Transferts de chaleur et de masse dans un bain liquide avec fusion de la paroi et effets de composition

Quynh Trang Pham

UNIVERSITÉ DE GRENOBLE

THÈSE

Pour obtenir le grade de

DOCTEUR DE L'UNIVERSITÉ DE GRENOBLE

Spécialité : Mécanique des fluides, Energétique, Procédés

Arrêté ministériel : 7 août 2006

Présentée par

Quynh Trang PHAM

Thèse dirigée par **Hervé COMBEAU** et
codirigée par **Jean-Marie SEILER**

préparée au sein du CEA Grenoble,
Laboratoire de Thermohydraulique Diphasique et Accidents graves
dans **l'École Doctorale I-MEP 2**

Transferts de chaleur et de masse dans un bain liquide avec fusion de la paroi et effets de composition

Thèse soutenue publiquement le **9 Avril 2013** ,
devant le jury composé de :

M. Yves FAUTRELLE
Professeur, Institut National Polytechnique de Grenoble, Président
M. Jacques POIRIER
Professeur, Université d'Orléans, Rapporteur
M. Florian FICHOT
HDR, Institut de Radioprotection et de Sûreté Nucléaire, Rapporteur
M. Bruno TOURNIAIRE
Dr, Electricité de France, Examinateur
M. Alexei MIASSOEDOV
Dr, Karlsruhe Institute of Technology, Examinateur
M. Hervé COMBEAU
Professeur, Ecole des Mines de Nancy, Directeur de thèse
M. Jean-Marie SEILER
Directeur de recherche, Commissariat à l'Energie Atomique et aux Energies Alternatives, Co-directeur de thèse

Acknowledgments

This work has been carried out at Laboratory of Two phase Thermal-hydraulic and Severe Accident, Atomic and Alternative Energy Commission (CEA de Grenoble), under the supervisions of Prof. Hervé Combeau and Dr. Jean-Marie Seiler. The project has been supported by the Atomic and Alternative Energy Commission, who is gratefully acknowledged.

Foremost, I would like to express profound gratitude to my supervisors, Hervé Combeau and Jean-Marie Seiler, for their guidance and encouragement throughout this work. In particular, I was inspired by Jean-Marie Seiler who gave me the passion of questioning about observed physical phenomenon and of giving explanations to them. I learnt from Jean-Marie Seiler the rigorous approach to research and the methods needed to be competent at synthesising information. My thanks and appreciations also go to Hervé Combeau who was always available for discussions about our research topics.

I would like also to thank Karine Froment for her kind help from my arrival in CEA Grenoble until the end of my thesis.

I would like also to acknowledge Gilles Ratel for his support in numerical calculations.

I would like to express my special gratitude to Anne-Marie Seiler for her encouragement throughout my thesis.

I gratefully acknowledge Prof. Jacques Poirier, Dr. Florian Fichot, Prof. Yves Fautrelle, Dr. Bruno Tourniaire and Dr. Alexei Miassoedov for their careful reading and review of this manuscript.

I am also grateful to my Ozturk Onur Can for his help during the thesis writing.

I would like to thank my parents, my sister and my husband for their love, support and encouragement all along of my residence in France.

Finally, I sincerely would like to thank every members in Laboratory of Two-phase Thermal-Hydraulic and Severe Accident, for being so helpful and supportive.

HEAT AND MASS TRANSFER IN A LIQUID POOL WITH WALL ABLATION AND COMPOSITION EFFECTS

Abstract

This work deals with the thermal-hydraulics of a melt pool coupled with the physical chemistry for the purpose of describing the behaviour of mixtures of materials (non-eutectic).

Evolution of transient temperature in a liquid melt pool heated by volumetric power dissipation has been described with solidification on the cooled wall. The model has been developed and is validated for the experimental results given by LIVE experiment, performed at Karlsruhe Institute of Technology (KIT) in Germany. Under the conditions of these tests, it is shown that the interface temperature follows the liquidus temperature (corresponding to the composition of the liquid bath) during the whole transient. Assumption of interface temperature as liquidus temperature allows recalculating the evolution of the maximum melt temperature as well as the local crust thickness.

Furthermore, we propose a model for describing the interaction between a non-eutectic liquid melt pool (subjected to volumetric power dissipation) and an ablated wall whose melting point is below the liquidus temperature of the melt. The model predictions are compared with results of ARTEMIS 2D tests. A new formulation of the interface temperature between the liquid melt and the solid wall (below liquidus temperature) has been proposed.

Key words - heat transfer, mass transfer, thermal-hydraulic, solidification, ablation, liquidus temperature, molten corium – concrete interaction (MCCI).

Résumé

Ce travail traite de la thermohydraulique d'un bain de melt couplée à la physicochimie pour la description du comportement de mélanges de matériaux (non-eutectiques).

On décrit le transitoire d'établissement de température dans un liquide avec dégagement de puissance volumique en présence de solidification sur une paroi refroidie. Le modèle développé à cet effet est validé par rapport aux résultats des essais LIVE réalisés à KIT. Dans les conditions de ces essais on montre que la température d'interface suit la température liquidus (correspondant à la composition du bain liquide) pendant le transitoire d'établissement de la température dans le bain et des croûtes solides.

Par ailleurs, on propose un modèle d'interaction entre un liquide non-eutectique (soumis à dissipation volumique de puissance) et une paroi fusible dont la température de fusion est inférieure à la température liquidus du bain. Les prédictions du modèle sont comparées aux résultats des essais ARTEMIS 2D. On en déduit une nouvelle formulation de la température d'interface (inférieure à liquidus température) entre le liquide et la couche pâteuse en paroi.

Mots clés - transfert de chaleur, transfert de masse, thermal-hydraulique, solidification, fusion, température liquidus, interaction corium – béton.

TABLE OF CONTENTS

LIST OF FIGURES

LIST OF TABLES

NOMENCLATURE

Small Latin letters

a, b	Coefficients of Nusselt correlation versus external Rayleigh number in natural convection	-
a', b'	Coefficients of Nusselt correlation versus internal Rayleigh number in natural convection	-
a^*, b^*	Coefficients of Nusselt correlation versus internal Rayleigh in gas-liquid convection	-
e^*	Equivalent non-dimensional thickness of the gap and the vessel wall	-
e_{gap}	Thickness of the gap between the crust and the inner vessel wall	m
e_{vessel}	Thickness of the vessel wall	m
g	Gravity acceleration	m s^{-2}
$h_{Bl}(x)$	Heat transfer coefficient in the boundary layer at level x	$W.m^{-2}.K^{-1}$
$h_{bulk}(x)$	Heat transfer coefficient in the bulk at level x	$W.m^{-2}.K^{-1}$
$\overline{h}_{bulk}$	Average heat transfer coefficient at the liquid-solid interface	$W.m^{-2}.K^{-1}$
h_{crust_vessel}	Equivalent heat transfer coefficient for the crust, the gap and the vessel wall	$W.m^{-2}.K^{-1}$
h_{gap}	Heat transfer coefficient in the gas gap between the solid crust and the inner vessel wall	$W.m^{-2}.K^{-1}$
$h_{local}(\theta)$	Local heat transfer coefficient at the liquid-solid interface in transient	$W.m^{-2}.K^{-1}$
h_{stt}	Steady state heat transfer coefficient at the melt-crust interface	$W.m^{-2}.K^{-1}$
$h_{stt}(\theta)$	Local heat transfer coefficient at the melt-crust interface in steady state	$W.m^{-2}.K^{-1}$
$\overline{h}_{stt}$	Average heat transfer coefficient at the melt-crust interface in steady state	$W.m^{-2}.K^{-1}$
h_{bottom}	Heat transfer coefficient from the bottom of the melt to the cake	$W.m^{-2}.K^{-1}$
j_{bulk}	Radial liquid entrainment velocity from the bulk to the boundary layer	$m.s^{-1}$
$j_{bulk,top}$	Radial liquid velocity entrainment from the bulk to the boundary layer in the top zone	$m.s^{-1}$
$j_{bulk,bot}$	Radial liquid velocity entrainment from the bulk to the boundary layer in the bottom zone	$m.s^{-1}$
$j_{Cheesewright,turbulent}$	Radial liquid velocity entrainment from the bulk to the boundary layer deduced from Cheesewright model	$m.s^{-1}$
$j_{FLUXBAIN,,turbulent}$	Radial liquid velocity entrainment from the bulk to the boundary layer deduced from FLUXBAIN model	$m.s^{-1}$
$j_{Alvarez,laminar}$	Radial liquid velocity entrainment from the bulk to the boundary layer deduced from Alvarez model	$m.s^{-1}$

k	Partition coefficient of the melt	-
k_{cake}	Permeability of the cake	m^2
k_j	Coefficient of the correlation to estimate the radial liquid velocity entrainment to the boundary layer	-
k_ρ	$\frac{V_{abl}}{j_{bulk}} = k_\rho$	-
k_T	Ratio between the average melt temperature and the maximum melt temperature	-
k_M	Mass transfer coefficient of solute in the boundary layer	$m.s^{-1}$
m_L	Slope of the liquidus line in the phase diagram	K
$\dot{m}_{BL}$	Variation of the mass in the boundary layer	$kg.s^{-1}$
$\dot{m}_{gas,in}$	Incoming gas flow rate	$kg.s^{-1}$
$\dot{m}_{gas,out}$	Outgoing gas flow rate	$kg.s^{-1}$
$\dot{m}_{MC}$	Mass flow rate of concrete ablation	$kg.s^{-1}$
$\dot{m}_{cake}$	Mass flow rate of cake formation	$kg.s^{-1}$
r	Radial distance from the axis of a duct	m
s	Non dimensional crust thickness, $s = \frac{z}{z_{stt}}$	-
t	Time	s
t^*	Non dimensional time in the model of the melt temperature evolution	-
t^{**}	Non dimensional time in the model of the crust thickness evolution	-
$u(r)$	Local velocity for a duct	$m.s^{-1}$
u_{max}	Maximum velocity in the boundary layer	$m.s^{-1}$
u_c	Characteristic velocity in the boundary layer	$m.s^{-1}$
u_{BL}	Mass-flow average velocity in the boundary layer	$m.s^{-1}$
w_{bulk}	Mass percentage of solute in the bulk	-
w_{BL}	Mass percentage of solute in the boundary layer	-
w_{MC}	Mass percentage of solute in the molten concrete	-
w_{bulk}^{LiCl}	Mass percentage of LiCl in the bulk	-
$w_{bulk,ini}^{LiCl}$	Mass percentage of LiCl in the bulk at initial condition	-
w_{BL}^{LiCl}	Mass percentage of LiCl in the boundary layer	-
w_{MC}^{LiCl}	Mass percentage of LiCl in the molten concrete	-
w_{cake}^{LiCl}	Mass percentage of LiCl in the molten concrete	-
w_{bulk}^{BaCl2}	Mass percentage of $BaCl_2$ in the melt	-
$w_{concrete}^{BaCl2}$	Mass percentage of $BaCl_2$ in the solid concrete	-

w_{MC}^{BaCl2}	Mass percentage of $BaCl_2$ in the molten concrete	-
w_{cake}^{BaCl2}	Mass percentage of $BaCl_2$ in the cake	-
$w_{concrete-cake}^{BaCl2}$	Mass percentage of $BaCl_2$ at the concrete-cake interface	-
$w_{bulk-cake}^{BaCl2}$	Mass percentage of $BaCl_2$ at the bulk-cake interface	-
$w_{concrete-cake}^{LiCl}$	Mass percentage of LiCl at the concrete-cake interface	-
$w_{bulk-cake}^{LiCl}$	Mass percentage of LiCl at the bulk-cake interface	-
z	Distance from the bottom of the cavity	m
z_{stt}	Crust thickness at steady state	m
z_{crust}^{*}	Equivalent thickness of the solid crust, the gap and the vessel wall for heat resistance calculation	m
z_{stt}^{*}	Steady state equivalent thickness of the crust, the gap and the vessel wall for heat resistance calculation	m
$z_{interface}$	Position of the interface between top and bottom zones in the melt cavity	m
z_{cake}	Thickness of the cake	m
$z_{top,heater}$	Distance from the top of heater to the bottom of initial melt cavity	m
$z_{bot,heater}$	Distance from the bottom of heater to the bottom of initial melt cavity	m
x	Vertical distance from the edge of the boundary layer	m
y	Distance normal to the vertical plate	m

Latin capital letters

A	Coefficient for calculation of friction factor in porous medium	-
B	Coefficient for calculation of friction factor in porous medium	-
C_0	Initial composition of the melt	$mol.mol^{-1}$
C_{bulk}	Bulk composition	$mol.mol^{-1}$
C_{bulk}^{BaCl2}	Mol percentage of $BaCl_2$ in the melt	$mol.mol^{-1}$
$C_{concrete}^{BaCl2}$	Mol percentage of $BaCl_2$ in the solid concrete	$mol.mol^{-1}$
C_{MC}^{BaCl2}	Mol percentage of $BaCl_2$ in the molten concrete	$mol.mol^{-1}$
C_{cake}^{BaCl2}	Mol percentage of $BaCl_2$ in the cake	$mol.mol^{-1}$
C_{bulk}^{LiCl}	Mol percentage of LiCl in the melt	$mol.mol^{-1}$
$C_{concrete}^{LiCl}$	Mol percentage of LiCl in the solid concrete	$mol.mol^{-1}$
C_{MC}^{LiCl}	Mol percentage of LiCl in the molten concrete	$mol.mol^{-1}$
C_{cake}^{LiCl}	Mol percentage of LiCl in the cake	$mol.mol^{-1}$
$C_{p,liquid}^{BaCl2}$	Specific heat of the pure liquid $BaCl_2$	$J.kg^{-1}.K^{-1}$

$C_{p,solid}^{concrete}$	Specific heat of solid concrete	J.kg^{-1}.K^{-1}
$C_{p,solid}^{crust}$	Specific heat of the solid crust	J.kg^{-1}.K^{-1}
$C_{p,gas}$	Specific heat of gas	J.kg^{-1}.K^{-1}
$C_{p,liquid}^{top}$	Specific heat of the melt in the top zone	J.kg^{-1}.K^{-1}
$C_{p,liquid}^{bot}$	Specific heat of the melt in the bottom zone	J.kg^{-1}.K^{-1}
D_{inner}	Inner diameter of the hemispherical test vessel	m
D_L	Diffusion coefficient of the solute in the liquid	m^2.s^{-1}
D_{LiCl}	Diffusion coefficient of LiCl in the liquid phase in the cake	m^2.s^{-1}
F	Friction coefficient	-
G_L	Temperature gradient in the liquid phase	°C.m^{-1}
G_S	Temperature gradient in the solid phase	°C.m^{-1}
H	Height of the melt cavity	m
H_{ini}	Initial height of the melt	m
H_{up}	Thickness of the Rayleigh-Bénard convection layer at the top of the melt cavity	m
H_{add}	Enthalpy of the added crust at the solid-liquid interface	J. kg^{-1}
H_{BL}	Average enthalpy of the liquid in the boundary layer	J. kg^{-1}
H_{bulk}	Enthalpy of the liquid bulk	J. kg^{-1}
$H_{bulk,ini}$	Enthalpy of initial melt	J. kg^{-1}
$H_{concrete}$	Enthalpy of solid concrete	J. kg^{-1}
$H_{concrete,ini}$	Initial enthalpy of solid concrete	J. kg^{-1}
H_{crust}	Average enthalpy of the solid crust	J. kg^{-1}
H_{gas}	Enthalpy of gas	J. kg^{-1}
H_{MC}	Enthalpy of the molten concrete	J. kg^{-1}
H_{ref}	Reference enthalpy of the solid phase of the considered material at reference temperature T_{ref}	J. kg^{-1}
H_{top}	Height of the top zone	m
H_{bot}	Height of the bottom zone	m
$K_{concrete}$	Permeability of concrete	m^2
K_u	Coefficient for average velocity in the boundary layer in Alvarez'model	-
K_δ	Coefficient for boundary layer thickness in the boundary layer in Alvarez'model	-
L	Length of test section for In-vessel corium behaviour experiments	m
$L'_{solidification}$	$L'_{solidification} = C_{p,solid}^{crust} \frac{\Delta T_{sol}}{2} + L_{solidification}^{melt}$	J. kg^{-1}
$L'_{melting}$	$L_{melting}' = L_{melting}^{concrete} + C_{p,concrete}\,\Delta T_{concrete}$	J. kg^{-1}

$L_{melting}^{concrete}$	Latent heat of melting of concrete	J. kg^{-1}
$L_{solidification}^{melt}$	Latent heat of solidification of the melt (equal to the latent heat of melting)	J. kg^{-1}
$L_{solidification}^{BaCl2}$	Latent heat of solidification of the $BaCl_2$	J. kg^{-1}
$M_{BaCl2,end}$	Mass of $BaCl_2$ in the final melt	kg
$M_{BaCl2,ini}$	Mass of $BaCl_2$ in the initial liquid melt	kg
$M_{BaCl2,\ MC}$	Mass of $BaCl_2$ in the molten concrete	kg
M_{BaCl2,MC_to_melt}	Mass of $BaCl_2$ from the molten concrete to the cake	kg
$M_{BaCl2,cake}$	Mass of $BaCl_2$ in the cake	kg
M_{bulk}	Mass of the liquid melt at instant *t*	kg
$M_{bulk,ini}$	Initial mass of the liquid melt	kg
$M_{concrete}$	Mass of the solid concrete at instant *t*	kg
$M_{concrete,ini}$	Initial mass of the solid concrete	kg
M_{cake}	Mass of the cake	kg
M_{MC}	Mass of molten concrete	kg
$\overline{M}_{LiCl}$	Molecular mass of LiCl	kg.mol^{-1}
$\overline{M}_{BaCl2}$	Molecular mass of $BaCl_2$	kg.mol^{-1}
$\dot{Q}_{add}$	Power dissipation in the melt cavity	W
$\dot{Q}_{conduction}$	Power serving for heating up the solid wall by conduction	W.
$\dot{Q}_{convection}$	Power transferred through the liquid-solid interface by convection	W
$\dot{Q}_{gas}$	Power served for gas heating	W
$\dot{Q}_{lost}$	Power lost through the upper surface of test section	W
$\dot{Q}_{MC}$	Incoming power from molten concrete to the melt cavity	W
$\dot{Q}_{v}$	Volumetric power dissipated in the melt cavity	W.m^{-3}
$\dot{Q}_{bot}$	Power dissipation in the bottom zone of the melt cavity	W
$\dot{Q}_{top}$	Power dissipation in the top zone of the melt cavity	W
R	Radius of the cylinder or hemisphere melt cavity	m
R_interface	Radius of the melt-concrete interface at a given cavity elevation	m
R(x)	Local radius of the melt cavity at level *x*	m
$R_{avg}(x)$	Average bulk radius of a melt slice located between *x* and ($x + \Delta x$)	m

$$R_{avg}(x) = \frac{R_b(x) + R_b(x + \Delta x)}{2}$$

$R_b(x)$	Bulk radius at level x of the melt cavity	m
$S_{BL}(x)$	Boundary layer flow cross section at level x, $S_{BL}(x) = 2\pi R_{avg}(x)\delta(x)$	m^2
$S_{bulk}(x)$	Flow cross section in the bulk at level x, $S_{bulk}(x) = \pi R_b^2(x)$	m^2
$S_{lat,bulk}(x)$	Lateral surface area of the bulk at level x, $S_{lat,bulk}(x) = 2\pi R_b(x)\Delta x$	m^2
$S_{lat,wall}(x)$	Lateral surface area of the boundary layer at level x, $S_{lat,wall}(x) = \frac{2\pi R_{avg}(x)\Delta x}{\cos\theta}$	m^2
$S_{lateral}$	Interface area of the melt cavity	m^2
S_{cross}	Cross section of the flow	m^2
$S_{lat,top}$	Lateral surface area in the top zone	m^2
$S_{lat,bot}$	Lateral surface area in the bottom zone	m^2
$T_{BL}(x)$	Local average boundary layer temperature at level x	°C
$T_{bulk}(x)$	Local melt temperature at level x	°C
$\overline{T}_{bulk}$	Average temperature of the melt	°C
$T_{bulk,max}$	Maximum melt temperature	°C
$T_{bulk,stt}$	Steady state maximum melt temperature in the melt cavity	°C
$T_{concrete}$	Average temperature of solid concrete	°C
$T_{concrete,i}$	Temperature of solid concrete near the liquid-solid interface	°C
T_{edge}	Temperature at the interface between bulk and boundary layer	°C
T_i	Liquid-solid interface temperature	°C
T_w	Surface temperature of the vertical plate	°C
T_f	Film temperature between T_{bulk} and T_w for vertical plate	°C
T_{ext}	Temperature at the interface between the solid crust and the gap	°C
$T_{gas,in}$	Incoming temperature of gas	°C
$T_{gas,out}$	Outgoing temperature of gas	°C
T_{inner}	Temperature of the inner test vessel wall	°C
T_{outer}	Temperature on the external surface of the steel vessel wall	°C
$T_{liquidus}$	Liquidus temperature of the melt	°C
$T_{solidus}$	Solidus temperature of the melt	°C
T_{melt}	Melting temperature of the concrete ($T_{melt}^{concrete}$)	°C
T_{melt}^{BaCl2}	Melting temperature of pure $BaCl_2$	°C
T_{ref}	Reference temperature to calculate enthalpy	°C
$\overline{T}_{crust}$	Average temperature in the solid crust	°C
$T_{bulk\text{-}cake}$	Temperature at the melt-cake interface	°C
$T_{concrete\text{-}cake}$	Temperature at the concrete-cake interface	°C
$\overline{U}_{bulk}$	Average flow velocity in the bulk centre	$m.s^{-1}$

$\dot{V}_{BL}$	Volumetric flow rate in the boundary layer	$m^3.s^{-1}$
V_{abl}	Concrete ablation velocity	$m.s^{-1}$
V_{sol}	Solidification velocity	$m.s^{-1}$
V_{cavity}	Volume of the melt cavity	m^3
$V_{bulk}(x)$	Volume of a melt slice located between x and $(x + \Delta x)$, $V_{bulk}(x) = \pi R_{avg}^2(x)\Delta x$	m^3
$V_{BL}(x)$	Volume of a boundary layer slice between x and $(x + \Delta x)$, $V_{bulk}(x) = 2\pi R_{avg}(x)\Delta x\,\delta(x)$	m^3
$\dot{V}_{top}$	Volumetric flow rate in the top zone	$m^3.s^{-1}$
$\dot{V}_{bot}$	Volumetric flow rate in the bottom zone	$m^3.s^{-1}$
W	Width of the vertical plate	m
Y	Non dimensional temperature difference between the melt and the interface, $Y = \frac{\Delta T_{p,\max}}{\Delta T_{stt}}$	-

Small Greek letters

α	Thermal diffusivity of the melt	$m^2.s^{-1}$
α_{gas}	Void fraction in the melt cavity	-
β_C	Solutal expansion coefficient	-
β_T	Thermal expansion coefficient	$°C^{-1}$
δ	Thickness of the viscous boundary layer	m
δ_{MT}	Thickness of the mass transfer boundary layer	m
δ_T	Thickness of the thermal boundary layer	m
ε	Porosity of solid concrete	-
θ	Polar angle of the cavity to vertical direction	°
θ_{max}	Maximum polar angle of the melt cavity	°
θ_{min}	Minimum polar angle of the melt cavity	°
λ_{bulk}	Thermal conductivity of the melt	$W.m^{-1}.K^{-1}$
λ_{crust}	Thermal conductivity of the solid crust	$W.m^{-1}.K^{-1}$
λ_{gap}	Thermal conductivity of the gas gap	$W.m^{-1}.K^{-1}$
λ_{vessel}	Thermal conductivity of the vessel wall	$W.m^{-1}.K^{-1}$
ρ_{BL}	Density of the boundary layer	$kg.m^{-3}$
ρ_{limit}	Limit density between top-bottom in the melt cavity	$kg.m^{-3}$
ρ_{bulk}	Density of the melt	$kg.m^{-3}$
ρ_{crust}	Density of the solid crust	$kg.m^{-3}$
ρ_{cake}	Density of the cake	$kg.m^{-3}$

ρ_{MC}	Density of the molten concrete	kg.m^{-3}
ρ_{solid}	Density of the solid concrete	kg.m^{-3}
$\tau_{99\%}$	Time delay to obtain 99% maximum crust thickness	s
$\tau_{crust,real}$	Time delay to reach steady state crust thickness	s
$\tau_{filling}$	Mushy zone filling time delay	s
τ_{PF}	Time delay to obtain planar front at the liquid-solid interface	s
τ_{sol}	Characteristic time for crust growth	s
τ_{TH}	Thermal hydraulic characteristic time	s
υ	Kinematic viscosity of the melt	m^2.s^{-1}

Capital Greek letters

Δ	$\Delta = \frac{\delta V_{sol}}{D_L}$	-
$\Delta\overline{T}_{bulk}$	Average temperature difference between the melt and the melt-crust interface $\Delta\overline{T}_{bulk} = \overline{T}_{bulk} - T_i$	°C
$\Delta\rho$	Density difference between bulk and boundary layer	kg.m^{-3}
ΔH_m	$= L_{solidification} + \frac{1}{2} C_{p,crust}\, \Delta T_{crust}$	J. kg^{-1}
$\Delta T_{bulk,ini}$	Initial temperature difference between the melt and the wall ($\Delta T_{bulk,ini}$ = $T_{bulk,ini}$ -T_i)	°C
$\Delta T_{bulk,stt}$	Steady state temperature difference between the melt and the wall (ΔT_{stt} = $T_{bulk,stt}$ -T_i)	°C
$\Delta T_{bulk,max}$	Maximum temperature difference between the melt and the melt-crust interface ($\Delta T_{bulk,max}$ = $T_{bulk,max}$ -T_i)	°C
$\Delta T_{concrete}$	Difference between concrete melting temperature and the actual solid concrete temperature	°C
ΔT_{crust_vessel}	Temperature difference between the melt-crust interface and the external surface of the vessel wall	°C
ΔT_{SL}	Solidification temperature interval of the melt ΔT_{SL} = $T_{liquidus}$ -$T_{solidus}$	°C
$\Delta T_{bulk,top}$	Temperature difference between the inlet and outlet of top zone	°C
$\Delta T_{bulk,bot}$	Temperature difference between the inlet and outlet of bottom zone	°C
ΔT_{sol}	Temperature difference over the solid crust ($\Delta T_{sol} = T_i - T_{ext}$)	°C
ΔT_{stt}	Steady state temperature difference between the melt and the wall	°C
Δz_{top}	Height of the heater located in the top zone	m
Δz_{bot}	Height of the heater located in the bottom zone	m
Δz_{heater}	Height of the heater	m
Γ	Gibbs-Thomson coefficient Γ	-

$\overline{\varphi}$	Average heat flux transferred to the liquid-solid interface in transient	W.m^{-2}
$\varphi_{conduction}$	Heat flux serving for heating up the solid wall by conduction	W.m^{-2}
$\varphi_{convection}$	Convective heat flux transferred to the liquid-solid interface	W.m^{-2}
φ_{local}	Local heat flux transferred at the liquid-solid interface	W.m^{-2}
φ_{stt}	Steady state average heat flux transferred to the liquid-solid interface	W.m^{-2}
φ	Heat flux transferred to the liquid-solid interface (transient)	W.m^{-2}
φ_{bottom}	Heat flux transferred to the bottom liquid-solid interface	W.m^{-2}
$\varphi(x)$	Local heat flux at distance *x* from the top of the melt (edge of boundary layer)	W.m^{-2}

Non-dimensional numbers

Gr	Grashof number $Gr = \frac{g\,\beta_T\,(T_{bulk,\max} - T_i)\,H^3}{\nu^2}$	-
Gr_x	Local Grashof number $Grx = \frac{g\,\beta_T\,(T_{bulk} - T_i)\,x^3}{\nu^2}$	-
Nu	Average Nusselt number $Nu = \frac{\overline{h}_{bulk}\,H}{\lambda_{bulk}}$	-
Nu_{BL}	Local Nusselt number in the boundary layer $Nu_{BL} = \frac{h_{BL}\,2\,\delta}{\lambda_{bulk}}$	-
Nu_{bulk}	Local Nusselt number in the bulk, $Nu_{bulk} = \frac{h_{bulk}\,x}{\lambda_{bulk}}$	-
Ra_{ex}	External Rayleigh number, $Ra_{ex} = \frac{g\,\beta_T\,H^3\,(T_{bulk,\max} - T_i)}{\alpha\,\upsilon}$	-
Ra_{in}	Internal Rayleigh number, $Ra_{in} = \frac{g\,\beta_T\,H^5\,\dot{Q}_v}{\alpha\,\lambda_{bulk}\,\upsilon}$	-
$Ra_{critical}$	Critical Rayleigh for determining heat transfer mechanism in the cake	-
Ra_{cake}	Rayleigh number in the cake	-
Re	Average Reynolds number in the bulk, $\mathrm{Re} = \frac{\overline{U}_{bulk}\,H}{\upsilon}$	-
Re_{bulk}	Local Reynolds number in the bulk, $\mathrm{Re}_{bulk} = \frac{U_{bulk}\,x}{\upsilon}$	-
Re_{BL}	Local Reynolds number in the boundary layer, $\mathrm{Re}_{BL} = \frac{U_{BL}\,2\,\delta}{\upsilon}$	-
Sc	Schmidt number, $Sc = \frac{\upsilon}{D_L}$	-
Pr	Prandtl number, $\mathrm{Pr} = \frac{\upsilon}{\alpha}$	-

INTRODUCTION

The current work is performed in the framework of severe accident analyses for Nuclear Reactors (PWR). Even with low probability of occurrence, and according to current safety practices, the severe accidents including core melting must be taken into account already at the stage of the plant design, and later on during the operation phase of a nuclear power plant in order to prevent the radiological threat. For the safety of nuclear power plants, the concept of "Defense in Depth" (introduced by IAEA (International Atomic Energy Agency), WENRA Western European Nuclear Regulators Association and NRC (USA)) which emphasizes five protection levels to compensate for potential human and component failures, to maintain the effectiveness of the barriers by averting damage to the plant and to the barriers themselves, and to protect the public and the environment from harm in the event that these barriers are not fully effective. The objective of the first level of protection is preventing the abnormal operation and system failures. The second level serves for detection of failures and for preventing the failures from evolving into accident. If the second level fails, the third level would ensure that safety functions are further performed by activating specific safety systems. The purpose of the fourth level is to limit the accident progression through accident management measures, so as to prevent the release of radioactive materials to the environment. In a very unlikely case that all these four protection levels fail, there is still the fifth protection level to mitigate the consequences of the radiological emissions. This work will deal with the fourth level of defense in depth, called severe accident management.

Severe accident is defined as an accident involving the loss of coolant, melting of reactor core potentially resulting in damage of reactor containment. In the beginning, due to the absence of adequate cooling inside the reactor vessel, the core materials would overheat and melt. The corium melt will accumulate in the core and at the bottom of the reactor vessel. If the external vessel is cooled sufficiently, the melt could be solidified and the spread of damage is limited inside the reactor. However, in case of inadequate or insufficient cooling, the reactor vessel may fail, resulting in the release of corium melt into the reactor pit. Melt-through of the reactor vessel leads to possible damage to the reactor containment building (including the basemat), which is the last barrier between the reactor and the environment. Therefore, severe accident management closely relates to keeping the containment intact.

During 50 years of civil nuclear power generation, severe accidents have occurred three times. The first severe accident was Three Mile Island (TMI), which occurred in USA in 1979. During TMI 2 accident, a part of the fuel rods melted but the reactor vessel remained intact and no adverse health or environmental consequences were detected. Chernobyl accident, which occurred in Ukraine in 1986, was the most severe accident wherein the fuel rods and the building were destroyed by a power excursion, plausibly followed by interaction between molten fuel and water and hydrogen combustion. 31 people were killed on the plant site. Since there was no containment building to protect the reactor, the radioactivity released directly into the environment, leading to significant health and environment consequences. More recently, the Fukushima accident occurred in Japan in 2011. In this accident, three rather old BWR reactor cores were molten due to the consequences of a huge tsunami. The Fukushima accident resulted in probably limited radiation exposure of workers at the plant, but not such as to threaten their health, unlike Chernobyl. Land contamination also obliged to displace population in a large area. Despite the accident prevention and management measures adopted in nuclear power plants, a very low probability remains that some accident scenarios may develop into a severe accident. The Fukushima accident has underlined strongly the significance of ongoing research on severe accident prevention and management.

This work contributes to the study of molten corium behaviour and molten corium-concrete interaction which are involved closely to the protection of reactor vessel retention as well as the prevention and mitigation of containment damage due to interaction of hot corium melt with sacrificial concrete.

Chapter 1 of this thesis provides background to the subject by introducing a survey of the current works on corium behaviour and corium-concrete interaction during a severe accident. The precise objective of the thesis will be defined at the end of this chapter.

Chapter 2 focuses on natural convection in a non-eutectic molten corium pool with internal heat dissipation and external cooling at boundaries. The work aims at developing a physical model to describe heat transfer and crust solidification at the liquid-solid interface during LIVE L3A experiment.

Chapter 3 introduces the 2D ARTEMIS Program carried out in CEA Grenoble for investigation of heat and mass transfer during molten corium-concrete interaction. Description of simulating materials employed in 2D ARTEMIS as well as test installation and performance will be given.

Chapter 4 and Chapter 5 are devoted to studies on melt-concrete interaction (MCCI) during ARTEMIS 11 (with eutectic materials) and ARTEMIS 10 (non-eutectic materials). Detailed analysis of the obtained experimental data will be performed for determining the main physical phenomena governing heat and mass transfer in each situation. The work continues with a modelling part to simulate these phenomena and to recalculate the parameters of interest such as the evolution of corium temperature, heat flux distribution along the liquid-solid interface and evolution of the corium cavity shape.

The development of an integral model coupling heat and mass transfer between bulk and boundary layer for the local calculation in natural convection with ablation or solidification at the wall is presented in Appendix 7. In addition, derivations of the constitutive laws required for the model such as the friction factor, the heat transfer coefficient and the radial liquid flow entrainment from the bulk to the boundary layer are also provided. Another part of the chapter shows validation of the model for a simple case with natural convection along a vertical plate. This model will be also applied for calculation of more complex cases with solidification or ablation at the wall as seen in LIVE L3A, ARTEMIS 11 and ARTEMIS 10.

The thesis ends with a summary of the main conclusions which have been made throughout the present thesis work.

CHAPTER 1: STATE OF THE ART

1.1 Context of severe accidents in nuclear reactors (PWR)

In a hypothetical severe accident of a nuclear power reactor, reactor core is supposed to be no more cooled. The core heats up under the influence of the residual power (~20 to 30 MW for a 1000 MWe reactor). Exothermal oxidation of zirconium by vapour releases hydrogen. Fission products that are volatile are generated and released in the containment. Within a few hours after the starting of the accident, a mixture of molten material called “corium” is formed in the reactor vessel. The molten corium relocates at the bottom of the reactor vessel and may destroy this barrier. Then the corium falls in the reactor pit and the molten corium will contact the concrete containment. Thus, interaction between molten corium and concrete occurs. Interaction between corium and concrete (MCCI) can last several days. The residual power decreases only very slowly within weeks and months.

The in-vessel retention (IVR) strategy of molten corium is the retention of corium in the lower head of the reactor pressure vessel (RPV) with external cooling by submergence of the reactor pit. It is one of the important Severe Accident Management (SAM) Strategies in nuclear power plants. Demonstration of the in-vessel melt retention capability of a plant is a demanding task in order to terminate the progress of a core melt accident and to ensure the integrity of the reactor vessel. To fulfil this task, heat flux distribution along the inner vessel wall is required to enssure that the vessel wall will not fail.

In addition, nuclear reactor severe accident management also requires a prevention of complete erosion of concrete containment in order to protect the third barrier (containment and basemat) between radioactive materials and the external environment. Ablation of concrete may occur in only radial direction or may be isotropic in both radial and axial directions, depending on the heat flux distribution along the interface between corium and concrete cavity. Moreover, the widening of the corium cavity due to concrete ablation results in a moving liquid-solid interface, leading to significant variation of the interface conditions (interface temperature and interface composition), which are closely linked to the evolution of the corium temperature and heat flux distribution. Since the characteristic time delay for molten corium-concrete interaction (MCCI) ranges between few hours (for experiments with a small thickness of concrete) and several days (for a thick concrete basemat of several meters), it is necessary to predict the transient evolution of heat flux distribution over a long time period.

Corium is formed by core materials, more or less oxidized (UO_2, Zr, ZrO_2, steel, control rod materials). Typical corium temperatures are between 2300 and 2700°C.

Concrete may have different compositions. The main species in the concrete are SiO_2 (siliceous concrete, melting temperature ~1850°C), and $CaCO_3$ (Limestone, decomposes in CaO and CO_2). Silica or limestone stones are bound by a cement of variable composition (containing H_2O). As concrete is not a pure material, it exhibits a melting range (typically between 1300°C and 1800°C). Since the melting temperature of concrete is lower than the freezing temperature of corium, solid material can deposit between corium and concrete which can influence the corium pool thermalhydraulics, and as a consequence, the heat flux distribution and the local concrete ablation rates.

In the following, the wording “corium” will more generally be used to designate the molten pool refractory material. The wording “concrete” will more generally be used to designate the ablated wall material with lower melting temperature.

1.2 In-vessel Retention with external cooling

In a hypothetical severe accident, the molten core containing an important heat source can relocate into the lower plenum (lower head) of the reactor vessel where it can form a corium pool. The corium retention capability and the vessel integrity depend on the rate of heat transfer (heat flux) from the corium pool to the vessel inner wall and on heat removal from the external vessel surface. Heat flux distribution along the interface between vessel and molten corium pool with internal power dissipation is, thus, one of the critical issues in severe accidents in Pressurized Water Reactors (PWR).

Average heat flux is calculated as the product of the average heat transfer coefficient $\overline{h}_{bulk}$ and, in principle, the maximum temperature difference between the corium ($T_{bulk,max}$) and the liquid-solid interface (T_i), as follows:

$$\overline{\varphi} = \overline{h}_{bulk} \, (T_{bulk,\max} - T_i) \tag{1-1}$$

As the solidification temperature of corium is much higher than the steel temperature, a corium crust forms at the interface. The corium is also characterized by a melting temperature interval. If the corium contains only 10% (mass percentage) of iron oxide, this melting interval may be as high as 1000 K (solidus temperature ~ 1700 K and liquidus temperature ~ 2700 K). Thus, a mushy zone may potentially form at the interface between the melt and the crust. The heat transfer between the melt pool and the crust may be affected by this mushy zone and the modelling of heat flux distribution may be more complex than given by relation (1-1).

1.2.1 Knowledge concerning heat transfer in a molten corium pool

Steady state heat transfer with simulant materials

When a liquid pool is heated volumetrically and is cooled at its walls, the buoyant and viscous forces act in opposite direction, leading to liquid recirculation in the pool, which is known as natural convection. The ratio of buoyant and viscous forces times the ratio of convective and conductive heat transfer is the characteristic dimensionless parameter, called Rayleigh number. Referring to the melt temperature, the “external” Rayleigh number is defined on the basis of temperature difference between the liquid and the wall as follows:

$$Ra_{ex} = \frac{g \, \beta_T \, \Delta T \, H^3}{\upsilon \, \alpha} \tag{1-2}$$

wherein:

- g: acceleration due to gravity;
- H: characteristic length of the liquid volume;
- ΔT: temperature difference between the liquid and the wall;

- β_T: thermal expansion coefficient of liquid
- α: thermal diffusivity of liquid;
- υ: kinematic viscosity of the liquid.

However, for reactor application, when the temperature difference between the bulk and the wall is not known, only the power dissipation in the corium cavity is known a specific Rayleigh number, called "internal" Rayleigh number is defined:

$$Ra_{in} = \frac{g\,\beta_T\,\dot{Q}_v\,H^5}{\lambda_{bulk}\,\upsilon\,\alpha} \tag{1-3}$$

wherein:

- $\dot{Q}_v$: volumetric power dissipation in the liquid volume;
- λ_{bulk}: thermal conductivity of the liquid.

In literature, natural convection heat transfer in a molten corium pool with decay heat source and wall cooling has been investigated widely in the last four decades in the framework of PWR severe accidents studies. The situation is represented by internal Rayleigh number to quantify the buoyancy force due to internal heat generation.

Table 1-1. In-Vessel corium test descriptions.

Experiment	Geometry	Dimension	Fluid	Heating method
[Jahn et Reineke, 1974]	2D slice hemi-cylinder	R = 75 mm L = 2R	Water	Joule effect
[Steinberner et Reineke, 1978]	2D slice square	H = 800 mm $L = H$	Water	Joule effect
COPO I [Helle et al, 1998]	2D slice elliptic (scale 1:2)	$L = H$ = 800 mm 0.34 < H/R < 0.45	Aqueous solution of ZnSO4	Joule effect
COPO II [Helle et al, 1999]	2D slice hemi-cylinder (scale 1:2)	R = 1000 mm L = 1770 mm	Aqueous solution of ZnSO4	Joule effect
BALI [Bonnet et Garré, 1999]	2D slice, hemi-cylinder (scale 1:1)	R = 2000 mm $L = H$ 0.5 < R/H < 1	Water	Joule effect
SIGMA-2D	2D slice hemiscylinder	R = 125 mm	Water	Joule effect
[Gabor, 1980]	3D hemisphere	R = 240 mm or 280 mm or 320 mm $L = R$ 0.5 < H/R < 1	Aqueous solution of ZnSO4	Joule effect
UCLA [Frantz et Dhir, 1992]	3D hemisphere	R = 220 mm or 601 mm $L = R$ 0.43 < H/R < 1	Fréon 113	Microwaves
ACOPO [Theofanous et al, 1996, 1997]	3D hemisphere	R = 1000 mm H/R = 1 $L = H$	Water	Transient cooling pool
Mini ACOPO [Theofanous et al, 1997]	3D hemisphere	R = 220 mm H/R = 1 $L = H$	Water	Transient cooling pool

Experiments have been conducted at all scales (pool radius from some centimetres to a few meters), with different geometries (2D or 3D, cylindrical, elliptical or hemispherical), with different test conditions (cooling uniformly at lateral wall and top surface or cooling only at lateral wall) and by different power dissipation method (Joule effect, heating wire, heating elements, microwaves, …) in order to represent different situations with internal Rayleigh number ranging from 10^5 (small scale) to 10^{14} (reactor scale). In these experiments, the main parameters of interest are pool temperature profile and heat flux distribution along the pool wall. Test conditions for certain representative experiments have been summarized in Table 1-1.

The flow structure in the volumetrically heated corium pool with cooled walls has been described by [Theofanous et al, 1997]. When the corium pool is cooled at the upper surface as well as at its lateral wall, three zones would be observed in the corium pool as seen in Figure 1-1, which are:

- Zone 1: A thick top layer with thickness H_{up} wherein the temperature is quasi-uniform and the unstable Rayleigh-Bénard flow exists due to top cooling [Bernaz et al., 1999]. This region has been also observed experimentally by [Jahn et Reineke, 1974] and [Bonnet et al., 1999]. In case of absence of top cooling, this zone will disappear or its thickness becomes very thin.
- Zone 2: A boundary layer downward flow along the cooled lateral wall.
- Zone 3: A central and lower zone which is thermally stratified corresponding to the recirculation of the boundary layer flow.

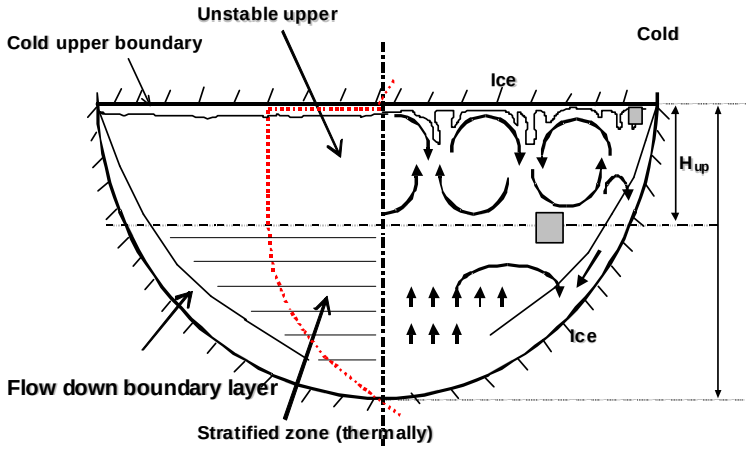

Figure 1-1. Existence of three flow zones in corium cavity in BALI experiment [Bernaz et al., 1999].

Distribution of heat flux along the surface of the reactor vessel is an important parameter because it has significant effect on the mass of corium that may escape the reactor vessel. For the test with uniform cooling (imposed temperature on the external surface of lateral wall and at the top surface), the heat flux transferred through the wall in the upper zone is constant and maximal. For the test with only lateral wall cooling (temperatureis imposed on the external surface of lateral wall), the flux reaches maximum at the top of the corium pool and decreases with the increase of the distance x from the top of the corium pool. Figure 1-2 shows the profiles of heat flux along the wall of the vessel given in BALI experiment [Bonnet et al, 1999]. In this figure, the ratio between local heat flux and maximum heat flux is depicted as function of the ratio x/H where in H is the height of the corium in the vessel. The shape of the heat flux distribution depends on the presence/absence of the top cooling.

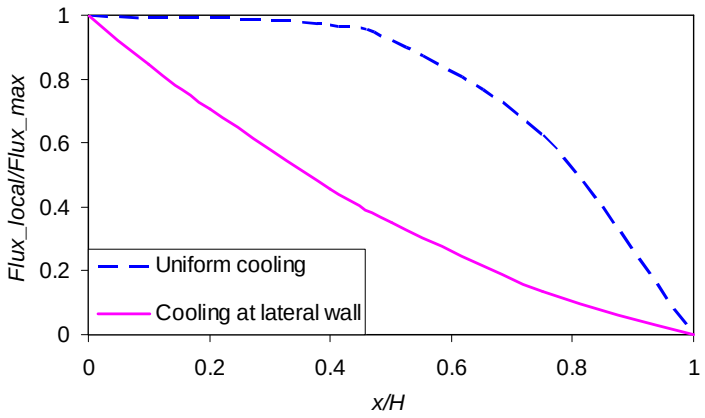

Figure 1-2. Heat flux distribution along the lateral vessel wall in BALI experiment [Bonnet et al., 1999].

Steady state heat transfer to the vessel wall has been investigated. Numerous correlations have been reported for estimation of natural convection average heat transfer in a volumetrically heated corium pool either by experimental or numerical method. In the existing correlations, the average heat transfer coefficient $\bar{h}_{bulk}$ (Equation (1-1)) from the corium to the wall is written in term of Nusselt number, which itself is a function of internal Rayleigh number, as follows:

$$\bar{h}_{bulk} = \frac{\lambda_{bulk}\, Nu}{H} \tag{1-4}$$

and

$$Nu = a' Ra_{in}^{b'} \tag{1-5}$$

Table 1-2. Correlations of Nusselt number to the vessel lateral wall.

Author	Correlation	Range of validity
[Jahn et Reineke, 1974]	$Nu_{dn} = 0.6\, Ra_{in}^{0.2}$	$Pr \sim 7$ $7.10^7 < Ra_{in} < 7.10^{11}$
[Mayinger et al, 1975]	$Nu_{dn} = 0.55\, Ra_{in}^{0.2}$	$7.10^6 < Ra_{in} < 5.10^{14}$
[Gabor et al, 1980]	$Nu_{dn} = 0.55\left(\frac{H}{R}\right)^{1.1} Ra_{in}^{0.15}$	$2.10^{10} < Ra_{in} < 2.10^{11}$ $0.5 < H/R < 1$
UCLA [Frantz et Dhir, 1992]	$Nu_{dn} = 0.54\left(\frac{H}{R}\right)^{0.25} Ra_{in}^{0.2}$	$8 < \mathrm{Pr} < 10$ $4.10^{11} < Ra_{in} < 10^{14}$ $0.43 < H/R < 1$
ACOPO [Theofanous et al., 1997]	$Nu_{dn} = 0.3\, Ra_{in}^{0.22}$	$10^{14} < Ra_{in} < 2.10^{16}$ $H/R = 1$
Mini ACOPO [Theofanous et al., 1997]	$Nu_{dn} = 0.048\, Ra_{in}^{0.27}$	$2 < Pr < 11$ $10^{12} < Ra_{in} < 3.10^{13}$ $H/R = 1$
	$Nu_{dn} = 0.0038\, Ra_{in}^{0.35}$	$2 < Pr < 11$ $10^{12} < Ra_{in} < 7.10^{14}$ $H/R = 1$
BALI [Bonnet et Seiler, 1999]	$Nu_{dn} = 0.131\left(\frac{H}{R}\right)^{0.19} Ra_{in}^{0.25}$	$5.8 < Pr < 8.2$ $10^{13} < Ra_{in} < 10^{17}$ $0.5 < H/R < 1$

Table 1-2 provides a number of Nusselt correlations for average heat transfer from corium to the vessel lateral wall. The range of validity for each correlation is also précised. It is seen that the heat transfer depends strongly on the physical properties of the simulant corium, the volumetric power dissipation (Internal Rayleigh and Prandlt numbers) and the configuration of the test section (the ratio *H/R* between the height and the radius of the corium pool).

Heat transfer through vessel lateral wall is the heat transfer through the boundary layer existing along this cooled wall (Zone 2). Two flow regimes are considered in this boundary layer region, which are laminar and turbulent. A criterion based on Grashof number (*Gr*) has been used to define the transition in between these two regimes. According to [Kutateladze et al, 1972], $Gr < 10^9$ corresponds to a laminar flow in boundary layer while $Gr > 10^9$ represents turbulent boundary layer flow. Since the reactor case is represented by internal Rayleigh number ranging from 10^{16} to 10^{17} corresponding to $10^{12} < Gr < 10^{13}$ (a PWR with volumetric power dissipation of 1 MW/m^3, $Pr = 1$ and $H = 2$ m), it corresponds to turbulent regime. Comparison of the heat transfer (represented by Nusselt number as written in Equations (1-4) and (1-5)) obtained by the listed correlations for laminar and turbulent regimes is shown in Figure 1-3, Figure 1-4. Agreement in order of magnitude of Nusselt number has been observed among the published correlations.

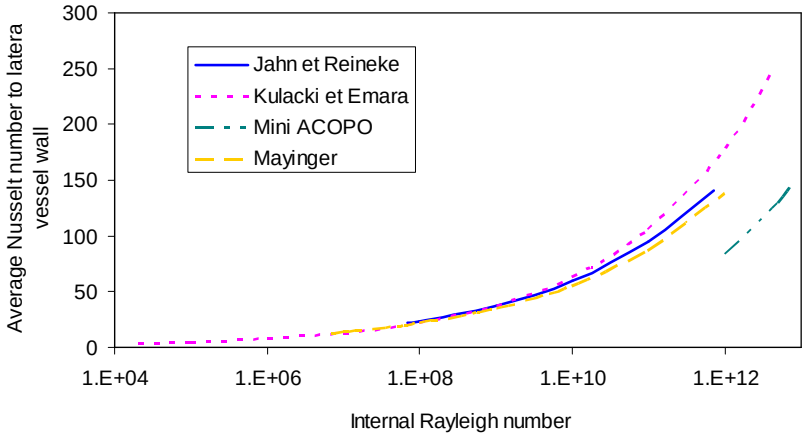

Figure 1-3. Average Nusselt number at lateral vessel wall for Gr < 10^9(laminar).

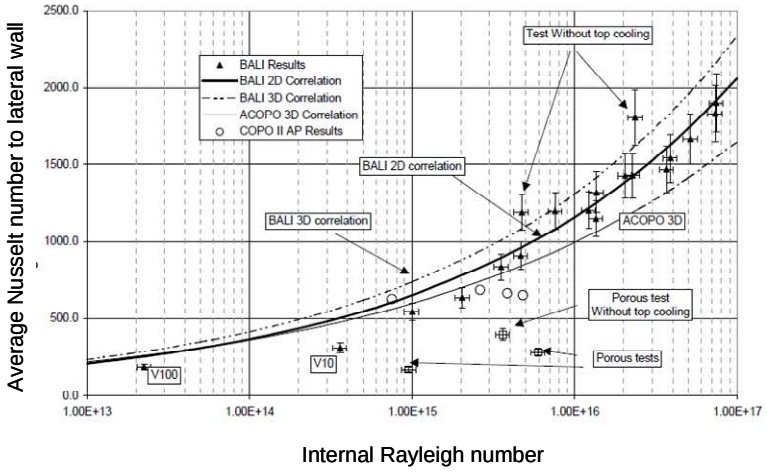

Figure 1-4. Average Nusselt number at lateral vessel wall for Gr > 10^9 (turbulent) [Bonnet et Seiler, 2001].

As presented previously, convection in the upper region of the corium vessel is characterized by an instability created by the cooled top surface. This cooling creates a cold layer at the top of a hotter layer. For a critical value of the temperature difference between the hot and cold layers, a movement appears inside the fluid. The denser cold fluid at the top moves downwards while the hot fluid moves upward from the lower layer. Cold plumes in the form of mushroom are formed (Figure 1-6) and an unstable layer is formed beneath the cooled top surface (Figure 1-5).

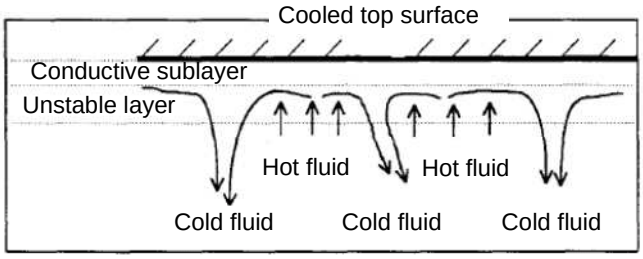

Figure 1-5. Rayleigh-Bénard convection underneath a cooled surface [Berg et al., 1966].

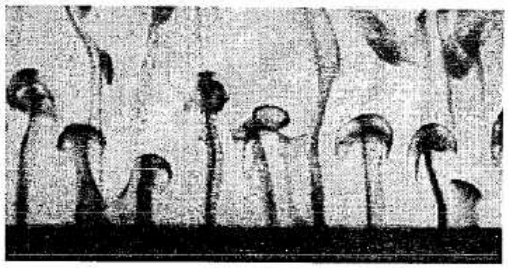

Figure 1-6. Formation of plumes inside the fluid layer due to top cooling [Sparrow et al, 1970].

The discussed situation is classically referred as Rayleigh-Bénard convection. Studies on these phenomena have been performed intensively during the last 40 years and a summary of the relating works has been reported by [Paul Manneville, 2005]. Heat transfer from the layer to the top surface has been correlated in terms of Nusselt and external Rayleigh numbers as $Nu = a\,Ra_{ex}^{b}$. Four flow regimes are considered which are laminar ($Ra_{ex} < 10^6$) [Krishnamurti, 1970], soft turbulent ($10^6 < Ra_{ex} < 4.10^7$) and hard turbulent ($4.10^7 < Ra_{ex} < 10^{11}$) [Castaing et al, 1989], and "asymptotic" regime ($Ra_{ex} > 10^{11}$) [Zaleski et al, 1991].

A situation of interest for nuclear reactor safety is slightly different from the classical Rayleigh-Bénard situation in the sense that the fluid layer can be volumetrically heated. The external Rayleigh in reactor case ranging in between 10^9 and 10^{12} emphasizes turbulent regime in such situation. [Bernaz et al., 1999] have investigated the possibility of transposition of results obtained for the classical Rayleigh-Bénard problem to real reactor situations. Experiments have been performed for the investigation of turbulent heat transport to the upper cooled top boundary layer of the heated pool. The plumes detaching from the top boundary were also observed (as seen in Rayleigh-Bénard situation). A model has been presented for the description of these plumes and the resulting heat transfer. A physical understanding of the effect of Rayleigh and Prandlt numbers on heat transfer in the layer has been gained. The so-called *soft turbulence* regime is associated with negligible interaction between the plumes and the main flow in the bulk. In this regime, the Nusselt number is proportional to $Ra_{ex}^{1/3}$. The so-called hard *turbulence regime* is related to an interaction between the plumes and the main flow. The plumes are locally and intermittently destroyed by a laminar boundary layer developing from large eddies issued from the main flow and impacting the boundary. Development of this laminar layer explains the dependency of the Nusselt number as approximately $Ra_{ex}^{2/7}$ for this regime. At high

Rayleigh numbers, increases of Reynolds number in the main flow results in development of fully turbulent boundary layers. In the so-called *asymptotic regime*, experiments of Rayleigh-Bénard turbulent natural convection in liquid helium and gas by [Chavanne, 1997] showed Nusselt is proportional to $Ra_{ex}^{0.4}$. Figure 1-7 provides a summary of different regimes in the upper layer.

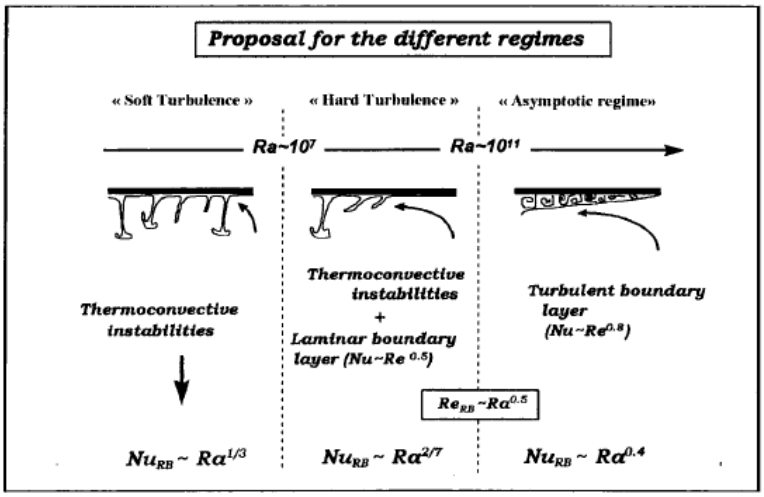

Figure 1-7. Synthesis of different regimes at the cooled top surface in reactor situation.

Heat transfer through the top cooled surface is also written in terms of Nusselt and internal Rayleigh numbers as done for lateral wall heat transfer. Some correlations are given in Table 1-3.

Table 1-3. Correlations of Nusselt number to cooled top surface.

Author	Correlation	Range of validity
[Kulacki et Emara, 1977]	$Nu_{up} = 0.345\, Ra_{in}^{0.226}$	$Pr \sim 7$ $2.10^4 < Ra_{in} < 4.4.10^{12}$
[Cheung, 1977]	$Nu_{up} = 0.208\ Ra_{in}^{0.25}$	$2\ .10^6 < Ra_{in} < 2.10^{11}$
[Steinberner et Reineke, 1978]	$Nu_{up} = 0.345\, Ra_{in}^{0.233}$	$Pr \sim 7$ $8.10^{12} < Ra_{in} < 4.10^{13}$
ACOPO [Theofanous et al., 1997]	$Nu_{up} = 1.95\, Ra_{in}^{0.18}$	$10^{14} < Ra_{in} < 2.10^{16}$ $H/R = 1$
BALI [Bonnet et al, 1999]	$Nu_{up} = 0.383\, Ra_{in}^{0.233}$	$5.8 < Pr < 8.2$ $10^{13} < Ra_{in} < 10^{17}$ $0.5 < H/R < 1$

In the previous experiments, the simulant corium contains only one material which was generally water, Freon, aqueous solution of $ZnSO_4$ in water (Physical properties of these solutions are close to water). In reactor case, the corium material is a mixture of oxides and metals. Recently, experiments have employed binary salt mixture as simulant corium for investigation of heat transfer in eutectic and non-eutectic mixture corium pools.

RASPLAV project was conducted at Kurchatov Institute (Russia) in the framework of OECD program. Objective of this project is to provide information on heat transfer in the curved corium vessel and to study the chemical interaction between the corium pool and the vessel wall. The RASPLAV-SALT experiment employs salt mixtures as simulant melt in order to investigate the effect of the solid crust (test with eutectic corium) and of a mushy zone (test with non eutectic corium) on

the heat transfer along the vessel wall [Asmolov et al., 1998]. Different salt mixtures are used as simulant corium:

- Eutectic mixture of NaF-$NaBF_4$: 8%-92% mol, $T_{liquidus}$ = 384 °C;
- Non eutectic mixture of NaF-$NaBF_4$: 25%-75% mol, $T_{liquidus}$ = 610 °C;
- Eutectic mixture of LiF-NaF-KF: 46.5%-11.5%-42% mol.

Qualitatively, the tests RASPLAV with salt mixtures show similar behaviours to the preceding tests in terms of heat flux distribution and temperature profile [Asmolov et al., 2000].

Transient heat transfer

[Kulacki et Emara, 1977], [Cheung, 1977] and [Keyhani et Kulacki, 1983] studied numerically a transient natural convection situation in a volumetrically heated layer. The work investigated the nature of developing and decaying turbulent convection in an internally heated fluid layer following a step change in volumetric power generation. It was shown that the time scale for natural convection establishment is much smaller than the time required for the temperature evolution. Therefore, the transient heat transport may be approached by a succession of steady state behaviour during transient. The transient model developed by [Cheung, 1977] was extended for the case of natural convection in a heated layer with solidification taking place at the cooled boundaries (i.e. formation of crust) by [Fan et Cheung, 1997]. Since the time scale of solidification is much larger than the time delay for reaching final steady state natural convection, the transient heat transfer is not influenced by solidification.

The previous works are performed for natural convection in a volumetric heated layer, which is the simplest configuration. In real reactor situation, the phenomena are predicted to be more complex because the interface condition will vary significantly during the whole transient. In fact, a mushy zone is supposed to form in front of the liquid-solid interface and evolution of this mushy zone to a planar front due to mass transfer is expectable. However, up to date, due to the lack of data, the question of transient natural convection heat transfer in a pool with internal heat generation and melt solidification is still open, including evolution of corium temperature, evolution of liquid-solid temperature and distribution of heat flux along the corium vessel wall. Therefore, more efforts are required for a full answer.

1.2.2 Investigations of interface conditions

In a PWR, the reactor vessel is made of stainless steel while the corium contains metals and oxides. As the corium mixture is not a pure material, the interface temperature between the corium and vessel wall is not a simple property of the corium. Lack of understanding of interface temperature would induce difficulties in calculation of heat flux distribution at the reactor vessel walls (since the heat flux depends on the heat transfer coefficient and the temperature at the interface).

This section is dedicated to discuss the state of the art on investigation of liquid-solid interface conditions during solidification of non-eutectic molten corium behaviour in between corium pool and vessel wall.

Interface temperature in steady state

[Seiler, 1996] developed a model referred as phase segregation model for melt thermal-hydraulics. The basic hypothesis in the model is that the melt separates into a solid part that is enriched in refractory species and a liquid part as in usual metallurgical solidification process. The solid part is deposited at the cooler boundary of the melt pool to form a crust in steady state.

The model has been developed for description of thermal-hydraulics in steady state in a corium vessel with internal power generation and external cooling. Following assumptions have been adapted in the model:

- The local crust thickness tends towards a constant value; thus the freezing rate tends towards zero on the entire interface area;
- When the freezing rate tends towards zero, the mushy zone disappears and the interface temperature tends towards the liquidus temperature of the actual melt composition;
- The composition of the liquid melt becomes uniform because of stirring of the pool by natural convection and because of the absence of further freezing.

Following consequences have been outlined:

- In steady state, the interface temperature between the melt and the crust is uniform (as it would be with a pure material with a given melting point) and there is no mushy zone,
- As the melt composition is also uniform, the thermal-hydraulics behaviour of the pool can be studied with a pure material,
- The thermal-hydraulic problem is completely defined as soon as the geometry, the power and fluid properties and the interface temperature are fixed;
- The heat flux distribution from the melt to the crust does, thus, not depend on external conditions.

Calculation of the model was also applied for end state of ACE experiments [Seiler, 1996] which is a set of large scale molten corium concrete interaction experiments. Solid crust develops in contact with the concrete or in contact with the two sides of the corium pool which is externally cooled. In addition, the model has been extended for different applications in late phases of severe accidents [Seiler et Froment, 2000].

This approach has first been validated by the PHYTHER experiment which was performed at CEA Saclay [Dauvois et al., 1999]. The test objective was to solidify a real corium mixture under controlled conditions. The test section consisted in a cylindrical copper crucible with 10 cm diameter and 5 cm height (Figure 1-8).

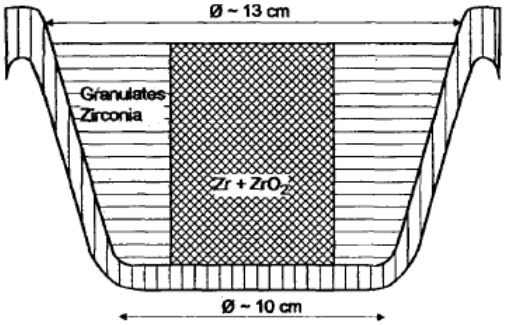

Figure 1-8. Crucible in PHYTHER experiment [Dauvois et al., 1999].

The corium contains a mixture of Zr and ZrO_2 with 50%-50% mol percentage. The external surface of the crucible was cooled by forced convection water flow in order to maintain a constant boundary temperature. The corium was heated from the upper surface of the crucible by Electron Bombardment (EB). After reaching steady state, the heat power was decreased stepwise. Solid deposits at the melt interface. Analyses proved that pure ZrO_2 layers formed during the different power plateaus at the interface between melt and lateral crust. Surface temperature of the melt was measured by pyrometer. Comparison of the measured temperature with the liquidus temperature corresponding to the actual melt composition ($T_{liquidus}$) inferred that $T_i = T_{liquidus}$ during steady state. No conclusion was drawn about the transient interface temperature.

As discussed in the preceding discussion on the molten corium behaviour in reactor vessel, non-eutectic and eutectic salt mixtures have also been employed as simulant non eutectic melts. The RASPLAV-SALT experiments show that the steady state temperature measured at the melt-crust interface tends to liquidus temperature of the actual corium melt composition [Asmolov et al. 2000]. The analysis of RASPLAV-SALT experimental data by the phase segregation approach developed by [Seiler, 1996] and [Seiler et Froment, 2000] leads to a conclusion that the mushy zone concept does not apply to corium pool thermal-hydraulics in steady state conditions. Moreover, the interface temperature between the solid and the liquid is now the liquidus temperature of the new remaining liquid at steady state [Froment et Seiler, 1999].

Experiments with prototypic corium have been conducted within the ECOSTAR project at NRI (small scale with 1 kg corium) and CEA Cadarache (large scale with 20 kg corium) to investigate the phase segregation during slow solidification in volumetrically heated pool of corium in late phases of severe accident [Journeau, 2003]. Plane front solidification of uranium-rich (U, Zr, Ca)O_2 crystals have been obtained from various prototypic corium compositions slowly cooled over hours. It was deduced that with prototypic materials during slow solidification (late phase of severe accident), there will be no mushy zone at the interface with corium pool. Moreover, the test gives evidence that the interface temperature is the liquidus temperature of the actual liquid. This is an important result in support of the approach introduced by [Seiler et Froment, 2000].

Briefly, the question of interface temperature in steady state solidification has been answered experimentally and theoretically for In-Vessel corium pools. However, the transient solidification behaviour has not been answered yet.

Interface temperature during transient

Although knowledge of transient interface condition for In-Vessel corium pools is of high importance, experimental data on this subject is still lacked. Up to now, only theoretical investigations have been reported. A summary of these theoretical bases will be recalled in the following.

A simple model was developed in [Seiler et Froment, 2000] for a volumetrically heated layer of molten corium which is suddenly cooled on its surfaces. Main assumptions of the model include:

- The external surface temperature is maintained at a constant temperature T_{ext};
- The solid crust forms at the interface with the molten corium;
- The temperature at the interface between solid crust and liquid corium is approximately constant, i.e, T_i = const;

- The heat flux φ_{stt} transmitted from the liquid to the crust is also constant (also absence of heating in the solid crust);
- The heat transfer through the crust is by steady state conduction.

With these assumptions, the freezing rate is obtained as:

$$V_{sol} = \frac{\lambda_{crust}\ \Delta T_{sol}}{z_{crust}\ \rho_{crust}\ L'_{solidification}} - \frac{\varphi_{stt}}{\rho_{crust}\ L'_{solidification}} \tag{1-6}$$

and the characteristics time required for crust growth was found as:

$$\tau_{sol} = \frac{\lambda_{crust}\ \rho_{crust}\ L'_{solidification}\ \Delta T_{sol}}{\varphi_{stt}^2} \tag{1-7}$$

wherein:

- λ_{crust} is the thermal conductivity of the solid crust;
- ρ_{crust} is the density of the solid crust;
- z_{crust} is the crust thickness;
- ΔT_{sol} is the temperature difference over the solid crust ($\Delta T_{sol} = T_i - T_{ext}$);
- $L'_{solidification} = C_{p,solid}^{crust}\ \frac{\Delta T_{sol}}{2} + L_{solidification}^{melt}$;
- $C_{p,solid}^{crust}$ is the specific heat of the solid crust;
- $L_{solidification}^{melt}$ is the latent heat of solidification;
- φ_{stt} is the heat flux transmitted to the solid crust in steady state.

According to [Seiler et Froment, 2000], the crust formation may be split into two main periods, depending on the solidification rate:

- Period 1: $t < \tau_{sol}$ for initial solidification with high freezing rate;
- Period 2: $t > \tau_{sol}$ for long term solidification with small freezing rates.

Two mass transport mechanisms can be encountered during the crust formation [Seiler et Froment, 2000] and [Combeau et al., 2010]. The first mechanism corresponds to the first period when solidification proceeds with a mushy zone and the second one is that when it comes to a planar front when the freezing rate is small enough. Understanding of the mass transfer kinetics associated with both solidification regimes is required.

Planar front associated with the long term solidification of multi-component materials has been studied widely in metallurgy. A model approach was introduced by [Rutter et Chalmers, 1953] and further developed by [Mullins et Sekerka, 1964]. According to this model approach, when the solidification of the melt occurs with a planar front at the liquid-solid interface, the interface temperature will stay in between the solidus and liquidus temperatures of the melt, depending on the freezing rate and on the thickness of the mass transfer boundary layer ahead of the liquid-solid

interface [Burton et *al.*, 1953]. In this situation, if the solidification rate is slow enough, then the interface temperature will approach the liquidus temperature.

The condition for plane front stability has been well established with assumptions of diffusion controlled mass transfer of solute in the liquid, as follows:

$$\frac{G_L}{V_{sol}} \Big/ \frac{-m_L C_{bulk}(1-k)}{D_L} \geq \frac{1}{k} \tag{1-8}$$

Criterion (1-8) is termed constitutional super-cooling criterion [Rutter et Chalmers, 1953]. When this criterion is satisfied, for constant freezing rate and mass transfer controlled by diffusion, the liquid composition at the interface will be $C_{L,i} = \frac{C_{bulk}}{k}$, the solid composition at the interface will be $C_{S,i} = C_{bulk}$ and the interface temperature will be equal to the solidus temperature for composition C_{bulk}.

In most real cases of solidification, convection is present due to temperature or solute concentration differences at the macroscopic scale. In the case of a planar front, solute redistribution has also been treated with an assumption of the existence of a mass transfer boundary layer, whose thickness is controlled by the convection [Burton et al. 1953]. It was assumed that outside of this boundary layer, the liquid composition is maintained uniform by convection, and inside of this layer, mass transport is by both by convection and diffusion. A sub-layer can be defined within which the mass transfer is by diffusion only by analogy with the thermal sub-layer in which heat transfer is governed by conduction. Several approaches are available for this problem in order to build a new criterion for the stability of a planar front, which couples the mass transfer effects due to both convection and diffusion of solute. As part of this model, the criterion developed by [Mullins et Sekerka, 1964] is modified by a factor of *1/k* in the case of a strong stirring [Hurle, 1968]**,** [Delves, 1968], [Hurle, 1976], as follows:

$$\frac{G_L}{V_{sol}} \Big/ \frac{-m_L C_{bulk}(1-k)}{D_L} \geq 1 \tag{1-9}$$

Under these conditions, for intense stirring conditions in case of a planar front solidification, the liquid composition on the interface tends towards C_{bulk} and the interface temperature towards $T_{liquidus}$ [Burton et *al.*, 1953]. [Burton et *al.*, 1953] have derived a relation between the interface temperature and the thickness δ of the mass transfer boundary sub-layer in the liquid ahead of this interface. Its expression is given below:

$$T_i = T_{liquidus} + m_L\, C_{bulk}\left[\frac{e^{\Delta}}{1-k\,(1-e^{\Delta})} - 1\right] \tag{1-10}$$

wherein: $\Delta = \frac{\delta_{MT}\, V_{sol}}{D_L}$, $\delta_{MT} = H\,(Sc\,Gr)^{-1/.3}$ and $Sc = \frac{\upsilon}{D_L}$.

According to Equation (1-10), the interface temperature varies between the solidus temperature in the case of a purely diffusive regime (infinite thickness of the boundary layer) and the liquidus temperature calculated at the bulk liquid concentration in the case of a strong stirring (thickness of the mass transfer boundary layer going to zero and/or solidification rate going to zero), which is in coherence with the phase segregation model reported by [Seiler et Froment, 2000].

One can also notice by comparing relations (1-8) and (1-9) that, for a partition coefficient lower than unity ($k < 1$), criterion (1-9) is fulfilled for a lower G_L/V_{sol} ratio. In other words, planar front is stabilized faster when both diffusion and convection contribute to the mass transfer. This means convection acts clearly in favour of a stabilization of a planar interface.

During short term solidification (period 1), cellular solidification and mushy zone must be considered which corresponds to unstable freezing front with formation of dendrites and a mushy zone exists in front of the solid crust [Dauvois et al., 2000]. Indeed, at the beginning of solidification when the freezing rate is not slow enough, criteria (1-8) and (1-9) are not yet satisfied. Hence, planar front could not be obtained during this rapid solidification period. In this period, solidification will proceed with a mushy zone and the temperature of the mush-liquid interface will be equal to the temperature at the tips the primary arms of the dendrite. This temperature can be evaluated by existing models such as the LGK model [Lipton, Kurz et Trivedi, 1987].

It is noted that transient heat transfer from the melt pool could be modified due to formation of this mushy zone. Therefore, question of transient behaviour of the mushy zone is of interest. [Combeau et al., 2010] and [Fischer, 2012] investigated the evolution of the mushy zone which was formed against a cooled surface and in a fixed temperature field. The mushy zone filling model developed by these authors owes to predict the evolution of the mushy zone. An important hypothesis is that the mass transfer is only by diffusion in the interdendrite liquid phase. The model enables to predict that the mushy zone is not stable and will evolve to a planar front due to the transport of solute by diffusion in the liquid phase in the mush. In addition, it was concluded that in final steady state, the liquid-solid interface temperature will be the liquidus temperature corresponding to the actual composition of the melt. This process will extend over a characteristic time delay ($\tau_{filling}$) which has been determined for the non eutectic solidification.

$$\tau_{filling} = \frac{\Delta T_{SL}{}^2}{G_S{}^2 D_L}\left(\frac{1+k}{2}\right) \tag{1-11}$$

in which ΔT_{SL} is the solidification temperature interval of the melt ($\Delta T_{SL} = T_{liquidus} - T_{solidus}$), G_S is the temperature gradient in the solid phase, which is given by:

$$G_S = \frac{\varphi_{stt}}{\lambda_{crust}} \tag{1-12}$$

wherein φ_{stt} is the heat flux transferred from the melt to the solid crust in steady state and λ_{crust} is the thermal conductivity of the solid crust.

1.2.3 Summary and unsolved issues

The question of steady state heat transfer and steady state interface temperature during solidification of liquid melt at the cooled boundaries of a melt pool with internal heat source has been clearly answered. The heat transfer from the melt pool to the upper pool surface and to the lateral liquid-solid interface could be evaluated by various Nusselt correlations in terms of internal or external Rayleigh number. The relation between correlations written in term of internal and external Rayleigh number has not been clarified.

When the upper surface of the pool is cooled, the top layer of the pool is quasi uniform in temperature and the heat flux distribution at this level is uniform (Rayleigh-Bénard layer) [Bernaz et al., 1999].

A stratification of pool temperature is observed in the bottom part of the melt pool. In this region, the heat transfer at the lateral boundary is controlled by a boundary layer flow. The heat flux increases with the polar angle of the pool but the distribution depends on the flow regime in the boundary layer.

In addition to heat transfer, the liquid-solid interface conditions are determined for the end state, wherein there is no mushy zone at the interface but planar front solidification and the interface temperature is the liquidus temperature of the actual liquid.

Work on transient heat transfer with crust formation has been limited to theoretical evaluations for the simplest configuration of a horizontal volumetrically heated layer [Fan et Cheung, 1997] and for a hemispherical geometry [Roux et Fichot, 2005]. In such situation, important effects of crust growth dynamics on heat transfer have been addressed. Analysis of time characteristic for thermal-hydraulics establishment and crust formation showed that these characteristic time delays are longer than the time required for establishment of natural convection flow in the heated layer. Therefore, the heat transfer in transient stays can be approached by a succession of steady state behaviours. However, the transient in reactor situation would be more complex due to possible establishment of a mushy zone variation or a planar front at the liquid-solid interface due to solute mass transfer, which results in significant variations on the liquid composition as well as the temperature at the interface. Therefore, it is not sure that the previous conclusion for transient heat transfer in a fluid layer is still valid in reactor situation. The main question is with the validity of the use of steady state heat transfer correlations for calculating transient evolution of heat flux and pool temperature.

Regarding to the liquid-solid interface conditions, the main question is the determination of the interface temperature evolution during the crust formation transient. This problem is still unresolved.

Investigations of these open issues are among the objectives of this thesis. Modelling will be performed to derive deterministic interface conditions and heat transfer in a physically consistent way to be applied for calculation of heat flux distributions along the vessel wall not only in steady state but also during transient.

1.3 Molten corium-concrete interaction (MCCI)

Containment integrity is a key objective in severe accident management since the containment structure and all associated systems provide the ultimate barrier against the release of fission products into the environment. In particular, containment integrity should be maintained even in the case of core melting leading to vessel melt-through. Containment capability to withstand all challenges resulting from severe accident sequences addresses the prevention of concrete basemat melt-through. In case of corium introduction in the reactor cavity, a direct interaction between molten corium and concrete occurs.

Experimental investigations have been performed widely to study the molten corium-concrete interaction under prototypic conditions of severe accident (ACE, MACE, CCI OECD, VULCANO) [Seiler et Tourniaire, 2008]. Concrete ablation kinetics with corium cavity evolution in 1D and 2D, effect of concrete material on concrete erosion, heat transfer from the melt to the concrete and liquid-solid interface conditions (composition and temperature), melt solidification, ejection of gas and fission products release, melt behaviour with respect to mixing by the percolating gases as well as fission products releases are among the objectives of MCCI experiments. Besides experimental works,

computer codes have been also developed to simulate these phenomena. Among them are the thermal-hydraulics models such as CORCON [Bradley et al, 1993] and WECHSL [Foit et al, 1995] and physico-chemical models such as CORQUENCH [Farmer, 2001], COSACO [Nie et al., 2002], TOLBIAC-ICB [Spindler et al., 2006] and MEDICIS [Cranga et al., 2005]. The available experimental data have been used for validation of these codes. The main lessons from the up-to-date investigations of MCCI will be briefly summarized in the next.

1.3.1 Learnings from 1D MCCI

ACE experiments

ACE experiments (Advanced Containment Experiment) were conducted at Argonne National Laboratory (ANL) from 1988 to 1991 [Thomson et Fink, 1988], [Thomson et al, 1997]. Seven large-scale tests were performed using four types of concrete (siliceous, limestone/sand, serpentine, and limestone). The test duration varies between 7 minutes (ACE L1) to 120 minutes (ACE L2). Objectives of ACE experiments were mainly to investigate the influences of concrete materials (siliceous, limestone or limestone with common sand…) and of the injected power on the ablation rate and melt temperature during MCCI and also to quantify the release of simulated fission products. The test installation is shown in Figure 1-9.

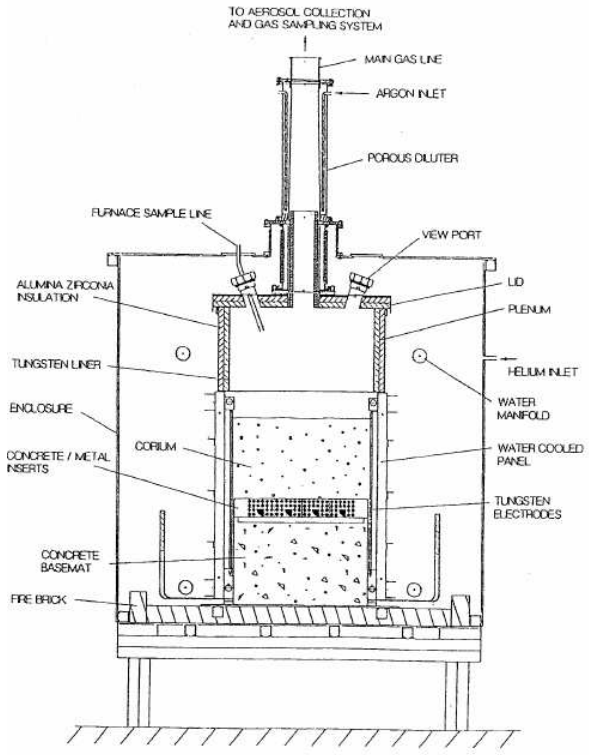

Figure 1-9. ACE test installation [Thomson et al., 1997].

The corium vessel is typically a horizontal square 50 cm x 50 cm, initially containing 300 kg of corium. The melt consisted of UO_2, ZrO_2, fission product simulants, concrete decomposition products, and some structural materials to obtain a typical corium mixture. Power is generated in the oxide melt by Joule effect (tungsten electrodes are implemented on two opposite walls). A concrete block is added at the bottom of the corium vessel and will be ablated vertically in 1D geometry. Initial mass of concrete is ~ 200 kg with typically 30 cm thickness. The top of the concrete layer is covered by a set

of concrete/metal inserts or a layer of zirconium rods to supply metallic additions to the melt as desired. Concrete attack was detected by a thermocouples imbedded in the concrete. The experiments were provided with measurement systems for gas and aerosol diagnostics, temperature measurements in concrete layer and melt pool, electrical power, and additional instrumentation for the cooling systems and a compensation system to prevent heat loss (to the upper surface of the test section). Lateral walls are thermally insulated at the best. Test conditions are summarized in Table 1-4. Figure 1-10 shows a typical final state of corium cavity that is observed after ACE L2 (siliceous concrete) and ACE L5 (LCS).

Table 1-4. ACE test conditions.

Test	Concrete material	Power (W/kg UO2)
ACE L1	Limestone-common sand	350
ACE L2	Siliceous	450
ACE L4	Serpentine layer over siliceous	250
ACE L5	Limestone-common sand and iron oxide	325
ACE L6	Siliceous	350
ACE L7	Limestone-common sand	250
ACE L8	Limestone	350/150

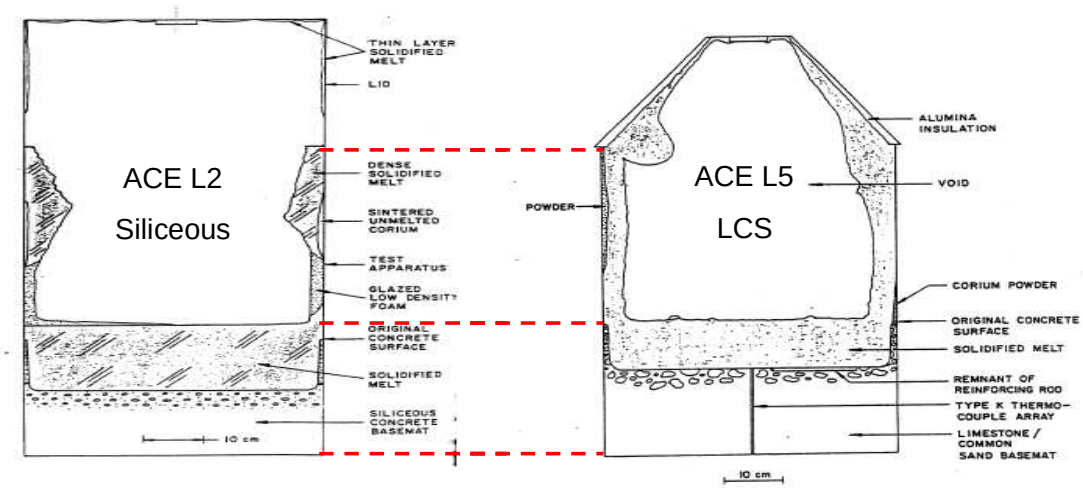

Figure 1-10. Final state of corium cavity ACE L2 and ACE L5 [Thomson et al. 1997].

Evolutions of melt temperatures in tests with siliceous concrete (ACE L2 and L6) are depicted in Figure 1-11 while Figure 1-12 presents evolutions of melt temperature in tests with limestone-common sand concrete (LCS) (ACE L5 and L7). It is seen that the melt temperature is much higher than the melting temperature of concrete (T_{melt} = 1250 K for siliceous concrete and T_{melt} = 1300 K for LCS concrete). The difference ranges from 500 K to 1000 K. This significant temperature difference shows evidence of an important thermal resistance existing at the corium-concrete interface.

The TOLBIAC code was developed by [Vandroux-Koenig et al., 1999a] based on the phase segregation model to simulate the thermal-hydraulics of a corium pool with sacrificial material. The model is an extrapolation of the model that has been developed for In-Vessel Corium pools. It is supposed that the interface temperature stays to the liquidus temperature of the melt. It is further supposed that a solid crust deposits at the interface and has the composition of the refractory phase. The liquidus temperature of the melt is calculated with the GEMINI code [Spindler et Veteau, 2006].

Calculations with this code have been done for ACE tests by [Vandroux-Koenig et al., 1999b]. As seen in Figure 1-11 and Figure 1-12, the melt temperature is close to the liquidus temperature in ACE L2; whereas, for ACE L5, L6 and L7, the former is lower than the latter but is still much nearer to the liquidus temperature than to the melting temperature of concrete.

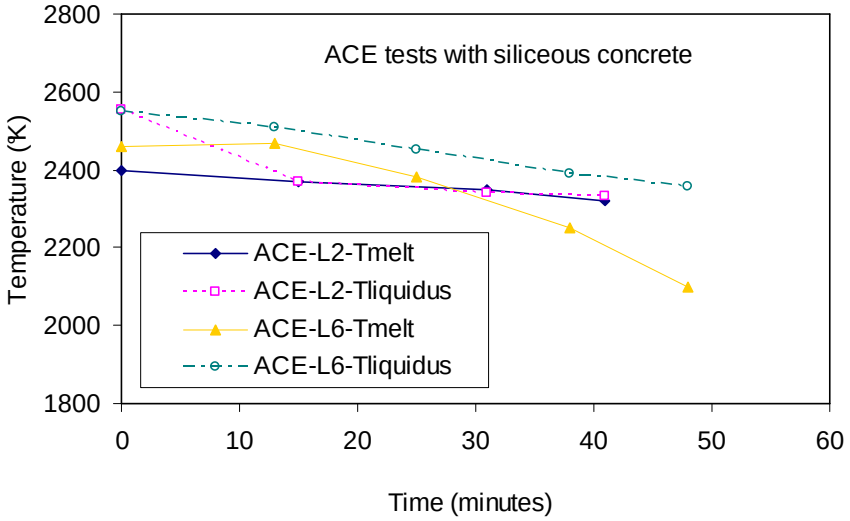

Figure 1-11. Melt and liquidus temperature evolutions in ACE experiments with siliceous concrete.

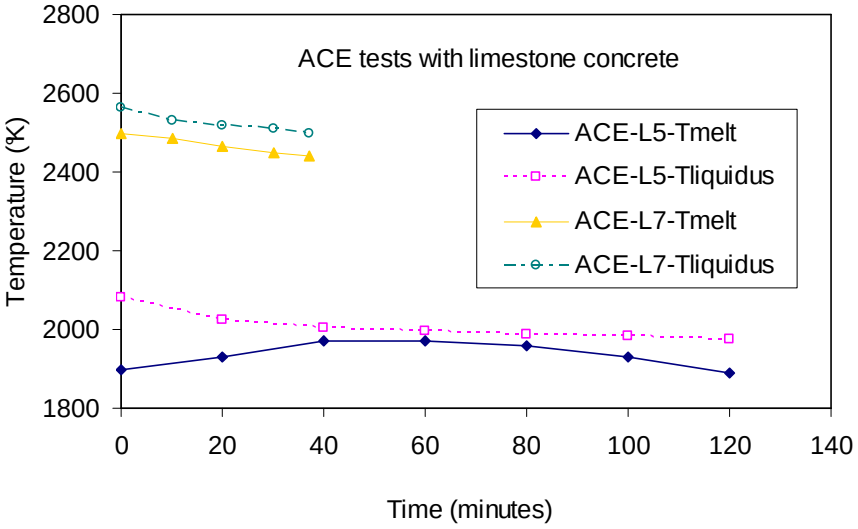

Figure 1-12. Melt and liquidus temperature evolution in ACE experiments in limestone-common sand and iron oxides (L5).

Gas ejection during ACE tests from concrete decomposition is evident which includes H_2O, CO_2 and H_2, CO and even SiO (when zirconium is present) due to decomposition of molten concrete and oxidation of metallic corium. Typical values of superficial gas velocities (1 to 8 cm/s) are given in Figure 1-13. Gas production with siliceous concrete is, in principle, much smaller than with limestone common-sand; in ACE L6 the high gas production seems to be linked to a transient acceleration of the concrete ablation.

As mentioned previously, one key issue in ACE experiment is to quantify the semi-volatile and refractory fission product (Ba, Sr, La,…) release during MCCI. It comes out that despite of the high melt temperature, the amount of fission product release is comparably small and that the release kinetics seems to be controlled by thermodynamic equilibrium [Cenerino et al., 1995] and is linked to the flow rate of sparging gas.

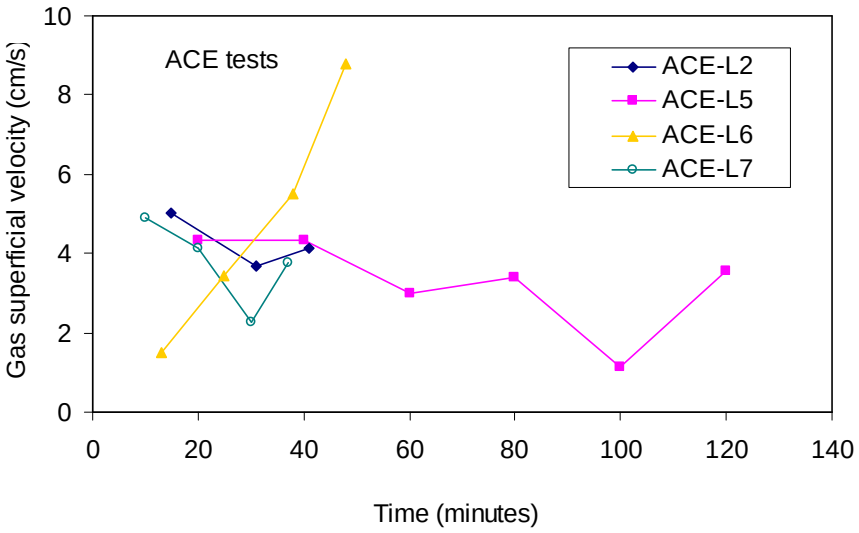

Figure 1-13. Superficial gas velocity in corium cavity in ACE experiments.

Figure 1-14 illustrates the vertical profiles of uranium concentration in the oxidic corium layer adjacent to the concrete in ACE L2 (siliceous) and ACE L5 (LCS) obtained from post-mortem examinations [Thompson et al., 1997]. Uranium and zirconium oxides are the refractory species in the corium melt. It can be seen that with LCS, the bottom region of the corium cavity near the interface with solid concrete is enriched in Uranium (uranium oxide is a refractory species) with 50 % mol of Uranium. The thickness of this layer is about 3 to 5 cm (Figure 1-14). Outside this layer, the Uranium concentration in the melt decreases sharply. At distance 11 cm from the interface with concrete, the mol percentage of Uranium is reduced to approximately 22%. By evidence, the layer near the interface is not formed of pure refractory phases. For ACE L2 with siliceous concrete, even though the mol percentage of uranium at the bottom is slightly higher than in upper part of the corium cavity, the difference is not significant enough for supporting refractory enrichment at the bottom. Macrosegregation seems not to be visible in this case.

In the phase segregation model applied to MCCI [Seiler, 1996], the thickness of the refractory enriched layer is estimated by assuming conduction heat transfer in the solid. Calculation by conduction model shows that the conduction thickness is significantly (factor 2 to 3) smaller than the one derived from the concentration measurements. This means that heat transfer by conduction is not sufficient to explain the heat transfer in the refractory enriched layer at the bottom of the corium cavity.

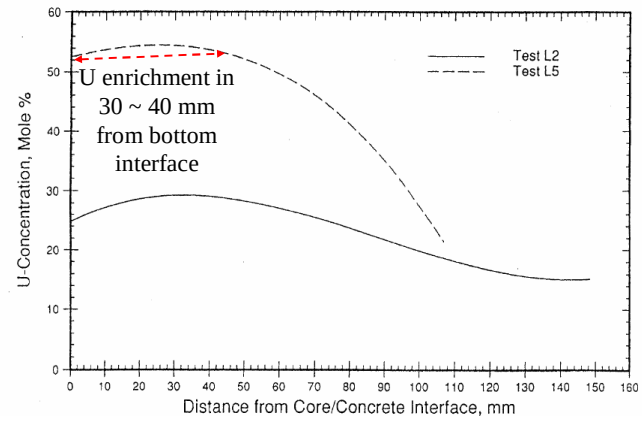

Figure 1-14. Uranium concentration near the bottom interface with concrete in ACE L2 and ACE L5 [Thomson et al. 1997].

MACE experiments

MACE (Melt Attack and Coolability Experiment) experiment was carried out in Argonne National Laboratory (ANL) after ACE experiment. The principle objective of this experiment is to investigate the coolability of the corium cavity if water is injected. In other words, can the corium melt pool be cooled by a water over-layer such that concrete ablation is halted [Farmer et al., 1997].

The experimental technique in the MACE experiment is similar to the ACE technique. An oxide UO2-rich melt is generated on top of a concrete basemat in an apparatus of 30 cm x 30 cm inner size for a pre-test, of 50 cm x 50 cm in regular tests and 120 cm x 120 cm for large scale test (MACE M3B). Melt masses have ranged from 100 kg to 2000 kg. The collapsed depth of the melt is 15 cm to 25 cm as is typically expected in severe accidents with large spreading areas under the Reactor Pressure Vessel (RPV). Heating is by tungsten electrodes by Joule effect with a power density representing the decay heat level at ~ 2 hours after shutdown. When the melt is completely liquid and after start of the ablation of concrete, water is added to the upper surface of the melt (Figure 1-15).

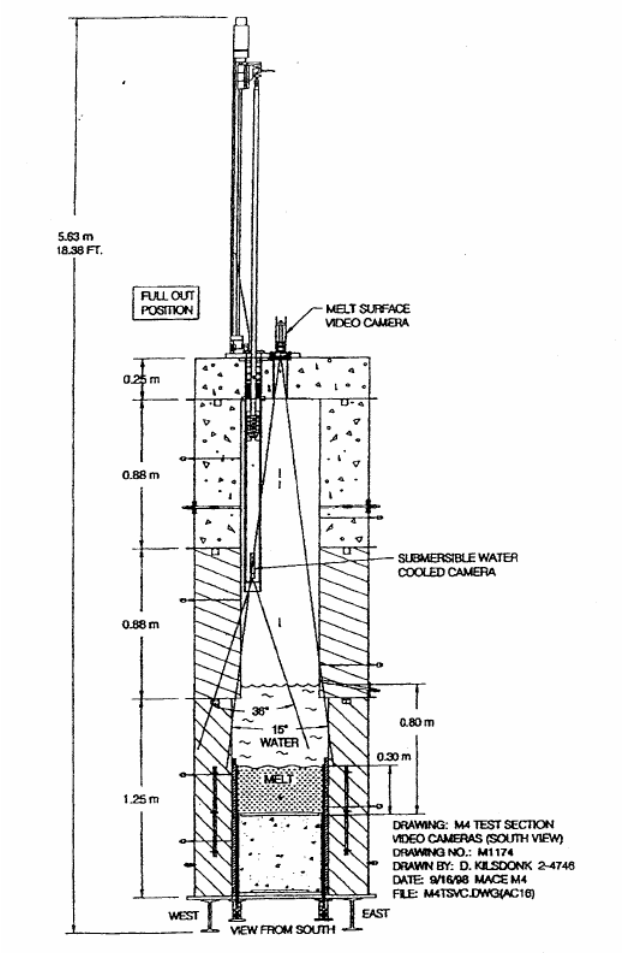

Figure 1-15. MACE installation [Thomson et al. 1997].

Figure 1-16 demonstrates evolutions of melt temperature measured in MACE M3B (LCS concrete) and liquidus temperature deduced from the work of [Vandroux-Koenig et al., 1999] using TOLBIAC-ICB code. Similarly to observation in ACE experiment, the melt temperature is lower than the liquidus temperature but seems to follow the liquidus temperature. In addition, when the power dissipation is doubled, the melt temperature still follows liquidus temperature. Moreover, measurement of gas superficial velocity also provides evidence of gas ejection from decomposition of ablated concrete during MCCI (Figure 1-17).

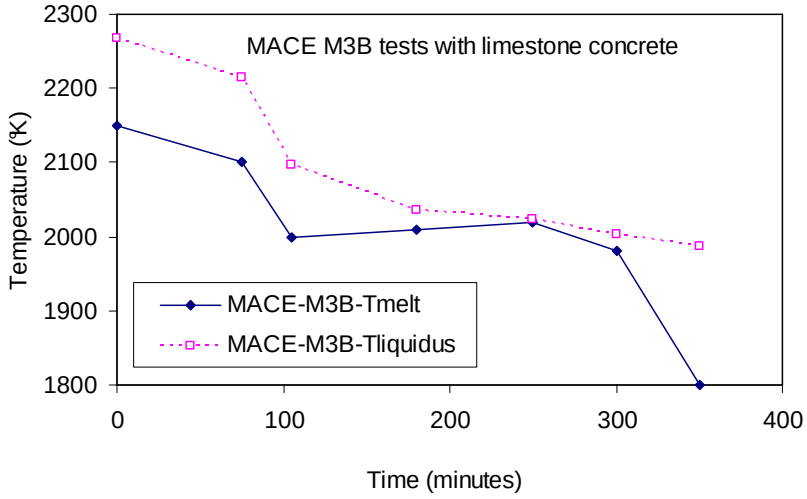

Figure 1-16. Melt temperature and liquidus temperature evolutions in MACE M3B (LCS).

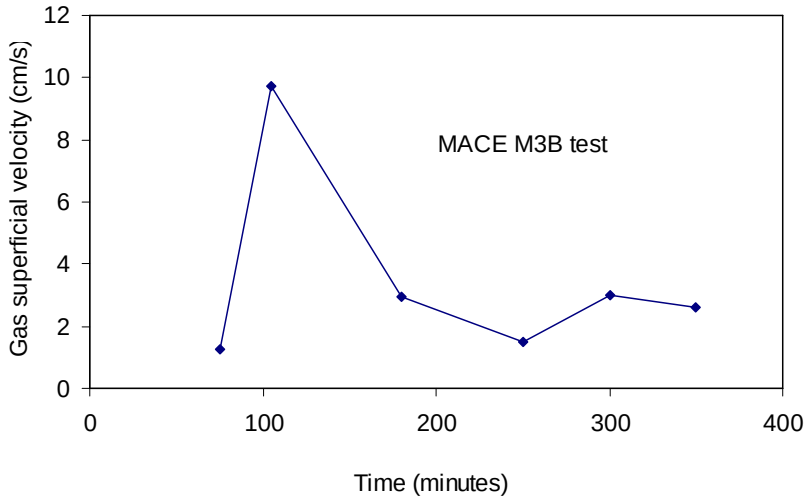

Figure 1-17. Superficial gas velocity in MACE M3B experiment.

As seen in Figure 1-18, post mortem exams show that there exists a refractory enriched layer at the bottom of the corium cavity with 2 ~ 3 cm thickness. This thickness is also greater than the conduction controlled thickness calculated with TOLBIAC-ICB code which is 1.5 cm [Vandroux-Koenig et al., 1999]. This layer is also probably a porous medium containing not only refractory but also a part of the ablated concrete products. Such a layer was also visible in MACE M1B which was performed with LCS concrete.

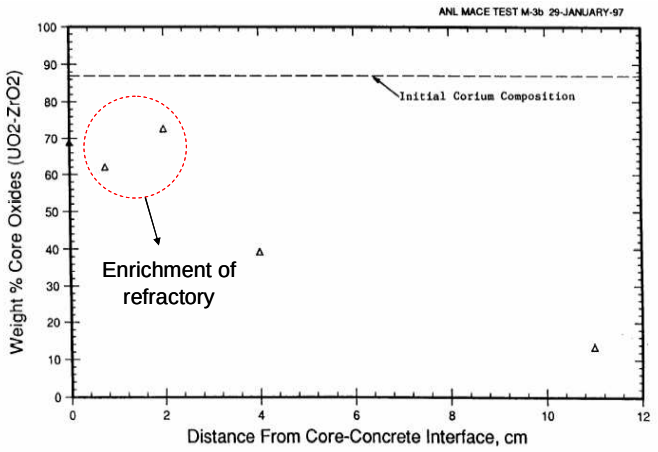

Figure 1-18. Oxide (UO_2+ZrO_2) concentration near the interface with concrete in MACE M3B experiments [Farmer et al., 1997].

ARTEMIS 1D

The ARTEMIS experimental program is devoted to the study of corium-concrete interaction using simulant materials [Michel et Cranga, 2008]. The aim of the ARTEMIS 1D tests was to study the phenomenology of MCCI in 1D geometry, in particular, behaviours on the bottom horizontal interface between liquid corium containing refractory species (with volumetric heat dissipation) and a low melting temperature solid concrete with gas injection. The concrete was composed of $BaCl_2$-LiCl mixture at its eutectic composition (25% $BaCl_2$-75% LiCl in mol, melting temperature: 522°C) and corium was simulated by pure $BaC1_2$ (Melting temperature: 960 °C) or a mixture of 80% mol $BaCl_2$-20%mol LiCl. The test installation is represented in Figure 1-19.

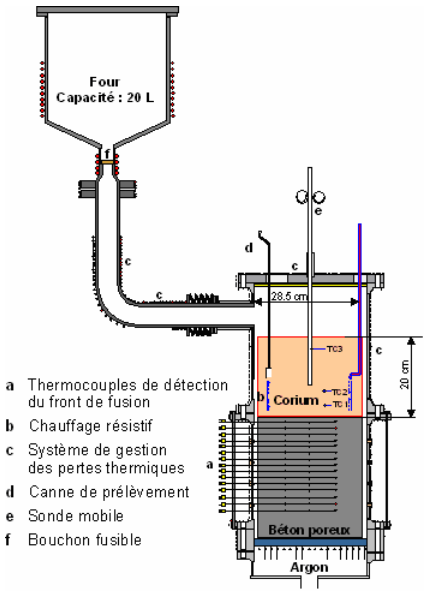

Figure 1-19. ARTEMIS 1D test description [Veteau, 2006].

The corium cavity is cylindrical with 28 cm diameter and a total 100 cm height. At the bottom of the corium cavity is situated a solid concrete layer with 46% porosity and 30 cm thickness. Argon gas is injected from the bottom of the concrete layer and is expected to penetrate the porous concrete to enter corium melt cavity [Guillaumé, 2008], [Guillaumé et al., 2009].

Table 1-5. ARTEMIS 1D test conditions and main results [Michel et Cranga, 2008].

	Test 1	Test 2	Test 3	Test 4	Test 5	Test 6
Duration	4h 40mins	1h 50mins	6h 30mins	4h 15mins	23mins	4h 25mins
Flux (W/m^2)	13000	24000	13100~25500	20000	41500	13400
Gas velocity (cm/s)	2	1	0.5	1~2	3	1
Initial superheat (°C)	96	109	34	31	26.5	47
Thickness of ablated concrete (cm)	31	26	28	45	33.5	30
Pool state	Semi-solid $T_i<T_{bulk}<T_{liquidus}$	Liquid $T_i<T_{bulk}\approx T_{liquidus}$	Liquid $T_{bulk}>T_i>T_{liquidus}$	Liquid $T_{bulk}>T_{liquidus}$	Semi-solid $T_{bulk}<T_{liquidus}$	Liquid $T_{bulk}\approx T_{liquidus}$
Interfacial layer (crust)	Yes	No (probe failed)	Yes	Yes	No	Yes
Crust thickness (mm)	0-90	Not remarked	80-120	50-120	0	0-80
Crust morphology	Globules of $BaCl_2$; Enrichent of LiCl	Grains of $BaCl_2$; Grains of molten and sintered concrete	Grains of $BaCl_2$; Dendrites	Grains of $BaCl_2$; Enrichment LiCl; Little dendrites	Mixed structure; Little dendrites	Dendrites surrounded by eutectic liquid
% mol $BaCl_2$_initial melt	80	100	100	100	100	100
% mol $BaCl_2$_final melt	46.3	57	45.9	46.1	57.7	52.9
% mass $BaCl_2$_final melt	72	86	80.6	80.7	87	84.6
% mol $BaCl_2$_crust	57	74.2	70.3	51.2	-	75.5
% mass $BaCl_2$_crust	86	93	92.1	83.7	-	93.8

A summary of the conditions of six ARTEMIS 1D tests and the key experimental results is given in Table 1-5. The melt and solid temperatures as well as position of ablated interface are measured during experiment. Interpretation has been made with the TOLBIAC-ICB code by [Spindler et Veteau, 2006].

Gas and concrete are heated up before the test beginning. Among the five tests with pure $BaCl_2$ corium, two trends were revealed. For the test with medium heat flux and gas velocity as tests 2, 3, 4, 6, an interfacial layer formed at the bottom of corium cavity, near the horizontal interface with concrete due to accumulation of refractory species $BaCl_2$. The post-mortem test shows that this layer is not solid but it is a porous medium containing not only refractory species but it is a mixture of solid particles and liquid at thermodynamics equilibrium. Morphology analysis provides evidences of holes on the surface of this layer and several chimneys along its height, indicating probably gas flow path as

well as molten concrete entrainment through this porous layer to the melt. In these tests, melt temperature is higher or approximately equal to liquidus temperature. [Guillaumé, 2008] calculated the thickness of this interfacial layer by conduction model and concluded that the experimental thickness of such a layer is 2 to 3 times thicker than the calculated one. This conclusion is, thus, similar to the conclusion derived from the LCS tests in ACE and MACE. In order to describe the heat transfer through this interfacial layer, a model taking into account both conduction and solute convection of interstitial liquid was developed. For test 5 with high heat flux and gas velocity, the melt temperature is lower than liquidus temperature. The melt must thus contain some solid.

Main results from 1D MCCI experiment

The 1D investigations of the Melt Coolability and Concrete Interaction (MCCI) program result in the following key outputs:

- Evolution of corium temperature follows approximately evolution of liquidus temperature for real corium material (ACE, MACE) as well as for simulant material (ARTEMIS 1D).
- Observation of a porous layer enriched in refractory species at the bottom interface with LCS concrete also observed in ARTEMIS. For tests with real reactor corium, this layer is only visible with limestone-common sand (LCS) concrete (MACE M1B, MACE M3B, ACE L5) but not with siliceous concrete (ACE L2). In ARTEMIS 1D (test 2, 3, 4, 6), this interfacial zone was also observed which contains solid particles and liquid at local thermodynamics equilibrium. Composition of this interfacial layer is enriched in refractory but not pure refractory.
- The thickness of this layer is higher (2 ~ 3 times) than the solid thickness calculated by conduction model. Heat transfer in this interfacial medium has been described by a model developed by [Guillaumé, 2008] in which both conduction and solutal convection in the interstitial liquid is taken into account.
- The post mortem analysis of the interfacial layer demonstrates existence of several holes and chimneys, indicating the gas flow path and molten concrete penetration into the corium cavity [Guillaumé, 2008].
- The model developed by [Guillaumé, 2008] allows recalculation of temperature evolution and ablation velocity as well as describes the mechanism which controls the behaviour of the interfacial layer for limestone-common sand concrete test in 1D. However, for siliceous concrete, the model was not applicable.
- Ablation instabilities were observed. These instabilities have been interpreted by [Seiler and Froment, 2000] as a result of molten concrete accumulation below the solid interface layer. If the interface layer is not permeable to molten concrete, the latter may accumulate below. This increases the heat transfer resistance between the melt and the concrete. The temperature at the interface between the molten concrete and the solid crust increases, which leads to a decrease of the thickness of the solid layer. When the thickness is sufficiently reduced, the sparging gas will help to break up the remaining of the solid accumulation. This leads to a direct contact between melt and concrete and to an acceleration of the ablation. The ablation slows again down as the interfacial layer reforms. This is a cyclic behaviour. This behaviour does not lead to a modification of the average ablation rate (since this average ablation rate is linked to the power dissipation) but to ablation instabilities that are superposed to the average ablation. The M3B (LCS) test has also shown that these instabilities have limited extends on the horizontal concrete surface (30 to 50 cm), which induces local penetrations.

1.3.2 Learnings from 2D MCCI

One important issue among the addressed issues that warrant further investigations concerns 2D concrete ablation. The question relates to the ablation shape of the corium cavity which can be preferentially radial or isotropic in both radial and axial directions. 2D MCCI experiments have been performed in order to investigate this task: CCI (ANL USA) and VULCANO (CEA France) experiments.

CCI program

CCI experiments (Core Concrete Interaction) were launched at Argonne National Laboratory (ANL) to address the 2D MCCI issue (axial and radial concrete ablation) by providing data for code verification and validation purposes [Farmer et al., 2004, 2005, 2006, 2007, 2008] for 2D ablation and for coolability with water flooding. In order to get more information about the coolability of corium by water in 2D geometry, the core-concrete facility was flooded from above after a pre-defined concrete ablation depth is reached. The tests employ real reactor corium (from a thermatic reaction) and two types of concrete which are limestone-common sand (LCS) and siliceous. The test section has rectangular shape with typically a 50 cm width (the width could reach 70 cm). The bottom and one of two lateral surfaces are ablated. The width of test section and the number of lateral concrete walls to be ablated vary between tests. The power dissipation in corium cavity is simulated by Joule effect with tungsten electrodes. The lateral walls with tungsten electrodes are insulated (by means of refractory material protection) The CCI test parameters are given in Table 1-6.

Table 1-6. CCI test conditions [Farmer et al, 2004, 2005, 2006, 2007, 2008].

	CCI-1	CCI-2	CCI-3	CCI-4	CCI-5
Concrete	Siliceous	LCS	Siliceous	LCS	Siliceous
Test section width (cm)	50	50	50	40	79
Duration (minutes)	68	300	107	458	928
Power (kW)	150	120	120	95	145
Initial corium mass (kg)	355.4	311.5	313.3	299.7	590
Initial corium temperature (°C)	1950	1900	1950	1950	1900

Figure 1-20 represents evolution of melt temperature in five CCI tests. Two tendencies are observed for the two types of concrete:

- For tests with siliceous concrete (CCI-1, CCI-3, CCI-5), melt temperature decreases in the beginning, then increases after a certain period of time before decreasing again until the test ending.
- For test with limestone-sand concrete (CCI-2, CCI-4), melt temperature decreases from the beginning to the end. Typically, two phases of decrease of melt temperature can be identified. Rapid temperature decrease is seen in the first phase. Then, the temperature decreases much more slowly in the second phase.

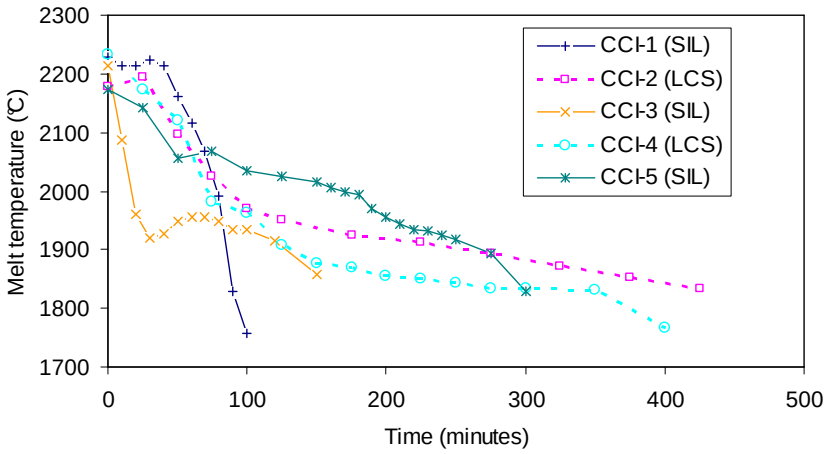

Figure 1-20. Evolutions of melt temperature in CCI tests.

[Cranga et al. 2008] performed an interpretation of these 2D experiments with ASTEC/MEDICIS code, developed by [Cranga et al. 2005]. The melt-concrete interface structure in MEDICIS code is described in Figure 1-21.

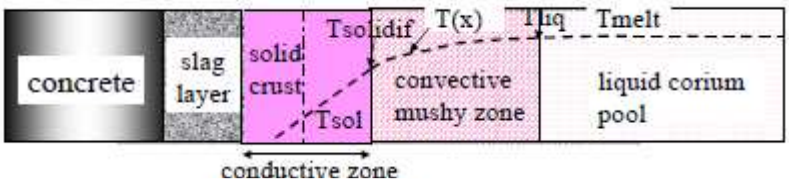

Figure 1-21. Melt-concrete interface structure in MEDICIS code [Cranga et al. 2005].

The main assumptions employed in this code are:

- A mushy zone exists in between the liquid melt and the formed crust
- The temperature at the crust-concrete temperature is the solidus temperature of the melt;
- Heat convection is governed by gas bubbling from the melt across the mushy zone. The convective two-phase heat transfer was evaluated by BALI experiments [Bonnet et Garré. , 1999] on a wide range of corium viscosity and superficial gas velocity;
- Underneath the mushy zone, the conduction controls heat transfer in the crust. Heat is transferred by conduction through this solid layer to the concrete and serves for concrete ablation;
- The temperature of the boundary between pool conductive and pool convective zones is evaluated by $T_{solidification} = \gamma T_{solidus} + (1-\gamma) T_{liquidus}$ where in γ is a parameter for evaluating the solidification temperature by interpolation between corium solidus and liquidus temperatures. γ is dependent on the molten fraction in the corium pool.

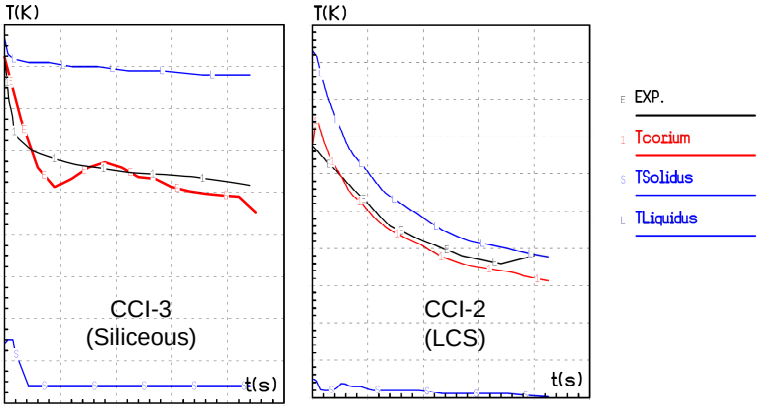

Figure 1-22. Comparisons of melt temperature and liquidus temperature in CCI-3 (siliceous concrete, γ = 0.4) and CCI-2 (limestone-sand concrete, γ = 0.1) [Cranga et al, 2008].

Results obtained from MECIDIS calculations for melt temperature evolution in CCI-2 (LCS concrete) and CCI-3 (siliceous concrete) with comparisons to corresponding liquidus temperature are displayed in Figure 1-22 (γ = 0.1 for LCS and γ = 0.4 for siliceous). The measured melt temperature stays below the liquidus temperature. Deviation between melt and liquidus temperature in siliceous concrete is more than in limestone-common sand concrete. Although water is flooded at the top of the corium cavity after a certain period of ablation, no decrease in overall melt temperature after flooding is exhibited.

The CCI tests provided information for evolution of corium cavity shape in 2D corium-concrete interaction. The corium cavity shape after concrete erosion observed at the end of CCI-3 (siliceous), CCI-2 (LCS) and CCI-5 (siliceous with wider test section) are displayed in Figure 1-23, Figure 1-24 and Figure 1-25.

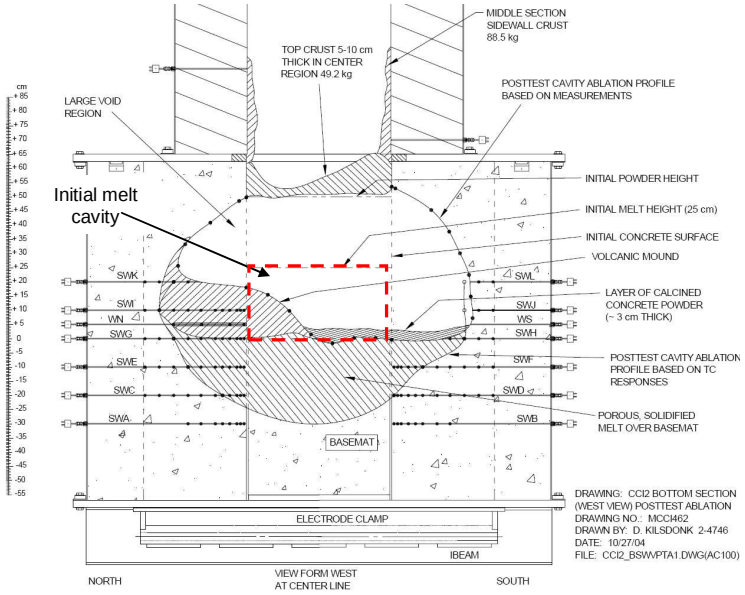

Figure 1-23. Final corium cavity in CCI-2 (LCS concrete).

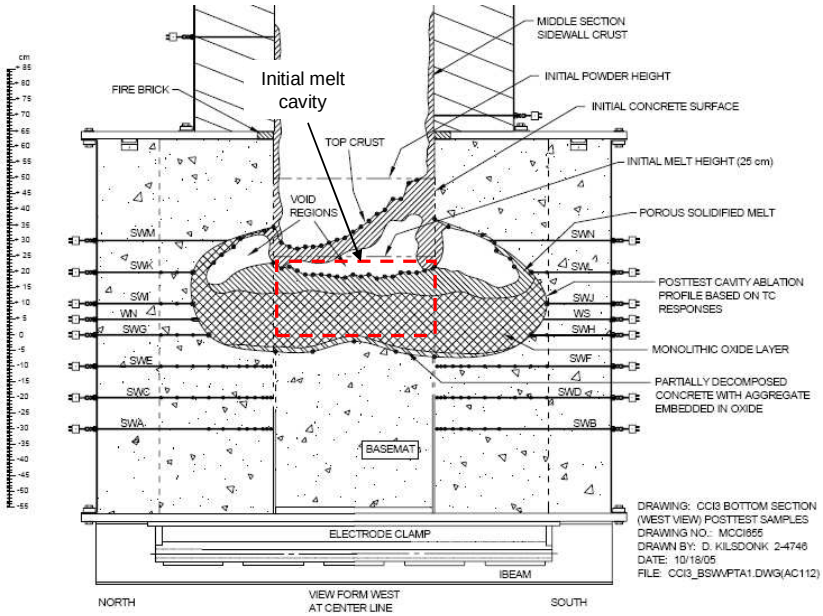

Figure 1-24. Final corium cavity in CCI-3 (siliceous concrete).

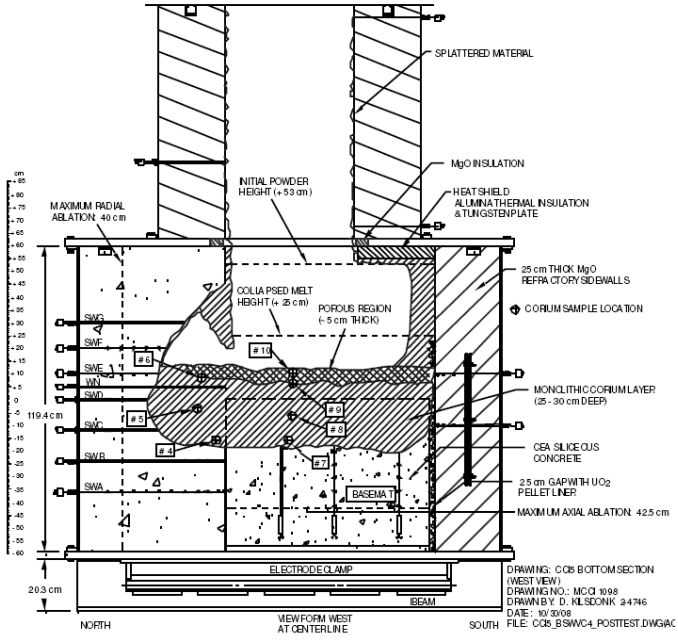

Figure 1-25. Final corium cavity in CCI-5 (siliceous concrete).

Two factors have important effect on the 2D concrete ablation shapes, which are the nature of concrete and the test section size.

The effect of concrete type is relatively clear. As shown in Table 1-7, the ratio between radial and axial maximum ablated concrete thicknesses for tests with LCS concrete (CCI-2 and CCI-4) ranges from 0.5 to 1; whereas, it is between 4 and 6 for siliceous tests (CCI-1 and CCI-3). Hence, for LCS concrete, axial and radial ablations are equivalent; whereas, radial ablation is more important than axial ablation with siliceous concrete.

Beside the effect of concrete type, test section size also influences significantly the ablation shape. As seen in Table 1-7, CCI-5 reveals different ablation behaviour from CCI-1 and CCI-3 with similar concrete material (siliceous). Ablation seems to be more uniform in CCI-5. Significant improvement of axial ablation in CCI-5 in comparison with CCI-1 and CCI-3 for the same concrete material (siliceous) might be explained by the enhancement of test section width (70 cm for CCI-5 compared to 50 cm for the CCI-1 and CCI-3). This effect is not clearly explained yet.

Table 1-7. Maximum ablated concrete thickness in radial and axial directions in CCI tests.

Maximum ablated thickness (cm)	CCI-1	CCI-2	CCI-3	CCI-4	CCI-5
Radial	34.2	24.1 ~ 29.2	24.1 ~ 34.3	15 ~ 25	20 ~ 25
Axial	7.56	29.2	5.1	35	22.5
Ratio radial/axial	4.5	0.82 ~ 1	4.73 ~ 6.7	0.43 ~ 0.71	0.89 ~ 1.11

Results of CCI tests have indicated trends of melt temperature evolution and 2D ablation front progression which are strongly dependent on the concrete type as well as on test section size. Evolution of melt temperature can be recalculated with the assumptions employed in the MEDICIS code for siliceous and limestone-sand concrete tests (CCI-3 and CCI-2). For LCS concrete, the melt temperature stays near liquidus temperature but for siliceous concrete, the melt temperature is significantly below liquidus temperature. Moreover, MEDICIS code enables description of transient concrete ablation (thickness of ablated concrete) in radial direction (for both siliceous and LCS). However, axial ablation kinetics is overestimated by the calculation. This issue needs to be investigated before further application for plant scale is applied. A first partial reason for this discrepancy is the underestimation in the late phase of the real axial ablation as deduced from thermocouples, which are lacking at a large enough concrete depth. Another possible reason is the initial formation of an unstable crust at the bottom interface which may reduce the axial ablation kinetics [Cranga et al., 2008]. These two possible phenomena that may occur in experiment are not described in the code.

Investigation of the corium-concrete morphology at the end of tests provides different observations. The corium-concrete interface for siliceous concrete consisted of a region where the core oxide has locally displaced the cement that bonded the aggregate (Figure 1-26). The melt with siliceous concrete looks also as a very dense melt without any gas inclusion. Conversely, the ablation front for LCS consisted of a powdery interface in which corium and concrete oxides are clearly separated (Figure 1-27). The melt with LCS concrete is also very porous. This tends to indicate that gas can penetrate in corium pool with LCS concrete but not with siliceous concrete. These observations led to an interpretation of concrete and size effect by [Tourniaire et Seiler, 2008]. A good stirring of the melt by sparging gas with LCS concrete can explain a homogeneous heat flux distribution and uniform ablation. If gas does not penetrate into the melt with siliceous concrete, the flow in the melt will be controlled by natural convection, which can explain the preferential radial ablation. For siliceous concrete and small scale tests, if the gas does not penetrate the melt, it must flow around, plausibly in the gap left by the erosion of cement between siliceous stones. But when the width of the test section increases, the gas may have more difficulties to flow around the melt and the gas may then be forced to flow through the melt, which leads to a modification of the flow in the melt and, consequently, to a modification of the heat flux distribution and ablation shape. All these events may of course be time dependent.

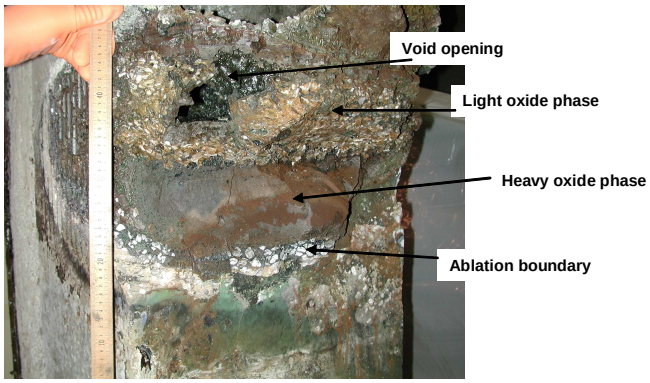

Figure 1-26. Final corium-concrete interface morphology in CCI-1 (siliceous concrete).

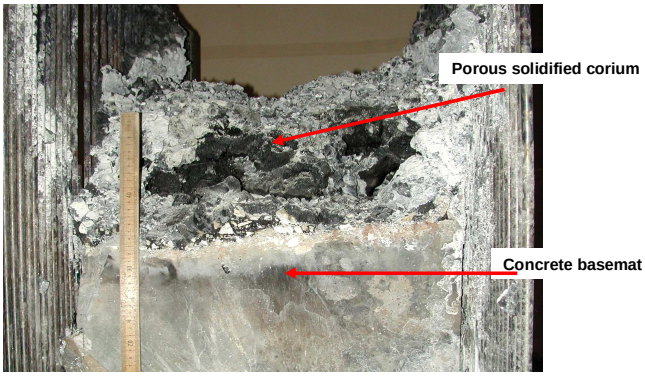

Figure 1-27. Final corium-concrete interface morphology in CCI-2 (LCS concrete).

VULCANO results

VULCANO experimental program was launched at CEA Cadarache (France) to study the 2D interaction between prototypic oxide corium and concrete. The test facility contains a block of 600 mm x 300 mm x 400 mm concrete with a hemi-cylindrical corium cavity with ~ 300 mm diameter and 250 mm height]. Several tests have been performed using two types of concrete: siliceous concrete, for instance for VB-U4 and VB-U5 and limestone-common sand for VB-U6 [Journeau et al. 2009].

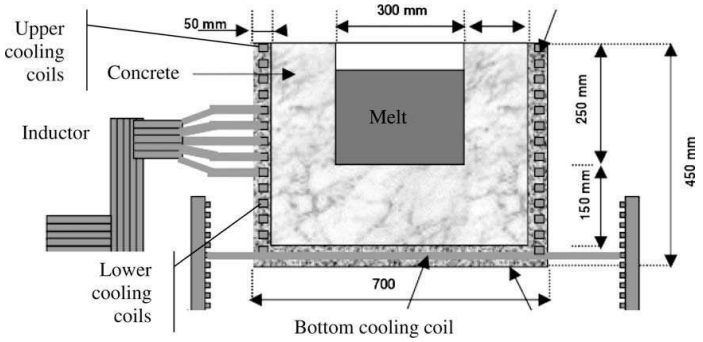

Figure 1-28. VULCANO test facility [Journeau et al. 2009].

VULCANO test conditions for these tests are summarized in Table 1-8.

Table 1-8. VULCANO test conditions [Journeau et al., 2009].

	VB-U4	VB-U5	VB-U6
Duration	1 h 40 minutes	2 h 30 minutes	2 h
Concrete	Siliceous	Siliceous	Limestone-sand
Initial melt temperature (K)	2200	2400	2400
Initial mass of corium (kg)	45	28	31
Power (kW)	14	12.5	9

Progression of the ablation interface is followed during each test and evolution of radial and axial fronts are reported by [Journeau et al., 2009] in Figure 1-29 for VB-U5 and Figure 1-30 for VB-U6. Similarity is obtained between CCI tests and VULCANO tests. The two test series both corroborate the CCI results, that ablation behaviour is strongly dependent on the type of concrete. Siliceous concrete is anisotropically radially ablated while limestone-common sand concrete ablation tends to isotropy.

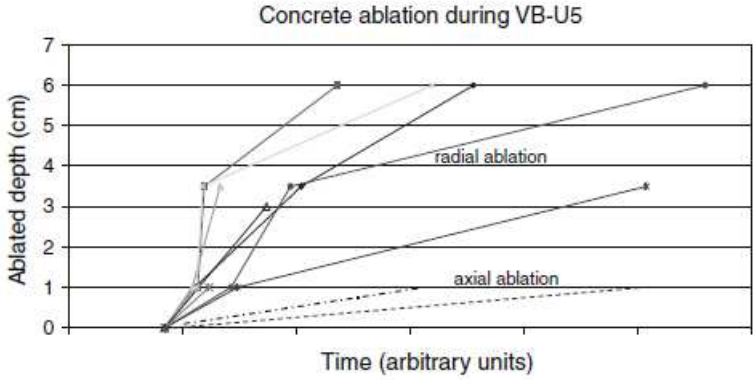

Figure 1-29. Progression of ablated front in VULCANO VB-U5 (siliceous).

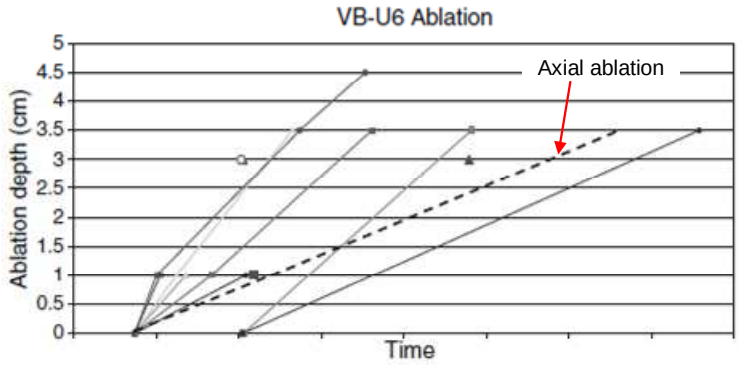

Figure 1-30. Progression of ablated front in VULCANO VB-U6 (Limestone-common sand). Dash line represents axial ablation and straight lines represent radial ablation at four azimuthal angles of cavity.

The average ratio between maximum ablation in radial and axial directions is shown in Table 1.

Table 1. Ratio between radial and axial ablations [Journeau et al., 2009].

VB-U4	VB-U5	VB-U6
2.5 : 1	5 : 1	2 : 1 for the first hour 1 : 1 for the second hour
Anisotropic	Anisotropic	Rather isotropic

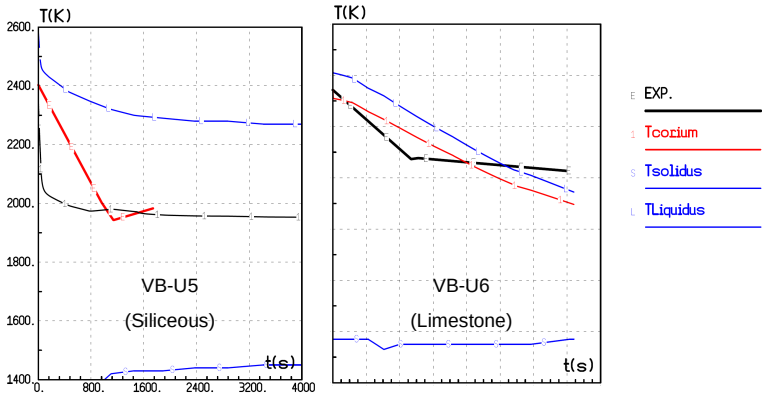

Figure 1-31. MEDICIS calculations of melt temperature and liquidus temperatures in VULCANO VB-U5 (γ = 0.4) and VB-U6 (γ = 0.1) [Cranga et al., 2008].

MEDICIS code also predicts that melt temperature follows liquidus temperature but is lower than liquidus temperature (maximum difference between the two temperatures is 350 K) for the two types of concrete as observed in CCI tests (Figure 1-31). As observed during CCI tests, the difference between melt and liquidus temperatures is for limestone-common sand concrete less than for siliceous. In general, observations in VULCANO tests show similarity to CCI tests for the same concrete type in tendency of melt temperature as well as progression of ablated front.

Interpretation of the VULCANO experimental results has been performed by TOLBIAC-ICB code [Journeau et al, 2009]. TOLBIAC-ICB [Spindler et al., 2005] assumes that the convective pool interface temperature is set to the pool liquidus temperature, according to the phase segregation model [Seiler and Froment, 2000]. The main hypotheses are that a solid crust deposits at the concrete walls and the pool is only composed of liquids and has thus a low viscosity. The crust thickness is estimated using a thermal steady-state model and local thermodynamic equilibrium is assumed at the crust–pool interface.

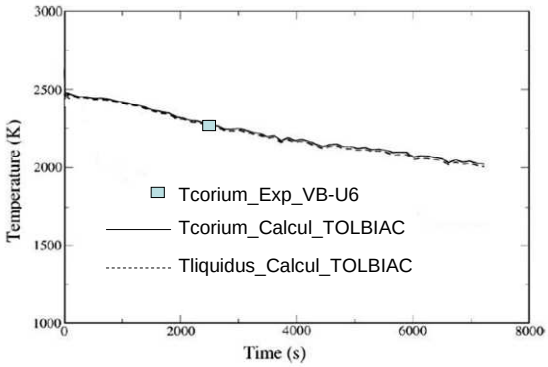

Figure 1-32. TOLBIAC-ICB calculation of melt temperature and liquidus temperatures in VB-U6 [Journeau et al., 2009].

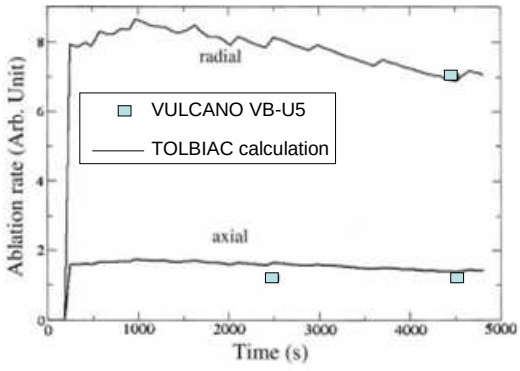

Figure 1-33. TOLBIAC-ICB calculation of ablation rate in VB-U6 [Journeau et al., 2009].

For test with limestone concrete (VB-U6), calculation with TOLBIAC-ICB indicates that the melt temperature follows liquidus temperature (Figure 1-32). This is coherent with the calculation by MEDICIS code as well as with the measured data. Moreover, evolution of ablation rate in radial and axial directions for test with siliceous concrete (VB-U5) has been reproduced by the code (Figure 1-33).

1.3.3 Major observations from 2D MCCI investigations

The recent studies on molten corium-concrete interaction focus on thermal-hydraulics of the melt (distribution of heat exchange coefficient) and phenomena occurring at the liquid-solid interface (governing the interface temperature) during 2D MCCI. Main findings from these works fall in the following points:

- The major observation is that siliceous concrete is preferentially radially ablated (CCI-1, CCI-3, CCI-5, VB-U4 and VB-U5) while limestone-common sand concrete ablation (CCI-2, CCI-4 and VB6-U6) tends towards isotropy (axial and radial ablations). For certain test, the radial ablation starts later than axial ablation.
- There exists an effect of test section size on ablation shape, but the experimental data basis is too scarce. In CCI-5 with siliceous concrete, when the width of the test section is increased from 50 cm to 70 cm, significant enhancement of axial ablation is obtained. Ablation in two directions was then relatively uniform. There was an acceleration of radial ablation at the end of the test. Therefore, the question of the effect of test duration stays open.
- The corium temperature follows evolution of the liquidus temperature for tests with limestone concrete CCI2, CCI4, VULCANO VB-U6. For siliceous concrete CCI-1, CCI-3 and CCI-5, the average melt temperature first decreases significantly, then re-increases before decreasing again. During the increase phase, it tends towards the liquidus temperature but stays generally below.
- There is a link between melt temperature decreases and instantaneous concrete ablation rate. The melt temperature becomes smaller than the liquidus temperature when radial ablation accelerates.
- CCI1, CCI2, CCI3 showed evidence of initial crust formation at the bottom and sidewalls at the beginning but the crust eventually disappeared at the end (dissolution of crust). Stability of the crust is predicted to play a major role in determining ablation progression [Farmer, 2007]. The question of existence of an interfacial layer at the liquid-solid interface between liquid melt and solid-concrete is still open for 2D ablation.

1.3.4 Unresolved issues

Despite intensive studies on molten corium-concrete interaction, there are still observations that are not explained for the time being:

- Why does the corium temperature follow the evolution of the liquidus temperature for limestone-common sand tests but not for siliceous concrete? Corium temperature can be more than 250 K lower than the liquidus temperature with siliceous concrete.
- What are the causes that lead to isotropic ablation with limestone-common sand concrete (VB-U6, CCI2, CCI-4) but preferentially radial ablation with siliceous concrete (CCI1, CCI3, VB-U5, VB-U4). Can the different behaviour for gas penetration as postulated by [Tourniaire et Seiler, 2008] be a sufficient reason?
- What are the causes and the consequences of ablation instabilities, such as observed with siliceous concrete (CCI-1, CCI-3, CCI-5, VB-U4, VB-U5); What is the minimum test size and test duration which would be necessary to observe representative average 2D ablation rates?

1.4 Objectives of the thesis

1.4.1 Study on in-vessel corium behaviour

The first objective of this thesis is to investigate the non-eutectic material effect on the thermal-hydraulics of a hemispherical shaped melt pool that is volumetrically heated and cooled on its lateral boundaries with melt solidification at the lateral wall.

The main questions to be addressed will focus on the transient molten pool behaviour, including:

- Transient heat transfer from the melt pool to the vessel wall;
- Kinetics of the macroscopic solid crust growth during transient;
- Mass transfer mechanism at the liquid-solid interface and interface temperature during transient and in the final steady state;
- Composition and temperature at the liquid-solid interface during transient and in steady state.

For the description of the transient molten pool thermal-hydraulics, a model will be developed and validated against LIVE tests to propose a physical approach to assess the mentioned parameters.

1.4.2 Study on 2D molten corium-concrete interaction

The state of the art shows existence of open issues that cannot be solved basing on the existing data. Furthermore, real material tests do not allow precise measurements of melt temperature distribution, solid behaviour at the interfaces and interface temperatures.

In order to get a closer view of phenomena, CEA, IRSN and EDF have launched the ARTEMIS 2D tests. The aim of the present work is to use the results of these experiments in order to investigate:

- The heat flux distribution along the corium cavity during transient;
- The evolution of the shape of the ablation interface;
- The evolution of corium temperature and the link to the melt composition;

- The evolution of interface conditions during MCCI, including composition distribution at the interfaces and interface temperatures;
- The effect of gas sparging on the flow recirculation in the corium cavity and its impacts on heat transfer.

CHAPTER 2: TRANSIENT HEAT TRANSFER & CRUST SOLIDIFICATION IN LIVE L3A

2.1 Context and objective of LIVE program

Steady state behaviour of core debris and of molten corium melt cavities in the lower head of a reactor power vessel (RPV) has been investigated widely in the last four decades by numbers of experimental and theoretical works [Gabor et al., 1980], [Theofanous et al., 1997], [Bonnet et al., 1999]. However, transient processes for crust growth and interface temperature are lacking.

The context of the LIVE Program at Karlsruhe Institute of Technology (KIT) is the investigation of core melt phenomena. The work is aimed at studying lower head formation and stability of melt cavities in RPV [Kretzschmar et Fluhrer, 2008]. Transient thermal-hydraulics of a hemispherical shaped non-eutectic melt cavity that is volumetrically heated and cooled on its lateral boundaries is the subject of this work. Information on transient heat flux distributions, melt temperature evolution as well as crust formation from melt release to final steady state are desired. In addition, better understanding of physical phenomena that govern solidification at the interface between core melt and its crust are of special attention.

2.2 LIVE L3A test description

2.2.1 Simulating materials

The simulating melt selected for LIVE experiments is a binary non-eutectic mixture of 80% mol KNO_3 – 20% mol $NaNO_3$ [Gaus-Liu et al., 2010]. A phase diagram proposed by [Levin et al., 1985] for this mixture is shown in Figure 2-1. An azeotrop (at 225 °C for 50% mol KNO_3-50% mol $NaNO_3$) is exhibited. The liquidus temperature for 80% mol KNO_3-20% mol $NaNO_3$ is approximately 285 °C. The solidus temperature for this composition is about 235 °C. The partition coefficient k (ratio between solidus/liquidus refractory (KNO_3) compositions) is taken equal to 0.2 in the present study. Recently, a new phase diagram for this mixture has been reported by [Zhang et al., 2003] (Figure 2-2). According to [Zhang et al., 2003], the liquidus and solidus temperatures of the mixture at the considered composition are respectively 565 K and 495 K (i.e. 292 °C and 222 °C) which are in agreement which those obtained by [Levin et al., 1985].

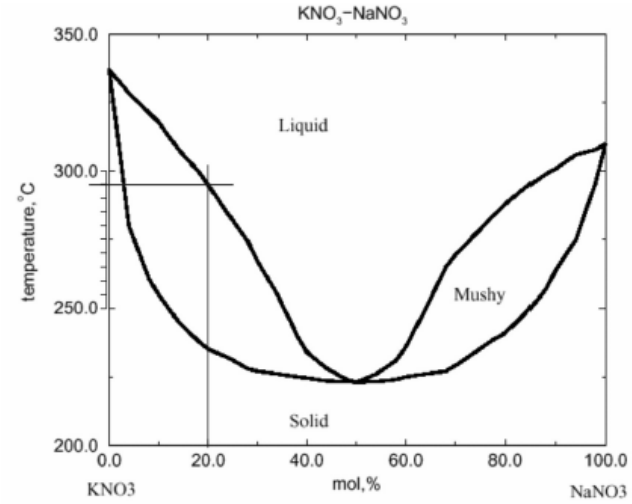

Figure 2-1. Phase diagram of KNO_3-$NaNO_3$ mixture [Levin et al., 1985].

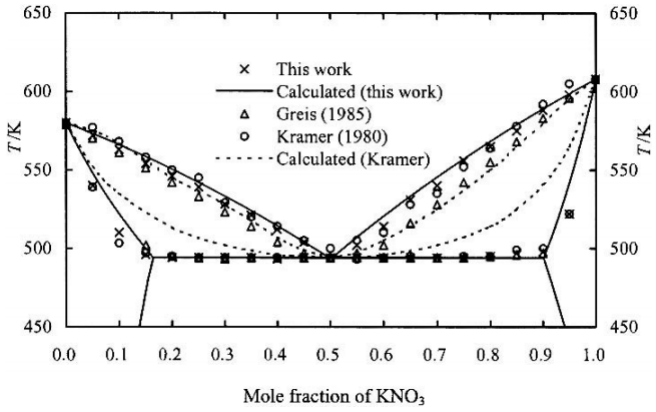

Figure 2-2. Phase diagram of KNO_3-$NaNO_3$ mixture [Zhang et al., 2003].

Physical properties of the mixture are given in Table 2-1.

Table 2-1. Physical properties of the simulating corium in LIVE L3A [Gaus-Liu et al., 2010].

Parameter		Unity	Value in LIVE L3A test
λ_{bulk}	Thermal conductivity	$W.m^{-1} K^{-1}$	0.44
υ	Kinematic viscosity	$m^2.s^{-1}$	$1.6\ 10^{-6}$
ρ_{bulk}	Density	$kg.m^{-3}$	1900
α	Thermal diffusivity	$m^2.s^{-1}$	$1.72\ 10^{-7}$
β_T	Thermal expansion coefficient	K^{-1}	$4.64\ 10^{-4}$
$C_{p,bulk}$	Specific heat	$J.kg^{-1}.K^{-1}$	1350
$L^{melt}_{solidification}$	Latent heat of solidification	$J.kg^{-1}$	$6\ 10^{4}$

2.2.2 Test installation

The LIVE test facility includes three main parts: the test vessel with its external cooling system, the volumetric heating system and a separate melting furnace [Kretzschmar et Fluhrer, 2008]; [Gaus-Liu et al., 2010]. The test vessel is a 1:5 scaled hemi-spherical lower head of a typical pressurized water reactor (PWR), fabricated from stainless steel. The inner diameter of the test vessel, Dinner, is 1 m and

the steel wall thickness is about 25 mm. The top of the vessel is covered with an insulation lid. The test vessel is embedded in a cooling vessel to simulate external cooling. The cooling water inlet is located at the bottom and the outlet is positioned at the top of the cooling vessel. The water temperature ranges from 20 °C (at the vessel bottom) to 90 °C (at the top region). The volumetric decay heat released from the corium melt is simulated by means of six heating coils supported by a steel structure (the total weight is 25 kg) attached in the vessel at six different elevations. The maximum temperature of the heating system is ~ 350 °C while its maximum power dissipation is 18 kW. To realize a homogenous heating power of the melt, the power in each heating coil is controlled separately [Gaus-Liu, 2010]. The sketch of LIVE test vessel facility is shown in Figure 2-3.

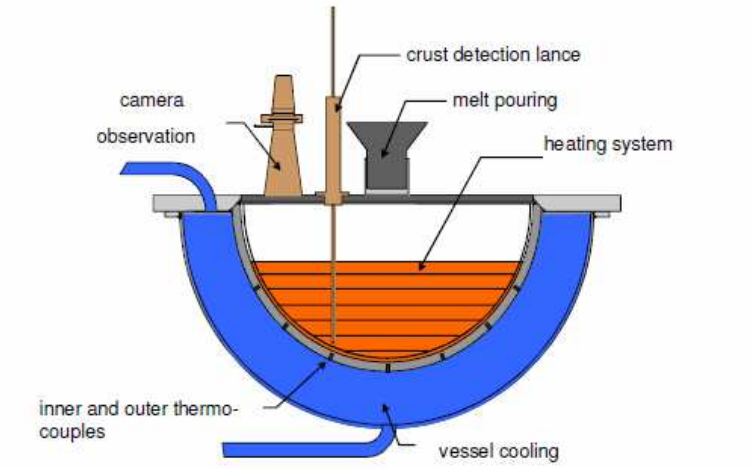

Figure 2-3. LIVE test vessel [Kretzschmar et Fluhrer, 2008].

The LIVE test facility has extensive instrumentation. The inner and outer temperatures of the test vessel are measured at five polar angles (0°, 30°, 51°, 65.5°, 76.5° where 0° corresponds to the vertical direction) and four azimuth angles (22.5° 112.5°, 202.5°, 292.5°) at each polar angle. Crust solidification process is monitored with thermocouple trees, attached at the inner vessel wall at three locations, which are respectively 100, 200 and 300 mm above the vessel bottom. A crust detection lance is aimed to detect precisely the position of the solid crust interface and measure the crust/melt interface temperature and the local, vertical melt temperature profile in the melt. The linear actuator is mounted on the lid of the test vessel. The lance can be driven at 0.1 mm accuracy. The crust detection system is put on the lid of the vessel (at polar angle 66.9° and at elevation 0.313 m from the bottom). The position of this system is at a radius of 365 mm and at azimuth angle 340° on the lid.

In the present work, only the results of LIVE L3A test are reviewed and analyzed. This experiment was conducted on April 23-25, 2008. In LIVE L3A, the vessel was cooled by water before the melt pouring and cooling was kept on during the whole test for simulation of external vessel cooling [Gaus-Liu et al., 2010]. The vessel and instrumentation are initially at ambient temperature. The power dissipation in the melt cavity is 10 kW in the beginning and 7 kW after 90000 s. The test conditions of LIVE L3A are given in Table 2-2.

During LIVE L3A, the total power transferred through the test vessel wall is measured and compared with the power dissipation in the melt cavity. There was a part of the power removed through the top surface but this part is less than 10% of the total power dissipation [Gaus-Liu et al., 2010].

Table 2-2. LIVE L3A test conditions.

Initial cooling condition	Water cooling
Water cooling flow rate	0.047 $kg.s^{-1}$
Melt pouring position	Lateral
Melt pouring flow rate	6 $kg.s^{-1}$
Melt volume	120 l
Initial melt temperature in the furnace	~ 350 °C
Heating power	Phase 1: 10 kW – duration: 90000 s followed by Phase 2: 7 kW – duration: 91800 s
Heat generation	Repartition of heaters in the melt for a homogeneous heating
Internal Rayleigh number	10^{12} - 10^{13}

2.3 LIVE L3A experimental results

This test provides information about the melt temperature evolution, heat flux distribution along the vessel wall during transient and steady state conditions, the crust thickness profile and the dependence of the crust formation on the heat flux distribution.

2.3.1 Evolution of melt temperature and temperature profiles

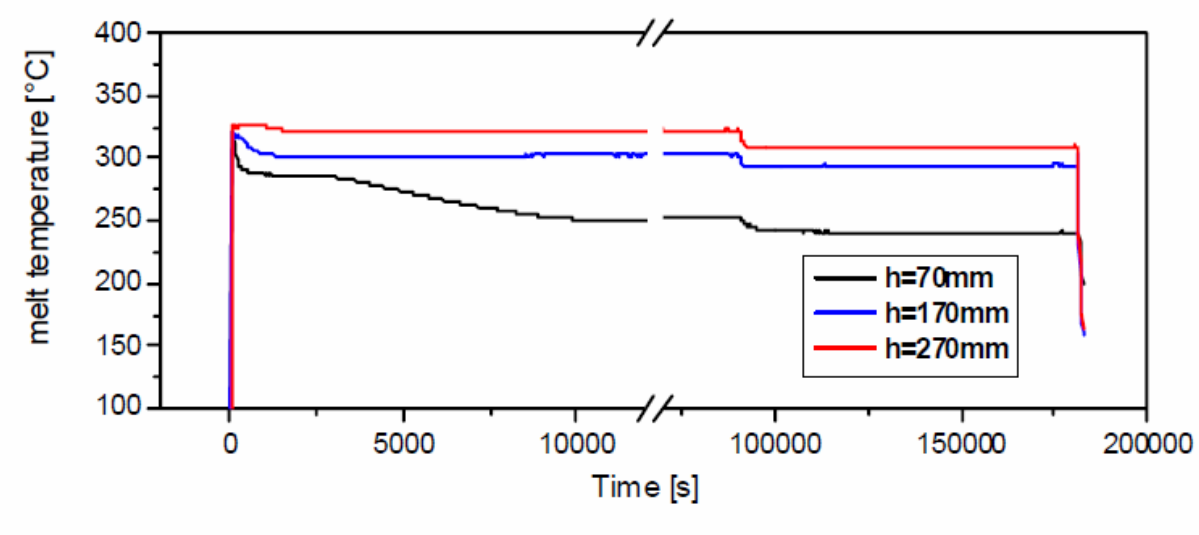

Figure 2-4. Melt temperature evolutions at three elevations in corium melt cavity [Gaus-Liu et al., 2010].

The experimental data of melt temperatures evolution during the two phases of heating (10 kW and 7 kW) at three different heights from the bottom of the vessel are reported (70 mm, 170 mm, 270 mm) in Figure 2-4; whereas, the melt temperature profiles in steady state at polar angle 47° for the two phases are depicted in Figure 2-5.

Figure 2-4 shows that at a level of 270 mm from the vessel bottom, i.e. near to the melt surface, the melt temperature gradually decreases from 327 °C to a steady value of about 320 °C (the initial melt cool down from 350 °C to approximately 327 °C is attributed to the heat up of the initially cold heater whose mass is 25 kg). After 90000 s, the heating power was reduced to 7 kW, and the melt temperature decreases again before reaching a constant value of 310 °C at level 270 mm.

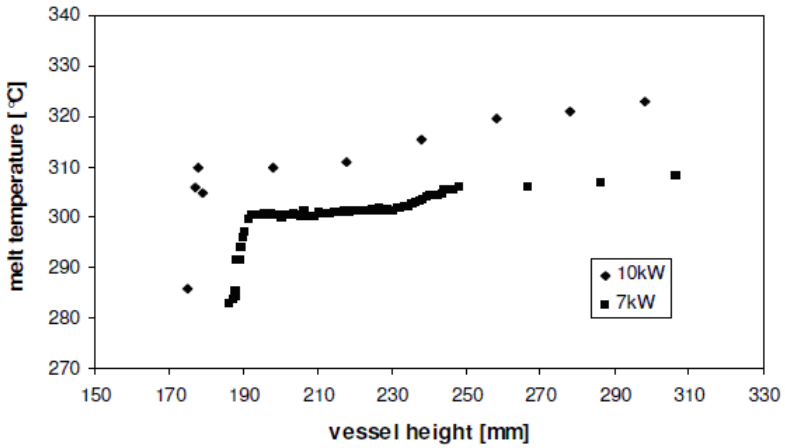

Figure 2-5. Steady- state axial temperature profile at polar angle 47° [Gaus-Liu et al., 2010].

Figure 2-5 exhibits a steep temperature gradient within the liquid boundary layer and a weak gradient outside the boundary layer to the melt surface in the molten part (about 10 °C in comparison to a temperature difference of 35 °C ~ 45 °C between the maximum melt temperature ($T_{bulk,max}$) and the liquidus temperature ($T_{liquidus}$ = 285 °C). In the molten part, the melt temperature increases quasi linearly, which is usually observed for volumetrically heated melt cavitys which are insulated at the top [Jahn et Reineke, 1974], [Theofanous et al., 1997], [Bonnet et Garré, 1999].

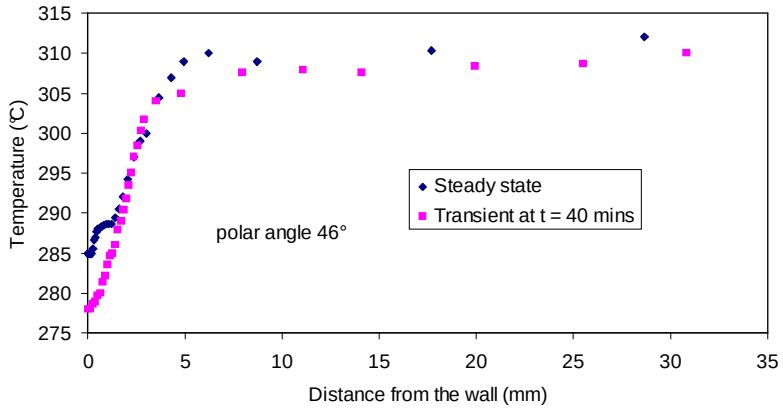

Figure 2-6. Radial melt temperature profile [Gaus-Liu et al., 2010].

Figure 2-6 presents the radial temperature profile near the lateral vessel wall in transient (measured at 40 minutes from the test beginning) and at steady state. It is seen that a boundary layer always exists in a small region of 5 ~ 7 mm thickness beside the vessel wall. A significant temperature gradient is obtained in this region. Outside of the boundary layer, the melt temperature is radially uniform. Additionally, it is observed that at t = 40 minutes, the wall temperature is 278 °C which is close to the liquidus temperature of the melt (285 °C) while it is exactly 285 °C in steady state. Therefore, it is reasonable to consider liquidus temperature as interface temperature.

2.3.2 Evolution of local crust thickness

The crust thickness evolutions at three different polar angles (37.6°, 52.9°, 66.9°) in 10 kW phase are illustrated in Figure 2-7.

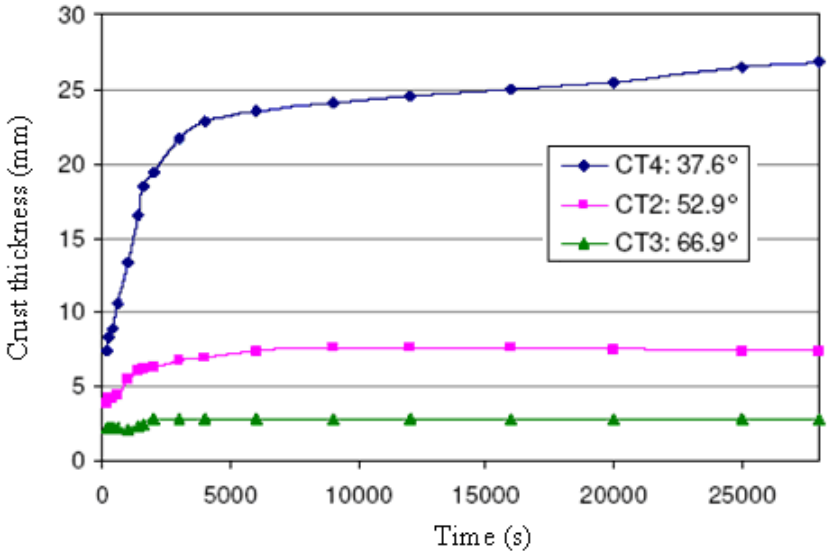

Figure 2-7. Crust thickness evolutions at three polar angles during 10 kW heating power phase in LIVE L3A [Gaus-Liu et al., 2010].

As observed in Figure 2-7, the crust growth period during the 10 kW phase in the lower part of the vessel is longer (at 37.6°, no real stabilization after 5000 s) than in the upper part (at 52.9°, stabilization after about 2000 s and at 66.9°, maximum crust thickness is obtained within only 500 s to 1000 s). The steady state thickness of the formed crust is greater in the lower part than in the upper part (about 27.5 mm at polar angle 37.6°, 8 mm at 52.9° and 2.5 mm at 66.9°).

2.3.3 Heat flux distribution along vessel wall

Calculation of heat flux through the vessel wall was based on the temperature difference between the inner and outer surfaces of the test vessel wall [Gaus-Liu et al., 2010], i.e.

$$\varphi = \lambda_{vessel} \frac{(T_{outer} - T_{inner})}{e_{vessel}} \frac{r_{inner}}{r_{outer}} \tag{2-1}$$

wherein:

- φ is the heat flux transferred through the vessel wall;
- λ_{crust} is the thermal conductivity of the vessel;
- e_{vessel} is the thickness of the vessel;
- T_{outer} and T_{inner} are respectively the temperature at the outer and inner vessel walls; measured by a set of thermocouples, located at six levels in the melt cavity;
- r_{inner} and r_{outer} are respectively the inner and outer radius of the vessel.

The distribution of the steady state heat flux in both 10 kW and 7 kW power heating periods are shown in Figure 2-8.

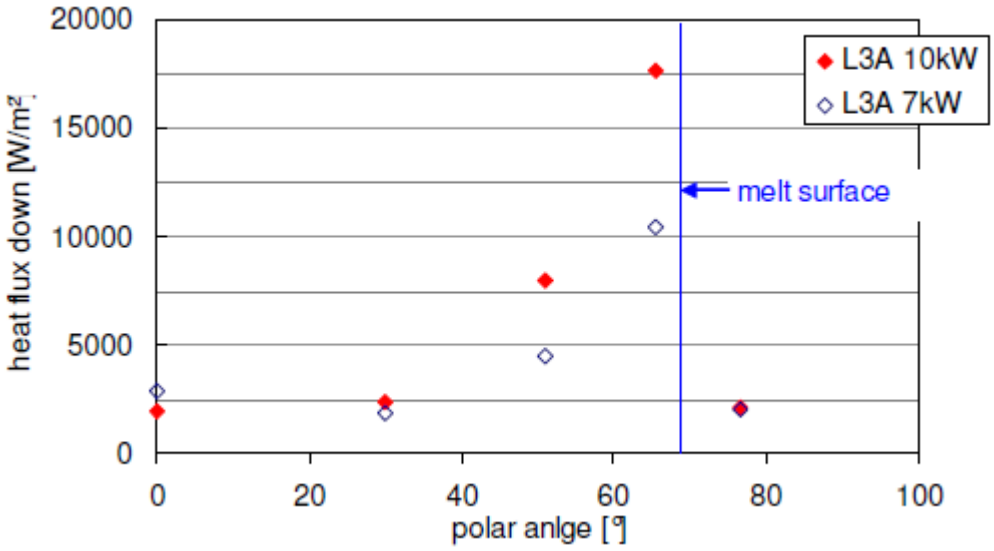

Figure 2-8. Steady state heat flux distribution in LIVE L3A.

It is noted that uncertainty on temperature measurement in the vessel wall would lead to uncertainty in heat flux. As the heat flux at the bottom is the smallest, the temperature difference is small and the maximum uncertainty on the heat flux could be obtained at this position. In fact, the heat flux should decrease continuously at the bottom and the minimum between 20 and 30 degrees polar angle observed in Figure 2-8 is an actually artefact. In any case the heat flux is very low at the bottom of the melt cavity.

2.4 0D modelling of heat transfer & solidification

This section is devoted to propose a physical approach for the description of the transient molten melt cavity thermal-hydraulics. For that purpose, a simplified model approach based on energy conservation will be used to assess the main physical aspects, including melt temperature evolution and transient solidification of the solid crust at the interface.

2.4.1 Model for melt temperature evolution

Main assumptions

To evaluate the evolution of the melt temperature, a control volume is defined which contains the liquid melt and the heating system. The energy balance for the considered control volume will be established using the following main assumptions:

- The physical properties of liquid melt in the melt cavity are supposed to be constant since the liquid melt temperature varies in a limited range from 350 °C to 310 °C; the thermal inertia of the internal heating device it is negligible compared to that of the liquid melt cavity;
- The variation of the mass of liquid melt in the melt cavity is negligible (M_{bulk} = constant) as the mass of solidified liquid is small in comparison to the total mass of the liquid melt cavity;
- The liquid-solid interface or the mush-liquid interface behaves like a no-slip boundary for the flow, the liquid velocity is equal to zero at that interface;

- The liquid-solid or mush-liquid interface temperature T_i during the transient is taken as the liquidus temperature of the final melt ($T_{liquidus}$) (which is in fact the final steady state temperature at the interface, the pertinence of this assumption will be further discussed later) [Seiler, 1996]; [Seiler et Froment, 2010], [Combeau et al; 2010];
- The variation of the solute concentration in the melt cavity notably due to macro-segregation during crust formation is assumed to be negligible as the volume of the solidified crust is small compared to the liquid melt volume;
- The melt temperature in the melt cavity is radially uniform at each melt cavity level (melt cavity height) and there is a stratified temperature distribution in the melt cavity. The time evolution of the average melt temperature difference ($\Delta\overline{T}_{bulk} = \overline{T}_{bulk} - T_i$) is assumed to be proportional to the variation of the maximum melt temperature difference ($\Delta T_{bulk,\max} = T_{bulk,\max} - T_i$) by a coefficient k_T. Since the measured axial temperature gradient in the melt cavity is linear and the slope of the axial temperature gradient is proportional to the volumetric power dissipation in the melt cavity which was adjusted to be constant during the test, coefficient k_T is supposed to be constant and time independent (i.e. $\Delta\overline{T}_{bulk} = k_T \Delta T_{bulk,\max}$ with an average value k_T = 0.8, determined from experimental data) [Gaus-Liu et al., 2010];
- The heat transfer at the interface between the liquid melt cavity and the solid crust is characterized by a surface averaged heat transfer coefficient $\overline{h}_{bulk}$ and an average heat flux $\overline{\varphi}$.

Assumptions b, d and g enable to solve separately the thermal-hydraulic behaviour of the melt cavity from the problem of crust growth.

Basic equations

With the above assumptions, the melt cavity energy balance can be written as:

$$k_T M_{bulk} C_{p,liquid}^{bulk} \frac{d\Delta T_{bulk,\max}}{dt} = \dot{Q}_{add} - \overline{\varphi}\, S_{lateral} \tag{2-2}$$

in which:

- $\dot{Q}_{add}$ is the power dissipation in the melt cavity;
- $S_{lateral} = \int_S dS = \int_{\theta_{\min}}^{\theta_{\max}} 2\pi r_{inner}^2 \sin\theta\, d\theta = 2\pi r_{inner}^2 (\cos\theta_{\min} - \cos\theta_{\max})$ wherein $S_{lateral}$ is the lateral surface of the melt cavity; θ_{min} and θ_{max} are the minimum and maximum polar angles of the melt cavity, respectively; whereas, H and r_{inner} are the height and the inner radius of the melt cavity (Figure 2-9);
- $\overline{\varphi} = \overline{h}_{bulk}\, \Delta T_{bulk,\max}$.

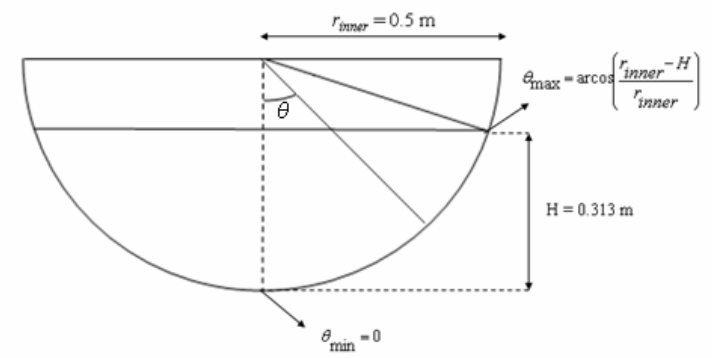

Figure 2-9. Definition of test vessel polar angle.

The average heat transfer coefficient is deduced from a natural convection correlation in which Nusselt number is written in the form of either internal Rayleigh number ($Nu = a' Ra_{in}^{b'}$) or external Rayleigh number ($Nu = a\, Ra_{ex}^{b}$). *a'* and *b'* are the coefficients taken from Nusselt number correlations written in terms of internal Rayleigh number [Mayinger et al., 1975], [Theofanous et al., 1997], [Bonnet et Garré, 1999]. An original methodology describing the link between coefficients *a*, *b*, *a'* and *b'* is detailed in Appendix 1. This methodology has seemingly not been published previously and is of interest for the transformation of known correlations and for the cross-check of correlations.

$$Nu = a\, Ra_{ex}^{b} = a\left(\frac{g\,\beta_T\,\Delta T_{bulk,\max}\,H^3}{\alpha\,\upsilon}\right)^{b} \tag{2-3}$$

Accordingly, the heat transfer coefficient writes:

$$\bar{h}_{bulk} = \frac{a\,\lambda_{bulk}}{H}\left(\frac{g\,\beta_T\,H^3}{\alpha\,\upsilon}\right)^{b}\Delta T_{bulk,\max}^{b} \tag{2-4}$$

The final form of the energy balance for the melt cavity then reads:

$$k_T\,M_{bulk}\,C_{p,liquid}^{bulk}\frac{d\Delta T_{bulk,\max}}{dt} = \dot{Q}_{add} - \frac{a\,\lambda_{bulk}\,S_{lateral}}{H}\left(\frac{g\,\beta_T\,H^3}{\alpha\nu}\right)^{b}\Delta T_{bulk,\max}^{1+b} \tag{2-5}$$

Taking into account that the average heat transfer coefficient in steady state, $\bar{h}_{stt}$, is written as:

$$\bar{h}_{stt} = \frac{a\,\lambda_{bulk}}{H}\left(\frac{g\,\beta_T\,H^3\,\Delta T_{stt}}{\alpha\nu}\right)^{b} \tag{2-6}$$

wherein ΔT_{stt} is the temperature difference between the maximum melt temperature ($T_{bulk,stt}$) and the interface temperature in steady state (T_i).

Alternatively:

$$\bar{h}_{stt} = \frac{\varphi_{stt}}{\Delta T_{stt}} = \frac{\dot{Q}_{add}}{S_{lateral}\,\Delta T_{stt}} = \frac{\dot{Q}_{add}}{2\pi r_{inner}^2(\cos\theta_{\min} - \cos\theta_{\max})\,\Delta T_{stt}} \tag{2-7}$$

wherein φ_{stt} is the average heat flux transferred from the melt cavity through the liquid-solid interface in steady state:

$$\varphi_{stt} = \frac{\dot{Q}_{add}}{S_{lateral}} \tag{2-8}$$

Then, a non-dimensional form of Equation (2-5) can be derived:

$$\frac{dY}{dt^*} = 1 - Y^{1+b} \tag{2-9}$$

wherein:

- $Y = \frac{\Delta T_{bulk,\max}}{\Delta T_{stt}}$ is the non-dimensional temperature difference between the melt and the liquid-solid interface. As the melt is initially superheated, Y is initially greater than 1.
- $t^* = \frac{t}{\tau_{TH}}$ is a non-dimensional time, $\tau_{TH} = \frac{k_T\, M_{bulk}\, C_{p,liq}^{bulk}\, \Delta T_{stt}}{\dot{Q}_{add}}$ called the characteristic thermal hydraulic time delay (the time necessary for heating adiabatically the melt cavity from the interface temperature to the steady state temperature).

Solving the energy balance equation in dimensional form (Equation (2-9)) or in non-dimensional form (Equation (2-5)) provides the evolution of the maximum melt temperature in the melt cavity ($T_{bulk,max}(t)$).

2.4.2 Model for crust thickness evolution

Main assumptions

During the solidification of the melt, a solid crust with thickness $z_{crust}(t)$ forms. The energy balance equation over the solid crust will be established under the following assumptions:

- The heat transfer through the solid crust and the vessel is purely conductive;
- The heat transfer is calculated under the assumption of successive steady state conductive heat transfer;
- The liquid-solid interface is either a planar front or a mushy zone. In both cases the interface temperature is taken at the liquidus temperature corresponding to the liquid melt composition. In case of solidification processing with a mushy zone this corresponds to the temperature at the tip of the primary arms of the dendrites and in case of a planar front it corresponds to a strong stirring intensity of the liquid ahead of the bulk. Thus , $T_i = T_{liquidus} =$ 285 °C;
- The temperatures on the external surface of the vessel (T_{outer}) is supposed to stay constant;

- Between the solid crust and the stainless steel wall, a gap is supposed to be formed (Figure 2-10). The thickness, thermal conductivity and heat transfer coefficient through this gap are assumed to be constant and are respectively noted as e_{gap}, λ_{gap} and h_{gap} where $h_{gap} = \frac{\lambda_{gap}}{e_{gap}}$;

- The total heat transfer coefficient between melt-crust interface and outer vessel surface at polar angle θ is $h_{crust\_vessel}(\theta)$, with $\frac{1}{h_{crust\_vessel}(\theta)} = \frac{z_{crust}(\theta)}{\lambda_{crust}} + \frac{1}{h_{gap}} + \frac{e_{vessel}}{\lambda_{vessel}}$;

- The physical properties of crust, gap and steel wall are constant and furthermore we will suppose that the properties of the crust are equal to the melt properties;

- The thickness of the crust is supposed to be small in comparison to the radius of the vessel;

- The local heat transfer coefficient h_{local} at the melt cavity boundary is assumed to be proportional to the average heat transfer coefficient by a coefficient $f(\theta)$ which is a function of the polar angle θ. This coefficient is derived from the LIVE L3A results by using the experimental data of the heat flux distribution in steady state as given in Figure 2-8. As mentioned in Equation (2-8), the average steady state heat flux is $\varphi_{stt} = \frac{\dot{Q}_{add}}{S_{lateral}}$. Knowing that $\varphi_{stt} = \bar{h}_{stt}\Delta T_{stt}$ and $\varphi_{stt}(\theta) = h_{stt}(\theta)\Delta T_{stt}$, then $f(\theta) = \frac{\varphi_{stt}(\theta)}{\varphi_{stt}} = \frac{h_{stt}(\theta)}{\bar{h}_{stt}}$. As a consequence, the values of $f(\theta)$ for different polar angles are deduced. An interpolation has been done as shown in Figure 2-11 and Figure 2-12 in order to approach $f(\theta)$ along the melt cavity lateral wall for both 10 kW and 7 kW heating powers.

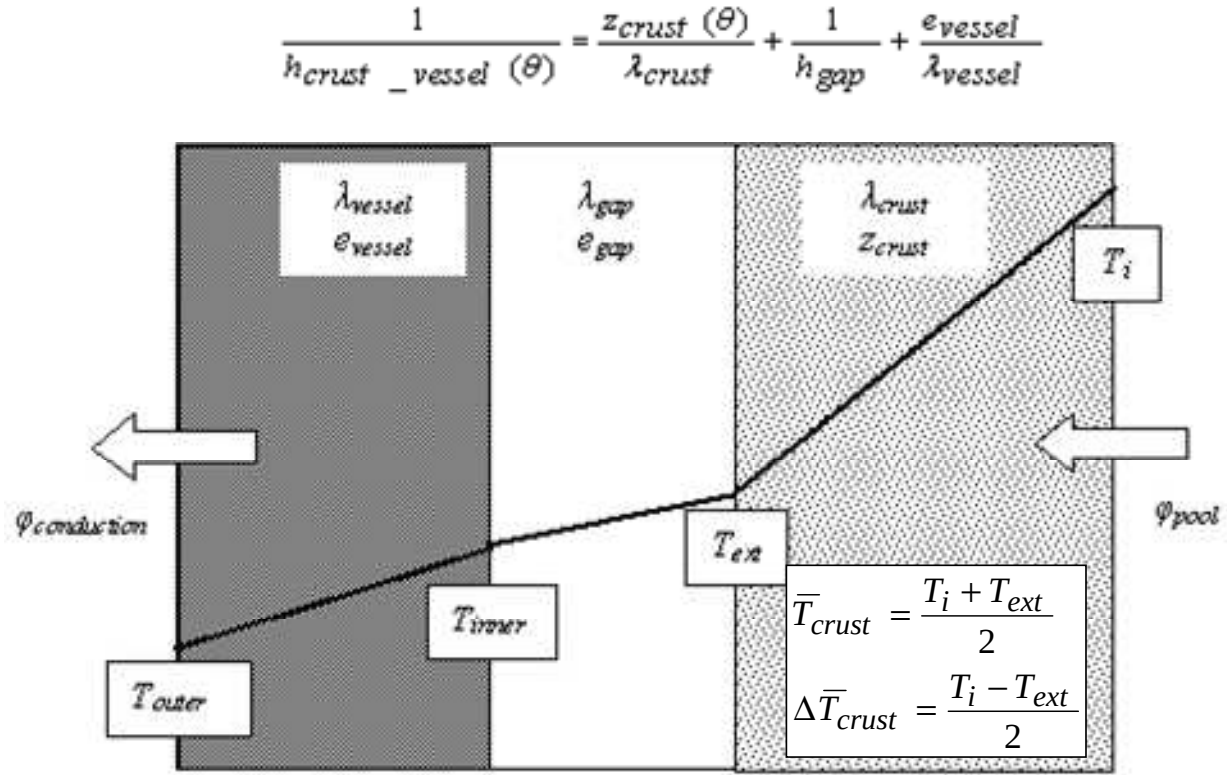

Figure 2-10. Temperature gradient in solid crust, gas gap and vessel wall.

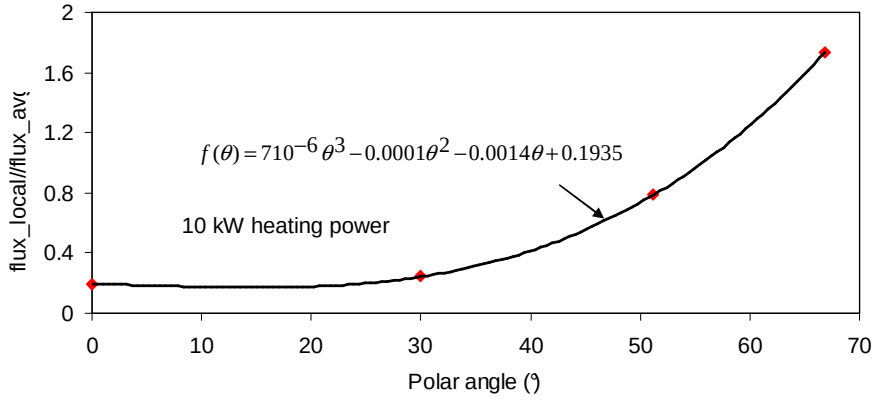

Figure 2-11. Ratio between local heat flux and average heat flux in steady state in 10 kW power heating phase during LIVE L3A.

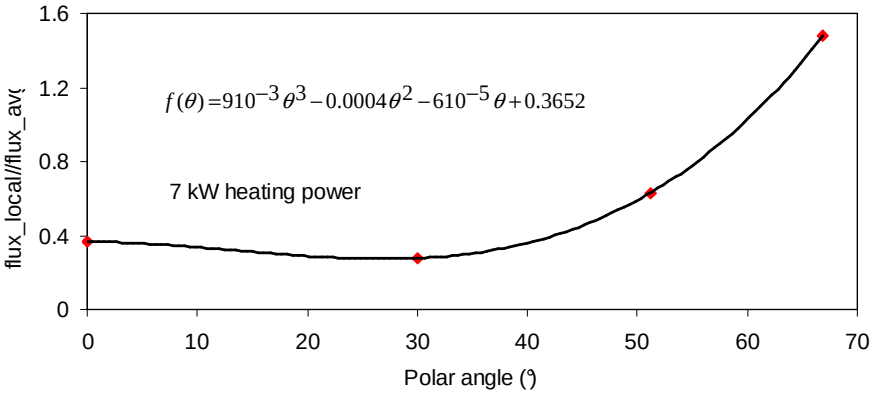

Figure 2-12. Ratio between local heat flux and average heat flux in steady state in 7 kW power heating phase during LIVE L3A.

Energy balance at the melt-crust interface

With preceding assumptions, the energy balance over the local thickness of solid crust is written as follows:

$$\frac{d}{dt}\left[\rho_{crust}\, z_{crust}(\theta)\, H_{crust}(\theta)\right] = \varphi_{local}(\theta) - \varphi_{conduction}(\theta) + \rho_{bulk}\frac{dz_{crust}}{dt} H_{add} \qquad (2\text{-}10)$$

in which :

- $\rho_{crust}\ z_{crust}(\theta)$ is the mass per unit surface of the formed solid crust at polar angle θ;
- ρ_{crust} is the density of solid crust, supposed to be that of liquid melt ρ_{bulk}, i.e. $\rho_{crust} = \rho_{bulk}$;
- The thermal conductivity of the solid crust and liquid melt are assumed to be the same, *i.e.* $\lambda_{crust} = \lambda_{bulk}$;
- $z_{crust}(\theta)$ is the local thickness of the solid crust at polar angle θ;

- H_{crust} is the crust enthalpy averaged over the solid crust thickness and is calculated by $H_{crust} = H_{ref} + C_{p,solid}^{crust}(\overline{T}_{crust} - T_{ref})$ where $C_{p,solid}^{crust}$ is the specific heat of the solid crust $\overline{T}_{crust}$ is the average temperature of the crust;
- H_{add} is the enthalpy of the added crust at liquid-solid interface at temperature T_i, $H_{add} = L_{solidification}^{melt} + H_{ref} + C_{p,solid}^{crust}(T_i - T_{ref})$ wherein $L_{solidification}^{melt}$ is the latent heat of solidification;
- $\varphi_{local}(\theta) = h_{local}(\theta)\Delta T_{bulk,\max} = f(\theta)\overline{h}_{stt}\Delta T_{bulk,\max}$ is the local heat flux transferred from the melt cavity through the liquid-solid interface at polar angle θ;
- $\varphi_{conduction}$ is the heat flux lost due to conduction from the solid crust through the vessel outer surface, $\varphi_{conduction}(\theta) = h_{crust\_vessel}(\theta)\Delta T_{crust\_vessel} = h_{crust\_vessel}(\theta)(T_i - T_{outer})$.

Equation (2-10) becomes:

$$\rho_{crust} H_{crust} \frac{dz_{crust}(\theta)}{dt} + \rho_{crust} z_{crust} \frac{dH_{crust}}{dt} = \varphi_{local}(\theta) - \varphi_{conduction}(\theta) + \rho_{bulk} H_{add} \frac{dz_{crust}(\theta)}{dt} \tag{2-11}$$

For purpose of simplification, the enthalpy variation of the solid crust is neglected, i.e. $\frac{dH_{crust}}{dt} = 0$. This would really be the case if the heat transfer resistance due to the gap and to vessel wall is small compared to the heat transfer resistance associated to the solid, $T_{ext} = T_{outer}$, $\overline{T}_{crust} = \frac{T_i + T_{ext}}{2}$. Since T_i and T_{outer} are constant, then $\frac{dH_{crust}}{dt} = 0$.

Equation (2-11) is now simply rewritten as:

$$\rho_{crust}(H_{crust} - H_{add})\frac{dz_{crust}(\theta)}{dt} = \varphi_{local}(\theta) - \varphi_{conduction}(\theta) \tag{2-12}$$

or:

$$\rho_{crust}\Delta H_m \frac{dz_{crust}(\theta)}{dt} = \varphi_{conduction}(\theta) - \varphi_{local}(\theta) \tag{2-13}$$

in which:

$$\Delta H_m = -(H_{crust} - H_{add}) = L_{solidification}^{melt} + \frac{1}{2} C_{p,solid}^{crust}\Delta T_{crust} \tag{2-14}$$

The heat flux lost due to conduction will be:

$$\varphi_{conduction}(\theta) = h_{crust\_vessel}(\theta)\Delta T_{crust\_vessel} \tag{2-15}$$

in which:

$$h_{crust\_vessel}(\theta) = \frac{\lambda_{crust}}{z_{crust} + e_{gap}\frac{\lambda_{crust}}{\lambda_{gap}} + e_{vessel}\frac{\lambda_{crust}}{\lambda_{vessel}}} \tag{2-16}$$

or:

$$\varphi_{conduction}(\theta) = \frac{\lambda_{crust}\,(T_i - T_{outer})}{z_{crust}(\theta) + e_{gap}\,\dfrac{\lambda_{crust}}{\lambda_{gap}} + e_{vessel}\,\dfrac{\lambda_{crust}}{\lambda_{vessel}}} \tag{2-17}$$

We define now: $z^*_{crust}(\theta) = z_{crust}(\theta) + e_{gap}\,\dfrac{\lambda_{crust}}{\lambda_{gap}} + e_{vessel}\,\dfrac{\lambda_{crust}}{\lambda_{vessel}}$ as the equivalent thickness of the crust, gap and vessel including the formed solid crust, the gap and the vessel.

With the formulation of the average heat transfer coefficient presented previously, the energy balance over the solid crust thickness is rewritten locally at a polar angle θ as follows:

$$\rho_{bulk}\;\Delta H_m\,\frac{dz_{crust}(\theta)}{dt} = \frac{\lambda_{crust}\;\Delta T_{crust\_vessel}}{z^*_{crust}} - f(\theta)\,\frac{a\;\lambda_{bulk}}{H}\left(\frac{g\;\beta_T\;H^3}{\alpha\,\nu}\right)^b Y^{1+b}\Delta T_{stt}^{1+b} \tag{2-18}$$

In steady state, the local steady state heat flux at polar angle θ is obtained from:

$$\varphi_{stt}(\theta) = f(\theta)\,\frac{a\;\lambda_{bulk}}{H}\left(\frac{g\;\beta_T\;H^3}{\alpha\,\nu}\right)^b Y^{1+b}\Delta T_{stt}^{1+b} \tag{2-19}$$

and the steady state equivalent crust thickness is:

$$z^*_{stt}(\theta) = \frac{\lambda_{crust}\;\Delta T_{crust\_vessel}}{\varphi_{stt}(\theta)} \tag{2-20}$$

For the purpose of transforming Equation (2-18) into a non-dimensional form, two dimensionless parameters are defined:

- Non-dimensional crust thickness: $s = \dfrac{z^*}{z^*_{stt}}$
- Non-dimensional time: $t^{**} = \dfrac{t}{\tau_{sol}}$ in which $\tau_{sol} = \dfrac{\lambda_{crust}\;\rho_{bulk}\;\Delta T_{crust\_vessel}\;\Delta H_m}{(\varphi_{stt})^2}$ is named as the characteristic time for solidification (for crust growth).

Consequently, the non-dimensional energy balance for the crust writes:

$$\frac{ds}{dt^{**}} = \frac{1}{s} - Y^{1+b} \tag{2-21}$$

- Solution for Y = const:

$$t^{**} = -\left[\frac{s}{Y^{1+b}} + \frac{\ln(Y^{1+b}s - 1)}{Y^{2(1+b)}}\right] \tag{2-22}$$

- When $Y \neq$ const, the variable s varies between $\frac{e^*}{z^*_{stt}}$ and unity. The solution of Equation (2-18) (or the equivalent non-dimensional form in Equation (2-21)) provides the evolution of the local crust thickness at different polar angles.

The actual solid crust thickness will be deduced:

$$z_{crust}(\theta) = z^*_{stt}(\theta)\ s - e^* \tag{2-23}$$

or:

$$z_{crust}(\theta) = \frac{\lambda_{crust}\,\Delta T_{crust\_vessel}}{\varphi_{stt}(\theta)}\, s - e^* \tag{2-24}$$

in which: $e^* = e_{gap}\frac{\lambda_{crust}}{\lambda_{gap}} + e_{vessel}\frac{\lambda_{crust}}{\lambda_{vessel}}$ is the equivalent thickness of the vessel and the gap.

2.4.3 Application for LIVE L3A

The developed models have been applied for the test conditions in LIVE L3A in order to evaluate their abilities in describing the evolutions of both the melt temperature inside the melt cavity and the local crust thickness.

Melt temperature evolution

A literature survey presented in Chapter 1 of the current thesis shows that during the last forty years, numbers of Nusselt correlations in terms of internal Rayleigh number have been built for the calculation of heat transfer from the liquid melt cavity to the wall for natural convection in a melt cavity with internal heat dissipation and external cooling in both laminar and turbulent regimes. In the current study, some correlations derived for laminar natural convection in hemispherical configuration have been employed for determination of average heat transfer coefficient from the melt to the curved vessel wall in LIVE L3A (the internal Rayleigh number in 10 kW and 7 kW phases respectively is 2.2 10^{12} and 1.5 10^{12} which belongs to laminar regime). These correlations are listed in Table 2-3 together with their transformed form written in terms of external Rayleigh number (transformation method is described in Appendix 1). The corresponding steady state heat transfer coefficient given by these correlations are also provided for LIVE.

Using the heat transfer coefficient given by Mayinger's correlation, the corresponding temperature difference between the melt and the interface in steady state is 40 °C and 30 °C respectively for 10 kW and 7 kW (average heat transfer coefficient is ~ 250 $W.m^{-2}.°C^{-1}$). Knowing that the steady state maximum melt temperature for these two power dissipating phases are 320 °C and 310 °C respectively, we can deduce the interface temperature of 280 °C for both 10 kW and 7 kW test phases, which is close to the liquidus temperature of the initial melt (285 °C).

Table 2-3. Average heat transfer coefficient from existing natural convection correlations for hemispherical geometry.

Author	Correlation	Transformed correlation	$\overline{h}_{bulk,10\ kW}$ ($W.m^{-2}.°C^{-1}$)	$\overline{h}_{bulk,7\ kW}$ ($W.m^{-2}.°C^{-1}$)
Mayinger's [Mayinger et al., 1975]	$Nu = 0.55 Ra_{in}^{0.2}$	$Nu = 0.59 Ra_{ex}^{0.25}$	249	233
ACOPO [Theofanous et al., 1997]	$Nu = 0.3 Ra_{in}^{0.22}$	$Nu = 0.28 Ra_{ex}^{0.28}$	291	265
Mini ACOPO [Theofanous et al., 1997]	$Nu = 0.048 Ra_{in}^{0.27}$	$Nu = 0.022 Ra_{ex}^{0.37}$	158	144
BALI [Bonnet et Garré, 1999]	$Nu = 0.131\left(\frac{H}{R}\right)^{0.19} Ra_{in}^{0.25}$	$Nu = 0.08 Ra_{ex}^{0.33}$	224	205

Furthermore, in the test report, the authors indicate that the composition of the melt slightly changes during the test (Table 2-4) [Gaus-Liu et al., 2010]. This is due to the higher concentration of refractory species (KNO_3) in the crust. Corresponding to the slight change of the melt composition, the liquidus temperature of the melt cavity was reduced from 285 °C to 278.5 °C, which agrees well with preceding calculated interface temperature of 280 °C.

Table 2-4. Melt composition during LIVE L3A [Gaus-Liu et al, 2010].

	Initial melt	End of 10 kW phase	End of 7 kW phase
$NaNO_3$ % mass	82.371	81.776	80.969
KNO_3 % mass	17.629	18.224	19.031
$T_{liquidus}$ (°C)	283.47	281.36	278.51

If we consider other heat transfer correlations given in Table 2-3, a lower average heat transfer coefficient of ~ 200 W.m-2.°C-1 would lead to an interface temperature of 270 °C, which is still closer to the actual liquidus temperature (~ 280 °C) than to the solidus temperature (~ 230 °C). Thus, we can justify the assumption that $T_i = T_{liquidus}$ when the steady state regime has been reached.

The Mayinger's correlation will be used in this analysis for the evaluation of the transient melt temperature evolution. However, with this correlation the heat transfer coefficient is solely a function of the volumetric power dissipation (internal Rayleigh number) and is only valid for the established thermal hydraulic steady state. It seems straightforward that the heat transfer coefficient cannot be constant versus time. For instance, if we suppose that the initial temperature of the melt is equal to the interface temperature (i.e. liquidus temperature and $\Delta T_{bulk} = 0$), there is no driving force for the boundary layer flow and the average heat transfer coefficient should then be equal to zero. If we express now the Nusselt number as a function of the external Rayleigh number ($Ra_{ex} = \frac{g\,\beta_T\,(T_{bulk} - T_i)\,H^3}{\upsilon\,\alpha}$), the effect of the temperature difference between the melt and the interface can be taken into account. Hence, for the purpose of evaluating the transient evolution of melt temperature, Mayinger's correlation has been re-written, on a physical basis (Appendix 1) as a function of the external Rayleigh number ($Nu = 0.59\,Ra_{ex}^{0.25}$). Coefficients *a* and *b* in Equation (2-5) are 0.59 and 0.25, respectively.

The temperature of the melt in the furnace is initially 350 °C. However, when the melt falls into the test section, the temperature may rapidly change because of the heating up of the instrumentation,

heater and associated support structures as well as the transient heat loss to the vessel wall. We can take into account the effect of the heat loss to vessel internal structure by supposing that a new thermal equilibrium is rapidly achieved in the vessel. Taking into account the thermal inertia of these internal structures, the initial melt temperature is reduced to 327 °C. This temperature will be taken as the initial melt temperature for the calculation. The transient heat losses to the vessel wall are governed by the transient heat transfer to the crust, which is supposed to be immediately formed on the vessel wall, and that is included in the model approach.

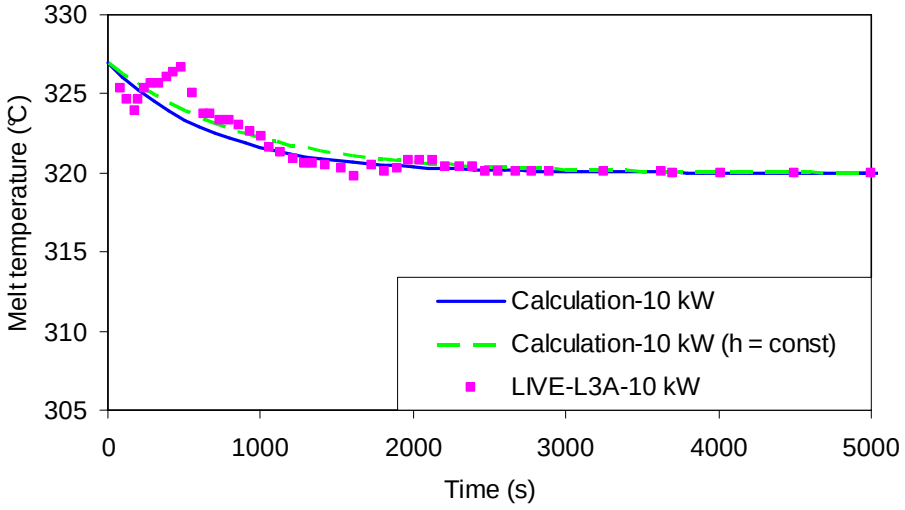

Figure 2-13. Calculation of melt temperature evolution in LIVE L3A in 10 kW phase.

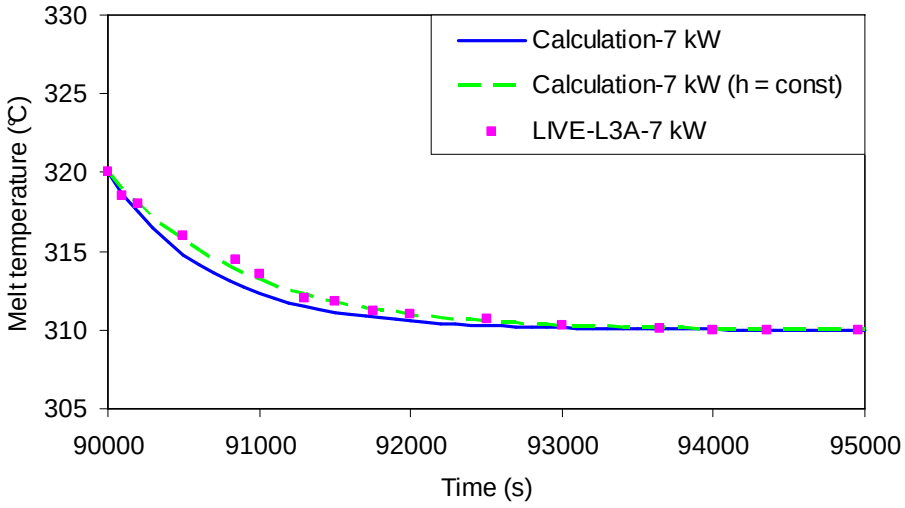

Figure 2-14. Calculation of melt temperature evolution in LIVE L3A in 7 kW phase.

Figure 2-13 and Figure 2-14 show the evolution of the maximum melt temperature during LIVE L3A experiment for both 10 kW and 7 kW dissipating power phases, calculated by the present model. The calculation results have been compared with those obtained from the experiment by KIT. An agreement between calculation and experiment is obtained in terms of the time required for the temperature to reach the steady state (about 3000 s for 10 kW phase and 3700 s for 7 kW phase). The maximum difference between the calculated melt temperature and the experimental one is about 5 °C (at $t \approx 500$ s in 10 kW phase). For the rest period during transient, the difference between calculated and experimental melt temperature is less than 2 °C.

The calculated thermal hydraulic time delay τ_{TH} is about 861 s for 10 kW phase and 879 s for 7 kW phase (with k_T = 0.8). If the heat transfer coefficient was constant ($\bar{h}_{bulk}(t) = \bar{h}_{stt}$), the solution of Equation (2-5) would take an exponential form, i.e. $\Delta T_{bulk} = \Delta T_{bulk,ini} + \left(\Delta T_{stt} - \Delta T_{bulk,ini}\right)\left(1 - e^{-\frac{t}{\tau_{TH}}}\right)$. The related total time delay to reach the steady state would be ~ $4\tau_{TH}$ ($\frac{T_{bulk} - T_{bulk,ini}}{T_{stt} - T_{bulk,ini}}$ ~ 98%), i.e. ~ 3500 s, which is near to the ones determined above. Calculations of the melt temperature evolution with constant heat transfer coefficient for 10 kW and 7 kW periods are given in Figure 2-13 and Figure 2-14. The difference between of melt temperature evolutions obtained by calculation either with varying transient heat transfer coefficient or with a constant heat transfer coefficient (steady state heat transfer coefficient) is not significant.

Crust thickness evolution

Calculation of the evolution of the local solid crust thickness has been done taking into account the heat transfer resistance of the gap existing between the solid crust and the inner vessel wall as well as the thermal resistance of the stainless steel vessel (25 mm thickness). Knowing the experimental heat flux distribution (Figure 2-8), the melt-crust interface temperature, the inner and outer wall temperature of the vessel and the crust thickness distribution from the experimental data, the heat transfer coefficient associated to the gap can be deduced in steady state for 10 kW and 7 kW phases.

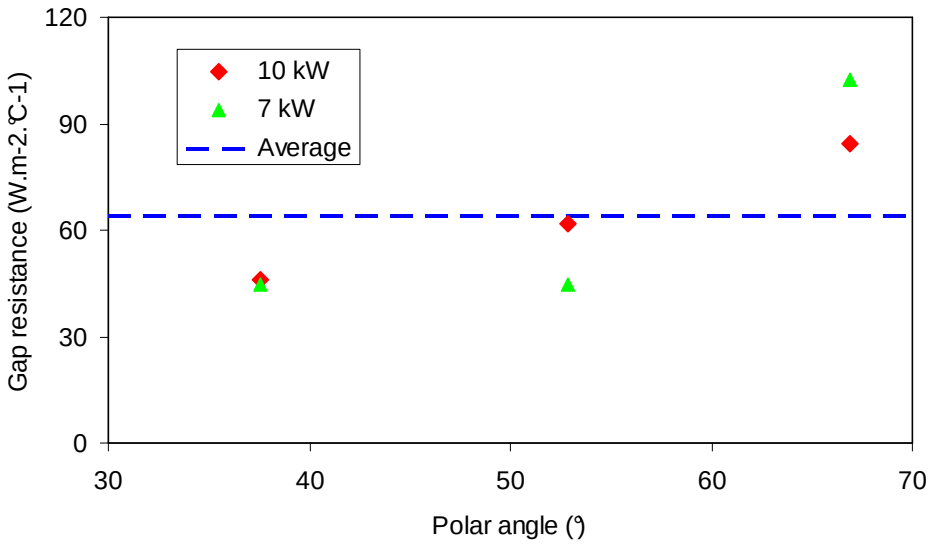

Figure 2-15. Heat transfer coefficient of gas gap.

Figure 2-15 presents the local heat transfer coefficient in the gap with its uncertainties in the two power dissipation phases. It is clearly shown that, at the lower part of the vessel (at polar angles 37.6° and 52.9°), the uncertainties of h_{gap} are smaller than near to the melt surface (at 66.9°). The large uncertainty of h_{gap} at the upper part of the vessel is mainly due to the reduced thickness of the crust in this region. Important is to notice that there exists an overlap associated to the gas gap data that corresponds to an average value of 64 ± 30 $W.m^{-2}.°C^{-1}$ for the three polar angles and for both 10 kW and 7 kW test phases. The fact that the gas gap has a constant heat transfer coefficient helps to justify the assumption of its existence. The calculated heat transfer coefficient would correspond to an

average gap thickness of about 0.5 mm if we suppose that the gap is filled with gas and that heat transfer through this gas gap is by conduction only (as assumed in the previous section).

Taking this value into account, Figure 2-16 depicts the calculated growth process of crust thickness at three polar angles (37.6°, 52.9° and 66.9°) during the 10 kW test phase obtained from the developed model calculation together with the experimental data. It is shown that the model well describes the crust growth process. Besides, both experiment and calculations demonstrate that the time required for the stability of the crust thickness is longer near the bottom of the melt cavity and higher at the upper part. Near the bottom, at 37.6°, the crust thickness keeps on increasing after 4000 s ~ 5000 s. At 52.9°, it stabilizes after ~ 2000 s. Near to the melt surface, at 66.9°, the crust thickness reaches the steady state value very rapidly (~ 500 s to 1000 s) after the test initiation.

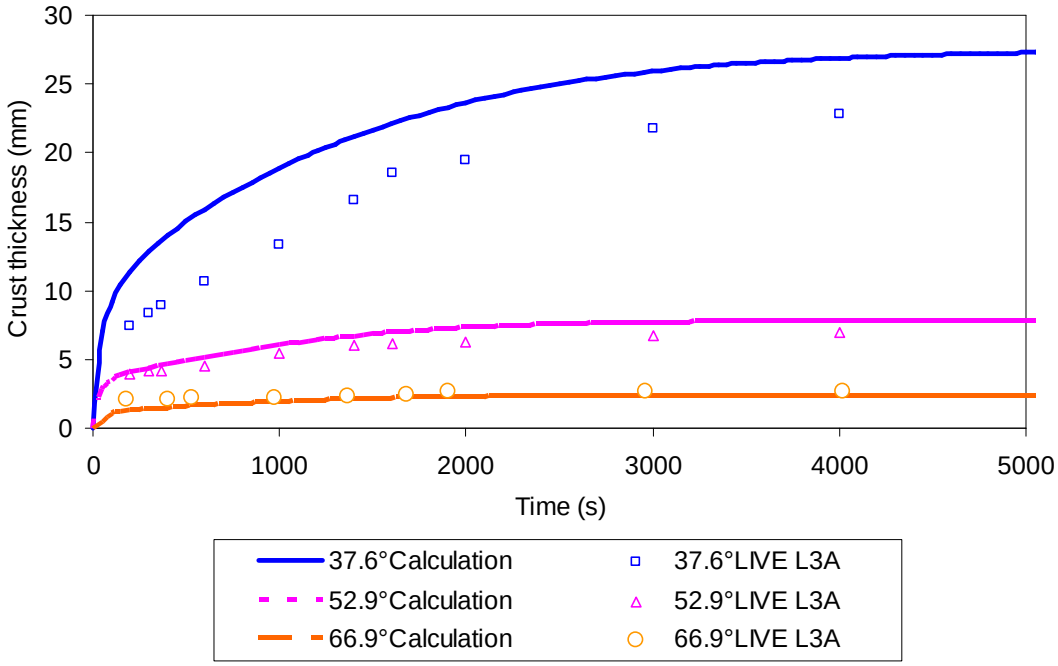

Figure 2-16. Crust thickness evolution in 10 kW phase.

Table 2-5. Solidification characteristic time for LIVE L3A during 10 kW phase.

Polar Angle	τ_{sol_10kW}	$\tau_{crust,real}$	$\tau_{crust,\exp}$
(°)	(s)	(s)	(s)
37.6	1189	4755	~ 5000
52.9	249	1000	2000
66.9	100	400	500 to 1000

In addition, due to the model of crust thickness evolution, the calculation of the local time characteristic for crust growth at different polar angles has been conducted and the results are given in Table 2-5 for 10 kW phase. The related time delay for the crust growth steady state is $\tau_{crust,real} = 4\tau_{sol}$ due to the exponential form of the solution.

The crust thickness at steady state during 7 kW phase is given in Table 2-6 and the corresponding solidification characteristic time delay is shown in Table 2-7.

Table 2-6. Steady state crust thickness in 7 kW phase.

Polar angle	Calculated z_{stt}	Experimental z_{stt}
(°)	(mm)	(mm)
37.6	42.86	41 ± 5
52.9	14.94	16.5 ± 5.5
66.9	7.09	7.5 ± 5

Table 2-7. Solidification characteristic times for LIVE L3A for 7 kW phase.

Polar Angle	τ_{sol_7kW}	$\tau_{crust,real}$
(°)	(s)	(s)
37.6	2008	8000
52.9	733	2900
66.9	177	800

As shown in Table 2-6, the calculated steady state crust thicknesses at different melt cavity levels for 7 kW phase taking into account the gap resistance are in agreement with the experimental ones. This again confirms the existence of the gap.

In addition, there is a relation between the thickness of the crust and the solidification characteristic time to the heat flux in each power dissipation phase. Indeed, since the heat flux transferred is lower during 7 kW phase, the crust obtained in this phase is thicker than in 10 kW phase because the thickness of the crust is proportional to the $1/\varphi_{stt}$. Moreover, the time required for crust formation is proportional to $1/\varphi_{stt}^2$, as consequences, the crust forms in a shorter time delay in 10 kW phase than in 7 kW phase.

2.4.4 Prediction of solidification regime

Review of solidification models

In the literature, there exist some investigations on the interface temperature during solidification of liquid melt when it contacts with a cooled solid wall as discussed in Chapter 1. Two situations can be encountered during the crust formation due to melt solidification. The first one is that solidification proceeds with a planar front and the second one is that with a mushy zone. Main conclusions from existing solidification models will be recalled below for the estimation methodology of the solidification regimes.

Planar front model

The physical model introduced by [Rutter et Chalmers, 1953] and developed by [Mullins et Sekerka, 1964] and [Hurle, 1976] leads to a conclusion that solidification due to contact of a liquid melt with a solid wall could process with a planar front at the liquid-solid interface. In addition, the model proposes a criterion for solidification rate which allows estimating the planar front stability, named as constitutional supercooling criterion.

Initially, ancient model accounted only solute diffusion for mass transfer in the boundary layer existing ahead the interface. As a result, interface temperature is the solidus temperature of the melt [Mullins et Sekerka, 1964]. [Hurle, 1976] improved the model by taking into account both diffusion and convection for mass transport. This results in a modified factor of $1/k$ in the so-called constitutional supercooling condition. In this situation, interface temperature stays in between the solidus and liquidus temperatures of the melt.

Determination of the interface temperature during planar front solidification is predicted by the formula reported by [Burton et *al*., 1953], in which the interface temperature is dependent on solidification rate and mass transfer boundary layer thickness. In the case when the solidification rate is slow enough or the mass transfer boundary layer existing in front of the liquid-solid interface is thin enough, the interface temperature tends to liquidus temperature [Seiler et Froment, 2000].

Mushy zone model

[Combeau et al. 2010] have studied the liquid-solid interface behaviour during transient freezing of non-eutectic melt cavity with internal power dissipation. This work demonstrates that at the initiation of solidification, planar front has not yet established and a mushy zone containing solid and liquid phases would form at the liquid-solid interface. The heat transfer in mushy zone is mainly governed by conduction while the mass transfer is controlled by solute diffusion and/or convection in the liquid phase. During the mushy zone solidification, the tip of the dendrites in the mushy zone is close to the liquidus temperature relative the melt composition. Due to diffusion and solute convective mass transport of solute, the mushy zone fills and will disappear at the end of solidification. The work gives a theoretical approach to determine the time delay for mushy zone evolution to reach planar front situation.

Table 2-8 summarizes the results of existing solidification models which have been presented in the above.

In reality, it is also possible to have during the process of the crust formation a transition between a mushy zone to a planar front. In fact, solidification starts first with higher solidification rate and, ultimately when the steady state regime is approached, with much lower solidification rate. In the final thermal hydraulic steady state, the solidification rate is equal to zero. This basically implies that solidification can proceed with a mushy zone at the beginning and come to plane front as the thermal hydraulic steady state is approached.

For the purpose of solidification regime determination, following questions are addressed:

- If a mushy zone forms during solidification, then how long will it take to fill up this zone?
- In case of a transition between a mushy zone to a planar front, it is required to precise the moment at which such transition between the two solidification regimes occurs.

Table 2-8. Solidification models.

Mushy zone filling	Planar front	
	Diffusion controlled	Diffusion and convection controlled
$C_{L,i} = C_{bulk}$	$C_{L,i} = \frac{C_{bulk}}{k}$	$C_{L,i} = C_{bulk}\,\frac{e^{\Delta}}{1-k(1-e^{\Delta})}$ $\Delta = \frac{\delta_{MT}\,V_{sol}}{D_L}\,;\ \delta_{MT} = H(Sc\,Gr)^{-1/3}$
$T_i = T_{tip} = T_{liquidus}(C_{bulk})$	$T_i = T_{solidus}(C_{bulk})$	$T_{solidus}(C_{bulk}) \le T_i \le T_{liquidus}(C_{bulk})$ $V_{sol} \to 0$ then $T_i \to T_{liquidus}(C_{bulk})$
$\tau_{MT,filling} = \frac{\Delta T_{SL}^{\ 2}}{G_S^{\ 2} D_L}\left(\frac{1+k}{2}\right)$	$\frac{G_L}{V_{sol}} \Big/ \frac{-m_L C_{bulk}(1-k)}{D_L} \ge \frac{1}{k}$	$\frac{G_L}{V_{sol}} \Big/ \frac{-m_L C_{bulk}(1-k)}{D_L} \ge 1$ (limit case for a strong stirring of the liquid phase)

Determination of solidification regime in LIVE L3A

In the preceding, the developed models propose a physical basis for the description of the transient melt cavity thermal-hydraulics behaviour in LIVE L3A in terms of the melt temperature evolution and the transient formation of the crust at the liquid-solid interface by imposing the liquidus temperature of the actual melt as the liquid-solid temperature for the whole transient. In this part, these conditions of melt temperature and crust evolutions obtained from the thermal hydraulic model will be used as inputs to investigate the transient solidification behaviour at liquid-solid interface in a deeper manner. Objective is first to figure out the mass transport mechanism that controls the non-eutectic melt solidification during LIVE L3A and then to answer the question of interface temperature evolution.

Firstly, application of the solidification models presented in Table 2-8 will be performed for determination of solidification regime in LIVE L3A.

It is noted that the mass of the solid crust is much smaller than the mass of the liquid melt, therefore, variation of the melt composition during the whole transient is negligible, i.e. $C_{bulk} = C_0$.

Assuming that solidification in LIVE L3A proceeds with a planar front at the interface, then the time delay to reach stable planar front is determined using the above mentioned constitutional supercooling criterion. Since natural convection controls heat transfer in LIVE L3A, it is believed that such flow recirculation also governs the mass transfer in such melt cavity. Therefore, both diffusion and convection would participate in solidification process. Comparisons of the characteristic time delay for stable planar front achievement to the time required for reaching steady state crust thickness (99% of the final crust thickness) at three different polar angles of the melt cavity during 10 kW and 7 kW phases are depicted from Figure 2-17 to Figure 2-22. In all cases, planar front stability is obtained before final steady state of solidification (i.e. $\tau_{PF} < \tau_{99\%}$).

- In the lower region of the melt cavity (37.6°), planar front solidification is reached later in the transient (~ 4400 s in 10 kW phase and ~ 6800 s at 7 kW phase) and practically just before the moment when ~ 99% of the final thickness of the crust is reached (~ 4800 s in 10 kW phase and ~ 7400 s at 7 kW phase);
- In the upper part of the melt cavity (66.9°), planar front is reached much earlier in time (~ 1400 s in 10 kW phase and ~ 1000 s in 7 kW phase) and well before the final crust thickness is reached (~ 3200 s in 10 kW phase and ~ 2800 s in 7 kW phase).

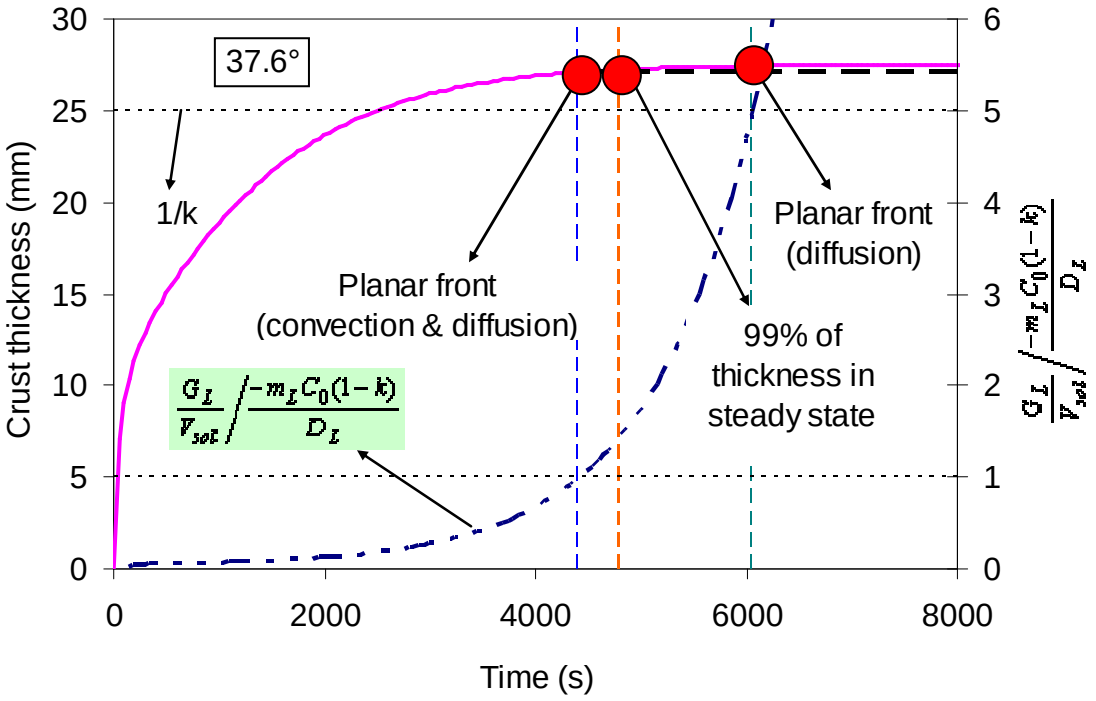

Figure 2-17. Characteristic time delay for planar front at 37.6° in 10 kW phase.

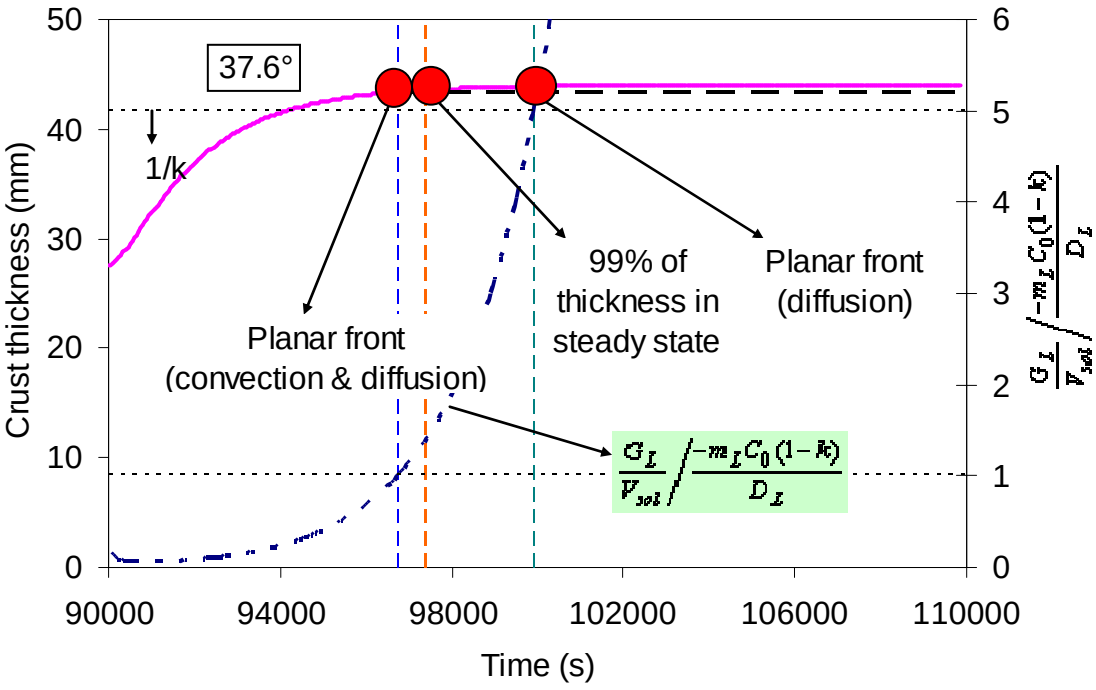

Figure 2-18. Characteristic time delay for planar front at 37.6° in 7 kW phase.

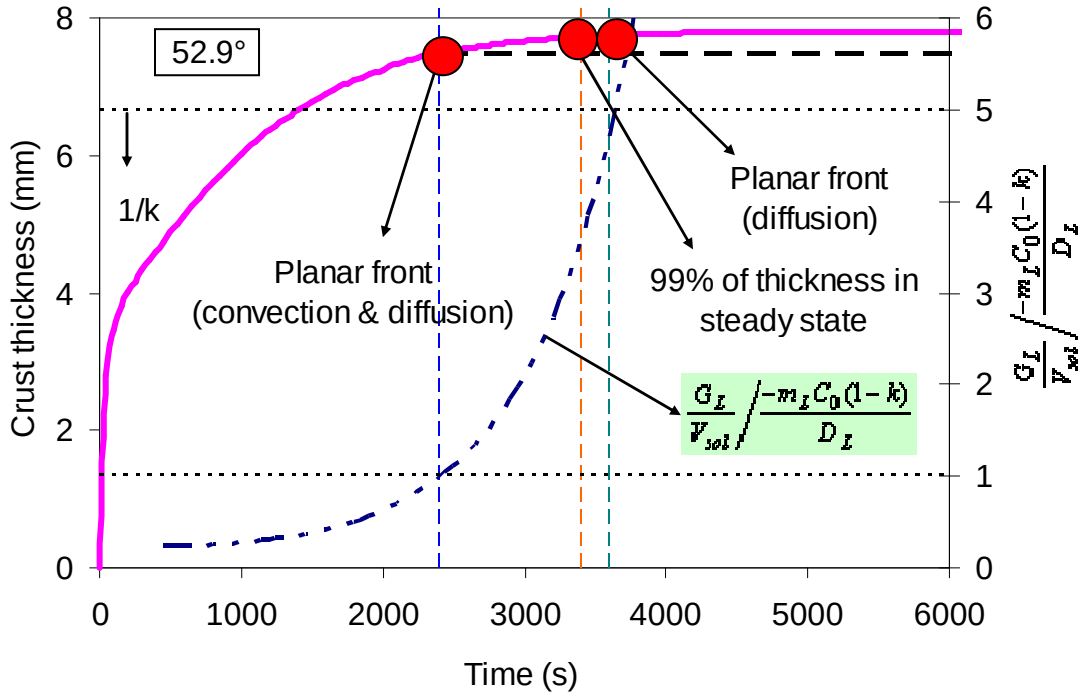

Figure 2-19. Characteristic time delay for planar front at 52.9° in 10 kW phase.

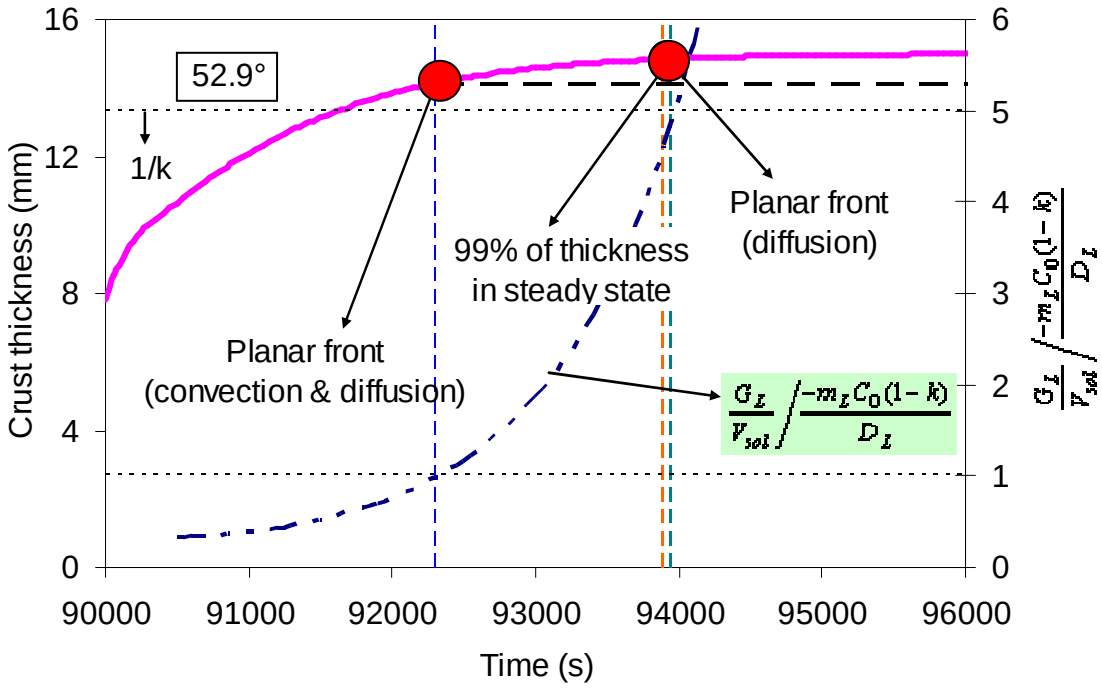

Figure 2-20. Characteristic time delay for planar front at 52.9° in 7 kW phase.

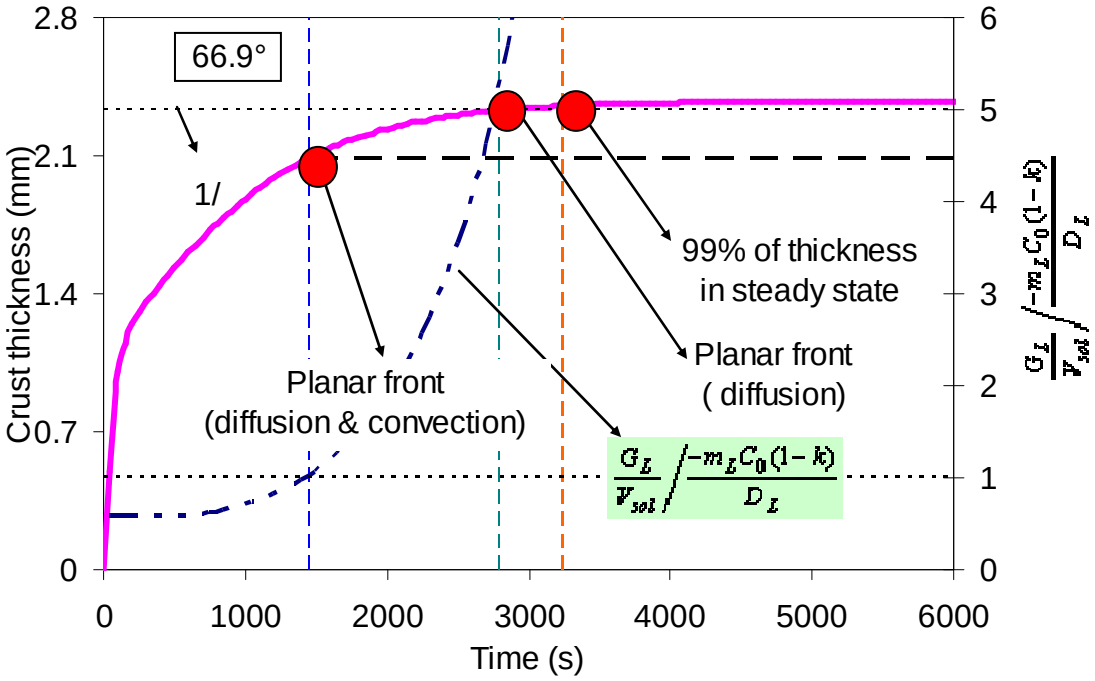

Figure 2-21. Characteristic time delay for planar front at 66.9° in 10 kW phase.

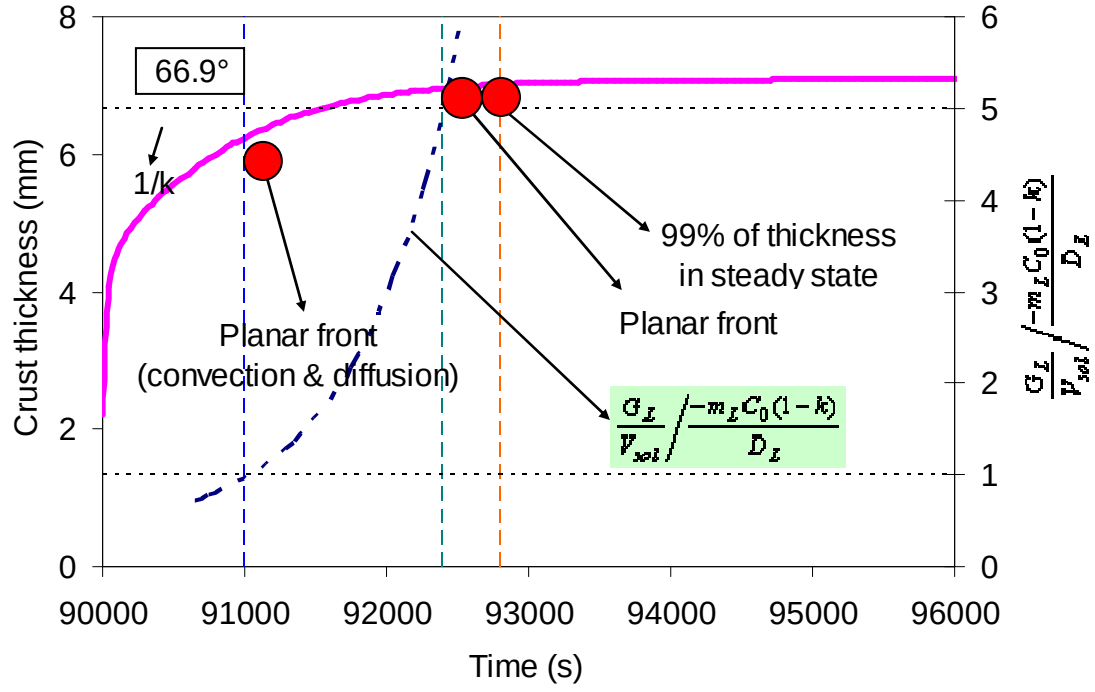

Figure 2-22. Characteristic time delay for planar front at 66.9° in 7 kW phase.

Supposing that the solidification proceeds with a mushy zone, then the time required for filling up of this zone in LIVE L3A is estimated. Calculation results of $\tau_{filling}$ for both 10 kW and 7 kW and comparisons to τ_{PF} and $\tau_{99\%}$ are reported in Table 2-9 and Table 2-10.

Table 2-9. Characteristic time delays in 10 kW phase.

Polar Angle (°)	$\tau_{99\%}$ (s)	τ_{PF} (s)	$\tau_{filling}$ (s)
37.6	4800	4400	5051
52.9	3400	2400	577
66.9	3200	1400	195

Table 2-10. Characteristic time delays in 7 kW phase.

Polar Angle (°)	$\tau_{99\%}$ (s)	τ_{PF} (s)	$\tau_{,filling}$ (s)
37.6	7400	6800	7373
52.9	3900	2300	1638
66.9	2800	1000	186

It is seen that at the upper part of the melt cavity (high heat flux region), the mushy zone is filled up relatively fast. Mushy zone filling up is completed before the solidification rate is low enough for planar front achievement (τ_{PF} is 6 to 8 times longer than $\tau_{filling}$). This means that almost the whole transient of solidification proceeds with a planar front at the liquid-solid interface.

At lower polar angle (37.6°), the time delay for mushy zone filling is a little bit longer than the time required for reaching planar front stability (only several hundreds of seconds in difference). This means that when planar front is reached, mushy zone is not yet completely filled. However, as seen in Table 2-9 and Table 2-10, complement of mushy zone filling occurs almost when 99% maximum crust thickness. This implies that at the steady state of solidification, mushy zone has disappeared.

The above analysis of the relating characteristic time delays comes to a prediction of solidification regime in LIVE L3A. At the initiation of solidification, a mushy zone is formed in front of the solid crust. Over a certain time delay (τ_{PF}), the solidification rate decreases to a critical value that is low enough to satisfy the constitutional supercooling criterion and a planar front is achieved. At this moment, mushy zone will disappear and solidification continues with planar front regime until maximum crust thickness is formed. During the transition from mushy zone to planar front, the mushy zone filling process occurs. At the upper zone of the melt cavity, this filling process might be completed rapidly before planar front obtainment; whereas, at the lower zone, it could be disturbed due to formation of planar front in a time delay less than the time required for mushy zone filling up.

Interpretation to transient liquid-solid interface temperature

Estimation of interface temperature for mushy zone solidification regime ($t < \tau_{PF}$)

According to the mushy zone filling model reported by [Combeau et al., 2010], the liquid-solid temperature is considered as the temperature at the tip of the dendrites. It has been reported that during mushy zone evolution, the tip temperature stays at liquidus temperature of the melt. In fact, tip temperature is strongly affected by convection in the boundary layer existing ahead the mush [Cantor et Vogel, 1977], [Ananth and Gill, 1991]. Globally, presence of convection would reduce significantly the tip undercooling, or, in other words, it could bring the tip temperature closer to the liquidus temperature. Another model for calculating the undercooling at the tip of the dendrites was presented in the work of [Ananth et Gill, 1991]. In the next, calculation with this model with varying Gibbs-Thomson coefficient and different boundary layer liquid velocity conditions will be performed for an alternative prediction of the dendrites' tip temperature during mushy zone solidification.

Figure 2-23 shows that the maximal difference between the temperature of the mushy zone's tip and the liquidus temperature is in the order of 10 °C. A variation of the Gibbs-Thomson coefficient Γ of 3 orders of magnitude does not affect significantly this undercooling. The lowest curve corresponds to $\Gamma = 10^{-6}$ m.°C with the fluid flow effect, for a value of the liquid velocity in the boundary layer U_{BL} = 0.01 m/s. This curve shows that the undercooling is small and that the convective effect is important. In this situation, the tip undercooling is less than 0.1 °C. These results again indicate that during the mushy state in LIVE L3A, the interface temperature stays close to the liquidus temperature.

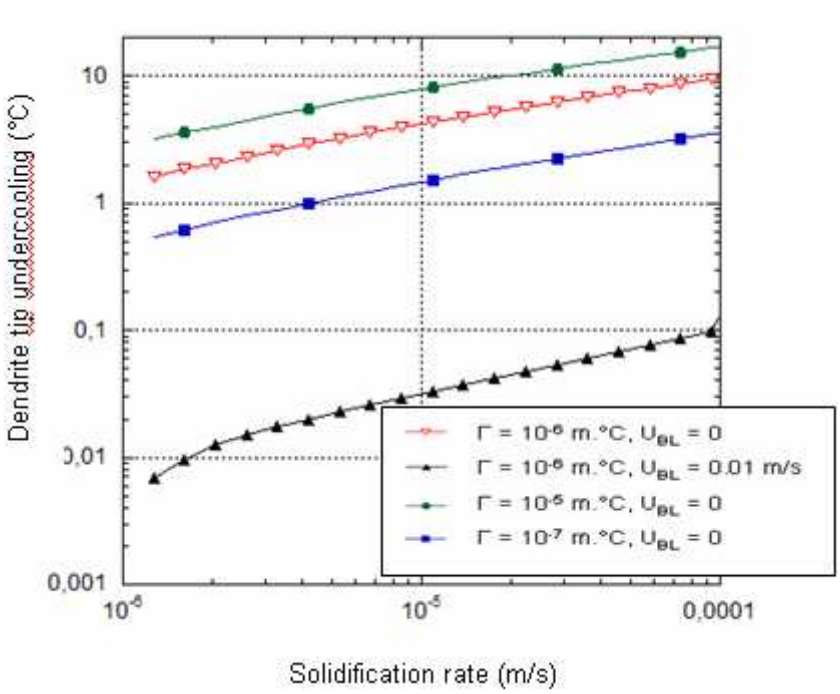

Figure 2-23. Calculation of dendrite tip undercooling by [Ananth et Gill, 1991] model.

Estimation of interface temperature for planar front solidification regime ($t > \tau_{PF}$)

Estimation of interface temperature during planar front regime ($t > \tau_{PF}$) is performed according to the works of [Hurle, 1976] and [Seiler et Froment, 2000]. Results are represented in Figure 2-24 for the 10 kW phase and in Figure 2-25 for 7 kW phase. It is clearly observed that the interface temperature stays closely to the liquidus temperature corresponding to the melt composition ($T_i \approx T_{liquidus}(C_0)$ = 285°C).

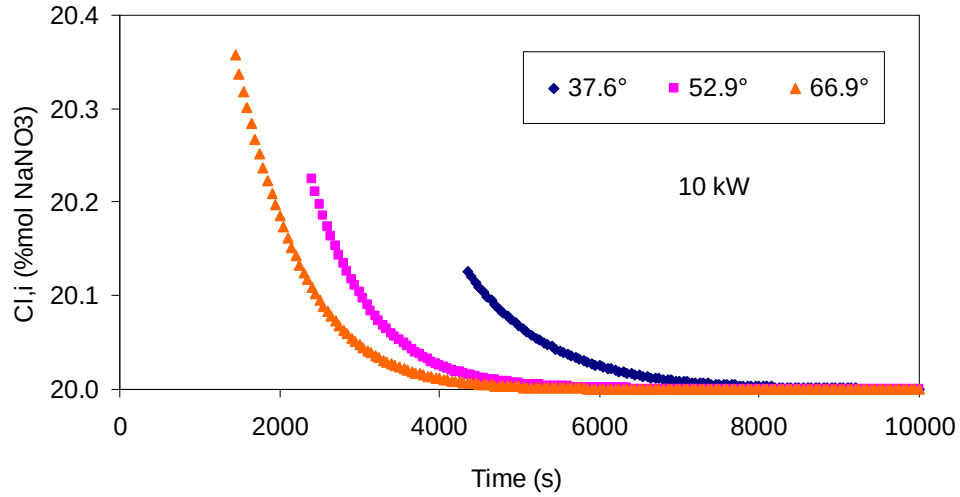

Figure 2-24. Evolution of solute concentration in liquid phase on the interface during planar front solidification regime in 10 kW phase.

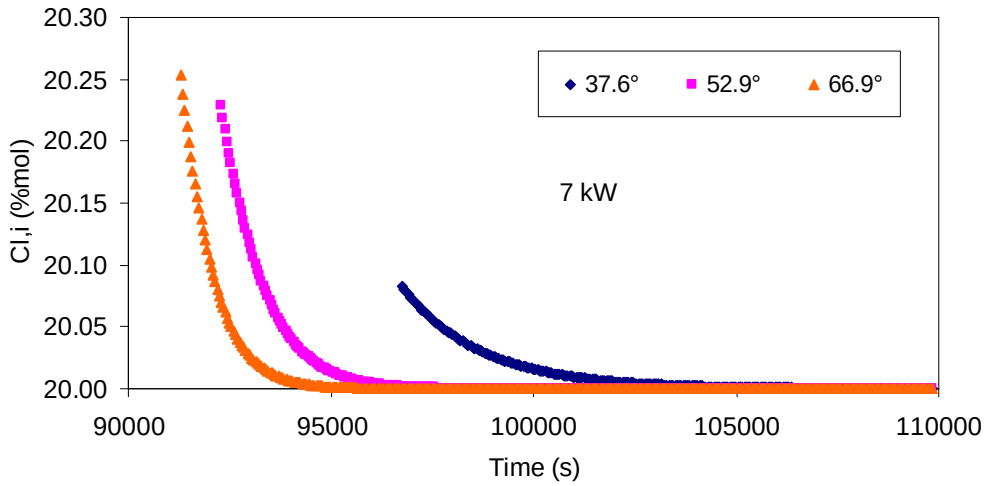

Figure 2-25. Evolution of solute concentration in liquid phase on the interface during planar front solidification regime in 7 kW phase.

2.4.5 Conclusion

The simple developed model allows simulating transient heat transfer and solidification in a melt cavity with volumetric heating for a non-eutectic material mixture as used in the LIVE L3A test performed by KIT. It has been demonstrated that the evolution of maximum melt temperature can be recalculated assuming liquidus temperature at the liquid-solid interface during the whole transient. The average transient heat transfer is well approached by supposing a succession of thermal-hydraulic steady states using a natural convection Nusselt correlation involving the external Rayleigh number calculated on the basis of the instantaneous temperature difference between the liquid melt and the liquid-solid interface. Moreover, calculation of melt temperature evolution using steady state heat transfer coefficient for the whole transient ($\overline{h}_{bulk}(t) = \overline{h}_{stt}$) shows very minor difference to the one with transient varying heat transfer coefficient. The characteristic time delay to reach steady state melt temperature is approximately the same for the two calculations.

In addition, it has been shown that the transient evolution of crust thickness at different elevations of the melt cavity can be calculated using the steady state heat flux distribution, taking into account a gap resistance existing in between the crust and the vessel wall.

Calculation results of solidification rate and crust thickness evolution obtained from the simplified model have been used for predicting the solidification regimes governing the liquid-solid interface temperature. An analysis of the relating characteristic time delays shows that the solidification starts with a mushy zone and finishes with a planar front. The time delay for the transition between mushy zone and planar front has been reported. During mushy zone regime, the temperature at the tip of the dendrites in the mushy zone is close to the liquidus temperature of the actual melt composition and so does the interface temperature during planar front growth regime.

2.5 1D modelling of local heat transfer and solidification

It is noted that in the previous section of this chapter, a simplified 0D model has been developed and validation of this model has been performed using the LIVE L3A experimental data. Although this model allows calculating the evolution of the maximum temperature in the melt cavity, it was not able to determine the temperature and heat flux profiles in the melt cavity. In addition, evolution of solid crust thickness formed at the liquid-solid interface has been calculated in 0D model by imposing the experimental heat flux measured in the experiment in steady state. In this step, calculations by a 1D boundary model will be applied for LIVE L3A conditions. The aim is to obtain the evolution of the melt temperature at different melt cavity levels as well as the melt temperature and heat flux distribution, not only in steady state but also in transient. Evolution of local crust thickness will be deduced from transient heat flux which is calculated locally.

Appendix 7 of the current thesis presents in detail the 1D model that has been developed for modelling of local physical parameters relating to interaction of a liquid melt cavity surrounded by a solid wall. The model couples heat and mass transfers between the bulk of the melt cavity and a boundary layer existing along the lateral wall. A radial liquid flow has been supposed to enter the boundary layer from the bulk. The development of the model bases on balances of mass, momentum and energy in the bulk and in the boundary layer. Constitutive laws for estimation of local radial liquid velocity, local heat transfer in the boundary layer and local friction coefficient are proposed which are dependent on the fluid properties (Prandlt number). The developed model together with these constitutive laws has been validated in the case of natural convection along a vertical wall with imposed bulk and wall temperatures. Calculation results provided by this model for local parameters in the boundary layer such as temperature profile, boundary layer thickness and fluid velocity confirm its ability to access local heat and mass transfer during contact of hot liquid melt with solid wall. In this section, in order to validate the model, calculation will be done for LIVE L3A which is a more complicated case wherein the wall temperature is considered constant but the bulk temperature varies versus time.

2.5.1 Constitutive laws

As discussed previously, the test vessel in LIVE L3A is a 1:5 scaled semi-spherical lower head of a typical pressurized water reactor (PWR) with 31.3 cm height and 1 m inner diameter. For such a small scale test, the Grashof number is less than $2\ 10^9$. Therefore, only laminar heat transfer in the boundary layer is considered in this situation.

According to the Appendix 7 presenting the boundary layer model and its constitutive laws, the friction coefficient in laminar regime is calculated by:

$$F = \frac{96}{\mathrm{Re}} \tag{2-25}$$

For LIVE L3A, Pr = 9.3, leading to the constitutive laws for j_{bulk} as follows:

$$j_{bulk} = 0.19\left[g\,\beta_T\,(T_{bulk} - T_{BL})\,\upsilon\right]^{1/3} \tag{2-26}$$

where in T_{bulk} and T_{BL} are the local bulk and boundary layer temperature at a given distance from the top of the boundary layer.

The heat transfer to the wall can be estimated using either Nu_{bulk} or Nu_{BL} correlations deduced previously for laminar natural convection as follows:

$$Nu_{bulk} = 4\frac{\delta}{\delta_T} = 4\,\mathrm{Pr}^{1/3} \approx 8.4 \tag{2-27}$$

or:

$$Nu_{BL} = \frac{4\dfrac{\delta}{\delta_T}}{\dfrac{4}{5}\dfrac{\delta}{\delta_T} - \dfrac{1}{5}\left(\dfrac{\delta}{\delta_T}\right)^2} = \frac{5}{1 - 0{,}275\,\mathrm{Pr}^{1/3}} \approx 11.86 \tag{2-28}$$

2.5.2 Calculation results by 1D model

The results of calculation for 10 kW phase in LIVE L3A with transient solidification are shown below. Figure 2-26 presents evolution of melt temperature at different elevations of the melt cavity. Initially, the melt temperature is assumed uniform in the cavity at 327 °C. It is observed from Figure 2-4 that the calculated temperature evolution at elevation H = 27 cm is in agreement with the experimental results. The calculated steady state temperature at 27 cm is about 320 °C which is in agreement with the experimental one (320 °C). In addition, the time delays for reaching steady state obtained by calculation and experiment are both approximately 3000 s. However, the model predicts a peak of melt temperature occurring at about 500 s which is considered as the time required for the recirculation in the melt cavity flowing from the bottom to the top. In experiment, this peak is observed at about 1000 s which is later than the calculated one. Moreover, the predicted temperature for this peak is 337°C which is 9°C higher than in LIVE L3A (328 °C). This might be due to a loss of heat at the top of the melt cavity by radiation which is not described in the model.

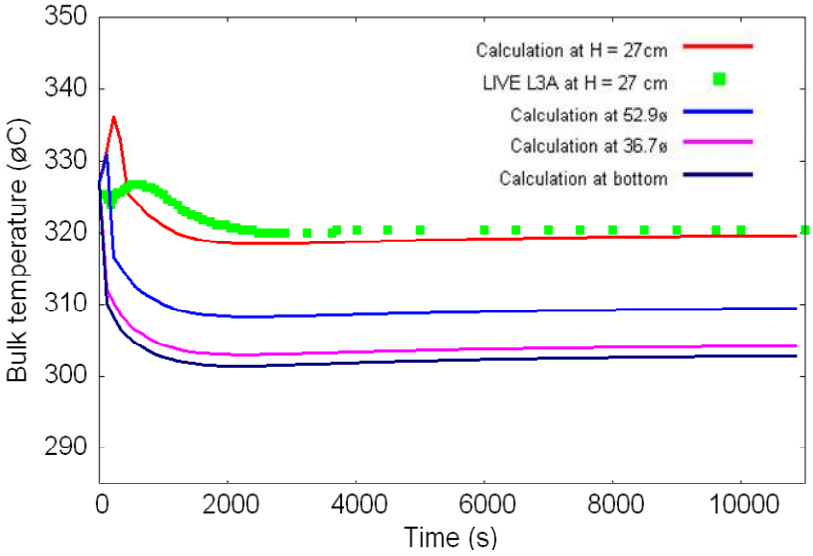

Figure 2-26. Calculation of melt temperature evolutions at different melt cavity elevations by 1D boundary layer model for 10 kW phase.

Besides, good agreements are also obtained for the temperature profile in the bulk at steady state (Figure 2-27) as well as the heat flux distribution along the melt cavity wall (Figure 2-28). The difference between calculation and experiment for steady state heat flux at 66.9° can be explained by the absence of heat loss by radiation to the upper surface of the melt, which is not described by the developed model.

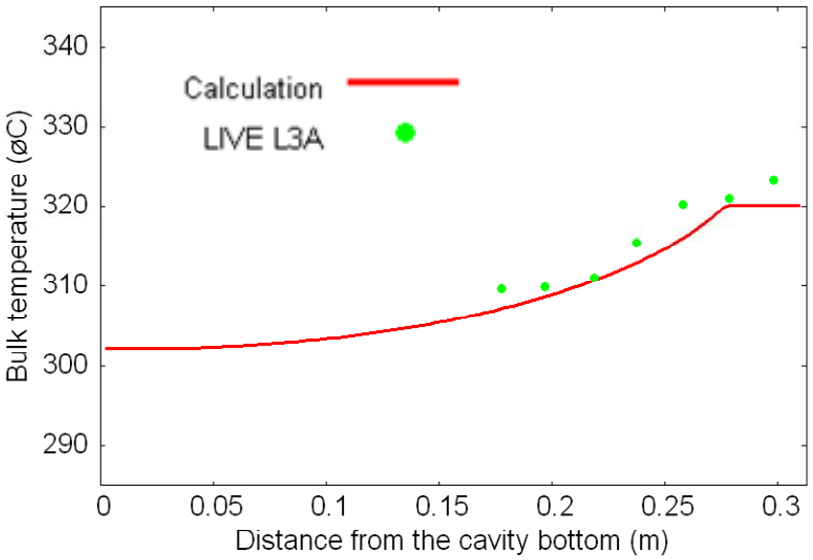

Figure 2-27. Steady state axial temperature profile in melt cavity in 10 kW phase.

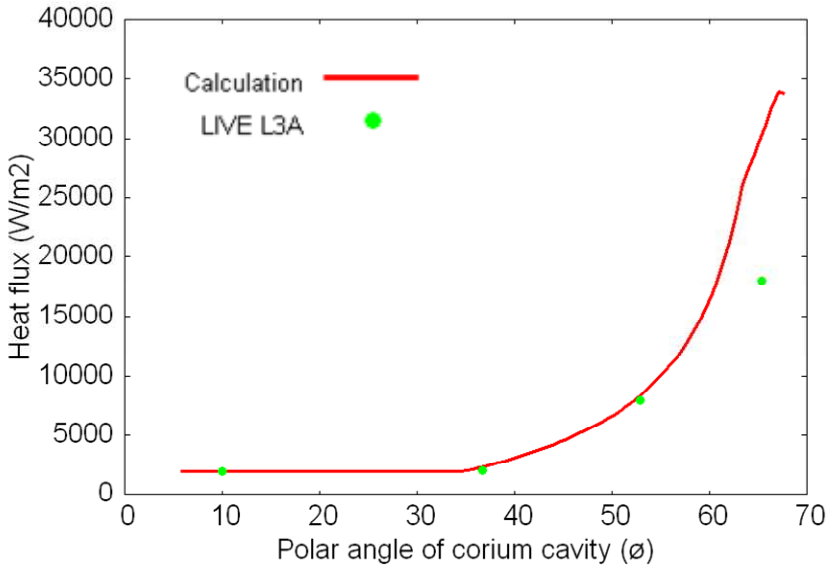

Figure 2-28. Steady state heat flux distribution in 10 kW phase.

The evolution of the solid crust thickness is also well described by the developed model (Figure 2-29 and Figure 2-30).

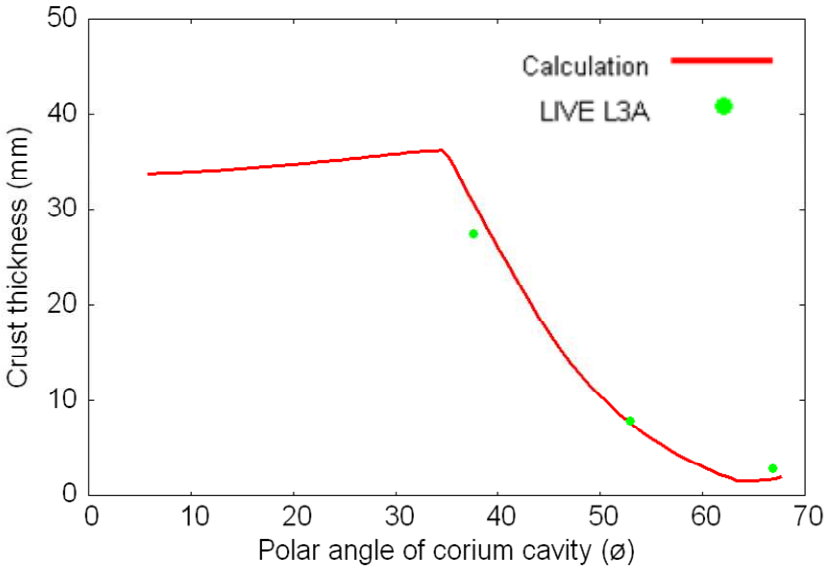

Figure 2-29. Distribution of solid crust thickness at the end of 10 kW phase.

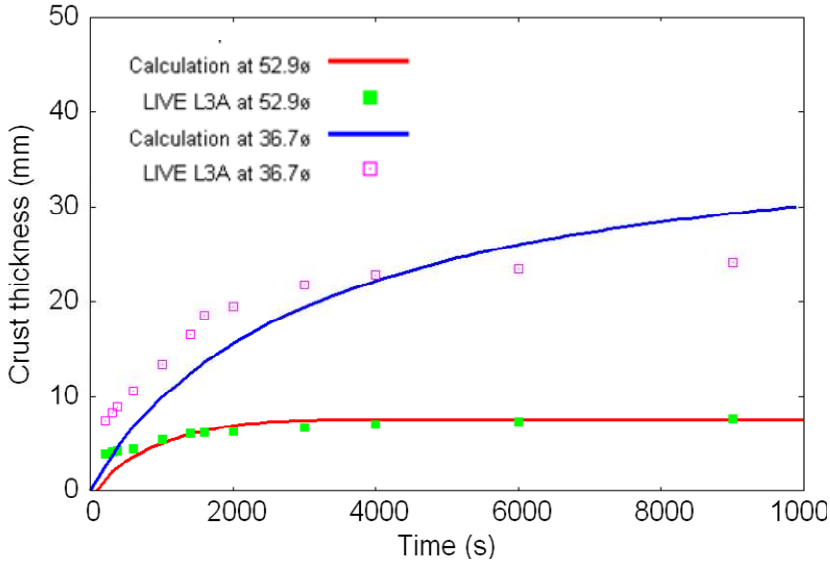

Figure 2-30. Crust thickness evolution at 37.6° and 52.9° in 10 kW phase.

2.5.3 Conclusion

The main conclusions from the calculation for LIVE L3A by 1D model approach are summarized as follows:

- The present results from the model are in good agreement with measurements of LIVE L3A not only in terms of evolutions of both bulk temperature and local solid crust thickness, but also in term of bulk temperature profile as well as heat flux and crust thickness distributions (along the melt cavity interface) in steady state conditions.
- The heat transfer mechanism from the bulk to the wall is the natural convection. The constitutive laws for friction coefficient and heat transfer coefficient deduced from the use of Eckert's velocity and temperature profiles, which were developed for natural-convection boundary layer along a vertical plate in laminar regime, are still valid for a hemispherical melt cavity with solidification at the wall.
- In comparison with the simple 0D model previously developed for describing the evolution of the maximum bulk temperature and of the crust thickness for LIVE L3A, this 1-D model allows calculating all the local parameters such as: bulk temperature and velocity, local boundary layer thickness, mass-flow-average velocity and temperature in the boundary layer, local heat flux and solidification rate at the wall. In particular, the model enables estimating the local melt cavity-shape variation due to solidification.

2.6 Conclusions

This chapter is devoted to the investigation of heat transfer and solidification in a simulating non-eutectic molten corium melt cavity with internal heating source and external cooling at boundaries. The work at simulating the in-vessel retention experiment LIVE L3A performed in KIT.

A simplified model has been developed for calculation of the evolution of maximum melt temperature and evolution of the solid crust thickness due to solidification. The model assumes liquidus temperature of the melt at the liquid-solid interface and employs an average heat transfer from an existing natural convection Nusselt number developed for steady state heat transfer. A transformation

of the correlation from internal Rayleigh number to external Rayleigh number has been performed in order to take into account the transient variation of temperature difference between the melt and the liquid-solid interface. The local crust thickness evolution has been calculated by imposing the steady state heat flux profile measured in the experiment. Agreement between the model and the experimental data in melt temperature evolution and crust thickness evolution proves that the heat transfer in transient has similar behaviour as in steady state. In addition, using the calculation results for transient solidification rate and applying the existing solidification models for planar front and mushy zone, a prediction of solidification regimes in LIVE L3A has been proposed, wherein a mushy zone regime occurs at the beginning and a planar front is obtained at the end. Recalculation of interface temperature during the whole transient again indicates that the interface temperature always stays close to liquidus temperature of the actual melt.

Application of the 1D boundary layer model for LIVE L3A has been carried out in the current chapter in order to validate the capability of the model for describing local physical parameters of heat and mass transfer for a hemispherical configuration with varying bulk temperature and changes in cavity shape due to solidification of liquid melt. The model gives access to recalculation of local melt temperature and heat flux distribution not only in steady state but also in transient. The constitutive laws for friction coefficient and heat transfer in the boundary layer as well as for radial liquid flow velocity from the bulk to the boundary layer which are derived for a vertical plate are also applicable for a hemispherical melt cavity.

CHAPTER 3: ARTEMIS PROGRAM: INVESTIGATION OF MOLTEN MELT-CONCRETE INTERACTION. DESCRIPTION OF ARTEMIS 2D TEST FACILITY

3.1 Objectives of ARTEMIS 2D

The ARTEMIS program, performed in Grenoble by DTN/SE2T/LPTM, common program between IRSN and EDF, CEA, is aimed to study the melt-concrete interaction with simulant materials. The main objective of ARTEMIS 2D tests is to investigate the 2D melt-concrete interaction phenomena, focusing on the determination of the heat flux distribution along the cavity wall of the melt and on interface conditions. The investigation of the heat transfer coefficient as well as the interface temperature between the liquid melt and the solid concrete become the key issues.

The interface temperature between the melt and the solid is dependent on the physico-chemistry and thermal-hydraulics of the non-eutectic melt. Besides, this interface temperature depends on the thickness of any melt crust which may form at the interface during melt-concrete interaction. The behaviour of this crust (evolution of the crust thickness, and the mechanical interaction of the crust with injected gas) governs also the release mode of the molten concrete into the melt. The related variation of the melt composition versus time may also have an effect on the interface phenomena. Therefore, the molten melt-concrete interaction phenomenon is a result of a strong coupling between thermal-hydraulics (interface temperature, heat transfer at the interface) and physico-chemistry (composition of the melt and of any solid layer forming at the interface).

3.2 Similarity analysis for material selection

Real material experiments, at very elevated temperatures (~ 2000 K - 2500 K) are technically complex to realize and have limited instrumentation possibilities. An alternative option is to use simulant materials and perform tests at lower temperature, which is more favourable for instrumentation. The difficulty resides then in the choice of these simulant materials. The phenomena to simulate are numerous and touch physico-chemical aspects as well as thermal-hydraulics aspects.

The simulant materials were selected based on a number of criteria. Basing on the similarity analysis conducted by [Veteau, 2006], the simulant materials were chosen for ARTEMIS 2D tests as:

- Melt: pure $BaCl_2$
- Concrete: mixture of $BaCl_2$-LiCl at eutectic composition (25% mol $BaCl_2$-75% mol LiCl)

The reasons for this material selection are explained in the next.

3.2.1 Physico-chemical and density aspects

Phase diagram

Concerning the physico-chemical aspects, the similarity criteria are, basically, dependent on the phase diagram. Figure 3-1 shows the analogy between the phase diagram for an actual oxidic melt (UO_2 + ZrO_2) -concrete mixture and the ARTEMIS salts ($BaCl_2$ + LiCl).

UO_2 and ZrO_2 are the refractory species in the reactor case (melting temperature is about 2700 °C ~ 2850 °C). These materials are simulated by pure $BaCl_2$ (melting temperature is ~ 960 °C). Concrete (melting temperature ranging between 1200 °C and 1500 °C) is represented by the eutectic mixture containing 75% LiCl mol percentage and 25% $BaCl_2$ mol percentage (melting temperature: 522 °C).

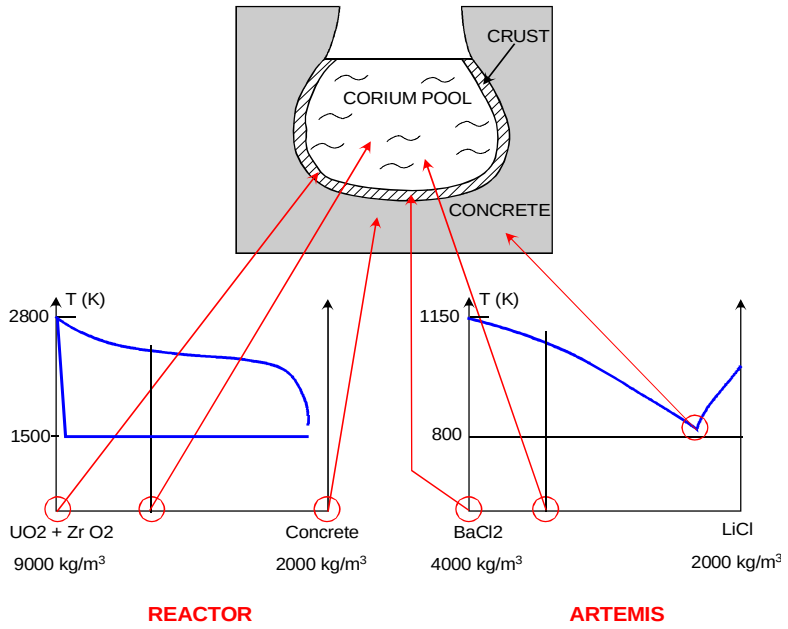

Figure 3-1. Phase diagrams in the case of reactor and the case of ARTEMIS.

The binary mixture of $BaCl_2$ and LiCl were chosen because their phase diagram shows the following criteria of similarity compared to the reactor materials:

- Solidus temperature of "melt" close to melting temperature of "concrete";
- A sufficiently large melting interval, i.e. $\frac{T_{liquidus} - T_{solidus}}{T_{melt}} = 0.5 \div 1$;
- A partition coefficient close to 0 in both cases. The solid, that is thermodynamic-equilibrium with a liquid melt at any composition, is solely composed of the refractory component.

Densities and other physical properties

To conserve the density ratios (that plausibly controls crust deposition), the following constraint concerning the densities is fulfilled: $\rho_{concrete} < \rho_{bulk} < \rho_{crust(refractory\ species)}$ (Table 3-1, Table 3-2 and Table 3-3).

Table 3-1. Physical properties of actual reactor melt (85% mass UO_2 and 15% mass ZrO_2) and an actual concrete.

	Density	Heat capacity	Thermal conductivity	Enthalpy of melting	Melting temperature
	$kg.m^{-3}$	$J.kg^{-1}.K^{-1}$	$W.m^{-1}.K^{-1}$	$J.kg^{-1}$	°C
Concrete	2390	860	1.3	$2.2\ 10^6$ (silicious) $2.4\ 10^6$ (LCS) $3.5\ 10^6$ (limestone)	~1500
Melt crust (refractory species)	8000	600	3	$3.7\ 10^5$	2600
Melt liquid	2500~7000	760	2.4		

Table 3-2. Physical properties of $BaCl_2$ (simulant material for refractory species of melt).

	Density	Thermal expansion coefficient	Solute expansion coefficient	Kinematic viscosity	Heat capacity	Thermal conductivity	Enthalpy of melting	Melting temperature
	$kg.m^{-3}$	K^{-1}	$kg.kg^{-1}$	$kg.m^{-1}.s^{-1}$	$J.kg^{-1}.K^{-1}$	$W.m^{-1}.K^{-1}$	$J.kg^{-1}$	°C
$BaCl_2$ solid	3500				594	0.5 (at 400 °C)	$7.4\ 10^4$	960
$BaCl_2$ liquid	3150 (at 960 °C)	$3.2\ 10^{-4}$	0.9	$1.5\ 10^{-6}$	522	0.8		

Table 3-3. Physical properties for simulant concrete (mixture of $BaCl_2$ 25% mol-LiCl 75% mol).

	Density	Thermal expansion coefficient	Kinematic viscosity	Heat capacity	Thermal conductivity	Enthalpy of melting	Melting temperature
	$kg.m^{-3}$	K^{-1}	$kg.m^{-1}.s^{-1}$	$J.kg^{-1}.K^{-1}$	$W.m^{-1}.K^{-1}$	$J.kg^{-1}$	°C
Solid	1638 (porous solid)			700		$2.6\ 10^5$	522
Liquid	2439	$3.2\ 10^{-4}$	10^{-6}	800	0.64		

3.2.2 Thermal-hydraulics aspects

To approach the similarity between the reactor case and the experiment in terms of thermal-hydraulics, the parameters to be set in an experiment are the superficial gas velocity j_{gas}, the imposed heat flux φ to the solid, the initial height of the melt H_{ini} and the transport properties of the melt (dynamic viscosity μ, thermal conductivity λ_{bulk}).

In the reactor case, range of values for j_{gas}, φ and H_{ini} of interest are:

- j_{gas} = a few cm/s;
- $2.10^4\ W.m^{-2} < \varphi < 2\ 10^5\ W.m^{-2}$;
- $0.4\ m < H_{ini} < 3\ m$;
- $0.1\ Pa.s < \mu < \sim 10\ Pa.s$.

Height of the melt

For the mixture $BaCl_2$-LiCl employed in ARTEMIS, the melt cavity is continuously enriched with LiCl by mixing of molten concrete and formation of a crust (plausible enriched in $BaCl_2$) at the interface between the melt and concrete with a significant thickness. At small scale, the enrichment rate of the melt with concrete will be faster, due to the small mass ratio between the melt and the concrete. The size of the test section is also constrained by economical aspects to ~ 40 litres.

A compromise had to be found between melt enrichment rate (that is mainly controlled by the power dissipation), and the thickness of any crust with refractory materials. This compromise kept a representative melt height of 0.3 ~ 0.5 m.

Crust thickness and power level

Preserving characteristics of the crust such as thickness and the characteristic time for crust formation are of special interest. Assuming that the thickness of the crust is controlled by heat conduction and assuming the temperature at the interface between melt-crust is the liquidus temperature of the melt and the temperature at the interface between crust-concrete is the melting temperature of the concrete T_{melt}, then the crust thickness is given by:

$$z_{crust} = \frac{\lambda_{crust}(T_{liquidus} - T_{melt})}{\varphi} \tag{3-1}$$

Besides, the time required for crust formation (τ_{sol}) is:

$$\tau_{sol} = \frac{\lambda_{crust}\rho_{crust}\Delta T_{sol} L^{refractory}_{solidification}}{\varphi^2} \tag{3-2}$$

where λ_{crust} and ρ_{crust} are the thermal conductivity and density of the crust material; φ is the heat flux transferred through the interface between melt and crust, ΔT_{sol} is the solidification interval of the melt material ($T_{liquidus}$-$T_{solidus}$) and $L^{refractory}_{solidification}$ is the latent heat of solidification of refractory species to form the crust.

Considering that the thickness of the crust had to be represented (centimetre range), and knowing the thermal conductivity and melting interval of the materials, leads to a specific heat flux range of 5000 to 15000 W/m²K. This heat flux range leads to total power dissipation in the experiment in the range of 2 kW to 10 kW.

Heat losses

This is a rather small power level for a test section working at elevated temperature (500 to 1000 °C) with a large external surface (~ 2 m²). Therefore, special care must be taken to reduce the heat losses in order to be able to ensure a good control of the power balance.

Superficial gas velocity

The superficial velocity of the injected gas at the concrete interface was preserved between the reactor and the experiment (j_{gas} ranging from 1 to 5 cm/s).

The ratio between the power absorbed for gas heating and the imposed power should also be preserved. For the reactor case, this ratio is small (typically less than 5%). In ARTEMIS, the power absorbed for gas heating is about 330 W (for j_{gas} = 1 cm/s and $T_{gas,\ in}$ = 400 °C and the dissipated power is ~ 4000 W). Therefore, the ratio is about 0.08, which is a little bit larger than the ratio in the reactor case but stays still at a reasonable low value.

Concrete ablation rate

The above consideration fixes the concrete ablation rate which is given by:

$$V_{abl} = \frac{\varphi}{\rho_{MC} L_{melting}^{concrete}} \tag{3-3}$$

where ρ_{MC} is the density of the molten concrete and $L_{melting}^{concrete}$ is the latent heat for melting of concrete.

In ARTEMIS, the ablation velocity of the concrete is between a few cm/h to ~10 cm/h. This ablation rate is similar to the ablation rates in the reactor situation

Viscosity

The viscosity of real corium might be small (in the case of limestone concrete, containing a small amount of silica) or elevated (in the case of siliceous concrete). Elevated viscosity could not be simulated with the materials chosen for ARTEMIS, which is an important limitation.

3.2.3 Phenomena to be captured in ARTEMIS

During the ARTEMIS 2D tests, the experimental data concerning the following parameters are expected to be collected.

- In terms of thermal hydraulic phenomena:
  - Melt temperatures evolution and temperature distribution in the melt
  - Interface(s) temperatures evolutions (lateral and axial)
  - Ablation rate of concrete (evolution of cavity shape)
  - Gas flow rate
  - Void fraction in the melt
- In terms of physico-chemical aspects:
  - Formation of crust at the liquid-solid interface
  - Crust thickness (position of melt interface(s) versus. time)

- Crust growth rate
- Crust composition
- Melt composition (average and distribution)

3.3 Description of the test facility

The description of ARTEMIS 2D test section is presented in details in the work of [Samaille et al., 2007]. Only main features are recalled in the next.

A general sketch of the ARTEMIS 2D installation is shown in Figure 3-2. The installation of the ARTEMIS 2D includes:

- A melt furnace for heating the liquid melt to a specified temperature before transferring it into the test section.
- A test section containing concrete and an initial cavity that will be filled with liquid melt. An electrical heating system is provided in the cavity to simulate the power dissipation.
- A lateral tank, initially empty, designed to receive the melt at the end of the experiment by tilting the test section. The aim is to separate the melt from the solid crust that is plausibly deposited at the interface(s).
- Insulation with a specific system to reduce the heat losses. A total compensation of heat loss consists of 18 independent zones of temperature control.
- Argon gas source for generating and providing gas to the test section, with preheating.
- A system of mobile instruments (mobile probes 1D at the melt centre and 2D at the lateral wall of the melt cavity) for measuring:
- The melt temperature distribution in the cavity and near the melt-concrete interface;
- The position of interfaces and interface temperatures;
- The melt composition distribution in the melt.

Details of each component are given in the next.

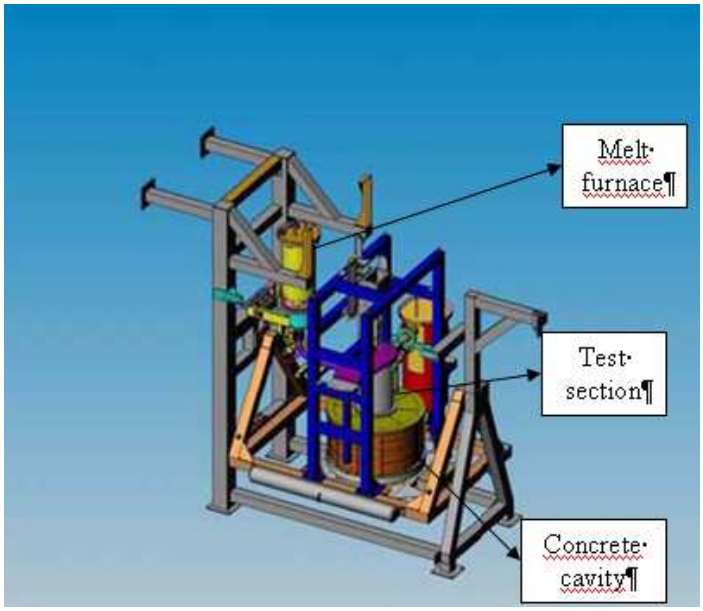

Figure 3-2. ARTEMIS 2D installation.

3.3.1 Melt furnace

The melt furnace, with a storage capacity of 40 litres, allows the melting of "melt material" to the temperature of maximum 1000 ° C. This furnace (Figure 3-3) composes of:

- The volume of liquid melt;
- A fusible plug at the lower end, allowing melt release from the furnace to the test section. It permits to drain the melt within a few seconds.

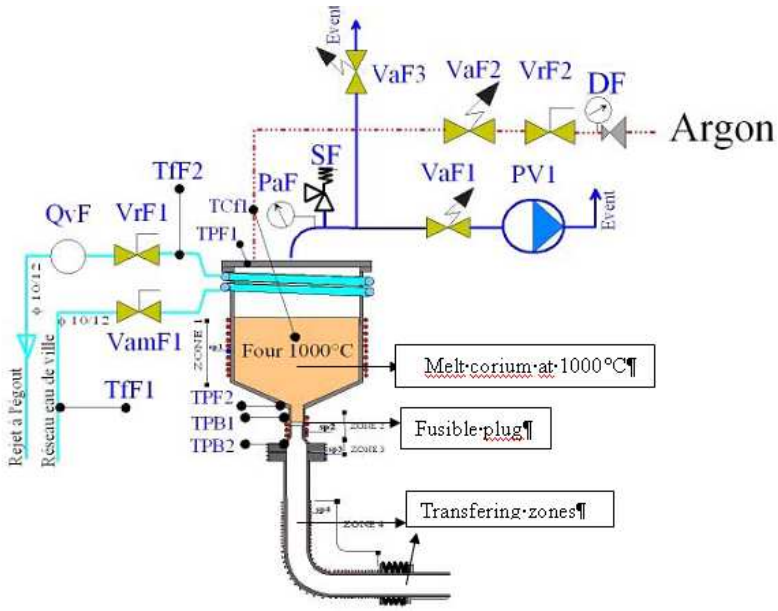

Figure 3-3. Melt furnace for ARTEMIS 2D.

3.3.2 Test section

The test section is composed of a mechanical assembly of several modules. Each module will be described in the followings.

Gas injection system

The gas injection system is designed for gas superficial velocities ranging from 1 to 5 cm/s (at the melt-concrete interface). The gas is injected at 5 levels (QM1 to QM5). Measurement of gas flow rate is performed using five mass flow meters (Figure 3-4). The measurement of gas inlet temperature is achieved (TR1) and the measurement of pressure drop across the test section is measured by a differential pressure sensor DP1 (Figure 3-4). During the test, the mass flow of gas in each injection section is recalculated every time the surface of the cavity changes in order to keep constant the superficial gas velocity at the melt-solid interface.

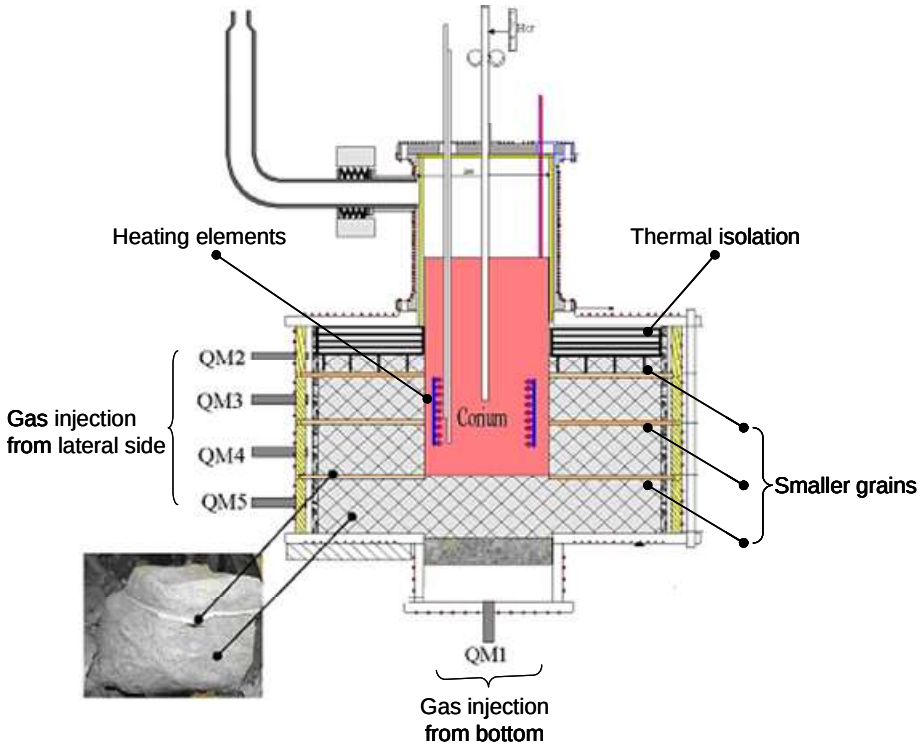

Figure 3-4. Gas injection system for ARTEMIS 2D.

Porous concrete

The concrete has 46 % porosity for the main part. The concrete grain size ranges between 200 µm and 900 µm. Its permeability has been measured by [Dupouy et Camel, 1998] and is about 3 10^{-12} m^2 to 6 10^{-11} m^2.

The concrete cavity, with a height of approximately 440 mm (this value may change for each test) and 800 mm in diameter, is divided into several parts. It consists of four independent axial rings, each ring has a separate lateral argon gas injection. Gas injection is connected to an annular external chamber. A porous sheath (inox) permits to control the uniformity of the gas injection. This is achieved by locating the main gas pressure drop through the porous sheath and not in the porous concrete. Special attention has been paid to the elimination of gaps between the inox porous sheath and the concrete. In order to

eliminate axial redistribution of gas within the concrete, horizontal separators (horizontal rings of small thickness) which are made of material identical to that of concrete but with much finer grain size (< 200 μm) are installed between each concrete section.

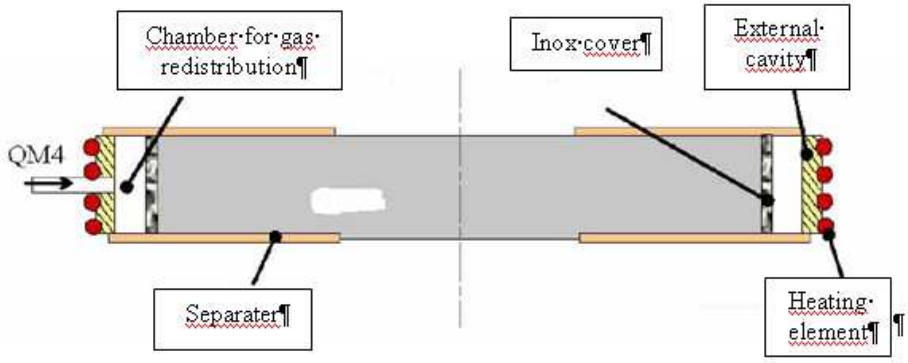

Figure 3-5. Gas injection and separation system.

Each axial zone in the concrete is also instrumented with 0.5 mm thermocouples that are embedded inside the concrete, arranged in 4 planes at 90° azimuthal intervals (45°, 135°, 225°, 315°). In total, there are 98 thermocouples. The thermocouples are radially uniformly spaced with a pitch of 80 mm, however, the distribution is closer (40 mm pitch) in 2 planes: the first being the vertical planes at the bottom centre line (TB4A, TB5A, TB6A, TB7A, TB8A, TB9A) and the second is radial and located in the top region TB3C, TB3D, TB3E, TB3F, TB3G, TB3H (Figure 3-6). Indication from these thermocouples not only provides the evolution of local concrete temperature but also the position of the ablation front and evolution of the corium cavity shape during molten corium-concrete interaction. During the test, the ablation front is followed on-line and interfacial area of the corium cavity is calculated continuously.

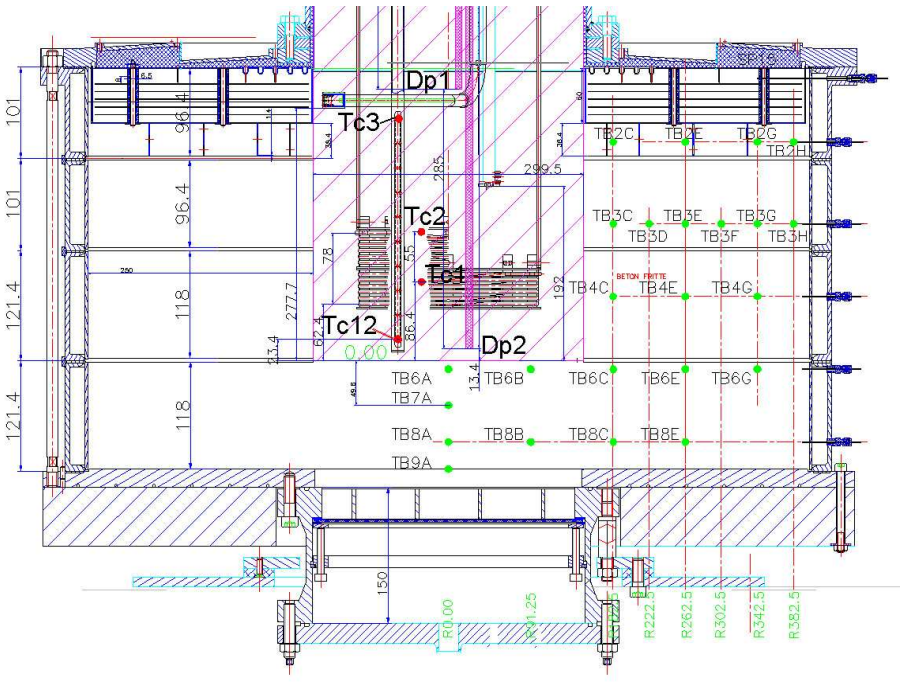

Figure 3-6. Thermocouples matrix inside the concrete.

Melt cavity

The melt cavity has cylindrical shape and is divided into two parts. The lower part is located inside the concrete region and the upper part is situated in the continuation of the upper cylindrical cavity of the test section and the melt may fill partially this top zone (Figure 3-7). The diameter of the melt cavity is 300 mm and its total height is 552 mm, receiving the liquid melt from the melt furnace. The height of the liquid melt is variable for each test (from 260 mm to 550 mm). Heat losses are controlled in Zone 7 (melt height), in zone 6 (argon gas) and Zone 5 (Top lid). A jet-braking system is also installed at the outlet of the drain tube that avoids jet impact on concrete material.

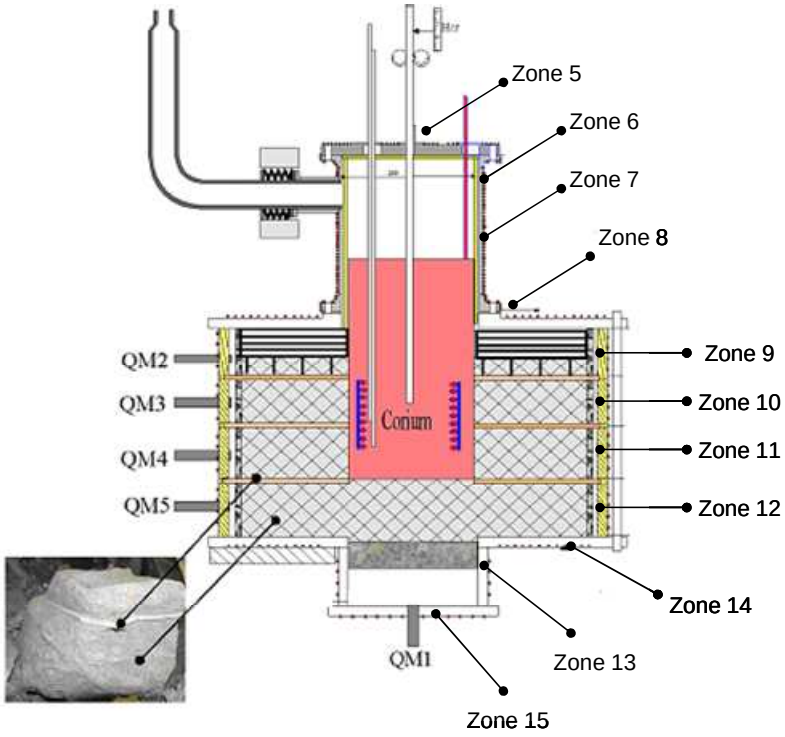

Figure 3-7. Melt cavity.

Simulation of heating power

An annular heating element is submerged in the liquid melt. The heating elements are electrically insulated from the melt material. They are composed of several modules with a rated output of 2 kW each module. These elements are fed continuously by a stabilized current supply. The diameter of the heater is about 20 cm and the height ~ 15 cm. Two thermocouples Ts1 and Ts2 are connected to the heating elements for security reason (to prevent the melt temperature exceeding 1000 °C).

3.3.3 Instrumentations in the melt cavity

Temperature measurement and melt sampling in the melt cavity

Several thermocouples located inside the corium cavity allow measurement of corium temperature.

Thermocouple TC1 (0.5 mm diameter) (Figure 3-6) measuring melt temperature is placed near the centre of the heating zone at distance 116 mm from the initial bottom of the melt cavity. In addition, 10 thermocouples from TC3 to TC12 are installed on a fix cane to measure the vertical temperature gradient in the corium cavity. These thermocouples are located from distance of 266.4 mm for TC3 to 23.4 mm for TC12 from the initial bottom of the corium cavity. The distance between them is fixed at 27 mm.

A sampling tube permits to take samples in the melt centre with a volume of 1cm^3 for each sample. From ARTEMIS 10, the samples can be taken simultaneously at different elevations at the same time (6 different elevations).

A mobile probe 1D (Figure 3-8) permits to detect the position of the melt solid interface at the cavity bottom and simultaneously to measure the axial temperature distribution in the vicinity of the interface. Its tip is initially placed at ~ 4 cm above the lower surface of the concrete. The probe is periodically moved. The displacement-length is possible up to 255 mm depth from the initial position of the concrete surface. A displacement sensor indicates the position of the current measuring point and a force sensor is aimed to help to avoid the stamping of the lower crust (But the lower crust revealed to be very soft and the probe probably penetrated the bottom cake layer). After each measurement, the probe returns to the "waiting position" 4 cm in elevation above the deepest position. The position of the thermocouples is shown inFigure 3-8.

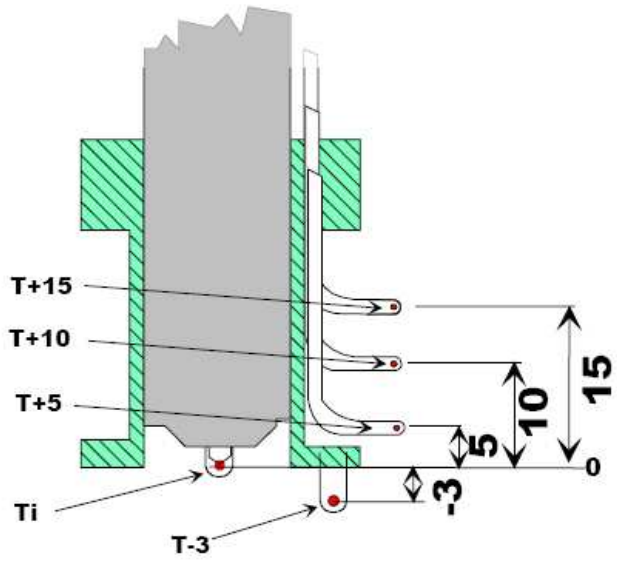

Figure 3-8. Sketch of the geometry at the tip of the mobile probe 1D.

The temperature measurement near the lateral wall of the melt cavity is performed by a mobile 2D probe equipped with 11 thermocouples (type N Class 1) (Figure 3-9). This 2D probe can move upwards and downwards in the vertical direction, rotates to detect the position of the lateral liquid-solid interface at a given elevation of the melt cavity and permits to measure interface temperature as well as the temperature in the vicinity of this interface. Knowing the distance between the thermocouples installed on the 2D mobile probe, the radial temperature profile at a given cavity elevation will be deduced. The commissioning of this probe was completed during the second 2D test (ARTEMIS 8). This probe was modified after ARTEMIS 8 in order to measure the temperature of the lateral interface in all configurations (concave or convex interface) (Figure 3-10). The working mechanism of the mobile probe 2D is described in the followings:

- When the desired vertical position is reached, the probe starts rotating until contact with the interface. This contact is detected by a torque limitation.
- Once the measurement is performed, the probe rotates back to the original position.
- The probe is positioned at a new vertical position.

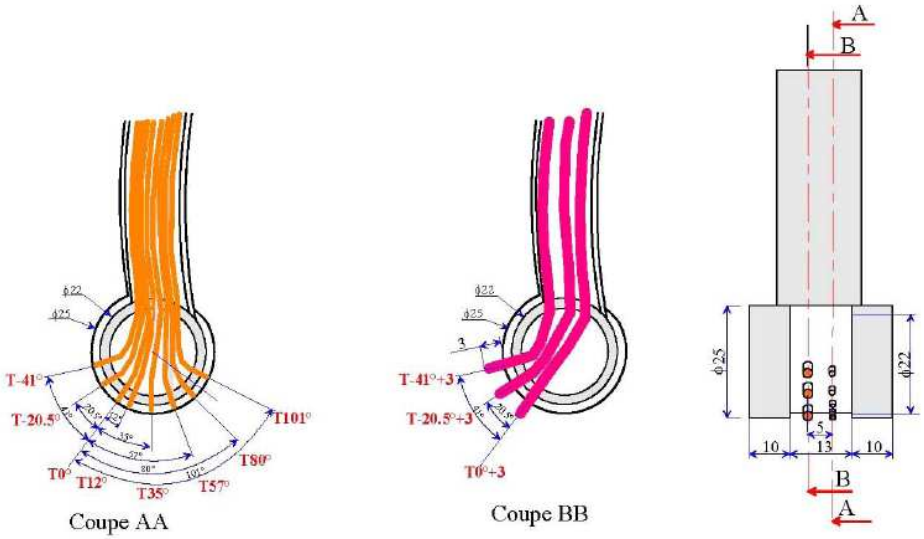

Figure 3-9. Schematic of 2D mobile probe for ARTEMIS.

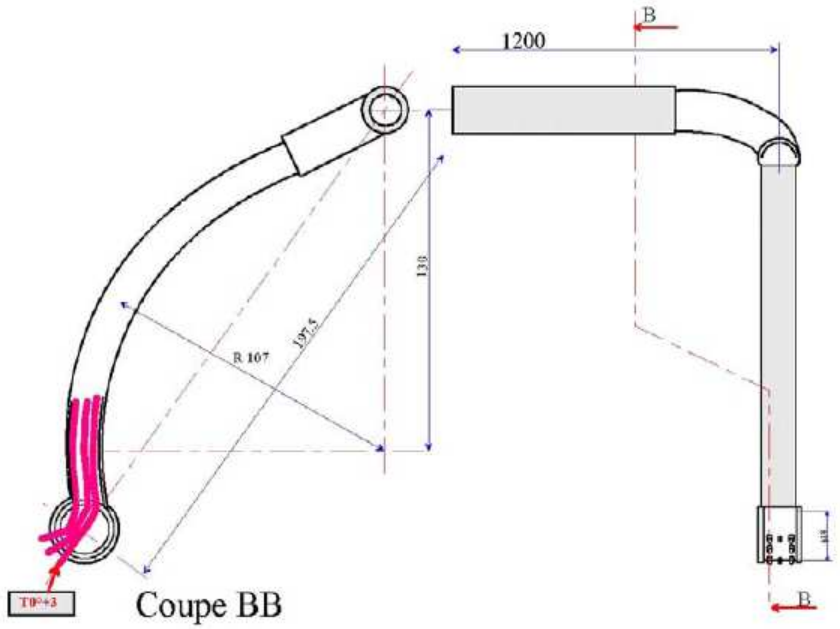

Figure 3-10. Schematic of 2D mobile probe from ARTEMIS 9 to ARTEMIS 13.

Measurement of void fraction in melt cavity

Measurement of void fraction α_{gas} in melt cavity is carried on by injecting a low gas flow in an immersed tube to measure a pressure equivalent to the immersion height of the tube by a sensor (the distance from the melt surface in the test section and the tip of the immersed tube, Figure 3-11). The

differential pressure drop between two tubes with immersed heights h_1 and h_2 in a distance ΔH between each other allows the determination of the average void fraction over the height ΔH. The link between the pressure in each tube and the height of the immersed tubes is as following:

$$\Delta PC1 = \rho_{bulk}\, g\, h_1 \left(1 - \alpha_{gas}\right) \tag{3-4}$$

$$\Delta PC2 = \rho_{bulk}\, g\, h_2 \left(1 - \alpha_{gas}\right) \tag{3-5}$$

where ρ_{bulk} is the density of liquid melt and g is the acceleration of gravity.

The average void fraction α_{gas} along the height ΔH is then deduced:

$$\alpha_{gas} = 1 - \frac{\Delta PC1 - \Delta PC2}{\rho_{bulk}\ g\, \Delta H} \tag{3-6}$$

where:

- ($\Delta PC1 - \Delta PC2$) is the pressure difference;
- $\rho_{bulk}\, g\Delta H$ is the pressure difference for pure liquid;
- $\Delta H = x_1 - x_2 = h_2 - h_1$ is the distance between the tip of the two tubes in which x_1 and x_2 are the distance from the melt cavity bottom to the tips of the tubes.

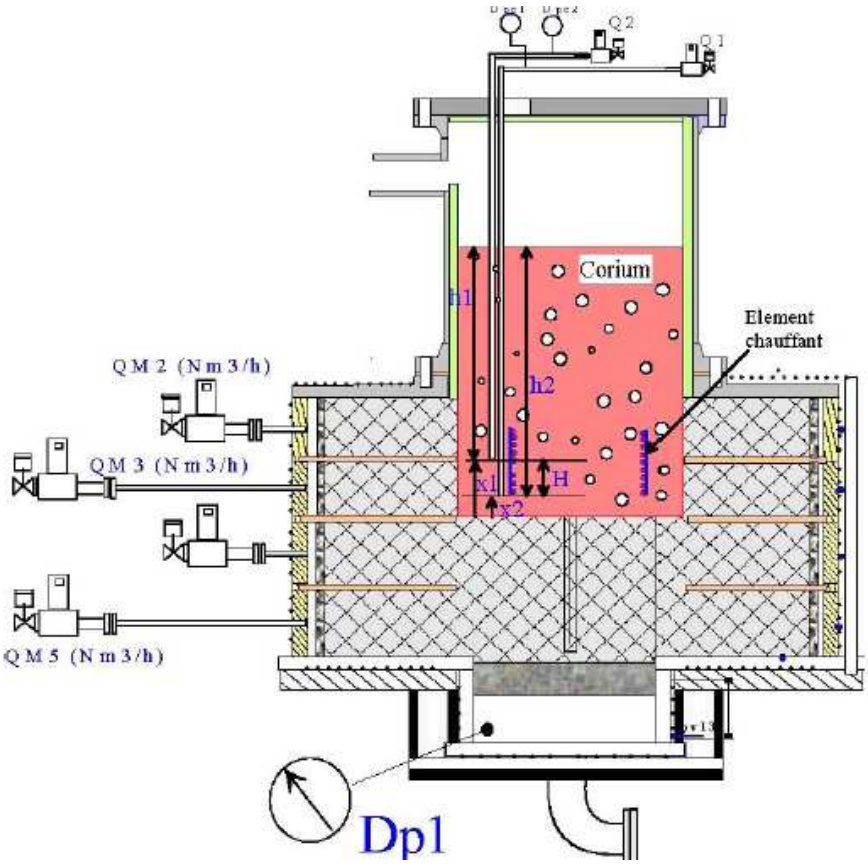

Figure 3-11. Void fraction measurement.

Control of heat losses during test

During the test, the concrete heat up and melt may also touch the external steel vessel. The temperature of the vessel will increase and calculations showed that heat losses may become very large (several kW). Therefore special care has been taken to reduce the heat losses under these conditions.

The thermal control of these three top zones section (zones 5, 6, 7 in Figure 3-7) is operated in order to regulate the wall temperature to the temperature of the melt in the top melt region. In that way the radiation heat losses are minimized. On the side walls (zones 9 to 12) a guard heating and thermal insulation are designed to ensure zero heat loss.

The ceiling of concrete (zone 8 and zone 8bis) (Figure 3-12) has been designed to limit heat loss by conduction and radiation.

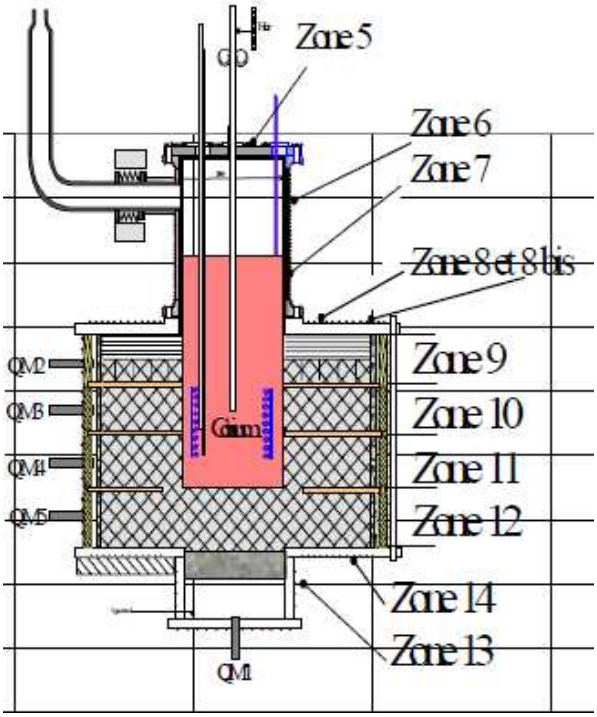

Figure 3-12. Heat loss control system.

3.4 Fabrication of concrete

The concrete is especially fabricated from a solidified melt having concrete composition. (75% mol LiCl – 25% mol $BaCl_2$%). After that, Crushing and sieving of solid concrete are carried out under dry gas. Sizes of concrete particles before completing the sintering in the test section are between 80 µm and 800 µm. The concrete particles are dropped into the test section and cold-pressed in place, layer by layer. The insertion of the 98 thermocouples is carried out during this process.

The next step is sintering at 400 °C with percolaging argon gas for several hours using external heating elements zones 8-15 (Figure 3-12). For the tests that are considered here, the test begins with this hot concrete (the concrete is not cooled down in order to avoid crack formations in the concrete).

3.5 Test matrix

ARTEMIS 2D series include seven tests, carried out between 9/2005 and 2/2008. The main test parameters are given in Table 3-4.

Table 3-4. ARTEMIS 2D test matrix.

Test	Melt simulant materials	Initial temperature of melt in furnace	Gas superficial velocity	Applied power	Initial melt height	Cavity geometry
		°C	m/s	W	m	
7	Pure $BaCl_2$	1005	0.01	4000	0.5	X = 0.25 m Z = 0.25 m H = 0.205 m D = 0.3 m
8	Concrete (25% mol $BaCl_2$, 75% mol LiCl)	562	0.01	4000	0.5	X = 0.25 m Z = 0.25 m H = 0.205 m D = 0.3 m
9	Pure $BaCl_2$	1005	0.01	4000	0.28	X = 0.2 m Z = 0.12 m H = 0.33 m D = 0.4 m
10	Pure $BaCl_2$	1005	0.02	6000	0.45	X = 0.25 m Z = 0.12 m H = 0.26 m D = 0.3 m
11	Concrete (25% mol $BaCl_2$, 75% mol LiCl)	562	0.02	6000	0.33	X = 0.25 m Z = 0.12 m H = 0.26 m D = 0.3 m
12	Concrete (25% mol $BaCl_2$, 75% mol LiCl)	712	0.04	4000	0.37	X = 0.25 m Z = 0.12 m H = 0.26 m D = 0.3 m
13	Pure $BaCl_2$	1005	0.04	9000	0.55	X = 0.25 m Z = 0.12 m H = 0.26 m D = 0.3 m

X: initial thickness of the lateral concrete wall

Z: initial thickness of the bottom concrete wall

H: the height of the melt cavity in the concrete part

D: the diameter of the melt cavity

ARTEMIS 7 was the first test in ARTEMIS 2D series, conducted on 16/09/2005. For this test, interaction between melt (pure $BaCl_2$) and concrete is investigated. This test showed a preferential radial ablation.

In order to analyse the origin of preferential radial ablation, it was decided that the objective of ARTEMIS 8 was to study pure 2D thermal-hydraulics phenomena only with elimination of the effects

related to physico-chemistry. For this purpose, the simulated melt was replaced by a liquid mixture of $BaCl_2$ and LiCl, having an identical composition to that of concrete (25% mol $BaCl_2$ and 75% mol LiCl). This test was also an opportunity to test the performance of the vertical mobile probe in measuring the interface temperature at the bottom of the melt cavity. Again, the test resulted in an ablation of concrete which is preferentially radial.

In ARTEMIS 7 and ARTEMIS 8, there was some possibility that the configuration of the cavity could be at the origin of the preferential radial ablation. The boundary layer flow induced by gas injection on the lateral surface of the concrete cavity impacts on the horizontal roof of the cavity. This impact could induce a local recirculation that could enhance local heat exchange and potentially increase the radial ablation (Figure 3-13).

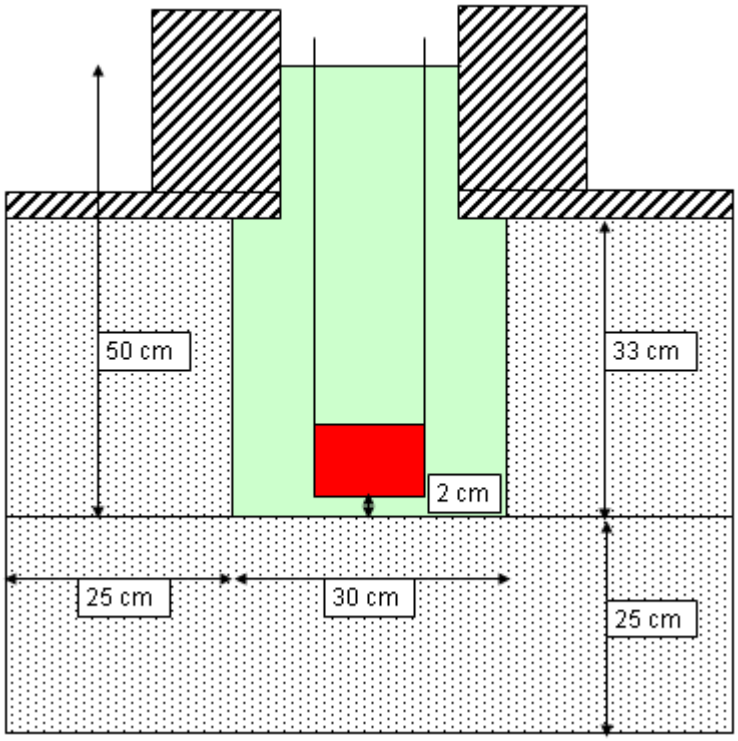

Figure 3-13. Geometries of ARTEMIS 7 and ARTEMIS 8.

In ARTEMIS 9 the top geometry of the concrete cavity was changed for the purpose of avoiding flow recirculation induced by the roof of the concrete cavity. The volume of the cavity in the concrete was increased and thus the initial level of the liquid melt was reduced, together with a reduction of the initial melt mass also. The heater was also raised up to prevent the direct contact of bottom solid cake with the heater) (Figure 3-14). The results of ARTEMIS 9 were compared with those in ARTEMIS 7 (similar materials) to obtain the effects of geometry modifications to the ablation of concrete.

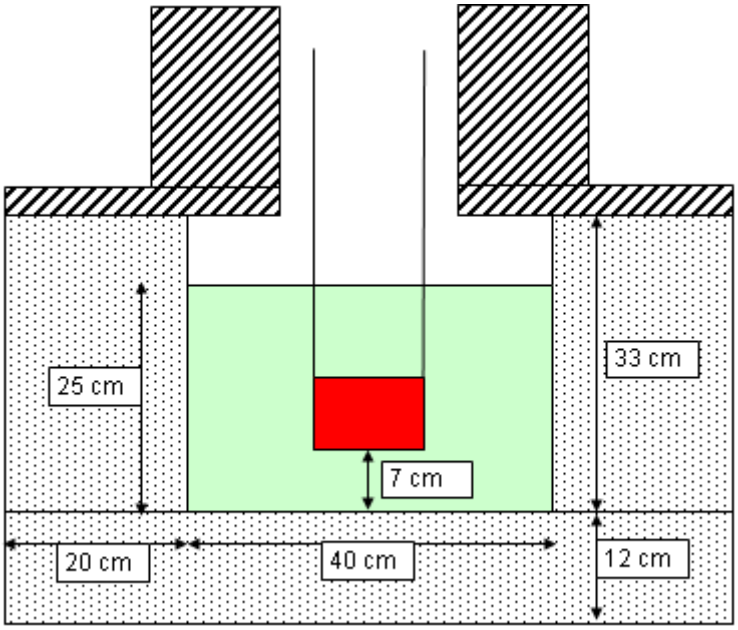

Figure 3-14. Geometry of ARTEMIS 9 (the heater is raised up and the thickness of the bottom wall of concrete cavity is reduced).

Results of test 9 were similar to those obtained in ARTEMIS 7 and ARTEMIS 8. A preferential radial ablation was observed after the test.

ARTEMIS 10 was conducted with similar materials as ARTEMIS 7 and ARTEMIS 8. However, in this test, significant technical modifications were made to the test installation. The ceiling between the concrete wall and the melt was amended to limit heat loss by radiation and conduction and also with the intention to block local recirculation (Figure 3-15). A temperature sensor was installed in order to measure the vertical temperature gradient in the melt. The sampling cane was modified in a way that it was possible to take more samples simultaneously (axial composition distribution in the melt). Besides, in order to avoid the formation of cracks in concrete, both sintering of the concrete at 400 °C and test were conducted continuously without cooling of the concrete. In test 10, the superficial velocity of the gas was doubled (2 cm/s) for the investigation of gas velocity effect on the concrete ablation.

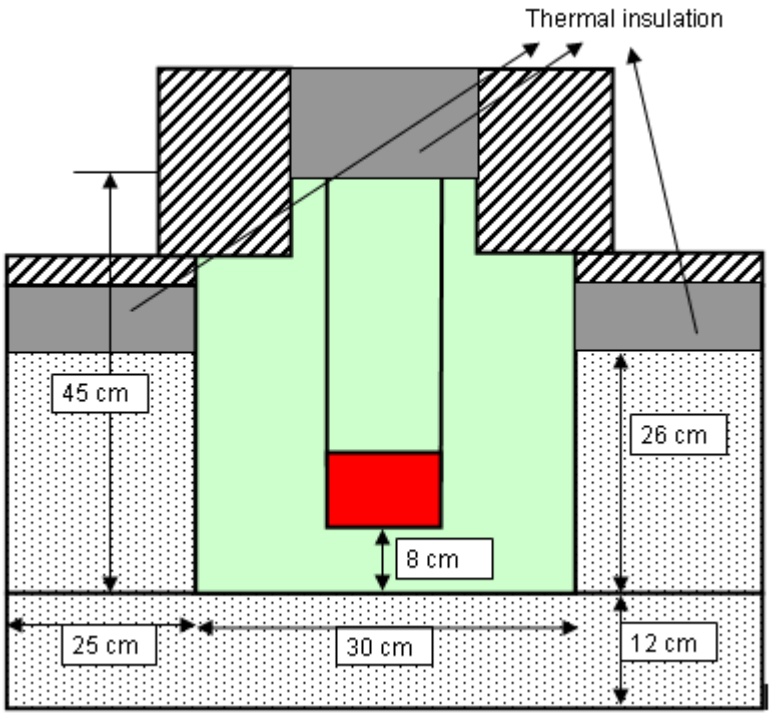

Figure 3-15. Geometry from test 10 (with upper thermal insulation).

ARTEMIS 11 was carried out with melt having the composition of concrete (as in ARTEMIS 8). The parameters of this test were identical to those of ARTEMIS 10, except the initial temperature of the melt and its composition. Initial temperature of the melt is T_{melt} + 40 °C = 562 °C, aiming at verifying the effect of initial temperature of melt onto the test results. The results of this test were compared to those of ARTEMIS 8 to see the effect of superficial gas velocity and those of ARTEMIS 10 to obtain the difference in concrete ablation with different simulant materials. It was shown that the ablation of concrete in radial direction was already dominant.

ARTEMIS 12 was another study of thermal-hydraulics effects with melt having the composition of concrete, as in ARTEMIS 11. The gas velocity was doubled in comparison to ARTEMIS 11 (4 cm/s) and the initial temperature of the melt is 722 °C which is 200 °C over T_{melt} (522 °C). The test was conducted with an expectation of enhancing the heat transfer to the bottom of the melt with a higher superficial velocity of gas (In ARTEMIS 11, with j_{gas} = 2 cm/s, only radial ablation was observed). Again, preferential radial ablation was observed.

ARTEMIS 13 was aimed to investigate the interaction between melt and concrete taking into account both thermal-hydraulics and physico-chemistry aspects. Hence, the simulating materials are similar to those of ARTEMIS 7, ARTEMIS 9 and ARTEMIS 10. The power dissipation was increased up to 9000 W. The gas velocity is the same as than in ARTEMIS 12 (0.04 m/s). Also, this test was done with the maximum value of the initial height of melt (H_{max} = 0.55 m) that is compatible with the capacity of the furnace (40 litres). The results also provide a preferential ablation of concrete, as obtained in all previous tests.

3.6 Test procedure

- Increase the setting temperature of the melt furnace to be higher than the liquidus temperature of the melt by, at least, about 20 °C.
- Start argon bubbling for void fraction measurements.
- For preventing heat shock in the corium cavity, turn on the heating elements a few minutes before transferring the liquid corium to the test section.
- Adjust the nominal gas mass flux (corresponding to superficial gas velocity).
- Thermally insulate the fusible plug and heat the outlet of the furnace to 1000 °C (melting temperature of the fusible plug).
- The test begins when the fusible plug is molten. When all the corium is transferred into the test section, the nominal power is set on the heating element. During the test, this power is readjusted due to variation of the electrical resistance of the heating element with temperature.
- Displacement (up/down/rotated) of the mobile probes should be made every 5 minutes. The measurement duration is about 3 minutes, which includes the time delay needed for going down, stabilization and measurement.
- The gas flow can be stopped or adjusted by the operator during the test for each separate injection zone.
- Evolution of the ablation interface can be observed using the installed instruments (mobile probe and thermocouples in the concrete).
- The test must be stopped when the temperatures at the lateral walls are greater than the melting temperature of the concrete (522 °C).
- The test section is tilted at the end of the experiment; the liquid melt is transferred into the dedicated tank.
- When the experimental apparatus is at ambient temperature, the test section can be removed from the concrete part.
- Finally, sampling at the interface can be made for composition analysis.

CHAPTER 4: MELT-CONCRETE INTERACTION WITH EUTECTIC MATERIALS

4.1 ARTEMIS 11 test description

ARTEMIS 11 is the fifth among the seven tests in 2D ARTEMIS series, carried out in 2007. This test was aimed at eliminating the physico-chemistry effects (i.e. segregation effect related to the refractory) and studying pure 2D thermal-hydraulics phenomena controlling the ablation of solid concrete (separate effect approach). For this purpose, the liquid melt was taken by a liquid mixture of $BaCl_2$ and LiCl having the eutectic composition that is identical to the composition of concrete.

4.1.1 Test initial conditions

Melt (corium)

- Eutectic composition: 25% mol $BaCl_2$-75% mol LiCl (62.04% mass $BaCl_2$-37.96% mass LiCl)
- Liquidus temperature (eutectic temperature): 522 °C
- Initial pouring temperature: 562 °C
- Initial mass: 57 kg
- Initial volume: 0.0233 m^3

Concrete

- Eutectic composition: 25% mol $BaCl_2$-75% mol LiCl (62.04% mass $BaCl_2$-37.96% mass LiCl)
- Melting temperature: 562 °C
- Initial temperature: 400 °C
- Initial mass: 259.25 kg
- Porosity: 46%
- Grain size: 0.2 ~ 0.9 mm

Argon gas

- Inlet temperature: 400 °C
- Superficial velocity at the melt cavity interface: 2 cm/s

4.1.2 Test installation

The test section characteristic and instrumentations are described in detail in the previous chapter (Chapter 3). Figure 4-1 represents the initial arrangement of ARTEMIS 11. The melt cavity has 30 cm diameter and initial height of the liquid melt in the cavity is 32 cm (among which only 26.5 cm is inside the concrete cavity). The heating elements are located from a distance of 6.24 cm to 14.04 cm

from the bottom of the melt cavity. The power dissipation from the heating element in ARTEMIS 11 is 6000 W while the superficial gas velocity at the melt-concrete interface is maintained at 2 cm/s. The test duration was 2 h 22 minutes 18 s but gas was cut off at 1 h 45 minutes.

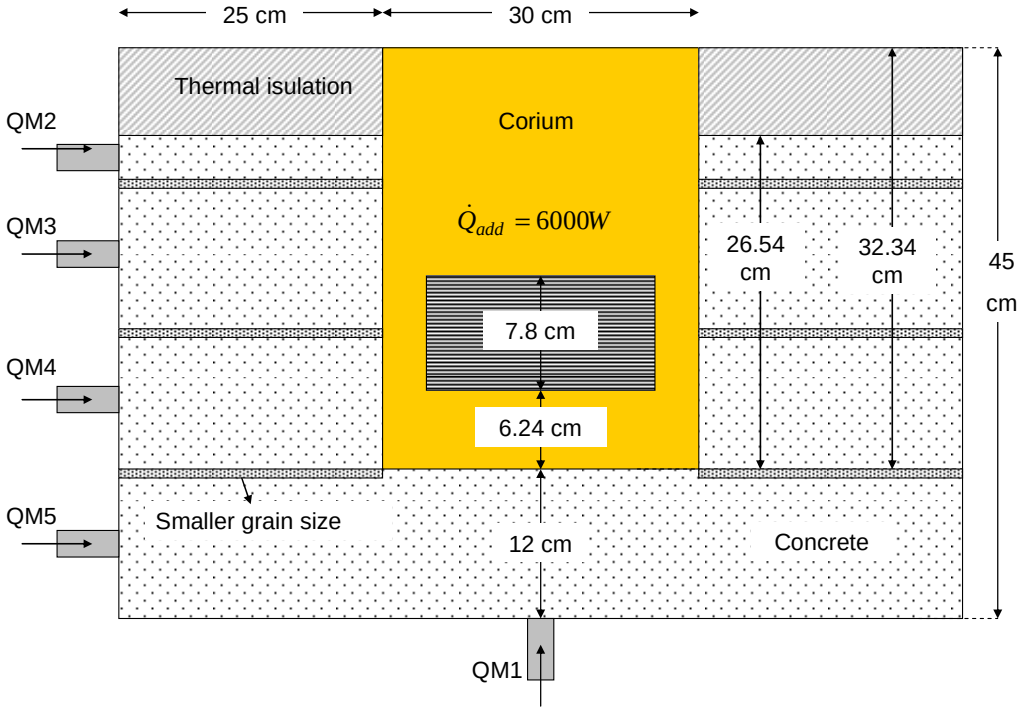

Figure 4-1. ARTEMIS 11 initial arrangement.

4.2 ARTEMIS 11 experimental data

4.2.1 Evolution of melt temperature

Evolutions of melt temperatures at different elevations *z* in the cavity (*z* is the distance from the initial melt cavity bottom) during ARTEMIS 11 test are illustrated in Figure 4-2. Minimum temperature is obtained in the bottom zone of the melt cavity (by TC12, *z* = 23.4 mm). In the heated zone, the bulk temperature increases with the increasing *z*. Maximum bulk temperature is measured at the output of the heated region (by TC2, *z* = 140 mm). The difference between maximum and minimum temperatures in the melt cavity is less than 25°C.

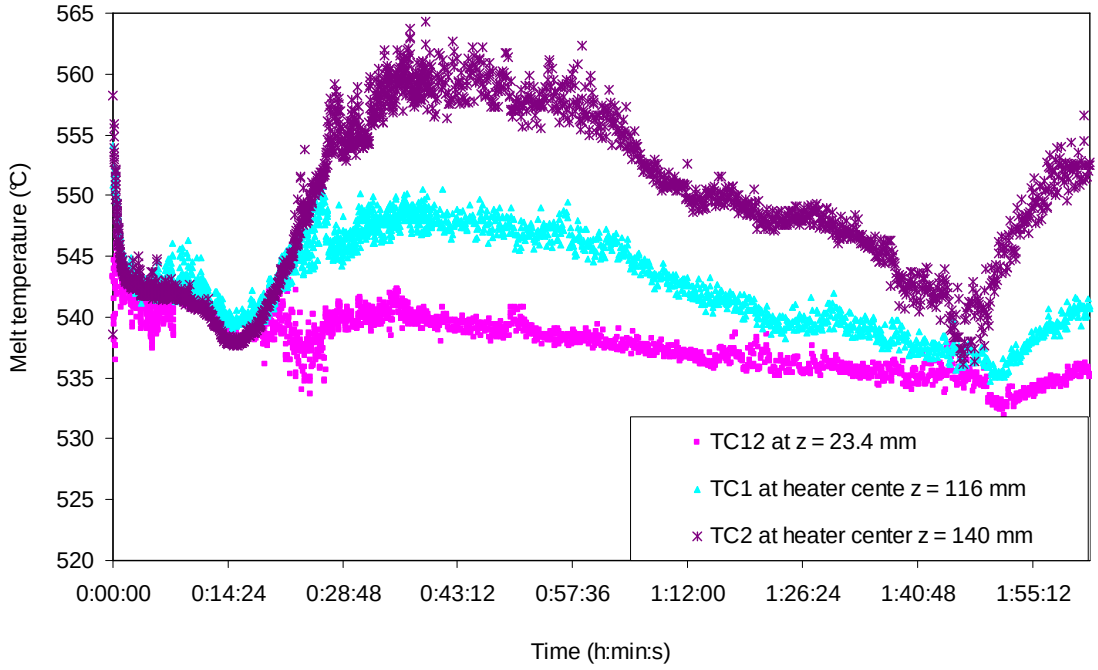

Figure 4-2. Evolution of bulk temperature at different cavity elevations in ARTEMIS 11.

During the first minutes, the melt temperature decreases from its initial temperature (562 °C) down to 535 °C at TC12 (z = 23.4 mm) or 540 °C at TC1 (z = 116 mm) and TC2 (z = 140 mm). After that, it stays quasi constant during approximately 17 minutes. Beyond 17 minutes, the melt temperature increases to a peak value (maximum temperature measured by TC2 increases to 564 °C at t = 40 minutes) then decreases again to 537 °C ~ 542 °C. After t = 1 h 45 minutes, the gas is cut partially, leading to a new increase of melt temperature.

4.2.2 Evolution of axial temperature distribution

Figure 4-3 depicts the evolution of the axial temperature distribution in the melt cavity (z = 0 corresponds to the bottom of the melt cavity which is reduced by 2 cm from the initial position of the cavity bottom due to the quick ablation at the bottom interface with the concrete only seen in the first few seconds). The temperature in the upper region is clearly higher than in the lower region. At t < 17 minutes, the temperature profile inside and above the heated zone is quite flat. An important temperature gradient is only seen in a region of approximately 30 mm thickness from the bottom of the melt cavity. At t > 17 minutes, a positive temperature gradient is observed inside the heated zone. The temperature distribution above the heated zone is still quasi uniform. At the bottom interface with concrete, the interface temperature is measured as the melting temperature of the concrete (T_{melt} = 522 °C).

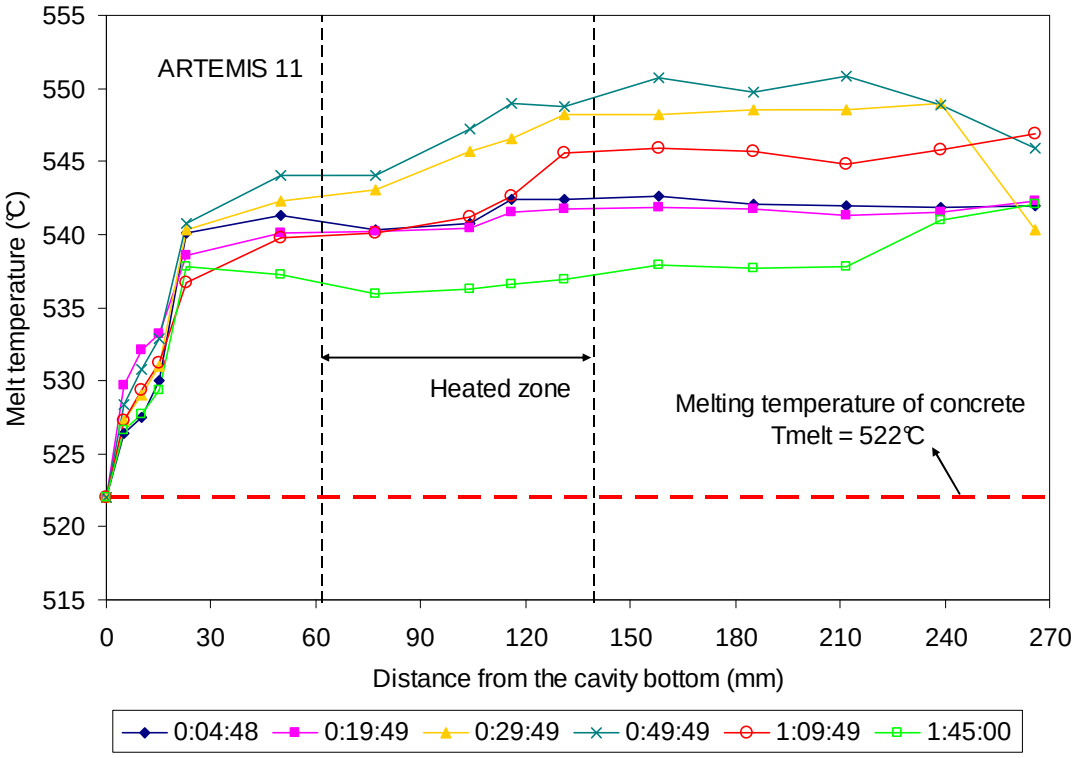

Figure 4-3. Evolution of axial bulk temperature distribution.

4.2.3 Evolution of radial temperature distribution

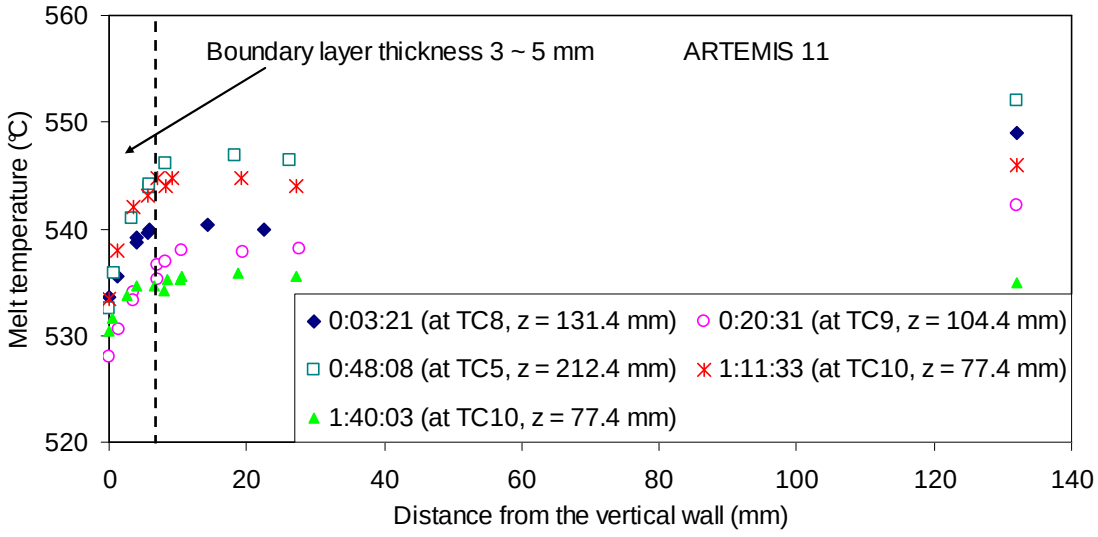

Figure 4-4. Evolution of radial bulk temperature distribution.

Regarding to the radial temperature distribution in the melt near to the lateral interface at different cavity elevations, Figure 4-4 indicates that the temperature in the cavity centre is greater than near the lateral wall (the position of the lateral is moving due to cavity evolution). A thermal boundary layer is observed within a distance of 3 ~ 5 mm from the lateral wall. In this region, a significant increase of temperature is measured. The radial temperature gradient in the centre of the cavity is much smaller

than in the boundary layer region. In addition, the measured temperature at the lateral liquid-solid interface is about 8 °C to 10 °C beyond the melting temperature of the concrete.

4.2.4 Evolution of average concrete temperature

The evolution of average concrete temperature is shown in Figure 4-5. This temperature is calculated by taking the volumetric average of the temperatures measured by maximum 85 thermocouples located inside the residual solid concrete. Only the thermocouples located in the residual solid volume are considered for this calculation. The detail of this calculation is presented in Appendix 6.

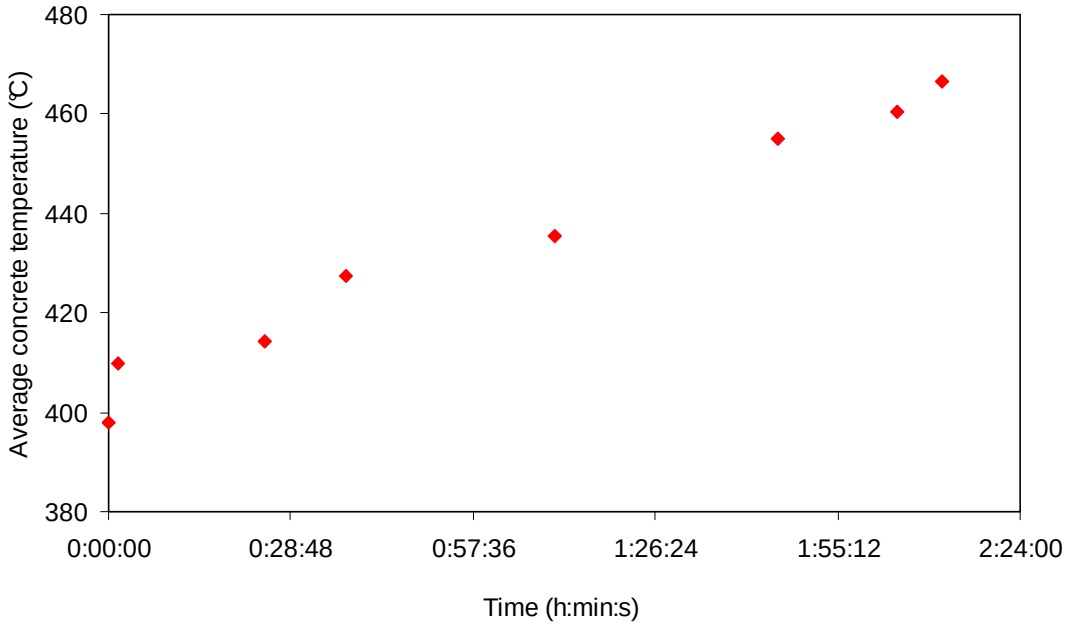

Figure 4-5. Evolution of average residual solid concrete temperature.

4.2.5 Evolution of melt cavity shape

Figure 4-6 illustrates the evolution of melt cavity shape at four azimuth angles (45°, 135°, 225° and 315°). The position of the melt cavity interface is detected by thermocouples located inside the concrete cavity. Determination method is described in details in Appendix 6. As seen in Figure 4-6, ablation occurs mainly in the radial direction (to the cavity lateral wall). Axial ablation at the cavity bottom is very minor (only 1 cm) and is observed only at test initiation (in the first minute). In addition, radial ablation is not uniform along the height of the melt cavity. Ablation at the top zone is stronger than in the bottom zone. At the end (t = 2 h 11 minutes), the thickness of ablated concrete at the top ranges between 34 ~ 38 cm while less than 4 cm of concrete are ablated in the lower part of the cavity bottom.

Evolution of the mass of molten concrete deduced from the cavity shape data is depicted in Figure 4-7. It is seen that about 83 kg of solid concrete has ablated at the end of ARTEMIS 11.

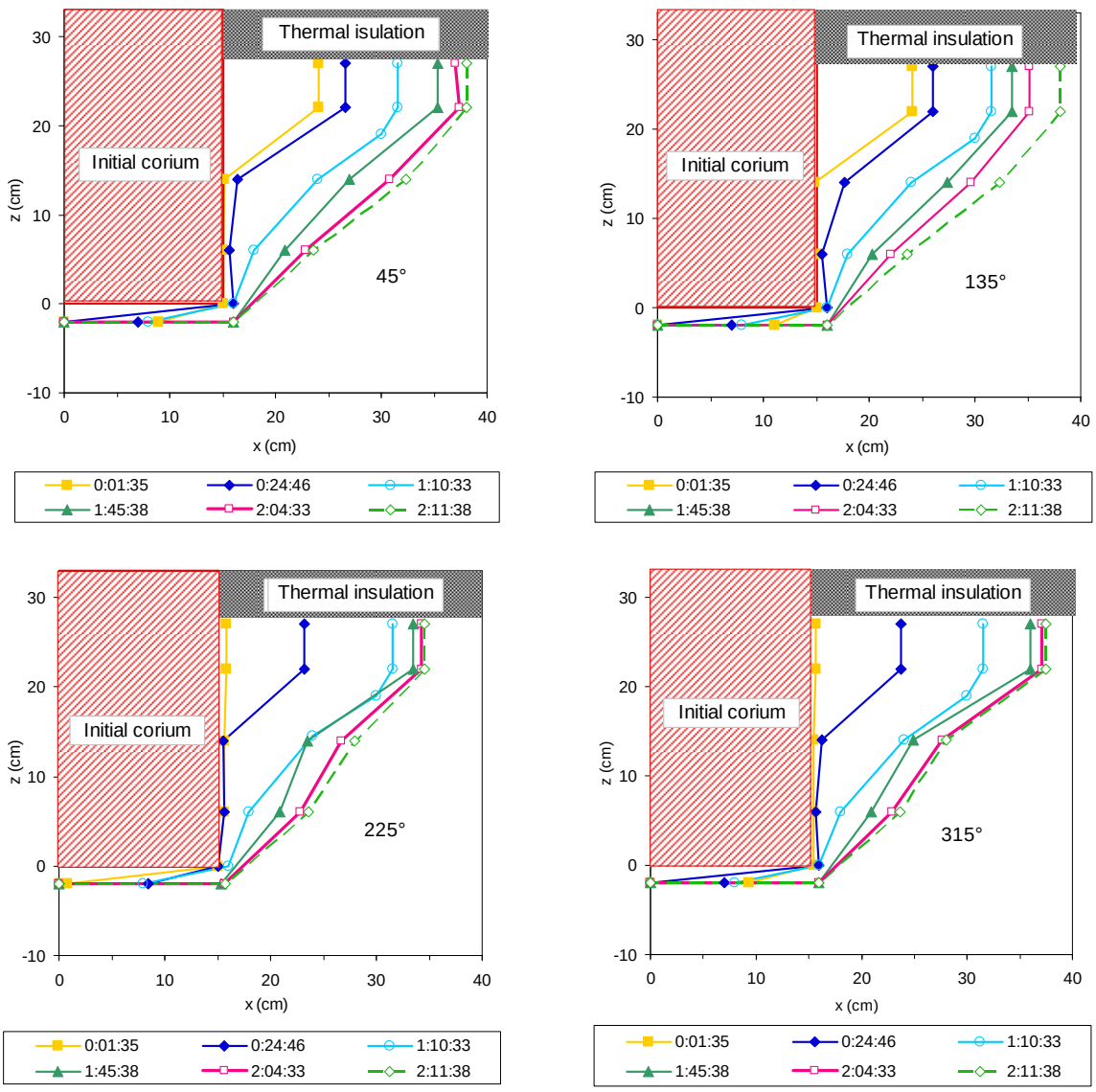

Figure 4-6. Evolution of melt cavity shape at four azimuthal angles.

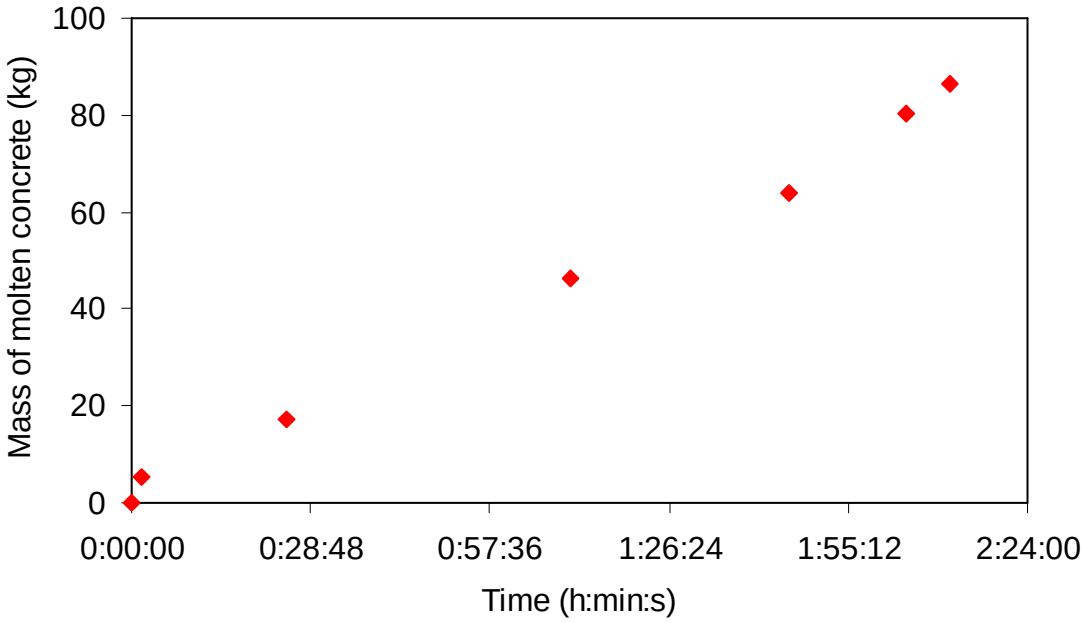

Figure 4-7. Evolution of molten concrete mass.

4.3 ARTEMIS 11 data analysis

4.3.1 Energy balance

In order to verify the energy conservation during ARTEMIS 11, the energy balance will be calculated using the reported experimental data for a control volume containing the liquid melt cavity and the surrounding solid concrete. Details of this calculation are given in Appendix 5.

Energy is conserved when the variation of the energy stored in the control volume between instant t and $t = 0$ is equal to the total energy dissipation from the heating elements minus the energy that serves for gas heating. The energy stored in the control volume includes:

- Energy due to cooling of the initial melt;
- Energy due to heating up of the solid concrete;
- Energy for melting part of the solid concrete;
- Energy for heating the molten concrete up to the melt temperature.

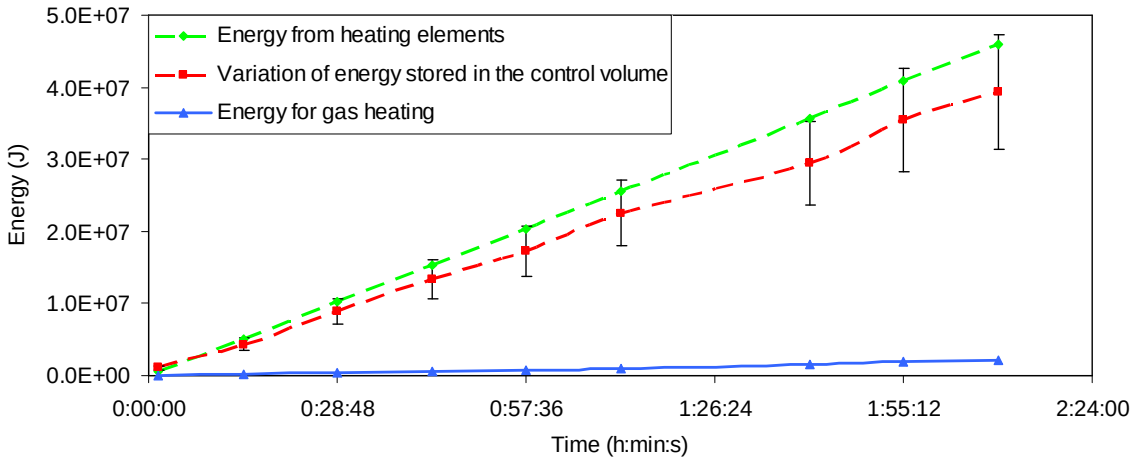

Figure 4-8. Energy balance in ARTEMIS 11.

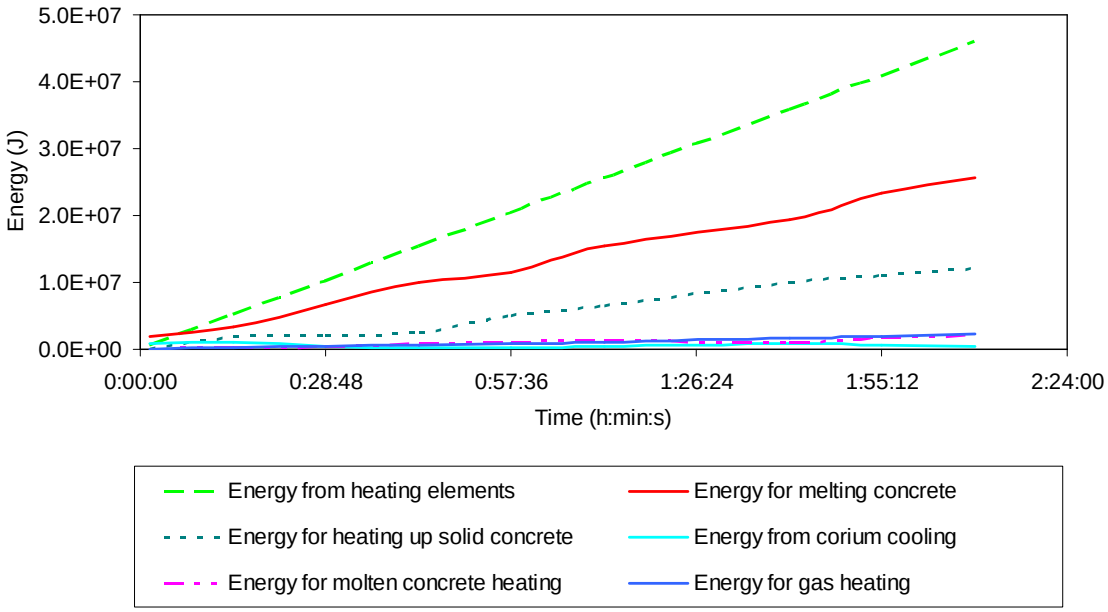

Figure 4-9. Energy distribution in ARTEMIS 11.

Figure 4-8 indicates that the energy that serves for gas heating is minor in comparison with the energy generated from heating elements and with the variation of energy stored in the materials of the control volume. Generally, energy is conserved. The energy loss is less than 10%. In addition, Figure 4-9 shows the distribution of energy. It is seen that the main energy in the control volume serves for concrete ablation. Another important part of energy is devoted for heating up the solid concrete. Energies related to melt cooling and molten concrete heating to the melting temperature are minor contributions.

4.3.2 Liquid-solid interface temperature

As observed in Figure 4-3, the interface temperature at the cavity bottom is the melting temperature of the concrete (522 °C). Figure 4-4 shows that the temperature at the lateral wall of melt cavity ranges

between 528 °C to 532 °C, which is a few degrees higher than the melting temperature of the concrete. This difference might be due to the position of the thermocouples relative to the interface and to the heat transfer in the thermocouples and in the supporting structure.

4.3.3 Prediction of heat transfer mechanism in the melt cavity

Analysis of flow recirculation in melt cavity

According to the axial and radial temperature distributions depicted in Figure 4-3 and Figure 4-4, the melt temperature in the upper part of the melt cavity is higher than in the lower part and the temperature in the cavity central is higher than near the lateral wall of the cavity. This observation indicates an upward flow in the cavity centre and a downward flow in the boundary layer near the liquid-solid interface. This behaviour emphasizes the existence of a flow recirculation in the melt cavity which is similar to what occurs under natural convection. This result seems to be surprising since gas is injected and is expected to induce a good gas-liquid mixing in the melt cavity, leading to uniform temperature.

Heat transfer coefficient relative to natural convection in a heated liquid cavity can be estimated by numbers of correlations developed in the literature. Therefore, it is interesting to compare these heat transfer coefficients with the data deduced from the experimental data of ARTEMIS 11 in order to determine if there is a gas release effect on the heat transfer in the melt cavity.

Calculation of heat transfer coefficient to the melt-concrete interface

From the experiments, the average heat transfer coefficient ($\overline{h}_{bulk}$) from the melt cavity to the liquid-solid interface in ARTEMIS 11 can be estimated as:

$$\overline{h}_{bulk} = \frac{\overline{\varphi}(t)}{T_{bulk,\max} - T_i} \tag{4-7}$$

wherein:

- $T_{bulk,max}$ is the maximum temperature of the melt (measured by TC2 at the outlet of the heater),
- T_i is the liquid-solid interface temperature which is taken as the melting temperature of the concrete (T_i = 522 °C),
- $\overline{\varphi}(t)$ is the average heat flux transferred from the melt cavity to the liquid-solid interface, determined by:

$$\overline{\varphi}(t) = \frac{\dot{Q}_{add}}{S_{lateral}(t)} \tag{4-8}$$

in which:

- $\dot{Q}_{add}$ is the power dissipation in the melt cavity,
- $S_{lateral}(t)$ is the interfacial area of the melt cavity, estimated at each time step by the method described in Appendix 6.

The average heat transfer coefficient deduced from ARTEMIS 11 will be compared with the ones obtained by existing heat transfer correlations developed for natural convection such as [Jahn et Reineke, 1974], [Mayinger et al., 1975], [Theofanous et al., 1997], etc…. The approximation of hemispherical shape or cylindrical shape is made. In these correlations, average heat transfer coefficient in volumetrically heated fluid cavity with wall cooling is written in terms of non-dimensional Nusselt number, as follows:

$$\bar{h}_{bulk} = \frac{\lambda_{bulk}\, Nu}{H} \tag{4-9}$$

wherein Nusselt is given as a function of internal Rayleigh number as:

$$Nu = a\, Ra_{in}^{b} \tag{4-10}$$

and:

$$Ra_{in} = \frac{g\, \beta_T \dot{Q}_v\, H^5}{\lambda_{bulk}\, \upsilon\, \alpha} \tag{4-11}$$

in which a and b are the coefficients of the correlations, g is the gravitational acceleration, H is the height of the fluid in the cavity, α is the thermal diffusivity of the fluid, β_T is the thermal expansion coefficient of the fluid, υ is the kinematic viscosity of the fluid, λ_{bulk} is the thermal conductivity of the fluid and $\dot{Q}_v$ is the volumetric power dissipation ($\dot{Q}_v = \frac{\dot{Q}_{add}}{V_{cavity}}$ wherein V_{cavity} is the volume of the melt cavity, determined by the method presented in Appendix 6).

It is shown in Figure 4-10 that the calculated heat transfer coefficient deduced from ARTEMIS 11 is close to those provided by natural convection correlations for certain time intervals (from 28 minutes to 57 minutes and at t > 1 h 20 minutes). However, for t < 17 minutes and at $t \approx 1$ h, the heat transfer coefficient seems to be higher than for natural convection. The difference in magnitude is however only about 2-3 times. This means that the flow recirculation in ARTEMIS 11 at these time instants seems to be more efficient than a pure natural convection. Such enhanced heat transfer coefficient could result from a gas-liquid mixing in the melt cavity, leading to an enhancement of heat transfer. If this is really the case, then the heat transfer during these periods should be compatible with a gas-liquid convection heat transfer.

A simple method to see if gas has certain effect on the heat transfer in ARTEMIS 11 is to compare the heat transfer coefficient calculated from experimental data with the heat transfer coefficient provided by gas-liquid convection correlations in literature wherein the recirculation is driven by gas along a flat plate [Gabor et al., 1976], [Gustavson et al., 1977], [Greene et al., 1980], [Chawla et al., 1984]. In these correlations, heat transfer is also calculated as a function of non-dimensional Nusselt and Rayleigh numbers as done in natural convection case. However, for the gas-liquid convection case, the Rayleigh number is written as function of void fraction (α_{gas}) of the gas in the liquid cavity, as follows:

$$Ra_{ex} = \frac{g\, \alpha_{gas} H^3}{\upsilon\, \alpha} \tag{4-12}$$

Comparison of the heat transfer coefficient deduced for ARTEMIS 11 with the ones given by gas-liquid convection heat transfer correlations is shown in Figure 4-11 with an assumption of 10% void fraction in the melt cavity. This average void fraction is calculated based on the drift model approach developed by [Zuber et Findlay, 1967].

It is seen that within the first 17 minutes, the heat transfer coefficient of ARTEMIS 11 is close to the one provided by Gustavson's and Chawla's correlations for gas-liquid convection. Hence, there is probably a gas-liquid mixing in the melt cavity that enhances the heat transfer during this time period. This is coherent with the flat axial temperature distribution observed experimentally in ARTEMIS 11 during this period. Starting from t = 17 minutes, the heat transfer coefficient of ARTEMIS 11 is lower than the heat transfer coefficient predicted from gas-liquid convection correlations. At t = 1 h, the heat transfer coefficient of ARTEMIS 11 becomes very close but still stays below the gas-liquid convection heat transfer coefficient.

By comparing Figure 4-10 and Figure 4-11, it is concluded that a gas-enhanced recirculation plausibly governs the heat transfer in the melt cavity at t < 17 minutes. During the remaining of the test, the flow recirculation in ARTEMIS 11 is closer to natural convection.

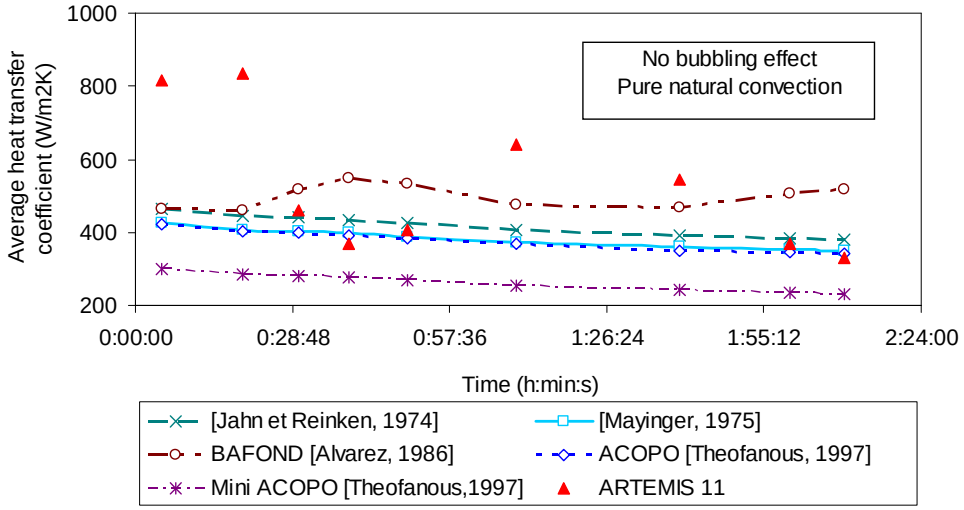

Figure 4-10. Comparison of average heat transfer coefficients between ARTEMIS 11 and natural convection correlations.

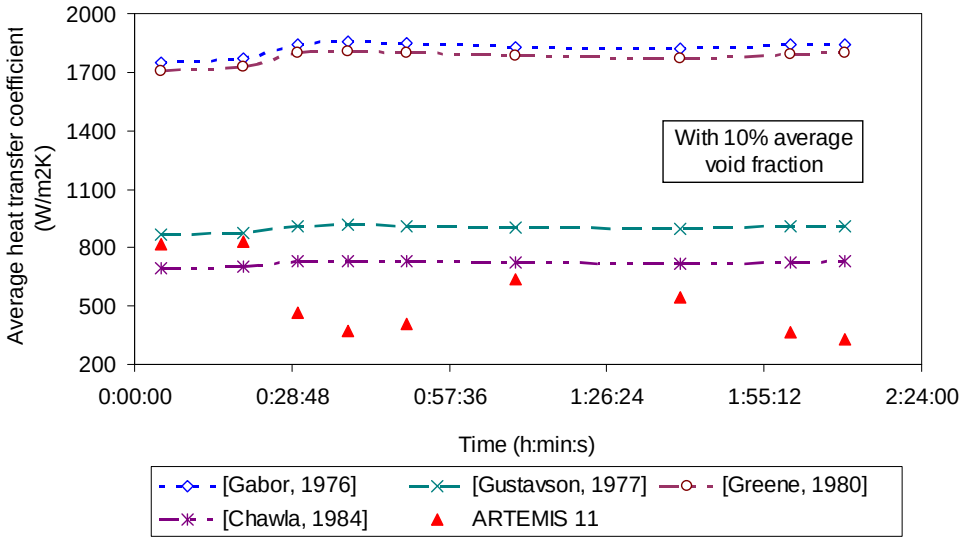

Figure 4-11. Comparison of average heat transfer coefficients between ARTEMIS 11 and gas-liquid convection correlations.

Estimation of flow velocity in the bulk

The average bulk velocity ($\overline{U}_{bulk}$) for ARTEMIS 11 is derived from the experimental data of maximum melt temperature $T_{bulk,max}(t)$ and melt cavity volume $V_{cavity}(t)$, as follow:

$$\overline{U}_{bulk}(t) = \frac{\dot{Q}_v \, H}{\rho_{bulk} \, C_{p,bulk} \, (T_{bulk,\max} - T_i)} \tag{4-13}$$

wherein:

- ρ_{bulk} is the density of the liquid melt,
- $C_{p,bulk}$ is the specific heat of the melt,
- H is the height of the melt cavity,
- $\dot{Q}_v$ is the volumetric power dissipation in the melt cavity.

Figure 4-12 shows the evolution of the estimated characteristic flow velocity in the cavity axis in ARTEMIS 11, which ranges between 3 10-4 m/s and 1.4 10-3 m/s. At t < 17 minutes when gas-enhanced convection controls the flow recirculation, the heat transfer is more efficient and the bulk velocity is about 2-3 times greater than for t > 17 minutes where the flow recirculation seems to be mainly governed by natural convection.

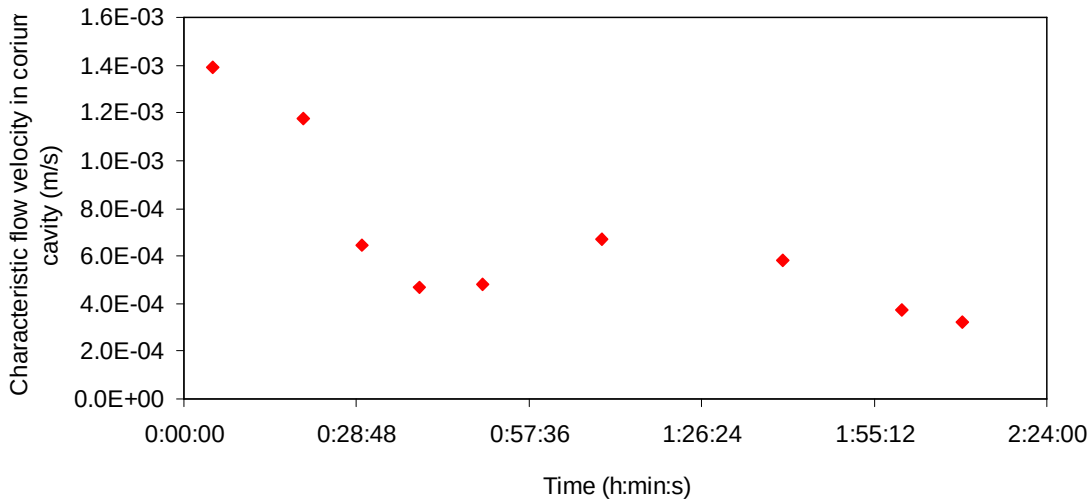

Figure 4-12. Estimation of characteristic flow velocity in melt cavity centre for ARTEMIS 11.

TRIO CFD calculation for transient natural convection heat transfer

The previous discussion allows a comparison of the heat transfer coefficient in ARTEMIS 11 with the heat transfer coefficient derived from known correlations in literature which are developed for natural convection and for gas-liquid convection. It has been deduced that in the beginning, gas-liquid convection controls heat transfer in the melt cavity and then, natural convection becomes the main heat transfer mechanism. However, it is noted that these correlations were developed only for steady state heat transfer. Hence, they may be not adapted for the transient. Besides, it is also interesting to investigate if the characteristic convection velocity that has been deduced from experiment is

compatible with the hypothesis of natural convection. For a better understanding of the transient heat transfer mechanism during ARTEMIS 11, a complementary calculation will be made with a CFD code.

To fulfil this task, TRIO code has been used for the calculation of natural convection in liquid melt for a cylindrical configuration with the test materials and same dimensions as in ARTEMIS 11. The initial test conditions are taken as the conditions of ARTEMIS 11 test in natural convection period (t > 17 minutes) with assumption of initial uniform bulk temperature in the melt cavity, i.e. T_{bulk} = 537 °C, the wall temperature is taken as the melting temperature of the concrete, i.e. $T_i = T_{melt}$ = 522 °C and the power dissipation in the heated zone of the melt cavity is $\dot{Q}_{add}$ = 6000W. The aim is to look at the transient thermal hydraulic behaviour of a heated liquid cavity with cooled wall in terms of temperature evolution, temperature gradients and flow velocity in the cavity centre if natural convection is assumed to be the main convection mechanism. The details of TRIO calculation are described in Appendix 3. Only main results are presented in Table 4-1.

It is demonstrated in Table 4-1 that the temperature distributions in axial and radial directions in the melt cavity obtained by TRIO code for natural convection are relatively similar to those observed in ARTEMIS 11. In addition, the flow velocity estimated by ARTEMIS 11 is of the same order of magnitude with the one calculated by TRIO for natural convection situation. However, the maximum bulk temperature measured in ARTEMIS 11 is smaller than the steady state bulk temperature predicted by TRIO. This means that the flow recirculation in ARTEMIS 11 is not totally similar to the classical natural convection occurring in a volumetrically heated pool with wall cooling which has been studied widely in the past.

Table 4-1. Comparison between TRIO calculation for natural convection and ARTEMIS 11.

	TRIO	ARTEMIS 11 at t > 17 minutes
Transient duration	Melt temperature increases from its initial value and reaches steady state after 800 s (~ 13 minutes)	Melt temperature increases from initial value of 537 °C to a maximum value at t = 40 minutes then gradually decreases again until t = 1 h 45 minutes. No steady state is observed
Maximum melt temperature	$T_{bulk,max} = T_{bulk,stt}$ = 573 °C	$T_{bulk,max}$ = 564° C (at $t \approx$ 40 minutes)
Axial temperature gradient	Above the heated zone: flat Linear increase of temperature from the cavity bottom to the top level of heated zone (from 522 °C at the cavity bottom to 586 °C at the exit of heater) in steady state	Above the heated zone: flat In the heated zone: linear Beneath the heated zone: quasi linear
Radial temperature gradient	Flat in the cavity centre and decreasing in the boundary layer Boundary layer thickness: 3 ~ 5 mm	Flat in the cavity central and quasi linear in the boundary layer Boundary layer thickness: 3 ~ 5 mm
Flow velocity on cavity axis	8.3 10^{-4} m/s	Transient between 3.2 10^{-4} and 7 10^{-4} m/s

At least two factors can be considered as a possible origin for the differences concerning the natural convection period between ARTEMIS 11 and TRIO calculation. First, the TRIO code did not take into account the effects of wall melting, thermal inertia associated to these materials entering the melt cavity and cavity shape modification during the whole transient. Second, the TRIO calculation does

not consider the modification of the geometry of the cavity (the increase if the interface area due to melting wall will be shown to have an influence on the evolution of the melt temperature). Furthermore, the injected gas should normally have effect on the heat transfer. Therefore, an analysis of gas flow path will be of interest.

Investigation of gas flow path

In this section, an analysis of gas distribution in ARTEMIS 11 will be presented to evaluate the behaviour of the injected gas when it flows through the porous concrete medium. The objective of this work is to investigate if gas could by-pass the melt cavity or not.

TRIO code has been used for an estimation of gas velocity on the interface between liquid melt and solid concrete with similar configuration and initial test conditions as given in ARTEMIS 11. This calculation allows determining the gas distribution in the porous concrete medium. An average superficial gas velocity was expected as 0.01 m/s in the calculation case (in ARTEMIS 11, the gas superficial velocity was 0.02 m/s) along the interfaces of the melt cavity (except for the three elevations at which the size of the concrete grains is reduced). The local superficial gas velocity on the liquid-solid interface is calculated as a function of the cavity height and the distance from the cavity centre to its lateral wall. Details of the calculation are given in Appendix 2. Only main results are shown below.

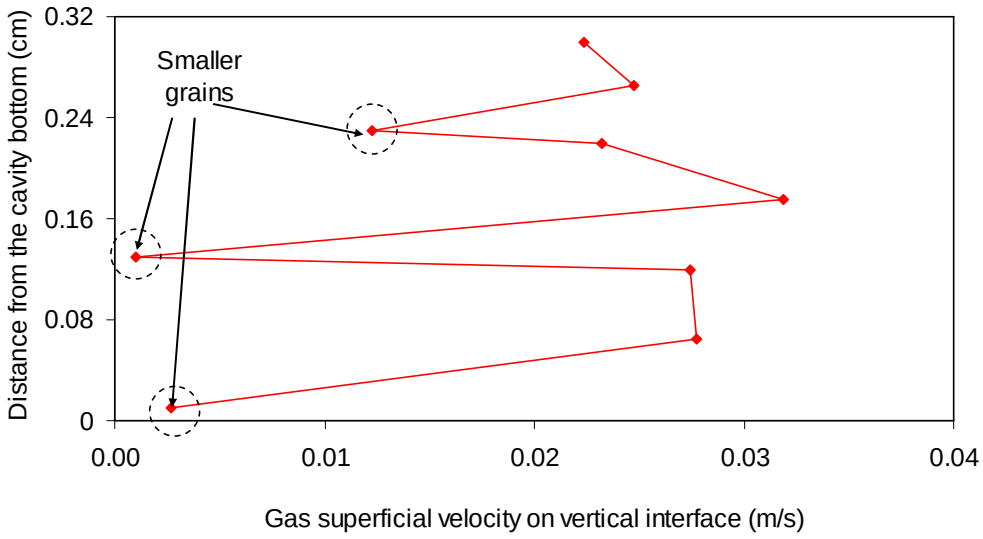

Figure 4-13. Estimation of gas velocity on the vertical interface of melt cavity.

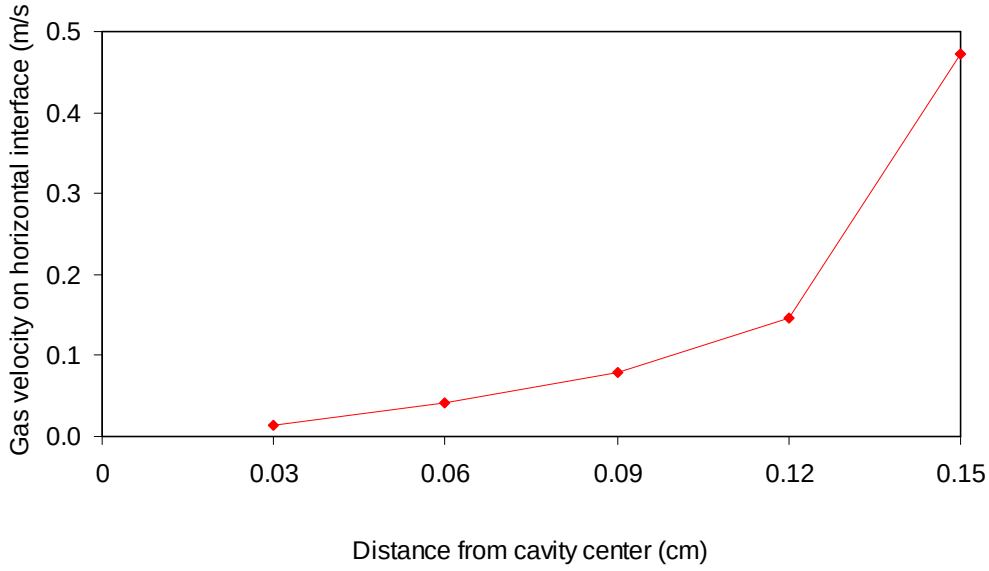

Figure 4-14. Estimation of gas velocity on the horizontal interface of melt cavity.

As seen in Figure 4-13 and Figure 4-14, with the initial condition and material physical properties given as in ARTEMIS 11, assuming that the permeability of the porous concrete medium does not change during the test, gas would penetrate the concrete and enter the melt cavity from both horizontal and vertical interfaces. The calculated superficial gas velocity ranges between 0.005 m/s to 0.5 m/s. On the horizontal interface, the superficial gas velocity is predicted to be higher in the periphery than in the centre (Figure 4-14). Figure 4-13 illustrates that at three elevations of the cavity at which the size of the concrete grains is smaller, gas still can enter the melt cavity but its superficial velocity is lower than at other elevations with larger grain size. At other elevations with normal size of concrete grains, the average gas velocity is about 0.01 m/s which is the expecting value.

Some sensitivity calculations have been made. The increase in concrete grain size leads to an increase in its permeability, resulting in a decrease of gas velocity at the melt cavity interface because the gas can by-pass the melt more easily.

The fact that gas flows through the melt cavity is coherent with the experimental observation of decreasing melt temperature evolution during the first 17 minutes of ARTEMIS 11 (gas-liquid mixing convection period). However, as discussed in the preceding, after 17 minutes, the temperature gradient in the melt cavity increases, indicating that there is less or even no more gas in the melt cavity. Existence of gas in the melt cavity at t < 17 minutes and its disappearance at t > 17 minutes are in agreement with the measurement of void fraction in ARTEMIS 11.

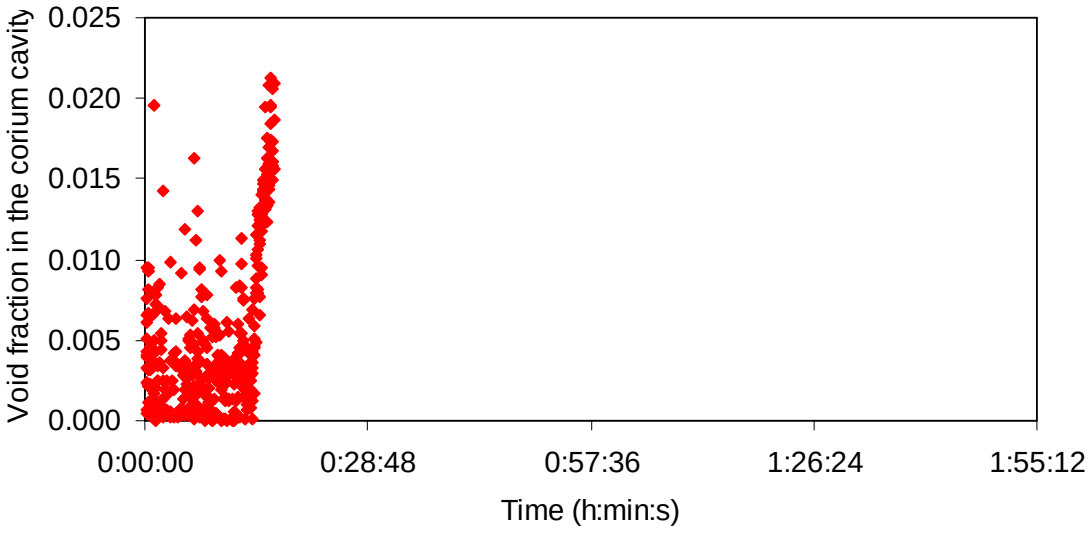

Figure 4-15. Void fraction measurement in ARTEMIS 11.

As seen in Figure 4-15, existence of gas in the melt cavity is detected only during the first 17 minutes from the test initiation. The gas void fraction is about 10% in average. After that, there is no more record of gas in the melt cavity.

Entrainment of gas during t < 17 minutes in ARTEMIS 11 can be explained by post-mortem observations of several gas blowing holes at the liquid-solid interface. These holes are seen at the end of the experiment after removing the remaining liquid melt from the cavity (Figure 4-16).

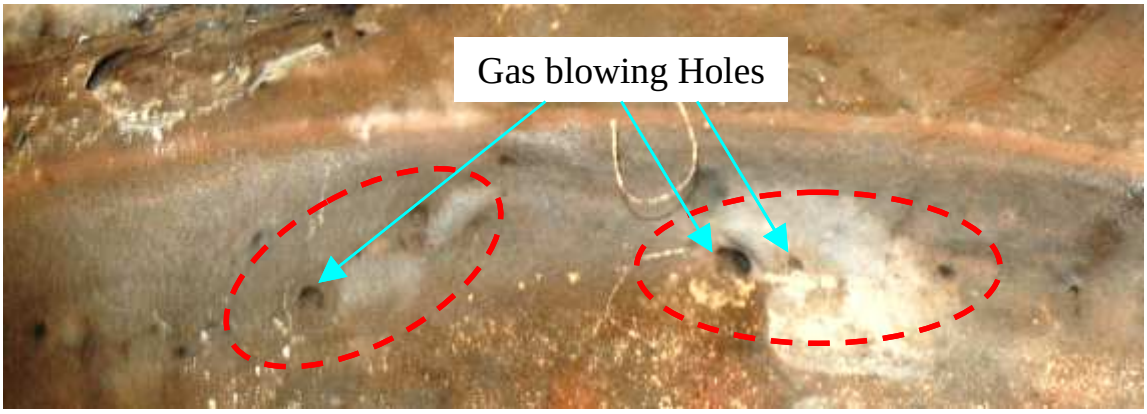

Figure 4-16. Existence of localized gas blowing holes at the melt cavity interface.

Figure 4-16 shows existence of certain holes at the melt cavity lateral wall after ARTEMIS 11. This means that the gas did probably not penetrate the melt interface uniformly but only at a reduced number of locations and probably only during the first 17 minutes in the test.

Disappearance of gas in the melt at t > 17 minutes can be explained by two possibilities.

- First, it might be due to an increase of permeability inside the concrete. Indeed, when the permeability of the concrete increases, gas can penetrate the concrete more easily and might no longer enter the melt cavity (Calculations with assumption of ten times and hundred times higher

permeability in the porous concrete have been performed to confirm this behaviour, shown in Appendix 2). The increase of permeability might be due to the formation of cracks inside the concrete linked to temperature gradients in the concrete and thermal expansion.

- Second, melting of concrete at the liquid-solid interface might plug the porosity at the interface between liquid melt and solid concrete, leading to a decrease of the number of gas blowing holes, preventing gas from entering the melt cavity. However, a limited number of holes were observed at the cavity interface at the test ending (Figure 4-16), indicating that gas still can enter the melt cavity but plausibly with a reduced flow rate.

4.3.4 Conclusion from the analysis

Main conclusions have been made from the preceding analysis of ARTEMIS 11 experimental data.

- First, there is evidence of a flow recirculation in the melt cavity. The fluid goes upwards in the cavity centre and downwards in the boundary layer existing along the lateral wall.
- Second, the interface temperature stays at melting temperature of the concrete at the bottom interface and is measured at a few degrees above the melting temperature of the concrete at the lateral interface.
- Third, an analysis on the heat transfer in the melt cavity has been carried out and led to the conclusion that:
  - During the first 17 minutes of ARTEMIS 11, there is an efficient gas-liquid mixing in the melt cavity and the heat transfer is controlled by gas-liquid convection. The deduced heat transfer coefficients in ARTEMIS 11 are close to the ones obtained from gas-liquid convection correlations.
  - However, for t > 17 minutes, a comparison with TRIO CFD calculations shows that the convection seems to be close to natural convection. The heat transfer coefficients become significantly smaller than the gas-liquid convection heat transfer coefficient.
  - The transition between gas-liquid flow configuration and natural convection flow configuration seems to be quite fast.
  - The calculations of gas flow in the porous concrete medium (with nominal characteristics) and superficial velocity at the melt-concrete interface by CFD code show percolation of gas in the melt cavity. It is emphasized that there is a significant increase in the permeability of the porous concrete by crack formation (making gas by-pass the concrete) and/or possible plugging of the porosity by the molten concrete at the liquid-solid interface (preventing gas from entering the melt cavity).

4.4 0D modelling of thermal-hydraulics and concrete ablation for ARTEMIS 11

4.4.1 Main assumptions of 0D model

The objective of this model development is to explain the melt temperature evolution versus time in the cavity and to bring more highlights to the nature of the internal convection. A system containing a melt cavity located inside a solid porous concrete cavity is considered. A schematic of the system is shown in Figure 4-17.

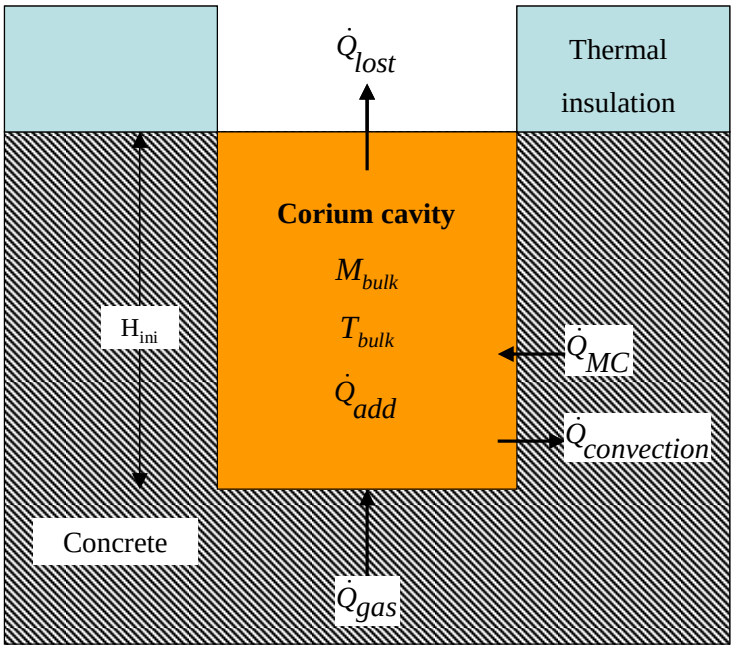

Figure 4-17. ARTEMIS 11 configuration for 0D model.

The following hypotheses are assumed for the simplified model approach:

- Solid concrete is ablated across the melt cavity surface;
- Variation of the melt cavity radius will be calculated with assumption of hemisphere or cylinder geometry of the cavity and the height of the melt cavity is assumed to be constant ($H(t) = H_{ini} = 33$ cm);
- The temperature at the interface between the cavity and the solid concrete, T_i, is taken as the melting temperature of the concrete as done in the model developed for LIVE L3A in Chapter 2;
- Since the melt cavity temperature is not uniform, an average temperature difference (with the boundary) is defined with an assumption that the variation of the average temperature difference with the interface in the cavity is proportional to the variation of the maximum temperature difference in the cavity, or $\Delta\overline{T}_{bulk} = k_T \Delta T_{bulk,\max}$ where k_T is a coefficient that is assumed to be time independent with $\Delta\overline{T}_{bulk} = \overline{T}_{bulk} - T_i$ and $\Delta T_{bulk,\max} = T_{bulk,\max} - T_i$;
- The average melt temperature in ARTEMIS 11 is taken as the mathematical average of the temperature measured by thermocouples located at different level in the melt cavity. Calculating the ratio $\frac{\overline{T}_{bulk} - T_i}{T_{bulk,\max} - T_i}$ leads to $k_T \approx 1$ during the first 17 minutes and $k_T \approx 0.75$ for the rest of the test (in LIVE L3A, $k_T \approx 0.8$).

4.4.2 Model basic equations

The model will be developed based on the mass and energy conservation in the melt cavity. The control volume is taken as the volume of the liquid melt.

Mass conservation

Changes in the mass of the cavity are caused by the molten concrete entering into the cavity and the gas entering and going out. The mass conservation equation for the cavity is written as following:

$$\frac{dM_{bulk}}{dt} = \dot{m}_{MC} + \dot{m}_{gas,in} - \dot{m}_{gas,out} \tag{4-14}$$

in which, M_{bulk} is the mass of the cavity, $\dot{m}_{MC}$ is the mass flow rate of the molten concrete entering the cavity, $\dot{m}_{gas,in}$ is the mass flow rate of the gas entering the cavity, and $\dot{m}_{gas,out}$ is the mass flow rate of the gas getting out from the cavity.

As mentioned before, the mass flow rate of gas is assumed to be unchanged across its path through the cavity. Therefore, Equation (4-14) can be rewritten as:

$$\frac{dM_{bulk}}{dt} = \dot{m}_{MC} = \rho_{MC} \frac{dV_{cavity}}{dt} \tag{4-15}$$

wherein V_{cavity} is the volume of the melt cavity.

Since the concrete has a porosity of ε = 46%, the density of the molten concrete will be given as:

$$\rho_{MC} = \rho_{solid} \ (1-\varepsilon) \tag{4-16}$$

wherein ρ_{solid} is the intrinsic density of concrete material.

Energy conservation

The causes that result in power dissipation and adsorption in the cavity include:

- The power dissipation $\dot{Q}_{add}$;
- The power related to gas flow $\dot{Q}_{gas}$;
- The power related to molten concrete entrance $\dot{Q}_{MC}$;
- The power lost by the melt towards the rest of the test section $\dot{Q}_{lost}$ (not including the concrete part);
- The power transferred from the cavity to the interface between the cavity and the solid concrete due to convection in the cavity $\dot{Q}_{convection}$. This power will be used for ablating the solid concrete as well as for heating the solid concrete near the interface by conduction ($\dot{Q}_{convection} = \dot{Q}_{MC} + \dot{Q}_{conduction}$) (Figure 4-18).

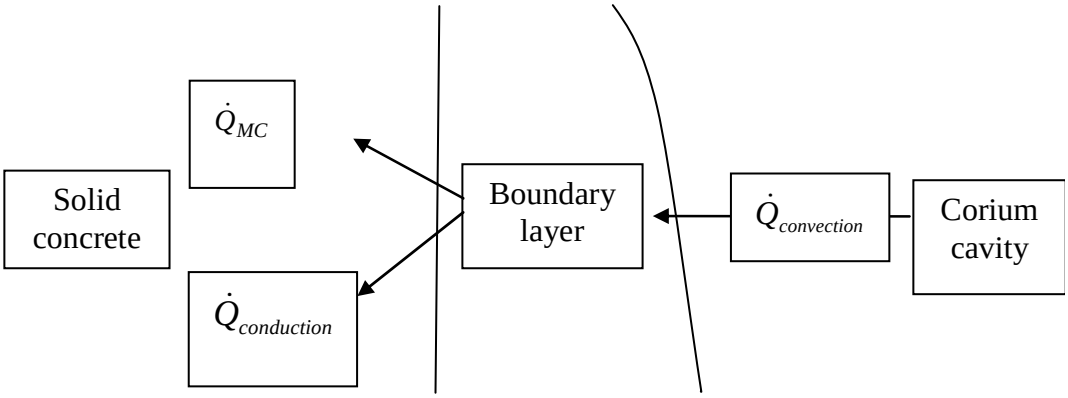

Figure 4-18. Heat transfer at the liquid-solid interface.

The power balance equation for the cavity is written as:

$$\frac{d}{dt}(M_{bulk}H_{bulk}) = \dot{Q}_{add} + \dot{Q}gas + \dot{Q}_{MC} - \dot{Q}_{lost} - \dot{Q}_{convection} \quad (4\text{-}17)$$

in which H_{bulk} is the average mass enthalpy of the melt.

The left hand side of Equation (4-17) can be rewritten as:

$$\frac{d}{dt}(M_{bulk}H_{bulk}) = M_{bulk}\frac{dH_{bulk}}{dt} + H_{bulk}\,\dot{m}_{MC} \quad (4\text{-}18)$$

The enthalpy of the cavity at a given average bulk temperature $\overline{T}_{bulk}$ is given by:

$$H_{bulk}(\overline{T}_{bulk}) = H^{concrete}_{melting}(T_{melt}) + C^{bulk}_{p,liquid}(\overline{T}_{bulk} - T_{melt}) \quad (4\text{-}19)$$

where $H^{concrete}_{melting}(T_{melt})$ is the enthalpy at a reference temperature T_{melt} (T_{melt} is the melting temperature of concrete),.

Hence, variation of the energy in the melt cavity can be rewritten as:

$$\frac{d}{dt}(M_{bulk}H_{bulk}) = k_T\,M_{bulk}\,C^{bulk}_{p,liquid}\frac{d\Delta T_{bulk,\max}}{dt} + H_{bulk}\,\dot{m}_{MC} \quad (4\text{-}20)$$

Part of the power dissipation will serve for gas heating from the initial temperature of the gas ($T_{gas,in}$ = 400 °C) (we consider here the total temperature increase for the gas) to the maximum cavity temperature $T_{gas,out} = T_{bulk,max}$. Thus, the power necessary for gas heating up is calculated as follows:

$$\dot{Q}gas = \dot{m}gas\left[H\,gas(T_{gas,in}) - H\,gas(T_{bulk,\max})\right] \quad (4\text{-}21)$$

in which, $H_{gas}(T_{gas,in})$ and $H_{gas}(T_{bulk,,max})$ are the mass enthalpies of the gas at $T_{gas,in}$ and at $T_{bulk,max}$, respectively.

Assuming that the molten concrete enters the cavity at T_{melt} and with a mass flow rate $\dot{m}_{MC}$, thus the power entering the cavity with molten concrete is written as:

$$\dot{Q}_{MC} = \dot{m}_{MC}\, H_{MC}(T_{melt}) \tag{4-22}$$

in which $H_{MC}(T_{melt})$ is the mass enthalpy of the molten concrete at T_{melt}.

The power that gets out from the cavity to the liquid-solid interface by convection is written as:

$$\dot{Q}_{convection} = \overline{\varphi}\ \mathrm{S}_{\mathrm{lateral}} = \overline{h}_{bulk}\ \mathrm{S}_{\mathrm{lateral}} \Delta T_{bulk,\max} \tag{4-23}$$

in which $\overline{\varphi}$ is the average heat flux transferred to the liquid-solid interface due to convection, $\overline{h}_{bulk}$ is the average heat transfer coefficient at the liquid-solid interface and $S_{lateral}$ is the lateral surface area of the melt cavity.

This power will be used to heat up the concrete from an average temperature $T_{concrete}$ of the concrete to the melting temperature T_{melt}, before ablating it (phase change) as well as to heat up the solid concrete left in the solid concrete by conduction. Thus, the power balance on the liquid-solid interface reads:

$$\dot{Q}_{convection} = \left[L_{melting}^{concrete} + C_{p,solid}^{concrete}\ (T_{melt} - T_{concrete}) \right] \dot{m}_{MC} + \dot{Q}_{conduction} \tag{4-24}$$

Hence, the ablation rate of the concrete will be deduced:

$$\dot{m}_{MC} = \frac{\dot{Q}_{convection} - \dot{Q}_{conduction}}{L_{melting}^{concrete} + C_{p,solid}^{concrete}\ \Delta T_{concrete})} \tag{4-25}$$

or:

$$\dot{m}_{MC} = \frac{h_{bulk}\ \mathrm{S}_{\mathrm{lateral}}\, \Delta T_{bulk,\max} - \dot{Q}_{conduction}}{L_{melting}^{concrete} + C_{p,solid}^{concrete}\ \Delta T_{concrete}} \tag{4-26}$$

with $\Delta T_{concrete} = T_{melt} - T_{concrete}$.

Combining the above relations, the final form of the energy balance in the melt cavity reads:

$$\begin{aligned} \frac{d\Delta T_{bulk,\max}}{dt} = {} & \frac{\dot{Q}_{add}}{k_T M_{bulk} C_{p,liquid}^{bulk}} - \frac{\dot{m}_{gas} C_{p,gas} \left(\Delta T_{bulk,\max} + T_{melt} - T_{gas,in} \right)}{k_T M_{bulk} C_{p,liquid}^{bulk}} \\ & - \frac{\dot{Q}_{lost}}{k_T M_{bulk} C_{p,liquid}^{bulk}} + \frac{\dot{Q}_{conduction}}{L_{melting}^{concrete} + C_{p,solid}^{concrete}\ \Delta T_{concrete}} \frac{\Delta T_{bulk,\max}}{M_{bulk}} \\ & - \frac{\overline{h}_{bulk}\ S_{lateral}\ \Delta T_{bulk,\max}}{k_T M_{bulk} C_{p,liquid}^{bulk}} \left[1 + \frac{k_T\ C_{p,liquid}^{bulk}\ \Delta T_{bulk,\max}}{L_{melting}^{concrete} + C_{p,solid}^{concrete}\ \Delta T_{concrete}} \right] \end{aligned} \tag{4-27}$$

As stated in the analysis of the ARTEMIS 11 experimental data, two flow regimes can be considered which are natural convection and gas-liquid convection. Therefore, in order to determine the evolution of the melt temperature by Equations (4-27), applications of existing correlations developed for these regimes will be used for estimation of heat transfer in the melt cavity.

Case 1. Natural convection heat transfer in the cavity

If natural convection controls heat transfer in the melt cavity, then the heat transfer coefficient to the cavity wall will be written as:

$$\bar{h}_{bulk} = \frac{a\lambda_{bulk}}{H}\left(\frac{g\,\beta_T\,H^3}{\upsilon\,\alpha}\right)^b \Delta T_{bulk,\max}^b \tag{4-28}$$

in which a and b are the coefficients of the correlation of the Nusselt number ($Nu = a\,Ra_{ex}^b$) which will be taken from different natural convection correlations, H is the height of the melt cavity, g is the gravitational acceleration; α, β_T, λ_{bulk} and ν are the thermal diffusivity, thermal expansion coefficient, thermal conductivity and kinematic viscosity of the melt, respectively.

Then the energy balance in the cavity can be rewritten as:

$$\frac{d\Delta T_{bulk,\max}}{dt} = A_0 + A_1\,\Delta T_{bulk,\max} - A_2\,S_{lateral}\,\Delta T_{bulk,\max}^{1+b} - A_3\,S_{lateral}\,\Delta T_{bulk,\max}^{2+b} \tag{4-29}$$

wherein:

$$A_0 = \frac{\dot{Q}_{add} - \dot{m}_{gas}\,C_{p,gas}\,(T_{melt} - T_{gas,in}) - \dot{Q}_{lost}}{k_T\,M_{bulk}\,C_{p,liquid}^{bulk}} \tag{4-30}$$

$$A_1 = \frac{\dfrac{\dot{Q}_{conduction}}{L_{melting}^{concrete} + C_{p,solid}^{concrete}\,\Delta T_{concrete}} - \dfrac{\dot{m}_{gas}\,C_{p,gas}}{k_T\,C_{p,liquid}^{bulk}}}{M_{bulk}} \tag{4-31}$$

$$A_2 = \frac{\dfrac{a\lambda_{bulk}}{H}\left(\dfrac{g\,\beta_T\,H^3}{\upsilon\,\alpha}\right)^b}{k_T M_{bulk} C_{p,liquid}^{bulk}} \tag{4-32}$$

$$A_3 = \frac{\dfrac{a\lambda_{bulk}}{H}\left(\dfrac{g\,\beta_T\,H^3}{\upsilon\,\alpha}\right)^b}{M_{bulk}\,(L_{melting}^{concrete} + C_{p,solid}^{concrete}\,\Delta T_{concrete})} \tag{4-33}$$

Case 2. Gas-liquid convection heat transfer in the cavity

If gas-liquid convection is assumed to govern the heat transfer in the melt cavity, then the heat transfer coefficient in the cavity is assumed to be given by:

$$\bar{h}_{bulk} = \frac{a^* \lambda_{bulk}}{H} \left(\frac{g \alpha_{gas} H^3}{\upsilon \alpha} \right)^{b^*} \tag{4-34}$$

in which α_{gas} is the void fraction in the bulk, a^* and b^* are the coefficients of the correlation of the Nusselt number ($Nu = a^* Ra_{ex}^{b^*}$ with $Ra_{ex} = \frac{g \alpha_{gas} H^3}{\upsilon \alpha}$) which will be taken from different gas-liquid convection correlations.

Then the energy balance in the cavity will be rewritten as:

$$\frac{d\Delta T_{bulk,\max}}{dt} = A_0 + A_1 \Delta T_{bulk,\max} - A_2 S_{lateral} \Delta T_{bulk,\max} - A_3 S_{lateral} \Delta T_{bulk,\max}^2 \tag{4-35}$$

wherein:

$$A_0 = \frac{\dot{Q}_{add} - \dot{m}_{gas} C_{p,gas} (T_{melt} - T_{gas,in})}{k_T M_{bulk} C_{p,liquid}^{bulk}} \tag{4-36}$$

$$A_1 = \frac{\frac{\dot{Q}_{conduction}}{L_{melting}^{concrete} + C_{p,solid}^{concrete} \Delta T_{concrete}} - \frac{\dot{m}_{gas} C_{p,gas}}{k_T C_{p,liquid}^{bulk}}}{M_{bulk}} \tag{4-37}$$

$$A_2 = \frac{\frac{a^* \lambda_{bulk}}{H} \left(\frac{g \alpha_{gas} H^3}{\upsilon \alpha} \right)^{b^*}}{k_T M_{bulk} C_{p,liquid}^{bulk}} \tag{4-38}$$

$$A_3 = \frac{\frac{a^* \lambda_{bulk}}{H} \left(\frac{g \alpha_{gas} H^3}{\upsilon \alpha} \right)^{b^*}}{M_{bulk} (L_{melting}^{concrete} + C_{p,solid}^{concrete} \Delta T_{concrete})} \tag{4-39}$$

In order to solve Equations (4-33) and (4-39) for calculation of melt temperature evolution, additional assumptions concerning the melt cavity shape and related interface area are required.

Since the convection heat flux transferred from the liquid cavity to the liquid-solid interface can be calculated from Equation (4-24), the ablation mass flow rate or the ablation velocity of the concrete can be deduced by using Equation (4-26). This allows estimating the volume of the liquid melt cavity.

Then, calculation of the radius of the cavity will be done by assuming either a hemisphere or cylinder geometry of the melt cavity.

Case 1: Hemisphere geometry

If a hemispherical geometry is assumed, then the interface area of the melt cavity is:

$$S_{lateral} = 2\,\pi\,R\,H \tag{4-40}$$

and the cavity volume is calculated by:

$$V_{cavity} = \frac{1}{3}\,\pi\,H^{2}\,(3\,R - H) \tag{4-41}$$

Therefore, the radius of the hemispherical melt cavity is:

$$R = \frac{1}{3}\,\left(\frac{3\,V_{cavity}}{\pi\,H^{2}} + H\right) \tag{4-42}$$

Case 2: Cylinder geometry

If cylinder geometry is assumed, then the interface area of the melt cavity is:

$$S_{lateral} = 2\,\pi\,R\,H \tag{4-43}$$

and its volume is:

$$V_{cavity} = \pi\,R^{2}\,H \tag{4-44}$$

Then, radius of the cylindrical melt cavity is:

$$R = \sqrt{\frac{V_{cavity}}{\pi\,H}} \tag{4-45}$$

4.4.3 Model application for ARTEMIS 11

The developed model has been applied for the test conditions of ARTEMIS 11. The main parameters of interest are the evolution of the maximum melt temperature and the evolution of the ablated mass of the concrete. Heat transfer correlations for natural convection as well as gas-liquid convection will be tested. Two configurations will be considered for the melt cavity, which are hemisphere and cylinder.

Melt temperature evolution

As discussed in the analysis of ARTEMIS 11 data, in the first period (t < 17 minutes), gas-liquid convection seems to govern the flow recirculation in the melt cavity. Therefore, calculations with the correlations developed by [Gabor et al., 1976], [Gustavson et al., 1977], [Greene et al., 1980] and [Chawla et al., 1984] have been carried out for this beginning period. Since the melt cavity is in cylinder shape initially, cylindrical geometry was assumed for this calculation.

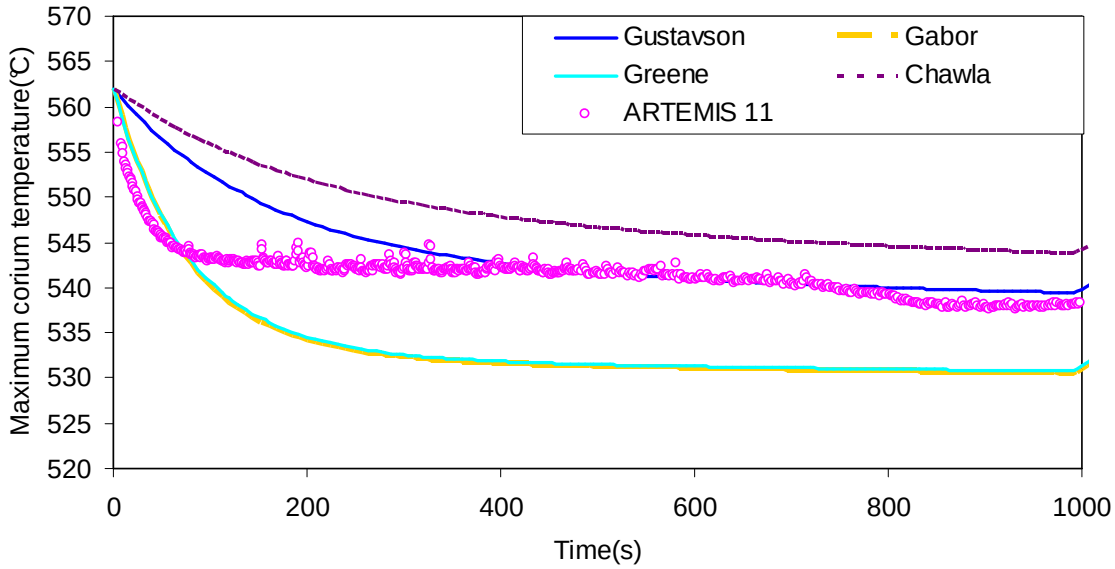

Figure 4-19. ARTEMIS 11 evolution of maximum melt temperature for t < 17 minutes using gas-liquid convection heat transfer correlations.

It is shown in Figure 4-19 that among the four applied gas-liquid convection heat transfer correlations, the one introduced by [Gustavson et al., 1977](Nu = 0.78 Ra0.25) allows a fair estimation of the bulk temperature evolution in comparison to the experimental data obtained in ARTEMIS 11. The difference between calculation and experiment is observed only in a very short period (at t < 200 s).

In the second period (t > 17 minutes), calculations will be performed for the two flow regimes, either natural convection or gas-liquid convection. The calculation results are shown in Figure 4-20 and Figure 4-21. It is seen that when the gas-liquid convection correlations are applied, the heat transfer coefficient is too high despite of the selected geometry (cylinder or hemisphere), resulting in a continuous decrease of melt temperature. The calculated melt temperature evolution is absolutely different from the experimental observation.

On the other hand, if heat transfer coefficient is estimated by natural convection correlations, similar tendency of temperature evolution in the melt cavity has been reproduced independent on the selected geometry (BAFOND and BALI correlations for cylinder or Mayinger, Jahn and Reineke, Gabor, Mini ACOPO correlations for hemisphere). As seen in Figure 4-20, the melt temperature reaches a maximum value at $t \approx$ 2000 s, then decreases gradually until the test end. In addition, the use of MiniACOPO and Gabor's correlations developed for natural convection in hemispherical geometry provides a good agreement between calculation and experiment in terms of the value of maximum temperature as well as the characteristic time to reach this value.

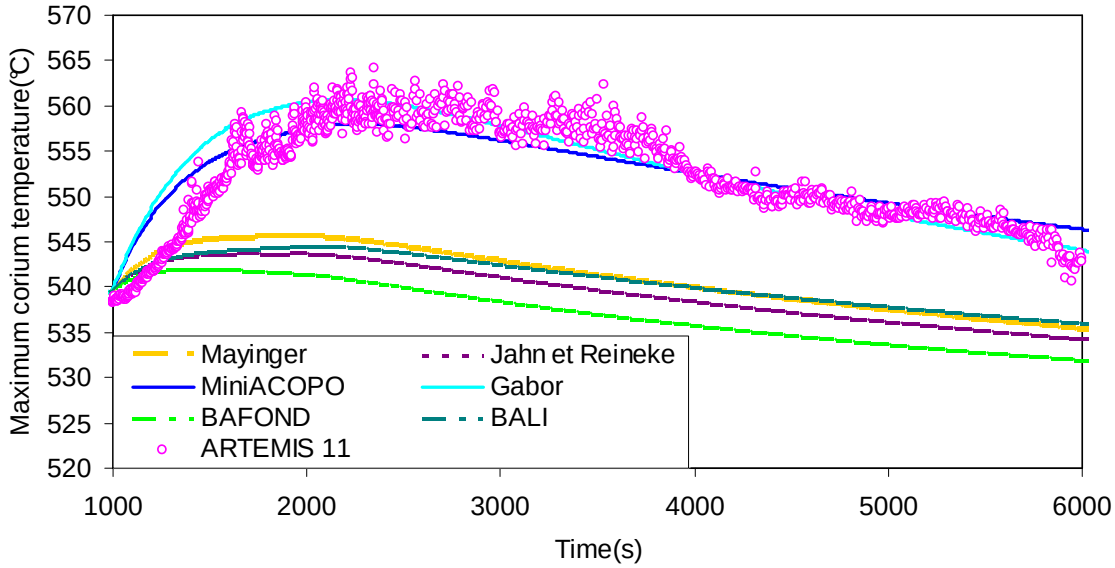

Figure 4-20. ARTEMIS 11 evolution of maximum melt temperature for t > 17 minutes using natural convection heat transfer correlations.

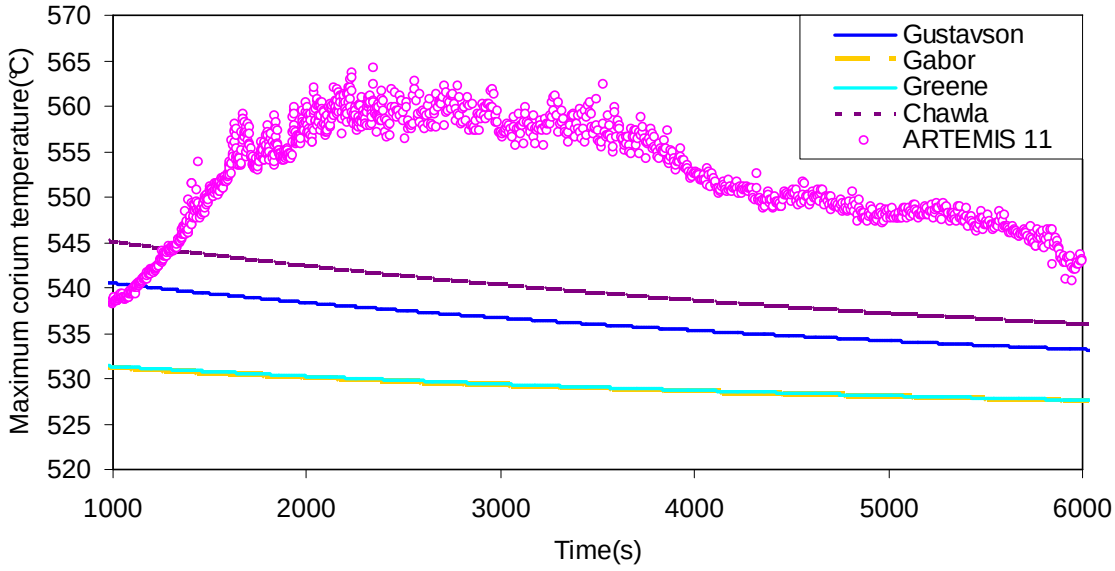

Figure 4-21. Evolution of maximum melt temperature for t > 17 minutes using gas-liquid convection heat transfer correlations.

From the above calculations, it is deduced that:

- The temperature increase is due to the decrease of the heat transfer coefficient after the initial period (t < 17 minutes) where heat transfer is governed by gas-liquid flow regime;
- The temperature decrease after $t \approx 2000$ s is due to the increase of heat transfer surface by cavity widening, leading to a decrease of heat flux (since the power dissipation is constant), and, as a consequence, to a decrease of the temperature difference between bulk and interface.

This reinforces the conclusion that for t > 17 minutes, natural convection is clearly the main heat transfer mechanism governing the heat transfer in the melt cavity.

Combining the calculation results using Gustavson's correlation for gas-liquid convection period (t < 17 minutes) and Mini-ACOPO correlation or Gabor's for the natural convection period (t > 17 minutes) gives the whole transient evolution of the maximum bulk temperature during ARTEMIS 11 as shown in Figure 4-22.

From these calculations, it is also concluded that the transition between gas-liquid convection and natural convection flow configurations are rather fast and takes probably less than ~ 200 s (i.e. ~ 3 minutes) and occurs between 1000 s and 1200 s in ARTEMIS 11.

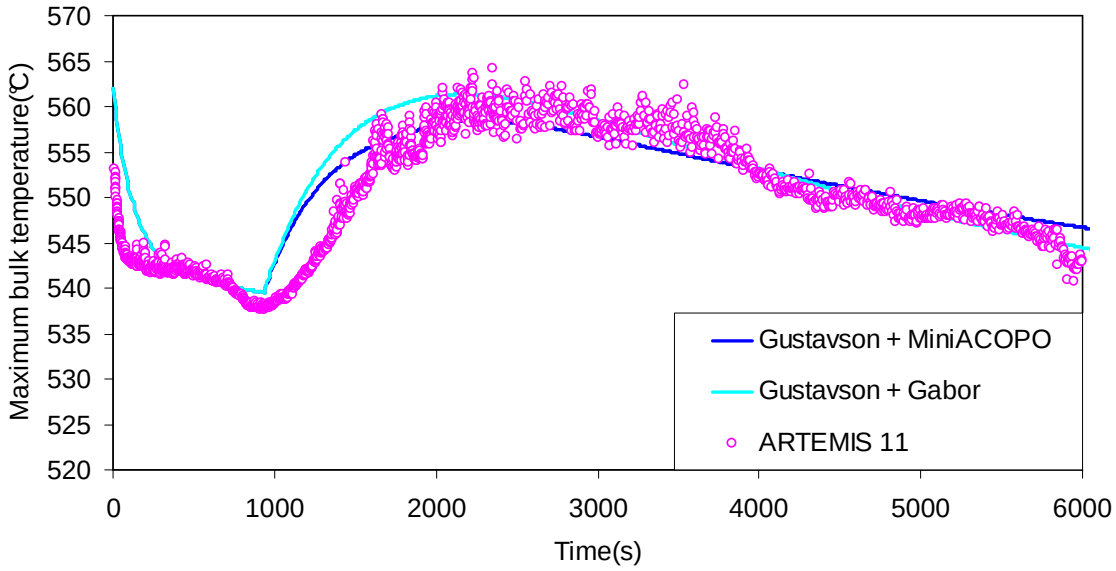

Figure 4-22. Evolution of maximum melt temperature during ARTEMIS 11.

Evolution of molten concrete mass

In addition, application of the developed model with the above optimized selection of heat transfer correlations also gives access to the evolution of the ablated mass of solid concrete as seen in Figure 4-23. Maximum difference between calculation and experimental data of about 5 kg is obtained at $t \approx$ 800 s ~ 1800 s, despite of the geometry.

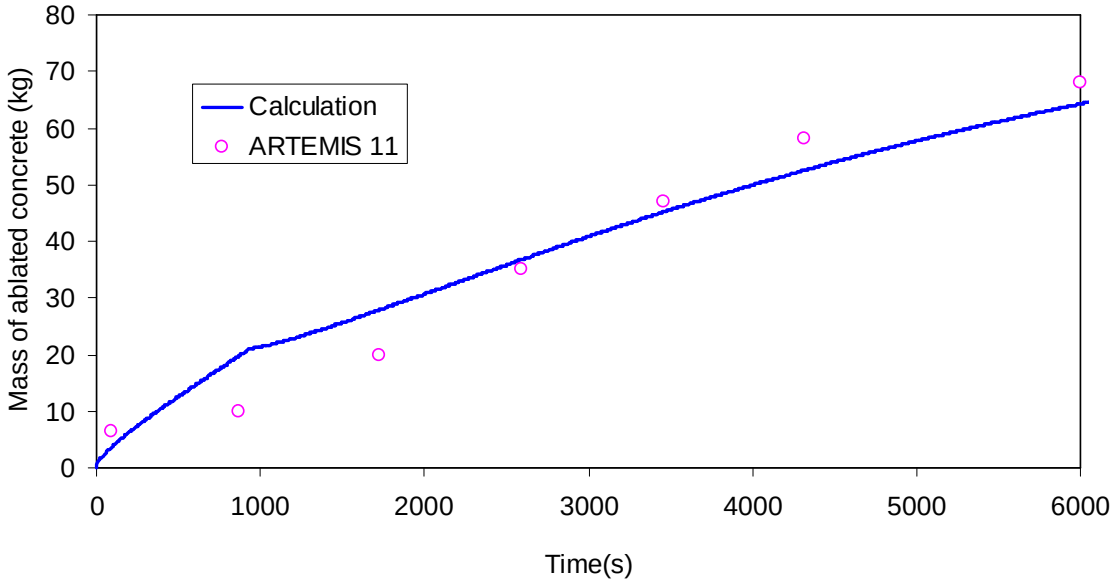

Figure 4-23. Evolution of maximum melt temperature during ARTEMIS 11.

4.4.4 Conclusion from 0D model calculations

It is confirmed from the application of the developed model that the flow recirculation in the melt cavity during t < 17 minutes is controlled by gas-liquid mixing convection. At t > 17 minutes, natural convection governs heat transfer in the melt cavity.

The heat transfer correlations reported by [Gustavson et al., 1977] for gas-liquid convection and by [Gabor et al., 1980] and Mini-ACOPO [Theofanous et al., 1997] for steady state natural convection heat transfer in hemispherical geometry are adopted to estimate the evolutions of the maximum bulk temperature as well as the mass of molten concrete in ARTEMIS 11.

Temperature increase is due to the decrease of heat transfer coefficient after the gas-liquid flow regime and temperature decrease is due to the cavity ablation and widening. This results are valid whatever the geometry assumed (either cylinder or hemisphere), which means that thermal effects are dominant.

The model is unable to describe the local parameters in the melt cavity such as the local melt temperature, local heat flux and the evolution of the local cavity radius, etc… Therefore, another model taking into account the evolution of these local parameters in the melt cavity has been developed.

4.5 1D modelling for calculation of local heat transfer and evolution of melt cavity shape for ARTEMIS 11

In Chapter 2, the developed 1D boundary layer model (presented in Appendix 7) has been applied for calculation of the evolution of local parameters in LIVE L3A. In this section, this model will be applied for ARTEMIS 11. The aim is to validate its ability for describing local heat transfer during melt-concrete interactions at eutectic composition. The main outcomes of interest include the

evolutions of the local temperature in the melt cavity, transient heat flux distribution along the cavity wall and evolution of the local cavity radius.

4.5.1 Constitutive laws

As presented in the description of ARTEMIS 11, the melt pool in ARTEMIS 11 has a small size (a few ten-centimeter scale), the Grashof number is smaller than 2 10^9. Therefore, the liquid flow in the boundary layer in this situation will be considered as a laminar flow.

According to the previous application of the 1D model for LIVE L3A (Chapter 2), the constitutive laws for friction coefficient and heat transfer coefficient derived from the velocity and temperature profiles introduced by Eckert for the description of the boundary layer along a vertical wall in laminar natural convection resulted in good agreement between calculation and experimental data. Therefore, these constitute laws will be also applied for the calculation of ARTEMIS 11.

The friction coefficient is calculated by:

$$F = \frac{96}{\mathrm{Re}} \tag{4-46}$$

For ARTEMIS 11, Pr = 3, which corresponds to a coefficient k_j equal to 0.36 in the correlation of superficial radial entrainment velocity of liquid from the bulk into the boundary layer (Appendix 7), i.e:

$$j_{bulk} = 0.36\left[g\,\beta_T\,(T_{bulk} - T_{BL})\,\upsilon\right]^{1/3} \tag{4-47}$$

where in T_{bulk} and T_{BL} are the local bulk and boundary layer temperature at a given distance x from the edge of the boundary layer (top surface of the melt).

With Pr = 3, as shown in Appendix 7, the heat transfer to the wall can be estimated using either Nu_{bulk} or Nu_{BL} as follows:

$$Nu_{bulk} = 4\frac{\delta}{\delta_T} = 4\,\mathrm{Pr}^{1/3} \approx 5.7 \tag{4-48}$$

$$Nu_{BL} = \frac{4\dfrac{\delta}{\delta_T}}{\dfrac{4}{5}\dfrac{\delta}{\delta_T} - \dfrac{1}{5}\left(\dfrac{\delta}{\delta_T}\right)^2} = \frac{5}{1 - 0{,}275\,\mathrm{Pr}^{1/3}} \approx 8.26 \tag{4-49}$$

The calculation is initiated at the time where natural convection becomes the governing heat transfer mechanism (t > 17 minutes).

4.5.2 1D model application for ARTEMIS 11

Application of the developed 1D model for ARTEMIS 11 with the above constitutive laws has been performed for the 2nd period of ARTEMIS 11 wherein natural convection controls heat transfer in the melt cavity. The calculated results including evolution of the melt temperature at different cavity elevations, temperature profile on the axis of the melt cavity and evolution of the melt cavity shape are shown in below.

Evolution of melt temperatures at different cavity elevations

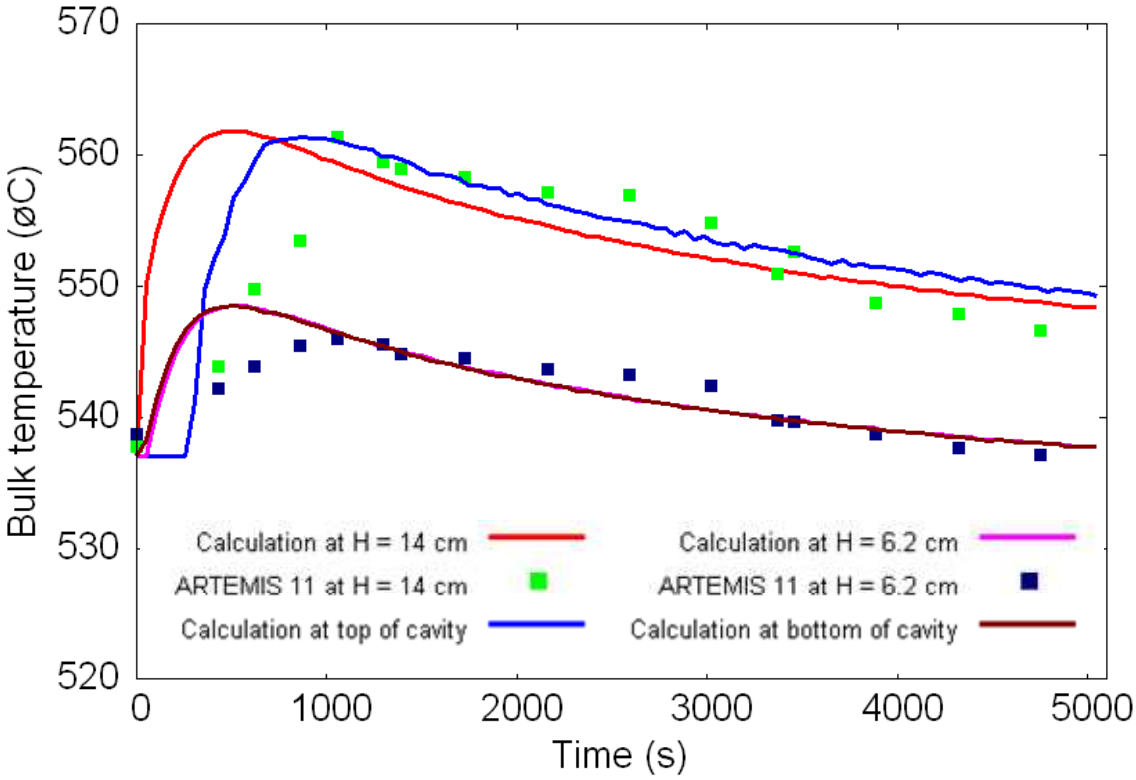

Figure 4-24. Bulk temperature evolutions at different melt cavity elevations in ARTEMIS 11 with 1D model.

The bulk temperature evolution at different melt cavity elevations are shown and compared with those measured in ARTEMIS 11 in Figure 4-24. Similar tendencies of temperature evolution have been observed between calculation and experiments. The calculated temperature at the top of the heater (z = 14 cm) reaches maximum temperature of about 562 °C while it is approximately 560 °C in ARTEMIS 11. After 5000s, the calculated temperature at this elevation reduces to 549 °C while it was about 545 °C in the experiment. At the melt cavity bottom, the difference between calculation and experiment is about 2 °C ~ 5 °C. However, the time to reach the maximum temperature in the calculation is shorter than in the experiment. Indeed, at the pool height z = 14 cm (top of the heater), the calculation shows that the temperature reaches maximum value after 600 s while this delay characteristic obtained in ARTEMIS 11 is about 1200s.

Bulk temperature profile at t = 5000 s

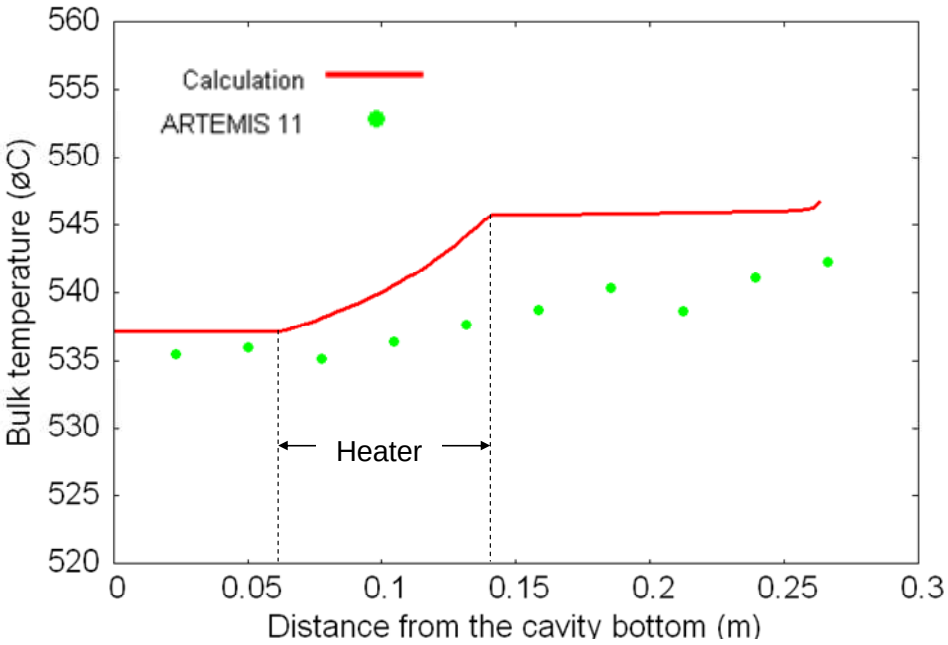

Figure 4-25. Bulk temperature profile at t = 5000 s in ARTEMIS 11.

Looking at the temperature profile in the pool after t = 5000 s (Figure 4-25) (at the end of the calculation), it is observed that the calculated temperature is higher than the experimental one (about 2 °C at the bottom and 5 °C at the top). Outside the heating region, the calculated temperature is uniform. The calculated temperature difference between top-bottom is approximately 10 °C while in ARTEMIS 11, a difference of 7 °C was observed.

Melt cavity shape at t = 5000 s

Figure 4-26 depicts the melt cavity shape at t = 5000 s. A rather good agreement is obtained between experiment and calculation. It is observed that ablation occurs mainly in the upper part of the cavity. This is clearly due to the heat flux profile linked to natural convection (high heat transfer coefficient and a big temperature difference between bulk and liquid-solid interface at the top). Near the bottom, there was almost no ablation since only cold liquid recirculates in this region from the lateral boundary layer flow.

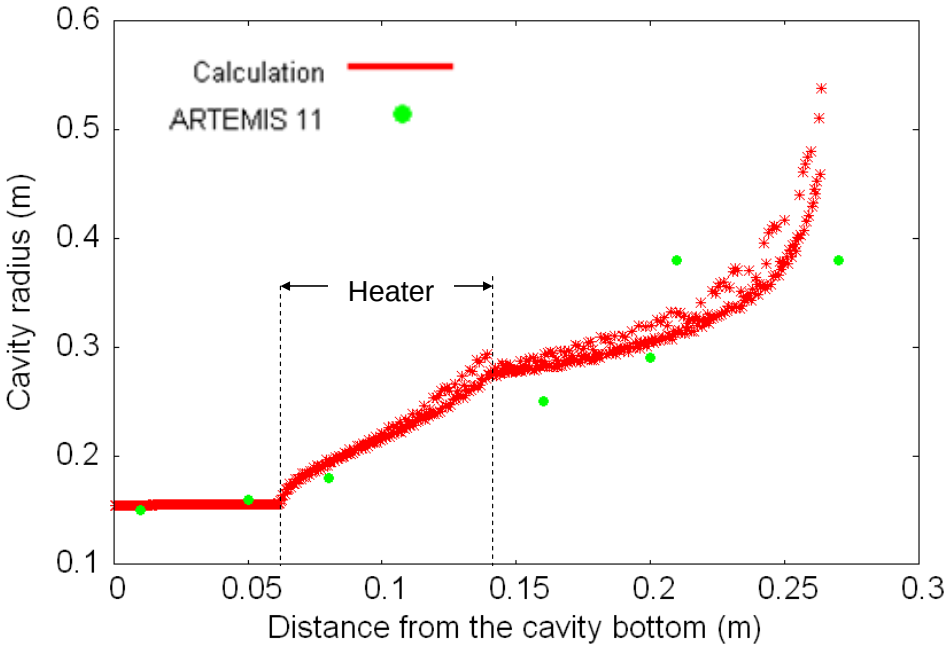

Figure 4-26. Melt cavity shape at t = 5000 s in ARTEMIS 11.

4.5.3 Conclusion from the 1D calculations

The main conclusions from the application of 1D model for ARTEMIS 11 are summarized as follows:

- The constitutive laws for friction coefficient and heat transfer coefficient deduced from the use of Eckert's velocity and temperature profiles, which were developed for natural-convection boundary layer along a vertical plate in laminar regime, seems to be valid for a cavity of variable shape with melting wall.
- Application of the model for the experimental conditions in ARTEMIS 11 allows a validation of the model for simulating not only the evolution of bulk temperatures at different melt cavity elevations but also the evolution of the cavity shape due to ablation of the solid concrete wall.
- The application confirms that natural convection dominates the flow regime at $t > 17$ minutes.
- The fast radial ablation at the top of the cavity is linked to the heat flux distribution associated to a laminar boundary layer flow.
- The low ablation at the bottom of the cavity is linked to the recirculation of cold liquid from the boundary layer in the bottom region.

4.6 Conclusions

This chapter is dedicated to the investigations of heat and mass transfers during ARTEMIS 11 experiment, which aimed to represent an eutectic solid material ablation by the eutectic melt with gas sparging and volumetric power dissipation in the melt cavity. The main conclusions are made as follows:

- Analysis of evolution of temperature gradient in the melt cavity reports existence of gas mixing in the melt cavity during the first 17 minutes. After that, natural convection controls heat transfer in the melt cavity.

- The melt temperature distribution is radially uniform at each cavity level except in the small region near the interface. Analysis of axial temperature gradient near to the liquid-solid interface indicates the existence of a boundary layer with a downward flow. This explains the preferentially radial ablation observed in ARTEMIS 11. Due to this boundary layer flow, the heat flux distributes non-uniformly along the lateral wall of the melt cavity, leading to maximum concrete ablation at the top and minimum concrete ablation at the bottom of the cavity.
- The temperature evolution in the melt cavity is recalculated by a 0D model. In the first 17 minutes, due to gas-liquid mixing convection regime, the two phase heat transfer correlation of Gustavson has been applied. After that, heat transfer was estimated by MiniACOPO correlation (or Gabor correlation) for natural convection heat transfer. The temperature decrease in the melt after 1 hour is attributed to the cavity widening due to ablation.
- Application of the 1D model already used for the interpretation of LIVE L3A test was made. This model couples the heat transfer between the bulk of the melt cavity and the boundary layer at the cavity wall. A radial liquid flow is assumed to enter the boundary layer from the bulk. Same local constitutive laws as for the interpretation of LIVE L3A test have been considered for friction, heat transfer and liquid entrainment velocity in the boundary layer. The 1D model calculation results proved to quite well reproduce the temperature evolutions as well as local ablation rates. From these calculations, it is concluded that the fast ablation at the top of the melt cavity is linked to the heat flux distribution associated to the laminar boundary layer flow. The low ablation rate at the melt cavity bottom is linked to the recirculation of cold liquid from the boundary layer at the bottom region.

CHAPTER 5: MELT-CONCRETE INTERACTION WITH SOLUTE MASS TRANSFER

5.1 ARTEMIS 10 test description

This chapter is dedicated to the investigation of the coupling between thermal-hydraulics and physico-chemistry effects during ARTEMIS 10 test. Simulant material for concrete in ARTEMIS 10 is a solid mixture of $BaCl_2$ and LiCl at eutectic composition (25% mol $BaCl_2$-75% mol LiCl, melting temperature: 522°C) as in ARTEMIS 11 while the melt is simulated by pure liquid $BaCl_2$ liquid (melting temperature: 960°C).

5.1.1 Initial test conditions

Melt (corium)

- 100% mol $BaCl_2$ (100% mass $BaCl_2$)
- Liquidus temperature: 960 °C
- Initial temperature: 960 °C
- Initial mass: 97.1 kg
- Initial volume: 0.0316 m^3

Concrete

- Eutectic composition: 25% mol $BaCl_2$-75% mol LiCl (62.04% mass $BaCl_2$-37.96% mass LiCl)
- Melting temperature (eutectic temperature): 522 °C
- Initial temperature: 400 °C
- Initial mass: 261.67 kg
- Porosity: 46%
- Grain size: 0.2 ~ 0.9 mm

Argon gas

- Inlet temperature: 400 °C
- Superficial velocity at the melt cavity interface: 2 cm/s (constant during test)

5.1.2 Test installation

Figure 5-1 represents the initial geometry for ARTEMIS 10. The melt cavity has 30 cm diameter and initial height of the liquid melt in the cavity is 44.3 cm (26.5 cm is initially inside the concrete cavity). The heating elements are located at a distance of 8.1 cm to 15.9 cm from the bottom of the melt cavity. The power dissipation in ARTEMIS 10 is 6000 W while the superficial gas velocity to the melt-

concrete interface is maintained at 2 cm/s (similar to ARTEMIS 11). The test duration was 1 h 31 minutes 30 s.

Thermocouple TC1 is located in the centre of the heated zone. In addition, measurements of the melt temperature near the axis of the melt cavity and at different elevations are performed by ten thermocouples (TC3 to TC12) attached in a vertical cane as in ARTEMIS 11. The distance between them is also fixed at 27 mm. For t < 28 minutes, these thermocouples are located between level 23.4 mm for TC12 to level 266.4 mm for TC3 from the initial bottom of the melt cavity, similarly to ARTEMIS 11. However, beyond t = 28 minutes until the end of the test, the cane is lowered by 8 cm as shown in Figure 5-2.

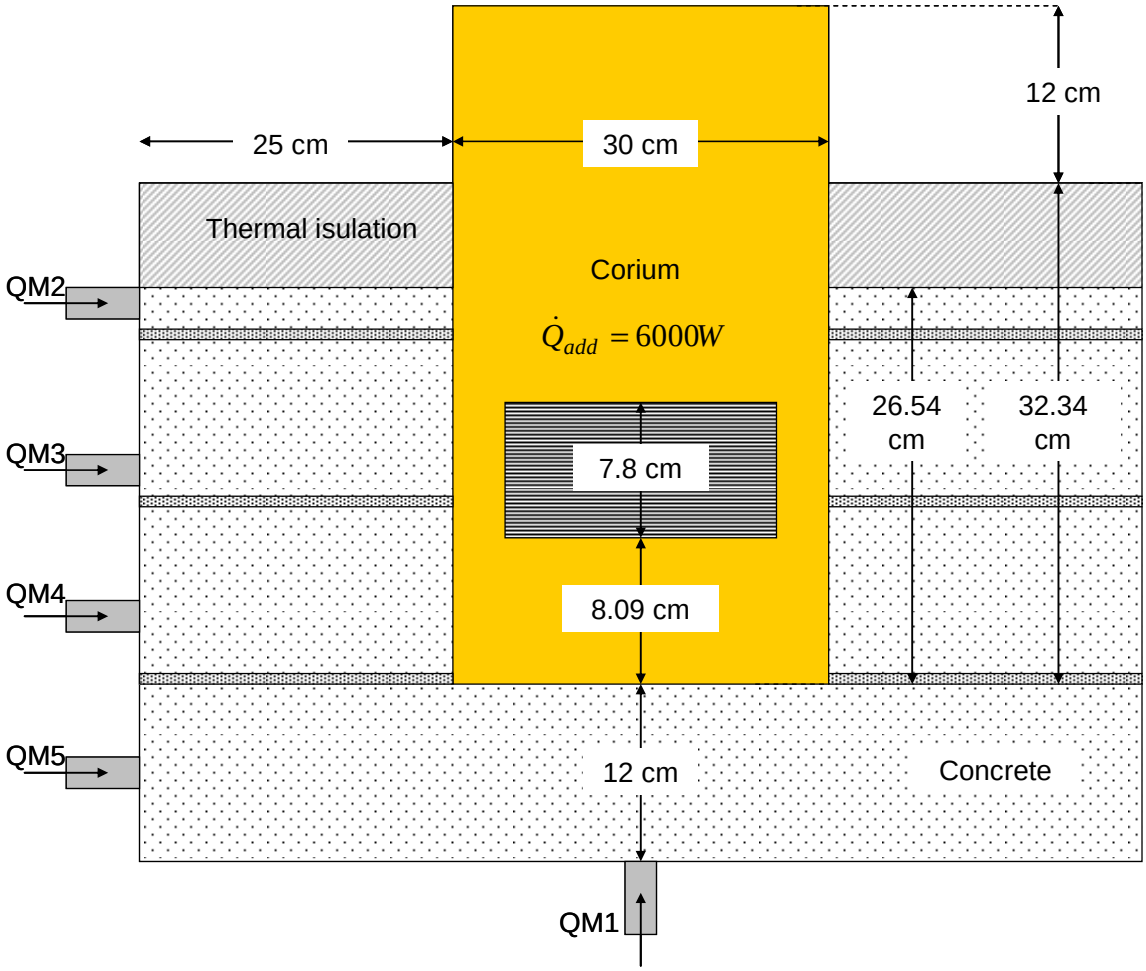

Figure 5-1. ARTEMIS 10 initial arrangement.

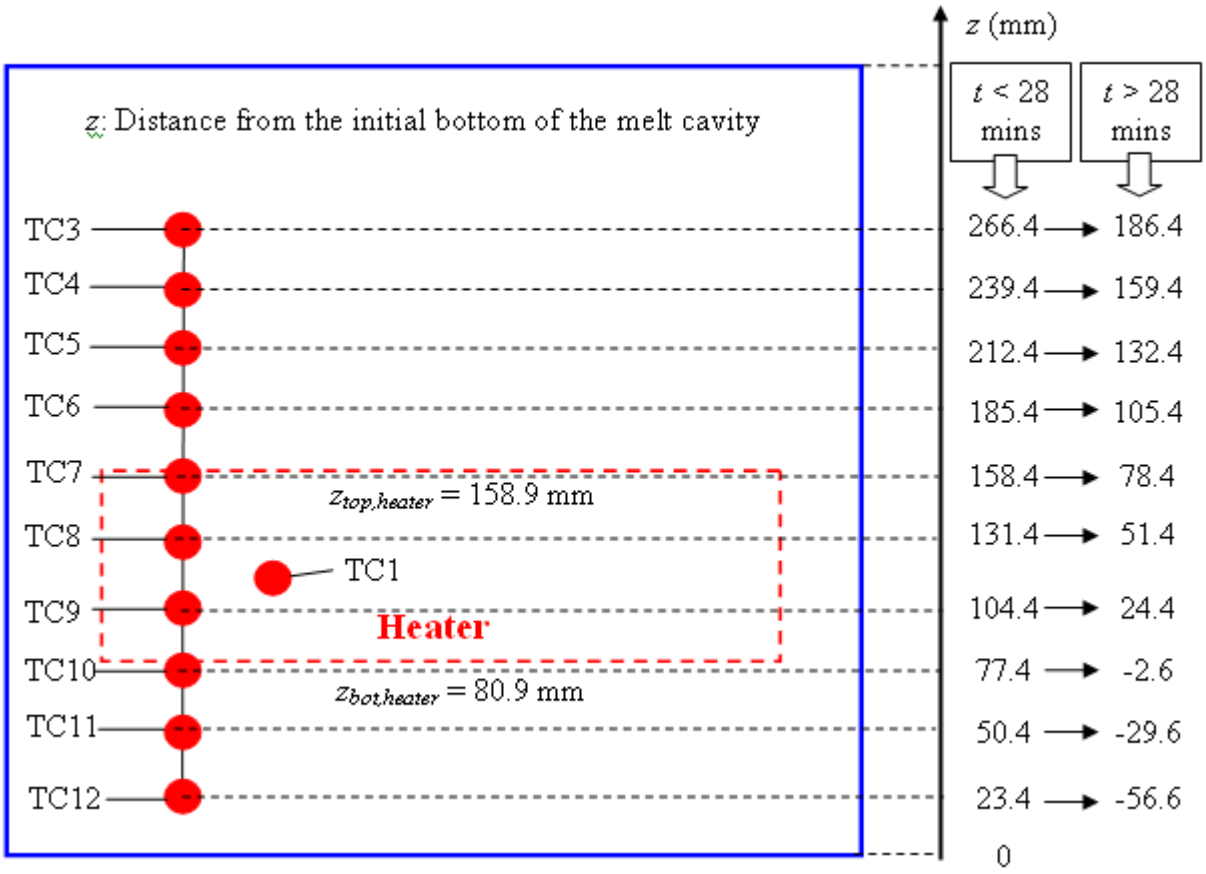

Figure 5-2. Position of thermocouples for axial melt temperature distribution measurement.

5.2 ARTEMIS 10 experimental data

5.2.1 Evolution of melt temperature

Evolution of melt temperatures at different elevations z (z is the distance from the initial cavity bottom) during ARTEMIS 10 test are illustrated in Figure 5-3.

The initial temperature observed in the experiment is lower than the initial melt temperature (960 °C). This fast cooling might be due to a strong ablation of the solid concrete at the test initiation by the superheated melt. This hypothesis will be investigated more in detail later

Figure 5-3 shows that minimum melt temperature corresponds to TC3 located in the top zone of the melt (z = 266.4 mm). The maximum melt temperature is obtained by TC12 near the bottom of the melt cavity (z = 23.4 mm). The cane lowering at 28 minutes leads to an increase of the temperatures by 10 °C approximately.

The difference between maximum and minimum melt temperatures in ARTEMIS 10 is about 100 °C, which is significantly more than the temperature difference measured in ARTEMIS 11 with a melt that had the same composition as concrete (about 20 °C ~ 25 °C).

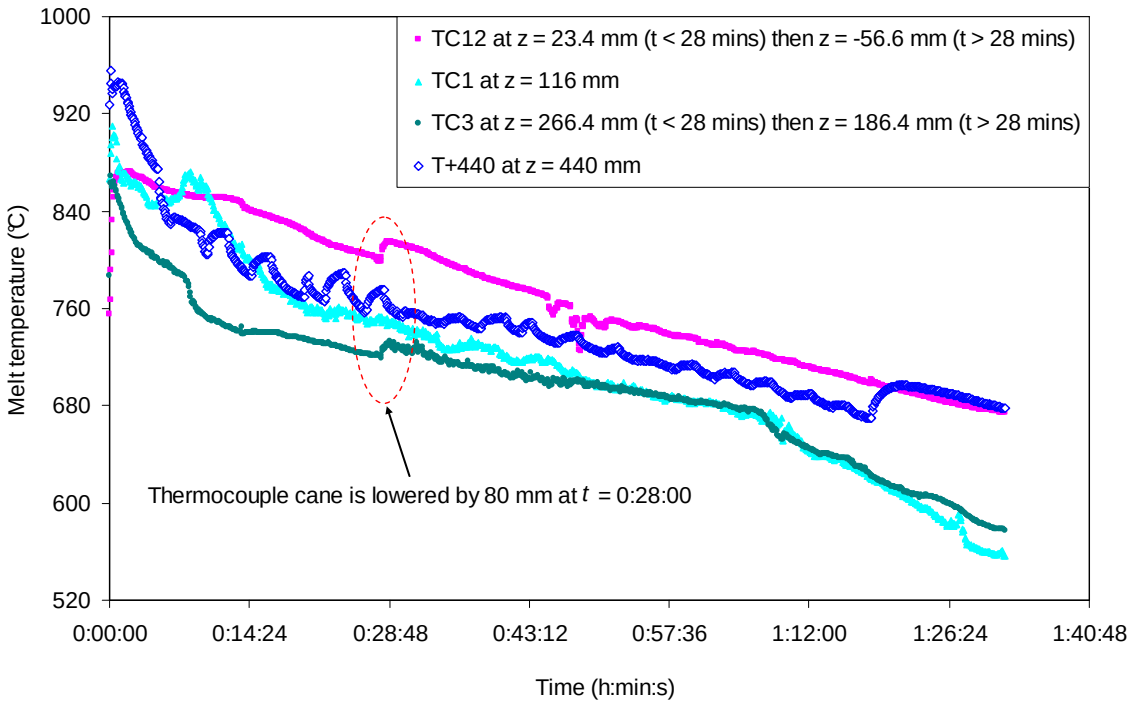

Figure 5-3. Evolution of melt temperature at different cavity elevations in ARTEMIS 10.

5.2.2 Evolution of axial temperature distribution

Figure 5-4 presents more precisely the temperature distribution near the melt cavity axis at different time instants. There is a global temperature decrease during the test (the maximum bulk temperature decreases from ~ 850 °C at t = 0:05:38 to t = 1:17:29. Three zones can be observed in the cavity, which are:

- In the top zone: the temperature gradient is slightly positive.
- In the middle zone: the temperature gradient is negative. This temperature gradient is displaced towards the bottom of the melt during the test. It is located in the heating zone (from z = 80.9 mm to z = 158.9 mm) at the beginning of the test and is lowered by approximately 110 mm (from z = -30 mm to z = 50 mm) at the end of the test.
- In the bottom zone: an important positive temperature gradient is observed. The location of this temperature gradient follows the progression of the melting front. This temperature gradient is very steep at the beginning (ΔT = 335 °C for elevations between z = -40 mm and z = 23 mm) and less at the end (ΔT = 195 °C between elevations z = -88 mm and z = -30 mm). By analogy with the interpretation of ARTEMIS 1D [Guillaumé, 2008], this positive temperature gradient at the bottom of the cavity could be an indication of the cake formation at the lower interface.

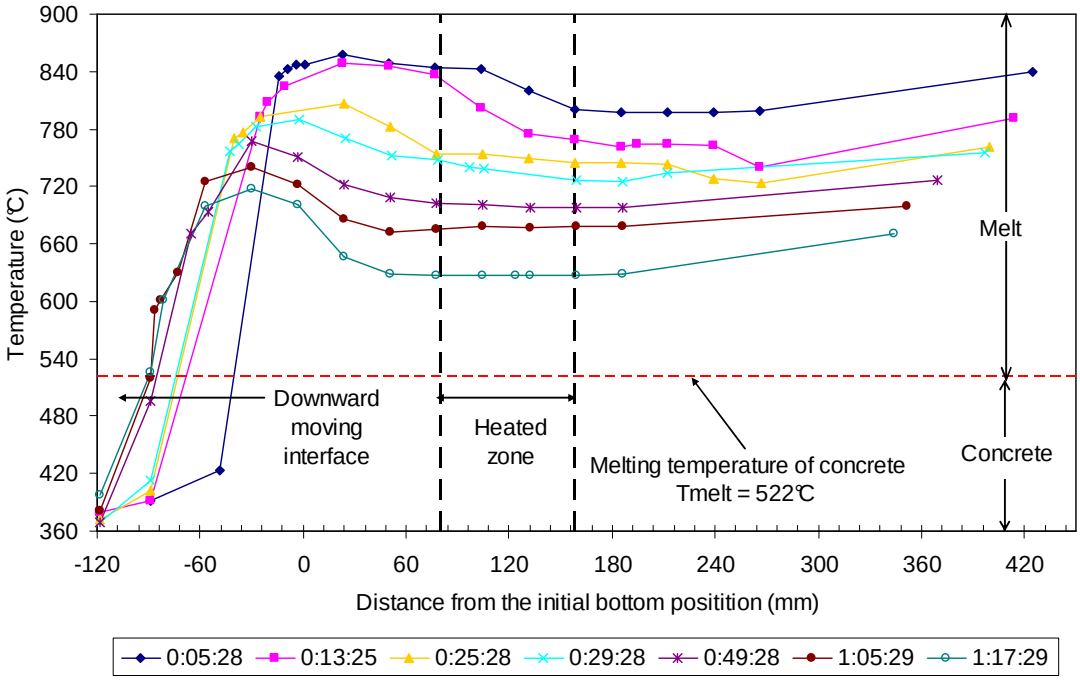

Figure 5-4. Evolution of axial temperature distribution near melt cavity axis.

The evolution of the position of the temperature gradients will be discussed more in details in the next part of this thesis. In addition, considering the bottom interface with the solid concrete as the position at which the melt temperature is equal to the melting temperature of the concrete (T_{melt} = 522 °C), then we can deduce the location of the bottom interface between melt cavity and solid concrete cavity versus time.

In the heated zone (from z = 80.9 mm to z = 158.9 mm), the temperature gradient is negative at t < 49 minutes and becomes slightly positive at t > 49 minutes. The existence of significant temperature gradient also indicates absence of (or poor) mixing of the melt by sparging gas, as observed for ARTEMIS 11. This is coherent with the measurement result of void fraction in the melt cavity which is always equal to zero during ARTEMIS 10. Therefore, in the following, we will suppose that natural convection is a first candidate hypothesis for the flow recirculation in the melt cavity.

5.2.3 Evolution of radial temperature distribution

Measurement of melt temperature near the cavity lateral wall performed by the 2D mobile probe provides evolution of the radial temperature distribution as shown in Figure 5-5. It is shown that the temperature in the cavity centre is greater than near the lateral wall. A thermal boundary layer is observed with a thickness of 3 ~ 5 mm from the lateral wall. In this region, a significant increase of temperature is obtained. The radial temperature gradient in the centre of the cavity is much smaller than in the boundary layer region.

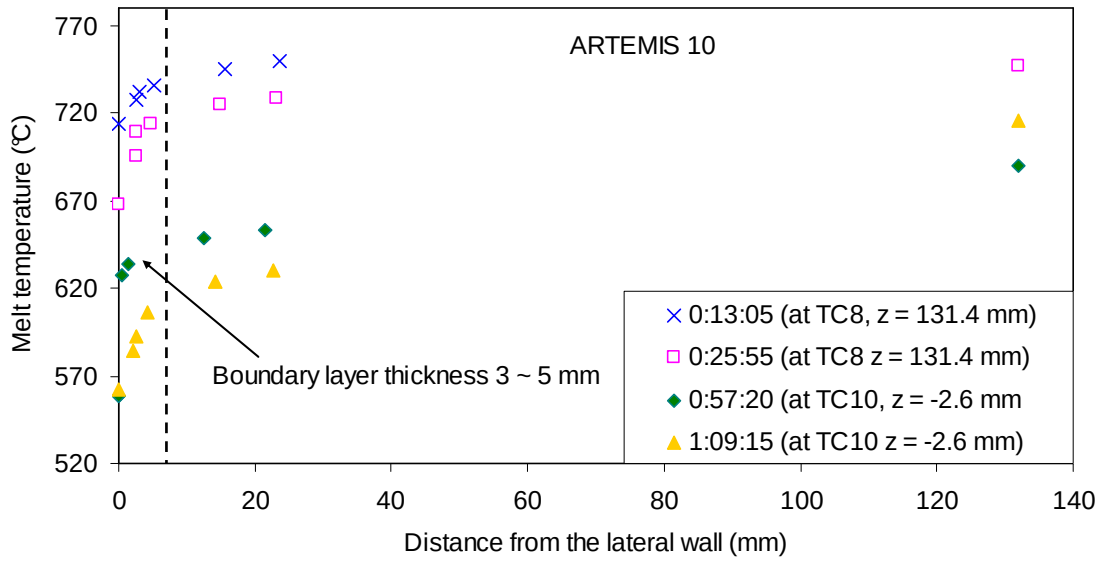

Figure 5-5. Evolution of radial temperature distribution in melt cavity at two different cavity elevations.

5.2.4 Evolution of average concrete temperature

The evolution of average concrete temperature is shown in Figure 5-6. This temperature is calculated by taking the volumetric average of the temperatures measured by maximum 85 thermocouples located inside the residual solid concrete. The detail of this calculation is presented in Annex 4.

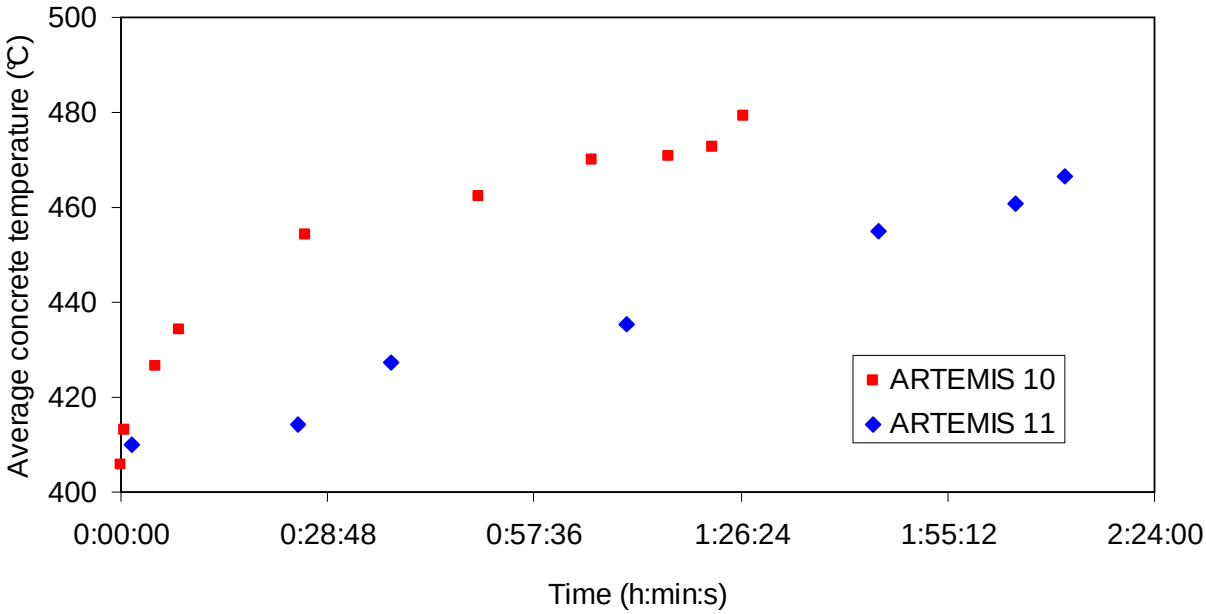

Figure 5-6. Evolution of the average residual solid concrete temperature in ARTEMIS 10.

It is seen that the average temperature of the residual solid concrete in ARTEMIS 10 increases more rapidly than in ARTEMIS 11. This means that the heat flux transferring from the melt cavity to solid

concrete to heat up the concrete at a given time instant in ARTEMIS 10 is higher than in ARTEMIS 11 for the same power dissipation in the melt cavity.

5.2.5 Evolution of melt cavity shape

Figure 5-7 illustrates the evolution of melt cavity shape at four azimuthal angles (45°, 135°, 225° and 315°). The position of the melt cavity interface is detected by thermocouples located inside the concrete cavity, and the methodology is described in Annex 4 and is similar to the methodology used for ARTEMIS 11.

It is seen that radial ablation at the top part of the cavity is stronger than at the bottom part. At the end of the test, the cavity radius at the top of the cavity (z = 265 mm) is about 40 cm. The vertical ablation is only about 8 cm at z = 0 mm (initial bottom of melt cavity). Axial ablation at the bottom of the melt cavity (8 cm to 10 cm) is more important than in ARTEMIS 11 (only about 20 cm).

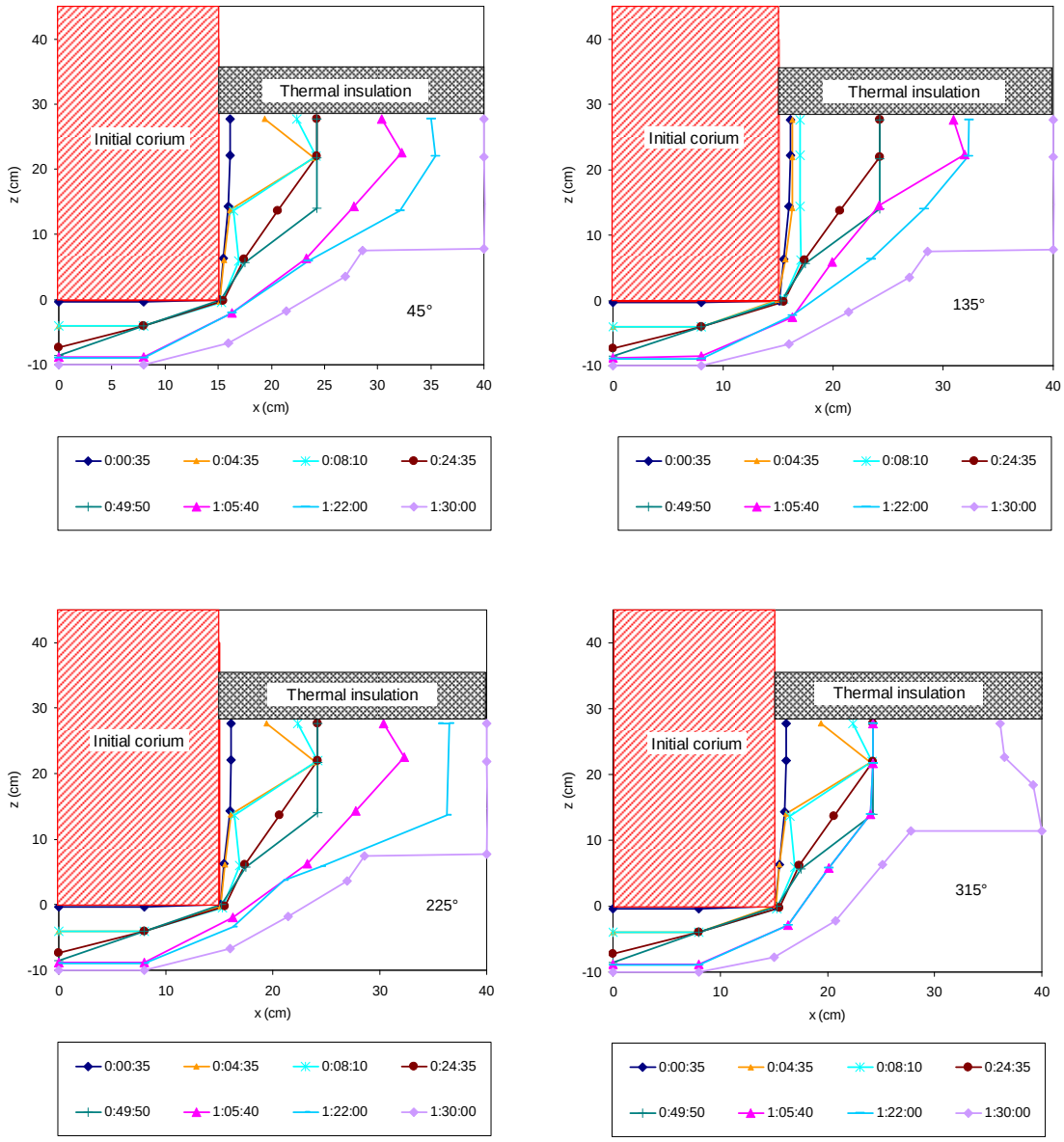

Figure 5-7. Metl cavity shape evolution in ARTEMIS 10.

Figure 5-8 compares the melt cavity shapes during ARTEMIS 10 and ARTEMIS 11. A significant difference in the cavity shape evolution has been observed between the two tests for the same power dissipation in the melt cavity. Indeed, axial concrete ablation at the bottom occurs only in the first minute with 2 cm of ablated concrete in ARTEMIS 11 while axial ablation is observed continuously during ARTEMIS 10 wherein 10 cm solid concrete ablates at the bottom of the melt cavity at the test ending. In addition, the radial ablation to the cavity lateral wall in ARTEMIS 10 seems to be stronger than in ARTEMIS 11, especially in the bottom zone of the melt cavity. After 24 minutes, about 5 cm of ablated concrete is observed at distance 15 cm from the initial bottom of the melt cavity in ARTEMIS 10, which is much thicker than 1 cm obtained in ARTEMIS 11 at the same cavity level. At the end of ARTEMIS 10, the top interface of the melt cavity approaches the lateral wall of the concrete cavity, indicating 25 cm thickness of ablated concrete; whereas only about 20 cm was obtained in ARTMIS 11 for the same time instant.

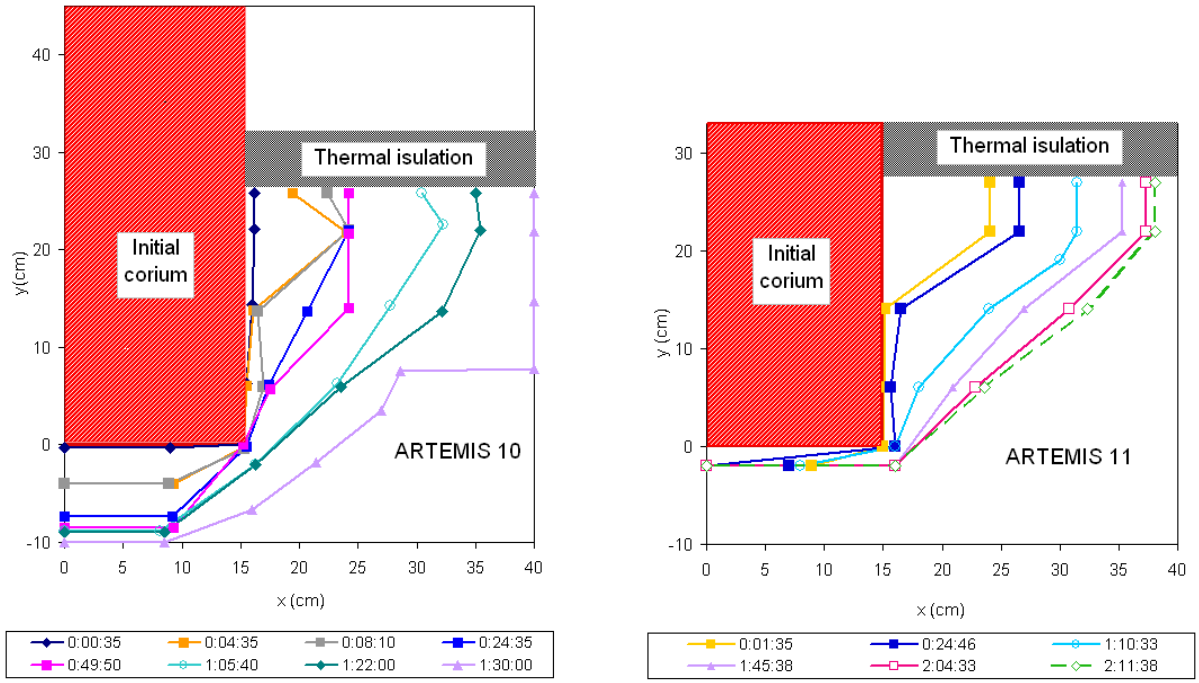

Figure 5-8. Comparison of cavity shape evolutions between ARTEMIS 10 and ARTEMIS 11.

The evolution of the mass of molten concrete, as deduced from the cavity shape data is depicted in Figure 5-9 and compared with the one deduced from ARTEMIS 11. It is seen that about 142 kg of solid concrete is ablated at the end of ARTEMIS 10 (t = 1:30:00) which is much more than 60 kg obtained in ARTEMIS 11 at the same time instant. Knowing that the power dissipation in the melt cavity is similar in the two tests (6000 W), one may raise a question of the reason for such difference in ablating behaviours in ARTEMIS 10 and ARTEMIS 11. The answers could be either the thermal effect of the initial melt temperature which is 960 °C in ARTEMIS 10 and 560 °C in ARTEMIS 11 or the mass transfer effect of solute species in ARTEMIS 10 which does not exist in ARTEMIS 11?

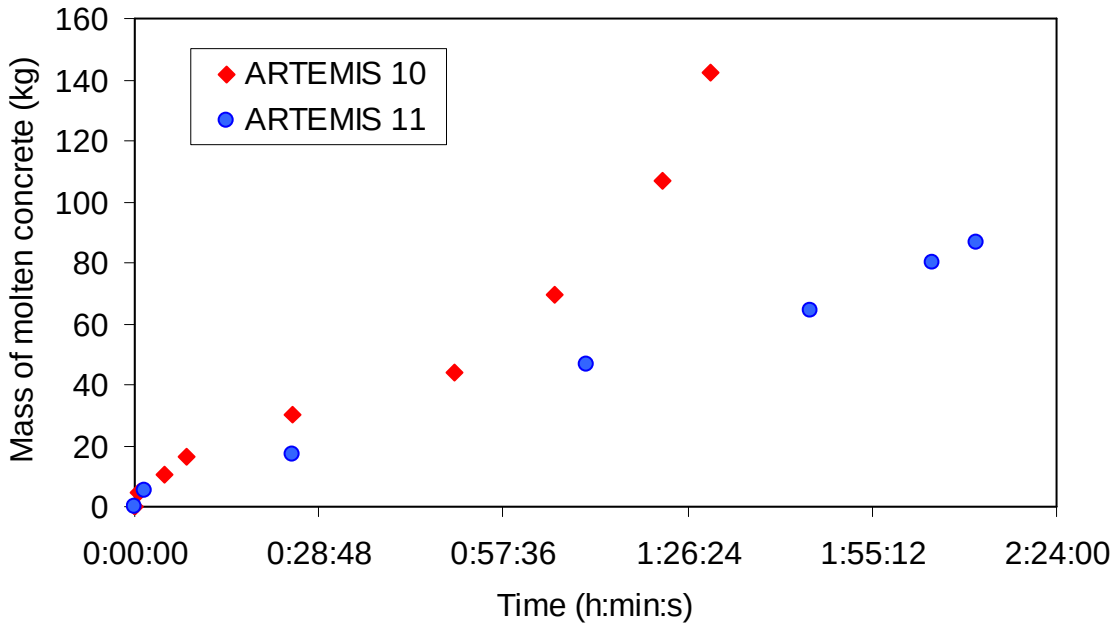

Figure 5-9. Evolution of molten concrete mass in ARTEMIS 10 and ARTEMIS 11.

5.2.6 Evolution of the melt composition

Since the initial melt contains 100% mass $BaCl_2$ while the solid concrete has 62.04% mass $BaCl_2$, during the mixing of the molten concrete with the liquid melt, the mass percentage of $BaCl_2$ in the melt will decrease and the mass percentage of LiCl will increase.

At a given instant, the average $BaCl_2$ mass percentage in the melt cavity is calculated by:

$$w_{bulk}^{BaCl2} = \frac{M_{bulk,ini}\, w_{bulk,ini}^{BaCl2} + M_{MC}\, w_{MC}^{BaCl2} - M_{cake}\, w_{cake}^{BaCl2}}{M_{bulk}} \quad (5\text{-}1)$$

wherein:

- M_{bulk},ini is the initial mass of the melt;
- M_{bulk} is the mass of the melt at instant *t*;
- M_{MC} is the mass of the molten concrete entering the melt cavity at instant *t*;
- M_{cake} is the mass of the cake forming at instant *t*;
- $w_{bulk,ini}^{BaCl2} = 100\,\%$ is the mass percentage of $BaCl_2$ in the initial melt;
- w_{bulk}^{BaCl2} is the mass percentage of $BaCl_2$ in the melt at instant *t*;
- $w_{bulk}^{BaCl2} = 62.04\,\%$ is the mass percentage of $BaCl_2$ in the molten concrete;
- $w_{bulk}^{BaCl2} = 94\,\%$ is the average mass percentage of $BaCl_2$ in the cake.

The average mol percentage of $BaCl_2$ in the melt (C_{bulk}^{BaCl2}) is deduced from the mass concentration as:

$$C_{bulk}^{BaCl2} = \frac{\overline{M}_{LiCl}\, w_{bulk}^{BaCl2}}{\overline{M}_{BaCl2} - (\overline{M}_{BaCl2} - \overline{M}_{LiCl})\, w_{bulk}^{BaCl2}} \tag{5-2}$$

wherein $\overline{M}_{BaCl2}$ and $\overline{M}_{LiCl}$ are the molecular masses of LiCl and $BaCl_2$, respectively.

Figure 5-10 shows measurement results of average melt composition during ARTEMIS 10. This measurement is performed on-line at different time instants during the test. Six samples of liquid melt are taken at different elevations in the melt cavity. It is seen that due to entrainment of molten concrete and formation of cake in the melt cavity, the average $BaCl_2$ concentration in the melt decreases from its initial concentration (pure $BaCl_2$) down to approximately 79 % in mass percentage or 39 % in mol percentage of $BaCl_2$ at the test ending.

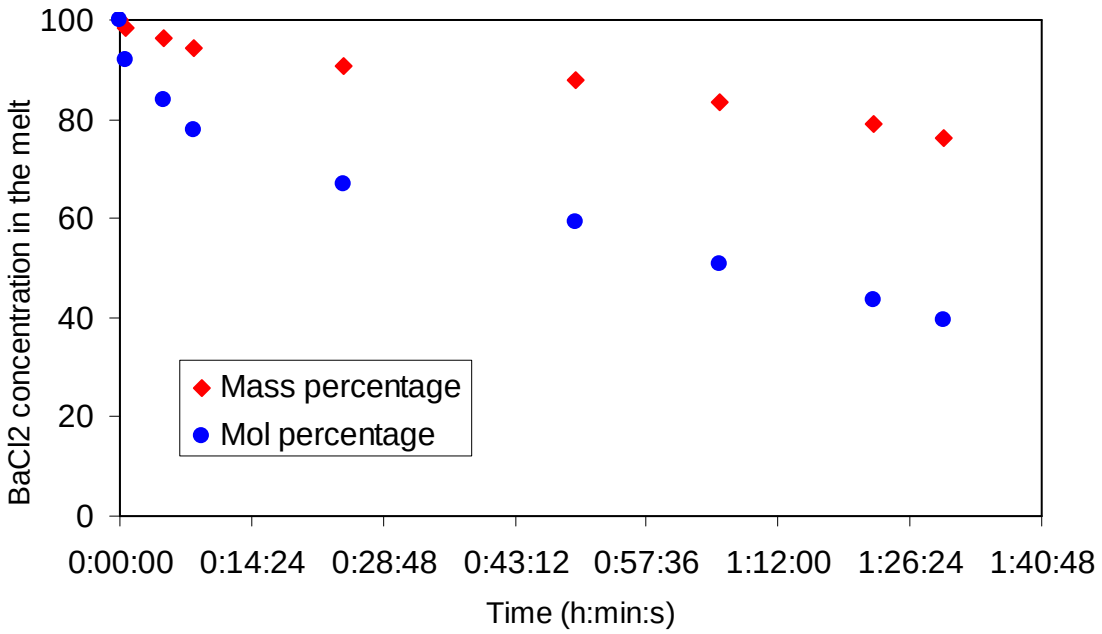

Figure 5-10. Measurement of average $BaCl_2$ concentration in the melt cavity in ARTEMIS 10.

The average mass and mol percentages of LiCl in the melt, denoted respectively as w_{bulk}^{LiCl} and C_{bulk}^{LiCl}, can be deduced:

$$w_{bulk}^{LiCl} = 100 - w_{bulk}^{BaCl2} \tag{5-3}$$

and:

$$C_{bulk}^{LiCl} = 100 - C_{bulk}^{BaCl2} \tag{5-4}$$

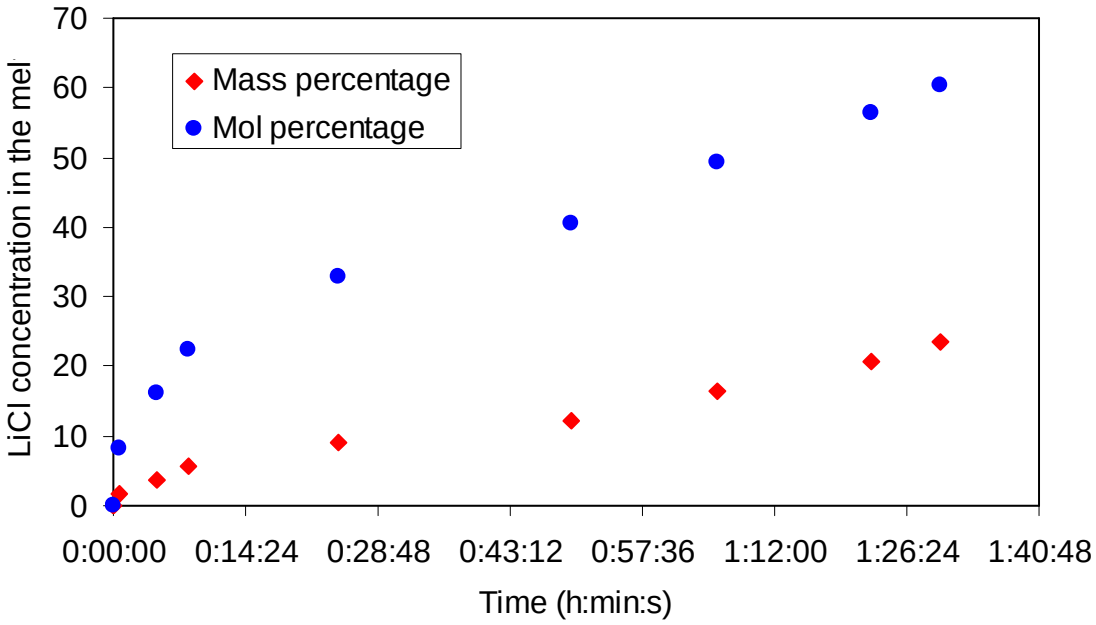

Figure 5-11. Measured average LiCl concentration in the melt in ARTEMIS 10.

Figure 5-11 provides the evolution of the average LiCl mass concentration in the melt cavity in ARTEMIS 10. It is seen that the LiCl mol composition increases gradually and at the end of the test, the average mass composition of LiCl in the bulk is increased to about 21% in mass percentage (~ 61% in mol percentage)

5.3 ARTEMIS 10 data analysis

5.3.1 Energy balance

Similarly to ARTEMIS 11, the energy balance for ARTEMIS 10 will be also calculated using the reported experimental data. The calculation method given in Annex 5 will be used as done for ARTEMIS 11.

Energy is conserved when the variation of the energy stored in the control volume between instant t and $t = 0$ is equal to the total energy dissipation from the heating elements minus the energy serving for gas heating. The energy stored in the control volume includes:

- Energy generated from cooling of the initial melt;
- Energy due to heating up of the solid concrete;
- Energy for melting part of the solid concrete;
- Energy for heating part of the solid concrete;
- Energy for heating the cake forming at the bottom of the melt cavity.

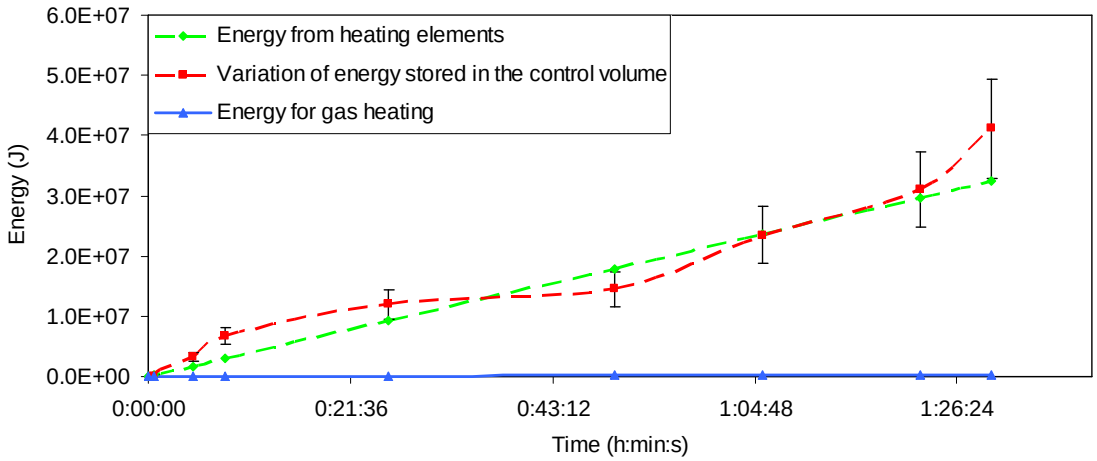

Figure 5-12. Energy balance in ARTEMIS 10.

Figure 5-12 shows the calculated energy balance in ARTEMIS 10. It is seen that energy is conserved during ARTEMIS 10. The energy serving for gas heating is minor in comparison to the energy from the heating elements and to the variation of the energy stored in the control volume. Discrepancy of less than 20% is observed which might come from the determination method of the ablated mass of concrete.

Figure 5-13 depicts the energy distribution in ARTEMIS 10. It is seen that the energy generated from melt cooling (from 960 °C to ~ 620 °C) takes an important role. This is different from ARTEMIS 11 in which the energy release from the initial melt cooling down is of minor contribution. A significant part of energy serves for heating up the solid concrete by conduction. In addition, other important parts of energy are devoted for concrete ablation and for heating up the molten concrete. As seen in Figure 5-13, the energies stored in the cake heating and related to gas heating is negligible.

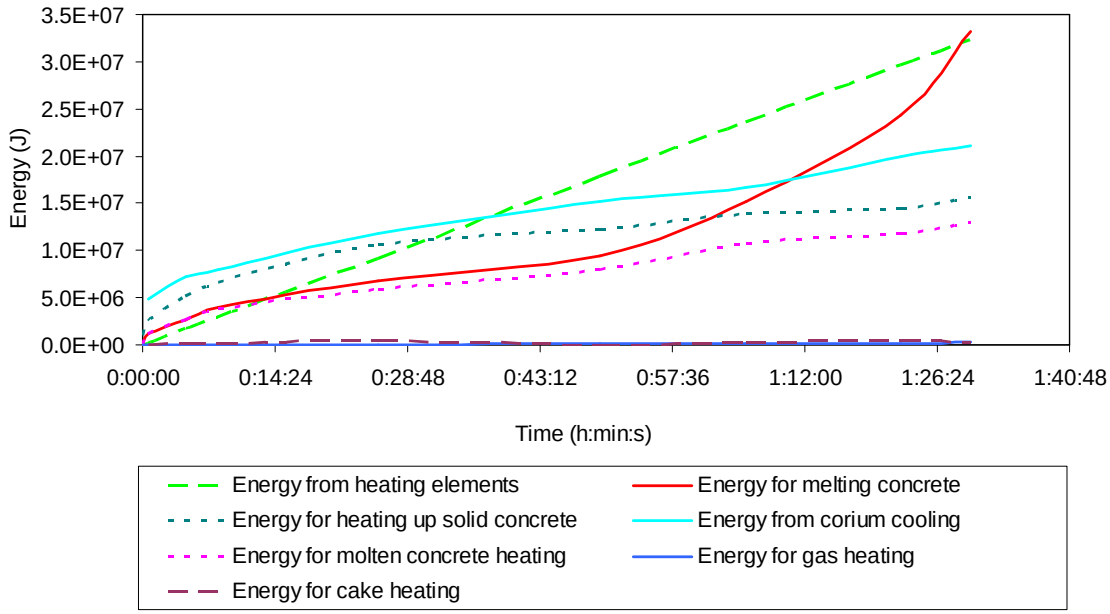

Figure 5-13. Energy distribution in ARTEMIS 10.

5.3.2 $BaCl_2$ mass conservation

- Mass of initial melt is 97.1 kg with 100% mass percentage of $BaCl_2$ → mass of $BaCl_2$ in the initial melt is $M_{BaCL2,ini}$ = 97.1 kg.
- Mass of molten concrete is 142 kg with 62.04% mass percentage of $BaCl_2$ → mass of $BaCl_2$ in the molten concrete is $M_{BaCl2,MC}$ = 88 kg.
- Mass of solid cake at the end of the test is 14.4 kg with 94% mass percentage of $BaCl_2$ → mass of $BaCl_2$ in the cake is $M_{BaCl2,cake}$ = 13.5 kg.
- Mass of melt cavity at the end is 224.7 kg with 79% mass percentage of $BaCl_2$ → mass of $BaCl_2$ in the final melt $M_{BaCl2,end}$ = 177.5 kg.
- Therefore, the mass of $BaCl_2$ from the molten concrete to the liquid melt is:
- $M_{BaCl2,MC\_to\_cavity} = M_{BaCl2,MC} - M_{BaCl2,cake}$ = 74.5 kg

Hence, the repartition of the $BaCl_2$ from the molten concrete is:

- ~ 15% to solid cake
- ~ 85% to the melt cavity

The mass balance of $BaCl_2$ is calculated by:

$$\Delta M_{BaCl2} = M_{BaCl2,end} - (M_{BaCl2,ini} + M_{BaCl2,MC} - M_{BaCl2,cake}) \approx 5.9 \text{ kg} \approx 3.3\ \% M_{BaCl2,end}$$

Therefore, it can be concluded that the mass of $BaCl_2$ is conserved during ARTEMIS 10.

5.3.3 Liquid-solid interface temperature

According to the analysis of ARTEMIS 11 for concrete-concrete interaction, the temperature at the liquid-solid interface is the melting temperature of the concrete. For ARTEMIS 10, the facts that the composition of the melt varies versus time and that the bulk composition may not be uniform (to be discussed in the next) lead to a question of how to determine the temperature at the liquid-solid interface? In chapter 2 (LIVE L3A) we arrived at the conclusion that the interface temperature, during crust formation and final steady state, is close to the liquidus temperature corresponding to the actual melt composition. The question is: “Does this hypothesis still hold for ARTEMIS 10, despite the ablation process and gas sparging through the liquid-solid interface?”

Figure 5-14, Figure 5-15 and Figure 5-16 provide comparisons of the temperature measured near the lateral liquid-solid interface (by the rotating 2D probe) and the liquidus temperature deduced from measurement of the local $BaCl_2$ concentration in the bulk at the same level at three different instants (the distribution of composition will be discussed later).

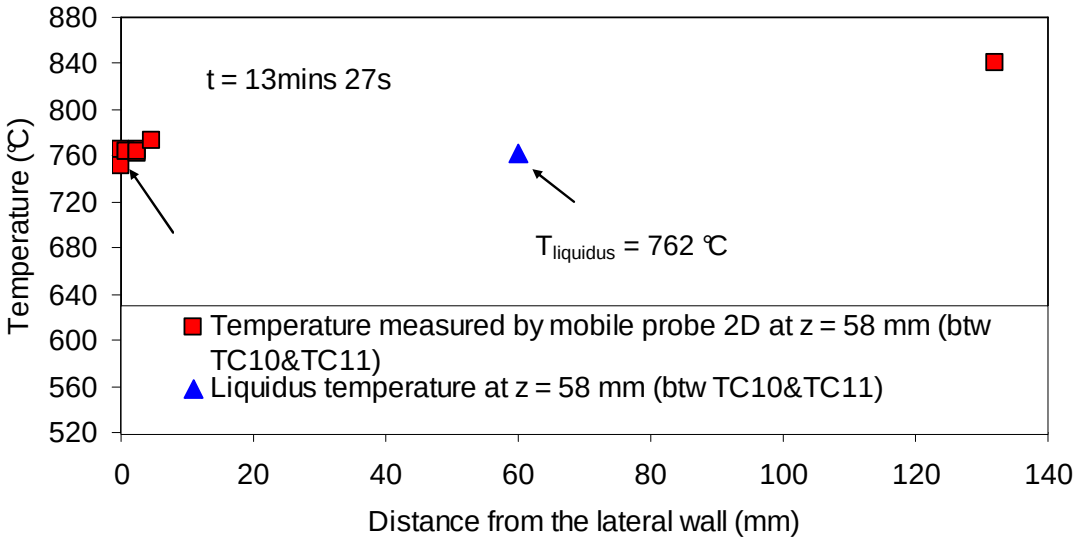

Figure 5-14. Comparison between measured interface temperature and liquidus temperature corresponding to the $BaCl_2$ concentration at z = 58 mm (between TC10 and TC11) at t = 0:13:27.

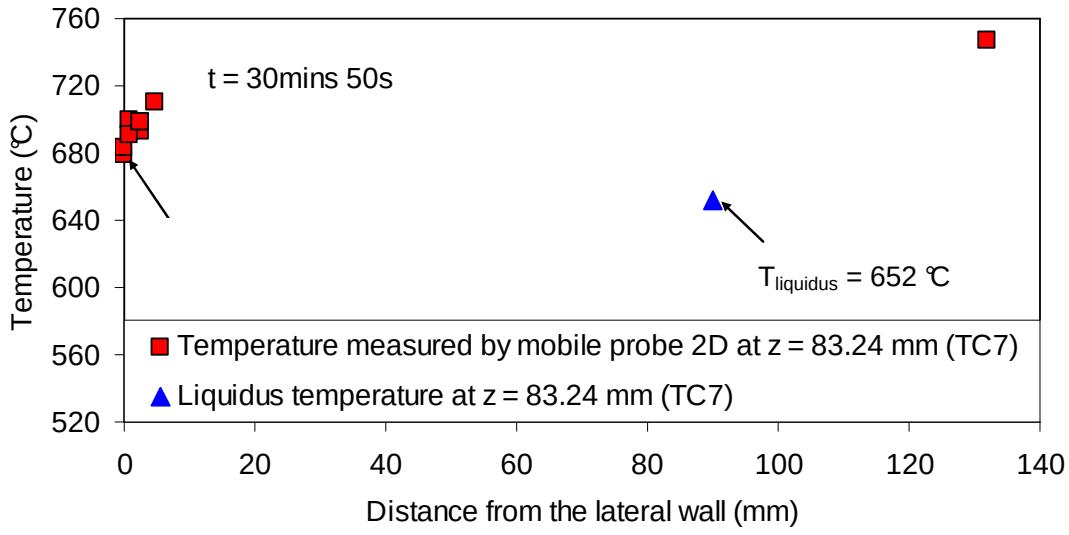

Figure 5-15. Comparison between measured interface temperature and liquidus temperature corresponding to the $BaCl_2$ concentration at z = 83.24 mm (TC7) at t = 0:30:50.

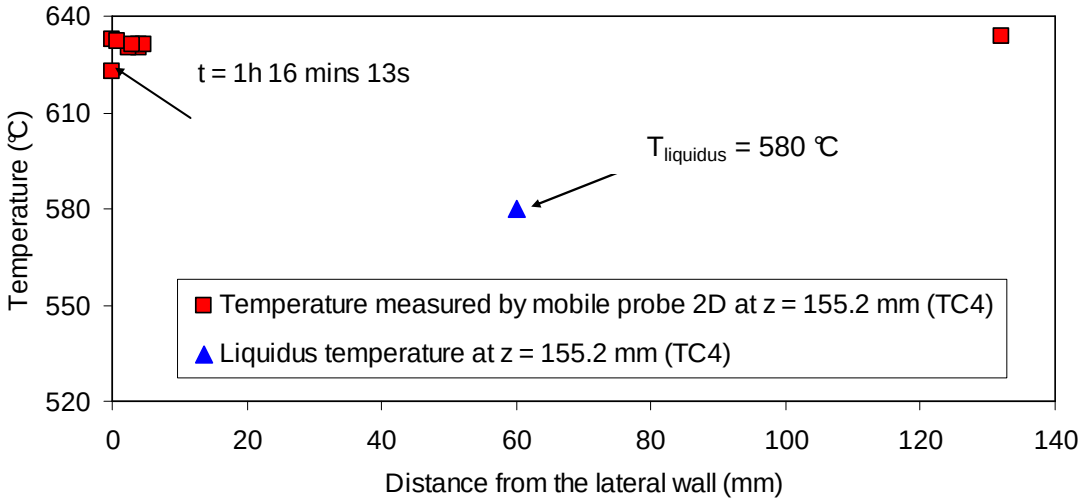

Figure 5-16. Comparison between measured interface temperature and liquidus temperature corresponding to the $BaCl_2$ concentration at z = 155.2 mm (TC4) at t = 1:16:13.

It is seen in Table 5-1 that the interface temperature is much greater than the melting temperature of the solid concrete (522 °C) and is closer to the liquidus temperature corresponding to the $BaCl_2$ concentration measured in the bulk at the same elevation. The difference between T_i and $T_{liquidus}(w_{bulk}^{BaCl2})$ for these three time instants is less than 40 °C while the difference between T_i and T_{melt} (melting temperature of concrete) ranges from 100 °C to 250 °C. The reader should also note that the melt composition near the interface might be different from the composition measured in the bulk. This aspect will be taken into account in the recalculation with the 1D model. The measurement error due to thermocouple positioning and conduction in the thermocouples is not known, but it can be estimated that the accuracy of the interface temperature measurement is of ± 8°C ~ 10°C as observed in the measurement of ARTEMIS 11 (the interface temperature is theoretically 522 °C while the measured one was of 8°C to 10 °C above the theoretical value).

Table 5-1. Interface temperature in ARTEMIS 10.

Time h:min:s	z mm	T_i °C	$T_{liquidus}$ °C	$T_{liquidus} - T_i$ °C	$T_i - T_{melt}$ °C
0:13:27	58	751	762	+11	229
0:30:50	83	679	652	-27	157
1:16:13	155	622	583	-39	100

5.3.4 Analysis of flow recirculation in the melt cavity

Knowledge of the flow behaviour in the melt cavity is required to understand the heat transfer mechanism in ARTEMIS 10. In order to describe how is the flow configuration in the cavity, information from the axial temperature profile and bulk composition distribution in the cavity will be analyzed.

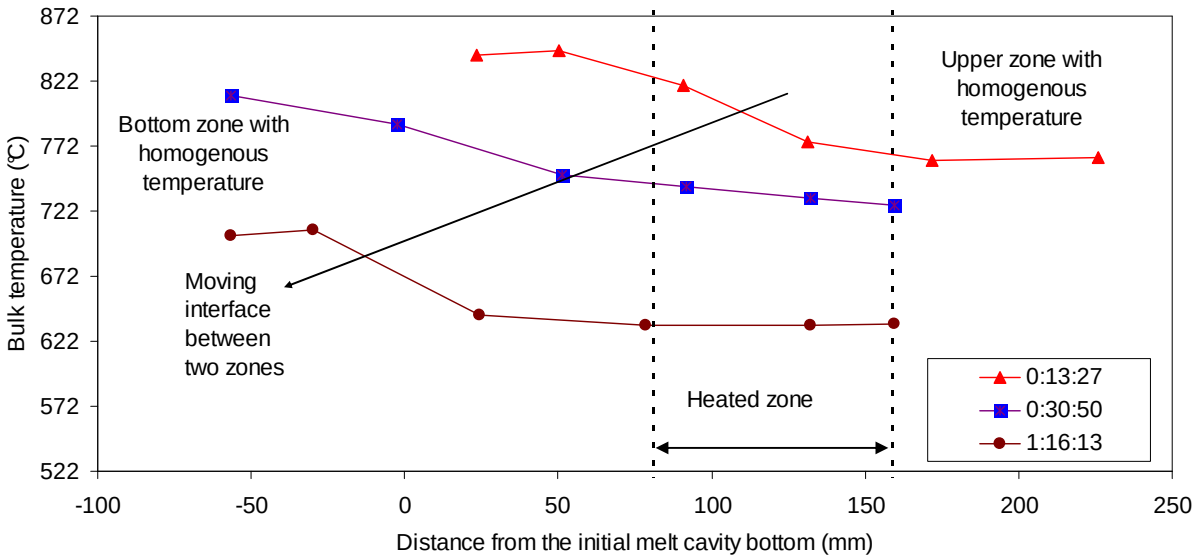

Figure 5-17. Two zones (top and bottom) with quasi-uniform temperature in the melt cavity.

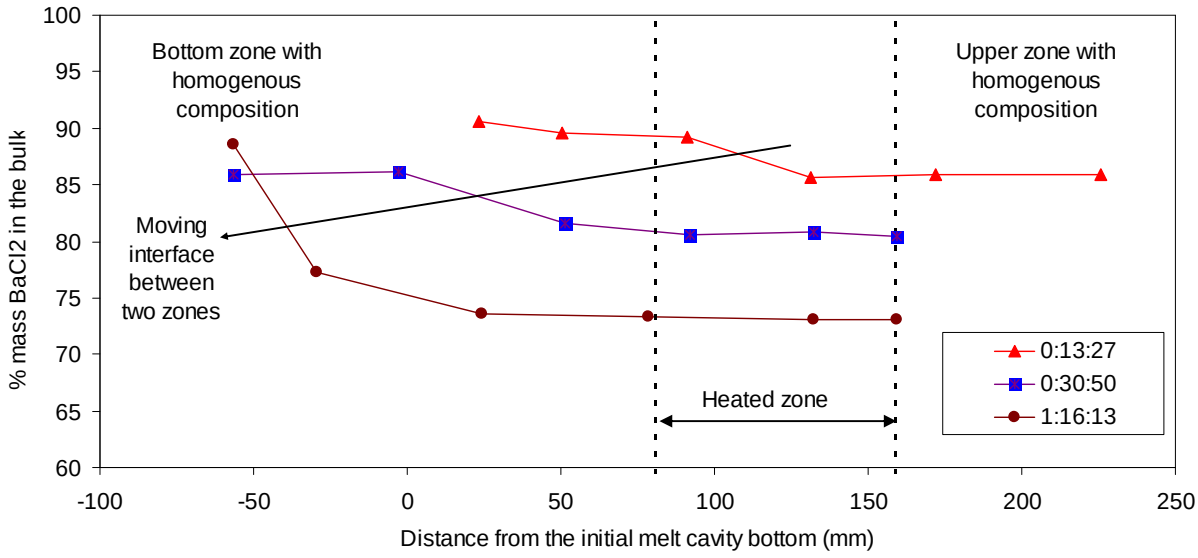

Figure 5-18. Two zones with uniform $BaCl_2$ concentration in the melt cavity.

As depicted in Figure 5-17 and Figure 5-18, the melt cavity is divided into two zones with uniform temperature and $BaCl_2$ concentration in each zone.

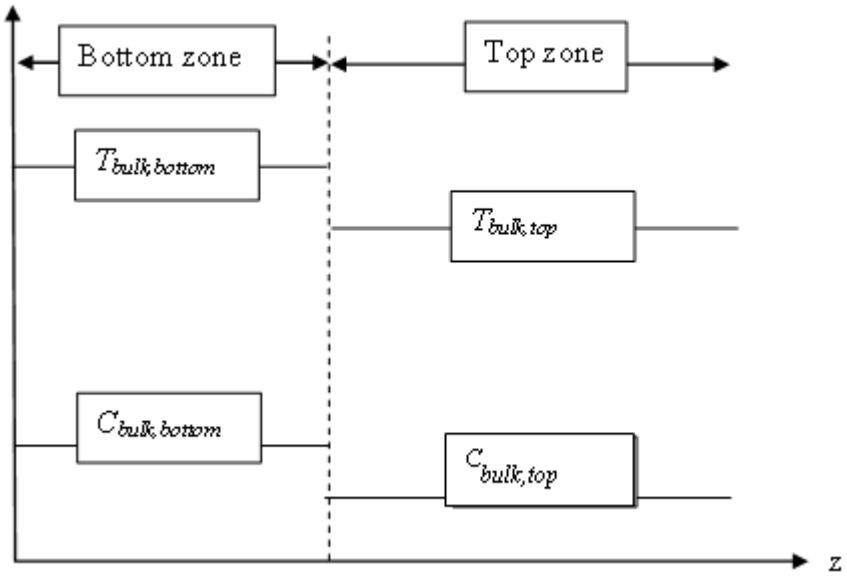

Figure 5-19. Schematic of two zones in the melt cavity.

The axial temperature profile indicates that the bulk temperature in the top zone is significantly lower than in the bottom zone. The interfaces between these two zones are moving in the same manner to the bottom of the cavity versus time.

Regarding to the distribution of $BaCl_2$ in the bulk, it is clearly seen that the bottom zone of the melt cavity is more enriched in $BaCl_2$ than the top zone. The mass percentage of $BaCl_2$ in the bottom zone is significantly higher than in the top zone. The difference of composition between the two zones increases versus time.

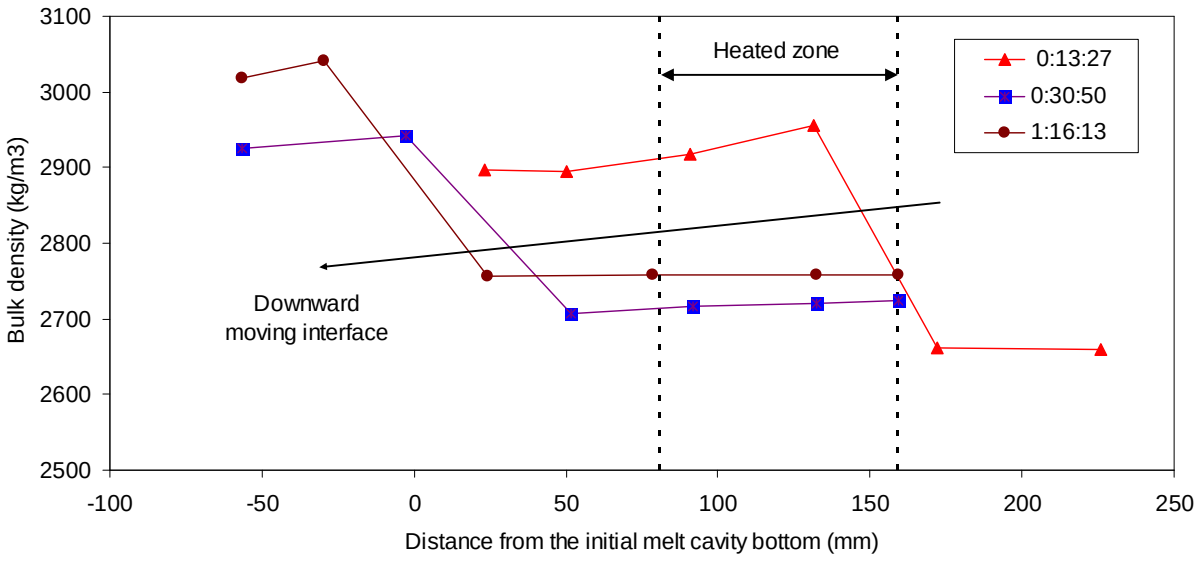

Figure 5-20. Density distribution in the top and bottom zones.

Using the local $BaCl_2$ concentration in the bulk at instant *t* together with the local bulk temperature presented previously, the local liquid density in the bulk could be deduced. Since the bottom zone is

more enriched by $BaCl_2$ than the top zone, the liquid density is higher in the bottom than in the top. The results are given in Figure 5-20.

The above analysis of the bulk temperature and the bulk composition in ARTEMIS 10 will be used in the next to propose a prediction of two recirculation loop configuration in the melt cavity. Flow directions in these recirculation loops will be determined in the following section.

5.3.5 Determination of recirculation flow direction

Estimation of the average density in the boundary layer

Since the melt cavity is divided into two parts, each part covering the bulk and a boundary layer zone, the flow recirculation in the melt cavity is governed by the density difference between the bulk and the boundary layer. This section proposes a simple method for estimating the boundary layer density.

As discussed previously, we will emphasize that natural convection is a first hypothesis concerning the flow recirculation in the melt. The calculation of boundary layer density is a simplified version of the 1D boundary layer model (Appendix 7). The boundary layer receives the molten concrete at melting temperature of concrete and the radial liquid melt from the bulk.

$$\rho_{BL}(T_{BL}) = \frac{\rho_{bulk}(T_{BL})\, j_{bulk} + \rho_{MC}(T_{BL})\, V_{abl}}{j_{bulk} + V_{abl}} \tag{5-5}$$

in which ρ_{bulk} is the density of the bulk at solute composition w_{bulk} and ρ_{MC} is the density of the molten concrete with solute composition w_{MC}. In this formula, the effects of temperature difference and of composition difference are taken into account.

Proposal of a criterion for flow direction prediction

As discussed in the previous section, the flow recirculation in the melt cavity is driven by the density difference between the liquid at the centre of the cavity and the liquid in the boundary layer. If the density in the bulk is higher than that in the boundary layer, then the flow moves downwards at the cavity centre and upwards in the boundary layer. By contrast, if the bulk has lower density than the boundary layer, the flow moves upward at the cavity centre and thus, the flow in the boundary layer is downward.

This section is dedicated to the estimation of the density difference between the bulk and the boundary layer. A criterion will be proposed for prediction the flow direction in the two recirculation loops in ARTEMIS 10.

The density difference between the bulk and the boundary layer is defined as:

$$\Delta\rho = \rho_{bulk}(T_{bulk}) - \rho_{BL}(T_{BL}) \tag{5-6}$$

Combining Equations (5-5) and (5-6) gives:

$$\Delta\rho = \rho_{bulk}(T_{bulk}) - \frac{\rho_{bulk}(T_{BL}) + k_\rho\, \rho_{MC}(T_{BL})}{1 + k_\rho} \tag{5-7}$$

with

$$\frac{V_{abl}}{j_{bulk}} = k_\rho \tag{5-8}$$

The density of the bulk at T_{BL} is written as:

$$\rho_{bulk}(T_{BL}) = \rho_{bulk}(T_{bulk})\left[1 - \beta_T (T_{BL} - T_{bulk})\right] \tag{5-9}$$

in which β_T is the thermal expansion coefficient of the melt and ρ_{bulk} depends on the composition in the bulk.

Combining Equations (5-7) and (5-9) leads to:

$$\Delta\rho = \frac{k_\rho \left[\rho_{bulk}(T_{bulk}) - \rho_{MC}(T_{BL})\right] + \beta_T\, \rho_{bulk}(T_{bulk})\left(T_{BL} - T_{bulk}\right)}{1 + k_\rho} \tag{5-10}$$

Assuming that the heat flux transferred from the bulk to the boundary layer will transfer through the interface with concrete and will serve for heating the solid concrete by conduction as well as for melting the solid concrete, the energy balance will be written as:

$$\begin{aligned} &\rho_{bulk}\, j_{bulk} C^{bulk}_{p,liquid} (T_{bulk} - T_{BL}) \\ &= \rho_{MC}\, V_{abl} \left[L^{concrete}_{melting} + C^{concrete}_{p,solid}\, \Delta T_{concrete} \right] + \varphi_{conduction} \end{aligned} \tag{5-11}$$

Assuming that the conduction heat flux is negligible in comparison with the heat flux serving for concrete melting, then Equation (5-11) is written alternatively as:

$$\rho_{bulk}\, j_{bulk} C^{bulk}_{p,liquid} (T_{bulk} - T_{BL}) = \rho_{MC}\, V_{abl} L'_{melting} \tag{5-12}$$

or

$$k_\rho = \frac{V_{abl}}{j_{bulk}} = \frac{\rho_{bulk}\, C^{bulk}_{p,liquid} \left(T_{bulk} - T_{BL}\right)}{\rho_{MC}\, L'_{melting}} \tag{5-13}$$

with $L'_{melting} = L^{concrete}_{melting} + C^{concrete}_{p,solid} \Delta T_{concrete}$.

Case 1: If the flow goes downwards at the cavity centre and upwards in the boundary layer, then the density in the bulk is greater than the one in the boundary layer. This means:

$$\Delta\rho \geq 0 \tag{5-14}$$

Equation (5-11) equals to:

$$\rho_{bulk}(T_{bulk}) - \rho_{MC}(T_{BL}) \geq \frac{\beta_T \ \rho_{bulk}(T_{bulk})\left(T_{BL} - T_{bulk}\right)}{k_\rho} \tag{5-15}$$

Combining Equations (5-13) and (5-15) leads to:

$$\rho_{bulk}(T_{bulk}) \geq \rho_{MC}(T_{melt}) \left[1 + \frac{\beta_T \ L'_{melting}}{C^{bulk}_{p,liquid}}\right] \tag{5-16}$$

Case 2: If the flow goes upwards at the cavity centre and downwards in the boundary layer, then the density in the bulk is lower than the one in the boundary layer. In this case:

$$\rho_{bulk}(T_{bulk}) \leq \rho_{MC}(T_{melt}) \left[1 + \frac{\beta_T \ L'_{melting}}{C^{bulk}_{p,liquid}}\right] \tag{5-17}$$

Define:

$$\rho_{\text{limit}} = \rho_{MC}(T_{melt}) \left[1 + \frac{\beta_T \ L'_{melting}}{C^{bulk}_{p,liquid}}\right] \tag{5-18}$$

Then an order of magnitude criterion is derived to predict the flow direction in the boundary layer (as well as the flow direction in the bulk centre), as follows:

- $\rho_{bulk}(T_{bulk}) \geq \rho_{limit}$: upward flow in the boundary layer
- $\rho_{bulk}(T_{bulk}) \leq \rho_{limit}$: downward flow in the boundary layer

Writing the density as a function of temperature and composition as follows:

$$\rho_{\text{bulk}}(T_{bulk}, w_{bulk}) = \rho^{T^{BaCl2}_{melt}}_{BaCl2} \left[1 - \beta_T (T_{bulk} - T^{BaCl2}_{melt}) - \beta_C w_{bulk}\right] \tag{5-19}$$

and

$$\rho_{\text{MC}}(T_{melt}, w_{MC}) = \rho^{T^{BaCl2}_{melt}}_{BaCl2} \left[1 - \beta_T (T_{melt} - T^{BaCl2}_{melt}) - \beta_C w_{MC}\right] \tag{5-20}$$

wherein β_T and β_C are respectively the thermal expansion coefficient and solute expansion coefficient which are assumed to be identical for the concrete and the melt (the values are taken in Table 3-2), $\rho_{BaCl2}^{T_{melt}^{BaCl2}}$ is the density of pure liquid $BaCl_2$ at melting temperature of $BaCl_2$.

Then the criterion of density is now written alternatively in terms of the solute composition difference between the molten concrete and the bulk.

Case 1: Upward flow in the boundary layer:

$$\frac{\beta_C}{\beta_T}(w_{MC}-w_{bulk})<\frac{\rho_{MC}(T_{melt})}{\rho_{BaCl2}^{T_{melt}^{BaCl2}}}\frac{L'_{melting}}{C_{p,liquid}^{bulk}}+T_{bulk}-T_{melt} \tag{5-21}$$

Case 2: Downward flow in the boundary layer:

$$\frac{\beta_C}{\beta_T}(w_{MC}-w_{bulk})>\frac{\rho_{MC}(T_{melt})}{\rho_{BaCl2}^{T_{melt}^{BaCl2}}}\frac{L'_{melting}}{C_{p,liquid}^{bulk}}+T_{bulk}-T_{melt} \tag{5-22}$$

The above criterion indicates that, as a first approximation, the direction of the flow in the melt cavity only depends on the density of molten concrete, on the concentration of the bulk and constant physical properties, and is not dependent on the boundary layer temperature or the temperature difference between the bulk and the boundary layer.

Application of the proposed criterion for ARTEMIS 10

The methodology presented in the preceding will be applied for ARTEMIS 10. The limit density between the top and the bottom zone calculated by Equation (5-18) is 2815 kg/m^3. As shown in Figure 5-21, this limit density is in between the density of the bulk in the top and bottom zones. This methodology allows determining more exactly the position of the interface between the top and the bottom zones ($z_{interface}$). It is seen that this interface moves downwards versus time.

- t_1 = 0:13:27: $z_{interface}$ = 152 mm
- t_2 = 0:30:50: $z_{interface}$ = 28 mm
- t_3 = 1:16:15: $z_{interface}$ = 13 mm

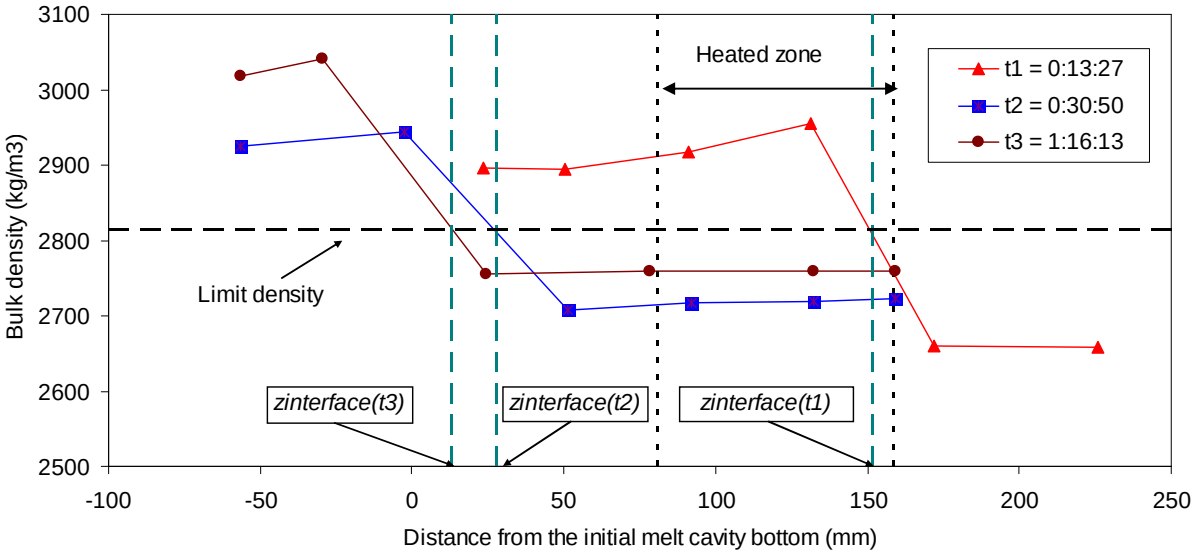

Figure 5-21. Evolution of interface position between top-bottom zones.

This leads to the conclusion that the top-bottom interface is lowered rather fast to the bottom of the cavity in the beginning. At t = 0:13:27, the interface already stays in the heated zone. After less than 30 minutes, this interface is located below the heating element zone. This indicates an increase of power dissipation in the top zone versus time while the power dissipation in the bottom zone declines as time goes on.

It is of importance that in the beginning, the heating power dissipates mainly in the bottom zone. Then, due to the downward movement of the interface, more and more power dissipates in the top zone and the power dissipation in the bottom zone is reduced.

According to the limit density criterion, the direction of the flow in each zone is deduced. In the top zone, since $\rho_{bulk}(T_{bulk}) < \rho_{limit}$, the flow should go upwards in the cavity centre and downwards in the boundary layer. In the bottom zone, $\rho_{bulk}(T_{bulk}) > \rho_{limit}$ indicates that the flow should go downwards in the cavity centre and therefore, upwards in the boundary layer (Figure 5-22). The downwards flow in the centre of the bottom zone explains the negative temperature gradient in this zone while the upwards flow in the centre of the top zone explains the positive temperature gradient in this zone.

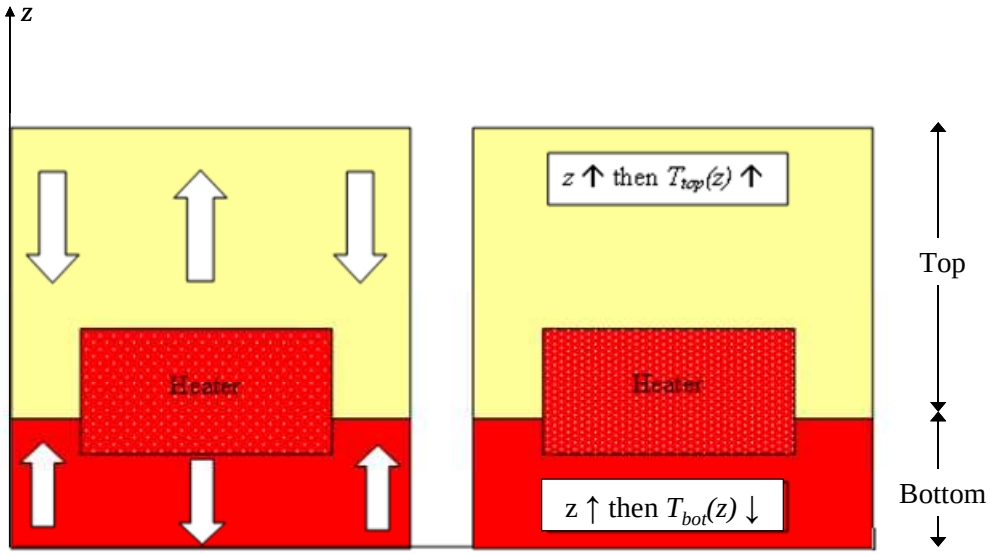

Figure 5-22. Flow directions in top and bottom zones.

5.3.6 Estimation of average volumetric flow rate in the melt cavity

As presented in the preceding, the position of the top-bottom interface has been determined using the proposed criterion for the density in the bulk. The power dissipation in each zone will be estimated by assuming that it is approximately proportional to the thickness of the heating zone located in each zone as depicted in Figure 5-23, i.e:

$$\dot{Q}_{top}(t) = \frac{\Delta z_{top}(t)}{\Delta z_{heater}} \dot{Q}_{add} \tag{5-23}$$

and

$$\dot{Q}_{bot}(t) = \frac{\Delta z_{bot}(t)}{\Delta z_{heater}} \dot{Q}_{add} \tag{5-24}$$

wherein:

$$\Delta z_{top}(t) = z_{top,heater} - z_{\mathrm{int}erface}(t) \tag{5-25}$$

and

$$\Delta z_{bot}(t) = z_{\mathrm{int}erface}(t) - z_{bot,heater} \tag{5-26}$$

wherein $z_{interface}(t)$ is the position of the interface between top and bottom zones at instant t (the distance from the initial bottom of the cavity to the top-bottom interface); $\dot{Q}_{top}(t)$ and $\dot{Q}_{bot}(t)$ are the power dissipation in the top and in the bottom zones at instant t, respectively.

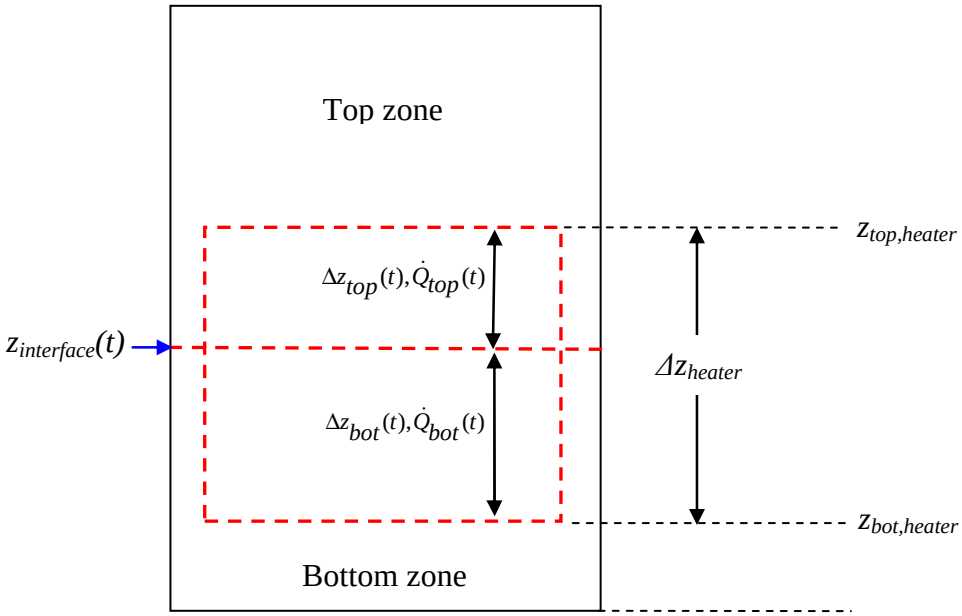

Figure 5-23. Schematic of power distribution in the top and bottom zones.

The volumetric flow rates in the top and bottom zones are calculated as follows:

$$\dot{V}_{top}(t) = \frac{\dot{Q}_{top}}{\rho_{bulk,top}\, C^{top}_{p,liquid}\, \Delta T_{bulk,top}} \tag{5-27}$$

and

$$\dot{V}_{bot}(t) = \frac{\dot{Q}_{bot}}{\rho_{bulk,bot}\, C^{bot}_{p,liquid}\, \Delta T_{bulk,bot}} \tag{5-28}$$

wherein $\rho_{bulk,top}$ and $\rho_{bulk,bot}$ are respectively the average density in the top and in the bottom zones, $\Delta T_{bulk,top}$ and $\Delta T_{bulk,bot}$ are the temperature difference between the inlet and outlet of the top zone and the bottom zone, respectively.

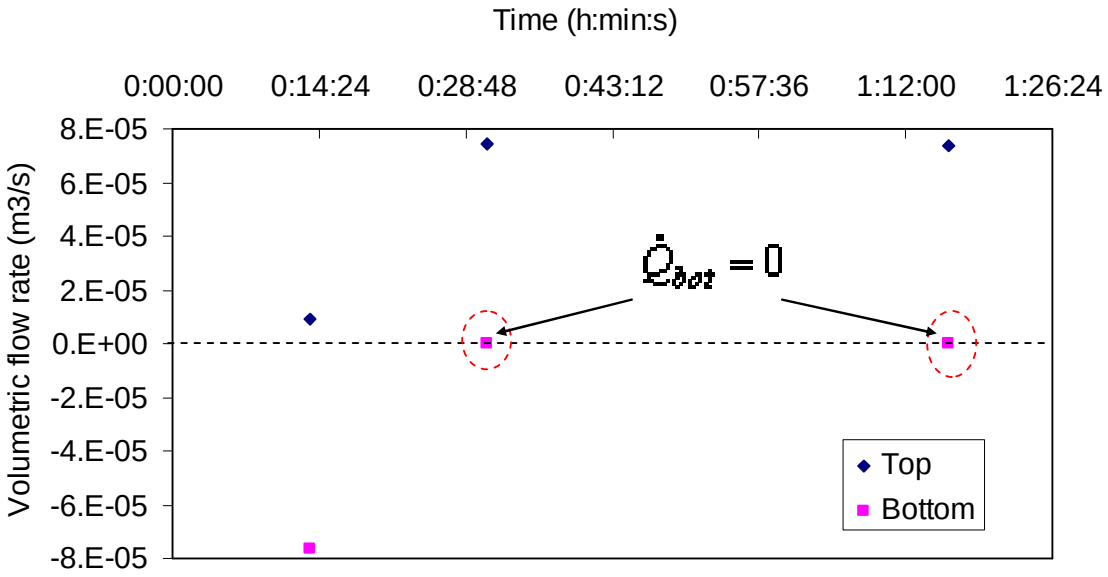

Figure 5-24. Average volumetric flow rate in the top and bottom zones.

The volumetric flow rate is positive at the top zone and negative at the bottom zone. The signs indicate that the fluid in the two zones flows in two opposite directions. After $t \geq$ 0:30:27, the volumetric flow rate in the bottom zone reduces to zero. This is an artefact; because there is no more power dissipation in this zone (The top-bottom interface is located below the heating zone). In the top zone, the volumetric flow rate increases versus time due to increasing power dissipation. The bulk velocity at the centre of the melt cavity ranges between 8 10^{-5} m/s to 4 10^{-4} m/s.

5.3.7 Estimation of the radial entrainment velocity to boundary layer

The average velocity of this radial liquid flow entrainment (into the boundary layer), denoted as j_{bulk}, is estimated for the top and the bottom zones of the cavity by knowing the average volumetric flow rate in each zone in the bulk, as follows:

$$j_{bulk,top}(t) = \frac{m_{v,top}(t)}{S_{lat,top}(t)} \tag{5-29}$$

and

$$j_{bulk,bot}(t) = \frac{m_{v,bot}(t)}{S_{lat,bot}(t)} \tag{5-30}$$

in which $S_{lat,top}(t)$ and $S_{lat,bot}(t)$ are the lateral surface areas of the top and the bottom zones, which is approximated by:

$$S_{lat,top}(t) = 2\pi R_{avg,top}(t) H_{top}(t) \tag{5-31}$$

and

$$S_{lat,bot}(t) = 2\pi R_{avg,bot}(t) H_{bot}(t) \tag{5-32}$$

wherein $R_{avg,top}(t)$ and $R_{avg,bot}(t)$ are the average radius of the top and the bottom zones, respectively, estimated as:

$$R_{avg,top}(t)=\frac{R_{top}(t)+R_{interface}(t)}{2} \tag{5-33}$$

and

$$R_{avg,bot}(t)=\frac{R_{bot}(t)+R_{interface}(t)}{2} \tag{5-34}$$

Besides, the heights of the top and the bottom zones are calculated by:

$$H_{top}(t)=H-z_{interface}(t) \tag{5-35}$$

and:

$$H_{bot}(t)=z_{interface}(t) \tag{5-36}$$

in which H is the height of the melt cavity and $z_{interface}(t)$ is the distance from the initial bottom of the melt cavity to the interface between the top and bottom zones at instant t.

Calculation results of j_{bulk} for the top and bottom zones are shown in Figure 5-26. It is observed that the radial liquid velocity in top and bottom zone varies as a function of time in the first 30 minutes before reaching a quasi-constant value. At t < 30 minutes, $j_{bulk,top}$ is smaller than $j_{bulk,bottom}$ while at t > 30 minutes, $j_{bulk,top}$ is greater than $j_{bulk,bottom}$.

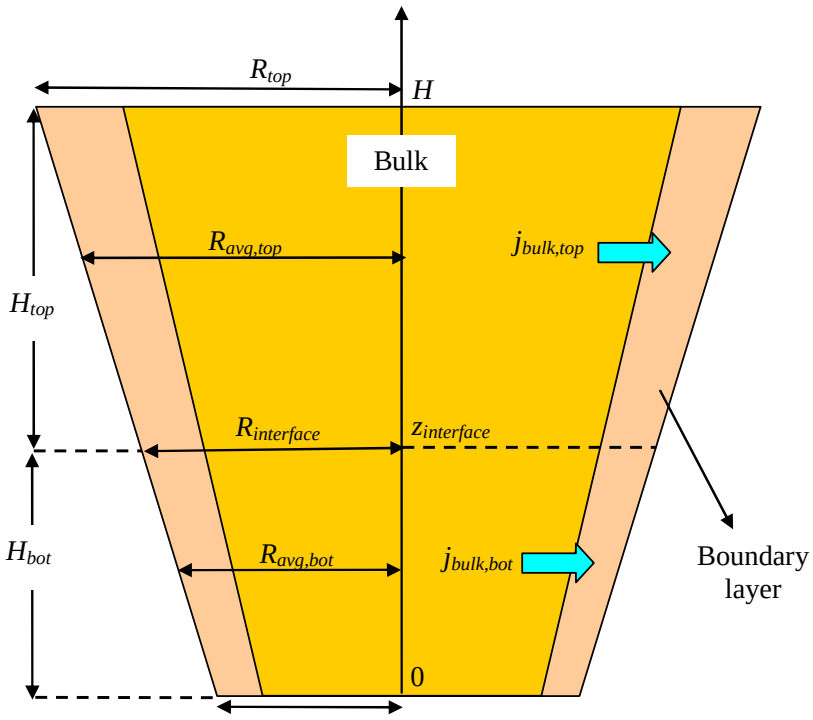

Figure 5-25. Entrainment of radial liquid flow from bulk to boundary layer.

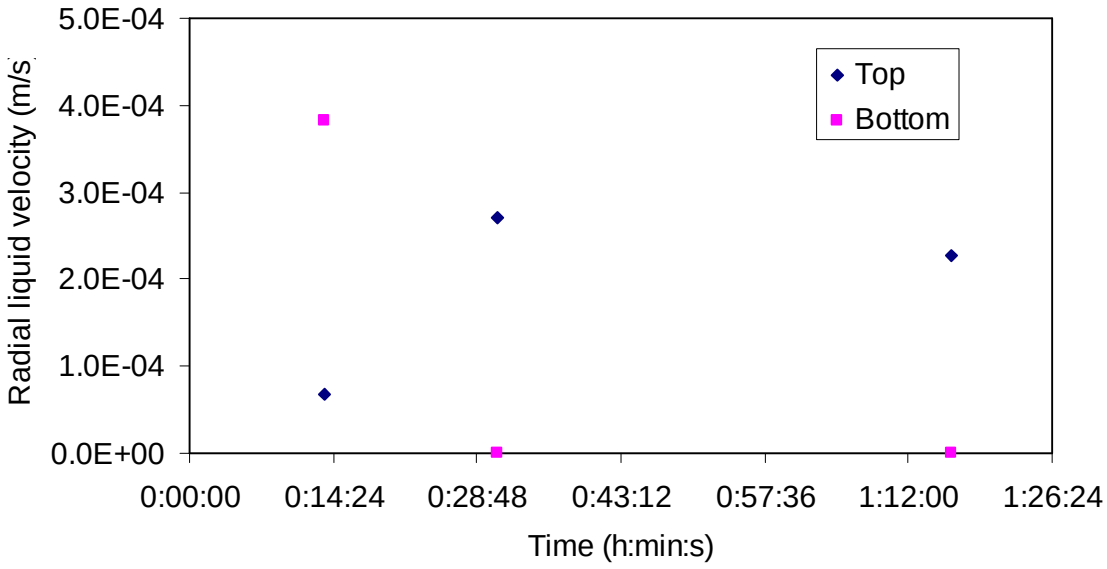

Figure 5-26. Estimation of radial liquid flow entrainment velocity from bulk to boundary layer.

5.3.8 Comparison of local ablation velocity and radial liquid velocity from bulk to boundary layer

On one hand, the boundary layer is fed by the radial liquid flow from the bulk. On the other hand, the boundary layer receives also the molten concrete from the ablation of the solid concrete. In this section, the velocity of the radial liquid flow from the bulk j_{bulk} will be compared to the ablation velocity of the concrete V_{abl}. Comparison is shown in Figure 5-27 for calculation in the top zone and in Figure 5-28 for calculation in the bottom zone. It is seen that in the top zone, the j_{bulk} is significantly greater (an order of magnitude) than V_{abl}. In the bottom zone, j_{bulk} is greater than V_{abl} in the beginning. Then velocities become very small (less than 10^{-5} m/s).

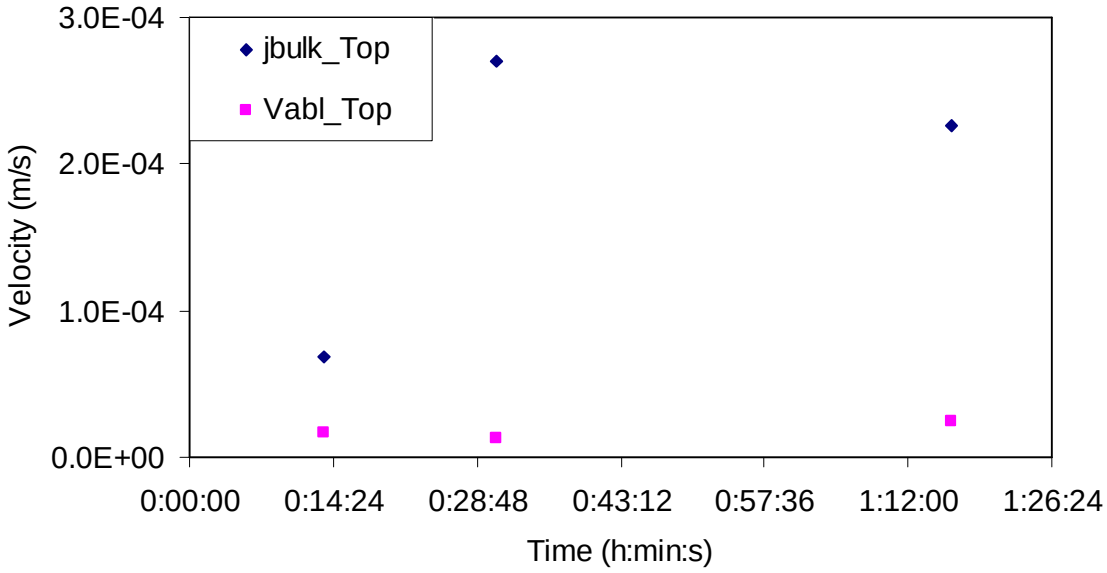

Figure 5-27. Comparison of j_{bulk} and V_{abl} in the top zone.

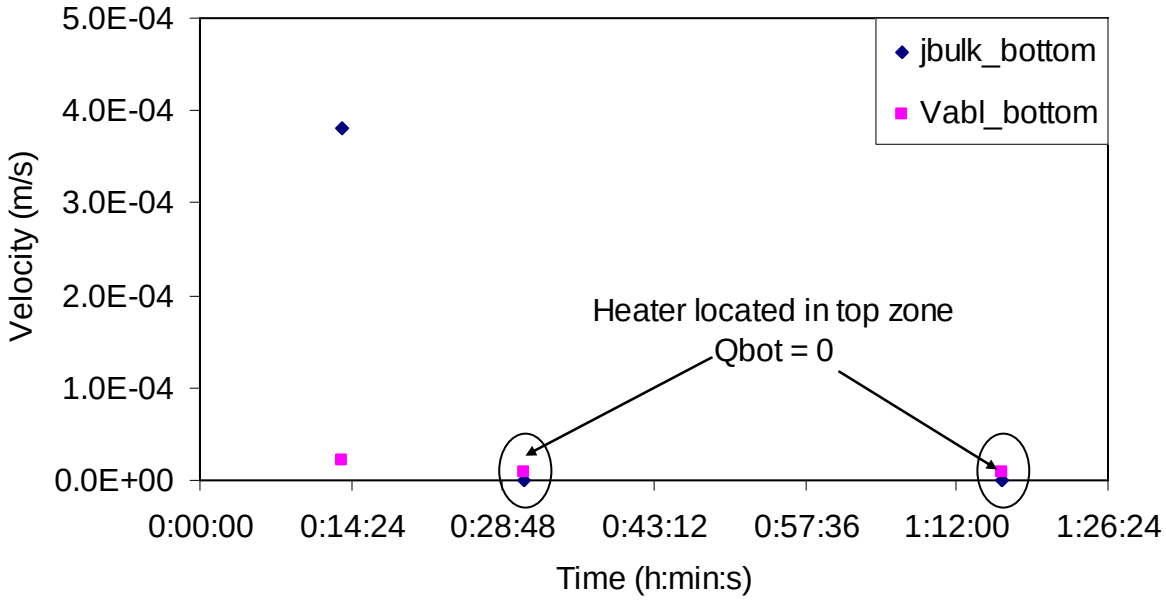

Figure 5-28. Comparison of j_{bulk} and V_{abl} in the bottom zone.

As seen in Figure 5-27 and Figure 5-28, the ratio k_ρ between ablation velocity and the radial liquid entrainment velocity into the boundary layer is between 0.07 to 0.25 which is in the same order of magnitude with the one calculated using Equation (5-13) which provides k_ρ in between 0.02 and 0.125.

5.3.9 Energy balance in the top and bottom zones

In order to estimate the energy balance in the top and the bottom zones of the melt cavity, a control volume will be defined for each zone. The top control volume contains the total volume of liquid melt and solid concrete located above the top-bottom interface in the melt while the control volume for the bottom zone is taken as the volume of liquid and solid below the interface. The position of top-bottom interface has been determined as a function of time in section 5.3.5. Calculations of energy balance for each zone are performed with the methodology given in Annex 5.

Since the energy serving for gas heating is of minor importance in comparison to the energy released from heating elements and to the variation of stored energy in the control volume, it will be neglected. Figure 5-29 represents a comparison of energy balance in the top and bottom zones in the melt cavity. It is seen that ablation in the top and bottom zones is directly linked to the distribution of heating power. At t > 1h when the top-bottom interface stays lower than the heated zone, there is no more ablation in the bottom zone while an acceleration of ablation and energy stored in the top zone is still observed.

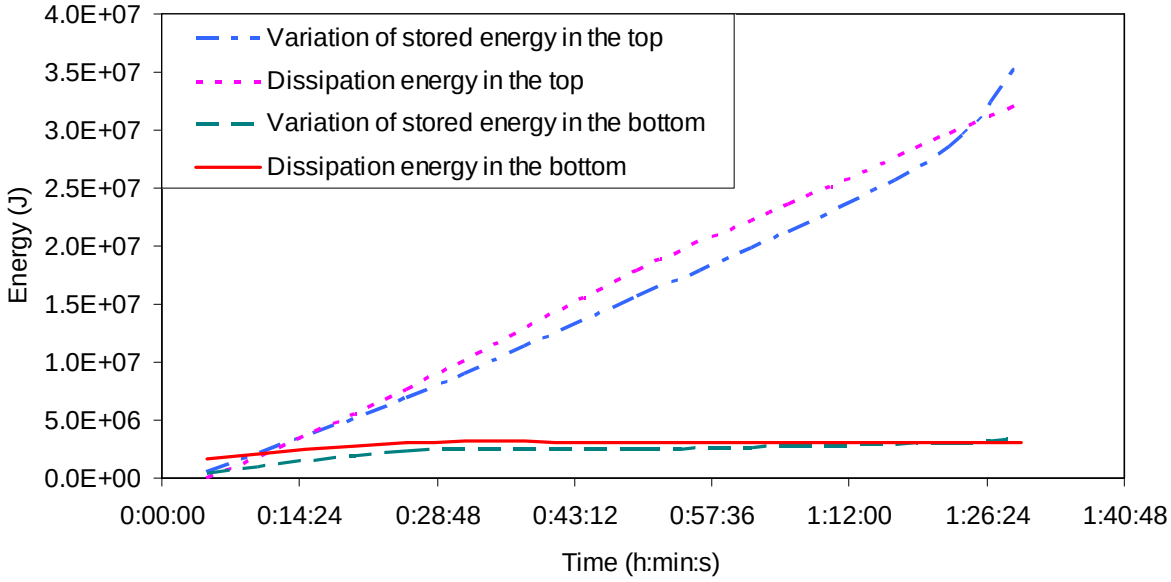

Figure 5-29. Energy partition and ablation in top and bottom zones.

5.3.10 Coherence between evolution of cavity shape and power distribution in the cavity

Figure 5-30 sketches the evolution of the power distribution in the cavity for two given time instants t_1 and t_2 with $t_1 < t_2$. The top-bottom interface is lowered versus time, leading to increasing power dissipation in the top zone and decreasing power dissipation in the bottom zone.

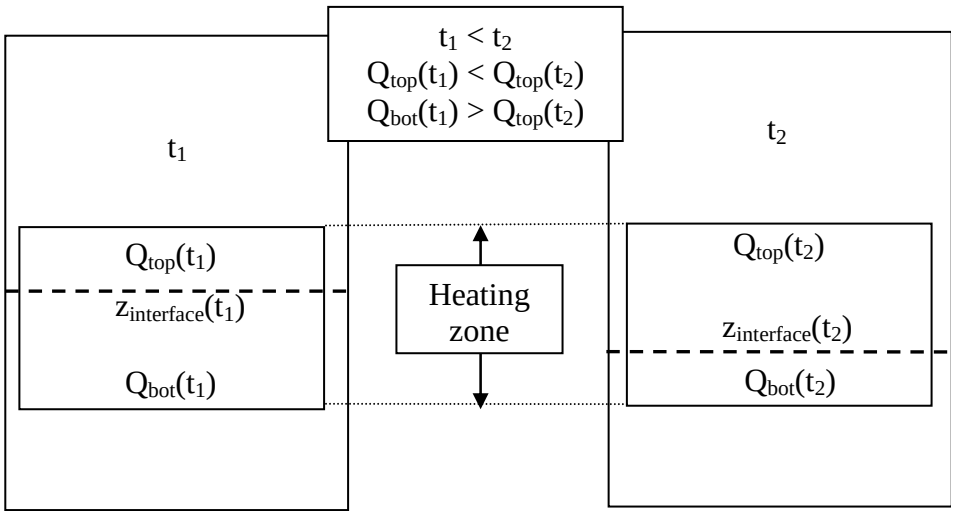

Figure 5-30. Sketch of the evolution of power distribution in top and bottom zones.

In the top zone, since the flow goes downwards in the boundary layer, the maximum heat flux and maximum ablation would be obtained at the top of the lateral wall. In the bottom zone, the flow goes upward in the boundary layer. Therefore, maximum heat flux should now occur at the bottom of the cavity. Hence, there would be ablation not only to the lateral wall of the melt cavity but also vertical ablation (i.e. melting of concrete at the bottom part of the cavity). At the top-bottom interface, the heat

flux is the minimum. Consequently, ablation at this elevation would be weaker than at other elevations in the melt cavity.

Combining the preceding discussions on the evolution of power distribution in the top and the bottom zones of the cavity and on the heat flux distribution at different cavity elevations leads to an explanation of the evolution of the cavity shape observed in ARTEMIS 10, as follows (Figure 5-7):

- In the top zone, since the flow in the boundary layer goes downwards, similarly to ARTEMIS 11, the boundary layer flow is plausibly laminar and the thickness of the boundary layer at the top of the lateral wall is very small, leading to a high heat transfer coefficient and high heat flux transferred from the melt cavity to the top. Therefore, strong ablation to the top of the lateral wall is seen. The energy for the ablation comes also from the melt cooling.
- At the beginning, a significant part of the power dissipation is in the bottom zone. In addition, the boundary layer flow in the bottom zone goes upwards in the boundary layer, leading to maximum heat flux at the bottom of the cavity. Consequently, beside the top lateral ablation, vertical ablation of the bottom interface is also observed.
- As time goes on, the top-bottom interface is lowered, then, the power dissipation in the bottom zone decreases and the power dissipation in the top zone increases. Hence, ablation to the bottom zone becomes less and less. After t = 0:30:27, the top-bottom interface locates lower than the heating elements. As a result, there will be no more power dissipating in the bottom zone. The energy used for concrete melting at the bottom is then only generated from the cooling of the melt. The heat flux transferred to the lateral wall of the bottom zone and to the bottom interface from the melt cavity is decreased significantly, leading to decrease of ablation in the bottom zone. In addition, due to the increasing thickness of the cake forming at the bottom of the melt cavity, the thermal resistance between melt and bottom concrete increases. Consequently, heat flux serving for concrete melting becomes very small and after 1 h, ablation to the bottom stops. In the mean time, the power in the top zone increases and therefore, ablation to the top lateral wall continues (after t = *1* h).
- According to the evolution of the cavity shape, at certain time instants, almost no lateral ablation can be observed for intermediate cavity elevations. As discussed in the above, these elevations could be considered as the position of the top-bottom interface in which the heat flux transferred to the lateral wall from the cavity is the minimum (in comparison with the heat flux at other cavity elevations). For example, between t = 0:04:35 and t = 0:08:10, no ablation is seen at z = 16 cm (z is the distance from the initial position of the cavity bottom). Hence, during this period, the interface between top and bottom zones locates at this elevation. Then, between t = 0:08:10 and t = 0:24:35, there is no ablation at z = 6 cm. This means the top-bottom interface has been lowered versus time. Moreover, between t = 1:05:40 and t = 1:22:00, minimum ablation occurs at z = 2 cm. This is coherence with the calculation of the densities at t = 1:16:15 which shows that the density in the boundary layer is similar to the density in the bulk (density difference is minor).

5.3.11 Prediction of heat transfer mechanism in the melt cavity

Since gas is injected into the system during ARTEMIS 10, it is expected to enter the melt cavity and this would affect the flow recirculation and heat transfer from the melt to the liquid-solid interface. If there exists a significant gas-liquid mixing interaction in the melt cavity, then, as discussed under Chapter 4 in the analysis of ARTEMIS 11, the temperature in the melt cavity would be uniform and quite no temperature gradient should be observed in the bulk (as seen in the first 16 minutes in ARTEMIS 11). This observation has been recently reported in the experimental results from CLARA tests. The test is performed at CEA Grenoble for a rectangular cavity (Figure 5-31) and water (with additives for variable viscosity) was employed as the working fluid. The fluid is volumetrically heated. Lateral and bottom walls are cooled. Gas is injected at different positions from either the lateral wall or the bottom interface of the water cavity in order to see the effect of gas on the heat transfer.

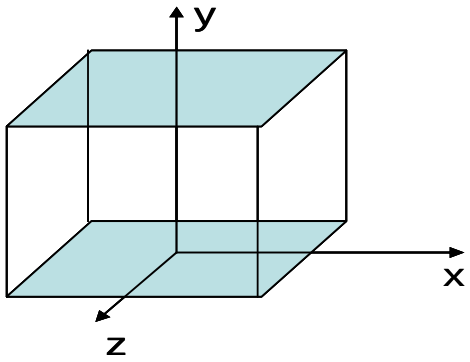

Figure 5-31. Sketch of water cavity in CLARA experiment.

According to the experimental results from CLARA test given in Figure 5-32 and Figure 5-33, no temperature gradient is visible in the bulk (outside lower interface) as soon as gas is injected in the liquid. A temperature gradient in the bulk (outside interface) exists only when no gas is injected and when the heat transfer in the liquid is controlled by natural convection. An indication of gas-liquid convection is a flat temperature gradient in the bulk. Since an important temperature gradient is always observed during ARTEMIS 10, it is plausible to conclude that there is no gas in the melt cavity and only natural convection governs the heat transfer from the bulk the wall.

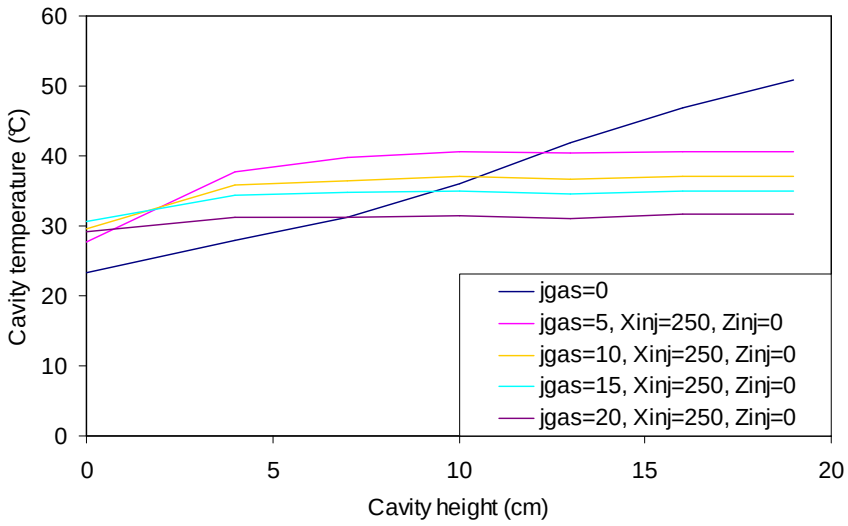

Figure 5-32. Bulk temperature profile with varying gas velocity.

jgas: Gas injection velocity (cm/s);

Xinj: Position of gas injection from the side wall (cm);

Zinj: Position of gas injection from the front wall (cm).

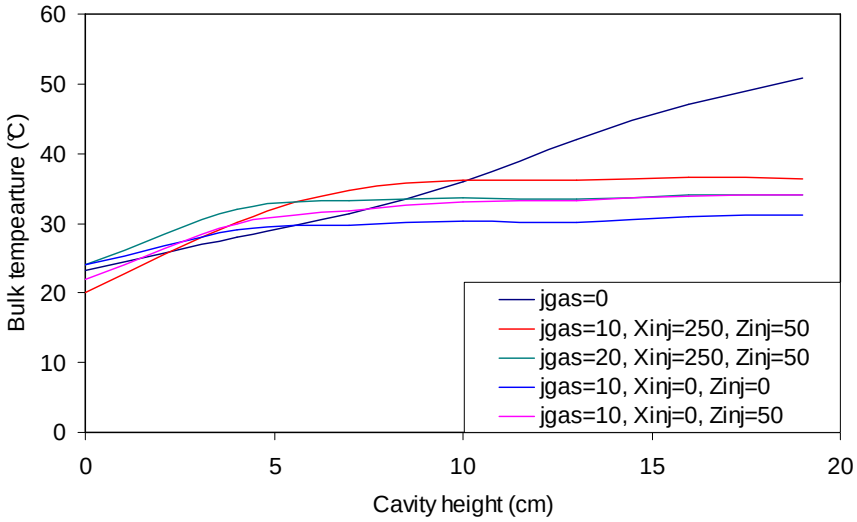

Figure 5-33. Bulk temperature profile with gas injected from different positions.

5.3.12 Analysis of cake formation

One important difference between melt-concrete interaction (ARTEMIS 10) and concrete-concrete interaction (ARTEMIS 11) is the formation of a cake at the bottom of the melt cavity. This cake forms at the bottom of the cavity under the liquid melt and beyond the interface with the solid concrete Figure 5-34.

Study on the formation mechanism, the structure of the cake as well as the heat and mass transfer inside the cake has been performed in the PhD thesis of [Guillamé, 2008] for ARTEMIS 1D. In the present analysis, only main conclusions will be recalled and analogy will be performed for interpretation of ARTEMIS 2D.

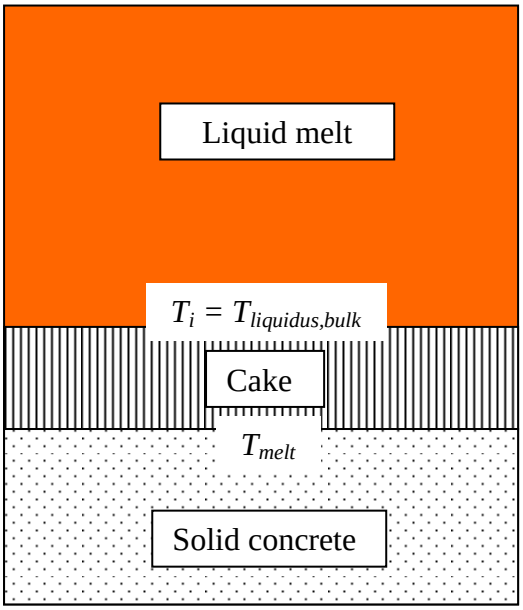

Figure 5-34. Schematic of cake formation at the cavity bottom.

Cake formation mechanism

Since the melting temperature of concrete is lower than the liquidus temperature of the melt, solidification can occur in the melt near to the interface. A porous medium, called a cake, enriched in refractory species ($BaCl_2$) is formed in between the solid and the liquid part due to formation of a mushy zone in front of the liquid-solid interface. This mushy zone contains both liquid and solid phases which are always in local thermodynamic equilibrium. Therefore, the cake is not a solid crust. The thickness of this mushy zone increases versus time until it reaches a quasi stable value which is also the final thickness of the cake.

Cake structure

The post-mortem test has shown that the cake has similar structure as observed during ARTEMIS 1D tests. [Guillaumé, 2008] concluded that it is not a solid crust of melt refractory particles. In fact, it is a porous medium formed of not only refractory particles with pores filled by liquid whose local composition is the composition corresponding to thermodynamic equilibrium with the solid. At the end of ARTEMIS 10, the final cake thickness is 83 mm and its mass is approximately 14 kg (Figure 5-35).

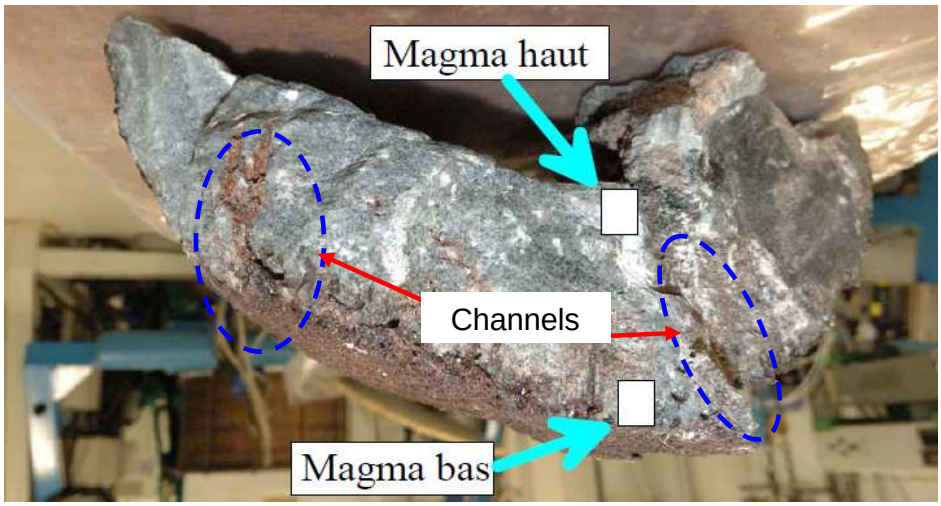

Figure 5-35. Cake sample at test ending of ARTEMIS 10.

The upper and bottom surfaces of the cake has quasi-hemispherical shape. The bottom surface of the cake is porous but the upper surface is smoother. There exist several channels in the cake (Figure 5-35). These channels could be considered as gas flow paths. They may have plugged during the test. A sketch of the cake is shown in Figure 5-36.

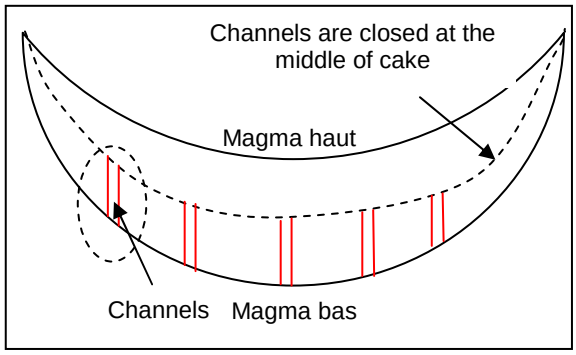

Figure 5-36. Cake configuration.

Samples of 5 to 10 cm^3 were taken at the upper and bottom surfaces of the cake for measurement of $BaCl_2$ concentration. $BaCl_2$ composition is not uniform in the cake but the cake is enriched in this refractory specie. The bottom is more enriched in $BaCl_2$ than the upper surface of the cake. Samples named as "magma haut" taken at top surface) and "magma bas" taken at bottom surface have respectively 91% and 96 % mass $BaCl_2$. It is noted that the mass percentage of $BaCl_2$ in the upper surface of the cake is higher than the mass percentage of $BaCl_2$ in the bulk at the bottom of the melt ($w_{bulk-cake}^{BaCl2}$ = 80% ~ 90%). In addition, the grains size at the upper surface of the cake ranges from 150 µm to 300 µm while, at the bottom surface, it is from 200 µm to 400 µm (Figure 5-37).

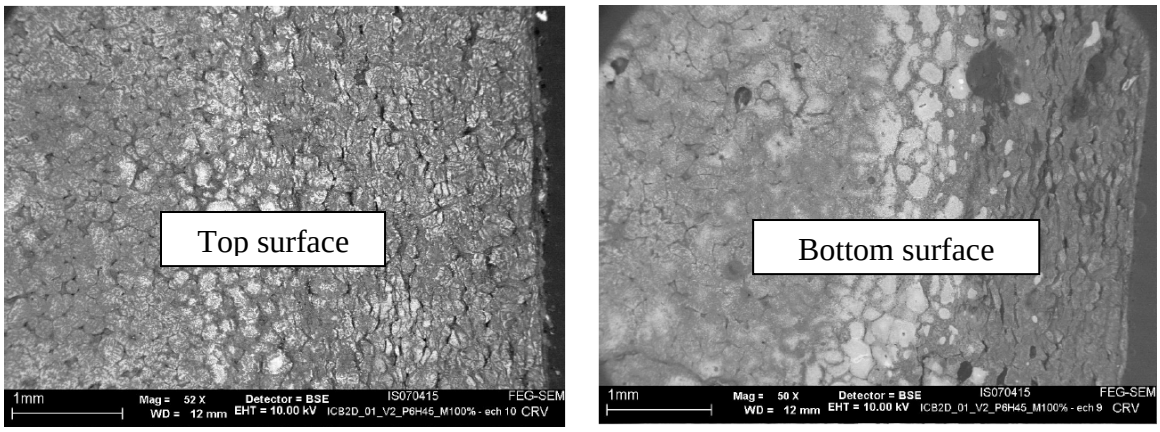

Figure 5-37. MEB measurement of cake samples.

Evolution of cake thickness

The mobile probe 1D was moving to detect the interface between the liquid melt and the cake (in case the cake is solid). The aim was to measure the variation of the cake thickness versus time as well as the temperature variation on this interface. The stop position of the probe could not be used for positioning the interface because the probe penetrated into the porous medium of the cake. Therefore, the thickness of the cake will more reliably be deduced from measured temperature profiles with followings assumptions:

- The temperature at the upper surface of the cake (between the cake and the liquid melt) is assumed as the liquidus temperature corresponding to the $BaCl_2$ composition at the bottom of the melt cavity, $T_{bulk\text{-}caket} = T_{liquidus}(w_{bulk-cake}^{BaCl2})$;

- The temperature at the lower surface of the cake(between the cake and the solid concrete)is assumed as the melting temperature of the solid concrete, $T_{concrete\text{-}cake} = T_{melt} = 522°C$;
- The temperature gradient in the cake is assumed to be linear;
- Accumulation of the molten concrete under the cake-concrete interface is neglected.

In the following, cake thickness is deduced from the temperature distribution for three time instants which are t = 0:13:50, t = 0:30:50 and t = 1:16:15. The thickness of the cake is considered as the region in between T_{melt} and $T_{liquidus}(w^{BaCl2}_{bulk-cake})$ (Figure 5-38, Figure 5-39, Figure 5-40).

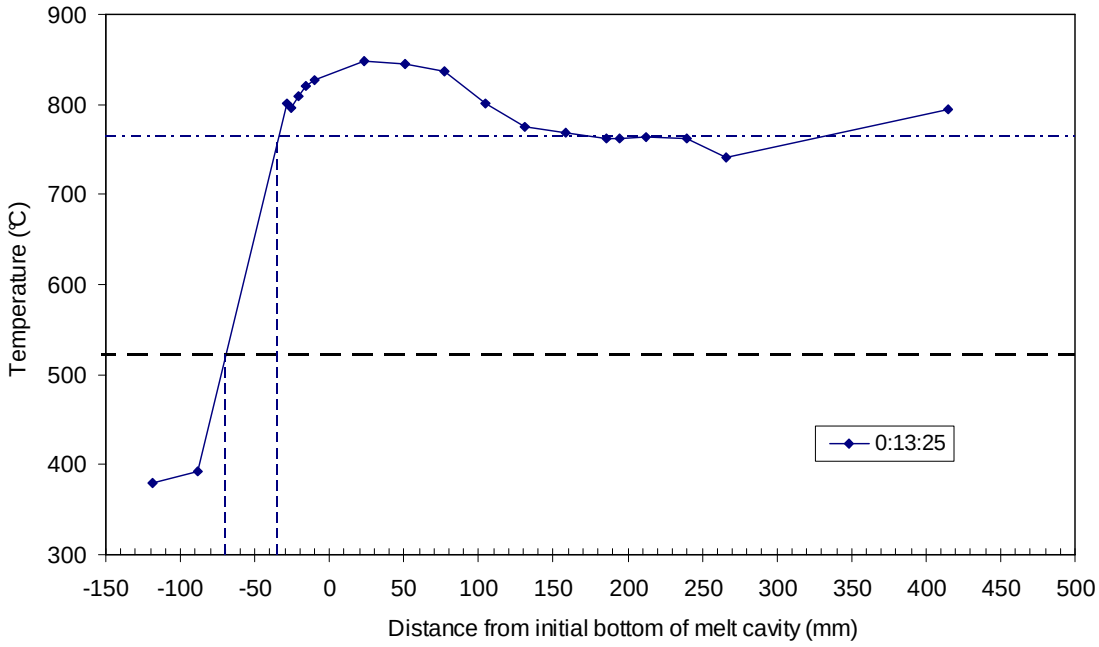

Figure 5-38. Location of cake boundaries with vertical temperature profile at t = 0:13:25.

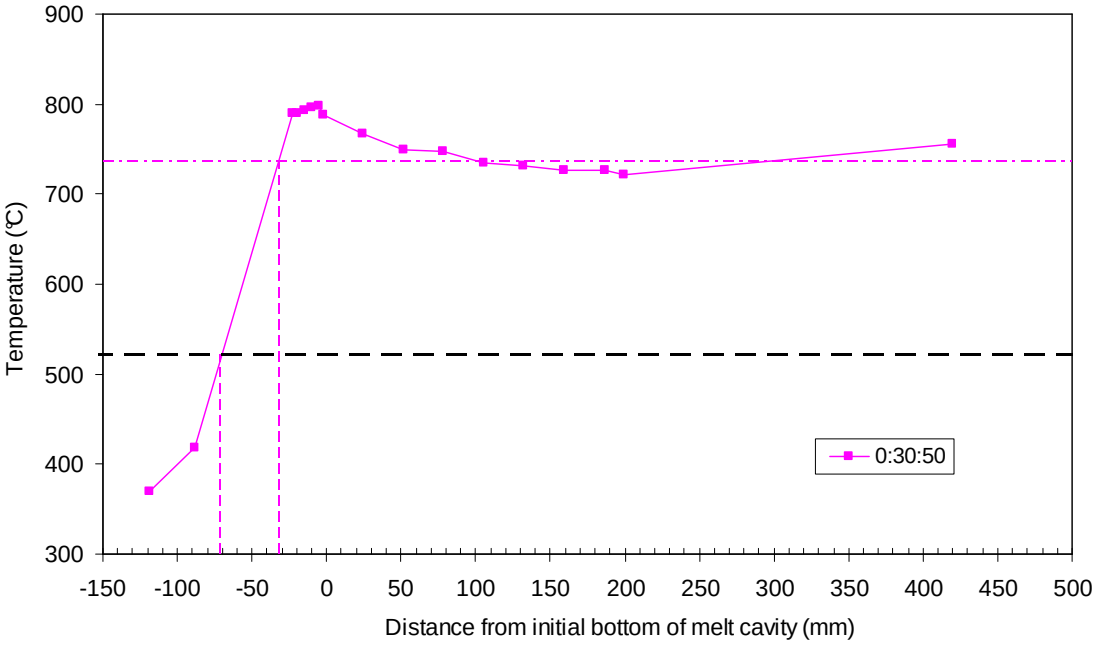

Figure 5-39. Location of cake boundaries with vertical temperature profile at t = 0:30:50.

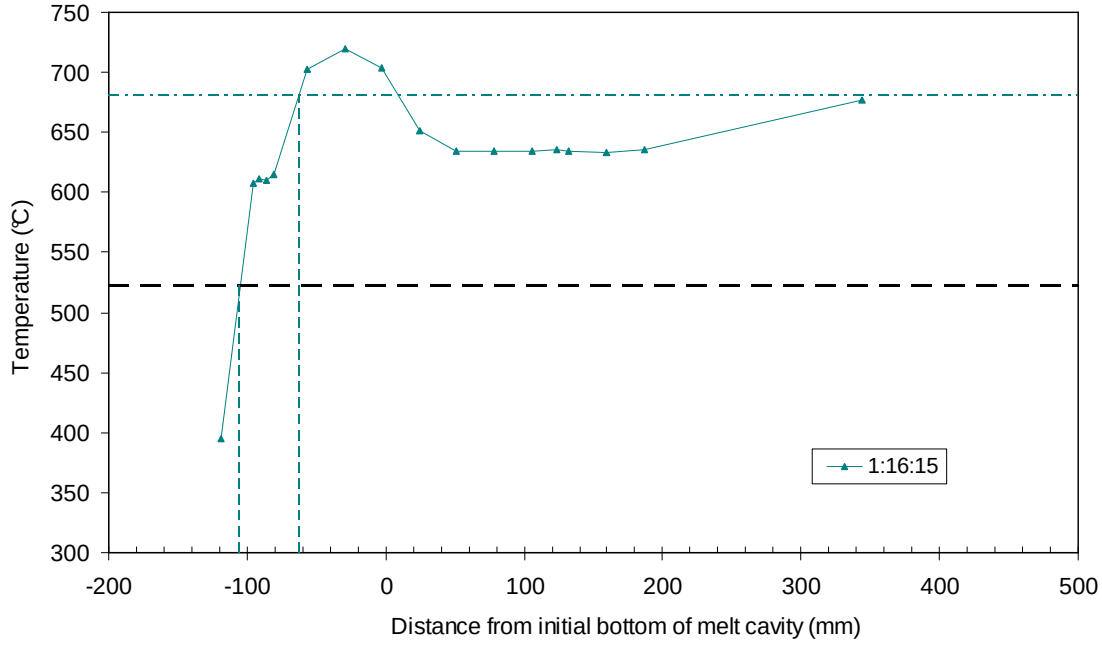

Figure 5-40. Location of cake boundaries with vertical temperature profile at t = 1:16:15.

Table 5-2. Estimation of cake thickness evolution.

Time	$w_{bulk-cake}^{BaCl2}$	$T_{liquidus}(w_{bulk-cake}^{BaCl2})$	T_{melt}	z_{cake}
h:min:s	% mass	°C	°C	mm
00:13:25	89	763	522	36
00:30:50	86	737	522	39
01:16:15	83	681	522	43

Estimation of the cake's thickness at three given instants is shown in Table 5-2. The estimated thickness of the cake is about 40 mm which is twice smaller than the one measured at the end of ARTEMIS 10 (83 mm).

Heat transfer in the cake

According to [Guillaumé, 2008], in ARTEMIS 1D, the heat transfer through the cake is not only by conduction. It was shown that an important contribution to the heat flux is due to an additional heat transfer by convection of solute in the liquid phase in the cake (the pores are filled with liquid). The liquid situated inside the pores (in the cake) is locally at thermodynamic equilibrium with the solid. Since the temperature in the cake increases from the interface between the cake and the solid concrete to the interface between the cake and the liquid melt (because $T_{melt} < T_{liquidus}$), this thermodynamic constraint implies that the LiCl concentration in the liquid increases. When concentration of LiCl in the interstitial in liquid increases, the density of the liquid decreases. The liquid at the bottom of the cake is less dense than the liquid at the top of the cake. Therefore, the liquid tends to move upwards due to the buoyancy force linked to the LiCl concentration gradient in the cake (solute convection).

There exists a criterion to have liquid movement in a porous medium, which is written in terms of Rayleigh number. According to the works of [Bories et Prat, 1995] and [Guillaumé, 2008], the Rayleigh number in a porous medium is calculated by:

$$Ra_{cake} = \frac{\rho_{cake}\, g\, \beta_C\, (w^{LiCl}_{bulk-cake} - w^{LiCl}_{concrete-cake})\, k_{cake}\, z_{cake}}{\mu\, D_{LiCl}} \tag{5-37}$$

wherein ρ_{cake} is the average density of the liquid in the cake, g is the gravity acceleration, β_C is the solute expansion coefficient, k_{cake} is the permeability of the cake, z_{cake} is the thickness of the cake, μ is the dynamic viscosity of the liquid, D_{LiCl} is the diffusion coefficient of LiCl in the mixture of LiCl and BaCl2, $w^{LiCl}_{bulk-cake}$ and $w^{LiCl}_{concrete-cake}$ are the LiCl concentration in the liquid at the interface between the bulk and the cake and between the cake and the solid concrete, respectively.

In order to have liquid movement in a porous medium, the buoyancy force must overcome the friction force and the solute diffusion. This means the Rayleigh number should be greater than a critical Rayleigh number, which was calculated by [Lapwood, 1948] as:

$$Ra_{critical} = 27.1 \tag{5-38}$$

In ARTEMIS 10, as the calculated Rayleigh number from Equation (5-37) is about 790 which is much greater than the critical Rayleigh number (the parameters for calculation are taken from [Guillaumé, 2008] because the morphology of the cake obtained in ARTEMIS10 is similar to the one obtained in ARTEMIS 1D), it is concluded that the liquid in the cake is in movement, leading to a solute convection in the cake. This convection induces convective heat transfer in the cake.

5.3.13 Conclusion from the analysis

Following conclusions could be deduced from the above analysis of the experimental.

- The melt cavity is divided into two zones. The temperature and composition are quasi-uniform in each zone.
- A thermal boundary layer of 3 ~ 5 mm thickness with linear increasing temperature exists along the lateral wall of the melt cavity.
- The liquid-solid interface temperature is close to the liquidus temperature corresponding to the $BaCl_2$ concentration in the bulk (this concentration varies significantly with the height, leading to a variable interface temperature).
- In both zones of melt cavity, there exists a flow recirculation, governed by natural convection. This means that concrete cracking or interface plugging mechanisms led to a by-pass of the melt by the gas, as observed at $t > 17$ minutes in ARTEMIS 11).
- The fluid flows in the two zones of the cavity in two opposite directions. In the top zone, the flow goes upwards in the cavity centre and downwards in the boundary layer. In the bottom zone, the flow goes downwards in the cavity centre and upwards in the boundary layer
- Maximum heat flux at the top zone is due to the recirculation in the top zone, in similar way as observed in ARTEMIS 11. For the bottom zone, natural circulation induces maximum heat flux at the bottom of the cavity.
- It has to be mentioned that there is no cake formation along the vertical wall of the melt cavity. In fact, the cake can form at the lateral wall of the melt cavity but due to precipitation, it may relocate at the cavity bottom. Another possibility is that the solid can be remelted right after it forms at the cavity lateral wall, leading to decrease of interface temperature. Therefore, cake is obtained only at the bottom of the cavity.
- The interface between the top and the bottom zones is moving downwards, leading to an evolution of the power distribution in each zone. The power dissipation in the top zone increases versus time while the power dissipation in the bottom zone decreases.
- There is a link between the power distribution between both zones and the ablation of the solid concrete. In the beginning, the power mainly dissipates in the bottom zone, leading to strong ablation to the bottom. After 1h, the top-bottom interface is lowered, leading to decrease of power dissipation in the bottom zone and increase of power dissipation in the top zone. Consequently, there is no more ablation to the bottom while ablation to the lateral wall in the top zone continues. Significant ablation of concrete is also due to melt cooling.
- In order to describe the global heat transfer in ARTEMIS 10, a 0D model will be developed in the next to corroborate the assumption of natural convection as the main heat transfer mechanism in the melt cavity. Various assumptions for the interface temperature should be made in order to justify whether it corresponds to the melting temperature of the concrete or the liquidus temperature of the $BaCl_2$ concentration in the bulk. Evolutions of the bulk temperature, the bulk composition and the ablated mass of the concrete can be calculated by the 0D model for comparison to ARTEMIS 10.
- For the purpose of local description of heat and mass transfer from the melt cavity to the liquid-solid interface, a more complex 1D model will be developed which is able to describe the evolution of the cavity shape in ARTEMIS 10.

5.4 0D modelling of thermal-hydraulics and concrete ablation for ARTEMIS 10

In Chapter 4, a 0D model has been developed for the description of melt temperature evolution during interaction of melt cavity and concrete wall at identical eutectic compositions of $BaCl_2$-LiCl mixture in ARTEMIS 11. In this chapter, the same methodology will be employed for modelling of thermal-

hydraulics and concrete ablation for ARTEMIS 10 in which melt and concrete have different compositions.

5.4.1 Main assumptions of 0D model

A system containing a liquid melt in a cavity located inside a solid concrete is considered. Gas is injected. One difference between ARTEMIS 10 and ARTEMIS 11 is the formation of a cake at the bottom of the melt cavity in ARTEMIS 10 which was not observed in ARTEMIS 11. Figure 5-41 provides a schematic of the considered system for the modelling of melt-concrete interaction in ARTEMIS 10.

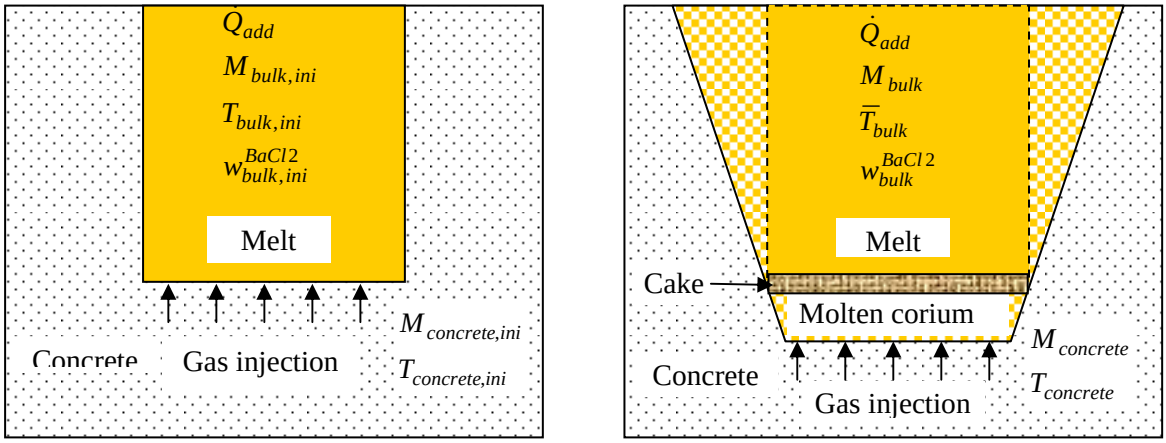

Figure 5-41. Schematic of melt cavity evolution during melt-concrete interaction in ARTEMIS 10.

The following hypotheses are assumed for the simplified model approach:

- The control volume is the volume of the melt cavity;
- Solid concrete is ablated across the melt cavity external surface;
- Variation of the melt cavity radius will be calculated with assumption of hemisphere or cylinder geometry of the cavity. The height of the melt is constant and is taken as the initial height (i.e. $H(t) = H_{ini}$ = 45 cm);
- A uniform bulk composition (represented by the mass percentage of $BaCl_2$, denoted by w_{bulk}^{BaCl2}) in the melt cavity is assumed at a given instant *t*;
- Since the temperature of the melt is not uniform, an average temperature difference (between the bulk and the liquid-solid interface) is defined as $\Delta\overline{T}_{bulk} = \overline{T}_{bulk} - T_i$ which is proportional to the maximum temperature difference between the bulk and the interface, i.e. $\Delta\overline{T}_{bulk} = k_T T_{bulk,\max}$ with $\Delta T_{bulk,\max} = T_{bulk,\max} - T_i$ in which k_T = 0.7 is independent on time and can be determined from experimental data of melt temperature measurement (as done in Chapter 4 for ARTEMIS 11).

An important aspect of the modelling concerns the interface temperature between the melt and the solid. Two extreme hypotheses have been emphasized:

- H1: the interface temperature is equal to the liquidus temperature corresponding to the instantaneous average composition in the bulk as assumed in Chapter 2 for LIVE L3A.

- H2: the interface temperature is equal to the melting temperature of concrete as done in Chapter 4 for ARTEMIS 11.

We will see that hypothesis H1 leads to a melt temperature decrease that will be too slow during the first 30 minutes. This hypothesis is not compatible with the fast decrease in temperature that is observed at the beginning of the test (as seen in Figure 5-3, the melt temperature drops by ~ 100 °C within a very short time (only a few minutes)). On the opposite, hypothesis H2 leads to a fast decrease in melt temperature (as experimentally observed in the beginning), but the temperature after that will be too low for the rest of the test.

Furthermore, the analysis of the interface temperature measurements has shown that the interface temperature is close to the liquidus temperature. The difference is about 20 °C to 40 °C. Thus, there are two problems for the modelling:

- It is required to propose a model for the interface temperature that is compatible with interface temperature measurements and that is able to reproduce the evolution of the average melt temperature.
- It is needed to take into account the possibility of solidification in the bulk, since the interface temperature may be less than the liquidus temperature.

In the following the model basis for $T_i = T_{liquidus}$ is first described. A new approach for the evaluation of the interface temperature ($T_i < T_{liquidus}$) is then presented. The necessary modifications of the equation taking into account solidification are discussed.

5.4.2 Model basic equations for $T_i = T_{liquidus}$

If the average melt temperature is higher than the liquidus temperature corresponding to actual the $BaCl_2$ concentration in the melt which is the case in LIVE L3A (Chapter 2) and ARTEMIS 11 (Chapter 4), then the simple model for description of heat and mass transfer for ARTEMIS 10 will be developed based on the mass and energy conservations in the melt cavity with the same methodology used for the two previous cases.

Mass conservation

Changes in the mass of the melt are caused by the molten concrete entering into the cavity and the gas entering and going out. The mass conservation equation for the cavity is written as follows:

$$\frac{dM_{bulk}}{dt} = \dot{m}_{MC} + \dot{m}_{gas,in} - \dot{m}_{gas,out} \tag{5-39}$$

in which, M_{bulk} is the mass of the liquid melt in the cavity, $\dot{m}_{MC}$ is the mass flow rate of the molten concrete entering the cavity, $\dot{m}_{gas,in}$ is the mass flow rate of the gas entering the cavity, and $\dot{m}_{gas,out}$ is the mass flow rate of the gas getting out from the cavity.

As mentioned before, the mass flow rate of gas is assumed to be unchanged across its path through the melt cavity. Therefore, Equation (5-40) can be rewritten as:

$$\frac{dM_{bulk}}{dt} = \dot{m}_{MC} \tag{5-40}$$

During the ablation of solid concrete, the molten concrete gets into the melt, leading to variation of the $BaCl_2$ composition in the liquid cavity versus time. The mass balance of $BaCl_2$ in the melt is written as:

$$M_{bulk} w_{bulk}^{BaCl2} = M_{bulk,ini}\, w_{bulk,ini}^{BaCl2} + M_{MC}\, w_{MC}^{BaCl2} \tag{5-41}$$

with:

$$M_{bulk} = M_{bulk,ini} + M_{MC} \tag{5-42}$$

where in M_{bulk} is the mass of the melt at time *t*, $M_{bulk,ini}$ is the initial mass of the liquid melt, M_{MC} is the mass of the molten concrete at instant *t*, w_{bulk}^{BaCl2} is the mass percentage of $BaCl_2$ in the melt liquid cavity at instant t, $w_{bulk,ini}^{BaCl2}$ is the mass percentage of $BaCl_2$ in the initial melt cavity ($w_{bulk,ini}^{BaCl2}$ = 100%), w_{MC}^{BaCl2} is the mass of $BaCl_2$ in the molten concrete (w_{MC}^{BaCl2} = 62.04%).

Then, the mass percentage of $BaCl_2$ in the melt at time *t* is estimated by:

$$w_{bulk}^{BaCl2} = \frac{M_{bulk} w_{bulk,ini}^{BaCl2} + M_{MC} w_{MC}^{BaCl2}}{M_{bulk}} \tag{5-43}$$

and the mass percentage of solute LiCl in the melt cavity is:

$$w_{bulk}^{LiCl} = \frac{M_{MC}}{M_{bulk}} w_{MC}^{LiCl} \tag{5-44}$$

Hence

$$\frac{dw_{bulk}^{BaCl2}}{dt} = \frac{\dot{m}_{MC}(w_{MC}^{BaCl2} - w_{bulk}^{BaCl2})}{M_{bulk}} \text{ (since } \frac{\dot{m}_{MC}}{M_{bulk}^2} \text{ is very small)} \tag{5-45}$$

and

$$\frac{dw_{bulk}^{LiCl}}{dt} = \frac{\dot{m}_{MC}}{M_{bulk}} w_{MC}^{LiCl} \tag{5-46}$$

Energy conservation

As presented in the 0D model developed under Chapter 4 for ARTEMIS 11, the energy variation in the melt includes:

- The power dissipation $\dot{Q}_{add}$;

- The power lost to structure $\dot{Q}_{lost}$ (not including the concrete part);
- The power related to gas entrance $\dot{Q}_{gas}$:

$$\dot{Q}gas = \dot{m}gas\left[H\,gas(T_{gas,in}) - H\,gas(T_{gas,out}) \right] \tag{5-47}$$

in which $H_{gas}(T_{gas,in})$ and $H_{gas}(T_{gas,out})$ are respectively the enthalpy of gas at entrance temperature $T_{gas,in} = T_i = T_{liquidus}(w_{bulk}^{BaCl2})$ and outgoing temperature $T_{gas,out} = \overline{T}_{bulk}$.

$$H\,gas(T_{gas,in}) = H_{gas}^{T_{ref}} + C_{p,gas}(T_{gas,in} - T_{ref}) \tag{5-48}$$

$$H\,gas(T_{gas,out}) = H_{gas}^{T_{ref}} + C_{p,gas}(T_{gas,out} - T_{ref}) \tag{5-49}$$

Hence:

$$\dot{Q}gas = \dot{m}gas\, C_{p,gas}\left[T_{liquidus}(w_{bulk}^{BaCl2}) - \overline{T}_{bulk} \right] \tag{5-50}$$

$$\dot{Q}gas = -\dot{m}gas\, C_{p,gas}\, \Delta\overline{T}_{bulk} \tag{5-51}$$

- The power related to molten concrete entrance $\dot{Q}_{MC}$:

$$\dot{Q}_{MC} = \dot{m}_{MC}\, H_{MC}(T_{melt}) \tag{5-52}$$

wherein $H_{MC}(T_{melt})$ is the enthalpy of the molten concrete, entering the melt cavity at melting temperature of concrete (T_{melt}):

$$\begin{aligned} H_{MC}(T_{melt}) = {} & w_{MC}^{LiCl} H_{ref,liquid}^{LiCl}(T_{ref}) + (1 - w_{MC}^{LiCl}) H_{ref,liquid}^{BaCl2}(T_{ref}) \\ & + C_{p,liquid}^{MC}(T_{melt} - T_{ref}) \end{aligned} \tag{5-53}$$

wherein w_{MC}^{LiCl} is the mass percentage of LiCl in the molten concrete, $C_{p,liquid}^{MC}$ is the specific heat of molten concrete, $H_{ref,liquid}^{LiCl}(T_{ref})$ and $H_{ref,liquid}^{BaCl2}(T_{ref})$ are respectively the reference enthalpies of liquid LiCl and $BaCl_2$ at reference temperature T_{ref}. If T_{ref} is taken as melting temperature of solid concrete, i.e. $T_{ref} = T_{melt}$, then enthalpy of molten concrete is:

$$H_{MC}(T_{melt}) = w_{MC}^{LiCl} H_{ref,liquid}^{LiCl}(T_{melt}) + (1 - w_{MC}^{LiCl}) H_{ref,liquid}^{BaCl2}(T_{melt}) \tag{5-54}$$

in which $H_{ref,liquid}^{LiCl}(T_{melt})$ and $H_{ref,liquid}^{BaCl2}(T_{melt})$ are the enthalpies of liquid LiCl and BaCl2 at T_{melt}

- The power transferred from the cavity to the interface between the cavity and the solid concrete due to convection in the cavity $\dot{Q}_{convection}$.

$$\dot{Q}_{convection} = \overline{\varphi}\ \mathrm{S}_{\mathrm{lateral}} = \overline{h}_{bulk}\ \mathrm{S}_{\mathrm{lateral}}\ \Delta T_{bulk,\max} \tag{5-55}$$

or:

$$\dot{Q}_{convection} = \overline{\varphi}\ \mathrm{S}_{\mathrm{lateral}} = \overline{h}_{bulk}\ \mathrm{S}_{\mathrm{lateral}}\ \frac{\Delta \overline{T}_{bulk}}{k_T} \tag{5-56}$$

wherein $\overline{\varphi}$ is the average heat flux transferred from the melt to the liquid-solid interface, $S_{lateral}$ is the lateral surface area of the melt cavity and $\overline{h}_{bulk}$ is the average heat transfer coefficient.

The power balance equation for the melt cavity is written as:

$$\frac{d}{dt}(M_{bulk} H_{bulk}) = \dot{Q}_{add} + \dot{Q}gas + \dot{Q}_{MC} - \dot{Q}_{lost} - \dot{Q}_{convection} \tag{5-57}$$

in which H_{bulk} is the average mass enthalpy of the melt at average temperature $\overline{T}_{bulk}$, calculated by:

$$\begin{aligned} H_{bulk}(\overline{T}_{bulk}) = {} & w_{bulk}^{LiCl} H_{ref,liquid}^{LiCl}(T_{melt}) + (1 - w_{bulk}^{LiCl}) H_{ref,liquid}^{BaCl2}(T_{melt}) \\ & + C_{p,liquid}^{bulk}(\overline{T}_{bulk} - T_{melt}) \end{aligned} \tag{5-58}$$

wherein $C_{p,liquid}^{bulk}$ is the average specific heat of the liquid melt with solute concentration w_{bulk}^{LiCl}.

Taking into account the entrainment of ablated concrete in the melt cavity, the energy variation of the melt in the left hand side of Equation (5-57) can be rewritten as:

$$\frac{d}{dt}(M_{bulk} H_{bulk}) = M_{bulk}\ \frac{dH_{bulk}}{dt} + H_{bulk}\ \dot{m}_{MC} \tag{5-59}$$

Then Equation (5-59) becomes:

$$\begin{aligned} \frac{d}{dt}(M_{bulk} H_{bulk}) = {} & M_{bulk}\ w_{bulk}^{LiCl}(H_{ref,liquid}^{LiCl} - H_{ref,liquid}^{BaCl2}) \\ & + M_{bulk}\ C_{p,liquid}^{bulk}\ \frac{d\overline{T}_{bulk}}{dt} + \dot{m}_{MC}\ H_{bulk} \end{aligned} \tag{5-60}$$

Combining Equations (5-51), (5-53), (5-56), (5-57), (5-58) and (5-60) and neglecting the heat loss to the structure $\dot{Q}_{lost}$ gives:

$$\begin{aligned} & M_{bulk}\ C_{p,liquid}^{bulk}\ \frac{d\overline{T}_{bulk}}{dt} = \dot{Q}_{add} - \dot{m}_{gas} C_{p,gas} \Delta \overline{T}_{bulk} - \overline{h}_{bulk} S_{lateral}\ \frac{\Delta \overline{T}_{bulk}}{k_T} \\ & - \dot{m}_{MC}\ C_{p,liquid}^{bulk}(\overline{T}_{bulk} - T_{melt}) - w_{MC}^{LiCl}\ \dot{m}_{MC}\ (H_{ref,liquid}^{LiCl} - H_{ref,liquid}^{BaCl2}) \end{aligned} \tag{5-61}$$

The convection heat transfer from the melt to the interface serves for ablating the solid concrete as well as for heating up the residual concrete by conduction. This means:

$$\dot{Q}_{convection} = \dot{Q}_{conduction} + \dot{m}_{MC}\left[L_{melting}^{concrete} + C_{p,solid}^{concrete}(T_{melt} - T_{concrete}) \right] \tag{5-62}$$

in which $\dot{Q}_{conduction}$ is the power serving for heating up the solid concrete by conduction, $L_{melting}^{concrete}$ is the latent heat of melting of concrete, $C_{p,solid}^{concrete}$ is the specific heat of solid concrete and $T_{concrete}$ is the average temperature in the concrete.

With the definition $\Delta T_{concrete} = T_{melt} - T_{concrete}$ then the ablated mass flow rate of concrete is estimated by:

$$\dot{m}_{MC} = \frac{\dot{Q}_{convection} - \dot{Q}_{conduction}}{L_{melting}^{concrete} + C_{p,solid}^{concrete} \Delta T_{concrete}} \tag{5-63}$$

or:

$$\dot{m}_{MC} = \frac{\bar{h}_{bulk} S_{lateral} \frac{\Delta \bar{T}_{bulk}}{k_T} - \dot{Q}_{conduction}}{L_{melting}^{concrete} + C_{p,solid}^{concrete} \Delta T_{concrete}} \tag{5-64}$$

Equation (5-61) will be solved using the ablated mass flow rate of concrete given in Equation (5-64) and the average heat transfer coefficient can be estimated using the existing Nusselt correlations as done in Chapter 2 for LIVE L3A and Chapter 4 for ARTEMIS 11.

From the test analysis, natural convection is the main heat transfer mechanism in the melt cavity, only the Nusselt correlations developed for natural convection will be employed for ARTEMIS 10. The average heat transfer coefficient in the melt cavity will be written as:

$$\bar{h}_{bulk} = \frac{a \lambda_{bulk}}{H} \left(\frac{g \beta_T H^3}{\upsilon \alpha} \right)^b \Delta \bar{T}_{bulk}^{b} \tag{5-65}$$

in which *a* and *b* are the coefficients of the correlation of the Nusselt number ($Nu = a\ Ra^b$) which will be taken from different natural convection correlations, *H* is the height of the melt cavity, g is the gravitational acceleration; α, β_T, λ_{bulk} and υ are the thermal diffusivity, thermal expansion coefficient, thermal conductivity and kinematic viscosity of the melt, respectively.

In order to solve Equation (5-61) for calculation of melt temperature evolution, additional assumptions concerning the melt cavity shape and related interface area are required.

The ablation mass flow rate or the ablation velocity of the concrete can be deduced by using Equation (5-64), allowing an estimation of the variation of volume of the melt cavity. Then, calculation of the radius of the cavity will be done by assuming either a hemisphere or cylinder geometry of the melt cavity (as done in Chapter 4 for ARTEMIS 11).

Case 1: Hemisphere geometry

If a hemispherical geometry is assumed, then the interface area of the melt cavity is:

$$S_{lateral} = 2\,\pi\,R\,H \tag{5-66}$$

and the cavity volume is calculated by:

$$V_{cavity} = \frac{1}{3}\,\pi\,H^{2}\,(3\,R - H) \tag{5-67}$$

Therefore, the radius of the hemispherical melt cavity is:

$$R = \frac{1}{3}\,\left(\frac{3\,V_{cavity}}{\pi\,H^{2}} + H\right) \tag{5-68}$$

Case 2: Cylinder geometry

If cylinder geometry is assumed, then the interface area of the melt cavity is:

$$S_{lateral} = 2\,\pi\,R\,H \tag{5-69}$$

and its volume is:

$$V_{cavity} = \pi\,R^{2}\,H \tag{5-70}$$

Then, radius of the cylindrical melt cavity is:

$$R = \sqrt{\frac{V_{cavity}}{\pi\,H}} \tag{5-71}$$

5.4.3 Model basic equations for $T_i < T_{liquidus}$

The previous model is developed with the same methodology as done for LIVE L3A wherein the interface temperature is taken as the liquidus temperature corresponding to the actual melt composition and the melt temperature always stays above the liquidus temperature. However, in ARTEMIS 10, the initial melt temperature is equal to the liquidus temperature of the melt. In this situation, if the interface temperature is taken as liquidus temperature, then there will be no heat transfer from the melt to the liquid-solid interface, leading to significant increase of melt temperature in the beginning due to the power dissipation. This was not seen in ARTEMIS 10. Indeed, a sharp decrease of melt temperature is observed in the first minutes of ARTEMIS 10 (The temperature decreases of approximately 100 °C in only 5 minutes). Therefore, we conclude that the interface temperature might not stay at the liquidus temperature of the melt. In order to have such significant decrease of melt temperature as observed in ARTEMIS 10 in the beginning, a high heat flux is expected to transfer from the melt to the interface.

It is of importance that, if the interface temperature is smaller than the liquidus temperature of the melt (ex: interface temperature is the melting temperature of the concrete), solidification of the melt can occur. If a succession of steady state situations (constant heat flux) are considered and supposing that

the ablation has no impact on the solid formation, the interface temperature could stay close to the liquidus temperature, as in LIVE 3A (Chapter 2).

However, in comparison to LIVE 3A, there are, in ARTEMIS 10, two main differences:

- In ARTEMIS 10, the heat flux to the wall (concrete) at the beginning of the test is an order of magnitude greater and decreases very fast in comparison to the situation in LIVE 3A. Thus, the assumption of steady state situation is certainly not valid, and the local mass transfer in the vicinity has to be taken into account
- The ablation rate leads to a moving interface. Thus, a stable solid crust can probably not form on the vertical interface.

Therefore, we were led to consider that solidification may occur and a mushy zone probably forms on the liquid-solid interface (as in LIVE L3A), but this mushy zone is not stable in the sense that it can disappear and reform again.

As a first approach, we might simply consider that convection does not take place in the mushy zone when the volumetric solid fraction is higher than a given threshold (α_{volsol}) and that convection is efficient when the volumetric solid fraction is less than this threshold. This leads then to following interface temperature:

$$T_i = T_{equ}(\alpha_{volsol}, w_{bulk}^{LiCl}) \tag{5-72}$$

This threshold temperature will, of course depend on the volumetric solid fraction and on the melt composition. Some problems can be anticipated with this formulation:

- At the beginning of the test, when the melt contains mainly refractory specie $BaCl_2$, this interface temperature would be very close to the liquidus temperature. Thus, it will not be possible to describe the steep melt temperature decrease at the beginning of the test.
- At the end of the test, the content in LiCl is sufficient so that the temperature corresponding to a reasonable value for α_{volsol} (for instance 0.2 to 0.3) is limited by the eutectic temperature (i.e. the melting temperature of concrete). This interface temperature would then be too low to explain the melt temperature that is measured at the end of the test.

A second approach has been emphasized. This approach is based on the assumption that the melt stays liquid in contact with the concrete. This means that the composition of the liquid on the interface is sufficiently enriched in solute (LiCl). The composition of the liquid on the interface depends on the mass transfer between the interface and the bulk. It is further supposed that this mass transfer is limited by diffusion in the mass transfer sub-layer. We thus write:

$$\left(\omega_{MC}^{LiCl} - \omega_i^{LiCl}\right) V_{abl} = k_M (\omega_i^{LiCl} - \omega_{bulk}^{LiCl}) \tag{5-73}$$

wherein k_M is the mass transfer coefficient through the boundary layer. As the ablation velocity never goes to zero (linked to power dissipation in the melt), the composition on the interface tends towards a value that depends on the ratio $\frac{k_M}{V_{abl}}$. If k_M is small in comparison to the ablation velocity, this model leads to an interface temperature that will stay close to the melting temperature of concrete. By contrast, if k_M is higher than the ablation velocity, then the interface temperature will approach the bulk temperature.

The discussion above leads to the conclusion that a mushy zone plausibly exists on the interface and that the thermal resistance associated to the presence of the solid fraction is important, but that a simple assumption of constant volumetric solid fraction on the interface does not lead to a temperature evolution that is coherent with the experimental observation. In the present approach, we will examine a possibility to determine the temperature at the tip of the dendrites within the mushy zone. Outside the mushy zone, the material is liquid. For ensuring no solid precipitation, following criterion must be fulfilled: the temperature gradient in the liquid nearby the interface must be greater than the liquidus temperature gradient associated to the composition gradient.

$$G_T > G_{Tliquidus} \tag{5-74}$$

in which G_T is the temperature gradient, which can be calculated from the average convection heat flux transferred from the melt to the thermal boundary layer existing in front of the liquid-solid interface and $G_{Tliquidus}$ is the liquidus temperature gradient, dependent on the concentration gradient $G_{LiCl} = \frac{\Delta w_{LiCl}}{\delta_{MT}}$ in the solute mass transfer boundary layer, i.e

$$G_T = \frac{\overline{\varphi}}{\lambda_{bulk}} \tag{5-75}$$

$$G_{Tliquius} = m_L G_{LiCl} = m_L \frac{\Delta w_{LiCl}}{\delta_{MT}} = m_L \frac{w_i^{LiCl} - w_{bulk}^{LiCl}}{\delta_{MT}} \tag{5-76}$$

in which w_i^{LiCl} and w_{bulk}^{LiCl} are respectively the concentration of solute (LiCl) at the interface between two sub-layers and in the melt, m_L is the slope of the liquidus curve in the phase diagram.

The thickness of the mass transfer boundary layer is calculated by:

$$\delta_{MT} = \frac{k_M}{D_{LiCl}} \tag{5-77}$$

wherein k_M is the mass transfer coefficient and D_{LiCl} is the mass diffusion coefficient of LiCl.

Combining Equations (5-75) to Equation (5-77), a criterion is obtained for the definition of the liquid-solid interface, which is:

$$\Delta w_{LiCl} = w_i^{LiCl} - w_{bulk}^{LiCl} < \frac{\overline{\varphi}\, D_{LiCl}}{m_L\, k_M\, \lambda_{bulk}} \tag{5-78}$$

Therefore:

$$T_i = T_{liquidus}(w_{bulk}^{LiCl}) - \frac{\overline{\varphi}\, D_{LiCl}}{k_M\, \lambda_{bulk}} \tag{5-79}$$

The mass transfer coefficient k_M is estimated using the mass transfer correlation written in terms of the Sherhood number, introduced in [Seiler et Froment, 2000]:

$$Sh = Nu\, Gr^{1/12}\, Sc^{1/3}\, \mathrm{Pr}^{-1/3} \tag{5-80}$$

wherein:

$$Sh = \frac{k_M \, H}{D_{LiCl}} \tag{5-81}$$

$$Sc = \frac{\upsilon}{D_{LiCl}} \tag{5-82}$$

$$Nu = a \, Ra_{ex}^{b} = a \, (Gr \, \mathrm{Pr})^{b} \tag{5-83}$$

$$\mathrm{Pr} = \frac{\upsilon}{\alpha} \tag{5-84}$$

$$Gr = \frac{g \, \beta_T \, (T_{bulk} - T_i) \, H^3}{\upsilon^2} \tag{5-85}$$

It is noted that the density variation is due to both the temperature difference and the concentration difference between the bulk and the interface. However, since the ablation velocity is approximately ten times lower than the velocity of the liquid entrainment from the bulk to the boundary layer, the density variation due to concentration difference is negligible in comparison to the effect of temperature difference.

Taking b = 0.25 for a laminar flow gives:

$$Sh = a \, Gr^{1/3} \, Sc^{1/3} \, \mathrm{Pr}^{-1/12} \tag{5-86}$$

Then:

$$k_M = a \, D_{LiCl}^{2/3} \left(\frac{g \, \beta_T \, (T_{bulk} - T_i)}{\upsilon} \right)^{1/3} \mathrm{Pr}^{-1/12} \tag{5-87}$$

With the physical properties of the melt given in Table 3-2, D_{LiCl} = 2 10^{-9} m^2/s, coefficient a is taken from existing Nusselt correlations, and the temperature difference between the bulk and the interface varies between 20 °C to 100 °C, the mass transfer coefficient k_M is obtained in between 3 10^{-6} m/s and 3 10^{-5} m/s.

In expression (5-79), the temperature difference $T_{liquidus} - T_i$ is proportional to the heat flux. When the heat flux is high, the temperature difference is important. This may then explain the fast temperature decrease at test beginning. When the heat flux is small, the temperature difference is small and the interface temperature tends towards the liquidus temperature. Furthermore, for a typical heat flux of ~ 15 000 W/m² (intermediate and late phase in ARTEMIS 10), the calculated temperature difference is approximately 30 °C with k_M = 3 10^{-6} m/s and is about 2 °C with k_M = 3 10^{-5} m/s. Thus, k_M = 3 10^{-6} m/s provides a temperature difference between the liquidus and interface temperatures hich is compatible with the interface temperature measurements. This approach is only an order of magnitude approach and would probably need further theoretical analyses.

Since the liquid-solid interface temperature is then lower than the liquidus temperature of the melt, the melt temperature may reach the liquidus temperature and solidification can thus occur. By this way, the formation of a cake enriched in refractory species $BaCl_2$ can be calculated. The formation of this cake will be taken into account in the modification of the mass and energy equations in the following development.

Mass conservation

Changes in the mass of the cavity are caused by the molten concrete entering into the cavity, formation of the cake. The mass conservation equation for the cavity is written as following:

$$\frac{dM_{bulk}}{dt} = \dot{m}_{MC} - \dot{m}_{cake} \tag{5-88}$$

in which $\dot{m}_{cake}$ is the mass rate of cake formation.

The mass balance of $BaCl_2$ in the melt cavity is modified as:

$$M_{bulk} w_{bulk}^{BaCl2} = M_{bulk,ini}\, w_{bulk,ini}^{BaCl2} + M_{MC}\, w_{MC}^{BaCl2} - M_{cake}\, w_{cake}^{BaCl2} \tag{5-89}$$

where in M_{cake} is the mass of the solid cake forming at the melt cavity bottom at instant *t* and w_{cake}^{BaCl2} is the mass percentage of $BaCl_2$ in the cake (w_{cake}^{BaCl2} = 94%) with:

$$M_{bulk} = M_{bulk,ini} + M_{MC} - M_{cake} \tag{5-90}$$

Then, the mass percentage of $BaCl_2$ in the melt cavity at instant *t* is estimated by:

$$w_{bulk}^{BaCl2} = \frac{M_{bulk} w_{bulk,ini}^{BaCl2} + M_{MC} w_{MC}^{BaCl2} - M_{cake}\, w_{cake}^{BaCl2}}{M_{bulk}} \tag{5-91}$$

Hence

$$\frac{dw_{bulk}^{BaCl2}}{dt} = \frac{\dot{m}_{MC}(w_{MC}^{BaCl2} - w_{bulk}^{BaCl2}) - \dot{m}_{cake}(w_{cake}^{BaCl2} - w_{bulk}^{BaCl2})}{M_{bulk}} \tag{5-92}$$

and

$$\frac{dw_{bulk}^{LiCl}}{dt} = \frac{\dot{m}_{MC} w_{MC}^{LiCl} - \dot{m}_{cake}\, w_{cake}^{LiCl}}{M_{bulk}} \tag{5-93}$$

Energy conservation

The power balance equation for the melt cavity is modified taking into account the formation of the cake due to solidification as:

$$\frac{d}{dt}(M_{bulk} H_{bulk}) = \dot{Q}_{add} + \dot{Q}gas + \dot{Q}_{MC} - \dot{Q}_{lost} - \dot{Q}_{convection} - \dot{Q}_{cake} \tag{5-94}$$

in which $\dot{Q}_{cake}$ is the power related to cake formation at the cavity bottom

$$\dot{Q}_{cake} = \dot{m}_{cake} H_{cake} \tag{5-95}$$

in which the cake is supposed to be solid, thus:

$$\begin{aligned} H_{cake} = {} & w_{cake}^{LiCl} H_{ref,solid}^{LiCl}(T_{melt}) + (1 - w_{cake}^{LiCl}) H_{ref,solid}^{BaCl2}(T_{melt}) \\ & + C_{p,solid}^{cake}(T_{cake} - T_{melt}) \end{aligned} \tag{5-96}$$

wherein $C_{p,solid}^{cake}$ is the specific heat of the cake, w_{cake}^{LiCl} is the solute concentration in the cake, $H_{ref,solid}^{LiCl}(T_{melt})$ and $H_{ref,solid}^{BaCl2}(T_{melt})$ are respectively the enthalpy of LiCl and $BaCl_2$ in solid phase at melting temperature of concrete.

The final energy balance equation becomes:

$$\begin{aligned} & M_{bulk} C_{p,liquid}^{bulk} \frac{d\overline{T}_{bulk}}{dt} = \dot{Q}_{add} - \dot{m}_{gas} C_{p,gas} \Delta\overline{T}_{bulk} - \overline{h}_{bulk} S_{lateral} \frac{\Delta\overline{T}_{bulk}}{k_T} \\ & + (\dot{m}_{cake} - \dot{m}_{MC}) C_{p,liquid}^{bulk} (\overline{T}_{bulk} - T_{melt}) + \dot{m}_{cake} L_{solidification}^{BaCl2} \\ & + (w_{bulk}^{LiCl} \dot{m}_{cake} - w_{MC}^{LiCl} \dot{m}_{MC})(H_{ref,liquid}^{LiCl} - H_{ref,liquid}^{BaCl2}) \\ & - w_{cake}^{LiCl} \dot{m}_{cake} (H_{ref,solid}^{LiCl} - H_{ref,solid}^{BaCl2}) \end{aligned} \tag{5-97}$$

5.4.4 Model application for ARTEMIS 10

In this section, several applications of the developed model will be performed for varying hypothesis of liquid-solid interface and melt temperatures.

- H1: $T_i = T_{liquidus}(w_{bulk}^{BaCl2})$.
- H2: $T_i = T_{melt}$.
- H3: $T_i = T_{equ}(\alpha_{volsol}, w_{bulk}^{LiCl})$.
- H4: $T_i = T_{liquidus}(w_{bulk}^{LiCl}) - \frac{\overline{\varphi}\, D_{LiCl}}{k_M\, \lambda_{bulk}}$.

With assumptions H2, H3 and H4, when the melt temperature reaches the liquidus temperature, the interface temperature stays below liquidus temperature of the melt and solidification will occur. Thus, the modified model for solidification will be used.

Melt temperature evolution

Calculations for average melt temperature will be performed using existing natural convection heat transfer coefficient as done for ARTEMIS 11 in Chapter 4. The calculation results with four different assumptions of interface temperature (H1, H2, H3, H4) are illustrated in Figure 5-42, Figure 5-43, Figure 5-44 and Figure 5-45, respectively.

The heat transfer coefficient is estimated using four different Nusselt correlation developed for natural convection, which are Mayinger, ACOPO, MiniACOPO and BAFOND. The correlation is chosen with the corresponding assumed geometry of melt cavity.

- Mayinger, ACOPO and Mini-ACOPO correlations are applied for calculation of heat transfer in hemisphere geometry (The surface area of the melt cavity is estimated by Equation (5-66)).
- BAFOND correlation is used for calculation in cylinder geometry (The surface area of the melt cavity is estimated by Equation (5-69)).

It is seen that if the liquidus temperature of the actual melt is taken as the interface temperature, the calculated melt temperature at t < 2000 s is much higher (more than 100 °C) than the experimental one and no steep temperature drop is obtained as observed in ARTEMIS 10. However, at t > 2000 s, this assumption seems to be a good approximation (Figure 5-42). In addition, among the four correlations of heat transfer, the ACOPO (for hemisphere) and BAFOND (for cylinder) correlations provide higher heat transfer coefficient than the other two correlations (Mini ACOPO and Mayinger's), leading to lower melt temperature which is closer to the experimental one. Moreover, the effect of geometry seems to be negligible (difference between the melt temperatures calculated with ACOPO and BAFOND correlations is not significant).

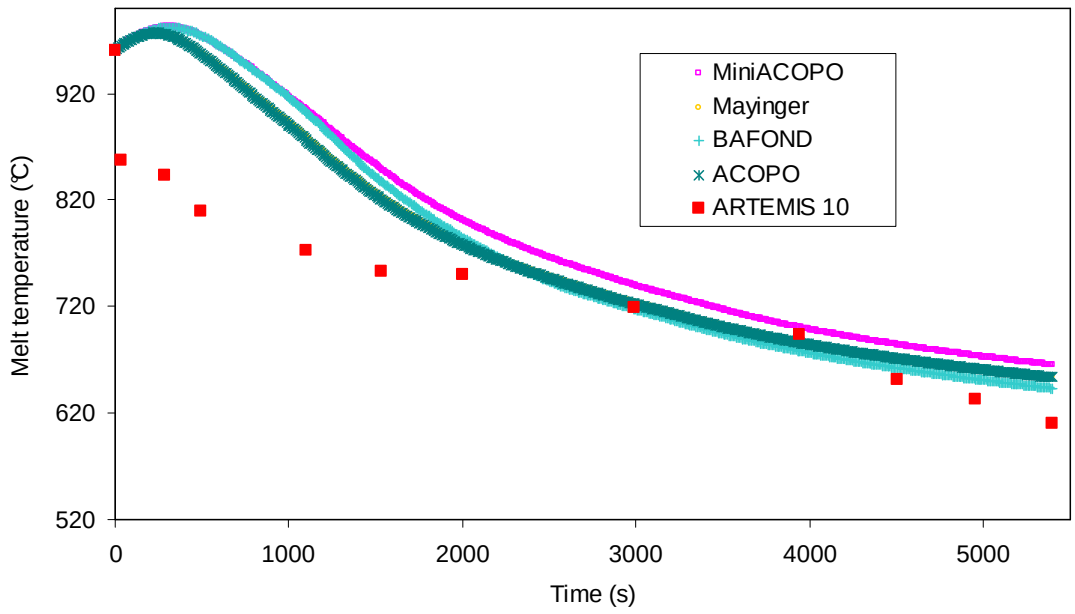

Figure 5-42. Average melt temperature evolution by 0D model for ARTEMIS 10 with $T_i = T_{liquidus}(w_{bulk}^{BaCl2})$.

Figure 5-43 shows the evolution of the melt temperature calculated with melting temperature of concrete at the liquid-solid interface. A sharp decrease of melt temperature is obtained at the beginning but after that, the calculated melt temperature stays far below the measured one. This means that the interface temperature is higher than the melting temperature of concrete.

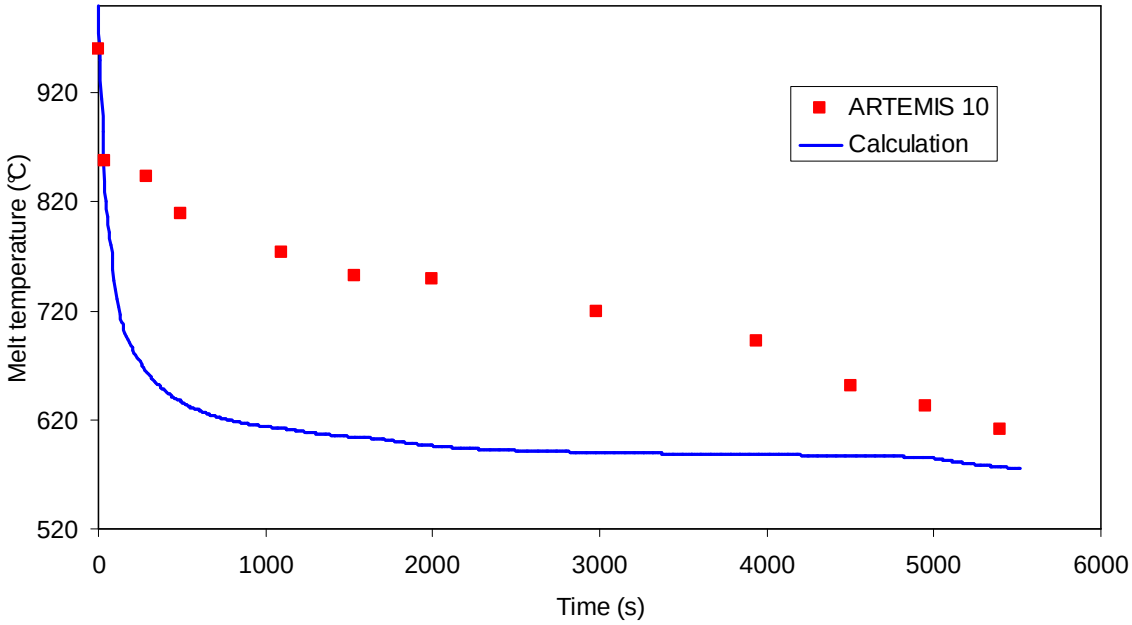

Figure 5-43. Average melt temperature evolution by 0D model for ARTEMIS 10 with $T_i = T_{melt}$ **.**

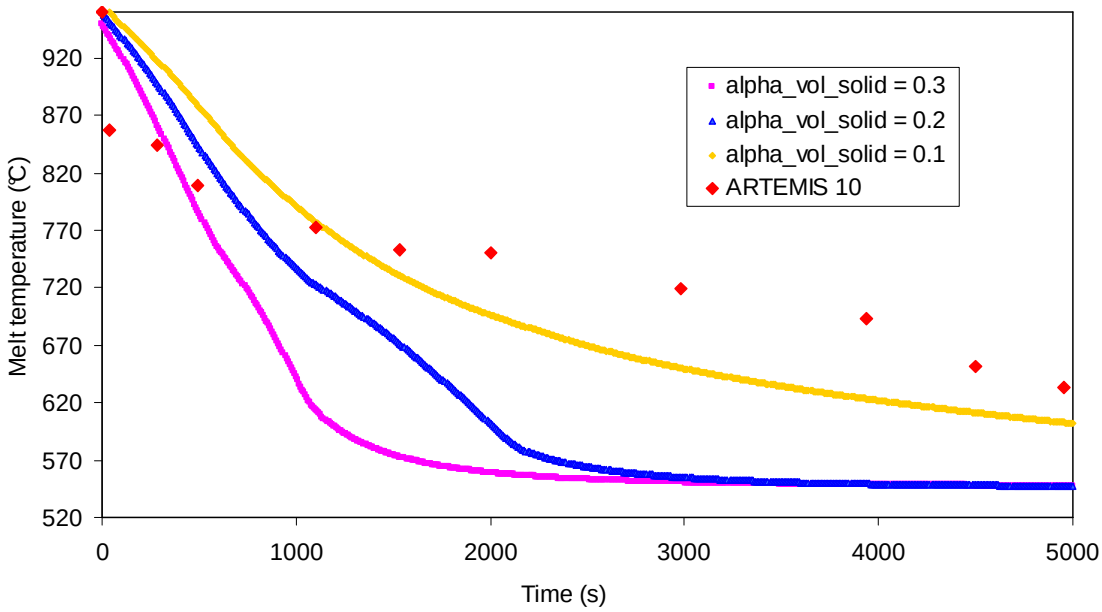

Figure 5-44. Average melt temperature evolution by 0D model for ARTEMIS 10 with $T_i = T_{equ}(\alpha_{volsol}, w_{bulk}^{LiCl})$ **.**

Using assumption H3 with the volume fraction of solid phase ranging from 0.1 to 0.3 and $T_i = T_{equ}(\alpha_{volsol}, w_{bulk}^{LiCl})$ reveals a melt temperature which is always too low in comparison with the melt temperature seen in ARTEMIS 10 (Figure 5-44) and the initial melt temperature decrease rate is too small.

With interface temperature estimated by assumption H4, D_{LiCl} = 2 10^{-9} m^2/s and k_M = 3 10^{-6} m/s (from Equation (5-87)), a tendency agreement has been obtained between the calculation results and the

experimental results. This assumption predicts a high temperature difference between the melt and the interface in the beginning, leading to steep temperature decrease as seen in ARTEMIS 10 (Figure 5-45).

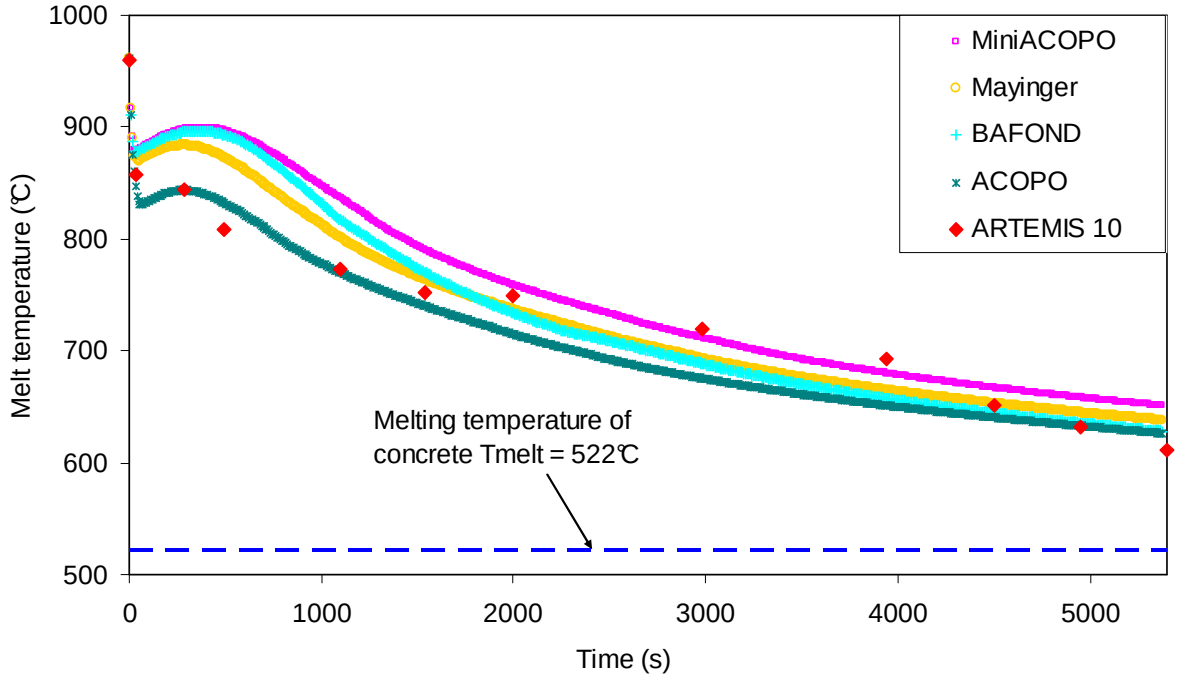

Figure 5-45. Average melt temperature evolution by 0D model for ARETMIS 10 with $T_i = T_{liquidus}(w_{bulk}^{LiCl}) - \dfrac{\overline{\varphi}\, D_{LiCl}}{k_M\, \lambda_{bulk}}$.

It is seen again in Figure 5-45 that the calculation results with hemisphere or cylinder geometry of melt cavity using different heat transfer correlations (corresponding to assumed geometry) seems to be not so different. Indeed, the results obtained from BAFOND correlation for cylindrical geometry stays in between the one given by the other three correlations developed for hemisphere geometry. Among the four applied heat transfer coefficient, it is seen that in the first 1000 s, the average melt temperature calculated with the ACOPO correlation shows a good agreement with the experimental data of ARTEMIS 10. The other three correlations provide the heat transfer coefficients which are not large enough in order to obtain a significant decrease of temperature as observed in the experiment. After 1000 s, the difference between the calculations given by different correlations becomes smaller. However, the calculation results with ACOPO correlation still fits best the ARTEMIS 10 data.

In Figure 5-46, the calculated evolution of melt temperature as well as the evolution of the interface temperature and the liquidus temperature of the actual melt with assumption H4 and ACOPO heat transfer correlation are depicted. At t < 100 s, the interface temperature is lower than the liquidus temperature corresponding to the actual melt composition, therefore, solidification of the melt occurs at the interface and the cake forms during this period. After t > 100 s, the melt temperature stays beyond the liquidus temperature and the model without solidification is applicable.

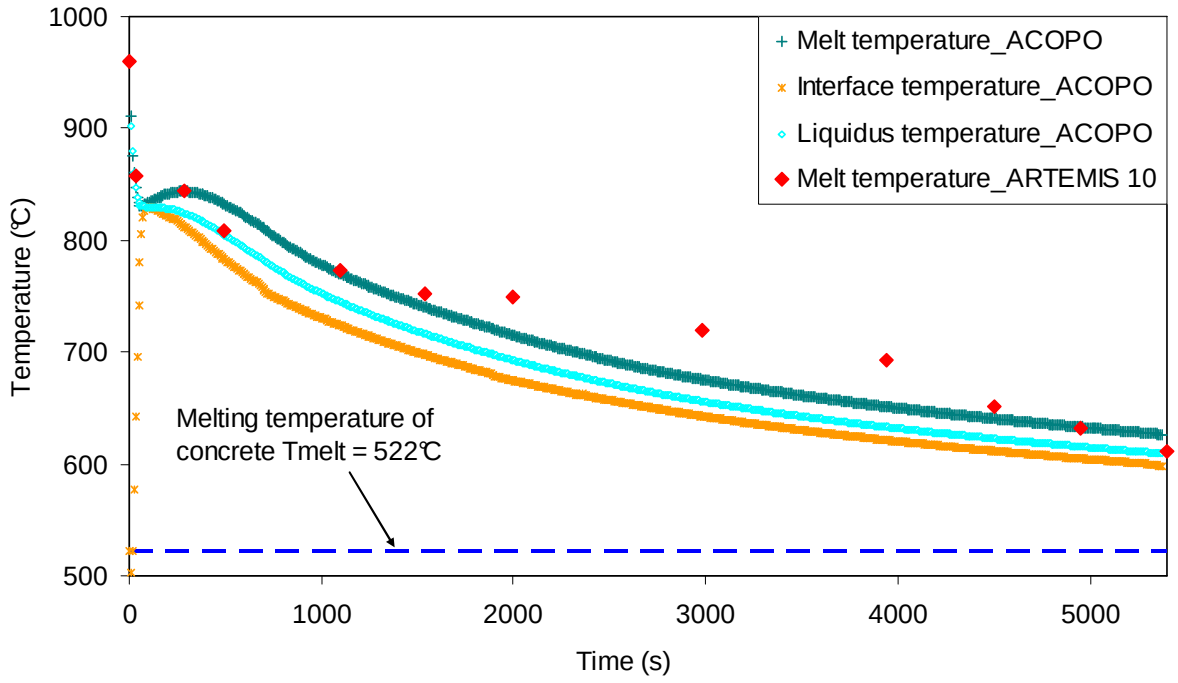

Figure 5-46. Evolutions of the average melt temperature and liquid-solid interface temperature calculated by 0D model using ACOPO natural convection heat transfer correlation.

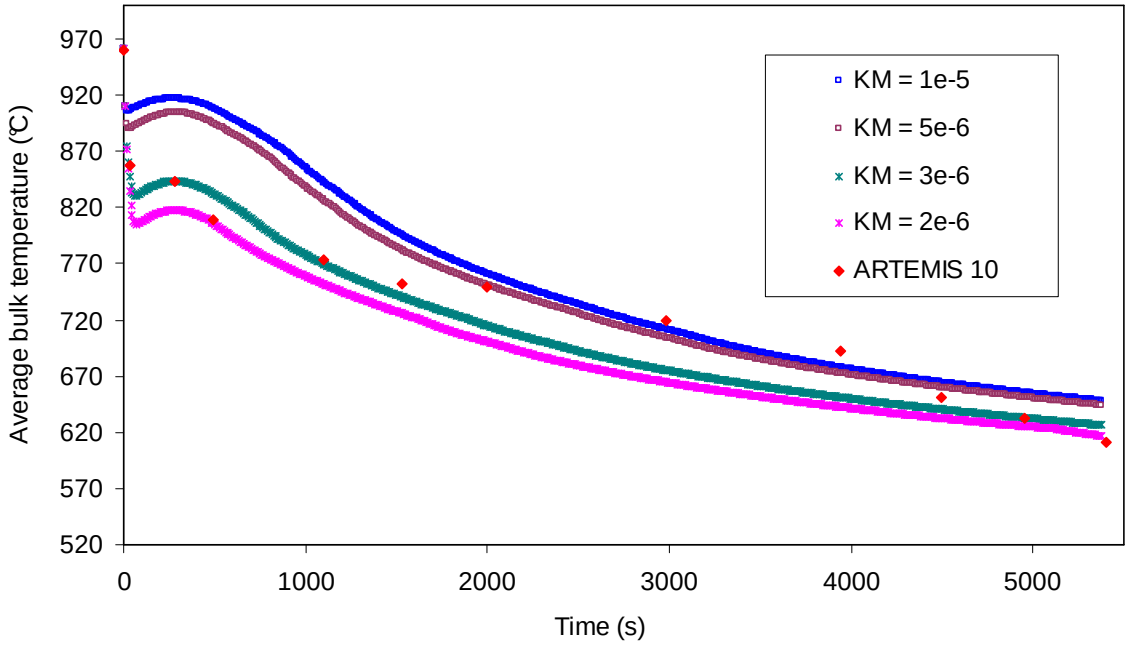

Figure 5-47. Evolution of average melt temperature with ACOPO correlation and varying mass transfer coefficient k_M.

For a verification of the sensibility of the mass transfer coefficient k_M, calculation has been done for k_M = 2. 10^{-6} m/s, k_M = 5 10^{-6} m/s and k_M = 10^{-5} m/s (Figure 5-47). It is seen that in order to have a significant temperature decrease in the beginning as observed in ARTEMIS 10, k_M should be taken as 2 10^{-6} m/s or 3 10^{-6} m/s. Otherwise, the interface temperature would approach the liquidus temperature of the bulk and the calculated melt temperature will stay far beyond the experimental one. However,

with k_M = 2 10^{-6} m/s, the calculated bulk temperature stays below the one obtained in ARTEMIS 10. Among the four tested values for k_M, the value k_M = 3 10^{-6} m/s gives the best agreement between calculation and experiment.

Evolution of molten concrete mass

Figure 5-48, Figure 5-49, Figure 5-50 and Figure 5-51 present evolutions of molten concrete mass obtained with different assumptions H1, H2, H3, H4. It is seen that using melting temperature of concrete at the liquid-solid interface (H2) or the interface temperature corresponding to a constant volume solid fraction at the interface (H3) results in over-estimations of the molten concrete mass as seen in Figure 5-49 and Figure 5-50.

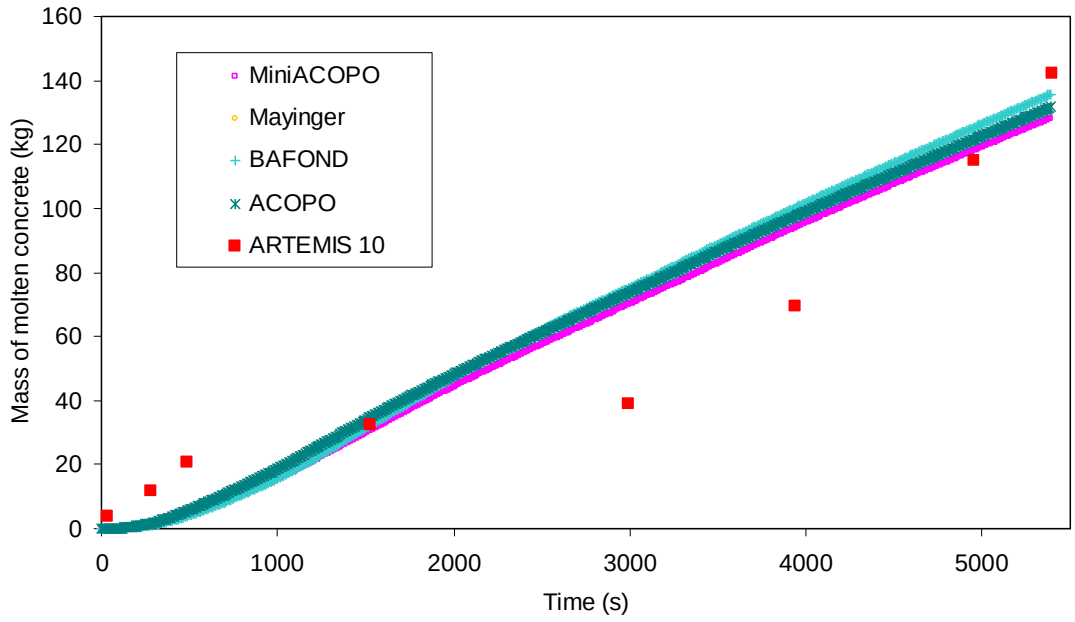

Figure 5-48. Evolution of molten concrete mass by 0D model for ARTEMIS 10 with $T_i = T_{liquidus}(w_{bulk}^{BaCl2})$ ***.***

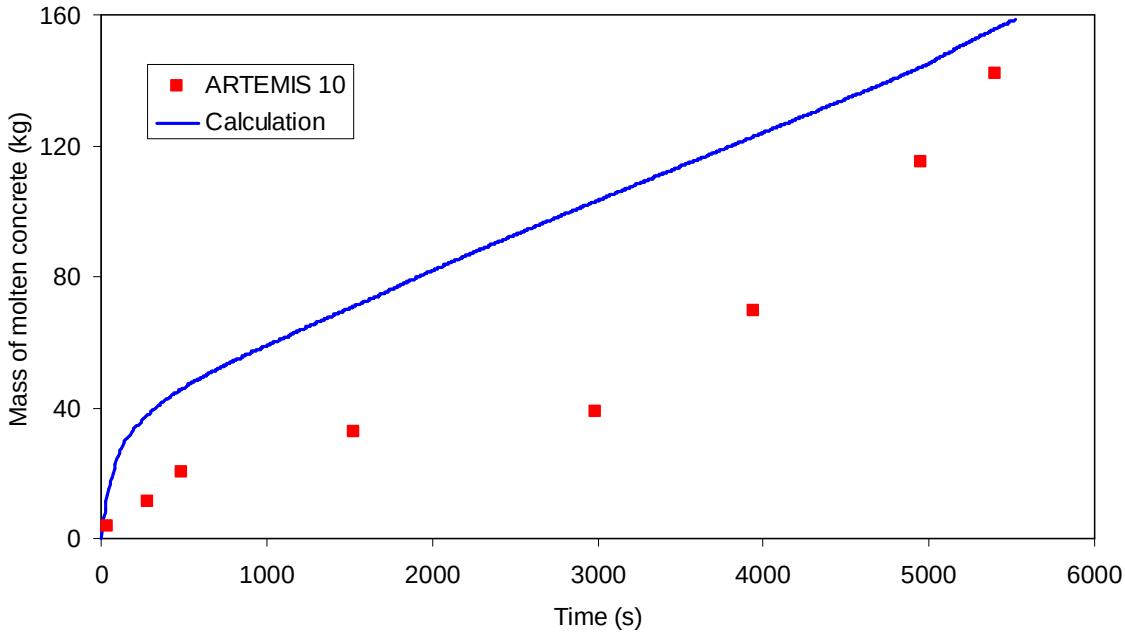

Figure 5-49. Evolution of molten concrete mass by 0D model for ARTEMIS 10 with $T_i = T_{melt}$ **.**

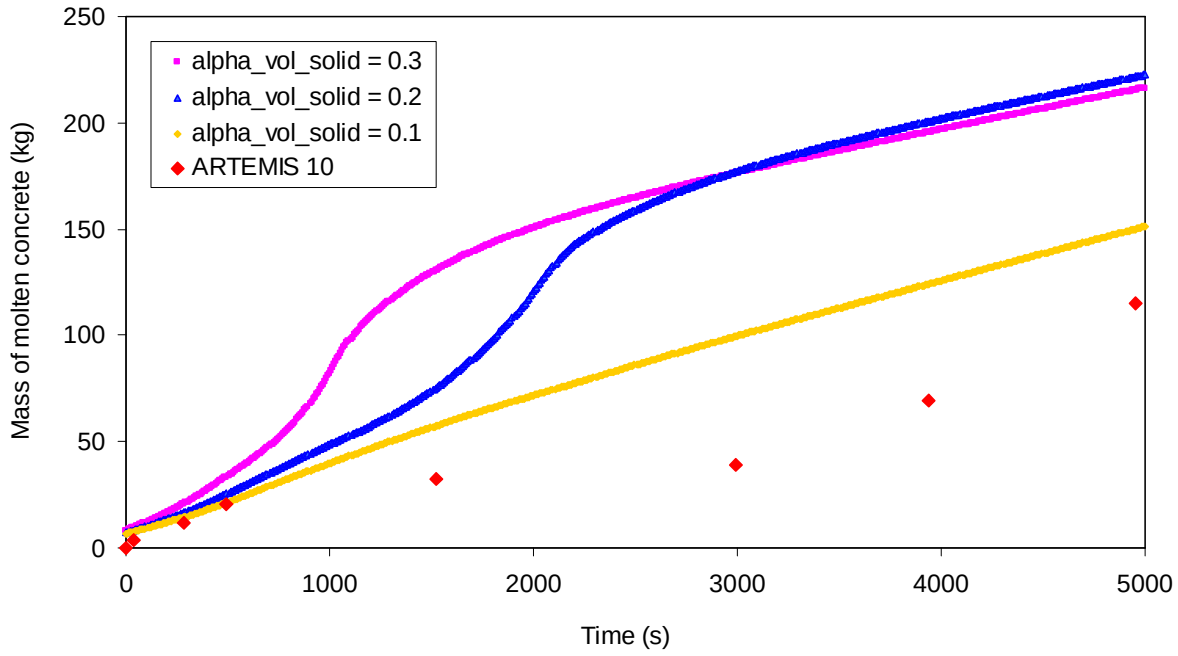

Figure 5-50. Evolution of molten concrete mass by 0D model for ARTEMIS 10 with $T_i = T_{equ}(\alpha_{volsol}, w_{bulk}^{LiCl})$ **.**

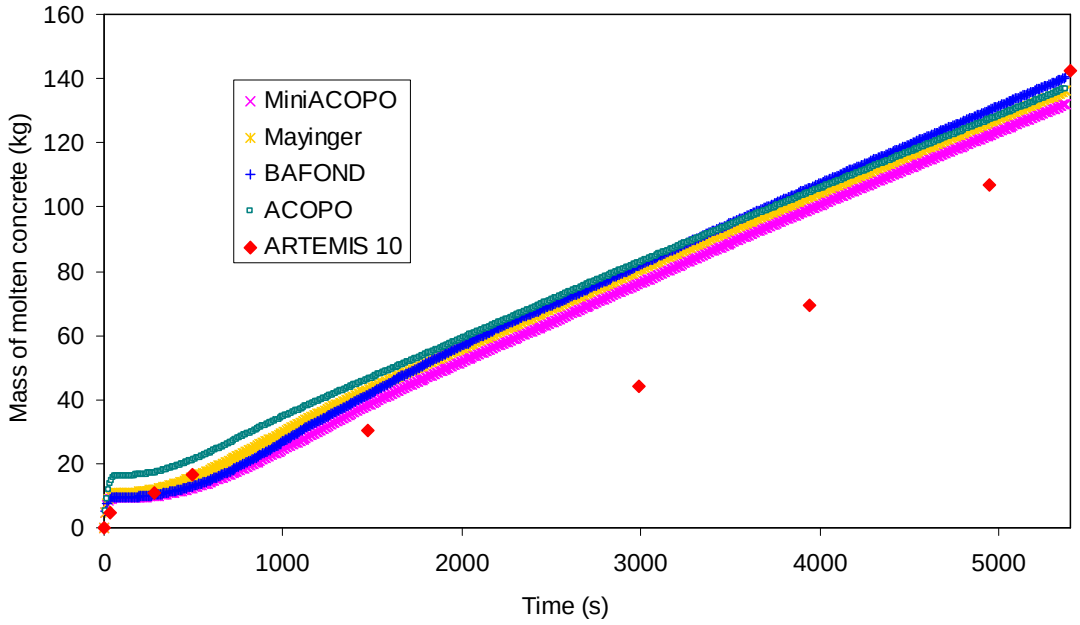

Figure 5-51. Evolution of molten concrete mass in ARTEMIS 10 with $T_i = T_{liquidus}(w_{bulk}^{LiCl}) - \dfrac{\overline{\varphi}\, D_{LiCl}}{k_M\, \lambda_{bulk}}$ ***.***

With liquidus temperature of the melt as the interface, the final calculated mass of molten concrete seems to be in qualitative agreement with the evolution obtained in ARTEMIS 10, however, it is impossible to reproduce the ablation in the beginning. According to Figure 5-51, it is seen that using the interface temperature calculated by Equation (5-79) provides a strong ablation of concrete just at the beginning. At the end of calculation, the final mass of concrete obtained by calculation is also in agreement with the experimental one (about 142 kg). The influence of geometry on the evolution of molten concrete mass is very minor.

Although the calculation with assumption H4 with a correction of temperature difference between interface temperature and liquidus temperature ($T_i = T_{liquidus}(w_{bulk}^{LiCl}) - \dfrac{\overline{\varphi}\, D_{LiCl}}{k_M\, \lambda_{bulk}}$) predicts well the initial ablation as well as the final mass of the molten concrete, there exists a difference between calculation and experiment in description of transient evolution of the mass of molten concrete,. At t < 1500 s, this difference is quite small but it becomes very significant at t > 1500 s. As discussed in the analysis of ARTEMIS 10, there is an acceleration of ablation between 3000 s and 4000 s. This phenomenon is not represented in the calculation results.

According to the experimental data of ARTEMIS 10, about 14 kg of cake was obtained at the end of the test. Regarding to the calculation of the mass of cake with assumption H4 shown in Figure 5-52, it is seen that among the four correlations applied for estimation of average heat transfer coefficient from the melt to the liquid-solid interface, ACOPO correlations gives the final mass of cake of 13.5 kg, which is the closest to the experimental data. The other three correlations provide very small masses of cake.

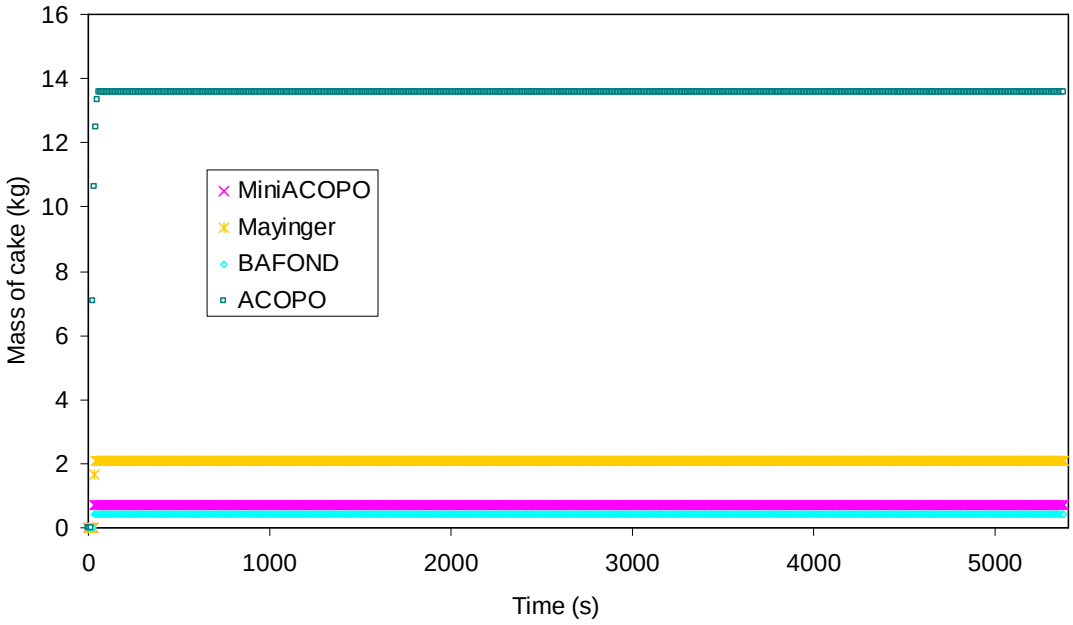

Figure 5-52. Evolution of cake mass in AREMIS 10.

Evolution of average melt composition

Calculation of the evolution of average melt composition obtained with assumption H4 for interface temperature, represented by the average mass percentage of $BaCl_2$ in the melt is given in Figure 5-53. In the beginning (t < 1500 s) and at the test ending (t > 4000 s), calculation shows relative agreement with experiment. However, at 1500 s < t < 4000 s, the calculated $BaCl_2$ mass percentage is lower than the one measured in the experiment.

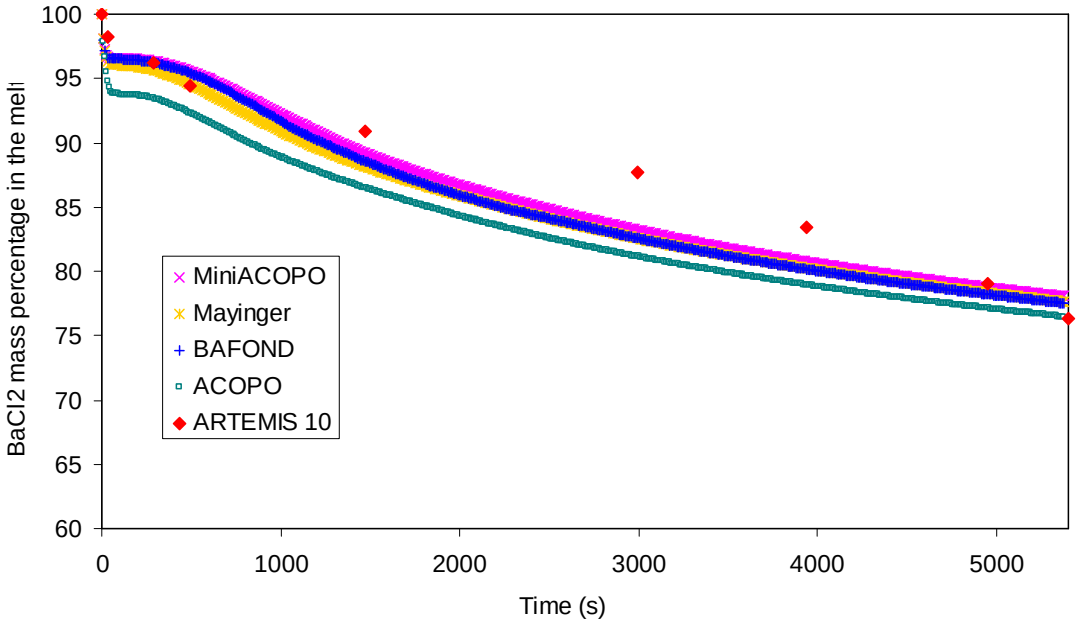

Figure 5-53. Evolution of average mass percentage of $BaCl_2$ in the melt AREMIS 10.

5.4.5 Conclusion from 0D model calculations

It is confirmed from the 0D model application that the flow recirculation in the melt cavity in ARTEMIS 10 is controlled by natural convection heat transfer. The effect of geometry on the melt temperature and molten concrete mass evolutions is negligible. This means the thermal effects are dominant in this situation.

Application has been performed with four different assumptions of liquid-solid interface temperature.

- H1: $T_i = T_{liquidus}(w_{bulk}^{BaCl2})$ shows good approximation of melt temperature evolution at t > 2000 s but at t < 2000 s, the calculated melt temperature is too high in comparison with the experimental one. The concrete ablation rate is also too small during that time period.
- H2: $T_i = T_{melt}$ gives fast initial temperature decrease but after that, the calculated melt temperature is much lower than the experimental one and the concrete ablation rate is too large.
- H3: $T_i = T_{equ}(\alpha_{volsol}, w_{bulk}^{LiCl})$ is also unable to describe the melt temperature evolution because the calculated melt temperature is too low in comparison with the measured one in ARTEMIS 10.
- H4: $T_i = T_{liquidus}(w_{bulk}^{LiCl}) - \frac{\overline{\varphi}\, D_{LiCl}}{k_M\, \lambda_{bulk}}$ reveals good description of melt temperature evolution with steep melt temperature drop at the beginning and the final calculated melt temperature is quite close to the experimental one.

The ACOPO heat transfer correlation reported by [Theofanous et al., 1997] for steady state natural convection heat transfer in hemispherical geometry is best adapted to estimate the evolutions of the average melt temperature, but the result is not very different when Mayinger's and ACOPO correlation are used (as for LIVE and ARTEMIS 11). However, the calculation with ACOPO correlation provides a good estimation of the mass of cake formed due to solidification of $BaCl_2$ in the melt.

The model is unable to describe the local parameters in the melt cavity such as the local melt temperature, local heat flux and the evolution of the local cavity radius, etc… Therefore, another model taking into account the evolution of these local parameters in the melt cavity has been developed.

5.5 1D modelling for calculation of local heat transfer and evolution of melt cavity shape for ARTEMIS 10

In chapter 2 and chapter 4, the developed 1D boundary layer model (presented in Annex 7) has been applied for calculation of the evolution of local parameters in LIVE L3A and ARTEMIS 11. In this section, this model will be applied again for ARTEMIS 10 test. The main outcomes of interest include the evolutions of the local temperature in the melt cavity, transient heat flux distribution along the cavity wall and evolution of the local cavity radius.

In the next 1D calculation, the model will be applied only for the top zone using increasing power dissipation versus time as derived from the analysis of ARTEMIS 10. The bottom zone is not described with the present model. Only the top zone is described. The power dissipation in the top zone increases versus time as determined under section 5.3.

5.5.1 Constitutive laws

As presented in the description of ARTEMIS 10, the melt pool in ARTEMIS 10 has a small size (a few ten-centimeter scale), the Grashof number is smaller than 2 10^9. Therefore, the liquid flow in the boundary layer in this situation will be considered as a laminar flow.

According to the previous application of the 1D model for LIVE L3A (Chapter 2) and for ARTEMIS 11 (Chapter 4), the constitutive laws for friction coefficient and heat transfer coefficient derived from the velocity and temperature profiles introduced by Eckert for the description of the boundary layer along a vertical wall in laminar natural convection resulted in good agreement between calculation and experimental data. Therefore, these constitute laws will be also applied for the calculation of ARTEMIS 10.

The friction coefficient is calculated by:

$$F = \frac{96}{\mathrm{Re}} \tag{5-98}$$

For ARTEMIS 10, Pr = 4, the coefficient k_j equals to 0.33 in the correlation of superficial radial entrainment velocity of liquid from the bulk into the boundary layer (Annex 3), i.e:

$$j_{bulk} = 0.33\left[g\,\beta_T\,(T_{bulk} - T_{BL})\,\upsilon\right]^{1/3} \tag{5-99}$$

wherein T_{bulk} and T_{BL} are the local bulk and boundary layer temperature at a given distance x from the top edge of the boundary layer.

With $Pr \approx 4$, as shown in Annex 3, the heat transfer to the wall can be estimated using either Nu_{bulk} or Nu_{BL} as follows:

$$Nu_{bulk} = 4\frac{\delta}{\delta_T} = 4\,\mathrm{Pr}^{1/3} \approx 6.4 \tag{5-100}$$

$$Nu_{BL} = \frac{4\dfrac{\delta}{\delta_T}}{\dfrac{4}{5}\dfrac{\delta}{\delta_T} - \dfrac{1}{5}\left(\dfrac{\delta}{\delta_T}\right)^2} = \frac{5}{1 - 0{,}275\,\mathrm{Pr}^{1/3}} \approx 8.9 \tag{5-101}$$

5.5.2 1D model application for ARTEMIS 10

According to the conclusion from the 0D model, the assumption that $T_i = T_{liquidus}$ leads to a high melt temperature at t < 2000s. During the rest of the test, liquidus temperature seems to be a good approximation for the interface temperature. Therefore, in the next 1D calculation with the boundary layer model, liquidus temperature corresponding to local liquid composition in the boundary layer will

be assumed as the local liquid-solid interface temperature in which the local liquid composition at a given elevation in the boundary layer is calculated by knowing the local radial liquid entrainment velocity from the bulk j_{bulk} with solute concentration w_{bulk} and the local ablation velocity of concrete V_{abl} with solute concentration of molten concrete w_{MC} according to Equation (A-7-31).

Evolution of average melt temperature

The average bulk temperature evolution is shown in Figure 5-54 and compared with the average temperature obtained in ARTEMIS 10 in. For t < 2000 s, a significant difference is observed between calculation and experiment. This is due to the assumption of liquidus temperature at the liquid-solid interface for this calculation.

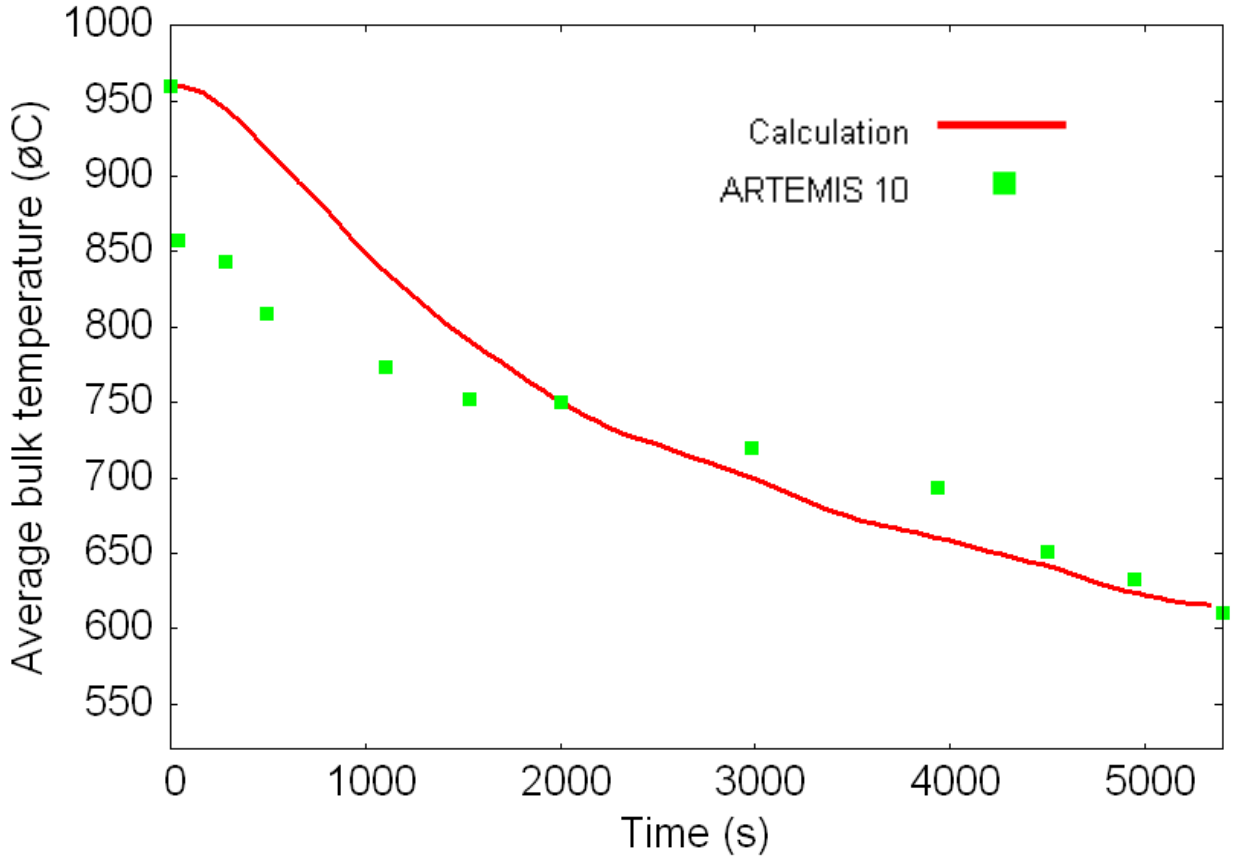

Figure 5-54. Average melt temperature evolution in ARTEMIS 10.

Melt cavity shape at test ending t = 5400 s

Figure 5-55 depicts the melt cavity shape at t = 5400 s. Due to 46% porosity of molten concrete, the height of the melt in the cavity is reduced to about 30 cm (the initial height is 45 cm). A rather good agreement is obtained between experimental ablation profile and calculation. It is observed that ablation occurs stronger in the upper part of the cavity than the bottom cavity. This is clearly due to the heat flux profile linked to natural convection (high heat transfer coefficient and a big temperature difference between bulk and liquid-solid interface at the top). Difference between calculation and experiment is seen in the bottom zone of the melt. This is due to the existence of the bottom recirculation in the melt cavity that is not described in the present model.

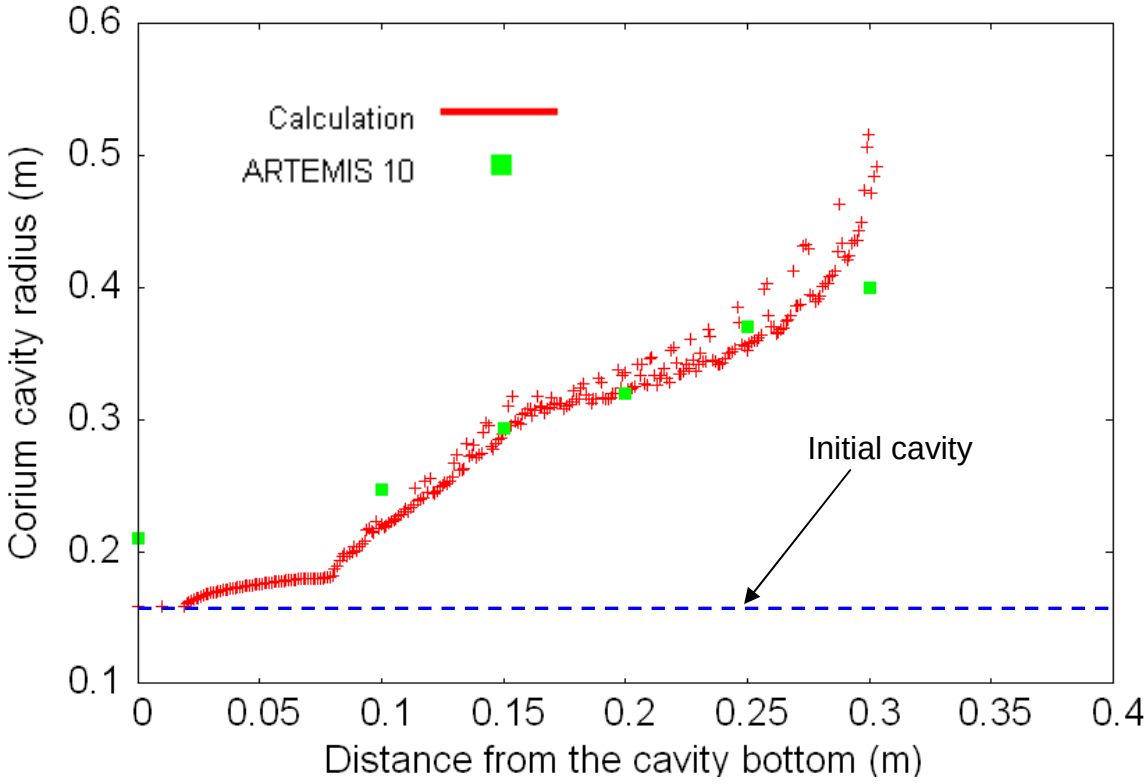

Figure 5-55. Melt cavity shape at t = 5400 s in ARTEMIS 10.

Evolution of molten concrete mass

Figure 5-56 shows the evolution of molten concrete mass. Agreement is obtained between calculation and experiment (blue points). The final mass of molten concrete was 142 kg in ARTEMIS 10 which is close to the calculated one of 141.5 kg. In transient, it is seen that the calculated ablated mass of concrete given by model 0D is higher than the one provided by model 1D. This is due to the fact that in the 1D calculation, only ablation in the top zone is considered with the increasing power dissipation versus time (gradually increases up to 6000 W after 2000 s); whereas, in the 0D model, calculation is performed for the whole melt cavity with a constant power dissipation of 6000 W.

Indeed, in the first 2000 s, only a part of the heater is located in the top zone of the cavity, then the total power dissipation in the top zone is less than 6000 W. The ablated mass of the concrete obtained in the top zone is proportional to the power dissipation in this zone and is less than the total mass of ablated concrete obtained in this period. As shown in Figure 5-56, if the mass of ablated concrete is adjusted (green points) taking into account the fact that the power dissipation in the top zone is less than 6000W at t < 2000 s as done in the calculation, then an agreement would be observed between calculation and experiment.

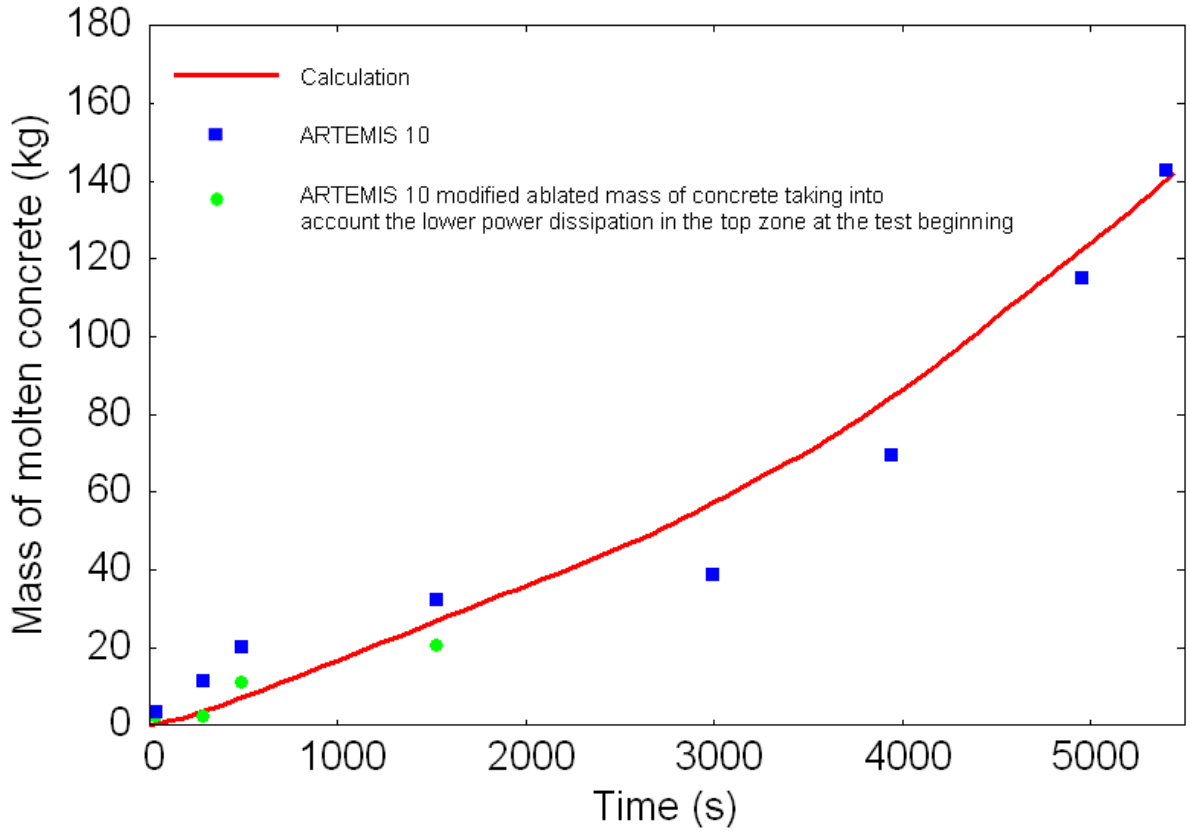

Figure 5-56. Evolution of molten concrete mass in ARTEMIS 10.

5.5.3 Conclusion from 1D calculations

The main conclusions from the application of 1D model for ARTEMIS 10 are summarized as follows:

- The constitutive laws for friction coefficient and heat transfer coefficient deduced from the use of Eckert's velocity and temperature profiles, which were developed for natural-convection boundary layer along a vertical plate in laminar regime, seem to stay valid for a hemispherical cavity with melting wall, not only for the case of identical composition of melt and concrete (ARTEMIS 11) but also for the case when melt and concrete have different composition (ARTEMIS 10).
- Liquidus temperature of the melt at the liquid-solid interface seems to be a good assumption for t > 2000 s. In the first 2000 s, the interface temperature is significantly lower than the liquidus temperature.
- Calculation of the model for the evolution of the cavity shape exhibits agreements to ARTEMIS 10, especially at the top zone of the melt cavity. However, the developed model was not able to describe the 2nd recirculation flow at the bottom of the melt cavity. Hence, it can not reproduce the ablation at the bottom as seen in ARTEMIS 10.
- The application confirms that natural convection dominates the flow regime in the melt cavity.

5.6 Conclusions

This chapter is dedicated to the investigations of heat and mass transfers during ARTEMIS 10 experiment, which aimed to represent the ablation of an eutectic solid concrete by a non-eutectic and

refractory melt with gas sparging and volumetric power dissipation in the melt cavity. The main conclusions are made as follows:

- Analysis of evolution of temperature distributions and heat transfer in the melt cavity shows that natural convection would be the main heat transfer mechanism. The heat transfer from the melt to the liquid-solid interface can best be estimated using the natural convection Nusselt correlation introduced for ACOPO experiment by [Theofanous et al., 2007].
- Two recirculation loops have been identified in the melt cavity. The composition and temperature in each zone are quasi-uniform but different. In the top zone, the flow goes upwards in the melt cavity centre and downwards in the boundary layer. In the bottom zone, the flow goes downwards in the cavity centre and upwards in the boundary layer. This leads to ablation of concrete not only at the lateral wall but also at the bottom interface of the melt cavity.
- A simple criterion for a density limit has been introduced to determine the position of the top-bottom interface. The interface between top and bottom zones moves downwards versus time, leading to increasing power dissipation in the top zone and decreasing one in the bottom zone. This helps explaining the termination of ablation at the bottom and an acceleration of the top ablation.
- A cake is formed at the bottom of the melt cavity due to deposition of $BaCl_2$. Although the cake is enriched in $BaCl_2$, it is not solid. It is a porous medium containing both solid and liquid at local thermodynamic equilibrium. Heat transfer in the cake is governed not only by conduction but also by solute convection. The convection explains the thickness of the cake, as for ARTEMIS 1D.
- The temperature evolution in the melt cavity is recalculated by a 0D model as done for LIVE L3A and ARTEMIS 11. The best agreement has been found for an interface temperature evolution depending on the heat flux. The interface temperature is significantly lower than liquidus at elevated heat flux, explaining the fast decrease of melt temperature at the test beginning. After approximately 1000 s, the heat flux decreases and the interface temperature can be assumed equal to the liquidus temperature of the melt.
- Application of the 1D model already used for the interpretation of LIVE L3A and ARTEMIS 11 tests was also made for ARTEMIS 10. This model couples the heat and mass transfer between the bulk of the melt and the boundary layer at the cavity wall. A radial liquid flow is assumed to enter the boundary layer from the bulk. Same local constitutive laws as for the interpretation of LIVE L3A test have been considered for friction, heat transfer and liquid entrainment velocity in the boundary layer. The model was applied only for the flow recirculation in the top zone and did not take into account existence of the bottom flow recirculation.
- The 1D model calculation results proved to quite well reproduce the ablation profile. From these calculations, it is concluded that the fast ablation at the top of the melt cavity is linked to the heat flux distribution associated to the laminar boundary layer flow, as in ARTEMIS 11.

CONCLUSIONS

This thesis work is a contribution to the study of molten corium behaviour and molten corium-concrete interaction during severe accident of nuclear reactors. In these situations, the main objective of interest for the reactor applications is to determine the heat flux distributions along the lower head and ablation rate of the concrete cavity.

Lessons from the state of the art

The first chapter covers a state of the art for In-vessel Retention and Molten Corium – Concrete Interaction. Among the work devoted to In-Vessel Retention, it has been shown that the question of steady state heat transfer and steady state interface temperature at the cooled boundaries of a melt cavity with internal heat source has been clearly answered. The steady state heat transfer from the melt cavity to the upper cavity surface and to the lateral liquid-solid interface can be determined by existing Nusselt correlations in terms of internal or external Rayleigh number. The liquid-solid interface conditions are also determined for the steady state situation: absence of mushy zone at the interface and the interface temperature is equal to the liquidus temperature of the actual liquid composition. However, available studies concerning the transient heat transfer with crust formation are limited. During the transient, a mushy zone can exist, which results in significant effect on the liquid composition near the interface and on the interface temperature. Due to the lack of precise experimental data, the question of transient natural convection heat transfer in a melt cavity with internal heat generation and melt solidification is still also open, including evolution of melt temperature, transient evolution of the liquid-solid interface temperature as well as the transient distribution of the heat flux along the vessel wall.

In the second part of the survey, main results from the MCCI program have been summarized. It has been emphasized that despite intensive studies on molten corium-concrete interaction, there are still open issues that are not yet explained:

- The evolution of the shape of the ablation interface in 2D configuration;
- The effect of gas sparging on the flow recirculation in the melt cavity and its impact on heat transfer;
- The effect of gas sparging and concrete melting on crust formation and interface temperature.

Investigations in this thesis

In order to answer the above mentioned questions, heat and mass transfer in a molten corium cavity surrounded by solid wall have been studied here for three different situations.

- The first situation deals with a volume heated non-eutectic melt contained in a hemispherical shaped cooled vessel, without gas sparging, simulating in-vessel corium with crust formation at the corium vessel wall. The situation corresponds to the LIVE L3A experiment which was performed at KIT, Germany.
- The second situation treats a 2D ablation of a concrete cavity with gas sparging. In order to separate the physico-chemical aspects and to first study purely thermal-hydraulic aspects, interaction with identical eutectic material is investigated. This situation is illustrated by ARTEMIS 11 test.

- The third situation concerns 2D concrete ablation by a melt that is more refractory. Both thermal-hydraulics and physico-chemical aspects are investigated. This situation involves the study of ablation of an eutectic solid concrete wall interacting with a heated liquid melt at different composition (refractory and non-eutectic melt) with gas injection. This situation is represented by the ARTEMIS 10 test.

Main results concerning in-vessel corium behavior with solidification at vessel wall

The analysis is devoted to the investigation of transient heat transfer and solidification in a simulated non-eutectic molten corium cavity with internal heating source and external cooling at boundaries.

A simplified model has been developed for calculation of the evolution of maximum melt temperature and evolution of the solid crust thickness due to solidification. The model assumes liquidus temperature of the actual melt at the liquid-solid interface and employs an average heat transfer from an existing natural convection Nusselt number developed for steady state heat transfer. A transformation of the correlation from internal Rayleigh number to external Rayleigh number has been performed in order to take into account the transient variation of temperature difference between the melt and the liquid-solid interface. The local crust thickness evolution has been calculated by imposing the steady state heat flux profile measured by experiment. Agreement between the model and the experimental data in melt temperature evolution and crust thickness evolution proves that the heat transfer in transient has similar behaviour as in steady state. In addition, using the calculation results for transient solidification rate and applying the existing solidification models for planar front and mushy zone, a prediction of solidification regimes in LIVE L3A has been proposed, wherein a mushy zone state occurs at the beginning and a planar front is obtained at the end. Recalculation of interface temperature during the whole transient again indicates that the interface temperature always stays close to the liquidus temperature of the actual melt composition.

Application of the 1D boundary layer model for LIVE L3A has been carried out. The model gives access to local melt temperature and heat flux distribution not only in steady state but also in transient. The constitutive laws for friction coefficient and heat transfer in the boundary layer as well as for the radial liquid flow velocity from the bulk to the boundary layer which are derived for a vertical plate are also applicable for a hemispherical melt cavity.

Main results concerning the second situation (wall ablation by a heated melt with uniform composition and gas sparging)

ARTEMIS 11 experiment is aimed to represent an eutectic solid material ablation by the eutectic melt with gas sparging and volumetric power dissipation in the melt cavity. The main conclusions are as follows:

- Analysis of evolution of temperature gradient in the melt cavity reports existence of gas mixing in the melt cavity during the first 17 minutes. After that, natural convection controls heat transfer in the melt cavity.
- The natural convection flow explains the preferential radial ablation. The heat flux distributes non-uniformly along the lateral wall of the melt cavity, leading to maximum concrete ablation at the top and minimum concrete ablation at the bottom of the cavity.
- The maximum temperature evolution in the melt cavity is recalculated by a 0D model. In the first 17 minutes, due to gas-liquid mixing convection regime, a two phase heat transfer correlation has

been applied. After that, heat transfer was estimated by a natural convection correlation. The temperature decrease in the melt after 1 hour is attributed to the cavity widening and the reduction of heat flux due to ablation.

- Application of the 1D model already used for the interpretation of LIVE L3A test was made. The 1D model calculation results show a good reproduction of the melt temperature evolutions as well as the local ablation rates. From these calculations, it is concluded that the fast ablation at the top of the melt cavity is linked to the heat flux distribution associated to the laminar boundary layer flow. The low ablation rate at the melt cavity bottom is linked to the recirculation of cold liquid from the boundary layer at the bottom region.

Main results concerning the third situation (wall ablation by a heated melt with non-uniform composition and gas sparging)

ARTEMIS 10 experiment is aimed to represent the ablation of an eutectic solid concrete by a non-eutectic and refractory melt with gas sparging and volumetric power dissipation in the melt cavity. The main conclusions are as follows:

- Analysis of evolution of temperature distributions and heat transfer in the melt shows that natural convection is the main heat transfer mechanism. The heat transfer from the melt to the liquid-solid interface can be estimated using the natural convection Nusselt correlation.
- Two recirculation loops have been identified in the corium melt cavity. The composition and temperature in each zone are quasi-uniform, but different. The temperature in the top zone is lower than in the bottom zone while the solute concentration in the top zone is greater than in the bottom zone. The flow in the top zone goes upwards in the corium cavity centre and downwards in the boundary layer. In the bottom zone, the flow goes downwards in the cavity centre and upwards in the boundary layer. This leads to ablation of concrete not only at the lateral wall but also at the bottom interface of the corium cavity.
- A criterion for a density limit has been introduced to determine the position of the top-bottom zone interface. The interface between top and bottom zones moves downwards versus time, leading to increasing power dissipation in the top zone and decreasing in the bottom zone. This helps explaining the termination of ablation at the bottom and acceleration of the top ablation.
- The cake is formed at the bottom of the melt cavity due to deposition of refractory ($BaCl_2$). Although the cake is enriched in $BaCl_2$, it is not solid but a porous medium containing both solid and liquid at local thermodynamic equilibrium as observed previously in the thesis work of [Guillaumé, 2008]. Heat transfer in the cake is governed not only by conduction but also by solute convection. The internal convection explains the thickness of the cake, as for ARTEMIS 1D.
- The temperature evolution in the melt cavity is recalculated by a 0D model as done for LIVE L3A and ARTEMIS 11. The best agreement has been found for an interface temperature evolution depending on liquidus temperature with a correction linked to the heat flux. The interface temperature is significantly lower than the liquidus at elevated heat flux, explaining fast decrease of melt temperature at test beginning. After approximately 1000 s, the heat flux decreases and the interface temperature can be assumed equal to the liquidus temperature of the melt.
- Application of the 1D model already used for the interpretation of LIVE L3A and ARTEMIS 11 tests was also made for ARTEMIS 10. Same local constitutive laws as for the interpretation of LIVE L3A test have been considered for friction, heat transfer and liquid entrainment velocity in the boundary layer. The 1D model calculation results proved to quite well reproduce the ablation profile for the top zone. From these calculations, it is concluded that the fast ablation at the top of the melt cavity is linked to the heat flux distribution associated to the laminar boundary layer flow, as in ARTEMIS 11.

General Conclusions

Conclusions in terms of ablation

In terms of ablated mass of concrete, the controlling parameters are

- The power dissipation in the melt cavity;
- The thermal inertia of the melt, which is linked to the temperature decrease of the melt. The rate of temperature decreases is associated to the evolution of the interface temperature and to the heat transfer in the melt. For materials with single melting temperature, the interface temperature is fixed. For non-eutectic mixtures, the evolution of the interface temperature is more difficult to predict, but for ARTEMIS 10, the hypothesis that the interface temperature follows the liquidus temperature provides good results in terms of evolution of the ablated mass of concrete.

For the long term, when the mass of ablated concrete becomes large, the temperature of the melt tends towards the melting temperature of the concrete and the ablation rate of concrete is then entirely controlled by the power dissipation.

Conclusions in terms of heat transfer

In terms of heat transfer from the melt cavity to the liquid-solid interface, it has been concluded that average steady state heat transfer coefficient can be a good approximation for the transient heat transfer coefficient. Existing heat transfer correlations for natural convection or gas driven convection recirculation can be used for the calculation of transient pool heat up and heat flux distribution. The statement can be explained by the fact that, in the cases analysed in this work, the characteristic time delay required for establishing the natural convection flow is mush shorter than the characteristic time delay associated to the heating up of the melt cavity (which is linked to the thermal inertia of the melt and to the power dissipation).

The predominant lateral material ablation observed in ARTEMIS 11 and ARTEMIS 10 tests is linked to two effects:

- The fact that natural convection dominates in the melt cavity (no or very little gas penetration in the melt cavity) and boundary layer flow is downward;
- The fact that buoyancy effects are more important than solute effects (for non uniform composition) due to the small ablation rate of solid concrete in comparison to the entrainment velocity of the liquid from the bulk to the boundary layer and due to a limited density difference between the melt and the concrete.

This analysis suggests that the preferential radial ablation observed in siliceous concrete ablation test might be due to existence of only one flow recirculation loop with downward boundary layer in the melt cavity and the heat transfer is controlled by natural convection which means that the gas may probably not flow through the corium cavity. This may explain the post-test observations that corium melt appears to be very dense with siliceous concrete (whereas it is very porous with limestone concrete).

Conclusions in terms of interface temperature

For LIVE L3A test conditions, involving solid crust formation on a steel vessel wall without gas sparging, it appears that the interface temperature stays close to the liquidus temperature during the transient crust formation.

For ARTEMIS 11 (materials with uniform eutectic composition), the interface temperature is equal or very close to the eutectic melting temperature.

For ARTEMIS 10 (non-uniform composition, sparging gas, moving interface), the situation is much more complex. The melt composition is not uniform (melt composition stratification in the vertical direction and composition variation in the boundary layer). The assumption that the interface temperature is equal to the liquidus temperature corresponding to the average actual melt composition leads to a reasonable melt temperature estimation for the long term. But this assumption leads to a significant over-estimation of the melt temperature at short term (< 1 hour). The 0D analysis suggests that for a short term, the interface temperature is below the liquidus and that the temperature difference with the liquidus depends on the heat flux. A relation has been proposed to approximate this temperature difference. The 1D calculation shows that the assumption of liquidus temperature corresponding to the local average boundary layer composition as local interface temperature is not sufficient to explain the short term discrepancy.

Conclusions in terms of prediction capability of 0D model

It is seen that the 0D model has a good capability of predicting concrete ablation, melt composition and average melt temperature evolution. This can be explained by the following statements:

- Concrete ablation is entirely controlled by power dissipation and thermal inertia of the melt;
- The interface temperature is mainly linked to the material properties while the properties of the melt are linked to the composition of the melt which is governed by concrete ablation.

Thus, the prediction of the evolution of the mass of ablated concrete, average melt temperature and average melt composition can be obtained with a simple 0D model. However, for the prediction of local ablation rates and evolution of the melt cavity shape, at least a 1D model is necessary.

Needs for future work

When two recirculation loops exist in the melt cavity as observed in ARTEMIS 10, due to the non-uniform composition distribution, the situation becomes more complicated and the introduced 1D model is not sufficient. While radial ablation of concrete is quite well described by this model, the axial ablation to the bottom of the melt cavity has not yet described. In the future, the model should be improved for describing the heat and mass transfer in a molten corium cavity with non-uniform composition distribution and non-uniform ablation in order to represent the two flow recirculation loops existing in ARTEMIS 10. In addition, formation of the cake due to deposition of refractory species observed experimentally in ARTEMIS 10 is not considered in the model. This point should be included in the future upgraded model.

It is noted that in ARTEMIS 10 and ARTEMIS 11, gas does not exist in the melt cavity (or only exist in a short period in the beginning of ARTEMIS 11). Therefore, the effect of gas on heat transfer in the melt cavity and on the liquid-solid interface conditions is not investigated in the framework of the thesis. Experimental data from another test in which the gas effect is clearer would be analysed for further study of gas sparging effect on MCCI.

REFERENCES

Al-Arabi M., Khamis M., Abd-Ul-Aziz M., Heat transfer by natural convection from the inside surface of a uniformly heated tube at different angles of inclination, International Journal of Heat and Mass Transfer, Vol. 34 (4,5) (1991), pp. 1019-1025.

Alvarez D., Analysis de la convection naturelle dans un fluide soumis a dissipation volumique de puissance, Note Technique CEA STT/STML/85-64-C, 1985.

Ananth R., Gill W.N., Self-consistent theory of dendritic growth with convection, Journal of Crystal Growth, Vol. 108 (1991), pp.173-189.

Asfia F.J., Dhir V.K., An experimental study of natural convection in a volumetrically heated spherical pool bounded on top with a rigid wall, Nuclear Engineering and Design, Vol.163 (3) (1996), pp. 333-348.

Asmolov V. G., Abalin S., Surenkov A., Gnidoi I., Strizhov V., Results of salt experiments performed during phase I of RASPLAV project, OECD RASPLAV Project, RP-TR-24, Kurchatov Institute, Russia, 1998.

Asmolov V.G., Strizhov V.F., Degaltsev Yu.G., RASPLAV Final Report – Behavior of the corium molten pool under external cooling, OECD RASPLAV Project, Russia, July 2000.

Bechta S.V., Khabensky V.B., Vitol S.A., Experimental studies of oxidic molten corium–vessel steel interaction, Nuclear Engineering and Design, Vol.210 (2001), pp. 193-224.

Bene O., Konings R.J.M., Wurzer S., Sierig M., Dockendorf A.M., A study of the NaNO3-KNO3 system using an innovative encapsulation technique, Thermochimica Acta, Vol.509 (1-2) (2010), pp. 62-66.

Berg J.C., Boudart M., Acrivos A., Natural convection in pools of evaporating liquids », Journal of Fluid Mechanics, Vol.24 (4) (1966), pp.721-735.

Bernaz L., Bonnet J.M., Seiler J.M., Investigation of natural convection heat transfer to the cooled top boundary layer of a heated pool, Proceedings of the Ninth International Topical Meeting on Nuclear Reactor Thermal-Hydraulics, NURETH-9, San Francisco, California, USA, October 3-8, 1999.

Bonnet J.M., An integral model for the calculation of heat flux distribution in a pool with internal heat generation, Proceedings of the Seventh International Topical Meeting on Nuclear Reactor Thermal-Hydraulics, NURETH7, New York, USA, September 10-15, 1995.

Bonnet J.M., Garré E., Présentation et synthèse des essays BALI-Configuration en cuve-Géométrie hémicylindrique", Note Technique CEA DRN/DTP/SETEX/LTEM/99-143, France, 1999.

Bonnet J.M., Seiler J.M., Thermal hydraulic phenomena in corium pools: the BALI experiment, Proceedings of the Seventh International Conference on Nuclear Engineering, ICONE-17, Tokyo, Japan, 1999.

Bonnet J.M., Seiler J.M., OECD RASPLAV Project: In-vessel corium pool thermalhydraulics for the bounding cases, Note Technique CEA SETEX/LTEM/01-247, France, 2001.

Bories J., Prat M., Transfert de chaleur dans les milieux poroux, Techniques de l'ingénieur, dossier B8250, 1995.

Bradley D.R., Gardner D.R., Brockmann J.E., Griffith R.O., CORCON-MOD3: an integrated computer model for analysis of molten core-concrete interactions, NUREG/CR-5843, USA, 1993.

Buck M., Burger M., Miassoedov A., Gaus-Liu X., Palagin A., Godin-Jacqmin L., Tran C.T., Ma W.M., Chudanov V., The LIVE Program: tests and joint interpretation within SARNET and ISTC, 3rd European Review Meeting on Severe Accident Research, ERMSAR-2008, Nesseber, Bulgaria, 2008.

Bui V.A., Dinh T.N., Sehgal B.R., In-Vessel Core Melt Pool Formation during Severe Accidents, Proceedings of the 1996 National Heat Transfer Conference, Session “Fundamental Phenomena in Severe Accidents”, Houston, Texas, USA, 1996.

Burton J.A., Prim R.C., Slichter W.P., The distribution of solute in crystals grown from the melt. Part I. Theoretical, Journal of Chemical Physics, Vol.11 (1953), pp. 1987-1991.

Cantor B., Vogel A., Dendritic solidification and fluid flow, Journal of Crystal Growth Vol. 41 (109) (1977).

Castaing B., Gunaratne G., Kadanoff L., Libchaber A., Thomae S., Wu X.Z., Zaleski S., Zanetti G., Scaling of hard thermal turbulentce in Rayleigh-Bénard convection, Journal of Fluid Mechanics, Vol. 204 (1989) pp.1-30.

Cenerino G., Cordfunke E.H.P, Hunterlaar M. E., Molten corium/concrete interaction and corium coolability. A state of the art report. Chapter 5. Fission product release during MCCI, Nuclear Science and Technology, European Commission, 1995.

Chavanne X., Etude du régime turbulent en convection de Rayleigh-Bénard dans l’hélium liquide ou gazeux autour de 5K, Thèse USM Grenoble, France, October 1997.

Chawla T.C., Chan S.H., Heat transfer from vertical/inclined boundaries of heat-generating boiling pools, Journal of Heat Transfer, Vol. 104 (1982), pp. 465-473.

Cheesewright R., Turbulent natural convection from a vertical plane surface, Journal of Heat Transfer (1968), pp. 1-8.

Chen T.S., Tien H.C., Armaly B.F., Natural convection on horizontal, inclined, and vertical plates with variable surface temperature or heat flux, International Journal of Heat and Mass Transfer, Vol. 29 (10) (1986), pp. 1465-1478.

Cheung F.B., Natural convection in a volumetrically heated fluid layer at high Rayleigh numbers, International Journal of Heat and Mass Transfer, Vol. 20 (1977), pp. 499-506.

Combeau H., Appolairea B., Seiler J.M., Interface temperature between solid and liquid corium in severe accident situations: A comprehensive study of characteristic time delay needed for reaching liquidus temperature, Nuclear Science and Engineering, Vol. 240 (8) (2010), pp. 1975-1985.

Coriell S.R., Hurle D.T.J., Sekerka R.F., Interface stability during crystal growth: The effect of stirring, Journal of Crystal Growth, Vol.32 (1976), pp. 1-7.

Cranga M., Fabianelli R., Jacq F., Barrachin M., Duval F., The MEDICIS code, a versatile tool for MCCI modeling, Proceedings of the Fifth International Congress on Advances in Nuclear Power Plants, ICAPP-05, Seoul, Korea, May 15-19, 2005.

Cranga M., Mun C., Michel B., Duval F., Barrachin M., Interpretation of real material 2D MCCI experiments in homogenous oxidic pool with the ASTEC/MEDICIS code, Proceedings of the Eighth International Congress on Advances in Nuclear Power Plants, ICAPP-08, Anaheim, California, USA, June 8-12, 2008.

Dauvois V., Lang J.P., Maillault C., Segregation de phases dans un corium en cours de refroidissement (Essais PHYTHER), Note technique DPE/SPCP/LEPCA/99-NT-001, France, 1999.

Delves R.T., Theory of stability of a solid-liquid interface during growth from stirred melts, Journal of Crystal Growth Vol. 3-4 (1968), pp. 562-568.

Eckert E.R.G., Jackson T.W., Analysis of turbulent free-convection boundary layer on flat plate, Report 1015, National Advisory Committee for Aeronautics, 1950.

Fan T.H., Cheung F.B., Modeling of Transient Turbulent Natural Convection in a Melt Layer With Solidification, Transactions of the ASME, Vol. 119 (1997), pp. 544-552.

Farmer M.T., Aeschlimann R.W., Kilsdonk D.J., Lomperski S., OECD MCCI Project - 2D Core Concrete Interaction (CCI) Tests: CCI-4 Quick Look Data Report, OECD/MCCI-2007-TR04, 2007.

Farmer M.T., Aeschlimann R.W., Kilsdonk D.J., Lomperski S., OECD MCCI Project - 2D Core Concrete Interaction (CCI) Tests: CCI-4 Final Report, OECD/MCCI-2007-TR06, 2007.

Farmer M.T., Kilsdonk D.J., Lomperski S., Aeschlimann R.W., OECD MCCI Project - 2D Core Concrete Interaction (CCI) Tests: CCI-5 Quick Look Data Report, OECD/MCCI-2008-TR07, 2008.

Farmer M.T., Lomperski S., Kilsdonk D.J., Aeschlimann R.W., OECD MCCI Project - 2D Core Concrete Interaction (CCI) Tests: CCI-2 Test Data Report - Thermal hydraulic Results, OECD/MCCI-2004-TR05, 2004.

Farmer M.T., Lomperski S., Kilsdonk D.J., Aeschlimann R.W., OECD MCCI Project - 2D Core Concrete Interaction (CCI) Tests: CCI-3 Test Data Report - Thermal hydraulic Results", OECD/MCCI-2005-TR04, 2005.

Farmer M.T., Lomperski S., Kilsdonk D.J., Aeschlimann R.W., OECD MCCI Project - 2D Core Concrete Interaction (CCI) Tests: Final Repor", OECD/MCCI-2005-TR05, 2006.

Farmer M.T., Modeling of ex-vessel corium coolability with the CORQUENCH code, Proceedings of the Ninth International Conference on Nuclear Engineering, ICONE-9, Nice, France, April 8–12, 2001.

Farmer M.T., Spencer B.W., Armstrong D.R., Kilsdonk D.J., Aeschlimann R.A., McUmber L.M., MACE Test M3b data report-Volume 1, MACE-TR-D13, EPRI TR-108806, 1997.

Fischer S., Zaloznik M., Seiler J.M., Rettenmayr M., Combeau H., Experimental verification of a model on melting and resolidification in a temperature gradient, Journal of Alloys and Compounds, Vol.540 (2012), pp. 85-88.

Foit J., Reimann M., Adroguer B., Cenerino G., Stiefel S., The WECHSL-Mod3 Code: a computer program for the interaction of a core melt with concrete including the long term behavior, Model description and User's manual, FZKA 5522, Germany, 1995.

Frantz B., Dhir D.K., Experimental investigation of natural convection in spherical segments of volumetrically heated pools, National Heat Transfer Conference, San Diego, USA, 1992.

Froment K., Seiler J.M., On the importance of a strong coupling between physico-chemistry and thermal hydraulics for modeling late phases of severe accidents in LWRs, Proceedings of the Ninth International Topical Meeting on Nuclear Reactor Thermal-Hydraulics, NURETH-9, San Francisco, California, USA, October 3-8, 1999.

Gabor J.D., Baker L., Cassulo J.C., Erskine D.J., Warner J.G., Heat transfer to curved surfaces from heating generating pools, ASME/AIChE 18th National Heat Transfer Conference, San Diego, California, USA, August 6-8, 1979.

Gabor J.D., Cassulo J.C., Ellison P.C., Heat transfer from internally heated hemispherical pool, National Heat Transfer Conference, Orlando, 1980.

Gaus-Liu X., Fluhrer B., Miassoedov A., Cron T., Foit J., Schmidt-Stiefel S., Wenz T., Results of the LIVE L3A Experiment, FZKA 7527, Forschungszentrum Karlsruhe, Germany, 2010.

Greene G.A., Jones O.C., Schwarz C.E., Abuaf N., Heat removal characteristics of volume heated boiling pools with inclined boundaries, NUREG/CR-1357, BNL-NUREG-51157, USA, 1980.

Guillaumé M., Combeau H., Seiler J.M., An improved interface model for molten corium–concrete interaction, Nuclear Engineering and Design, Vol.239 (6) (2009), pp. 1084-1094.

Gustavson R., Chen J.C., Kazimi M.S., Heat Transfer and Fluid Dynamic Characteristics of Internally Heated Boiling Pools, BNL-NUREG-50759, USA, 1977.

Helle M., Experimental COPO II data on natural convection in homogenous and stratified pools, Proceedings of the Ninth International Topical Meeting on Nuclear Reactor Thermal-Hydraulics, NURETH-9, San Francisco, USA,1999.

Helle M., Kylakainen O., Tuomisto H., Experimental data on heat flux distribution from a volumetrically heated pool with frozen boundaries, OECD/CSNI Workshop on In vessel core debris retention and coolability, Garching, Germany, 1998.

Hofmann P., Hagen S., Schanz G., Schumacher G., Sepold L., Chemical-physical behavior of LWR core components in severe reactor accidents, Proceedings of IAEA Technical Committee Meeting, Aix-en-Provence, France, 1992.

Hurle D.T.J., Interface stability during the solidification of a stirred binary-alloy melt, Journal of Crystal Growth, Vol.5 (1969), pp. 162-166.

Jahn M., Reineke H.H., Free convection heat transfer with internal heat sources calculations and measurements, Proceedings of the Fifth International Heat Conference, Tokyo, Japan, 1974.

Journeau C., Jegou C., Monerris J., Piluso P., Fromov K., Phase macrosegregation during the slow solidification of prototypic corium, Proceedings of the Tenth International Topical Meeting on Nuclear Reactor Thermal-Hydraulics, NURETH-10, Seoul, Korea, October 5-9, 2003.

Journeau C., Piluso P., Haquet J.F., Boccaccio E., Saldo V., Bonnet J.M., Malaval S., Carénini L., Brissonneau L., Two-dimensional interaction of oxidic corium with concretes: The VULCANO VB test series, Annals of Nuclear Energy, Vol. 36 (2009), pp. 1597-1613.

Kang K.H., Park R.J., Kim S.B., Sur K.Y., Cheung S.B., Rempe J.L., Simulant Melt Experiments for the Investigations of the In-vessel Core Catcher Performance during Severe Accidents, Proceedings of the of International Congress on Advances in Nuclear Power Plants, ICAPP-05, Seoul, Korea, May 2005.

Keyhani M., Kulacki F.A., Experiments on transient thermal convection with internal heat sources – Large time results, ASME Journal of Heat Transfer, Vol.105 (1983), pp. 261-266.

Kolb G., Theerthan S.A., Sehgal B.R., Experimental results of natural convection of stratified pool on SIMECO facility, RASPLAV Program Meeting, Madrid, Spain, 2009.

Kolb G., Theerthan S.A., Sehgal B.R., Experiments on in-vessel melt pool formation and convection with NaNO3-KNO3 salt mixture as melt simulant, Proceedings of the Eighth International Conference on Nuclear Engineering, ICONE-8, Baltimore, USA, 2000.

Kretzschmar F., Fluhrer B., Behavior of the melt pool in the power plenum of the Reactor Pressure Vessel - Review of experimental programs and background of the LIVE Program, Report FZKA 7382, Forschungszentrum Karlsruhe, Germany, 2008.

Krishnamurti R., On the transition to turbulent convection, Journal of Fluid Mechanics, Vol. 42 (2) (1970), pp. 295-320.

Kulacki F.A., Emara A.A., Steady and transient thermal convection in a fluid layer with uniform volumetric energy sources, Journal of Fluid Mechanics, Vol.83 (1977), pp. 375-395.

Kymäläinen O., Tuomisto H., Hongisto O., Theofanous T. G., Heat flux distribution from a volumetrically heated pool with high Rayleigh number, Nuclear Engineering and Design, Vol.149 (1994), pp. 401-408.

Lapwood E.R., Convection of a fluid in a porous medium, Proceedings of The Cambridge Philosophical Society, Vol. 44 (1948), pp. 508-512.

Levin E.M., Robbins C.R., McMurdie H.F, Phase diagram for ceramists_Vol. 1: Oxides and salts, American Ceramic Society, ISBN-10:0916094049, 1985.

Lipton J., Kurz W., and Trivedi R., Rapid dendrite growth in undercooled alloys, Acta Metall, Vol 35 (4) (1987), pp. 957-964.

Manneville P., Rayleigh-Bénard convection, thirty years of experimental, theoretical and modeling work, Journée Henri Bénard, ESPCI, France, 2001.

Mayinger F., Jahn. M., Reineke H.H., Steinberner U., Examination of thermal hydraulic processes and heat transfer in a core melt, Report BMFT RS 48/1, Hanover, Germany, 1976.

McAdams W.H., Heat Transmission, 3rd Edition, New York: McGraw Hill, 1954.

Miassoedov A., Cron T., Foit J., Gaus-Liu X., Schmidt-Stiefel S., Wenz T., LIVE experiments on melt behavior in the RPV lower head, Proceedings of the Sixteenth International Conference on Nuclear Engineering, ICONE16, Orlando, Florida, USA, 2008.

Michel B., Cranga M., Interpretation and calculation for the first series of tests for the ARTEMIS program (Corium-Concrete interaction with simulating materials), Note IRSN, France, 2008.

Mullins W. W., Sekerka R. F., Stability of a planar interface during solidification of a dilute binary alloy, Journal of Applied Physics, Vol.35 (1964), pp. 444-452.

Nie M., Fischer M., Advanced MCCI Modeling Based on Stringent Coupling of Thermal Hydraulics and Real Solution Thermo-chemistry in COSACO, Proceedings of Tenth International Conference on Nuclear Engineering, ICONE-10, Arlington, VA, April 14–18, 2002.

Ostrach S., An analysis of laminar free-convection flow and heat transfer about a flat plate parallel to the direction of a generating body force, Report 1111, National Advisory Committee for Aeronautics, 1952.

Park R.J., Choi S.M., Kim S.B., Kim H.D., Natural convection heat transfer with crust formation in the molten metal pool, Nuclear Technology, Vol.127 (1) (1999), pp. 66-80.

Rohsenow W.M., Hartnett J.P., Cho Y.I., Handbook of heat transfer, 1998, pp.5-6.

Roux P., Fichot F., De Pierrepont S., Modelling of binary mixture phase change: assessment on RASPLAV-SALT experiments, Proceedings of the Eleventh International Topical Meeting on Nuclear Reactor Thermal-hydraulics, NURETH-11, Avignon, France, 2005.

Rutter J.W., Chalmers B., A prismatic substructure formed during solidification of metals, Canadian Journal of Physics, Vol. 31 (1953), pp. 15-39.

Schlichting H., Boundary layer theory, 1955, pp.602.

Seiler J.M., Analysis of test 55-59 and 60 from fourth series of RASPLAV salt tests, Note technique CEA SETEX/LTEM/98-85, 1998.

Seiler J.M., Fouquet A., Froment K., Defoort F., Theoretical analysis for corium pool with miscibility gap, Nuclear Technology, Vol.141 (3) (2003), pp. 233-243.

Seiler J.M., Froment K., Material effects on multiphase phenomena in late phases of severe accidents of nuclear reactors, Multiphase Science and Technology, Vol.12 (2) (2000), pp. 217-257.

Seiler J.M., Model simplifié de calcul de distribution de flux en conditions aux limites d'un bain de corium soumis a un dégagement volumique de puissance, Note Technique CEA, STR/LETC/92-60, CEA Grenoble, France, 1992.

Seiler J.M., Phase segregation model and molten pool thermal-hydraulics during MCCI, Nuclear Engineering and Design, Vol.166 (2) (1996), pp. 259-267.

Seiler J.M., Tourniaire B., Mise à jour de l'Analyse phénoménologique de l'interaction corium-béton, apport des experiences ARTEMIS, Note technique CEA DTN/SE2T/LPTM/2008-268, Grenoble, France, 2008.

Sparrow E.M., Husar R.B., Goldstein R.J., Observations and other characteristics of thermals, Jounal of Fluid Mechanics, Vol. 41 (1970), pp.793-800.

Spindler B., Tourniaire B., Seiler J.M., Simulation of MCCI with the TOLBIAC-ICB code based on the phase segregation model, Nuclear Engineering and Design, Vol.236 (2006), pp. 2264 – 2270.

Spindler B., Veteau J.M., Molten corium concrete interaction: post-calculations of 1D ARTEMIS tests with the TOLBIAC-ICB Code, Proceedings of the Sixth International Congress on Advances in Nuclear Power Plants - ICAPP-06, Reno – Nevada, USA, June 4-8, 2006.

Steinberner U., Reineke H.H., Turbulent buoyancy convection heat transfer with internal heat source, Proceedings of the Sixth International Heat Transfer Conference, Toronto, Canada, Vol.2 (21) (1978), pp. 305-311.

Stepanyan A.V., Nayak. A.K., Sehgal B.R., Experimental investigations of natural convection in three layer stratified pool with internal heat generation, Proceedings of the Eleventh International Topical Meeting on Nuclear Reactor Thermal-Hydraulics, NURETH-11, Avignon 23-28, 2005.

Stewart W.E., Lightfoot E.N., Transport Phenomena, R.B. Bird, 1960, pp.155.

Theofanous T.G., Angelini S., Natural convection for in-vessel retention at prototypic Rayleigh numbers, Nuclear Engineering and Design, Vol.200 (2000) pp.1-9.

Theofanous T.G., Liu C., Additon S., Angelini S., Kymäläinen O., Salmassi T., In-vessel coolability and retention of a core melt, Report DOE/ID-10460, Vol.11 (Chapter 5), USA, 1995.

Theofanous T.G., Maguire M., Angelini S., Salmassi T., The first results from the ACOPO experiment, Proceedings of International Topical Meeting on Probabilistic Safety Assessment (PSA ’96), 1996, pp. 1343-1350.

Theofanous T.G., Maguire M., Angelini S., Salmassi T., The first results from the ACOPO experiment, Nuclear Engineering and Design, Vol.169 (1997).

Thomson D.H., Farmer M.T., Fink J., Armstrong D.R., Spencer B.W., Compilation, Analysis and Interpretation of ACE Phase C and MACE Experiment Experimental Data-Volume 1: MCCI Thermal hydraulic Results, ACEX TR-C-14, 1997.

Thomson D.H., Fink J., Advanced Containment Experiments, ACE MCCI Test L5: Test data report, ACE-TR-C7, 1988.

Tiller W.A., Jackson K.A., Rutter J.W., Chalmers B., The redistribution of solute atoms during the solidification of metals, ActaMetallurgica, Vol. l (1953), pp. 428-437.

Tran T.C., Kudinov P., Dinh T.N., An approach to numerical simulation and analysis of molten corium coolability in a boiling water reactor lower head, Experiments and CFD code applications to Nuclear Reactor Safety, OECD/NEA & IAEA Workshop, Grenoble, France, 2008.

Vandroux-Koenig S., Seiler J.M., Spindler B., Frédéric G., Froment K., Simulation of ACE and MACE experiments with a phase segregation model using the TOLBIAC code, OECD Workshop on Ex-Vessel Debris Coolability, Karlsruhe, Germany, November 15-18, 1999.

Vandroux-Koenig S., Spindler B., Moreau G.M., Pelisson R., TOLBIAC version 4.2: code description, Note technique CEA SMTH/LM2-99-36, Grenoble, France, 1999.

Veteau J.M., ARTEMIS program: Investigation of MCCI by means of simulating material experiments, Proceedings of the Sixth International Congress on Advances in Nuclear Power Plants, ICAPP-06, Reno – Nevada, USA, June 4-8, 2006.

Zaleski S., Boundary layer stability and heat flux in Rayleigh-Bénard experiments, Comptes Rendus de l’Académie des Sciences, Serie II, Vol.10 (1991), pp. 1099-1103.

Zhang X., Tian J., Xu K., Gao Y., Thermodynamic Evaluation of Phase Equilibria in NaNO3-KNO3 System, Journal of Phase Equilibria, Vol. 24 (5) (2003), pp. 441-446.

Zuber N., Findlay J.A., Average volumetric concentration in two phase flow systems, Journal of Heat Transfer, Vol. 87 (1965), pp. 453-467.

Appendix 1. Transformation of Nusselt correlation from internal Rayleigh into external Rayleigh

In order to determine the heat flux transferred from a hemispherical cavity containing liquid melt, it is needed to evaluate Nusselt number (Nu). In fact, Nu can be written in terms of either internal Rayleigh number ($Ra_{in} = \frac{g\,\beta_T\,H^5\,\dot{Q}_v}{\alpha\,\lambda_{bulk}\,\upsilon}$) or external Rayleigh number ($Ra_{ex} = \frac{g\,\beta_T\,\Delta T_{bulk,\max}\,H^3}{\alpha\,\upsilon}$) where g is the gravitational acceleration; α, β_T, ν, λ_{bulk} are respectively the thermal diffusivity, thermal expansion coefficient, kinematic viscosity and thermal conductivity of the melt; H is the height of the melt cavity, $\Delta T_{bulk,max}$ is the difference between the maximum melt temperature ($T_{bulk,max}$) in the melt cavity and the liquid-solid interface temperature (T_i) and $\dot{Q}_v$ is the volumetric power dissipation in the melt cavity.

For the purpose of evaluating the transient evolution of melt temperature, it is more practical to use external Rayleigh number for the Nusselt correlation for the calculation of the variation of average heat transfer coefficient versus time and temperature difference ($\Delta T_{bulk,\max} = T_{bulk,\max} - T_i$). However, there exist in literature numbers of Nusselt correlation which are written in terms of internal Rayleigh number. These correlations are only valid for established thermal-hydraulics steady state.

When the heat loss from the melt cavity to its upper surface is negligible, the heat flux transferred through the lateral wall of the hemispherical melt cavity in steady state (φ_{stt}) is given by:

$$\varphi_{stt} = \frac{\dot{Q}_v\,V_{cavity}}{S_{lateral}} = \frac{\dot{Q}_v\,\frac{1}{3}\pi H^2\,(3R-H)}{2\pi R H} = \frac{\dot{Q}_v\,H\,(3R-H)}{6R} \qquad \text{(A-1-1)}$$

in which $\dot{Q}_v$ is the volumetric power dissipation in the melt cavity, R, H, $S_{lateral}$ and V_{cavity} are respectively the radius, the height, the interfacial area and the volume of the melt cavity.

The average heat flux ($\overline{\varphi}$) can be also expressed in terms of the average heat transfer coefficient ($\overline{h}_{bulk}$) and the average temperature difference between the melt and the interface (ΔT_{bulk}), i.e:

$$\overline{\varphi} = \overline{h}_{bulk}\,\Delta T_{bulk} \Rightarrow \Delta T_{bulk} = \frac{\overline{\varphi}}{\overline{h}_{bulk}} = \frac{\varphi_{stt}}{\overline{h}_{bulk}} \qquad \text{(A-1-2)}$$

Therefore,

$$\Delta T_{bulk} = \frac{\dot{Q}_v\,H\,(3R-H)}{6R\,\overline{h}_{bulk}} \qquad \text{(A-1-3)}$$

The average heat transfer coefficient $\overline{h}_{bulk}$ is calculated as:

$$\bar{h}_{bulk} = \frac{\lambda_{bulk}\ Nu}{H} \tag{A-1-4}$$

From Equations (A-1-1), (A-1-2), (A-1-3) and (A-1-4) we have:

$$\Delta T_{bulk} = \frac{\dot{Q}_v\ H^2\ (3R - H)}{6R\ \lambda_{bulk}\ Nu} = \frac{\frac{1}{6}\dot{Q}_v\ H^2 (3 - \frac{H}{R})}{\lambda_{bulk}\ Nu} \tag{A-1-5}$$

Applying Equation (A-1-5) in the expression of external Rayleigh number leads to:

$$Ra_{ex} = \frac{g\ \beta_T\ H^3 \Delta T_{bulk}}{\nu\ \alpha} = \frac{g\ \beta_T\ H^3}{\nu\ \alpha} \frac{\frac{1}{6}\dot{Q}_v H^2 (3 - \frac{H}{R})}{\lambda_{bulk}\ Nu} = \frac{g\ \beta_T\ \dot{Q}_v\ H^5}{\lambda_{bulk}\ \nu\ \alpha} \frac{\frac{1}{6}(3 - \frac{H}{R})}{Nu} \tag{A-1-6}$$

or

$$Ra_{ex} = \frac{1}{6\,Nu}(3 - \frac{H}{R}) Ra_{in} \tag{A-1-7}$$

The Nusselt number is now obtained as:

$$Nu = a' Ra_{in}^{\ b'} = a' \left(\frac{6}{3 - \frac{H}{R}} \right)^{b'} Nu^{b'}\ Ra_{ex}^{\ b'} \tag{A-1-8}$$

$$Nu^{1-b'} = a' \left(\frac{6}{3 - \frac{H}{R}} \right)^{b'} Ra_{ex}^{\ b'} \Rightarrow Nu = a'^{\frac{1}{1-b'}} \left(\frac{6}{3 - \frac{H}{R}} \right)^{\frac{b'}{1-b'}} Ra_{ex}^{\frac{b'}{1-b'}} \tag{A-1-9}$$

Now, Nusselt is written in terms of both internal and external Rayleigh numbers, as follows:

$$Nu = a' Ra_{in}^{\ b'} = a Ra_{ex}^{\ b} \tag{A-1-10}$$

wherein:

$$a = a'^{\frac{1}{1-b'}} \left(\frac{6}{3 - \frac{H}{R}} \right)^{\frac{b'}{1-b'}} \text{ and } b = \frac{b'}{1 - b'} \tag{A-1-11}$$

Appendix 2. Gas flow path in porous medium

In ARTEMIS experiment, gas is injected into a porous concrete cavity. Knowing the permeability of the porous medium allows characterization of the gas distribution and the gas flow path as well.

The gas velocity in a 1D porous concrete is calculated by Darcy's law as follows:

$$j_{gas} = \frac{K_{concrete}}{\mu_{gas}} \frac{\Delta P}{L} \tag{A-2-1}$$

or:

$$\Delta P = \frac{\mu_{gas}\ j_{gas}\ L}{K_{concrete}} \tag{A-2-2}$$

in which j_{gas} is the superficial gas velocity injected into the test section (m.s-1), $K_{concrete}$ (m2) and μ_{gas} (Pa.s) are respectively the permeability and the dynamic viscosity of gas, ΔP is the pressure drop and L is the thickness of the porous concrete layer.

In TRIO the pressure drop is given by:

$$\Delta P = F \frac{L}{D_h} \frac{1}{2} \rho_{gas}\ j_{gas}^2 \tag{A-2-3}$$

in which D_h is the hydraulic diameter (the size of the pores in the porous concrete layer), ρ_{gas} is the density of the gas and F is the pressure factor, which can be expressed in terms of Reynolds number as follows:

$$F = \frac{A}{\mathrm{Re}^B} \tag{A-2-4}$$

For laminar regime, B = 1. Therefore

$$\Delta P = \frac{A}{\mathrm{Re}} \frac{L}{D_h} \frac{1}{2} \rho_{gas}\ j_{gas}^2 \tag{A-2-5}$$

or

$$\Delta P = \frac{A \mu_{gas}\ L\ j_{gas}}{2\, D_h^2} \tag{A-2-6}$$

Then:

$$\Delta P = \frac{A \mu_{gas}\ L\ j_{gas}}{2\, D_h^2} = \frac{\mu_{gas}\ j_{gas}\ L}{K_{concrete}} \tag{A-2-7}$$

and

$$A = \frac{2\,D_h^2}{K_{concrete}} \qquad \text{(A-2-8)}$$

In ARTEMIS 1D pretest, a measurement of pressure drop in the porous concrete medium was carried out. The pressure drop along a system composed of a concrete layer deposited on the surface of a graphite plate was measured. The concrete layer has 30 cm thickness. Gas is injected from the bottom (Figure A-2-1). The superficial velocity of the gas is 3.14 cm/s. The pressure drop along the graphite plate alone was about 890 mb while the pressure drop along the combined section of graphite plate and porous concrete was 1700 mb. Therefore, the pressure drop across the concrete layer was about 810 mb.

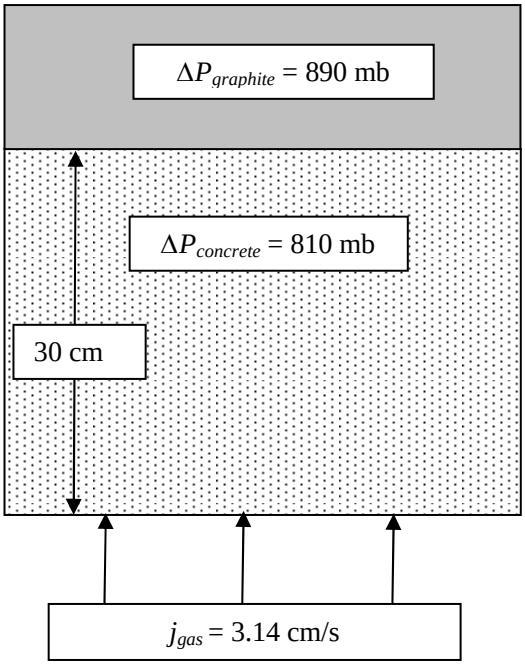

Figure A-2-1. Test section for pressure drop measurement in ARTEMIS 1D pretest.

In order to obtain $\Delta P_{concrete} \approx 810$ mb as measured in the pretest, with $\mu_{gas} = 2\ 10^{-5}$ Pa.s, $D_h = 5.10^{-5}$ m, L = 30 cm, j_{gas} = 3.14 cm/s, the value of A will be about 2300.

Calculation by TRIO code with A = 2300 provides the pressure drop in the concrete layer of 810 mb which is in agreement with the measured one in the pretest. Therefore, A = 2300 will be applied as a reference value for the calculation of pressure drop in the porous concrete in ARTEMIS 2D.

The first calculation has been performed with A = 2300 for the same configuration as in ARTEMIS 11. The concrete cavity has 40 cm radius and 45 cm height. At the centre of the concrete cavity, there is a cylindrical cavity (15 cm radius and 33 cm height) representing the melt cavity as in ARTEMIS 11 (Figure A-2-2).

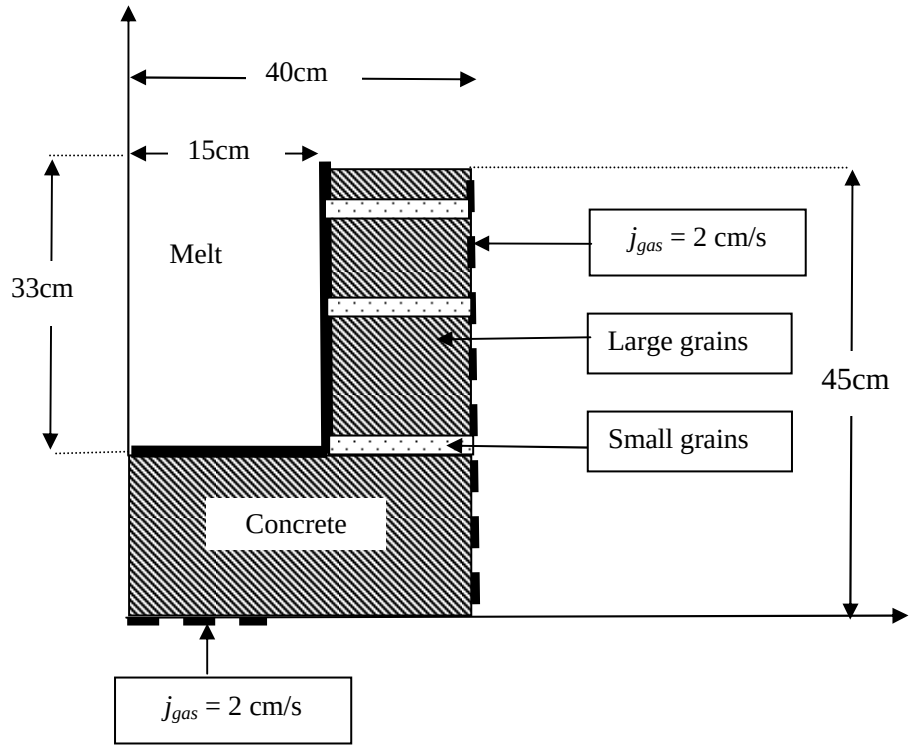

Figure A-2-2. Configuration for 2D pressure drop calculation by TRIO code.

It is noted that in ARTEMIS 2D, the permeability of the porous concrete is not uniform. In the lateral wall of the concrete cavity, there are three layers containing finer concrete grains with smaller size of pore. Each layer is 1 cm thick and is located at 10 cm, 24 cm and 34 cm from the bottom of the concrete cavity. Gas is injected from the bottom and from the lateral walls of the porous concrete cavity between the three layers with small size concrete grains and through the bottom. The average superficial gas velocity at the central cavity interface is 2 cm/s.

The gas velocity field in the concrete cavity is shown in Figure A-2-3. It is seen that gas can enter the melt cavity from the horizontal and vertical interfaces.

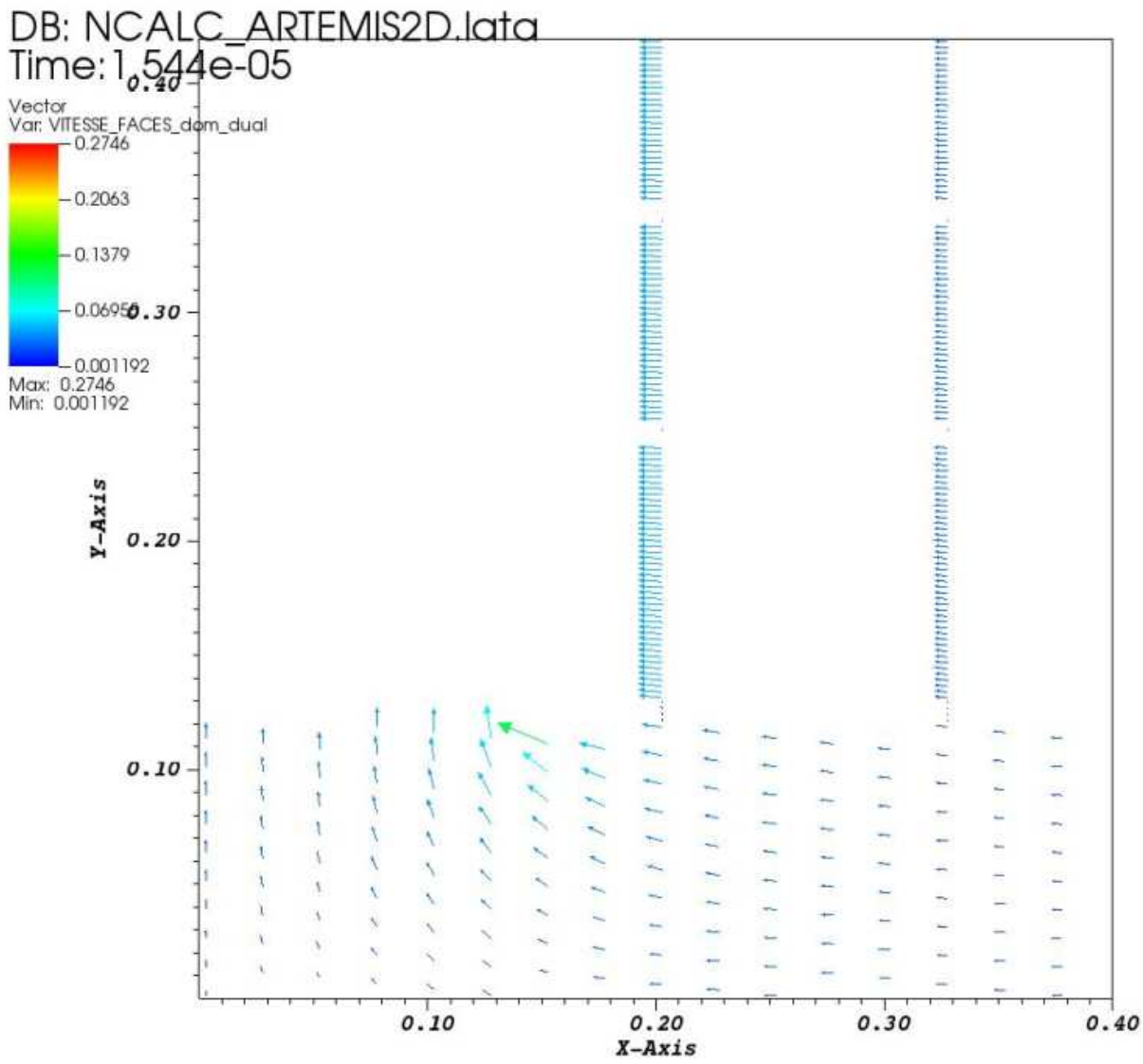

Figure A-2-3. Velocity field of gas in the concrete cavity in ARTEMIS 2D.

The superficial gas velocities, provided by the TRIO code for A = 2300, are shown in Figure A-2-4 and Figure A-2-5. On the horizontal interface, the gas enters the melt cavity with a superficial velocity ranging from 0.013 m/s (at 3 cm from the melt cavity axis) to 0.47 m/s (at the melt cavity lateral wall, i.e. 15 cm from the melt cavity axis. At the bottom interface near the lateral wall of the melt cavity, the superficial gas velocity is even higher than the expected one.

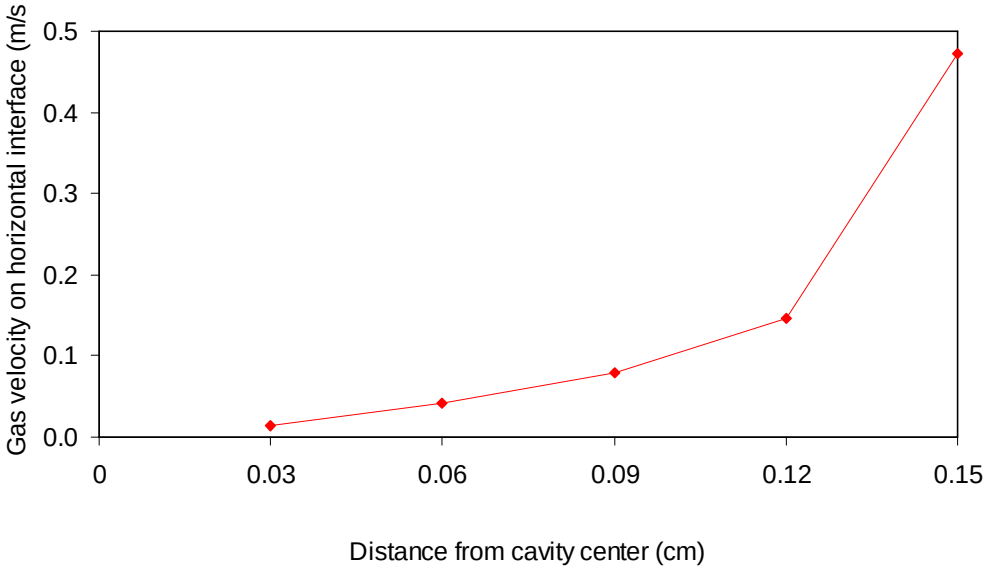

Figure A-2-4. Superficial gas velocity on horizontal interface for ARTEMIS 2D.

On the vertical interface, the gas flows through the three layers with small grains with very small superficial velocity (less than 0.01 m/s). In the region with larger size grains, the mean superficial velocity at the cavity interface is about 0.02 m/s which is the intended value.

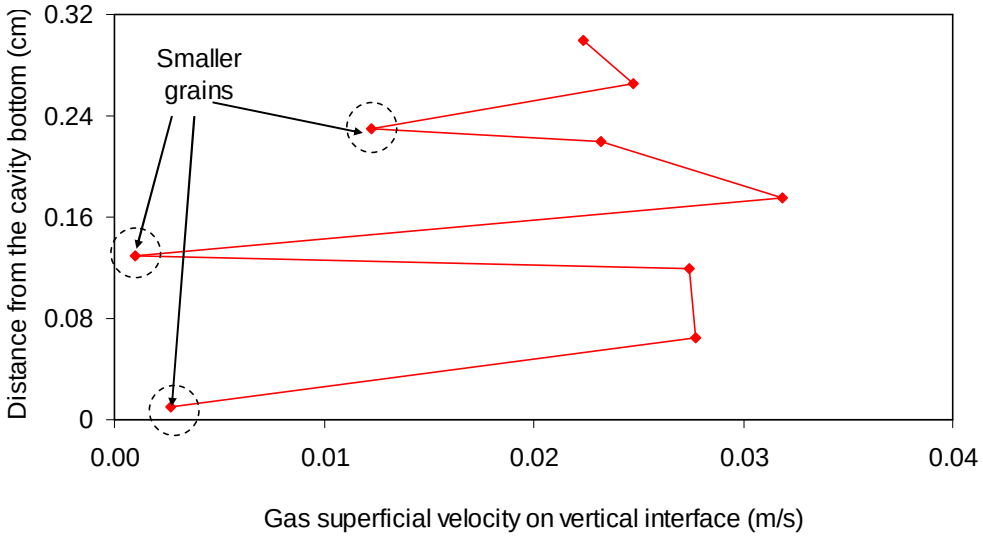

Figure A-2-5. Superficial gas velocity on vertical interface for ARTEMIS 2D.

In fact, in ARTEMIS 11, the existence of gas in the melt cavity during the first 20 minutes from the test beginning has been observed by a flat temperature gradient in the melt cavity during this period and void fraction measurement. Since the temperature gradient in the melt cavity is no more flat after 20 minutes, it seems that there is less or no more gas in the melt cavity.

The flow of the gas is closely dependent on the permeability of the porous concrete. When there is no more gas in the melt cavity, it could mean that there might be an increase of the permeability of the concrete. As consequences, the gas flow may by-pass the melt cavity. This could be related to the formation of numbers of cracks inside the porous concrete due to the thermal expansion of concrete at high temperature. Another possibility is that the porous concrete interface might plug.

To analyse the potential consequences of above assumptions, calculations have been performed for increased permeability of the porous concrete. To have a 10 time higher permeability of the concrete, coefficient *A* has been divided by 10, i.e. *A* = 230. The calculation with *A* = 230 exhibits that the gas still flows through the melt cavity (Figure A-2-6 and Figure A-2-7 and Figure A-2-8). If A is divided by 100 (i.e. *A* = 23), the gas will by-pass to the top of the melt cavity (Figure A-2-6, Figure A-2-7 and Figure A-2-9).

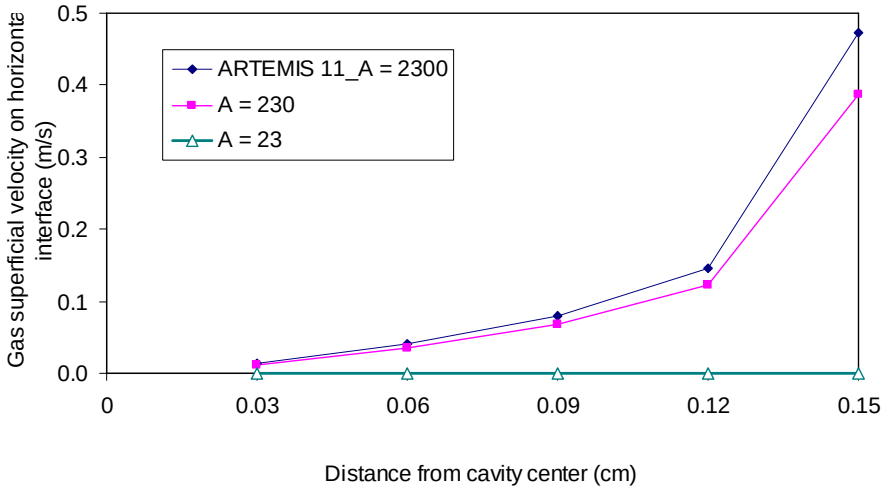

Figure A-2-6. Superficial gas velocity on horizontal interface for different coefficients A.

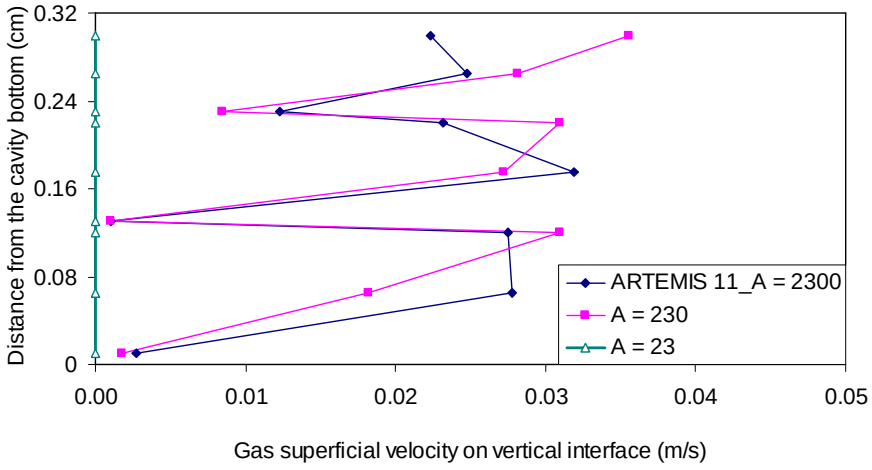

Figure A-2-7. Superficial gas velocity on vertical interface for different coefficients A.

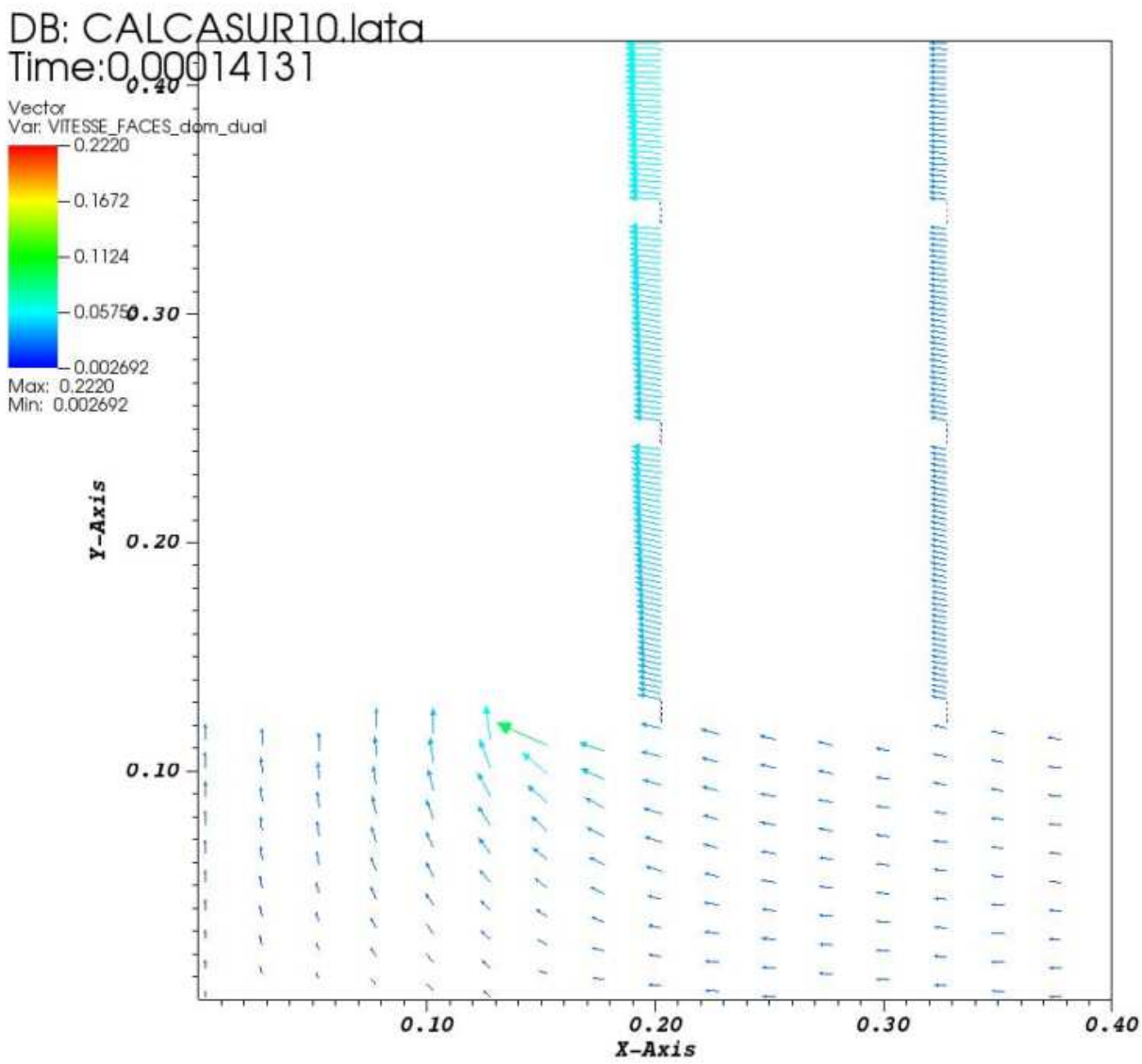

Figure A-2-8. Gas velocity field in concrete cavity with A = 230.

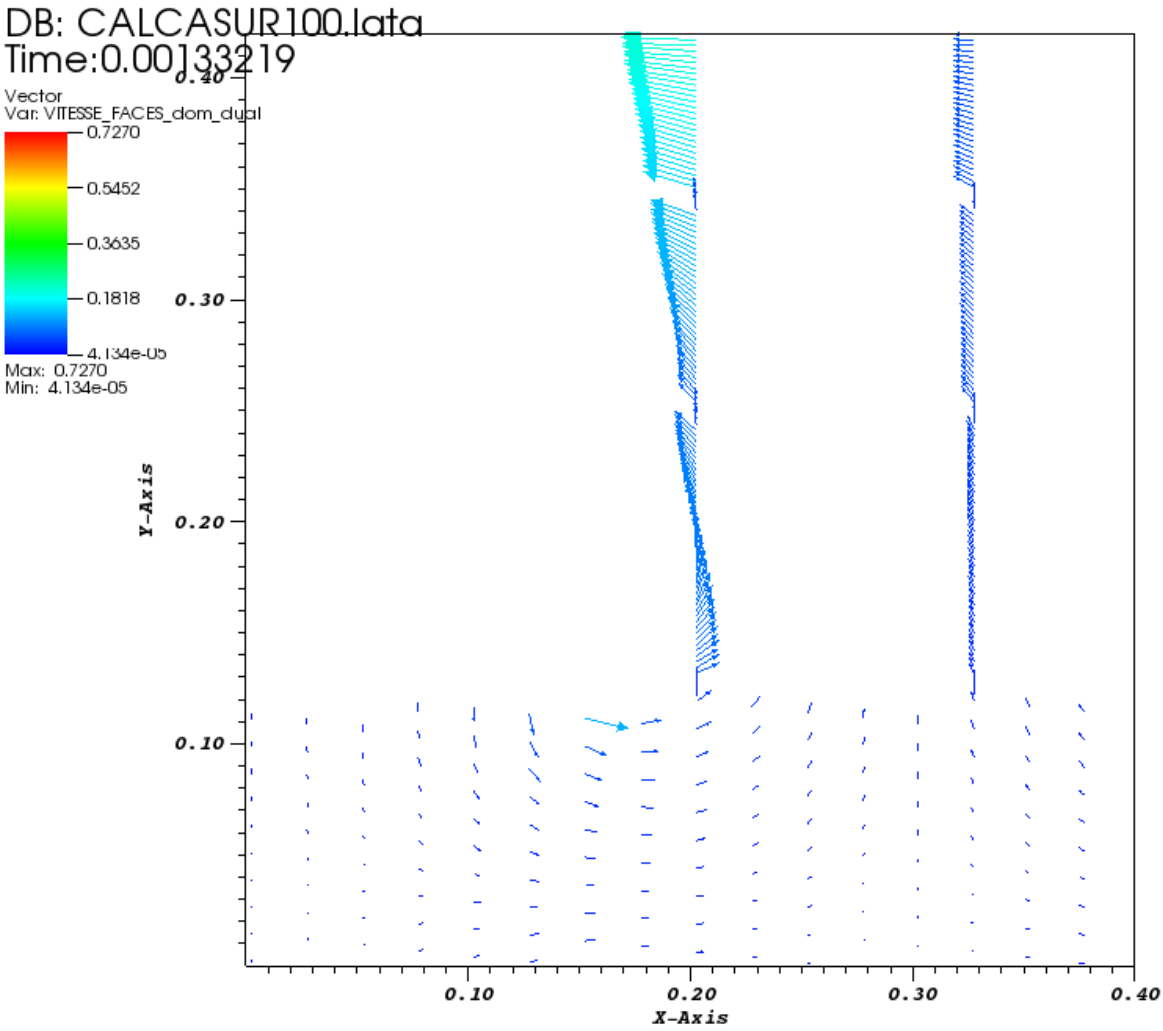

Figure A-2-9. Gas velocity field in concrete cavity with A = 23.

Appendix 3. Natural convection calculation by TRIO code

TRIO code has been used for the calculation of liquid natural convection in a cylindrical configuration with the same dimension as in ARTEMIS 11 (t > 17 minutes) to see the transient effect and the distribution of the melt temperature and to have a better understanding of the heat transfer mechanism The aim is to look at the behaviour of a heated melt in terms of temperature evolution and temperature distribution if natural convection is assumed to be the main heat transfer mechanism.

The calculation with TRIO code has been done for a cylindrical cavity with 15 cm radius and 33 cm height. Two heating elements 7.8 cm in height are located inside the cavity at the level of 6.2 to 14 cm from the cavity bottom and between 10 and 12 cm in diameter. Each heating element has 2 cm width. The total power dissipation from the heating elements is 6000 W (Figure A-3-1).

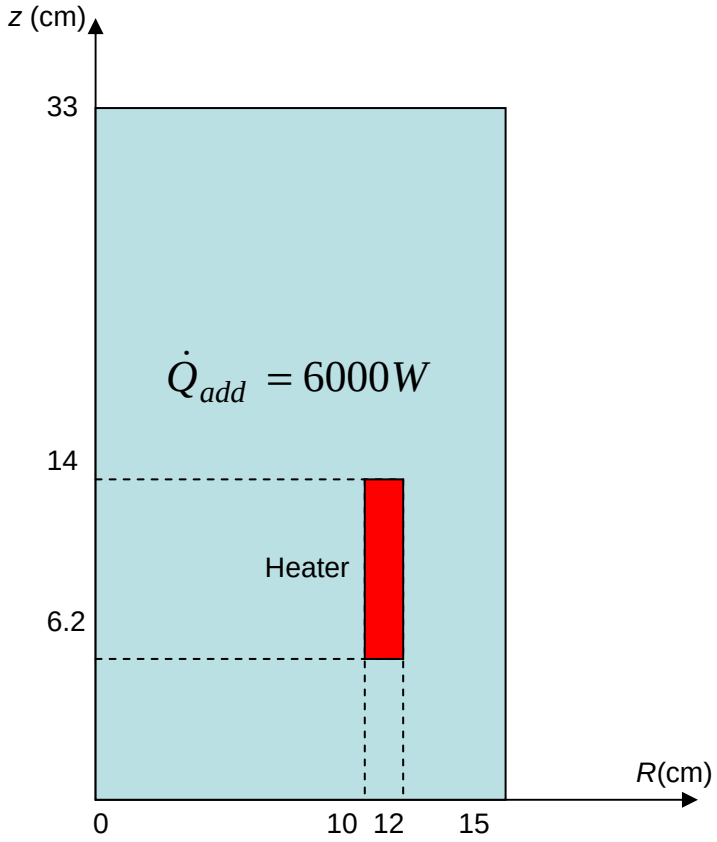

Figure A-3-1. Configuration for natural convection calculation by TRIO.

The initial conditions are at uniform bulk temperature in the melt cavity, T_{bulk} = 537 °C, the lateral and bottom wall temperature is taken as the melting temperature of the concrete, i.e. $T_i = T_{melt}$ = 522 °C and the power dissipation in the heated zone of the melt cavity is $\dot{Q}_{add}$ = 6000W. The heat flux on the top surface is equal to zero. Material properties correspond to molten eutectic.

The calculating results given by TRIO are as follows:

- At steady state, $\Delta T_{bulk,\ TRIO}$ = 51 °C which is only 20% higher than $\Delta T_{bulk,\ ARTEMIS111}$ (42 °C);

- The melt temperature reaches steady state (573 ^{o}C) after 800 s (13 minutes), i.e. faster in ARTEMIS 11 (23 minutes);
- The radial temperature gradient in the melt cavity is flat (except in the boundary layer region of 3 ~ 5 mm from the lateral wall) and the axial temperature gradient is linear in the heated zone (increases gradually from 522 ^{o}C at the bottom interface of the cavity up to 573 ^{o}C at the top of the heated zone);
- The average flow velocity on cavity axis is U_{bulk} = 8.4 10^{-4} m/s.

Evolutions of melt temperatures at different cavity elevations calculated by TRIO code is shown in Figure A-3-2.

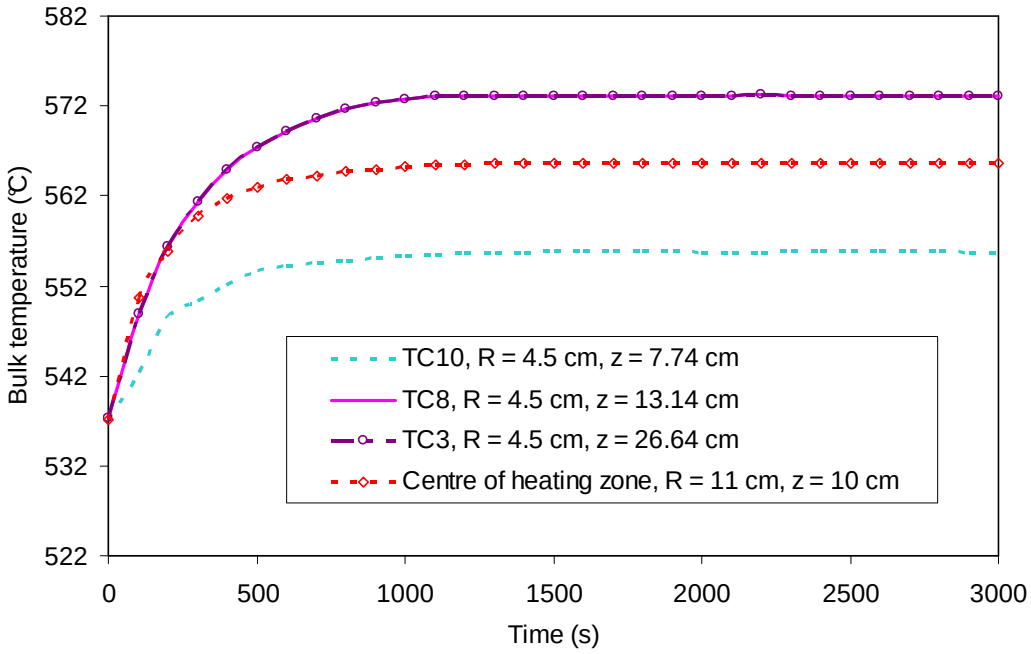

Figure A-3-2. Transient evolution of bulk temperature at different cavity elevations from TRIO calculation.

Figure A-3-3 and Figure A-3-4 show the temperature field in the cavity at t = 400 s and at steady state t = 800 s. A temperature stratification is clearly observed.

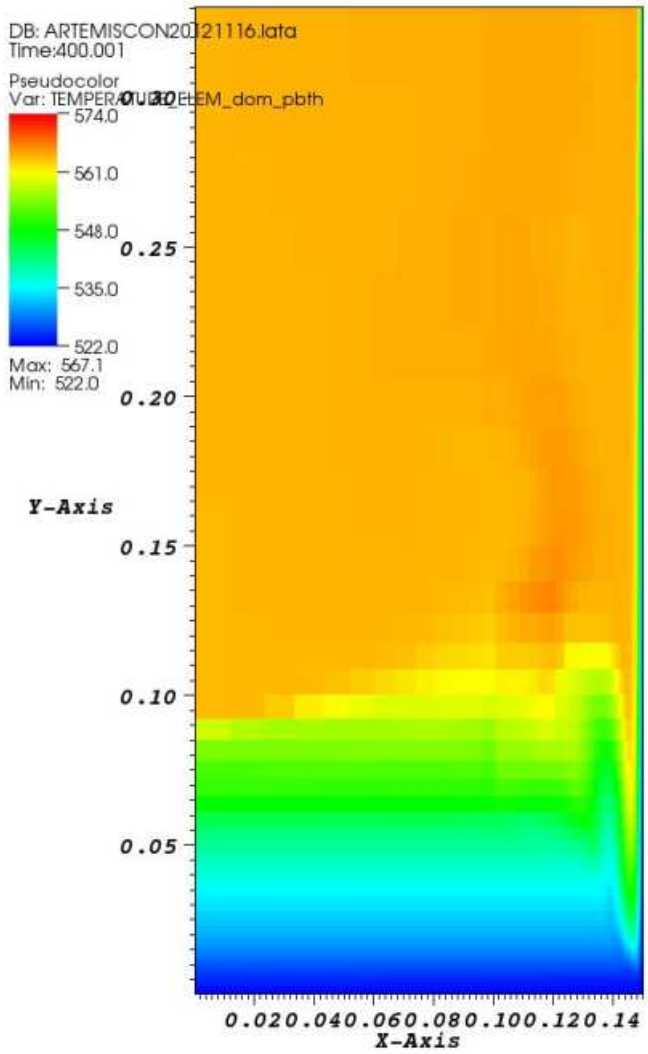

Figure A-3-3. Temperature distribution in the cavity at t = 400 s (transient).

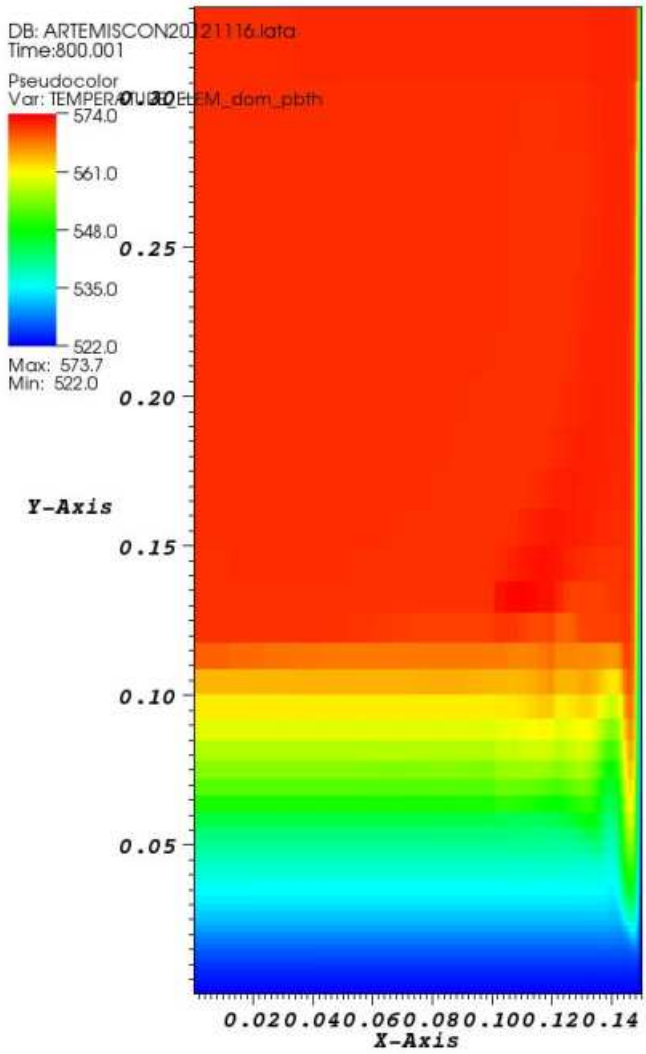

Figure A-3-4. Temperature distribution in the cavity at t = 800 s (steady state).

The steady state radial temperature distributions for three different cavity elevations are illustrated in Figure A-3-5. A boundary layer is observed near the lateral wall with a thickness of approximately 5 mm. In this boundary layer region, an important temperature gradient is seen. Inside the heated region and in its vicinity, there is a small temperature gradient but near the cavity axis (in the region where $R < 8$ cm), the temperature is uniform.

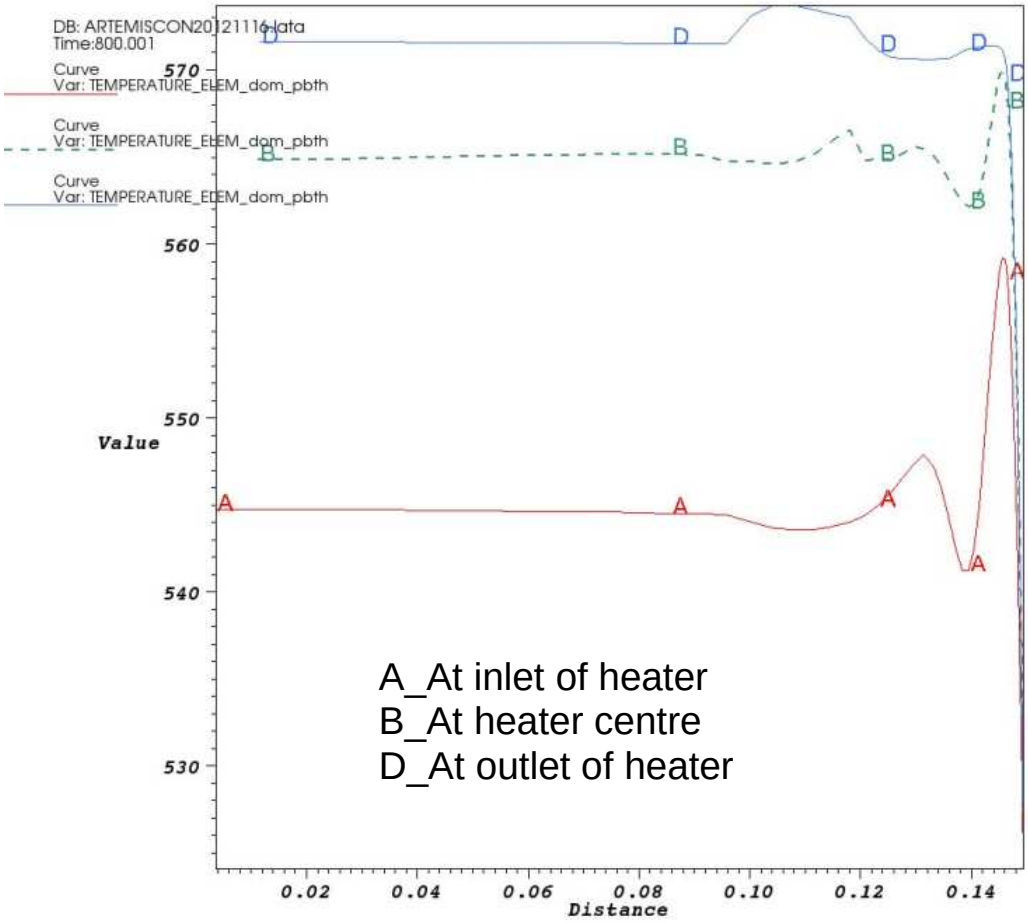

Figure A-3-5. Steady state radial temperature distribution in the cavity.

The axial temperature gradient in the cavity in steady state is depicted in Figure A-3-6 at two distances from the axis of the cavity (inside and outside of heater).

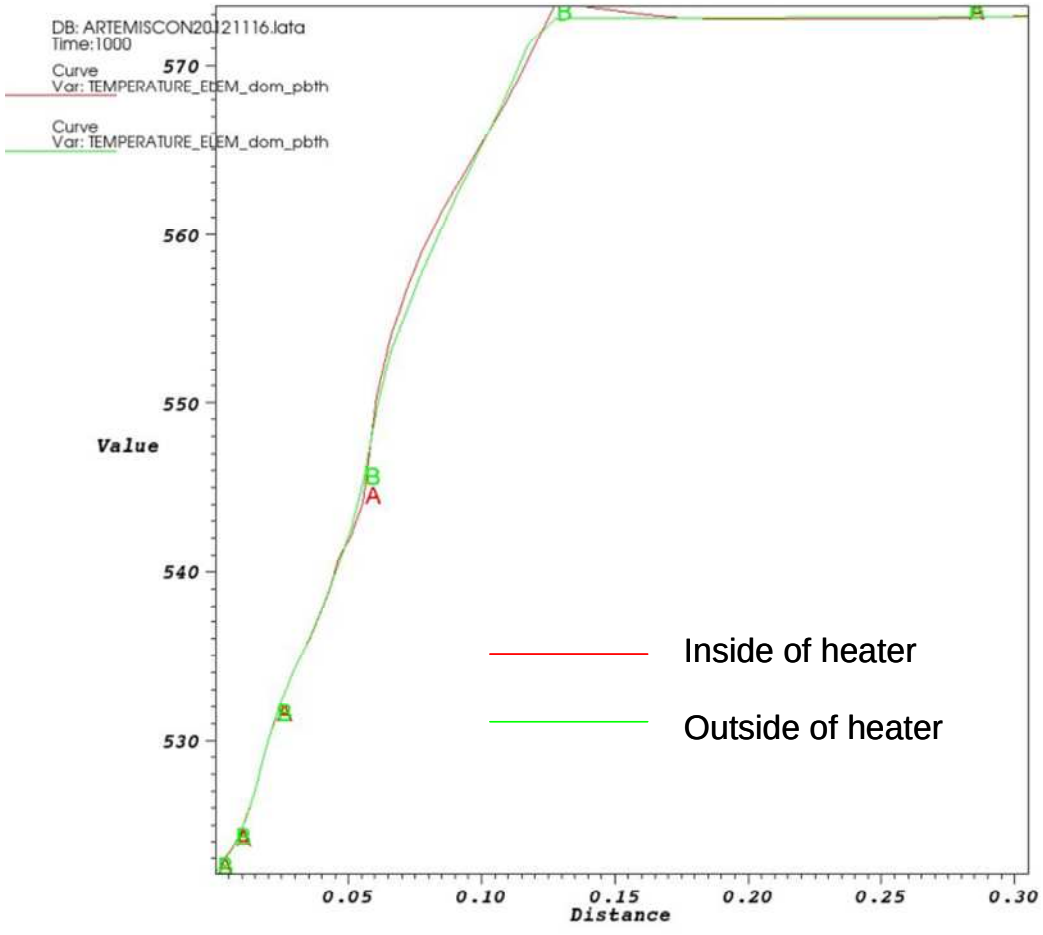

The

Figure A-3-6. Steady state axial temperature distribution in the cavity.

Important conclusions from these calculations are:

- The assumption of natural convection after time 17 minutes is corroborated;
- The radial temperature gradient is uniform, despite the radially non-uniform distribution of the heat source. This justifies the radially uniform temperature field considered in the 1D model approach.

Appendix 4. Energy balance in ARTEMIS 10

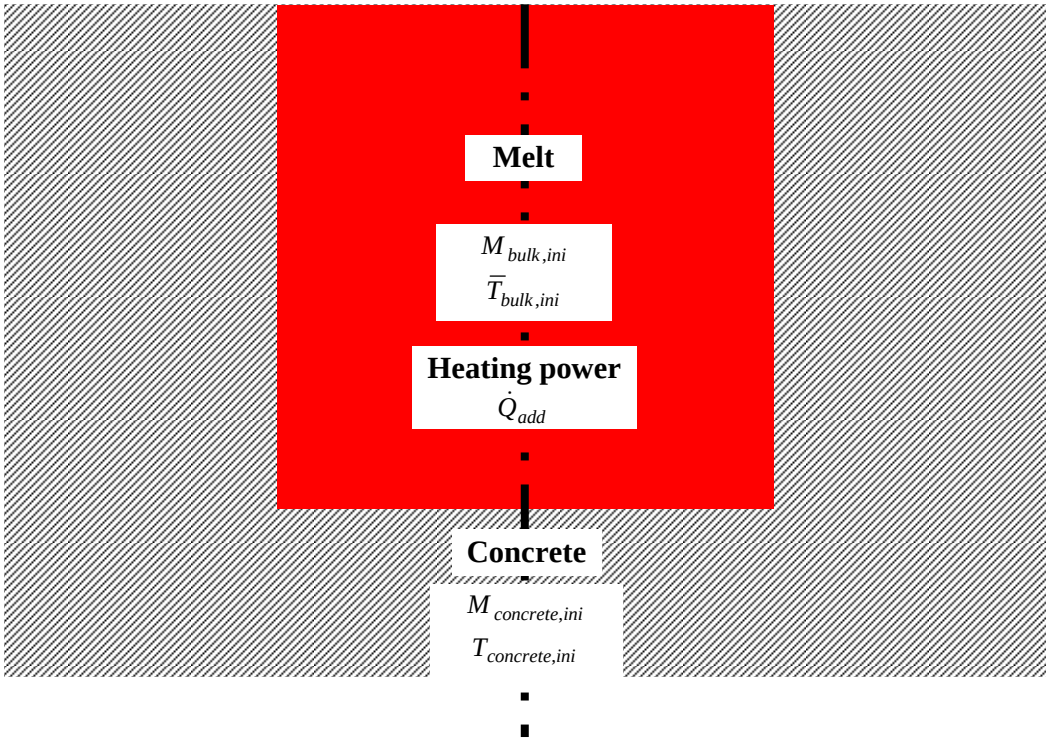

Figure A-4-1. System at t = 0.

We consider the initial situation of ARTEMIS 10 system in Figure A-4-1 which includes:

- A cylinder cavity with initial radius 15 cm and height 45 cm containing liquid melt
  - Initial temperature of the melt: $T_{bulk,ini} = 960\,°C$;
  - Initial melt mass: $M_{bulk,ini} = 97.1\,kg$;
  - Initial mass percentage of $BaCl_2$ in the liquid melt: $w_{bulk,ini}^{BaCl2} = 100\,\%$;
  - Initial enthalpy of the melt: $H_{bulk,ini} = H_{liquid}^{BaCl2}(T_{melt}^{BaCl2}) + C_{p,liquid}^{BaCl2}\left[T_{bulk,ini} - T_{melt}^{BaCl2}\right]$;
  - Energy stored in the initial melt is calculated by:

$$E_{bulk}(0) = M_{bulk,ini}\ H_{bulk,ini} = M_{bulk,ini}\left\{H_{liquid}^{BaCl2}(T_{melt}^{BaCl2}) + C_{p,liquid}^{BaCl2}\left[T_{bulk,ini} - T_{melt}^{BaCl2}\right]\right\} \quad \text{(A-4-1)}$$

- A cylinder concrete cavity with radius 40 cm surrounding the melt cavity and containing a solid mixture $BaCl_2$ and LiCl
  - Concrete porosity: ε = 46%;
  - Initial temperature of solid concrete: $T_{concrete,ini} = 400°C$;
  - Initial mass of solid concrete: $M_{concrete,ini} = 267.1\,kg$;
  - Mass percentage of BaCl2 in the solid concrete: $w_{concrete}^{BaCl2} = 62.04\,\%$ (corresponding to a mol percentage of $C_{concrete}^{BaCl2} = 25\,\%$);
  - Initial enthalpy of solid concrete:

$$H_{concrete,ini} = H_{solid}^{concrete}(T_{melt}) + C_{p,solid}^{concrete}\left[T_{concrete,ini} - T_{melt}\right] \quad \text{(A-4-2)}$$

- Energy stored in the solid concrete at t = 0:

$$E_{concrete}(0) = M_{concrete,ini}\ H_{concrete,ini} \quad \text{(A-4-3)}$$

$$E_{concrete}(0) = M_{concrete,ini}\left\{H_{solid}^{concrete}(T_{melt}) + C_{p,solid}^{concrete}\left[T_{concrete,ini} - T_{melt}\right]\right\} \quad \text{(A-4-4)}$$

The total energy stored in the system at t = 0 is the sum of energies stored in the melt and in the concrete. This means:

$$E_{total}(0) = E_{bulk}(0) + E_{concrete}(0) \quad \text{(A-4-5)}$$

or:

$$E_{total}(0) = M_{bulk,ini}\left\{H_{liquid}^{BaCl2}(T_{melt}^{BaCl2}) + C_{p,liquid}^{BaCl2}\left[T_{bulk,ini} - T_{melt}^{BaCl2}\right]\right\} + M_{concrete,ini}\left\{H_{solid}^{concrete}(T_{melt}) + C_{p,solid}^{concrete}\left[T_{concrete,ini} - T_{melt}\right]\right\} \quad \text{(A-4-6)}$$

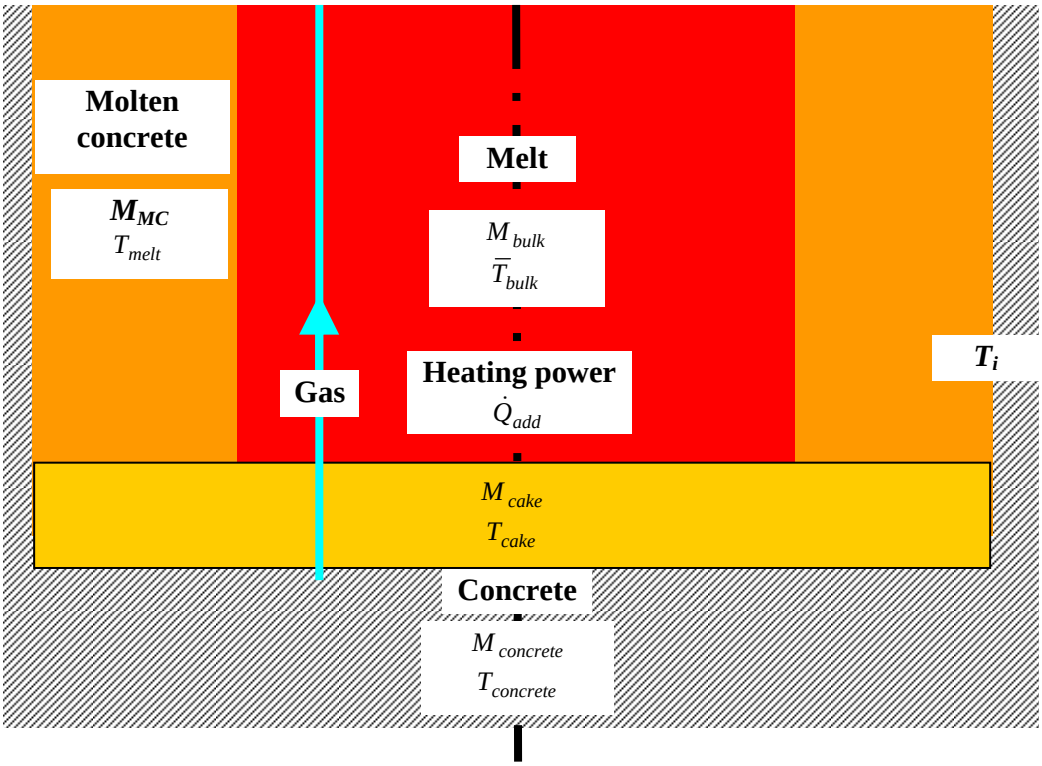

Figure A-4-2. System at instant t.

Figure A-4-2 shows the schematic of the system at instant t, including:

- Melt cavity
  - Average temperature of the melt: $\overline{T}_{bulk}$ (which is taken as the volume average of the bulk temperatures distribution measured by TC3 to TC12 which are located from the top to the bottom of the liquid melt cavity);

- Melt mass M_{bulk} which contains the mass of initial liquid melt and the added mass due to molten concrete entrance minus cake, i.e. $M_{bulk} = M_{bulk,ini} + M_{MC} - M_{cake}$;
- Mass percentage of $BaCl_2$ in the melt w_{bulk}^{BaCl2} (corresponding to C_{bulk}^{BaCl2} mol percentage of $BaCl_2$);
- Enthalpy of the melt: H_{bulk};
- Energy stored in the bulk is the sum of the energy from the mass initial liquid melt at temperature $\overline{T}_{bulk}$ and the energy added due to the ablated molten concrete and the solid cake, as follows:

$$E_{bulk}(t) = \left(M_{bulk,ini} - M_{cake}\right)\left\{H_{liquid}^{BaCl2}(T_{melt}^{BaCl2}) + C_{p,liquid}^{BaCl2}\left[\overline{T}_{bulk} - T_{melt}^{BaCl2}\right]\right\} + M_{MC}\left\{H_{liquid}^{concrete}(T_{melt}) + C_{p,liquid}^{concrete}\left[\overline{T}_{bulk} - T_{melt}\right]\right\} \quad \text{(A-4-7)}$$

- Concrete cavity
  - Concrete porosity: ε = 46%;
  - Average temperature in the solid concrete: $T_{concrete}$ (this temperature is deduced by volume averaging the temperature measured by thermocouples located inside the residual solid concrete, the details of the calculation method has been presented in Appendix 6);
  - Mass of solid concrete: $M_{concrete}$;
  - Mass percentage of $BaCl_2$ in the solid concrete: $w_{concrete}^{BaCl2} = 62.04\,\%$ (corresponding to a mol percentage of 25 % $BaCl_2$);
  - Enthalpy of the solid concrete: $H_{concrete}$;
  - Energy stored in the solid concrete is then:

$$E_{concrete}(t) = \left[M_{concrete,ini} - M_{MC}\right]\left\{H_{solid}^{concrete}(T_{melt}) + C_{p,solid}^{concrete}\left[T_{concrete} - T_{melt}\right]\right\} \quad \text{(A-4-8)}$$

- Solid cake forms at the bottom of the melt cavity
  - Average temperature in the cake: T_{cake} which is taken as average between the maximum bulk temperature (obtained by TC12) and the temperature measured by thermocouple T_i positioned at the bottom of the mobile probe 1D, $T_{cake} = \frac{T_{bulk,\max} + T_i}{2}$;
  - Mass of the cake: M_{cake};
  - Mass percentage of $BaCl_2$ in the solid cake $w_{cake}^{BaCl2} = 94\,\%$ (measured at the end of the experiment);
  - Enthalpy of the cake: H_{cake};
  - Energy stored in the cake is given by:

$$E_{cake}(t) = M_{cake}(t)\left\{H_{solid}^{BaCl2}(T_{melt}^{BaCl2}) + C_{p,solid}^{BaCl2}\left[T_{cake}(t) - T_{melt}^{BaCl2}\right]\right\} \quad \text{(A-4-9)}$$

- Argon gas is injected into the melt cavity
  - Superficial gas velocity: $j_{gas} = 0.02\,m/s$;
  - Specific heat of gas: $C_{p,gas} = 520\ J.kg^{-1}.K^{-1}$;

- Incoming gas temperature: $T_{gas,in} = 400°C$;
- Outgoing gas temperature: $T_{gas,out} = \overline{T}_{bulk}$;
- Incoming enthalpy of gas: $H_{gas,in} = H_{ref} + C_{p,gas}\,(T_{gas,in} - T_{ref})$;
- Outgoing enthalpy of gas: $H_{gas,out} = H_{ref} + C_{p,gas}\,(T_{gas,out} - T_{ref})$;
- Energy serving for gas heating is:

$$E_{gas}(t) = \int_0^t \dot{m}_{gas}\,(H_{gas,in} - H_{gas,out})\,dt \tag{A-4-10}$$

in which $\dot{m}_{gas}$ is the mass flow rate of gas.

The total energy stored in the system at instant t is the sum of the energies in the liquid melt, the solid concrete and the cake, as follows:

$$E_{total}(t) = E_{bulk}(t) + E_{concrete}(t) + E_{cake}(t) \tag{A-4-11}$$

or

$$\begin{aligned} E_{total}(t) = {} & \left[M_{bulk,ini} - M_{cake}\right]\left\{H_{liquid}^{BaCl2}(T_{melt}^{BaCl2}) + C_{p,liquid}^{BaCl2}\left[\overline{T}_{bulk} - T_{melt}^{BaCl2}\right]\right\} \\ & + M_{MC}\left\{H_{liquid}^{concrete}(T_{melt}) + C_{p,liquid}^{concrete}\left[\overline{T}_{bulk} - T_{melt}\right]\right\} \\ & + \left[M_{concrete,ini} - M_{MC}\right]\left\{H_{solid}^{concrete}(T_{melt}) + C_{p,solid}^{concrete}\left[T_{concrete} - T_{melt}\right]\right\} \\ & + M_{cake}\left\{H_{solid}^{BaCl2}(T_{melt}^{BaCl2}) + C_{p,solid}^{BaCl2}\left[T_{cake} - T_{melt}^{BaCl2}\right]\right\} \end{aligned} \tag{A-4-12}$$

Variation of the stored energy in the system between two instants is equal to the difference between the energy generated from the heating elements and the energy used for gas heating, as follows:

$$E_{total}(t) - E_{total}(0) = \dot{Q}_{add}\;t - E_{gas} \tag{A-4-13}$$

or:

$$\Delta E = E_{total}(t) - E_{total}(0) - \dot{Q}_{add}\;t + \int_0^t \dot{m}_{gas}\,(H_{gas,in} - H_{gas,out})\,dt \tag{A-4-14}$$

in which $\dot{Q}_{add} = 6000W$ is the power dissipation in the melt cavity.

Combining Equations (A-4-6), (A-4-12) and (A-4-14) gives the variation of energy in ARTEMIS 10 as:

$$\begin{aligned} \Delta E = {} & M_{bulk,ini}\,C_{p,liquid}^{BaCl2}\left[\overline{T}_{bulk} - T_{bulk,ini}\right] + M_{concrete,ini}\,C_{p,solid}^{concrete}\left[T_{concrete} - T_{concrete,ini}\right] \\ & + M_{cake}\left\{H_{solid}^{BaCl2} - H_{liquid}^{BaCl2} + C_{p,solid}^{BaCl2}\left[T_{cake} - T_{melt}^{BaCl2}\right] - C_{p,liquid}^{BaCl2}\left[\overline{T}_{bulk} - T_{melt}^{BaCl2}\right]\right\} \\ & + M_{MC}\left\{H_{liquid}^{concrete} - H_{solid}^{concrete} + C_{p,liquid}^{concrete}\left[\overline{T}_{bulk} - T_{melt}\right] - C_{p,solid}^{concrete}\left[T_{concrete} - T_{melt}\right]\right\} \end{aligned} \tag{A-4-15}$$

or:

$$\begin{aligned}\Delta E = {} & M_{bulk,ini}\, C_{p,liquid}^{BaCl2} \left[\overline{T}_{bulk} - T_{bulk,ini}\right] + M_{concrete,ini}\, C_{p,solid} \left[T_{concrete} - T_{concrete,ini}\right] \\ & + M_{cake} \left\{C_{p,solid}^{BaCl2} \left[T_{cake} - T_{melt}^{BaCl2}\right] + C_{p,liquid}^{BaCl2} \left[T_{melt}^{BaCl2} - T_{bulk}\right] - L_{solification}^{BaCl2}\right\} \\ & + M_{MC} \left\{C_{p,liquid}^{concrete} \left[\overline{T}_{bulk} - T_{melt}\right] + C_{p,solid}^{concrete} \left[T_{melt} - T_{concrete}\right] + L_{melting}^{concrete}\right\}\end{aligned} \quad \text{(A-4-16)}$$

The calculation of the energy balance will be performed in the next, using the given data from ARTEMIS 10 which are:

- The average bulk temperature (calculated by mathematical average of temperature measured by TC3 to TC12) (Figure A-4-3).

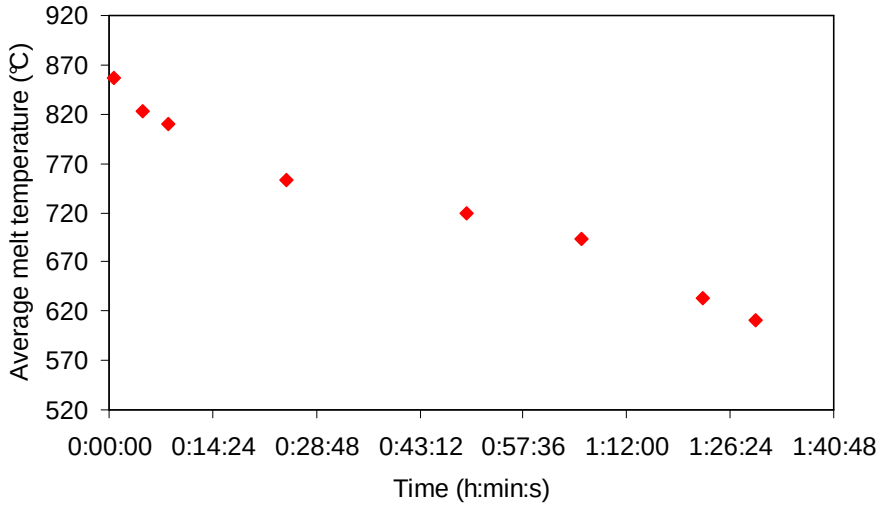

Figure A-4-3. Evolution of average bulk temperature in ARTEMIS 10.

- The evolution of the mass of the molten concrete (deduced from the position of the thermo-couples located in the solid concrete) (Figure A-4-4).

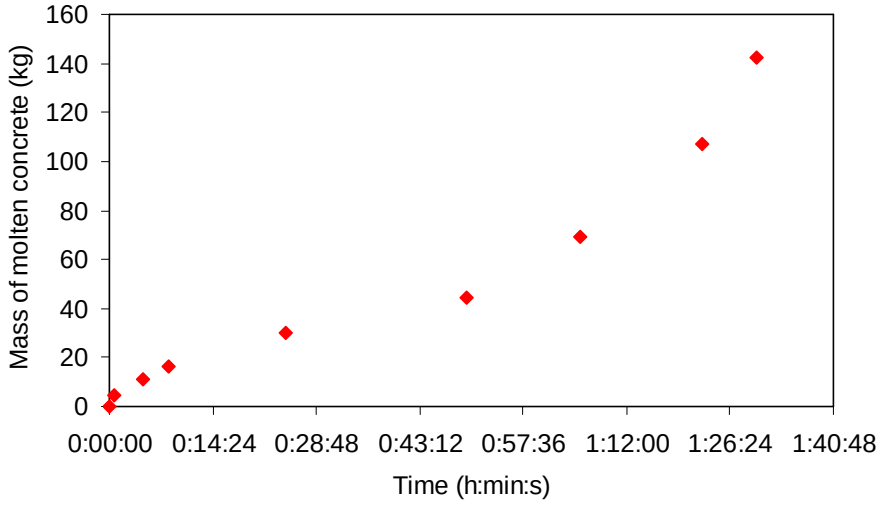

Figure A-4-4. Evolution of molten concrete mass in ARTEMIS 10.

- The average $BaCl_2$ concentration in the melt cavity (Figure A-4-5).

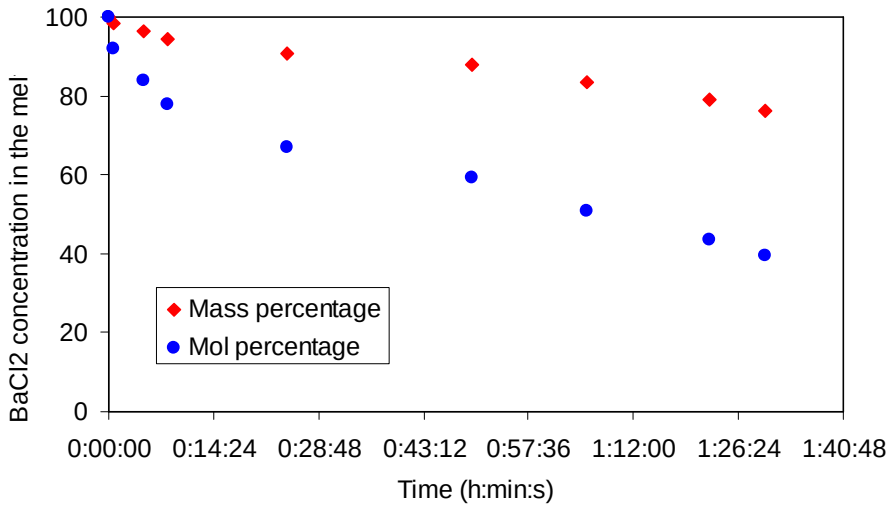

Figure A-4-5. Evolution of $BaCl_2$ concentration in the bulk in ARTEMIS 10.

- The average temperature in the solid concrete (determined by volume averaging of all the temperatures measured by thermocouples in the solid concrete cavity) (Figure A-4-6).

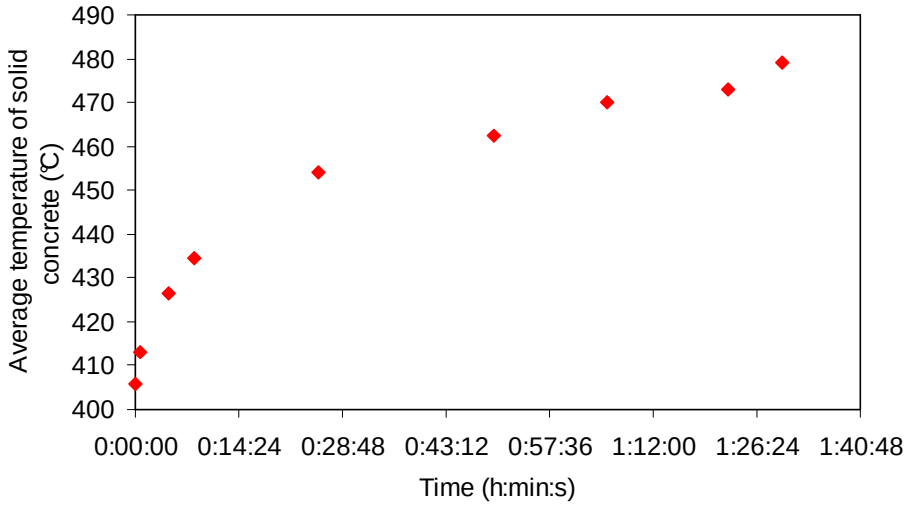

Figure A-4-6. Evolution of average concrete temperature in ARTEMIS 10.

Knowing the mass of the solid cake at the end of ARTEMIS 10 and assuming that the mass of the cake increases linearly versus time allows an estimation of the cake mass.

- The average temperature in the cake (estimated by mobile probe 1D).
- The heat capacities of the liquid melt and of the solid concrete are calculated as functions of the mol percentage of $BaCl_2$ and of the temperature |Veteau, 2004].

The global energy balance in ARTEMIS 10 is shown in Figure A-4-7. It is seen that energy is conserved during ARTEMIS 10. The energy serving for gas heating is minor in comparison to the energy from the heating elements and to the variation of the energy stored in the different materials. Uncertainty of less than 20% is observed which might come from the determination method of the ablated mass of concrete.

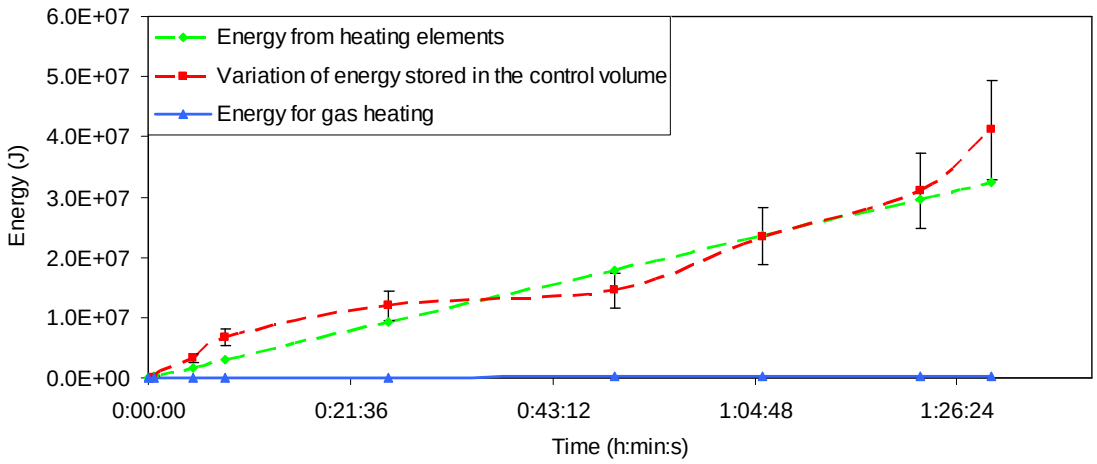

Figure A-4-7. Energy calculation for ARTEMIS 10.

Figure 4-8 shows a detailed partition of the energy. It is seen that the energy generating from melt cooling is important. This is different from ARTEMIS 11 in which the energy released from the initial melt is of minor distribution because the initial temperature is much lower. A significant part of energy serves for heating up the solid concrete by conduction. Other important parts of energy are devoted for concrete ablation and for heating up the molten concrete. In addition, the energies related to cake heating and gas heating are negligible.

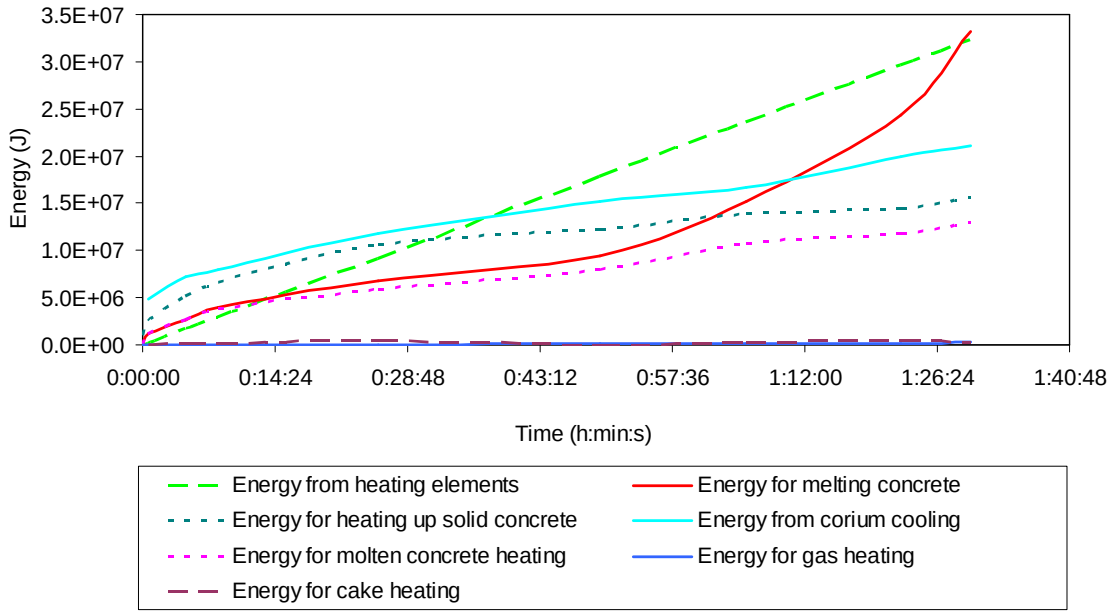

Figure A-4-8. Energy partition in ARTEMIS 10.

Appendix 5. Energy balance in ARTEMIS 11

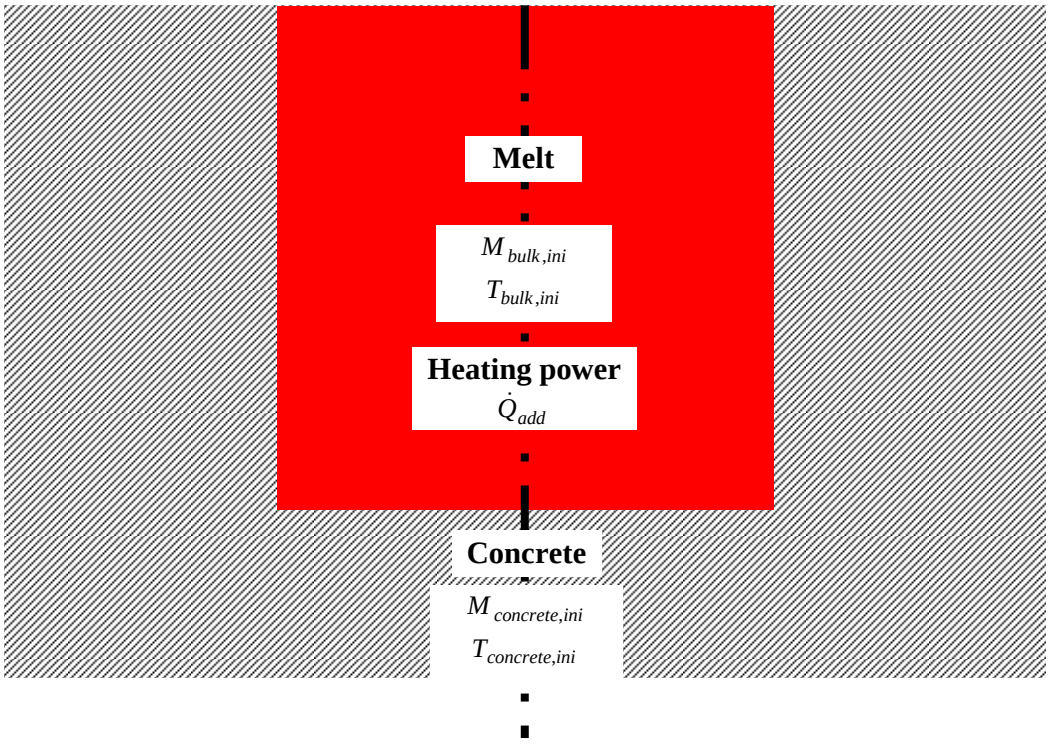

Figure A-5-1. System at t = 0.

We consider the initial situation of ARTEMIS 11 system in Figure A-5-1 which includes:

- A cylinder cavity with initial radius 15 cm and height 33 cm containing liquid melt
  - Initial temperature of the melt: $T_{bulk,ini} = 560\,°C$;
  - Initial melt mass: $M_{bulk,ini} = 57\,kg$;
  - Mass percentage of $BaCl_2$ in the melt: $w_{bulk}^{BaCl2} = 62.04\,\%$ (eutectic composition corresponding to a mol percentage of 25% and similar to the composition of solid concrete);
  - Initial enthalpy of the melt: $H_{bulk,ini} = H_{liquid}^{concrete}(T_{melt}) + C_{p,liquid}^{concrete}\left[T_{bulk,ini} - T_{melt}\right]$;
  - Energy stored in the initial melt is calculated by:

$$E_{bulk}(0) = M_{bulk,ini}\ H_{bulk,ini} = M_{bulk,ini}\left\{H_{liquid}^{concrete}(T_{melt}) + C_{p,liquid}^{concrete}\left[T_{bulk,ini} - T_{melt}\right]\right\} \quad \text{(A-5-1)}$$

- A cylinder concrete cavity with radius 40 cm surrounding the melt cavity and containing a solid mixture $BaCl_2$ and LiCl
  - Concrete porosity: ε = 46%;
  - Initial temperature of solid concrete: $T_{concrete,ini} = 400°C$;
  - Initial mass of solid concrete: $M_{concrete,ini} = 259.25\,kg$;
  - Mass percentage of $BaCl_2$ in the solid concrete: $w_{concrete}^{BaCl2} = 62.04\,\%$ (eutectic composition);
  - Initial enthalpy of solid concrete:

$$H_{concrete,ini} = H_{solid}^{concrete}(T_{melt}) + C_{p,solid}^{concrete}\left[T_{concrete,ini} - T_{melt}\right] \quad \text{(A-5-2)}$$

- Energy stored in the solid concrete at t = 0:

$$E_{concrete}(0) = M_{concrete,ini}\ H_{concrete,ini} \quad \text{(A-5-3)}$$

$$E_{concrete}(0) = M_{concrete,ini}\left\{H_{solid}^{concrete}(T_{melt}) + C_{p,solid}^{concrete}\left[T_{concrete,ini} - T_{melt}\right]\right\} \quad \text{(A-5-4)}$$

The total energy stored in the system at t = 0 is the sum of energies stored in the melt and in the concrete. This means:

$$E_{total}(0) = E_{bulk}(0) + E_{concrete}(0) \quad \text{(A-5-5)}$$

or:

$$\begin{aligned} E_{total}(0) = {} & M_{bulk,ini}\left\{H_{liquid}^{concrete}(T_{melt}) + C_{p,liquid}^{concrete}\left[T_{bulk,ini} - T_{melt}\right]\right\} \\ & + M_{concrete,ini}\left\{H_{solid}^{concrete}(T_{melt}) + C_{p,solid}^{concrete}\left[T_{concrete,ini} - T_{melt}\right]\right\} \end{aligned} \quad \text{(A-5-6)}$$

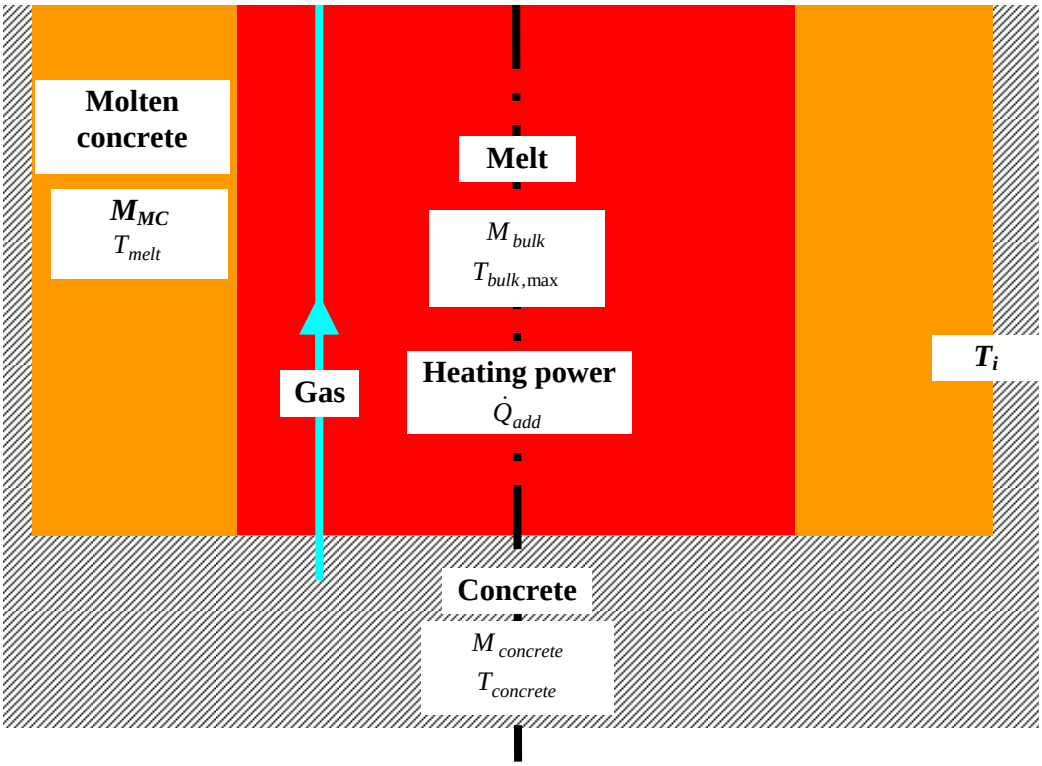

Figure A-5-2. System at instant t.

Figure A-5-2 shows the schematic of the system at instant t, including:

- Melt cavity
  - Maximum temperature of the melt: $T_{bulk,\max}$;

- Melt mass M_{bulk} which contains the mass of initial liquid melt and the added mass due to molten concrete entrance, i.e. $M_{bulk} = M_{bulk,ini} + M_{MC}$;
- Mass percentage of $BaCl_2$ in the melt $w_{bulk}^{BaCl2} = 62.04\%$;
- Enthalpy of the melt: H_{bulk};
- Energy stored in the bulk is the sum of the energy from the initial liquid melt at temperature $T_{bulk,max}$ and the energy added due to the ablated molten concrete and the solid cake, as follows:

$$E_{bulk}(t) = M_{bulk,ini}\left\{H_{liquid}^{concrete}(T_{melt}) + C_{p,liquid}^{concrete}\left[T_{bulk,\max} - T_{melt}\right]\right\} + M_{MC}\left\{H_{liquid}^{concrete}(T_{melt}) + C_{p,liquid}^{concrete}\left[T_{bulk,\max} - T_{melt}\right]\right\} \quad \text{(A-5-7)}$$

- Concrete cavity
  - Concrete porosity: ε = 46%;
  - Average temperature in the solid concrete: $T_{concrete}$ (this temperature is deduced by volume averaging the temperature measured by thermocouples located inside the residual solid concrete, the details of the calculation method has been presented in the energy balance calculation for ARTEMIS 11, described in Appendix 6);
  - Mass of solid concrete: $M_{concrete}$;
  - Mass percentage of $BaCl_2$ in the solid concrete: $w_{concrete}^{BaCl2} = 62.04\%$ (corresponding to a mol percentage of 25 % $BaCl_2$);
  - Enthalpy of the solid concrete: $H_{concrete}$;
  - Energy stored in the solid concrete is then:

$$E_{concrete}(t) = \left[M_{concrete,ini} - M_{MC}\right]\left\{H_{solid}^{concrete}(T_{melt}) + C_{p,solid}^{concrete}\left[T_{concrete} - T_{melt}\right]\right\} \quad \text{(A-5-8)}$$

- Argon gas is injected into the melt cavity
  - Superficial gas velocity: $j_{gas} = 0.02\,m/s$;
  - Specific heat of gas: $C_{p,gas} = 520\ J.m^{-1}.K^{-1}$;
  - Incoming gas temperature: $T_{gas,in} = 400°C$;
  - Outgoing gas temperature: ; $T_{gas,out} = T_{bulk,\max}$
  - Incoming enthalpy of gas: $H_{gas,in} = H_{ref} + C_{p,gas}(T_{gas,in} - T_{ref})$;
  - Outgoing enthalpy of gas: $H_{gas,out} = H_{ref} + C_{p,gas}(T_{gas,out} - T_{ref})$;
  - Energy serving for gas heating is:

$$E_{gas}(t) = \int_0^t \dot{m}_{gas}\,(H_{gas,in} - H_{gas,out})\,dt \quad \text{(A-5-9)}$$

in which $\dot{m}_{gas}$ is the mass flow rate of gas.

The total energy stored in the system at instant *t* is the sum of the energies in the liquid melt, the solid concrete and the cake, as follows:

$$E_{total}(t) = E_{bulk}(t) + E_{concrete}(t) \tag{A-5-10}$$

or

$$\begin{aligned} E_{total}(t) = {} & M_{bulk,ini}\left\{H_{liquid}^{concrete}(T_{melt}) + C_{p,liquid}^{concrete}\left[T_{bulk,\max} - T_{melt}\right]\right\} \\ & + M_{MC}\left\{H_{liquid}^{concrete}(T_{melt}) + C_{p,liquid}^{concrete}\left[T_{bulk,\max} - T_{melt}\right]\right\} \\ & + \left[M_{concrete,ini} - M_{abl}\right]\left\{H_{solid}^{concrete}(T_{melt}) + C_{p,solid}^{concrete}\left[T_{concrete} - T_{melt}\right]\right\} \end{aligned} \tag{A-5-11}$$

Variation of the stored energy in the system between two instants is equal to the difference between the energy generated from the heating elements and the energy used for gas heating, as follows:

$$E_{total}(t) - E_{total}(0) = \dot{Q}_{add}\ t - E_{gas} \tag{A-5-12}$$

or:

$$\Delta E = E_{total}(t) - E_{total}(0) - \dot{Q}_{add}\ t + \int_0^t \dot{m}_{gas}\ (H_{gas,in} - H_{gas,out})\, dt \tag{A-5-13}$$

in which $\dot{Q}_{add} = 6000 W$ is the power dissipation in the melt cavity.

Combining Equations (A-5-6), (A-5-11) and (A-5-13) gives the variation of energy in ARTEMIS 11 as:

$$\begin{aligned} \Delta E = {} & M_{bulk,ini}\ C_{p,liquid}^{concrete}\left[T_{bulk,\max} - T_{bulk,ini}\right] + M_{concrete,ini}\ C_{p,solid}^{concrete}\left[T_{concrete} - T_{concrete,ini}\right] \\ & + M_{MC}\left\{H_{liquid}^{concrete} - H_{solid}^{concrete} + C_{p,liquid}^{concrete}\left[T_{bulk,\max} - T_{melt}\right] - C_{p,solid}^{concrete}\left[T_{concrete} - T_{melt}\right]\right\} \end{aligned} \tag{A-5-14}$$

or:

$$\begin{aligned} \Delta E = {} & M_{bulk,ini}\ C_{p,liquid}^{concrete}\left[T_{bulk,\max} - T_{bulk,ini}\right] + M_{concrete,ini}\ C_{p,solid}^{concrete}\left[T_{concrete} - T_{concrete,ini}\right] \\ & + M_{MC}\left\{C_{p,liquid}^{concrete}\left[T_{bulk,\max} - T_{melt}\right] + C_{p,solid}^{concrete}\left[T_{melt} - T_{concrete}\right] + L_{melting}^{concrete}\right\} \end{aligned} \tag{A-5-15}$$

The calculation of the energy balance will be performed in the next, using the given data from ARTEMIS 11 which are:

- The evolution of maximum bulk temperature (Figure A-5-3).

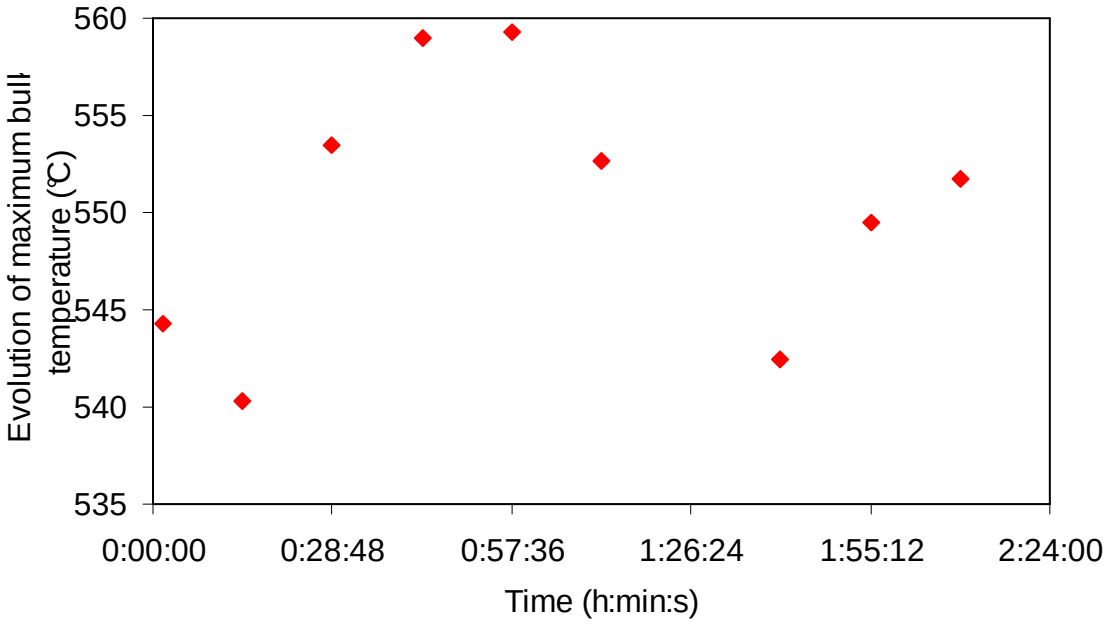

Figure A-5-3. Evolution of maximum bulk temperature in ARTEMIS 11.

- The evolution of the mass of the molten concrete (deduced from the position of the thermo-couples located in the solid concrete) (Figure A-5-4).

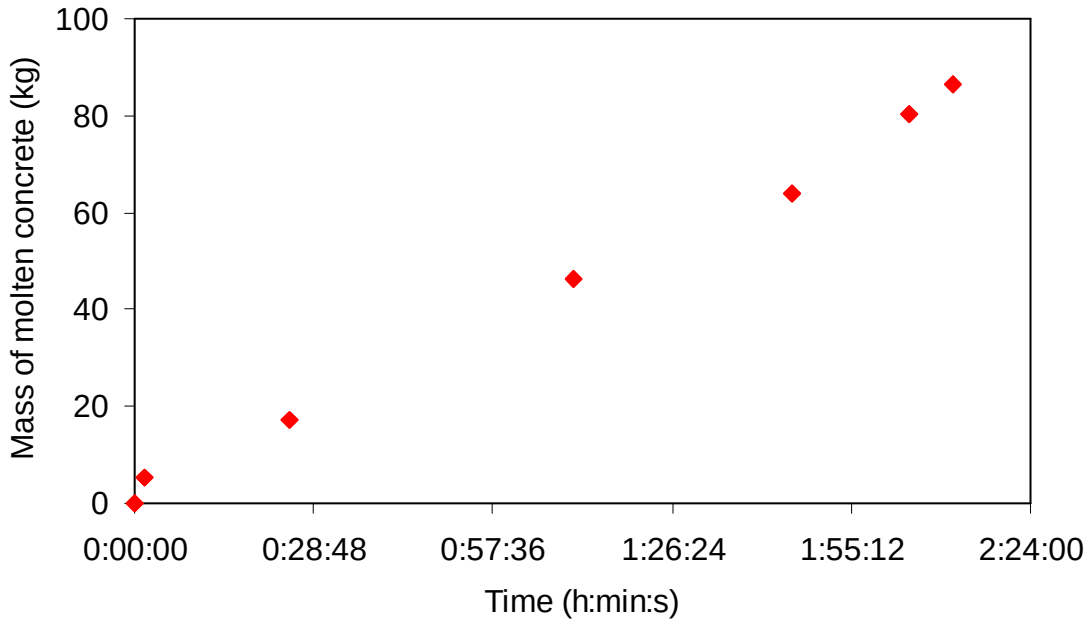

Figure A-5-4. Evolution of molten concrete mass in ARTEMIS 11.

- The average temperature in the solid concrete (determined by volume averaging of all the temperatures measured by thermocouples in the solid concrete cavity) (Figure A-5-5).

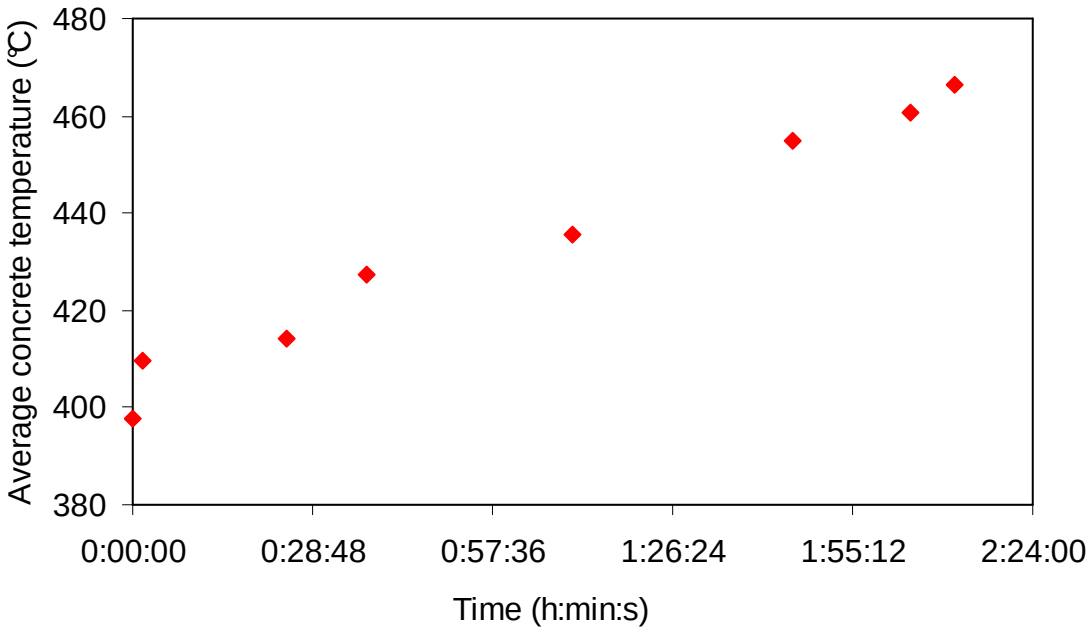

Figure A-5-5. Evolution of average concrete temperature in ARTEMIS 11.

Knowing the mass of the solid cake at the end of ARTEMIS 11 and assuming that the mass of the cake increases linearly versus time allows an estimation of the cake mass.

- The average temperature in the cake (estimated by mobile probe 1D).
- The heat capacities of the liquid melt and of the solid concrete are calculated as functions of the mol percentage of $BaCl_2$ and of the temperature |Veteau, 2004].

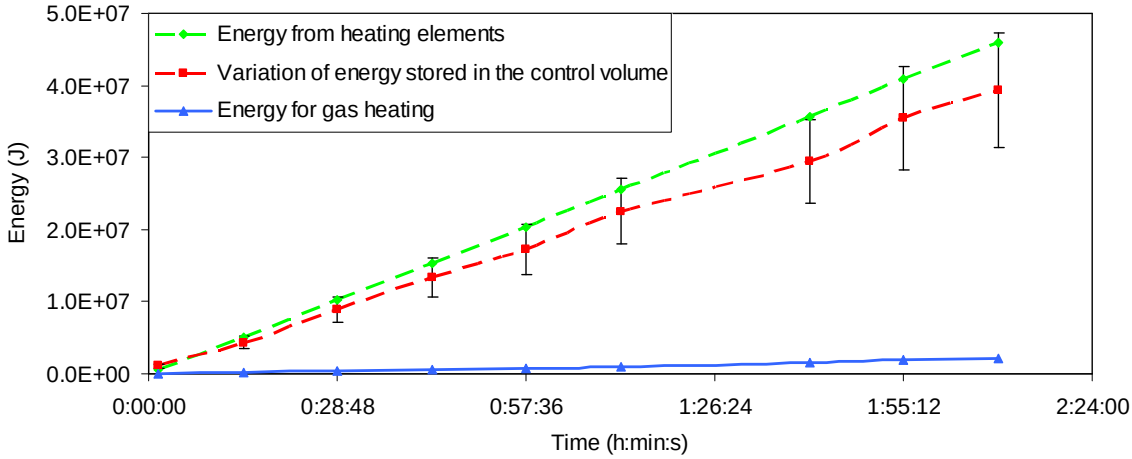

Figure A-5-6. Energy calculation for ARTEMIS 11.

Figure A-5-6 indicates that the energy that serves for gas heating is minor in comparison with the energy generated from heating elements and with the variation of energy stored in the materials of the control volume. Generally, energy is conserved. The energy loss is less than 10%. In addition, Figure A-5-7 shows the distribution of energy. It is seen that the main energy in the control volume serves for concrete ablation. Another important part of energy is devoted for heating up the solid concrete.

Energies related to melt cooling and molten concrete heating to the melting temperature are minor contributions.

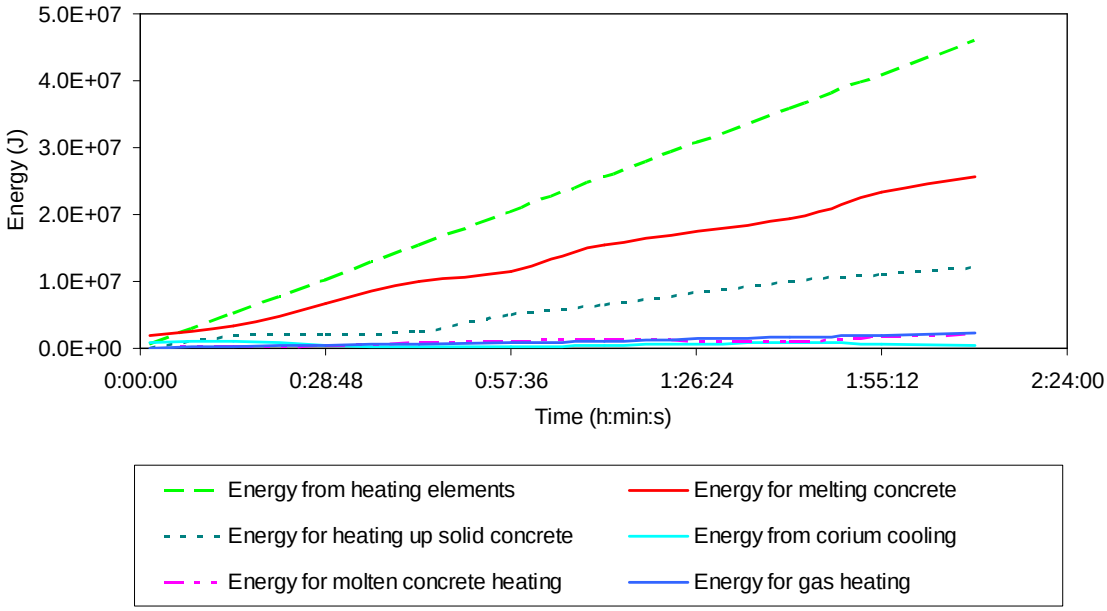

Figure A-5-7. Energy distribution in ARTEMIS 11.

Appendix 6. Determination of position of liquid-solid interface during melt-concrete interaction and calculation of the average temperature of the residual solid concrete

Method for determination of liquid-solid interface

The melting front locates at the positions at which the temperature reaches the melting temperature of the solid concrete (522 °C). The position of the melting front (interface between liquid melt and solid concrete) may be deduced from the measurements of local concrete temperatures, indicating by maximum 98 thermocouples in 8 planes (TB2 to TB9) attached inside the concrete cavity (Figure A-6-1).

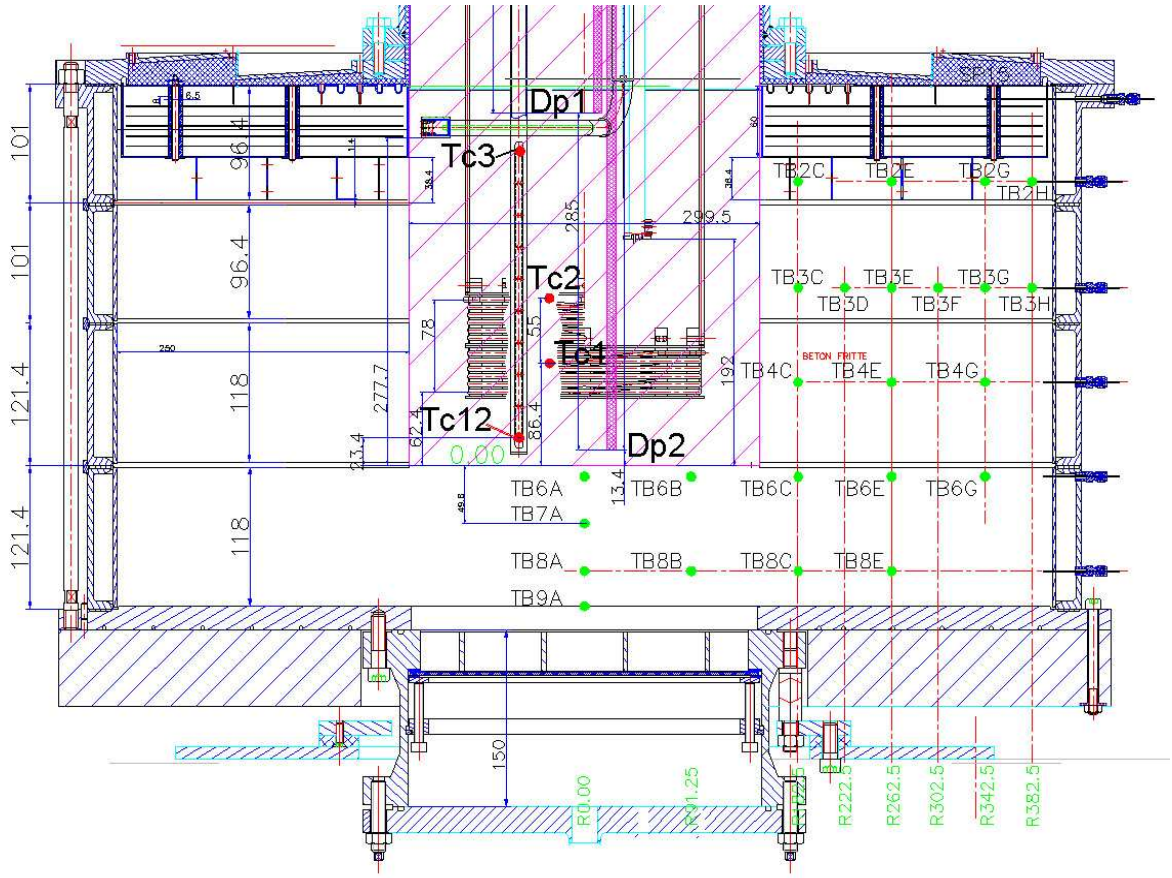

Figure A-6-1. Thermocouple matrix in solid concrete cavity.

From the indications of temperature from these thermocouples, the time required for them to reach melting temperature of the concrete **can be determined**. Knowing the distance between the thermocouples in each plane helps to plot a curve which describes the relation between the position of thermocouple and the time required for this thermocouple to reach the melting temperature. This curve also presents the evolution of the melting front in this plane. Fitting this curve by a polynomial function allows deducing the position of the melting front at given time instant *t*. This method is repeated for all the thermocouple planes in order to obtain the evolution of the liquid-solid interface at all elevations of the concrete volume.

Figure A-6-2, Figure A-6-3, Figure A-6-4 and Figure A-6-5 show evolutions of the melting front positions at four different elevations of the melt cavity, corresponding to four different thermocouple planes (TB2, TB3, TB4, TB6).

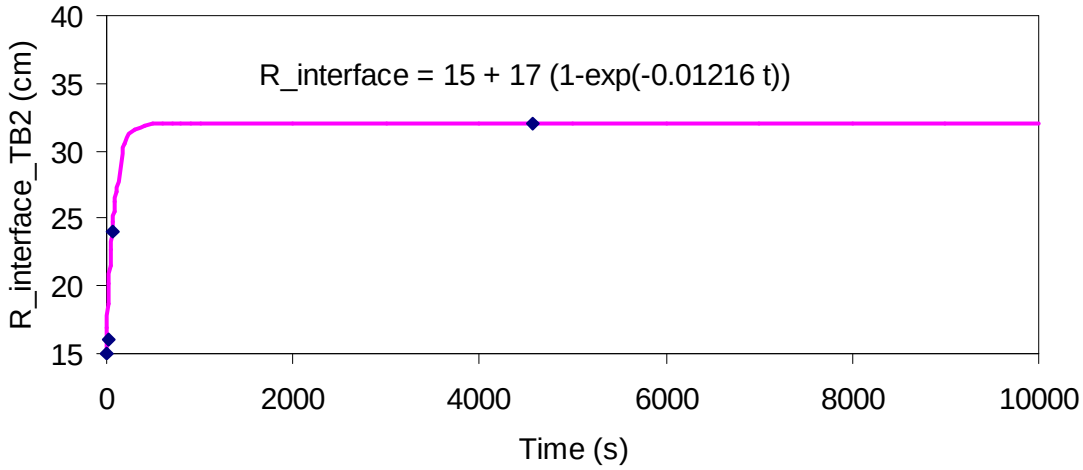

Figure A-6-2. Evolution of the melting radius at thermocouple plane TB2 in ARTEMIS 11.

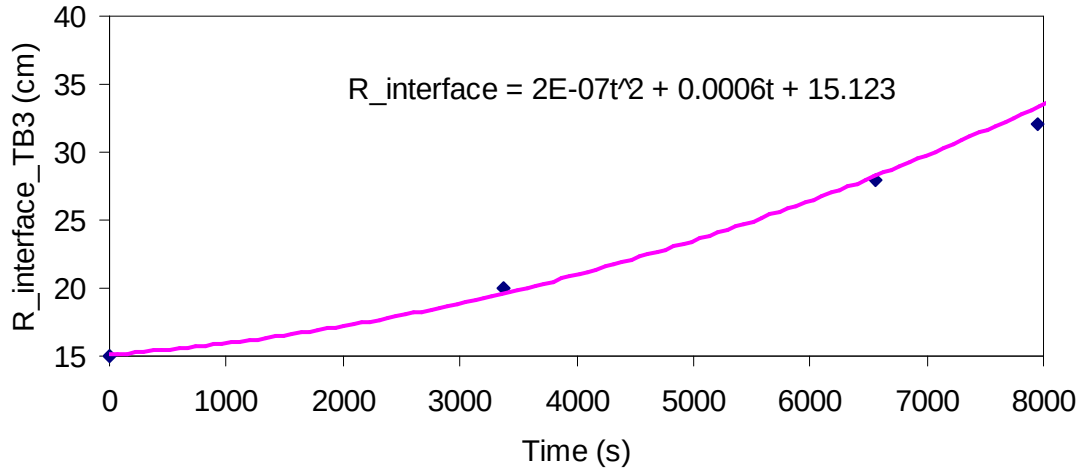

Figure A-6-3. Evolution of the melting radius at thermocouple plane TB3 in ARTEMIS 11.

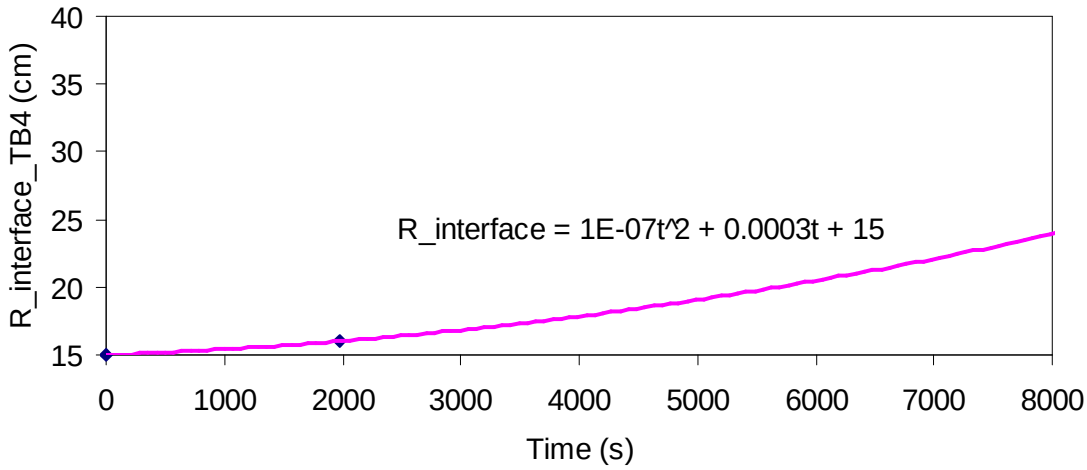

Figure A-6-4. Evolution of the melting radius at thermocouple plane TB4 in ARTEMIS 11.

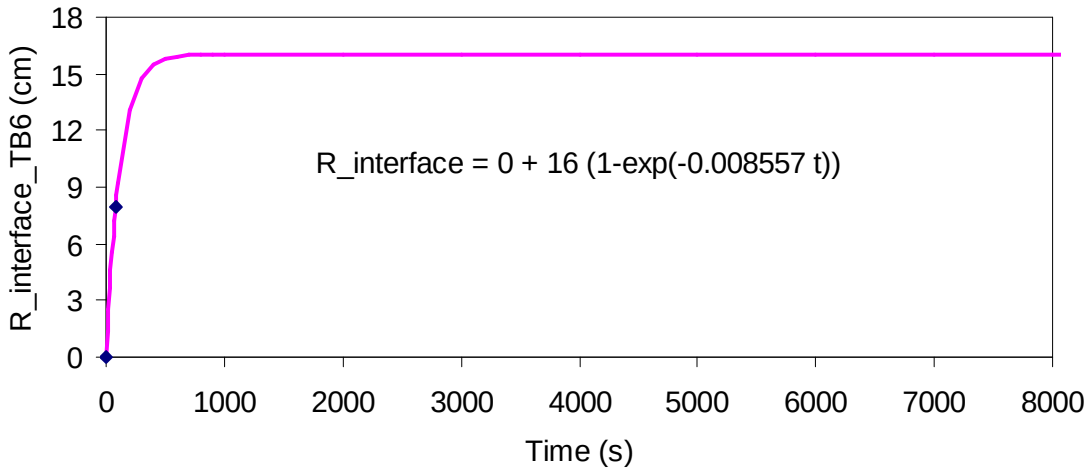

Figure A-6-5. Evolution of the melting radius at thermocouple plane TB6 in ARTEMIS 11.

Then, the melt cavity radius at a given instant for each cavity elevation can be deduced using the above polynomial functions. As a result, the evolution of the melt cavity shape is obtained for ARTEMIS 11 as shown in Figure A-6-6.

The evolution of the melt cavity shape in ARTEMIS 10 is shown in Figure A-6-7.

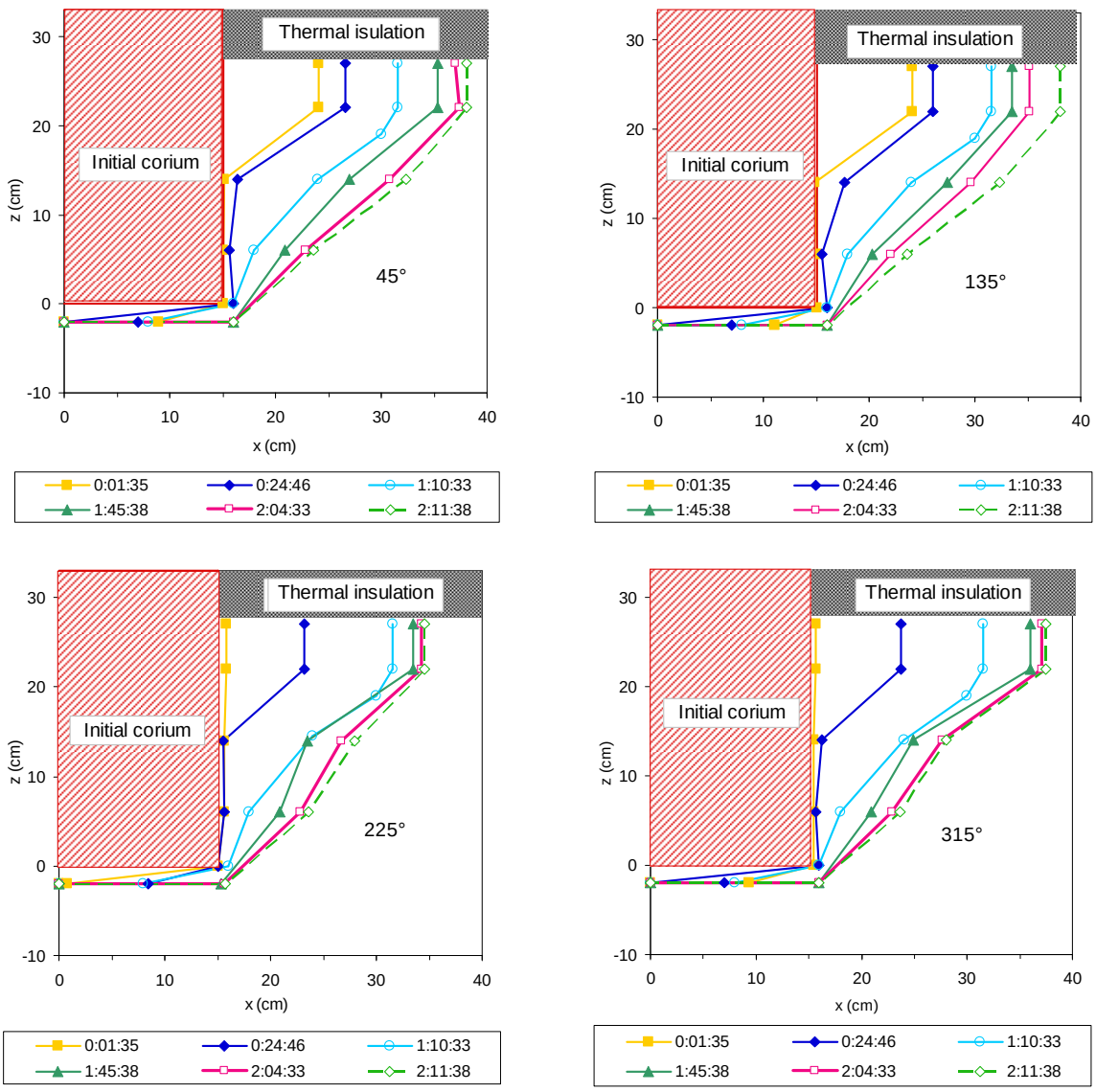

Figure A-6-6. Evolution of the melt cavity shape in ARTEMIS 11.

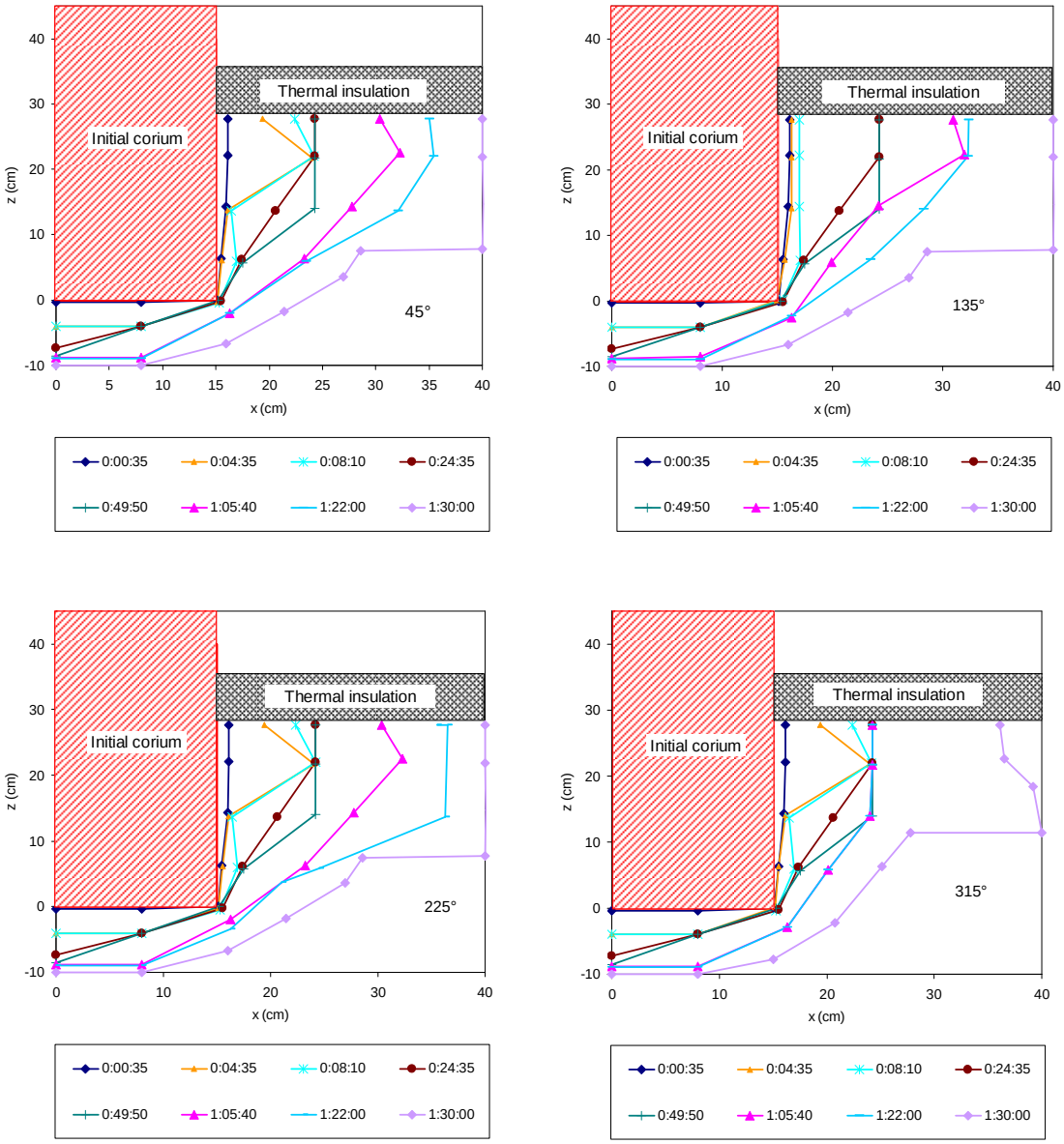

Figure A-6-7. Evolution of the melt cavity shape in ARTEMIS 10.

In addition, with the information of the melt cavity shape evolution or the evolution of the melt cavity radius at each elevation of the melt cavity, the volume of the melt can be deduced. Consequently, the mass of the melt in the cavity for a given time instant *t* can also be calculated.

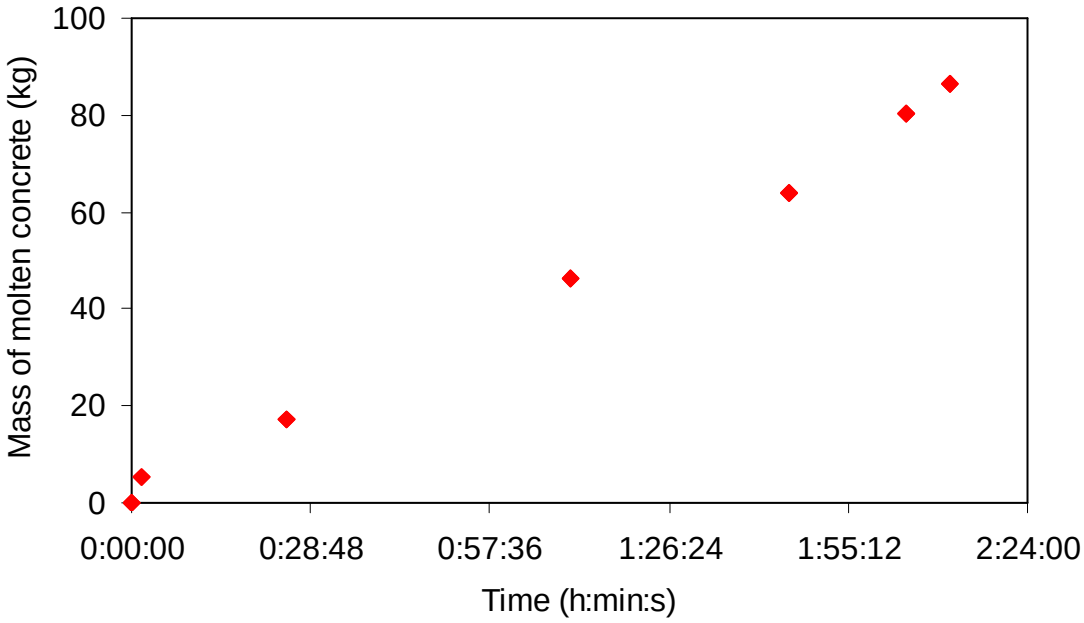

Figure A-6-8. Evolution of the ablated mass of concrete in ARTEMIS 11.

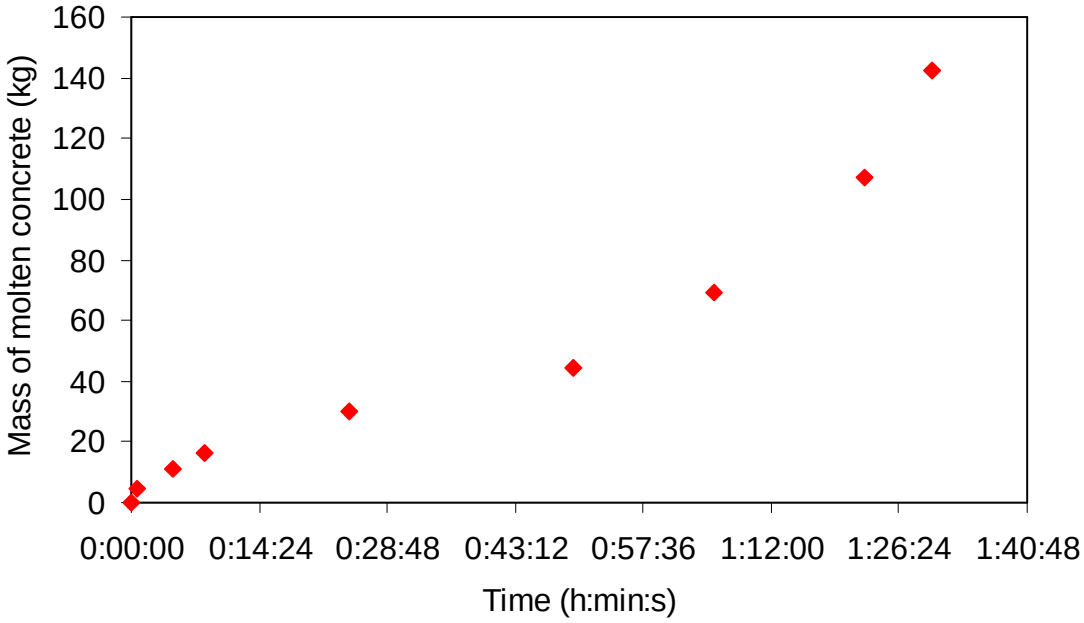

Figure A-6-9. Evolution of the ablated mass of concrete in ARTEMIS 10.

Method to estimate the average temperature in the residual solid concrete

We divide the concrete cavity into slices with uniform thickness Δz. Each slice contains one plane of thermocouples installed inside the solid concrete part. The radial distance between thermocouple is uniform Δr and the distance from the cavity centre to thermocouple is named R_i where i is the order of the thermocouple in the considered plane.

First of all, we determine an average radial temperature $\overline{T}_z$ which is the average of all the temperatures of the thermocouples located in this slice weighted by the specific area encompassed by each thermocouple. The energy stored in the concrete part located between two thermocouple R_i and R_{i+1} is:

$$dE_i = \rho_{concrete}\, C_{p,solid}^{concrete}\, S_i\, \Delta z\, (T_{z,i} - T_{ref}) \tag{A-6-1}$$

where $\rho_{concrete}$ is the density of the concrete, $C_{p,\,solid}^{\,concrete}$ is the heat capacity of the solid concrete, S_i is the surface area encompassed by the thermocouple between R_i and R_{i+1}, $T_{z,i}$ is the temperature of the thermocouple installed inside this slice unit and T_{ref} is a reference temperature.

Since $S_i = 2\pi R_i\, dr\, \Delta z$, we can alternatively write:

$$dE_i = \rho_{concrete}\, C_{p,solid}^{concrete}\, 2\pi R_i\, \Delta r\, \Delta z\, (T_{z,i} - T_{ref}) \tag{A-6-2}$$

Then the total energy stored in one slice is:

$$E_{slice} = \sum_{i=1}^{N} dE_i = \sum_{i=1}^{N} \rho_{concrete}\, C_{p,solid}^{concrete}\, 2\pi R_i\, \Delta r\, \Delta z\, (T_{z,i} - T_{ref}) \tag{A-6-3}$$

Since we assume that each slice is represented by an average temperature $\overline{T}_z$, we can also express the total energy stored in this slice in terms of this average temperature, as following:

$$E_{slice} = \rho_{concrete}\, C_{p,solid}^{concrete}\, (\overline{T}_z - T_{ref}) \sum_{i=1}^{N} S_i\, \Delta z \tag{A-6-4}$$

or, alternatively:

$$E_{slice} = \rho_{concrete}\, C_{p,solid}^{concrete}\, (\overline{T}_z - T_{ref}) \sum_{i=1}^{N} 2\pi R_i\, \Delta r\, \Delta z \tag{A-6-5}$$

From Equations (A-6-3) and (A-6-5), we have:

$$E_{slice} = \sum_{i=1}^{N} \rho_{concrete}\, C_{p,solid}^{concrete}\, 2\pi R_i\, \Delta r\, \Delta z\, (T_{z,i} - T_{ref}) \tag{A-6-6}$$

or:

$$E_{slice} = \rho_{concrete}\, C_{p,solid}^{concrete}\, (\overline{T}_z - T_{ref}) \sum_{i=1}^{N} 2\pi R_i\, \Delta r\, \Delta z \tag{A-6-7}$$

Since Δr = constant, we can deduce the radial average temperature for each slice as following:

$$\overline{T}_z = \frac{\sum_{i=1}^{N} R_i T_{z,i}}{\sum_{i=1}^{N} R_i} \tag{A-6-8}$$

Now, we can calculate the average temperature for each slice inside the concrete cavity. In order to determine the average temperature for the whole volume of the cavity, we have to rewrite the problem as follows.

There are N^* slices, located at different vertical levels from positions z_1 to z_{N^*}. The distance between two slices is Δz which is assumed to be constant. Each slice has a representative radial average temperature $\overline{T}_z$ and a total surface $S_{z,i}$.

The energy stored in one slice is:

$$dE_{z,i} = \rho_{concrete}\, C_{p,solid}^{concrete}\, S_{z,i}\, \Delta z\, (\overline{T}_{z,i} - T_{ref}) \tag{A-6-9}$$

Then the energy stored in the whole solid concrete cavity is the sum of the energy stored in all slices, which is:

$$E_{total} = \rho_{concrete}\, C_{p,solid}^{concrete} \sum_{i=1}^{N} S_{z,i}\, \Delta z\, (\overline{T}_{z,i} - T_{ref}) \tag{A-6-10}$$

If the whole solid concrete volume has an average temperature $T_{concrete}$ then the total energy E_{total} is written as:

$$E_{total} = \rho_{concrete}\, C_{p,solid}^{concrete}\, (T_{concrete} - T_{ref}) \sum_{i=1}^{N} S_{z,i}\, \Delta z \tag{A-6-11}$$

From (A-6-10) and (A-6-11), we obtain the average temperature of the whole solid concrete volume:

$$\overline{T}_{concrete} = \frac{\sum_{1}^{N^*} S_{z,i} \overline{T}_z}{\sum_{1}^{N^*} S_{z,i}} \tag{A-6-12}$$

Application of the above method has been carried out for calculation of average temperature in the residual solid concrete in ARTEMIS 11 and ARTEMIS 10. Calculation results are shown in Figure A-6-10 and Figure A-6-11.

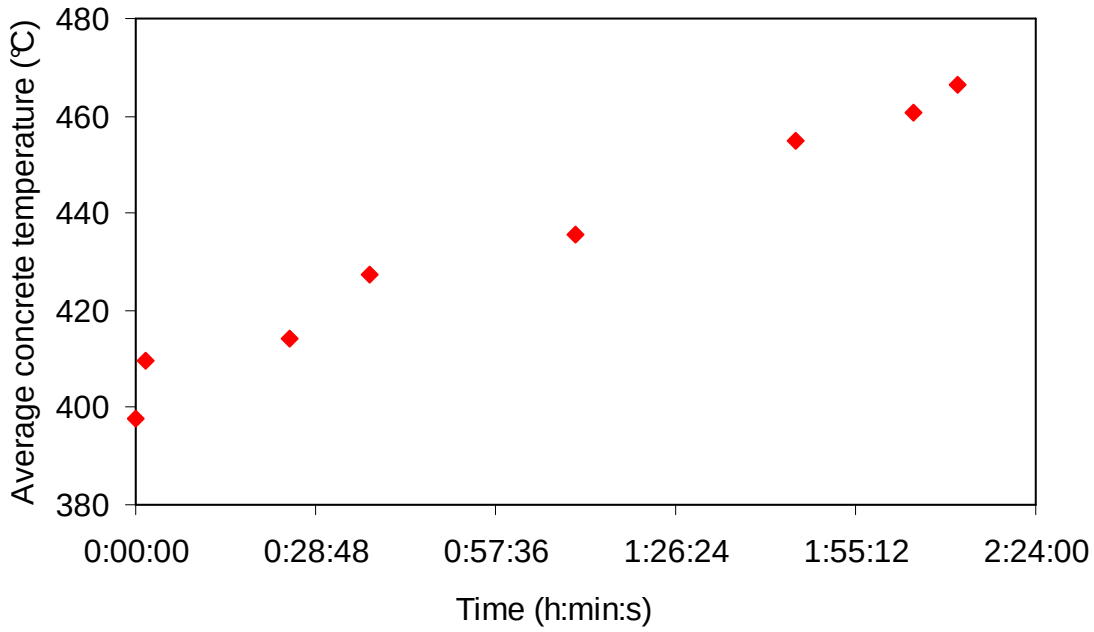

Figure A-6-10. Evolution of average concrete temperature in ARTEMIS 11.

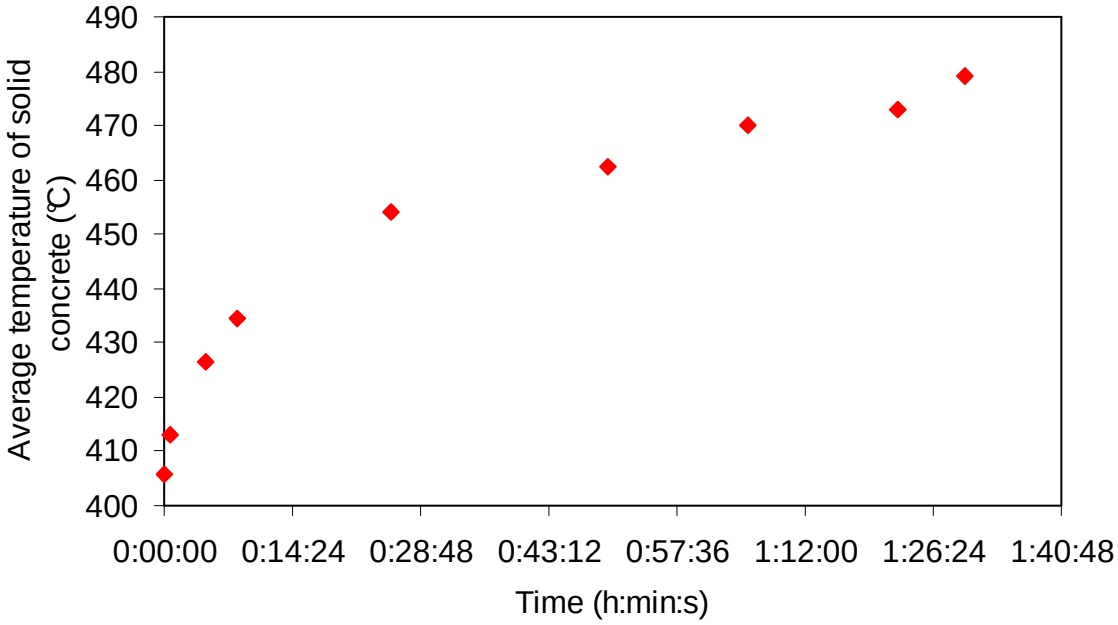

Figure A-6-11. Evolution of average concrete temperature in ARTEMIS 10.

Appendix 7. 1D integral model coupling heat and mass transfer between bulk and boundary layer

A.7.1 Model development for melt-concrete interaction

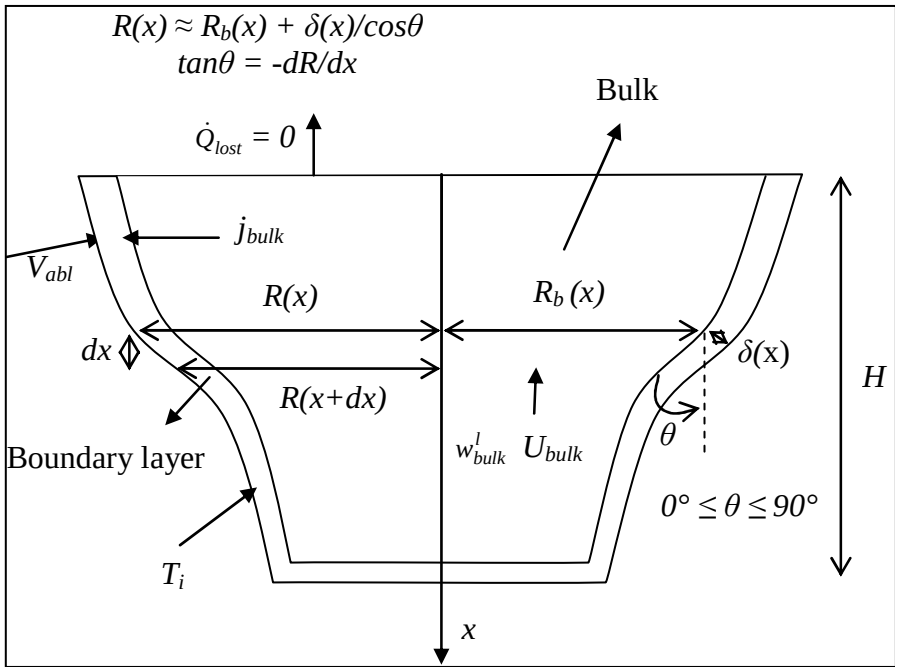

Figure A-7-1. Model 1D schematic for an axisymmetric melt cavity.

An axisymmetric liquid cavity with a height H as shown in Figure A-7-1 is considered. The radius of the cavity at level x (x is the distance from the top of the melt surface) is $R(x)$. The melt cavity is separated into two regions, the boundary layer with thickness $\delta(x)$ and the bulk with radius $R_b(x)$. The bulk flow goes upwards while the boundary layer flow goes downwards. The power transferred to the top of the melt surface is assumed to be zero. The cavity is heated volumetrically with a given axial power dissipation. The volumetric power dissipation is assumed to be uniform radially in the heated zone and is denoted as $\dot{Q}_v(x)$. Assuming a uniform radial temperature distribution in the bulk, then for a given distance x from the top of the melt surface, the bulk is represented by an average temperature $T_{bulk}(x)$, a flow velocity $U_{bulk}(x)$, a liquid composition represented by the mass percentage of solute ($w_{bulk}(x)$) and a corresponding average density $\rho_{bulk}(x)$. The inclination angle of the cavity interface from vertical direction at this position is θ (Figure A-7-1). At the outer surface of the cavity, an interface temperature profile is imposed, i.e. $T_i(x)$. A radial liquid flow with velocity $j_{bulk}(x)$ is assumed to be entrained from the bulk into the boundary layer (Figure A-7-1).

A.7.1.1 Equations for the bulk

In the following, balance equations will first be written for a bulk control volume V_{bulk} located between distance x and distance $(x + \Delta x)$ from the top of the melt surface as depicted in Figure A-7-2.

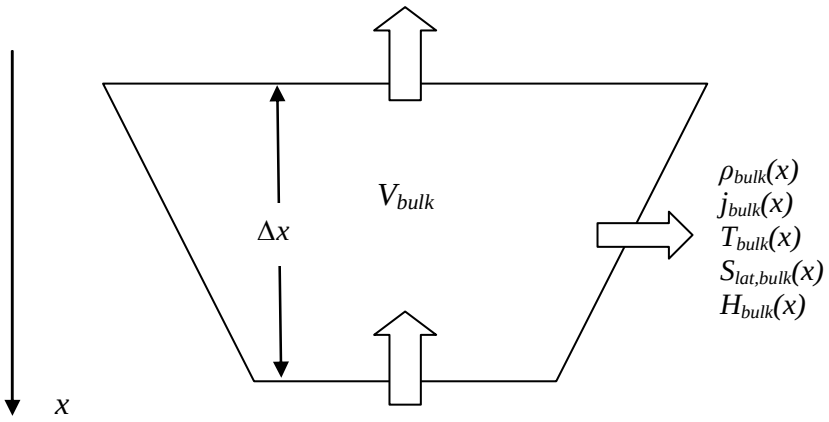

Figure A-7-2. Control volume of the bulk.

Mass balance in the bulk

Variation of the mass in the considered control volume is equal to the difference between the incoming and the outgoing masses.

- The incoming mass flow rate at (x + Δx) is: $S_{bulk}(x+\Delta x)\,\rho_{bulk}(x+\Delta x)\,U_{bulk}(x+\Delta x)$ in which $S_{bulk}(x + \Delta x)$ is the flow cross section at (x + Δx), i.e.

$$S_{bulk}(x+\Delta x) = \pi R_b^2(x+\Delta x) \tag{A-7-1}$$

- The outgoing mass flow rate at x is $S_{bulk}(x)\,\rho_{bulk}(x)\,U_{bulk}(x)$ in which $S_{bulk}(x)$ is the flow cross section at x, i.e.

$$S_{bulk}(x) = \pi R_b^2(x) \tag{A-7-2}$$

- The outgoing mass flow rate due to the radial liquid flow from the bulk to the boundary layer is $S_{lat,bulk}(x)\,\rho_{bulk}(x)\,j_{bulk}(x)$ in which $S_{lat,bulk}(x)$ is the lateral surface area of the bulk, which is calculated by:

$$S_{lat,bulk}(x) = 2\pi R_{avg}(x)\Delta x \tag{A-7-3}$$

wherein $R_{avg}(x)$ is the average radius of the considered control volume:

$$R_{avg}(x) = \frac{R_b(x) + R_b(x+\Delta x)}{2} \tag{A-7-4}$$

The mass variation in the considered control volume V_{bulk} is written as:

$$\frac{d\left[\rho_{bulk}(x)V_{bulk}(x)\right]}{dt} = S_{bulk}(x+\Delta x)\,\rho_{bulk}(x+\Delta x)\,U_{bulk}(x+\Delta x) - S_{lat,bulk}(x)\Delta x\,\rho_{bulk}(x)\,j_{bulk}(x) - S_{bulk}(x)\,\rho_{bulk}(x)\,U_{bulk}(x) \tag{A-7-5}$$

in which

$$V_{bulk}(x) = \pi R_{avg}^2(x)\,\Delta x \tag{A-7-6}$$

NB: j_{bulk} is the liquid entrainment velocity in the boundary layer, in the direction perpendicular to the pool axis.

Combining Equations from (A-7-1) to (A-7-6) gives:

$$\frac{d}{dt}(\pi R_b^2\,\rho_{bulk}) - \frac{d}{dx}(\pi R_b^2\,\rho_{bulk}\,U_{bulk}) = -2\pi R_b\,\rho_{bulk}\,j_{bulk} \tag{A-7-7}$$

wherein the bulk radius is calculated by:

$$R_b(x) = R(x) - \frac{\delta(x)}{\cos\theta} \tag{A-7-8}$$

Since the thickness of the boundary layer is generally much smaller than the radius of the cavity, the radius of the bulk will be considered as the radius of the cavity, i.e.

$$R_b(x) \approx R(x) \tag{A-7-9}$$

Hence, the mass balance in the bulk control volume reads:

$$\frac{d\rho_{bulk}}{dt} + \frac{2\rho_{bulk}}{R_{avg}}\frac{dR_{avg}}{dt} - \frac{R^2}{R_{avg}^2}\frac{d(\rho_{bulk}U_{bulk})}{dx} - \frac{2R\rho_{bulk}U_{bulk}}{R_{avg}^2}\frac{dR}{dx} = -\frac{2\,\rho_{bulk}\,j_{bulk}}{R_{avg}} \tag{A-7-10}$$

in which:

$$\frac{dR}{dx} = -\tan\theta \text{ (Figure A-7-3)} \tag{A-7-11}$$

As seen in Figure A-7-4, the ablation rate of the inclined wall and the variation of the average bulk radius versus time can be calculated by:

$$V_{abl}\,dt = dR_{avg}\cos\theta \Rightarrow \frac{dR_{avg}}{dt} = \frac{V_{abl}}{\cos\theta} \tag{A-7-12}$$

NB: The ablation velocity is defined in the direction that is perpendicular to the interface.

$$\tan\theta = \frac{R(x) - R(x+\Delta x)}{\Delta x} = -\frac{dR}{dx}$$

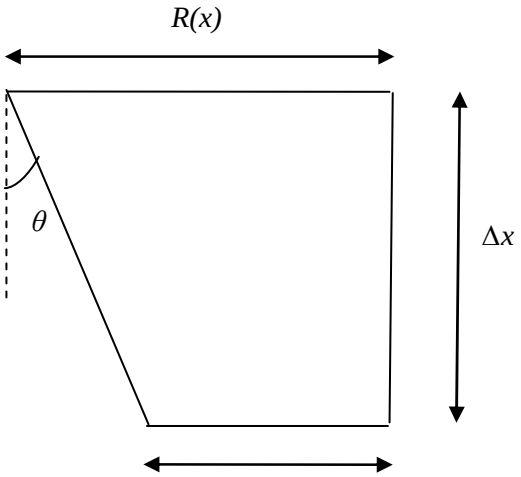

Figure A-7-3. Schematic of the wall inclined angle.

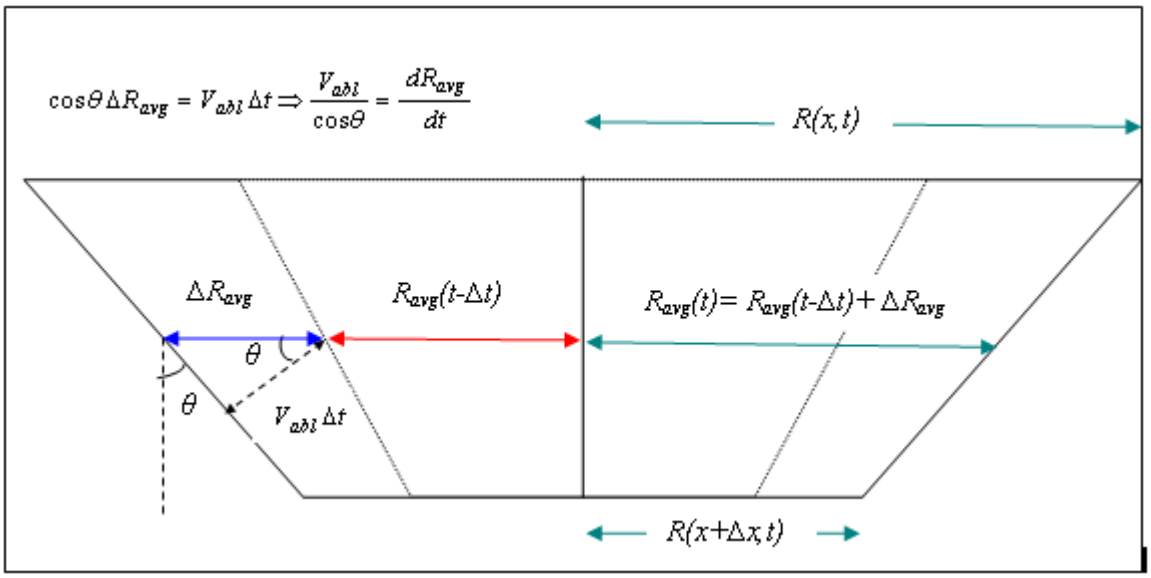

Figure A-7-4. Schematic of ablation velocity.

Combining Equations (A-7-10), (A-7-11) and (A-7-12) gives variation of the bulk velocity in x direction as:

$$\frac{dU_{bulk}}{dx} = \frac{-U_{bulk}}{\rho_{bulk}}\frac{d\rho_{bulk}}{dx} + \frac{1}{\rho_{bulk}}\left(\frac{R_{avg}}{R}\right)^2\frac{d\rho_{bulk}}{dt} + \frac{2}{R}\left[U_{bulk}\tan\theta + \left(j_{bulk} + \frac{V_{abl}}{\cos\theta}\right)\frac{R_{avg}}{R}\right] \tag{A-7-13}$$

In addition, the mass balance for solute in the bulk is written as:

$$\frac{d}{dt}(\pi R_{avg}^2\ \rho_{bulk}\ w_{bulk}) - \frac{d}{dx}(\pi R^2\ \rho_{bulk}\ U_{bulk}\ w_{bulk}) = -2\pi R_{avg}\ \rho_{bulk}\ j_{bulk}\ w_{bulk} \quad \text{(A-7-14)}$$

or:

$$w_{bulk}\left[\frac{d}{dt}(\pi R_{avg}^2\ \rho_{bulk}) - \frac{d}{dx}(\pi R^2\ \rho_{bulk}\ U_{bulk})\right] + \pi R_{avg}^2\ \rho_{bulk}\ \frac{dw_{bulk}}{dt} - \pi R^2\ \rho_{bulk}\ U_{bulk}\ \frac{dw_{bulk}^l}{dx} = -2\pi R_{avg}\ \rho_{bulk}\ j_{bulk}\ w_{bulk} \quad \text{(A-7-15)}$$

Combining Equations (A-7-13) and (A-7-15) leads to:

$$\frac{dw_{bulk}}{dt} - U_{bulk}\left(\frac{R}{R_{avg}}\right)^2 \frac{dw_{bulk}}{dx} = 0 \quad \text{(A-7-16)}$$

Energy balance in the bulk

Variation of energy versus time in the bulk layer located between x and (x + Δx) is written as the difference between the incoming and outgoing powers.

- The incoming power at ($x+\Delta x$) is $S_{bulk}(x+\Delta x)\,\rho_{bulk}(x+\Delta x)\,U_{bulk}(x+\Delta x)\,H_{bulk}(x+\Delta x)$ wherein $H_{bulk}(x+\Delta x)$ is the enthalpy of the bulk at $(x+\Delta x)$.
- The outgoing power at x is $S_{bulk}(x)\,\rho_{bulk}(x)\,U_{bulk}(x)\,H_{bulk}(x)$ in which $H_{bulk}(x)$ is the enthalpy of the bulk at x.
- The power dissipation in the control volume is $\dot{Q}_v(x)\ V_{bulk}(x)$ in which $\dot{Q}_v(x)$ is the local volumetric power dissipation at x ($\dot{Q}_v(x) = 0$ outside of the heated zone and $\dot{Q}_v(x) > 0$ and uniform inside the heated zone).
- The power loss due to the radial liquid flow going from the bulk to the boundary layer is $S_{lat,bulk}(x)\,\rho_{bulk}(x)\,j_{bulk}(x)H_{bulk}(x)$.

The power balance for the bulk reads:

$$\frac{d}{dt}[V_{bulk}(x)\,\rho_{bulk}(x)\ H_{bulk}(x)] = S_{bulk}(x+\Delta x)\,\rho_{bulk}(x+\Delta x)U_{bulk}\ (x+\Delta x)H_{bulk}(x+\Delta x) - S_{bulk}(x)\,\rho_{bulk}(x)U_{bulk}\ (x)H_{bulk}(x) + \dot{Q}_v(x)V_{bulk}(x) - S_{lat,bulk}(x)\,\rho_{bulk}(x)\ j_{bulk}(x)\,H_{bulk}(x) \quad \text{(A-7-17)}$$

Rearranging Equation (A-7-17) with the use of Equations from (A-7-1) to (A-7-6) provides:

$$\frac{d}{dt}(\pi R_{avg}^2\ \rho_{bulk}\ H_{bulk}) - \frac{d}{dx}(\pi R^2\ \rho_{bulk}\ U_{bulk}\ H_{bulk}) = \dot{Q}_v\ \pi R_{avg}^2 - 2\pi R_{avg}\ \rho_{bulk}\ j_{bulk}\ H_{bulk} \quad \text{(A-7-18)}$$

in which the enthalpy of the bulk can be written as:

$$H_{bulk}(T_{bulk}(x)) = w_{bulk} H_{ref,liquid}^{LiCl}(T_{melt}) + (1-w_{bulk}) H_{ref,liquid}^{BaCl2}(T_{melt}) + C_{p,liquid}^{bulk}\left[T_{bulk}(x) - T_{melt}\right] \quad \text{(A-7-19)}$$

with $H_{ref,liquid}^{LiCl}(T_{melt})$ and $H_{ref,liquid}^{BaCl2}(T_{melt})$ are the enthalpies of liquid LiCl and $BaCl_2$ at reference temperature $T_{ref} = T_{melt}$, $C_{p,liquid}^{bulk}$ is the average specific heat of the liquid melt.

Developing Equation (A-7-18) and combining with Equations (A-7-16) and (A-7-19) leads to the variation of the bulk temperature versus time as:

$$\frac{dT_{bulk}}{dt} - U_{bulk}\left(\frac{R}{R_{avg}}\right)^2 \frac{dT_{bulk}}{dx} = \frac{\dot{Q}_v}{\rho_{bulk}\ C_{p,liqui}^{bulk}} \quad \text{(A-7-20)}$$

A.7.1.2 Equations for the boundary layer

The control volume includes two zones which are the boundary layer and the solid concrete as shown in Figure A-7-5 . At a given distance *x* from the top of the boundary layer (the top of the melt surface), the normal thickness of the boundary layer is $\delta(x)$ (the thickness perpendicular to the interface). The boundary layer flow is represented by a normal velocity $U_{BL}(x)$ (perpendicular to the flow cross section) which is the mass-flow average velocity at *x*, an average temperature $T_{BL}(x)$ corresponding to an enthalpy $H_{BL}(x)$.

In one side of the boundary layer, a radial liquid flow containing the liquid corium from the bulk will enter the boundary layer at velocity $j_{bulk}(x)$, temperature $T_{bulk}(x)$, density $\rho_{bulk}(x)$ and enthalpy $H_{bulk}(x)$. In the other side of the boundary layer, the liquid-solid interface has temperature T_i. The solid concrete (depicted in the dotted part) with enthalpy $H_{concrete}$ and initial temperature $T_{concrete}$ lower than the concrete melting temperature T_{melt} will be melted by the heat flux transferred from the boundary layer to the wall. The molten concrete with density ρ_{MC} is considered to enter the boundary layer with a local velocity $V_{abl}(x)$ (perpendicular to the cavity wall).

An integral model for the boundary layer flow will be developed in the next for the volume control ABCD located in between *x* and $(x+\Delta x)$, aiming at describing the velocity and temperature profile in the boundary layer as well as to determine the thickness of the boundary layer and the heat transfer along the liquid-solid interface.

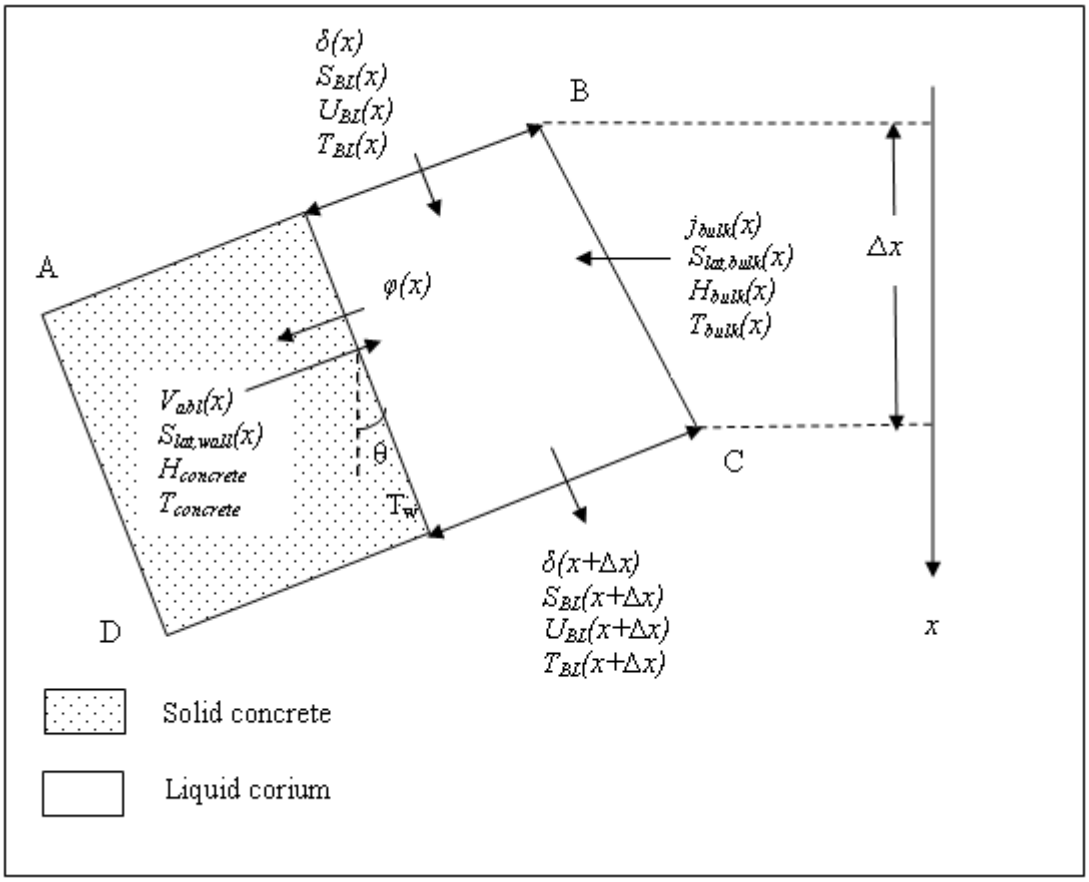

Figure A-7-5. Schematic of the boundary layer.

Mass balance in the boundary layer

The mass variation in the considered control volume ABCD is due to the addition of the incoming masses of the radial liquid flow from the bulk and the molten solid from the ablated solid concrete.

- The incoming mass flow rate due to the radial liquid flow from the bulk to the boundary layer is $S_{lat,bulk}(x)\,\rho_{bulk}(x)\,j_{bulk}(x)$ in which:

$$S_{lat,bulk}(x) = 2\,\pi\,R_{avg}(x)\,\Delta x \tag{A-7-21}$$

- The incoming mass flow rate of the molten concrete due to solid concrete ablation is $S_{lat,wall}(x)\,\rho_{MC}(x)\,V_{abl}(x)$ in which

$$S_{lat,wall}(x) = \frac{2\,\pi\,R_{avg}(x)\,\Delta x}{\cos\theta(x)} \tag{A-7-22}$$

- The incoming mass flow rate at the bulk depth x is $S_{BL}(x)\,U_{BL}(x)\,\rho_{BL}(x)$ in which

$$S_{BL}(x) = 2\,\pi\,R(x)\,\delta(x) \tag{A-7-23}$$

- The outgoing mass flow rate at the $(x + \Delta x)$ is $S_{BL}(x+\Delta x)\,\delta(x+\Delta x)\,U_{BL}(x+\Delta x)\,\rho_{BL}(x+\Delta x)$ in which

$$S_{BL}(x+\Delta x) = 2\,\pi\,R(x+\Delta x)\,\delta(x+\Delta x) \tag{A-7-24}$$

The mass balance for the boundary layer control volume ABCD is written as:

$$\begin{aligned}&\frac{d}{dt}[V_{ABCD}\,\rho_{BL}(x)] = -S_{BL}(x+\Delta x)U_{BL}(x+\Delta x)\rho_{BL}(x+\Delta x)\\&+S_{BL}(x)U_{BL}(x)\rho_{BL}(x)+S_{lat,bulk}(x)\,\rho_{bulk}(x)\,j_{bulk}(x)\\&+S_{lat,wall}\,\rho_{MC}(x)\,V_{abl}(x)\end{aligned} \tag{A-7-25}$$

in which:

$$V_{ABCD} = 2\pi\, R_{avg}(x)\,\delta(x)\,\Delta x \tag{A-7-26}$$

Rearranging Equation (A-7-25) provides:

$$\begin{aligned}&R_{avg}\,\frac{d}{dt}(\delta\,\rho_{BL})+(\delta\,\rho_{BL})\frac{dR_{avg}}{dt}+R\frac{d}{dx}(\,\delta U_{BL}\,\rho_{BL})+(\,\delta U_{BL}\,\rho_{BL})\frac{dR}{dx}\\&=R_{avg}\;\left(\rho_{MC}\,\frac{V_{abl}}{\cos\theta}+\rho_{bulkl}\;j_{bulk}\right)\end{aligned} \tag{A-7-27}$$

Combining Equations (A-7-11), (A-7-12) and (A-7-27) leads to:

$$\begin{aligned}\frac{d(\delta U_{BL}\,\rho_{BL})}{dx} &= \frac{R_{avg}}{R}\left(\frac{\rho_{MC}\,V_{abl}}{\cos\theta}+\rho_{bulk}\;j_{bulk}\right)-\frac{R_{avg}}{R}\frac{d(\delta\,\rho_{BL})}{dt}\\&\quad-\frac{\delta\,\rho_{BL}\,V_{abl}}{R\cos\theta}+\frac{\delta U_{BL}\,\rho_{BL}\tan\theta}{R}\end{aligned} \tag{A-7-28}$$

or:

$$\begin{aligned}\frac{d\delta}{dx} &= \frac{-\delta}{\rho_{BL}}\frac{d\rho_{BL}}{dx}-\frac{\delta}{U_{BL}}\frac{dU_{BL}}{dx}+\frac{R_{avg}}{R}\left(\frac{\frac{\rho_{MC}\,V_{abl}}{\cos\theta}+\rho_{bulk}\;j_{bulk}}{U_{BL}\,\rho_{BL}}\right)\\&\quad-\frac{R_{avg}}{R}\frac{1}{U_{BL}\,\rho_{BL}}\frac{d(\delta\,\rho_{BL})}{dt}-\frac{\delta\;V_{abl}}{U_{BL}\,R\cos\theta}+\frac{\delta\tan\theta}{R}\end{aligned} \tag{A-7-29}$$

Assuming that the mass fraction of solute in the boundary layer liquid flow is w_{BL}, then the mass balance of solute in the boundary layer is written similarly as the way for the mass balance in the bulk, i.e.

$$\begin{aligned}&\frac{d}{dt}(R_{avg}\,\delta\,\rho_{BL}\,w_{BL})+\frac{d}{dx}(R\,\delta U_{BL}\,\rho_{BL}\,w_{BL})\\&=R_{avg}\,(\frac{\rho_{MC}\,V_{abl}\,w_{MC}}{\cos\theta}+\rho_{bulk}\;j_{bulk}\,w_{bulk})\end{aligned} \tag{A-7-30}$$

After intermediate derivation steps, the final form for variation of solute mass fraction in the boundary layer reads:

$$\frac{dw_{BL}}{dt} = -U_{BL}\frac{R}{R_{avg}}\frac{dw_{BL}}{dx} + \frac{\rho_{MC}}{\rho_{BL}}\frac{V_{abl}\,(w_{MC} - w_{BL})}{\delta\cos\theta} + \frac{\rho_{bulk}}{\rho_{BL}}\frac{j_{bulk}\,(w_{bulk} - w_{BL})}{\delta} \tag{A-7-31}$$

Momentum balance in the boundary layer

The momentum balance in the boundary layer contains the following terms:

- The flow momentum at x is $S_{BL}(x)U_{BL}^2(x)\rho_{BL}(x)$.
- The flow momentum at $(x + \Delta x)$ is $S_{BL}(x+\Delta x)\delta(x+\Delta x)U_{BL}^2(x+\Delta x)\rho_{BL}(x+\Delta x)$.
- The gravity force is written as $V_{ABCD}\,g[\rho_{BL}(x) - \rho_{bulk}(x)]$.
- The friction force is calculated from the pressure drop along the flow path in the boundary layer, which is $F\frac{\frac{\Delta x}{\cos\theta}}{D_h}\frac{\rho_{BL}(x)U_{BL}^2(x)}{2}S_{BL}(x)$ in which F is the friction factor, D_h is the hydraulic diameter which is defined locally as $D_h(x) = 2\delta(x)$.

The momentum balance in the boundary layer in between x and $(x + \Delta x)$ is written as follows:

$$\begin{aligned}&\frac{d}{dt}[V_{ABCD}\,U_{BL}(x)\rho_{BL}(x)] = -\rho_{BL}(x+\Delta x)\,U_{BL}^2(x+\Delta x)\,S_{BL}(x+\Delta x)\\&+\rho_{BL}(x)\,U_{BL}^2(x)\,S_{BL}(x) + g[\rho_{BL}(x) - \rho_{bulk}(x)]V_{ABCD}\\&-F\frac{\Delta x}{\cos\theta}\frac{\rho_{BL}(x)U_{BL}^2(x)}{2D_h}S_{BL}(x)\end{aligned} \tag{A-7-32}$$

or:

$$\begin{aligned}&\frac{d}{dt}(R_{avg}\,\delta U_{BL}\,\rho_{BL}) + \frac{d}{dx}(R\,\delta U_{BL}^2\,\rho_{BL})\\&= R_{avg}\,\delta\,g\,(\rho_{BL} - \rho_{bulk}) - F\frac{R}{\cos\theta}\frac{\rho_{BL}\,U_{BL}^2}{4}\end{aligned} \tag{A-7-33}$$

Developing Equation (A-7-33) and combining with the mass balance in the boundary layer leads to the final form of the momentum balance in the boundary layer as:

$$\begin{aligned}&\frac{dU_{BL}}{dx} = \frac{g\,(\rho_{BL} - \rho_{bulk})}{\rho_{BL}\,U_{BL}} - F\,\frac{U_{BL}}{4\delta\cos\theta}\\&-\frac{R_{avg}}{R}\left(\frac{\rho_{MC}\,V_{abl}}{\rho_{BL}\,\delta\cos\theta} + \frac{\rho_{bulk}\,j_{bulk}}{\rho_{BL}\,\delta} + \frac{1}{U_{BL}}\frac{dU_{BL}}{dt}\right)\end{aligned} \tag{A-7-34}$$

Energy balance in the boundary layer

The variation of the power in boundary layer is expressed in terms of:

- The outgoing power at $(x + \Delta x)$ is $\rho_{BL}(x+\Delta x)U_{BL}(x+\Delta x)S_{BL}(x+\Delta x)H_{BL}(x+\Delta x)$;
- The incoming power at x is $\rho_{BL}(x)U_{BL}(x)S_{BL}(x)\ H_{BL}(x)$ in which:

$$H_{BL}(T_{BL}(x)) = w_{BL}H^{LiCl}_{ref,liquid}(T_{melt}) + (1-w_{BL})H^{BaCl2}_{ref,liquid}(T_{melt}) + C^{BL}_{p,liquid}[T_{BL}(x) - T_{melt}] \quad \text{(A-7-35)}$$

- The incoming power due to the entrance of concrete is $\rho_{MC}V_{abl}(x)\ S_{lat,wall}(x)\ H_{concrete}$;
- The incoming power due to the radial liquid flow from the bulk to the boundary layer is $\rho_{bulk}(x)\,j_{bulk}(x)S_{lat,bulk}(x)H_{bulk}(x)$.

The power balance for the considered control volume ABCD is given by

$$\begin{aligned}&\frac{d}{dt}[V_{ABCD}H_{BL}(x)\rho_{BL}(x)] = \rho_{BL}(x)U_{BL}(x)S_{BL}(x)H_{BL}(x)\\&-\rho_{BL}(x+\Delta x)U_{BL}(x+\Delta x)S_{BL}(x+\Delta x)H_{BL}(x+\Delta x)\\&+\rho_{MC}V_{abl}(x)S_{lat,wall}(x)H_{concrete}\\&+\rho_{bulk}(x)\,j_{bulk}(x)\,S_{lat,bulk}(x)H_{bulk}(x)\end{aligned} \quad \text{(A-7-36)}$$

or:

$$\begin{aligned}&\frac{d}{dt}[V_{ABCD}H_{BL}(x)\rho_{BL}(x)] = \rho_{BL}(x)U_{BL}(x)S_{BL}(x)H_{BL}(x)\\&-\rho_{BL}(x+\Delta x)U_{BL}(x+\Delta x)S_{BL}(x+\Delta x)H_{BL}(x+\Delta x)\\&+\rho_{bulk}(x)\,j_{bulk}(x)\,S_{lat,bulk}(x)H_{bulk}(x)\\&-\rho_{MC}V_{abl}(x)S_{lat,wall}(x)\left(H_{MC}-H_{concrete}\right)\\&-\rho_{MC}V_{abl}(x)S_{lat,wall}(x)\left(H_i(x)-H_{MC}\right)\\&-\rho_{MC}V_{abl}(x)S_{lat,wall}(x)\left(H_{BL}(x)-H_i\right)\\&+\rho_{MC}V_{abl}(x)S_{lat,wall}(x)H_{BL}(x)\end{aligned} \quad \text{(A-7-37)}$$

in which $H_{concrete}$ is the enthalpy of the solid concrete at $T_{concrete}$ and H_{MC} is the enthalpy of the molten concrete at T_{melt}.

Since the heat flux transferred from the boundary layer to the liquid-solid interface serves to melt the solid concrete, then:

$$\begin{aligned}\varphi(x) &= \rho_{MC}\, V_{abl}(x)\,\left(H_i - H_{concrete}\right)\\ &= \rho_{MC}\, V_{abl}(x)\left(H_i - H_{MC} + H_{MC} - H_{concrete}\right)\\ &= \rho_{MC}\, V_{abl}(x)\left[C_{p,liquid}^{concrete}\left(T_i - T_{melt}\right) + L_{melting}^{concrete} + C_{p,solid}^{concrete}\left(T_{melt} - T_{concrete}\right)\right]\end{aligned} \tag{A-7-38}$$

in which $L_{melting}^{concrete}$ is the latent heat of melting of concrete, $C_{p,liquid}^{concrete}$ is the specific heat of molten concrete and $C_{p,solid}^{concrete}$ is the specific heat of solid concrete.

Hence, Equation (A-7-37) becomes:

$$\begin{aligned}&\frac{d}{dt}\left[V_{ABCD}\, H_{BL}(x)\,\rho_{BL}(x)\right] =\\ &-\rho_{BL}(x+\Delta x)\,U_{BL}\,(x+\Delta x)\,S_{BL}(x+\Delta x)\,H_{BL}(x+\Delta x)\\ &+\rho_{BL}(x)\,U_{BL}\,(x)\,S_{BL}(x)\,H_{BL}(x) + \rho_{bulk}(x)\,j_{bulk}(x)\,S_{lat,bulk}(x)\,H_{bulk}(x)\\ &-\varphi(x)\,S_{lat,wall}(x) - \rho_{MC}\,V_{abl}(x)\,S_{lat,wall}(x)\left(H_{BL}(x) - H_i\right)\\ &+\rho_{MC}\,V_{abl}(x)\,S_{lat,wall}(x)\,H_{BL}(x)\end{aligned} \tag{A-7-39}$$

After intermediate deriving of Equation (A-7-40), combining Equations (A-7-31) and (A-7-35), the final form of the energy balance in the boundary layer reads:

$$\frac{dT_{BL}}{dx} = \frac{R_{avg}}{R}\left[\begin{aligned}&-\frac{1}{U_{BL}}\frac{dT_{BL}}{dt} - \frac{\varphi(x)}{C_{p,liquid}^{BL}\,\rho_{BL}\,U_{BL}\,\delta\cos\theta}\\ &+\frac{\rho_{bulk}\,j_{bulk}}{\rho_{BL}\,U_{BL}\,\delta}\left(T_{bulk} - T_{BL}\right) + \frac{\rho_{MC}\,V_{abl}}{\rho_{BL}\,U_{BL}\,\delta\cos\theta}\left(T_i - T_{BL}\right)\end{aligned}\right] \tag{A-7-40}$$

The convection heat flux transferred to the wall can be written alternatively in terms of the heat transfer coefficient from the bulk to the liquid-solid interface as:

$$\varphi(x) = h_{bulk}(x)\left(T_{bulk}(x) - T_i\right) \tag{A-7-41}$$

wherein the heat transfer coefficient is calculated from Nusselt number defined as:

$$h_{bulk}(x) = \frac{\lambda_{bulk}\, Nu_{bulk}}{2\,\delta(x)} \tag{A-7-42}$$

in which λ_{bulk} is the thermal conductivity of the melt.

A.7.2. Constitutive laws

In the previous section A.7.1, the integral model coupling the bulk and the boundary layer has been developed based on the balance equations in the bulk and in the boundary layer. However, in order to solve the system of equations, the expressions for the friction factor, the heat transfer coefficient and

the radial liquid flow from the bulk to the boundary layer are required. This section is dedicated to fulfil this task.

A.7.2.1 Friction coefficient

Forced convection in a circular duct

In literature, the friction factor for a forced convection in a circular duct has been estimated by derivation of the radial velocity profile in the duct. The details of these works have been reported by [Rohsenow, Hartnett et Cho, 1998, pp. 5-6] for laminar flow and by [Bird, Stewart et Lightfoot, 1960, pp. 155] for turbulent flow. Only a summary of these works will be recalled here.

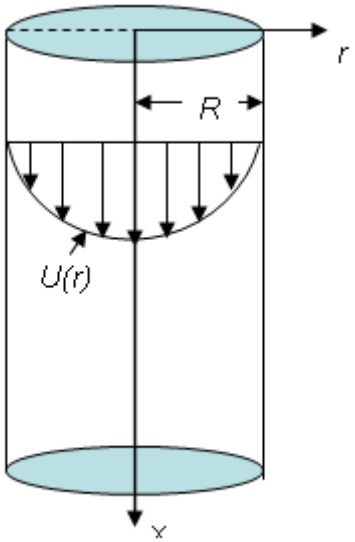

Figure A-7-6. Velocity profile for laminar flow in forced convection in a duct.

For a circular duct with a diameter $D = 2R$, the radial velocity profile of a fully developed laminar flow in forced convection is given analytically by the Hagen-Poiseuille parabolic profile [Handbook of heat transfer, Rohsenow, Hartnett, Cho, 1998, pp.5-6], as follow

$$u(r) = u_{\max}\left[1-(\frac{r}{R})^2\right] \qquad \text{(A-7-43)}$$

in which r is the radial distance from the duct axis and u_{max} is the maximum velocity which is obtained for $\frac{du}{dr}=0$ corresponding to $r=0$.

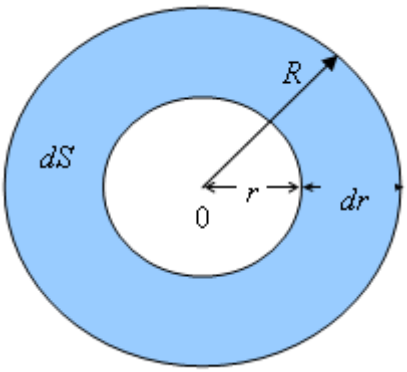

Figure A-7-7. Flow cross section in a duct.

The mass-flow average velocity u_{BL} is given by:

$$u_{BL} = \frac{1}{S_{cross}} \int_0^R u(r)\ dS \qquad \text{(A-7-44)}$$

in which S_{cross} is the flow cross section, $S = \pi R^2$ and $dS = 2\pi R\, dr$ (Figure A-7-7).

Hence:

$$u_{BL} = 0.5 u_{\max} \qquad \text{(A-7-45)}$$

Then, the velocity in the duct can be rewritten as:

$$u(r) = 2 u_{BL}\left[1 - (\frac{r}{R})^2\right] \qquad \text{(A-7-46)}$$

The pressure drop for a given length Δx of the duct is calculated by:

$$\Delta P = F \frac{\Delta x}{D} \frac{\rho u_{BL}^2}{2} \qquad \text{(A-7-47)}$$

in which F is the friction coefficient and ρ_{bulk} is the density of the fluid.

With $D = 2R$, the friction pressure gradient is deduced as:

$$\frac{dP}{dx} = \frac{\Delta P}{\Delta x} = \frac{F}{2R} \frac{\rho\ u_{BL}^2}{2} \qquad \text{(A-7-48)}$$

Besides, the pressure drop along the duct can be determined from the wall shear stress as follows:

$$\Delta P\, S_{cross} = \tau_w\, S_{lateral} \qquad \text{(A-7-49)}$$

in which $S_{lateral}$ is the lateral surface of the duct's wall ($S_{lateral} = 2\pi R \Delta x$).

The wall shear stress τ_w is also defined by:

$$\tau_w = \frac{1}{2} f \rho u_{BL}^2 \tag{A-7-50}$$

On the other hand, the shear stress is written alternatively in terms of the velocity gradient at the wall as:

$$\tau_w = \mu \left. \frac{du}{dr} \right|_{r = R} \tag{A-7-51}$$

in which μ is the dynamic viscosity of the fluid.

Taking into account the velocity profile given by Equation (A-7-43) gives:

$$\tau_w = \frac{2 \mu u_{\max}}{R} \tag{A-7-52}$$

Consequently,

$$F = 4 f \tag{A-7-53}$$

Then the friction coefficient is rewritten, for a circular duct, in terms of the wall shear stress as:

$$F = 4 \frac{\tau_w}{\frac{1}{2} \rho u_{BL}^2} \tag{A-7-54}$$

Replacing $u_{BL} = 0.5 u_{\max}$ and $\tau_w = \frac{2 \mu u_{\max}}{R}$ in Equation (A-7-54) results in:

$$F = 4 \frac{\frac{2 \mu u_{\max}}{R}}{\frac{1}{2} \rho u_{BL}^2} = 16 \frac{\mu}{\rho} \frac{2}{u_{BL}^2 R} = \frac{32 \upsilon}{u_{BL} R} \tag{A-7-55}$$

Defining $\mathrm{Re} = \frac{2 R u_{BL}}{\upsilon}$ leads to:

$$F = \frac{64}{\mathrm{Re}} \tag{A-7-56}$$

According to [Transport Phenomena, Bird, Stewart, Lightfoot, 1960, pp.155], for forced convection in a duct with diameter *D = 2R*, the forced convection velocity profile in turbulent regime is approximately given, for the viscous layer, by the power law velocity distribution as:

$$u(r) = u_{\max}\left(1 - \frac{r}{R}\right)^{1/7} \tag{A-7-57}$$

in which u_{max} is the maximum velocity obtained on the duct axis.

The mass flow average velocity is calculated by integrating the velocity profile given in (A-7-57) as:

$$u_{BL} = \frac{1}{S_{cross}} \int_0^R u(r)\, dS = \frac{49}{60} u_{\max} \tag{A-7-58}$$

For the evaluation of the wall shear stress, we cannot use Equation (A-7-51) since the velocity gradient at the wall is infinite. This is not physically possible. In fact, in the vicinity of the wall in a turbulent boundary layer, there exists a viscous layer, called laminar sub-layer. Inside this region, the temperature gradient is linear. Outside of this layer, the temperature follows the one-seventh power law as in Equation (A-7-57). According to Equation (20.12a) in [Boundary layer theory, Schlichting, 1955, pp.602], the wall shear stress on a wall for turbulent forced and free convection can be approached alternatively by:

$$\tau_w = 0.0225 \rho u_{\max}^2 \left(\frac{\upsilon}{u_{\max} R}\right)^{1/4} \tag{A-7-59}$$

in which υ is the kinematic viscosity of the fluid and u_{max} is, in the case of a duct, the maximum velocity on the axis.

Combining Equations (A-7-54) and (A-7-59) leads to:

$$F = \frac{4}{\frac{1}{2}\rho u_{BL}^2} 0.0225 \rho u_{\max}^2 \left(\frac{\upsilon}{u_{\max} R}\right)^{1/4} \tag{A-7-60}$$

Since $u_m = \frac{49}{60} u_{\max}$, the friction coefficient becomes:

$$F = \frac{4}{\frac{1}{2}\rho u_{BL}^2} \frac{0.0225 \rho u_{BL}^2}{0.146^2} \left(\frac{0.146 \upsilon}{u_{BL} R}\right)^{1/4} \tag{A-7-61}$$

With the definition of $\mathrm{Re} = \frac{2 R u_{BL}}{\upsilon}$ as done for laminar flow, we find:

$$F = 0.31 \mathrm{Re}^{-0.25} \tag{A-7-62}$$

In fact, Equation (A-7-62) corresponds to the Blasius's law of friction in pipe flow [Rohsenow, Hartnett, Cho, 1998, pp.5-22] for the calculation of friction coefficient in a duct for turbulent flow.

Natural convection along a vertical plate

In this section, similar methodology will be applied for calculation of friction factor for natural convection along a vertical plate.

In free convection, the viscous boundary layer velocity profile of a laminar flow along a vertical plate is taken from the Eckert's profile [Alvarez, 1985] as:

$$u(y) = u_c \frac{y}{\delta}\left(1-\frac{y}{\delta}\right)^2 \text{ for } 0 < y < \delta \text{ (Figure A-7-8)} \qquad \text{(A-7-63)}$$

in which y is the distance from the vertical plate, δ is the thickness of the viscous boundary layer and u_c is the characteristic velocity which was introduced by [Eckert et Jackson, 1950]as:

$$u_c = 1.185\left[1+0.494\,\mathrm{Pr}^{2/3}\right]^{-1/2} \frac{\upsilon}{x} Gr_x^{1/2} \qquad \text{(A-7-64)}$$

$$u_c = 1.185\left[1+0.494\,\mathrm{Pr}^{2/3}\right]^{-1/2} \sqrt{g\beta_T (T_{bulk}-T_w)x} \qquad \text{(A-7-65)}$$

wherein g is the gravitational acceleration, β_T is the thermal expansion coefficient, T_{bulk} and T_w are the bulk and the wall temperatures, respectively, and x is the distance from the edge of the boundary layer.

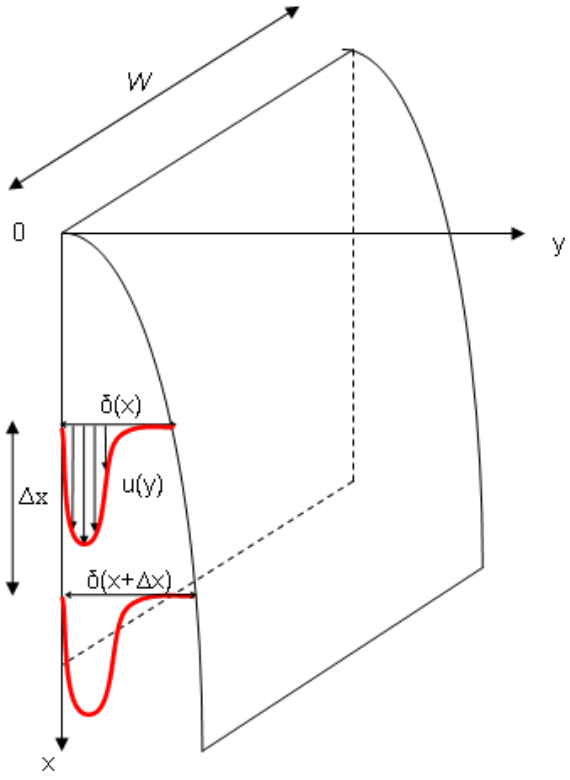

Figure A-7-8. Free convection along a vertical plate with Eckert's velocity profile.

At a given distance x from the edge of the boundary layer, the maximum boundary layer velocity is obtained at $y = \frac{\delta}{3}$ as:

$$u_{\max} = \frac{4}{27} u_c \tag{A-7-66}$$

The boundary layer thickness δ at a given distance x from the edge of the boundary layer is defined as the distance from the plate to a position y at which, typically $\frac{u(y)}{u_{\max}} < 1\%$. The mass-flow average velocity is deduced from:

$$u_{BL} = \frac{1}{W\delta} \int_0^{\delta} u(y) W \, dy \tag{A-7-67}$$

in which W is the width of the plate.

Hence:

$$u_{BL} = \frac{1}{12} u_c \tag{A-7-68}$$

The wall shear stress obtained by taking the derivative of the velocity profile at $y = 0$ is given by:

$$\tau_w = \frac{\mu \, u_c}{\delta} \tag{A-7-69}$$

The friction coefficient F will be calculated from the pressure drop ΔP along the vertical plate over a given length Δx, i.e:

$$\Delta P = F \frac{\Delta x}{D_h} \frac{\rho \, u_{BL}^2}{2} \tag{A-7-70}$$

in which $D_h = 2\delta$.

Besides, the pressure drop can be written in terms of the wall shear stress as follows:

$$\Delta P \, S_{cross} = \tau_w \, S_{lateral} \tag{A-7-71}$$

in which $S_{lateral}$ is the lateral surface of the vertical plate only ($S_{lateral} = W \, \Delta x$) (no friction on the fluid side) and S_{cross} is the flow cross section ($S_{cross} = W \, \delta$).

As a result:

$$F = \frac{96}{\mathrm{Re}} \tag{A-7-72}$$

with $\mathrm{Re} = \frac{2\delta u_{BL}}{\upsilon}$.

According to [Eckert and Jackson, 1950], the velocity profile in a turbulent free convection boundary layer along a vertical plate can be approached by:

$$u(r) = u_c \left(\frac{y}{\delta}\right)^{1/7} \left(1 - \frac{y}{\delta}\right)^4 \quad \text{for } 0 < y < \delta \tag{A-7-73}$$

The maximum velocity is obtained at $y = \frac{\delta}{29}$ as:

$$u_{\max} = 0.5372\, u_c \tag{A-7-74}$$

The mass-flow average velocity is calculated by integrating the velocity profile as:

$$u_{BL} = 0.146\, u_c \tag{A-7-75}$$

This result is coherent with the experimental data for a turbulent boundary layer along a vertical plate reported by [Cheesewright, 1968] which is:

$$u_{BL} = 0.15\, u_c \tag{A-7-76}$$

Since the derivative of the velocity at the wall is infinite (as in the case for turbulent forced convection in a duct, the wall shear stress in turbulent convection along a vertical plate is also estimated by:

$$\tau_w = 0.0225\ \rho u_c^2 \left(\frac{\upsilon}{u_c\, \delta}\right)^{1/4} \tag{A-7-77}$$

as done for a duct.

Finally, the friction coefficient for turbulent natural convection along a vertical plate is derived as:

$$F = 3.1\,\mathrm{Re}^{-0.25} \tag{A-7-78}$$

with $\mathrm{Re} = \frac{2\delta u_{BL}}{\upsilon}$.

A.7.2.2 Heat transfer coefficient

Laminar flow

We consider the temperature profile in laminar free convection along a vertical plate which is given by Eckert [D.Alvarez, 1985], as:

$$\frac{T_{bulk}-T}{T_{bulk}-T_w}=\left(1-\frac{y}{\delta_T}\right)^2 \tag{A-7-79}$$

in which δ_T is the thickness of the thermal boundary layer, T_{bulk} and T_w are respectively the bulk and the wall temperatures and T is the local temperature in the thermal boundary layer at position y.

The heat flux transferred to the plate is calculated by:

$$\varphi=\lambda\left.\frac{dT}{dy}\right|_{y=0} \tag{A-7-80}$$

Therefore:

$$\varphi=\frac{2\lambda}{\delta_T}(T_{bulk}-T_w) \tag{A-7-81}$$

The heat transfer coefficient from the bulk to the vertical plate is defined as:

$$h_{bulk}=\frac{\varphi}{T_{bulk}-T_w} \tag{A-7-82}$$

Hence:

$$h_{bulk}=\frac{2\lambda_{bulk}}{\delta_T} \tag{A-7-83}$$

The corresponding Nusselt number from the bulk to the wall can be introduced as:

$$Nu_{bulk}=\frac{h_{bulk}D_h}{\lambda_{bulk}}=\frac{h_{bulk}2\delta}{\lambda_{bulk}} \tag{A-7-84}$$

As a consequence:

$$Nu_{bulk}=4\frac{\delta}{\delta_T} \tag{A-7-85}$$

The ratio between the viscous and thermal boundary layer thicknesses for laminar flow in natural convection along a flat plate has been obtained analytically by [Ostrach, 1952] for Pr = 0.3, 1, 2, 10, 100, 1000 (shown in Figure A-7-9).

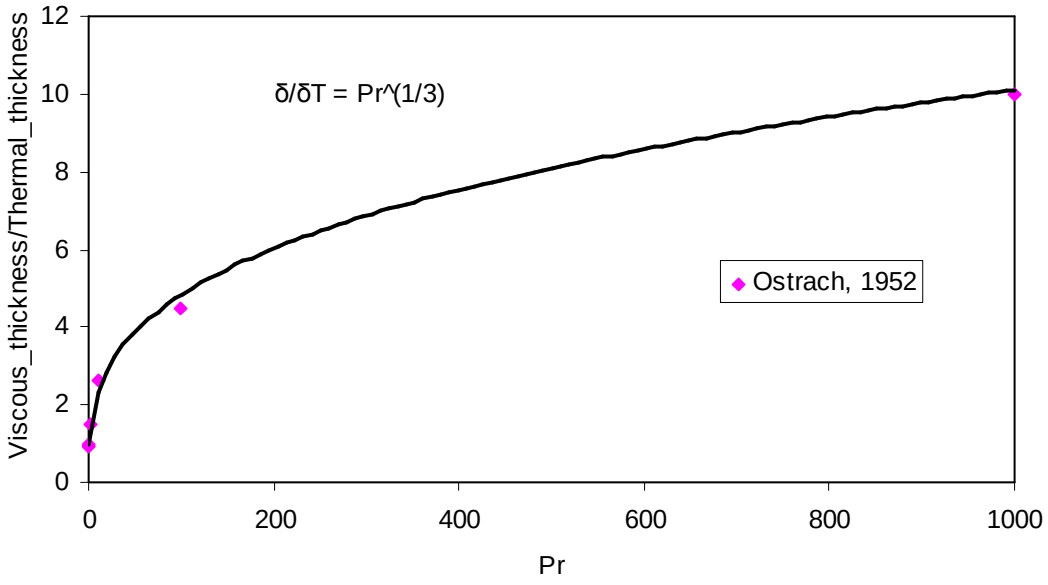

Figure A-7-9. Ratio between viscous boundary layer thickness and thermal boundary layer thickness in laminar natural convection.

The results show $\frac{\delta}{\delta_T}$ as a function of Pr number for Pr ≥ 1 as follows:

$$\frac{\delta}{\delta_T} = \mathrm{Pr}^{1/3} \tag{A-7-86}$$

Thus:

$$Nu_{bulk} = \frac{h_{bulk} D_h}{\lambda_{bulk}} = 4\,\mathrm{Pr}^{1/3} \tag{A-7-87}$$

Turbulent flow

The temperature profile in a turbulent free convection boundary layer along a vertical plate is approached by [Eckert et Jackson, 1950] as:

$$\frac{T_{bulk} - T}{T_{bulk} - T_w} = 1 - \left(\frac{y}{\delta_T}\right)^{1/7} \quad \text{for } 0 < t < \delta_T \tag{A-7-88}$$

in which δ_T is the thickness of the thermal boundary layer and y is the distance from the surface of the vertical plate.

It is observed from the experimental results reported by [Cheesewright, 1968] that in turbulent natural convection; the thicknesses of the viscous and thermal boundary layers are the same. Therefore, Equation (A-7-88) can be also written as:

$$\frac{T_{bulk}-T}{T_{bulk}-T_w}=1-\left(\frac{y}{\delta}\right)^{1/7} \quad \text{for } 0<t<\delta_T \tag{A-7-89}$$

Since the derivative of the boundary layer temperature in Equation (A-7-88) is infinite at the surface of the vertical plate, the heat flux transferred to the plate cannot be calculated as done for laminar regime. However, according to [Eckert et Jackson, 1950], the heat flux transferred to the wall can be estimated by Reynolds analogy between the turbulent exchange of momentum and heat as:

$$\varphi=k_s\tau_w C_p\frac{T_{bulk}-T_w}{u_c}\mathrm{Pr}^{-2/3} \tag{A-7-90}$$

in which k_s is an adjustable coefficient.

Consequently, the heat flux is written by:

$$\varphi=0.0225\,k_S\,\mathrm{Pr}^{-2/3}\,\rho_{bulk}\,C_{p,liquid}^{bulk}\,u_C(T_{bulk}-T_w)\left(\frac{\upsilon}{u_C\,\delta}\right)^{1/4} \tag{A-7-91}$$

The heat transfer coefficient from the bulk to the wall is defined as

$$h_{bulk}=0.0225\,k_S\,\mathrm{Pr}^{-2/3}\,\rho_{bulk}\,C_{p,liquid}^{bulk}\,u_C\left(\frac{\upsilon}{u_C\,\delta}\right)^{1/4} \tag{A-7-92}$$

and:

$$Nu_{bulk}=\frac{h_{bulk}D_h}{\lambda_{bulk}} \tag{A-7-93}$$

in which D_h is the hydraulic diameter which is 2δ for a flat plate.

Therefore:

$$Nu_{bulk}=0.0225\,k_S\,\mathrm{Pr}^{-2/3}\,\frac{\rho\,C_{p,liquid}^{bulk}}{\lambda}\,2\delta\,u_C\left(\frac{\upsilon}{u_C\,\delta}\right)^{1/4} \tag{A-7-94}$$

Replacing $u_{BL}=0.146\,u_c$ for turbulent flow in natural convection along a vertical wall gives:

$$Nu_{bulk}=0.113\,k_S\,\mathrm{Pr}^{1/3}\,\mathrm{Re}^{3/4} \tag{A-7-95}$$

A.7.2.3 Estimation of the radial velocity from bulk to boundary layer

In the literature, several boundary layer models have been developed for natural convection along a vertical wall with constant temperature at the wall and in the bulk or in volume-heated peripherally cooled pools. These models have proposed profiles of boundary layer velocity and boundary layer thickness. According to the mass balance equation, the velocity of the radial liquid flow entering the boundary layer from the bulk (j_{bulk}) can be deduced, as follows:

$$\frac{d}{dx}(\rho_{BL}\, u_{BL}\, \delta) = \rho_{bulk}\, j_{bulk} \tag{A-7-96}$$

in which ρ_{BL} is the density of the boundary layer, u_{BL} is the mass-flow average velocity of the boundary layer, δ is the thickness of the viscous boundary layer and ρ_{bulk} is the density of the bulk.

In this analysis, three of such models taken from the works of [Cheesewright, 1968], [Alvarez, 1985] and [Bonnet, 1994] will be considered to determine the expression of the radial liquid entrainment velocity j_{bulk}.

Cheesewright boundary layer model

Cheesewright investigated experimentally the boundary layer along a vertical wall in natural convection [Cheesewright, 1968]. From this work, the boundary layer thickness profile for both laminar and turbulent flow regimes have been provided, which are:

- For laminar regime:

$$\delta = 3.5x\left(\frac{Gr_x}{4}\right)^{-0.25} \tag{A-7-97}$$

- For turbulent regime:

$$\delta = 0.16xGr_x^{-0.1} \tag{A-7-98}$$

in which:

$$Gr_x = \frac{g\,\beta_T\,(T_{bulk} - T_w)\,x^3}{\upsilon^2} \tag{A-7-99}$$

wherein T_{bulk} and T_w are the bulk and the wall temperatures respectively, g is the gravity acceleration, β_T is the thermal expansion coefficient, υ is the kinematic viscosity of the fluid and x is the distance from the edge of the boundary layer.

Using the mass balance in the boundary layer (Equation (A-7-96)), the radial liquid velocity will be deduced. It is noted that in, the work of [Cheesewright, 1968], only the profile of average boundary layer velocity in turbulent regime was reported, which is:

$$u_m = 0.15\sqrt{g\beta_T\,(T_{bulk} - T_w)x} \tag{A-7-100}$$

Therefore, the liquid entrainment velocity j_{bulk} is only calculated for turbulent regime, as follows:

$$j_{Cheesewright,turbulent} = 0.024\left[g\beta_T (T_{bulk} - T_w)\right]^{0.4} \upsilon^{0.2} x^{0.2} \quad \text{(A-7-101)}$$

Alvarez boundary layer model

Alvarez proposed a boundary layer model which was developed using the integral method [Alvarez, 1985]. In this model, the thickness and the average velocity for a liquid laminar flow boundary layer are given by the following formulas:

$$\delta = K_\delta Gr_x^{-1/4} \quad \text{(A-7-102)}$$

$$u_m = K_u \frac{Gr_x^{1/2}}{x} \quad \text{(A-7-103)}$$

with

$$K_\delta = (80\times 3)^{1/4} \left(\frac{20}{21} + \mathrm{Pr}\right)^{1/4} \mathrm{Pr}^{-1/2} \quad \text{(A-7-104)}$$

$$K_u = \frac{1}{12}\left(\frac{80}{3}\right)^{1/2} \left(\frac{20}{21} + \mathrm{Pr}\right)^{-1/2} \upsilon \quad \text{(A-7-105)}$$

wherein T_{bulk} and T_w are the bulk and the wall temperatures respectively, g is the gravity acceleration, β_T is the thermal expansion coefficient, υ is the kinematic viscosity of the fluid and x is the distance from the edge of the boundary layer.

Using the mass balance in the boundary layer (Equation (A-7-96)), the velocity of the radial liquid flow can be deduced as:

$$j_{Alvarez,laminar} = \frac{1}{16} K_\delta K_u \left[g\beta_T (T_{bulk} - T_w)\right]^{1/4} \upsilon^{-1/2} x^{-1/4} \quad \text{(A-7-106)}$$

FLUXBAIN boundary layer model

In FLUXBAIN model approach [Bonnet, 1995], the boundary layer model is developed for a volume-heated cylindrical pool. The expressions of local boundary layer thickness and mean velocity in turbulent regime are reported as:

$$\delta = \frac{\left[8(0.0784 + 0.0366\,\mathrm{Pr}^{2/3})\right]^{1/2}}{0.0366\,\mathrm{Pr}} \frac{0.15\,\mathrm{Pr}^{1/3}}{\left[1 + \left(\frac{0.492}{\mathrm{Pr}}\right)^{9/16}\right]^{16/27}} x Gr_x^{-1/6} \quad \text{(A-7-107)}$$

$$u_{BL} = \left[8\,(0.0784 + 0.0366\,\mathrm{Pr}^{2/3}\right]^{-1/2} \sqrt{g\beta_T (T_{bulk} - T_x) x} \quad \text{(A-7-108)}$$

with $Gr_x = \frac{g\,\beta\,(T_{bulk} - T_w)\,x^3}{\upsilon^2}$ wherein T_{bulk} and T_w are the bulk and the wall temperatures respectively, g is the gravity acceleration, β_T is the thermal expansion coefficient, υ is the kinematic viscosity of the fluid and x is the distance from the edge of the boundary layer.

Combining the profiles of boundary layer velocity and boundary layer thickness given in Equations (A-7-107) and (A-7-108) with Equation(A-7-96), the radial liquid velocity from the bulk to the boundary layer in natural convection is estimated by:

$$j_{FLUXBAIN,turbulent} = F(\mathrm{Pr})\left[g\,\beta_T\,\left(T_{bulk} - Tw\right)\upsilon\right]^{1/3} \tag{A-7-109}$$

with

$$F(\mathrm{Pr}) = \frac{0.598\,\mathrm{Pr}^{-2/3}}{\left[1+\left(\frac{0.492}{\mathrm{Pr}}\right)^{9/16}\right]^{16/27}} \tag{A-7-110}$$

Proposal of a correlation for estimation of the radial liquid velocity from bulk to boundary layer

From the three mentioned correlations for j_{bulk}, it is observed that in the case when the bulk and the wall temperature are constant, supposing that the physical properties of the fluid are maintained constant, then $j_{Cheesewright,turbulent}$ and $j_{Alvarez,laminar}$ are dependent on the distance x from the edge of the boundary layer and Pr number while $j_{FLUXBAIN,turbulent}$ is only dependent on Pr number. Besides, each of these three correlations is applicable for either laminar or turbulent regime.

For our needs, we are looking to find a correlation for j_{bulk} that satisfies the following constraints:

- First, the correlation should be applicable at any position in the boundary layer, even if the surface is curvilinear in the case of a melting wall. Therefore, we cannot use the distance x from the edge and we are searching a correlation that is only a function of local parameters;
- Second, the correlation should be applicable when the density difference between the boundary layer and the bulk is also linked to variable composition (case of wall ablation with different composition), and not only to the temperature difference. In that case, the motor of bulk liquid entrainment into the boundary layer is the density difference. Extending to the case of uniform composition but different temperature, the entrainment is also linked to the density difference which is connected to the temperature difference between the boundary layer and the bulk (not to the temperature difference between the wall and the bulk).

Therefore, we propose the following expression, derived from Equation (A-7-109):

$$j_{bulk} = k_j\left\{g\,\upsilon\left[\beta_T\left(T_{bulk} - T_{BL}\right) + \beta_c\left(w_{bulk} - w_{BL}\right)\right]\right\}^{1/3} \tag{A-7-111}$$

in which k_j is supposed to be a function of Pr number, T_{BL} is the average temperature in the boundary layer, w_{bulk} and w_{BL} are respectively the average compositions in the bulk and in the boundary layer, β_T is the thermal expansion coefficient of the fluid and β_C is the concentration expansion coefficient of the fluid.

Coefficient k_j will be deduced for varying Pr number.

$$k_j = F(\mathrm{Pr})\left(\frac{T_{bulk} - T_w}{T_{bulk} - T_{BL}}\right)^{1/3} \quad \text{(A-7-112)}$$

The mass flow average temperature in the boundary layer is calculated by integrating the temperature profile, given in Equation (A-7-79) for laminar flow and Equation (A-7-88) for turbulent flow.

$$T_{BL} = \frac{1}{u_{BL}\delta}\int_0^{\delta} T(y)\,u(y)\,dy \quad \text{(A-7-113)}$$

Then, for laminar flow:

$$\frac{T_{BL} - T_w}{T_{bulk} - T_w} = \frac{4}{5}\frac{\delta}{\delta_T} - \frac{1}{5}\left(\frac{\delta}{\delta_T}\right)^2 \text{ with } \frac{\delta}{\delta_T} = \mathrm{Pr}^{1/3} \text{ (Equation (A-7-86))} \quad \text{(A-7-114)}$$

and for turbulent flow:

$$\frac{T_{BL} - T_w}{T_{bulk} - T_w} = 0.7515 \quad \text{(A-7-115)}$$

Consequently, coefficient k_j can be deduced as:

$$k_{j,laminar} = \frac{F(\mathrm{Pr})}{\left[1 - \frac{4}{5}\left(\frac{\delta}{\delta_T}\right) + \frac{1}{5}\left(\frac{\delta}{\delta_T}\right)^2\right]^{1/3}} \text{ with } \frac{\delta}{\delta_T} = \mathrm{Pr}^{1/3} \quad \text{(A-7-116)}$$

$$k_{j,turbulent} = \frac{F(\mathrm{Pr})}{0.2485^{1/3}} \quad \text{(A-7-117)}$$

with $F(\mathrm{Pr}) = \dfrac{0.598\,\mathrm{Pr}^{-2/3}}{\left[1 + \left(\frac{0.492}{\mathrm{Pr}}\right)^{9/16}\right]^{16/27}}$ (Equation (A-7-110)).

Figure A-7-10 shows the calculated value of k_j as functions of Pr number in laminar and turbulent regimes with Pr number varying from 1 to 10. It is observed that for Pr > 1, k_j in laminar and turbulent regimes are relatively the same.

- For Pr = 2.56 (water in test conditions of [Cheesewright, 1968]), k_j = 0.41;
- For Pr = 9.3 (LIVE L3A), k_j = 0.19;
- For Pr = 3.3 (ARTEMIS 11), k_j = 0.36.
- For Pr = 4 (ARTEMIS 10), k_j = 0.33.

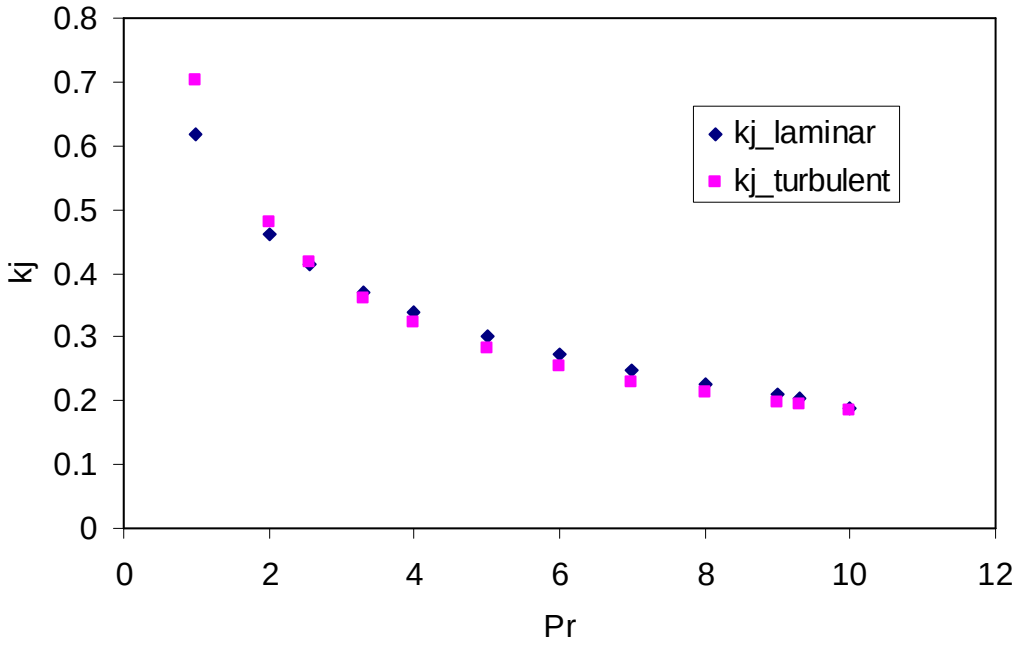

Figure A-7-10. Dependence of coefficient kj on Prandt number.

A.7.3 Model validation for natural convection along a vertical plate

A.7.3.1 Conditions and constitutive laws for calculation

Calculation with the developed boundary layer model has been carried for a vertical plate in water with T_{bulk} = 85°C and T_w = 55°C. The physical properties is taken at film temperature ($T_f = \frac{T_{bulk} + T_w}{2} = 70°C$) corresponding to Pr = 2.56. These conditions have been chosen in order to allow a comparison with experimental results from [Cheesewright, 1968].

The radial liquid velocity from the bulk to the boundary layer is estimated by:

$$j_{bulk} = 0.41\left[g\,\beta_T\,(T_{bulk} - T_{BL})\,\upsilon\right]^{1/3} \qquad \text{(A-7-118)}$$

The friction coefficient and Nusselt number in the bulk are calculated using the equations derived in the previous section for free convection along a vertical plate, as follows:

- For laminar regime ($Gr_x < 2\ 10^9$):

$$F = \frac{96}{\mathrm{Re}} \qquad \text{(A-7-119)}$$

$$Nu_{bulk} = 4\frac{\delta}{\delta_T} = 4\,\mathrm{Pr}^{1/3} \quad \text{(A-7-120)}$$

- For turbulent regime ($Gr_x > 10^{10}$):

$$F = 3.1\,\mathrm{Re}^{-0.25} \quad \text{(A-7-121)}$$

$$Nu_{bulk} = 0.113 k_s\,\mathrm{Pr}^{1/3}\,\mathrm{Re}^{3/4} \quad \text{(A-7-122)}$$

In the transition zone (2 109 < Gr_x < 1010), the friction factor and Nusselt in the boundary layer are estimated by interpolated functions of local Reynolds.

A.7.3.2 Calculation results

In the next, calculation will be done to evaluate the boundary layer behaviour along a vertical plate in natural convection for water with Pr = 2.56. In turbulent, various values for k_s are applied for the calculation of heat transfer from the bulk to the wall. For the validation of the developed boundary layer model, the calculated boundary layer thickness will be compared with the ones given by [Eckert et Jackson, 1950], [Cheesewright, 1968] and [Alvarez, 1985].

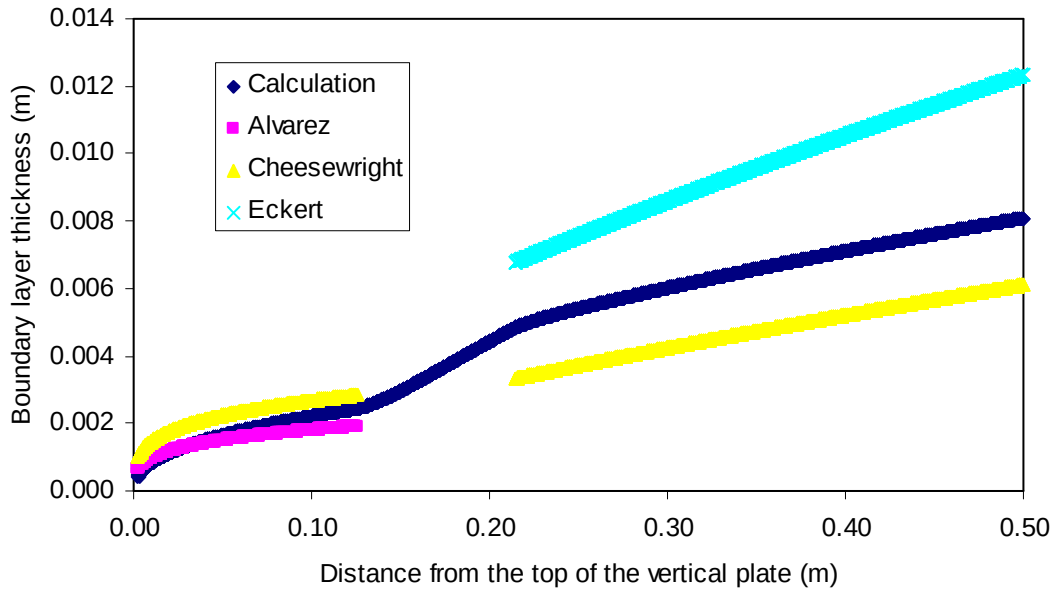

Figure A-7-11. Boundary layer thickness along a vertical plate in natural convection.

As seen in Figure A-7-12, the thickness of the calculated boundary layer in laminar regime is similar to those given by Cheesewright and Alvarez. In turbulent regime, the calculation results are in between the reference ones reported by Cheesewright and Eckert. This allows a validation of the model in describing the boundary layer along a vertical wall in natural convection.

In addition, calculated heat transfer coefficient is also compared with those given by existing correlations such as [Chawla et Chan, 1982], [McAdams, 1954], [Al-Arabi et al., 1991], [Chen et al.,

1986] … It is observed from Figure A-7-13 to Figure A-7-16 that the calculated results are in agreement with the references. For turbulent regime, with k_s = 1, k_s = 0.67 and k_s = 0.5, the calculated heat transfer coefficient is higher than the correlations while with k_s = 0.3, it is smaller. With k_s = 0.4, the calculated heat transfer coefficient stays in between the references and therefore, it is selected for the calculation of heat transfer during turbulent regime for a vertical plate.

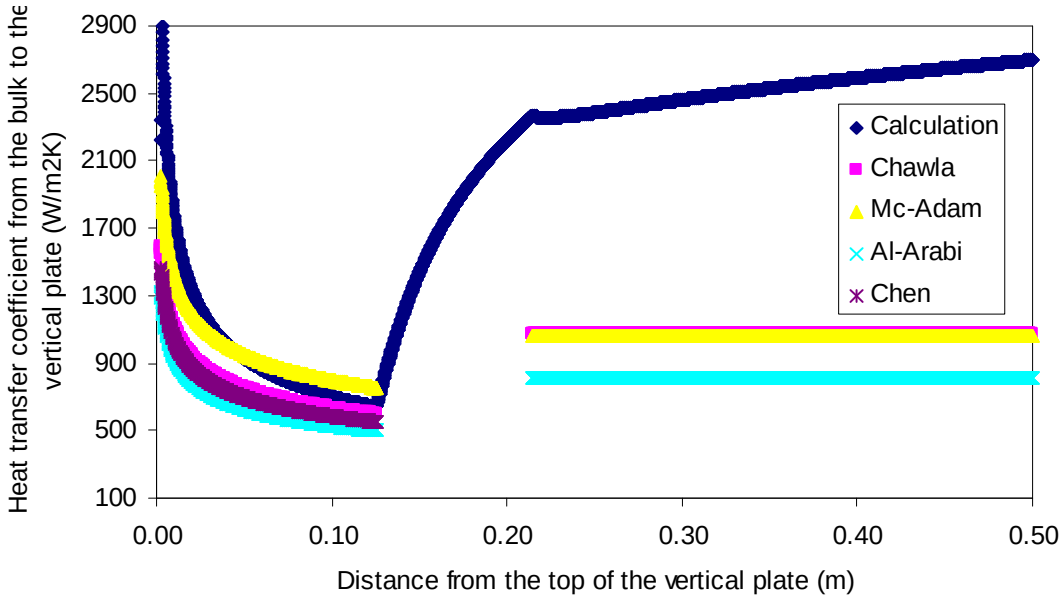

Figure A-7-12. Heat transfer coefficient from the bulk to the vertical plate in natural convection k_s = 1.

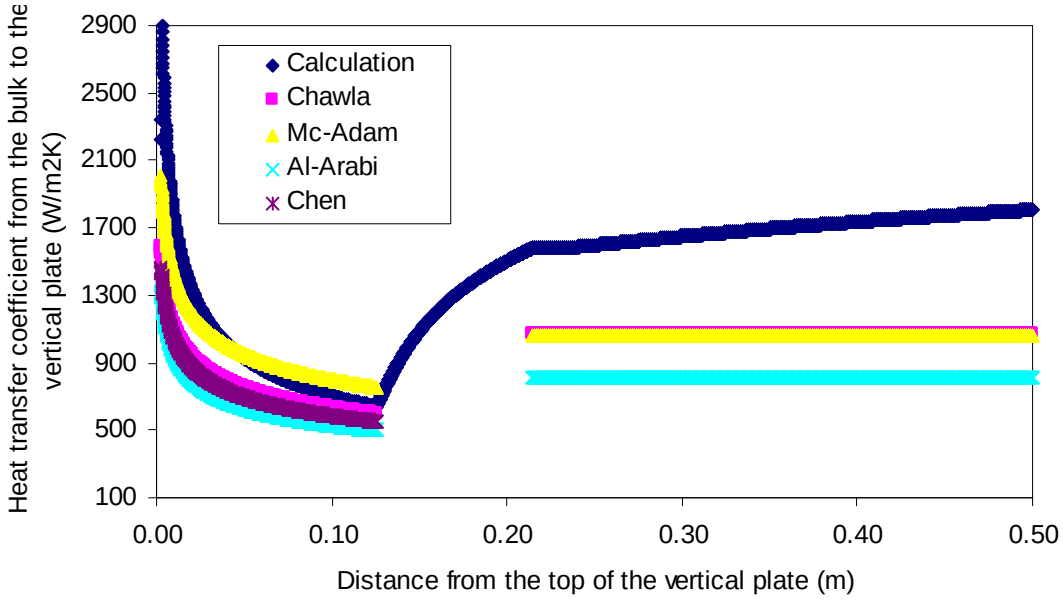

Figure A-7-13. Heat transfer coefficient from the bulk to the vertical plate in natural convection k_s = 0.67.

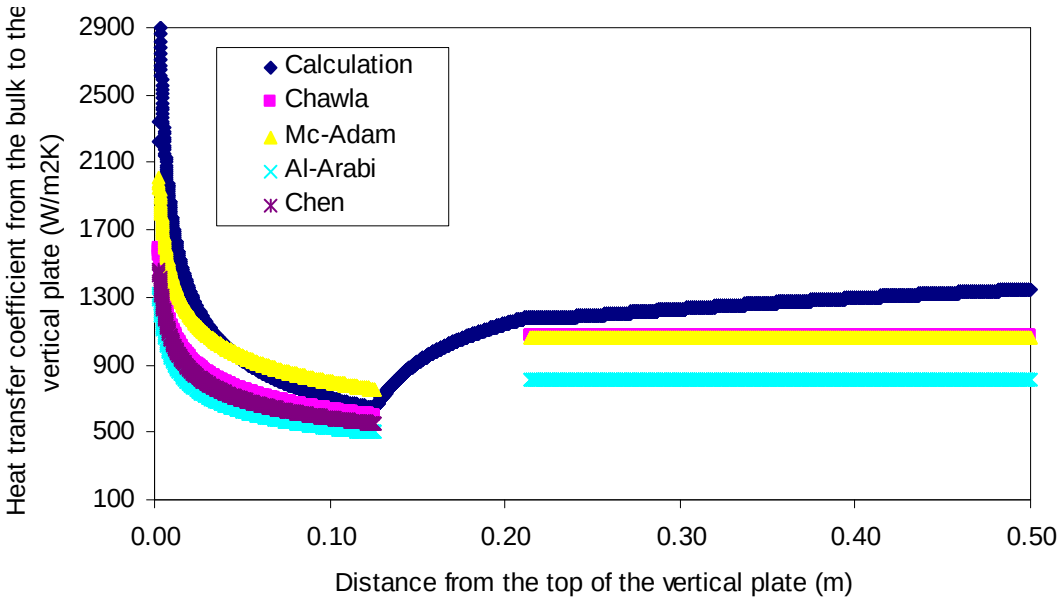

Figure A-7-14. Heat transfer coefficient from the bulk to the vertical plate in natural convection $k_s = 0.5$.

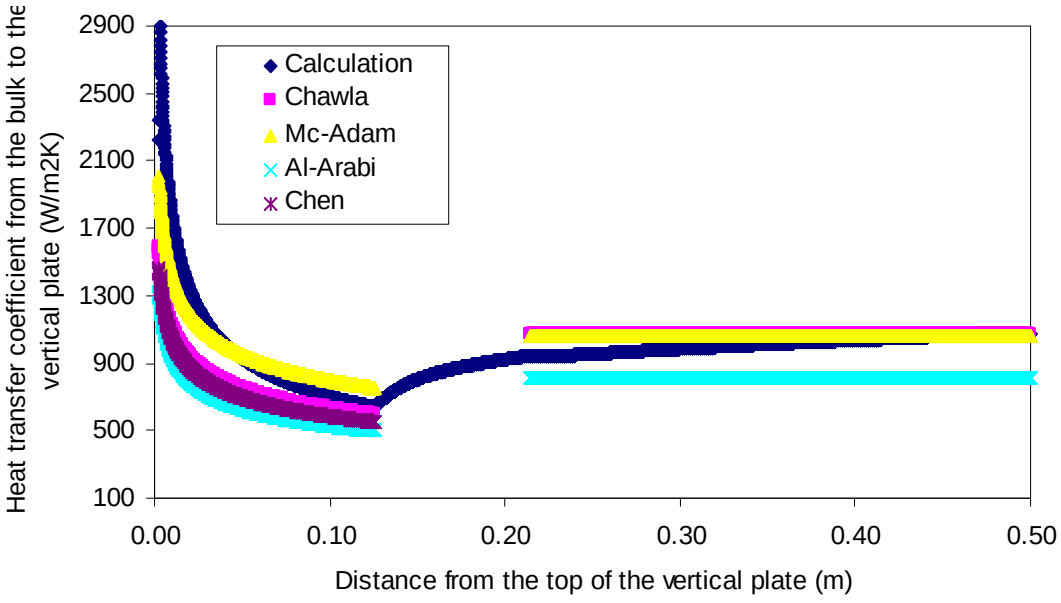

Figure A-7-15. Heat transfer coefficient from the bulk to the vertical plate in natural convection with $k_s = 0.4$.

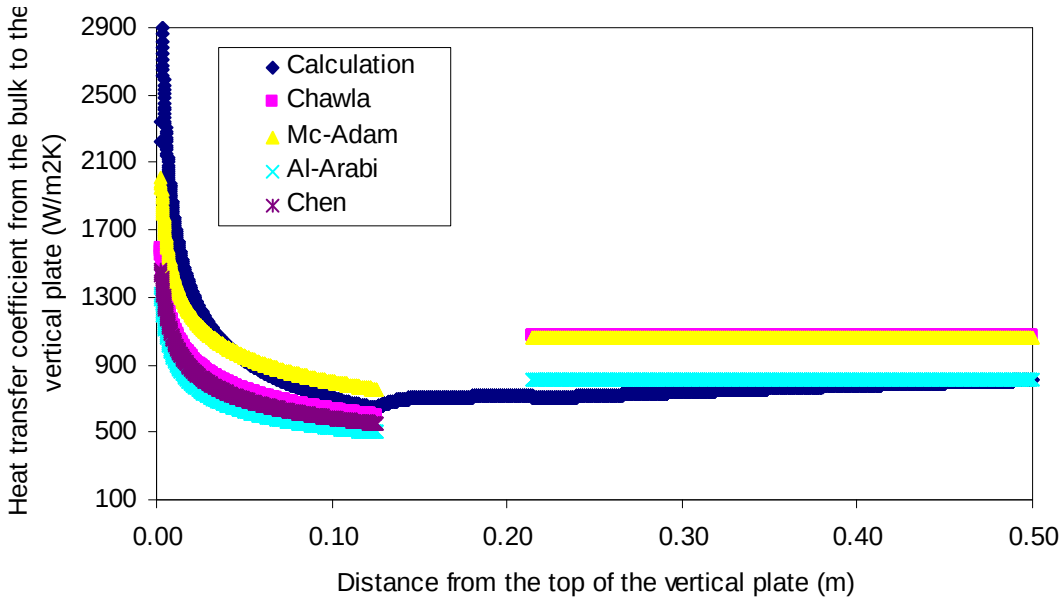

Figure A-7-16. Heat transfer coefficient from the bulk to the vertical plate in natural convection with $k_s = 0.3$.

After the developed integral model is validated for the simple case for a vertical plate, it has been applied for the test conditions of LIVE L3A, ARTEMIS 11 and ARTEMIS 10 for calculation of natural convection in cylinder or hemisphere melt cavity with transient evolution of melt temperature and solidification (LIVE L3A, Chapter 2) or ablation (ARTEMIS 11, Chapter 4 and ARTEMIS 10, Chapter 5) at the liquid-solid interface.

RESUME FRANCAIS

1. Contexte

Ce travail de thèse a été réalisé dans le cadre de l'analyse des phénomènes physiques concernant les accidents graves hypothétiques dans un réacteurs nucléaires (REP).

Dans un hypothétique accident grave de réacteur nucléaire, le cœur du réacteur ne serait plus refroidi par le système de refroidissement. Dans ce scénario, à cause de la puissance résiduelle (de l'ordre de 20 à 30 MW pour un réacteur de 1000 MWe), le combustible s'échauffe. Par ailleurs, l'oxydation exothermique du zirconium. Les produits de fission qui sont volatiles sont également générés dans le bâtiment réacteur. En quelques heures après le démarrage de l'accident, un mélange de matériaux fondus appelé «corium» est formé dans la cuve du réacteur. Le corium fondu migre vers le fond de la cuve et la chaleur dégagée par celui-ci peut faire dégrader la cuve. Ensuite, le corium tomerait dans le puits de cuve en béton. Par conséquence, une interaction entre le corium fondu et le béton (MCCI) a lieu. Cette interaction peut durer plusieurs jours. La puissance résiduelle diminue très lentement dans les semaines et les mois ultérieurs.

La stratégie de rétention en cuve (IVR) a pour objectif de retenir le corium dans le fond de la cuve du réacteur (RPV) en appliquant un refroidissement externe autour de la cuve. Cette approche fait partie des stratégies importantes permettant de gérer les accidents graves dans les centrales nucléaires. En effet, la rétention du corium est essentielle pour mettre fin la progression de l'accident, assurant ainsi l'intégrité de la cuve du réacteur (confinement secondaire). La compréhension de la distribution du flux de chaleur à la paroi interne de la cuve est dans ce cas.

En outre, la gestion des accidents graves dans les réacteurs nucléaires nécessite également la prévention du percement du radier en béton afin de protéger cette troisième barrière de sécurité entre les matériaux radioactifs et l'environnement externe. L'ablation du béton peut se produire uniquement dans la direction radiale ou de manière isotrope dans les deux directions radiale et axiale, en fonction de la distribution du flux de chaleur à l'interface entre le corium et le béton. Par ailleurs, le flux de chaleur dépend des variations des conditions d'interface (la température et la composition).

Le corium est composé de plusieurs matériaux de base tels que UO_2, Zr et ZrO_2, etc.. La température typique du corium est comprise entre 2300 °C et 2700 ° C.

Le béton peut également avoir des compositions différentes dont les principaux composants sont SiO_2 (béton siliceux, température de fusion ~ 1850 ° C), et $CaCO_3$ (calcaire, se décompose en CaO et CO2). Puisque le béton n'est pas un matériau pur, sa température de fusion peut varier entre 1300 ° C et 1800 ° C. Cette température est très inférieure à celle de solidification du corium (UO_2+ZrO_2, ~ 2500°C), par conséquent, du solide peut se déposer à l'interface corium-béton, impactant la thermohydraulique du bain de corium et, ainsi, la répartition du flux de chaleur et les vitesses d'ablation du béton.

Dans la suite de ce document, l'expression «corium» sera utilisée pour désigner le matériau fondu plutôt réfractaire et l'expression «béton» sera utilisée pour désigner le matériau de la paroi ablatée.

2. Etat de l'art

Dans le cadre des recherches sur l'Accident Grave, beaucoup d'études ont été effectuées concernant le comportement du corium en cuve ainsi que sur l'interaction corium-béton. L'objectif est de mieux comprendre le transfert de chaleur et les conditions à l'interface liquide-solide en régime permanent ou en régime transitoire au cours de la progression de l'accident.

2.1. Comportement du corium en cuve avec un refroidissement externe

Dans un hypothétique accident grave, le cœur fondu contient une source de chaleur importante et il peut se déplacer vers la partie inférieure de la cuve du réacteur où il peut créer un bain de corium. La capacité de rétention du corium et l'intégrité de la cuve dépendent de la distribution du flux de chaleur (provenant du bain de corium à la paroi intérieure de la cuve du réacteur) ainsi que du refroidissement à la surface extérieure de la cuve.

Les travaux récents sur la rétention en cuve du corium ont souligné que la question du transfert de chaleur et de la température à l'interface solide-liquide (lors de la solidification du liquide aux frontières refroidies du bain avec la source de chaleur interne) a été clairement résolue en régime permanent. En effet, le transfert de chaleur à la surface supérieure et à l'interface latérale entre le

liquide et le solide peut s’estimer par des corrélations du nombre de Nusselt en fonction du nombre de Rayleigh (interne ou externe). Cependant, le lien entre les différentes corrélations développées avec un nombre de Rayleigh interne ou externe n'a pas été précisé. Lorsque la surface supérieure du bain est refroidie, la couche supérieure du bain est quasiment uniforme en termes de la température et de la distribution du flux de chaleur. Une stratification de température du bain est observée dans la partie inférieure du bain. Dans cette région, le transfert de chaleur à la paroi latérale est contrôlé par un écoulement de couche limite. Le flux de chaleur augmente avec l'angle polaire du bain, mais sa répartition est fonction du régime d'écoulement dans cette couche limite. Par ailleurs, les conditions à l’'interface liquide-solide sont déterminées pour le régime permanent, dans lequel il n'y a pas de zone pâteuse à l’interface qui présente un front plane pour lequel la température d'interface est aussi la température liquidus du corium liquide. En régime permanent, la composition du corium liquide est uniforme.

Les études concernant le transfert de chaleur en régime transitoire avec la formation de croûte sont limitées à l’aspect théorique avec des configurations simples, telle que celle d’une couche liquide horizontale chauffée par une source de chaleur volumétrique. Dans une telle situation, les effets importants de la dynamique de croissance de la croûte sur le transfert de chaleur ont été abordés. Les analyses du temps caractéristique de l’établissement thermohydraulique ainsi que du temps caractéristique pour la formation de croûtes ont montré que ces retards de temps sont plus longs que le temps nécessaire à l'établissement d’un écoulement de convection naturelle. Par conséquent, le transfert de chaleur en régime transitoire peut être estimé par une succession de régimes permanents. Cependant, la situation en réacteur est plus complexe en raison de l'établissement, en transitoire, d’une zone pâteuse devant l'interface liquide-solide à cause du transfert de masse, ce qui entraîne des variations significatives de la composition du liquide ainsi que de la température à l'interface liquide-solide. Il est ainsi important de comprendre si on peut utiliser les corrélations du transfert de chaleur en régime permanent pour déterminer l'évolution temporelle du flux de chaleur et la température du corium.

En ce qui concerne les conditions à l'interface liquide-solide, l’objectif principal est de déterminer l'évolution de la température d'interface lors de la formation de la croûte transitoire. Ce problème n'est toujours pas résolu.

3.1. Interaction Corium-Béton

L'intégrité du puits de réacteur est un objectif clé de la gestion des accidents graves car le radier fournit une barrière de sécurité pour empêcher la sortie des produits de fission dans l'environnement. En particulier, l'intégrité du radier doit être assurée même en cas de fusion du cœur. En cas, de la présence du corium dans le puits de cuve, une interaction directe entre le corium et le béton fondu se produit.

Malgré des études approfondies sur l'interaction corium-béton, il y a encore des observations qui ne sont pas expliqués jusqu'à l'heure actuelle:

- Pourquoi la température du corium suit l'évolution de la température liquidus pour les tests de béton calcaire, mais ce n'est pas le cas pour les tests avec le béton siliceux dont la température du corium peut être de 250 K inférieure à la température liquidus du mélange corium-béton.
- Quelles sont les causes qui entrainent l'ablation isotrope lors de l'utilisation du béton calcaire (VB-U6, CCI2, ICC-4), mais une ablation radiale préférentielle pour béton siliceux (CCI1, CCI3, VB-U5, VB-U4).
- Quelles sont les causes et les conséquences des instabilités d'ablation observées avec le béton siliceux (CCI-1, CCI-3, CCI-5, VB-U4, U5-VB)? Quelle est la taille minimale de la section d'essai et quelle est la durée de test nécessaire pour observer une vitesse d'ablation 2D représentative?

3. Objectifs de la thèse

Corium en cuve

L'objectif de ce travail est d'étudier les effets du matériau non-eutectique sur la thermohydraulique d'un bain de corium en géométrie hémisphérique chauffé par une puissance.

Les principales questions à aborder mettront l'accent sur le comportement transitoire du bain de corium, y compris:

- Le transfert de chaleur transitoire du bain à la paroi de la cuve;
- La cinétique de la croissance de la croûte solide en régime transitoire;
- Le mécanisme de transfert de masse à l'interface liquide-solide et les conditions d'interface en régimes transitoire et permanent (la composition et la température à l'interface liquide-solide).

Pour la description de la thermohydraulique du bain en régime transitoire, un modèle a été développé et validé par le test LIVE L3A en proposant une approche physique pour évaluer les paramètres clés.

L'état de l'art montre l'existence des questions ouvertes qui ne peuvent être résolues en s'appuyant sur les données existantes. En outre, les essais en matériaux réels ne permettent pas des mesures précises de la distribution de température du corium, du comportement du solide à l'interface ainsi que la température d'interface.

Interaction corium-béton

Afin d'obtenir une analyse des phénomènes, le CEA, l'IRSN et l'EDF ont lancé les essais ARTEMIS 2D. L'objectif de ce travail est d'utiliser les résultats de ces expériences afin d'étudier:

- La distribution du flux de chaleur à l'interface de la cavité en régime transitoire;
- L'évolution de la forme de la cavité;
- L'évolution de la température du corium et le lien avec la composition du corium;
- L'évolution des conditions d'interface au cours d'une interaction corium-béton, recourant la distribution de composition à l'interface et la température d'interface;
- L'effet de l'injection de gaz sur la recirculation dans la cavité du corium et ses impacts sur le transfert de chaleur.

4. Des études menées dans cette thèse

Afin de répondre aux questions précédemment mentionnées, le transfert de masse et de chaleur dans une cavité du corium entouré par une paroi solide a été étudié via cas test différents : LIVE L3A, ARTEMIS 11 et ARTEMIS 10.

4.1. LIVE L3A

Cette première situation traite d'un bain du corium non-eutectique de forme hémisphérique qui est chauffé par une dissipation de puissance volumique et refroidi à la paroi latérale sans injection de gaz. Le cas simule un bain de corium en cuve avec la formation d'une croûte à la paroi. La situation correspond à l'expérience LIVE L3A qui a été réalisée à KIT, Allemagne.

Description du test

L'installation d'essai LIVE comprend trois parties principales: une cuve en acier avec son système de refroidissement externe, le système de chauffage volumétrique et un four de fusion [Kretzschmar et Fluhrer, 2008], [Gaus-Liu et al, 2010.]. La cuve est à l'échelle 1/5 d'un fond hémisphérique de cuve d'un réacteur à eau pressurisée type (REP), fabriquée à partir d'acier inoxydable (Figure 1).

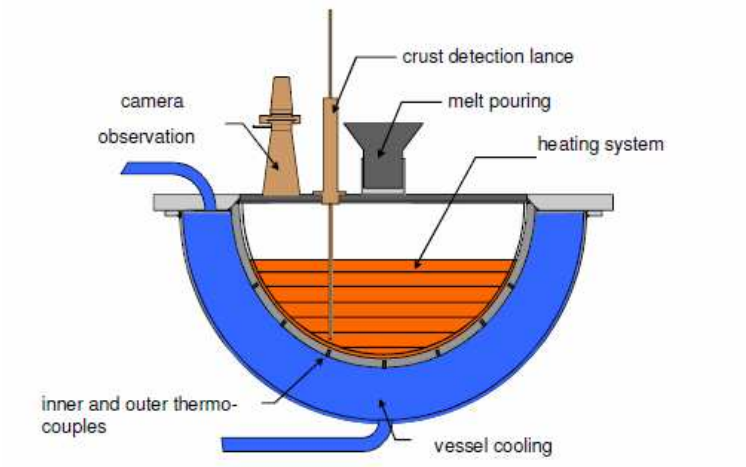

Figure 1. La cuve de l'essai LIVE.

Table 1. Propriétés physiques du corium de l'essai LIVE L3A.

Paramètre		Unité	Valeur dans LIVE L3A
λ_{bulk}	Conductivité thermique	$W.m^{-1} K^{-1}$	0.44
υ	Viscosité cinématique	$m^2.s^{-1}$	$1.6\ 10^{-6}$
ρ_{bulk}	Densité	$kg.m^{-3}$	1900
α	Diffusivité thermique	$m^2.s^{-1}$	$1.72\ 10^{-7}$
β_T	Coefficient de dilatation thermique	K^{-1}	$4.64\ 10^{-4}$
$C_{p,liquid}^{bulk}$	Capacité calorifique	$J.kg^{-1}.K^{-1}$	1350
$L_{solidification}^{melt}$	Chaleur latente de solidification	$J.kg^{-1}$	$6\ 10^4$

Le matériau simulant pour les expériences LIVE est un mélange binaire non-eutectique de 80% en mole de KNO_3 - 20% en mole de $NaNO_3$. La température liquidus de cette composition est d'environ 285 ° C et sa température solidus est d'environ 235 °C. Le coefficient de partage *k* (rapport entre compositions solidus et liquidus des réfractaires KNO_3) est pris égal à 0,2. Les propriétés physiques du corium et les conditions initiales de l'essai LIVE L3A sont données au Table 1 et Table 2.

Table 2. Conditions initiales de l'éssai LIVE L3A.

Condition initiale de refroidissement	refroidissement à l'eau
Débit d'eau de refroidissement	0.047 $kg.s^{-1}$
Volume initial du corium	120 l
Température initiale du corium dans le four de fusion	~ 350 °C
Puissance de chauffage	Phase 1: 10 kW – duré: 90000 s Phase 2: 7 kW – duré: 91800 s
Generation de chaleur	Répartition des éléments chauffants dans le corium pour un chauffage homogène
Nombre de Rayleigh interne	10^{12} - 10^{13}

Principaux résultats concernant le comportement du corium en cuve avec solidification à la paroi

L'analyse est consacrée à l'étude du transfert de chaleur en régime transitoire et la solidification dans un bain de corium non-eutectique avec une source de chaleurvolumique et un refroidissement à la surface extérieure. Un modèle simplifié a été développé pour le calcul de l'évolution de la température maximale du corium ($T_{bulk,max}$) et l'évolution de l'épaisseur de la croûte solide (z_{crust}) lors de la solidification.

L'équation permettant calculer la température maximale du corium est:

$$k_T M_{bulk} C_{p,liquid}^{bulk} \frac{d\Delta T_{bulk,\max}}{dt} = \dot{Q}_{add} - \overline{\varphi}\, S_{lateral} \quad (1)$$

où:

- M_{bulk} est la masse du corium;

- $C_{p,liquid}^{bulk}$ est la capacité calorifique du corium;
- $T_{bulk,max}$ est la température maximale du corium ;
- T_i est la température à l'interface liquide-solide ($T_i = T_{liquidus}(C_0)$ = 285 °C et C_0 est la composition initiale du corium) ;
- $\Delta T_{bulk,max} = T_{bulk,max} - T_i$;
- $\dot{Q}_{add}$ est la puissance volumique dissipée dans le bain de corium ;
- $\overline{\varphi}$ est le flux moyen transferé du bain à l'interface liquide-solide $\overline{\varphi} = \overline{h}_{bulk}\ \Delta T_{bulk,\max}$
- $\overline{h}_{bulk}$ est le coefficient moyen de transfert de chaleur du bain, qui est calculé par :

$$\overline{h}_{bulk} = \frac{a\,\lambda_{bulk}}{H}\left(\frac{g\,\beta_T\,H^3}{\alpha\,\upsilon}\right)^b \Delta T_{bulk,\max}^b \qquad (2)$$

où a et b sont des coefficients dans les correlations du nombre de Nusselt écrites en terme du nombre de Rayleigh externe ($Nu = a\,Ra^b$).

L'equation pour calculer l'éppaiseur de la croûte solide locale est donnée par:

$$\frac{d}{dt}\left[\rho_{crust}\, z_{crust}(\theta)\, H_{crust}(\theta)\right] = \varphi_{local}(\theta) - \varphi_{conduction}(\theta) + \rho_{bulk}\frac{dz_{crust}}{dt} H_{add} \qquad (3)$$

où:

- $\rho_{crust}\ z_{crust}(\theta)$ est la masse par unité de surface de la croûte solide formé à l'angle polaire θ;
- ρ_{crust} est la densité de la croûte solide, supposée égale à celle du corium ρ_{bulk}, i.e. $\rho_{crust} = \rho_{bulk}$;
- La conductivité thermique de la croûte solide et du corium sont supposées être les mêmes, *i.e.* $\lambda_{crust} = \lambda_{bulk}$;
- $z_{crust}(\theta)$ est l'épaisseur locale de la croûte solide à l'angle polaire θ;
- H_{crust} est l'enthalpie moyenne de la croûte $H_{crust} = H_{ref} + C_{p,solid}^{crust}(\overline{T}_{crust} - T_{ref})$ où $C_{p,solid}^{crust}$ est la capacité calorifique de la croûte et $\overline{T}_{crust}$ est la température moyenne de la croûte;
- H_{add} est l'enthalpie de la croûte solidifiée à l'interface liquide-solide, $H_{add} = L_{solidification}^{melt} + H_{ref} + C_{p,solid}^{crust}(T_i - T_{ref})$ où $L_{solidification}^{melt}$ est la chaleur latente de solidification;

- $\varphi_{local}(\theta) = h_{local}(\theta)\Delta T_{bulk,\max} = f(\theta)\bar{h}_{stt}\Delta T_{bulk,\max}$ est le flux de chaleur local transféré à partir du bain liquide à l'interface liquide-solide à l'angle polaire θ;
- $\varphi_{conduction}$ est le flux de chaleur perdu par conduction de la croûte solide vers la surface extérieure de la cuve.

Le modèle suppose que la température liquidus correspondant à la composition moyenne du bain est la température à l'interface liquide-solide et emploie un coefficient moyen de transfert de chaleur d'une correlation de nombre Nusselt développé pour la convection naturelle en régime permanent. Une transformation de la corrélation du nombre de Nusselt écrit en fonction du nombre de Rayleigh interne vers le nombre de Rayleigh externe a été réalisée.

$$Nu = a' Ra_{in}^{\ b'} = aRa_{ex}^{\ b} \tag{4}$$

où:

$$Ra_{ex} = \frac{g\,\beta_T\,\Delta T_{bulk,\max}\,H^3}{\alpha\,\upsilon} \tag{5}$$

$$Ra_{in} = \frac{g\,\beta_T\,H^5\,\dot{Q}_v}{\alpha\,\lambda_{bulk}\,\upsilon} \tag{6}$$

$$a = a'^{\frac{1}{1-b'}}\left(\frac{6}{3-\frac{H}{R}}\right)^{\frac{b'}{1-b'}} \tag{7}$$

$$b = \frac{b'}{1-b'} \tag{8}$$

Table 3. Coefficients du transfert de chaleur calculé par les correlations de nombre de Nusselt.

Auteur	Correlation	Correlation transformé	$\overline{h}_{bulk\ ,10\ kW}$ ($W.m^{-2}.°C^{-1}$)	$\overline{h}_{bulk\ ,7\ kW}$ ($W.m^{-2}.°C^{-1}$)
Mayinger's [Mayinger et al., 1975]	$Nu = 0.55Ra_{in}^{0.2}$	$Nu = 0.59Ra_{ex}^{0.25}$	249	233
Mini ACOPO [Theofanous et al., 1997]	$Nu = 0.0038Ra_{in}^{0.35}$	$Nu = 0.0003Ra_{ex}^{0.54}$	121	107
ACOPO [Theofanous et al., 1997]	$Nu = 0.048Ra_{in}^{0.27}$	$Nu = 0.022Ra_{ex}^{0.37}$	158	144
BALI [Bonnet et Garré, 1999]	$Nu = 0.131\left(\frac{H}{R}\right)^{0.19} Ra_{in}^{0.25}$	$Nu = 0.08Ra_{ex}^{0.33}$	224	205

Les calculs par le modèle ont été effectués en utilisant un coefficient moyen variable de transfert de chaleur estimée par la corrélation de Nusselt écrite en termes de nombre de Rayleigh externe (en tenant compte de la variation transitoire de la différence de température) et un coefficient moyen de chaleur de transfert constant calculée par la corrélation de Nusselt donnée en termes de nombre de Rayleigh interne (pour le régime permanent) (Table 3). On montre que les résultats des calculs d'évolution de la température maximale du corium dans les deux phases 10 kW et 7 kW sont assez similaires pour les deux approches du coefficient moyen de transfert de chaleur (Figure 2, Figure 3). Par conséquent, il est conclu que le transfert de chaleur en régime transitoire est proche de celui du régime permanent.

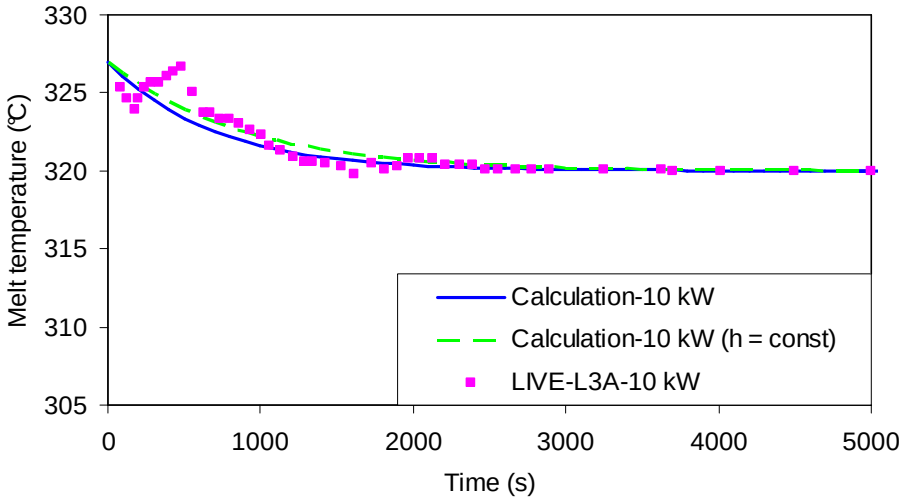

Figure 2. L'evolution de la température du bain pour la phase 10 kW.

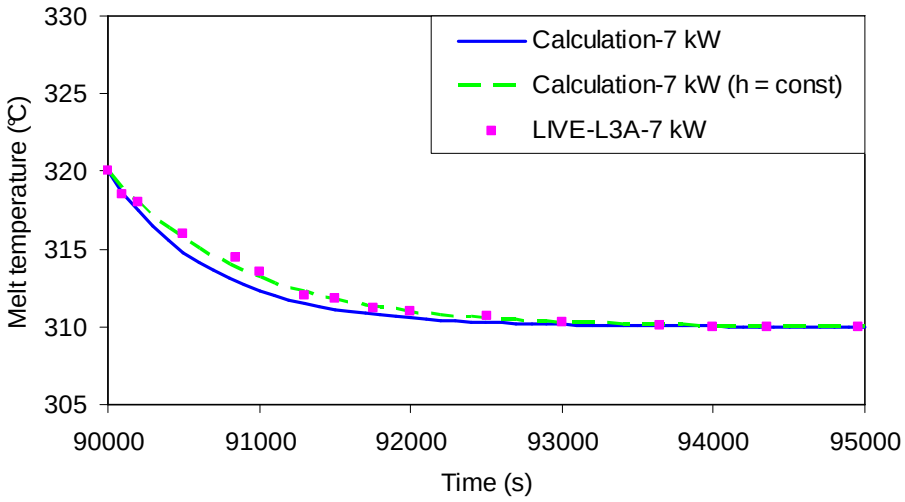

Figure 3. L'evolution de la température du bain pour la phase 7 kW.

L'épaisseur de la croûte locale a été calculée en imposant la répartition du flux de chaleur mesurée en régime permanent sur l'expérience (Figure 4 pour la phase 10 kW et Table 4 pour la phase 7 kW).

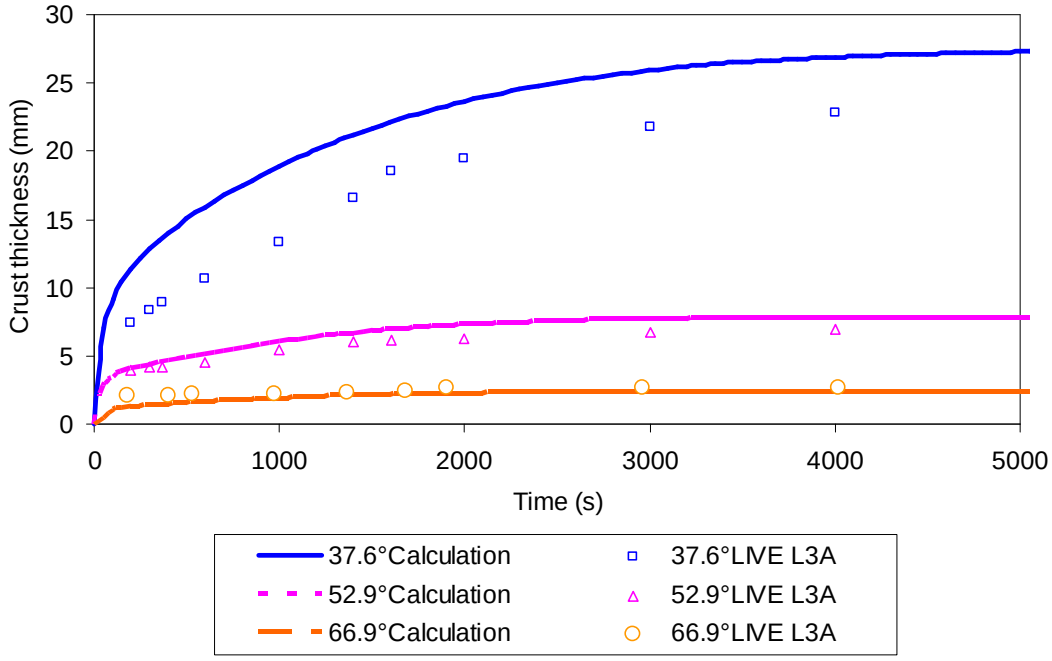

Figure 4. Evolution de l'éppaiseur de la croûte locale dans la phase 10 kW.

Table 4. L'éppaiseur finale de la croûte locale dans la phase 7 kW.

Angle polaire (°)	z_{stt} calculaté (mm)	z_{stt} Expérimentale (mm)
37.6	42.86	41 ± 5
52.9	14.94	16.5 ± 5.5
66.9	7.09	7.5 ± 5

L'accord entre le calcul et les données expérimentales de l'évolution de la température maximale du corium et l'évolution de l'épaisseur de la croûte locale aux niveaux différents de la cavité prouve que le transfert de chaleur en régime transitoire a un comportement similaire à celui en régime permanent.

En outre, en utilisant les résultats des calculs de la vitesse de solidification transitoire et en appliquant les modèles de solidification existants pour le front plan et la zone pâteuse (Table 5), une prédiction de régimes de solidification en LIVE L3A a été proposée.

Table 5. Modèles de solidification.

Zone pâteuse remplissage	Front plan	
	Diffusion contrôlée	Diffusion et convection contrôlé
$C_{L,i} = C_{bulk}$	$C_{L,i} = \frac{C_{bulk}}{k}$	$C_{L,i} = C_{bulk} \frac{e^{\Delta}}{1-k(1-e^{\Delta})}$ $\Delta = \frac{\delta_{MT} V_{sol}}{D_L}$; $\delta_{MT} = H(Sc\,Gr)^{-1/3}$
$T_i = T_{tip} = T_{liquidus}(C_{bulk})$	$T_i = T_{solidus}(C_{bulk})$	$T_{solidus}(C_{bulk}) \leq T_i \leq T_{liquidus}(C_{bulk})$ $V_{sol} \rightarrow 0$ then $T_i \rightarrow T_{liquidus}(C_{bulk})$
$\tau_{MT,\,filling} = \frac{\Delta T_{SL}{}^2}{G_S{}^2 D_L}(\frac{1+k}{2})$	$\frac{G_L}{V_{sol}} \Big/ \frac{-m_L C_{bulk}(1-k)}{D_L} \geq \frac{1}{k}$	$\frac{G_L}{V_{sol}} \Big/ \frac{-m_L C_{bulk}(1-k)}{D_L} \geq 1$

où :

- $C_{L,i}$ est la composition du liquide à l'interface liquide-solide ;
- C_{bulk} est la composition moyenne du corium ;
- G_L est le gradient de température dans sous couche thermique;
- G_S est le gradient de température dans la phase solide ;
- V_{sol} est la vitesse de solidification ;

- m_L est la pente de liquidus ;
- $T_{liquidus}(C_{bulk})$ est la température liquidus à la composition C_{bulk} ;
- $T_{solidus}(C_{bulk})$ est la température solidus à la composition C_{bulk} ;
- $\Delta T_{SL} = T_{liquidus} - T_{solidus}$;
- k est le coefficient de partage;
- D_L est le coefficient de diffusivité de soluté dans la phase liquide ;
- δ_{MT} est l'éppaiseur de la couche limite de transfert de masse ;
- H est la longeur caractéristique;
- $\tau_{MT,filling}$ est le temps requis pour le remplissage de la zone pâteuse.

Pour un angle polaire faible du bain de corium (37,6 °), le délai pour le remplissage de la zone pâteuse est un peu plus long que le temps nécessaire pour atteindre la stabilité du front plan. Cela signifie que lorsque le front plan est atteint, la zone pâteuse n'est pas encore complètement remplie. Cependant, comme on le voit dans Figure 7 et Figure 8, le complément du remplissage de la zone pâteuse se produit lorsque l'épaisseur de presque 99% au maximum de la croûte forme. Cela signifie que la solidification termine avec un front plan à l'interface liquide-solide mais la zone pâteuse ne disparaît pas.

On voit que dans la partie supérieure de la cavité du corium (52.9°), la zone pâteuse est remplie relativement rapide (Table 6, Table 7). Le remplissage de la zone pâteuse est terminé quand la solidification est suffisamment faible pour atteindre le front plan (Figure 7, Figure 8). Cela implique que, à la fin de la solidification, la zone pâteuse disparaît et un front plan est obtenu.

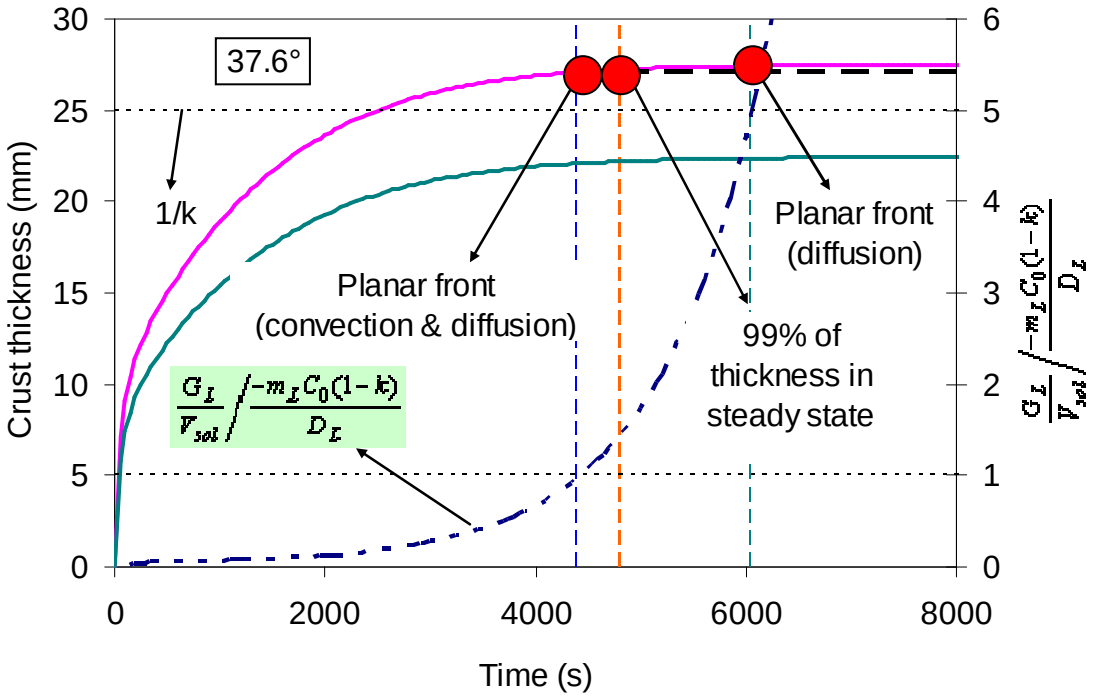

Figure 5. Temps caractéristique pour l'obtention d'un front plan à 37.6° dans la phase 10 kW.

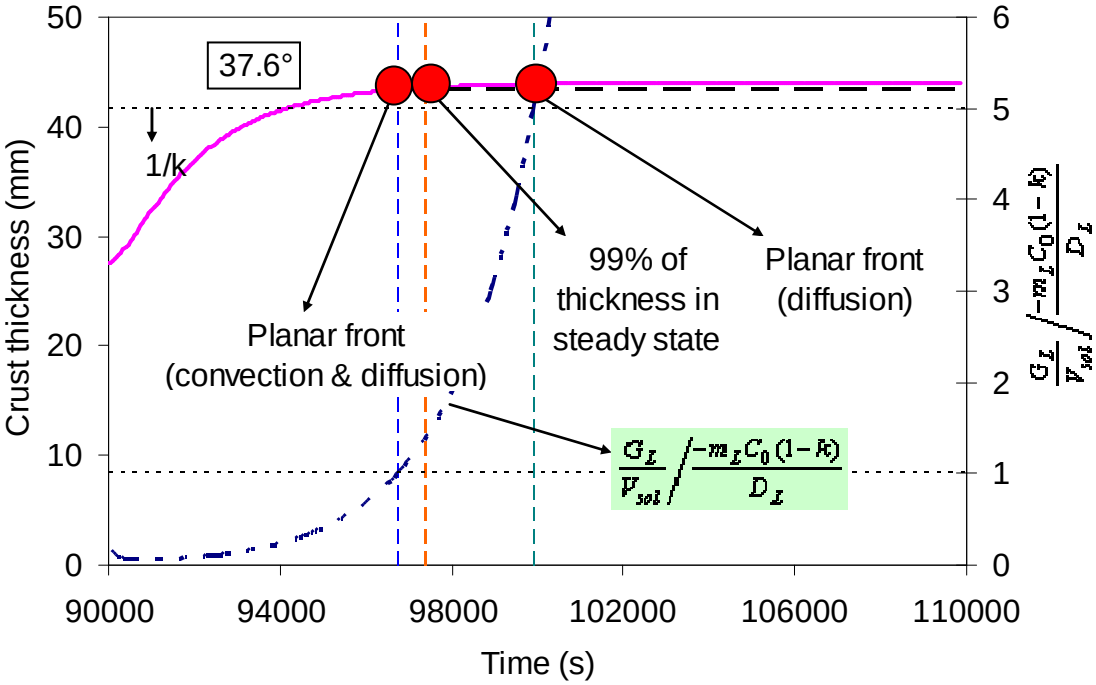

Figure 6. Temps caractéristique pour l'obtention l'un front plan à 37.6° dans la phase 7 kW.

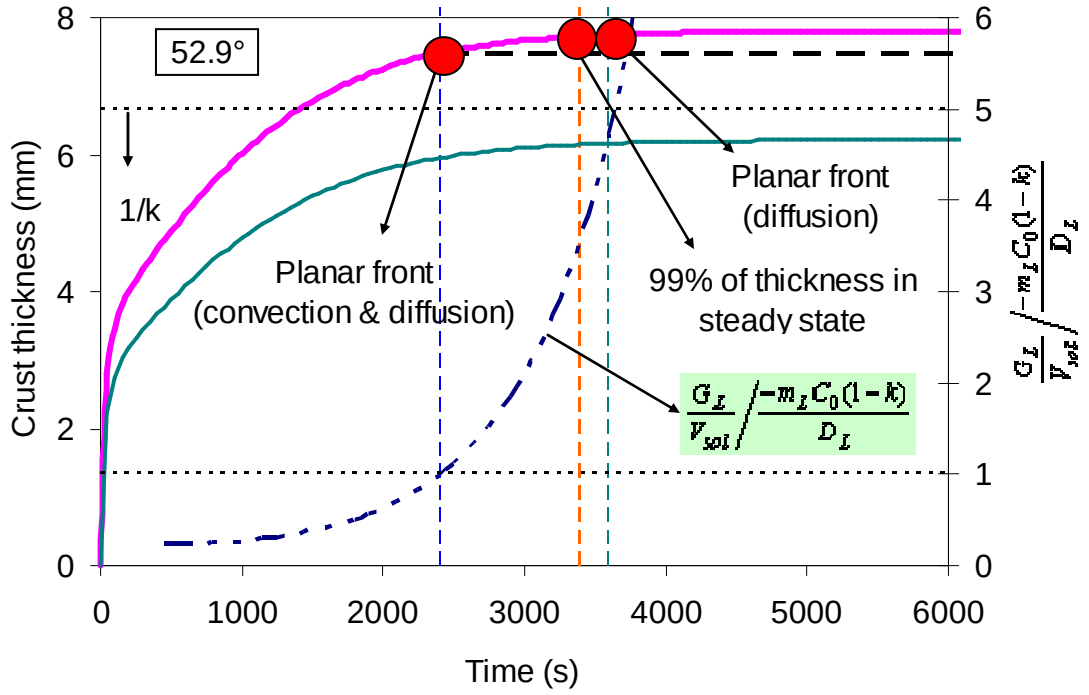

Figure 7. Temps caractéristique pour l'obtention l'un front plan à 52.9° dans la phase 10 kW.

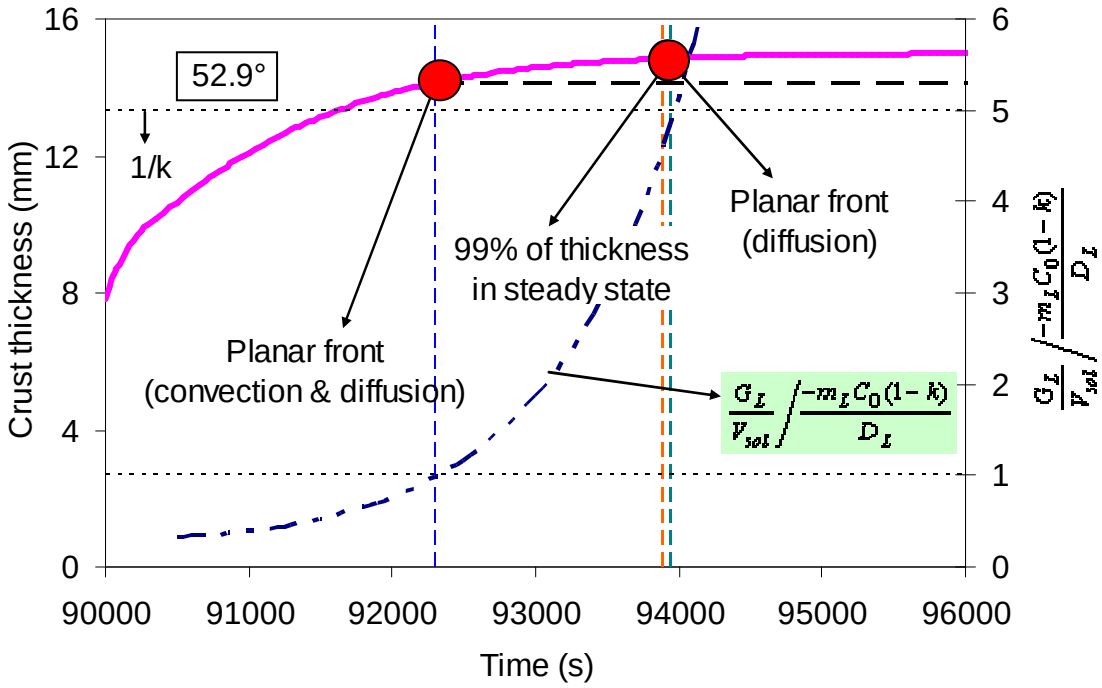

Figure 8. Temps caractéristique pour l'obtention l'un front plan à 52.9° dans la phase 7 kW.

Table 6. Comparaison entre le temps de remplissage de la zone pâteuse et le temps pour obtenir un front plan dans la phase 10 kW.

Angle polaire (°)	$\tau_{99\%}$ (s)	τ_{PF} (s)	$\tau_{filling}$ (s)
37.6	4800	4400	5051
52.9	3400	2400	577
66.9	3200	1400	195

Table 7. Comparaison entre le temps de remplissage de la zone pâteuse et le temps pour obtenir un front plan dans la phase 7 kW.

Angle polaire (°)	$\tau_{99\%}$ (s)	τ_{PF} (s)	$\tau_{,filling}$ (s)
37.6	7400	6800	7373
52.9	3900	2300	1638
66.9	2800	1000	186

Le calcul de la température d'interface pendant le régime transitoire indique que la température à l'interface liquide-solide reste toujours proche de la température liquidus correspondant à la composition moyenne du corium liquide.

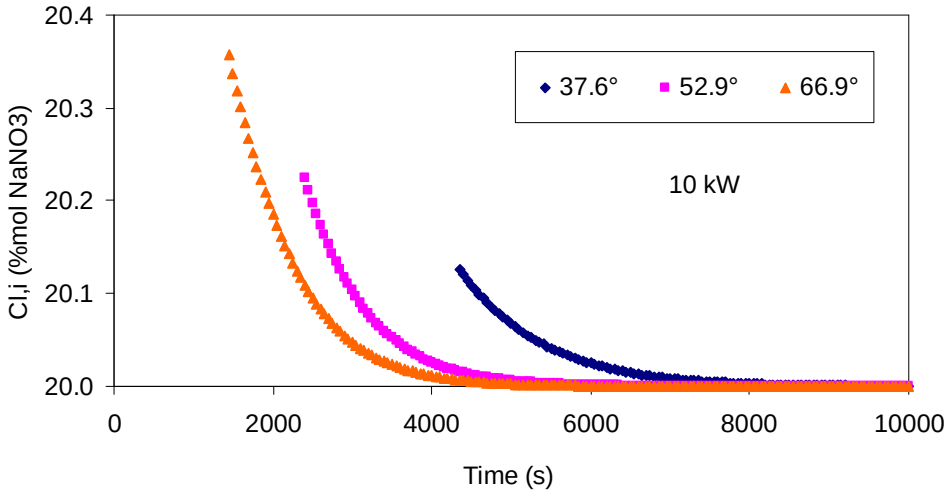

Figure 9. Evolution de la composition du liquide à l'interface dans la phase 10 kW.

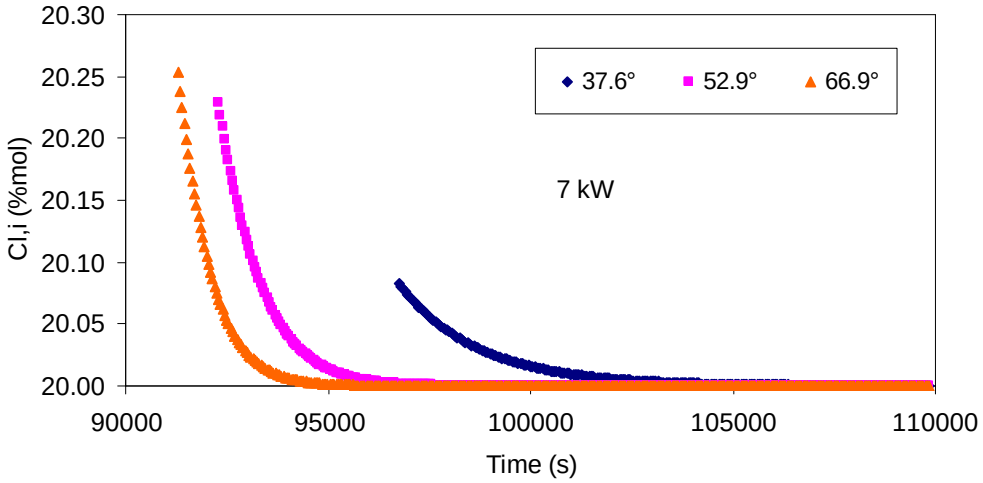

Figure 10. Evolution de la composition du liquide à l'interface dans la phase 7 kW.

L'application d'un modèle 1D développé à LIVE L3A a été effectuée. Le modèle donne accès à la température du corium et la distribution du flux de chaleur en régime transitoire et aussi en régime permanent (Figure 11, Figure 12, Figure 13, Figure 14). Les lois constitutives du coefficient de frottement et du transfert de chaleur dans la couche limite, ainsi que de la vitesse d'entraînement radiale du liquide du bain vers la couche limite, qui sont calculées pour une plaque verticale sont également applicables pour un hémisphère.

- Le coefficient de frottement

$$F = \frac{96}{\mathrm{Re}} \tag{9}$$

ou $\mathrm{Re} = \frac{2\,\delta\,u_{BL}}{\upsilon}$, δ et l'épaisseur de la couche limite locale, u_{BL} est la vitesse moyenne dans la couche limite et υ est la viscosité cinématique du fluide.

- Le coefficient de transfert de chaleur

$$Nu_{bulk} = 4\frac{\delta}{\delta_T} = 4\,\mathrm{Pr}^{1/3} \approx 5.7 \tag{10}$$

où Nu_{bulk} est le nombre de Nusselt dans le bulk ($Nu_{bulk} = \frac{2\,\delta\,h_{bulk}}{\lambda_{bulk}}$, h_{bulk} est le coefficient moyen de transfert de chaleur dans le bulk, λ_{bulk} est la conduction thermique du fluide) et le nombre de Prandtl est défini par $\mathrm{Pr} = \upsilon/\alpha$ avec α est la diffusivité thermique du fluide.

- La vitesse d'entraînement radiale du liquide du bain vers la couche limite est, pour Pr = 9.3, dans LIVE L3A :

$$j_{bulk} = 0.19\left[g\,\beta_T\,(T_{bulk} - T_{BL})\,\upsilon\right]^{1/3} \tag{11}$$

où g est l'accélération de la gravité, β_T est le coefficient de dilatation thermique, T_{bulk} est la température locale du bulk et T_{BL} est la température moyenne locale de la couche limite.

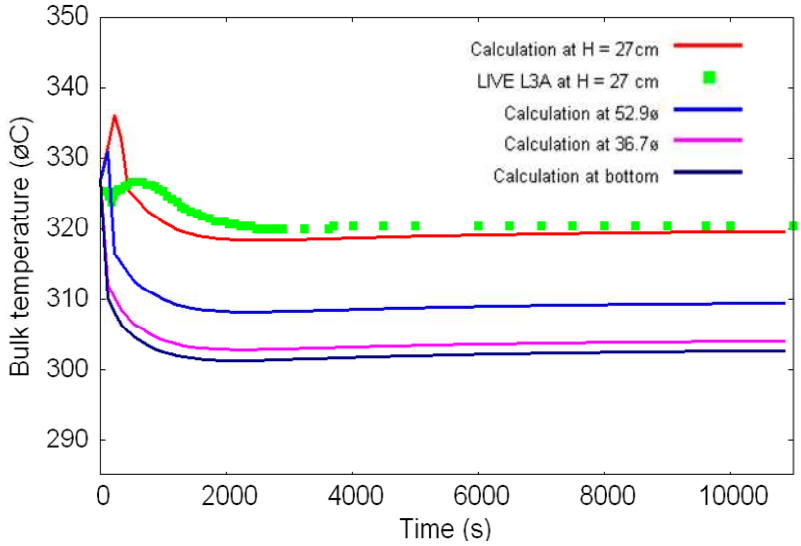

Figure 11. Evolution de la température du bain à différents niveaux.

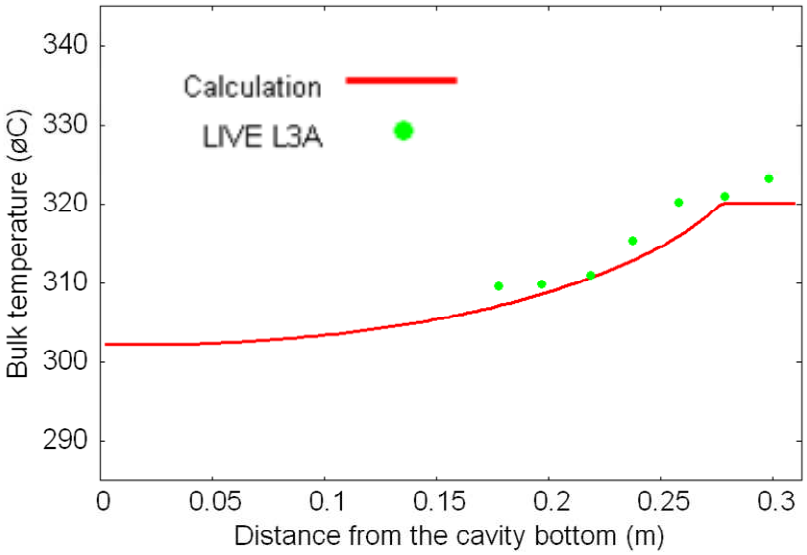

Figure 12. Profil vertical de la témperature du bain en régime permanent.

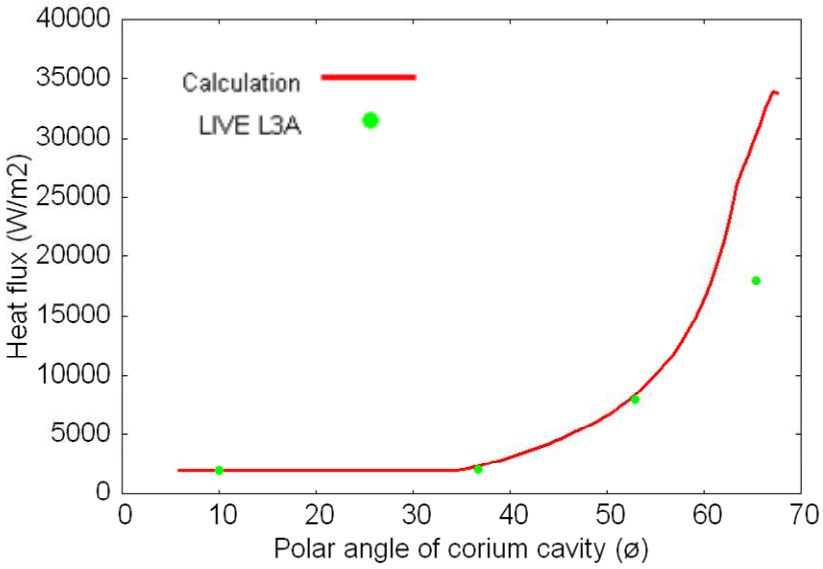

Figure 13. Profil du flux de chaleur en régime permanent.

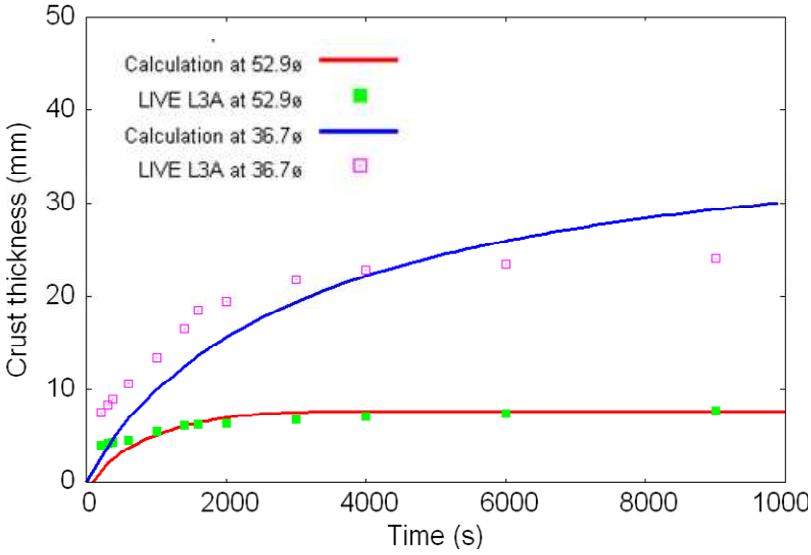

Figure 14. Evolution de l'épaisseur de la croûte locale.

5.1. ARTEMIS 11

La deuxième situation traite de l'ablation 2D d'une cavité de béton avec une percolage de gaz. Afin de séparer les aspects physico-chimiques et d'étudier d'abord des aspects thermo-hydrauliques, l'interaction identiques est étudiée en matériau eutectique. Cette situation est illustrée par le test ARTEMIS 11.

Description du test

Corium

- Composition eutectique: 25% en mole de $BaCl_2$ – 75% en mole de LiCl (62,04% en masse de $BaCl_2$ - 37,96% en masse de LiCl)
- Température de fusion (température eutectique): 522 ° C
- Température initiale: 562 ° C
- Masse initiale: 57 kg
- Volume initial: 0,0233 m^3

Béton

- Composition eutectique: 25% en mole de $BaCl_2$-75% en mole de LiCl (62,04% en masse de $BaCl_2$ - 37.96% en masse de LiCl)
- Température de fusion: 522 ° C
- Température initiale: 400 ° C
- Masse initiale: 259.25 kg
- Porosité: 46%
- Tailles des grains: 0,2 ~ 0,9 mm

Gaz d'Argon

- Température d'entrée: 400 ° C
- Vitesse superficielle à l'interface cavité: 2 cm/s

Table 8. Proprietés physiques du mélange eutectique dans ARTEMIS 11.

	Densité	Coefficient de dilatation thermique	Viscosité cinématique	Capacité calorifique	Conductivité thermique	Chaleur latente de fusion	Température de fusion
	$kg.m^{-3}$	K^{-1}	$kg.m^{-1}.s^{-1}$	$J.kg^{-1}.K^{-1}$	$W.m^{-1}.K^{-1}$	$J.kg^{-1}$	°C
Solide	1638 (solide avec porosité)			700		$2.6\ 10^{5}$	522
Liquide	2439	$3\ 10^{-4}$	10^{-6}	800	0.64		

Les caractéristiques de la section d'essai et de l'instrumentation sont décrites en détail dans le Chapitre 3 de la thèse. La Figure 15 représente la configuration initiale d'ARTEMIS 11. La cavité du corium a un diamètre de 30 cm et la hauteur initiale du liquide dans la cavité est de 32 cm (dont seulement 26,5 cm est à l'intérieur de la cavité de béton). Les éléments chauffants sont situés à une distance de 6,24 cm à 14,04 cm du fond initial de la cavité. La puissance dissipée par les éléments chauffants dans ARTEMIS 11 est 6000 W et la vitesse superficielle du gaz à l'interface liquide-béton est maintenue à 2 cm / s. La durée du test est 2 h 22 minutes 18 s mais le débit de gaz a été coupé à 1 h 45 minutes.

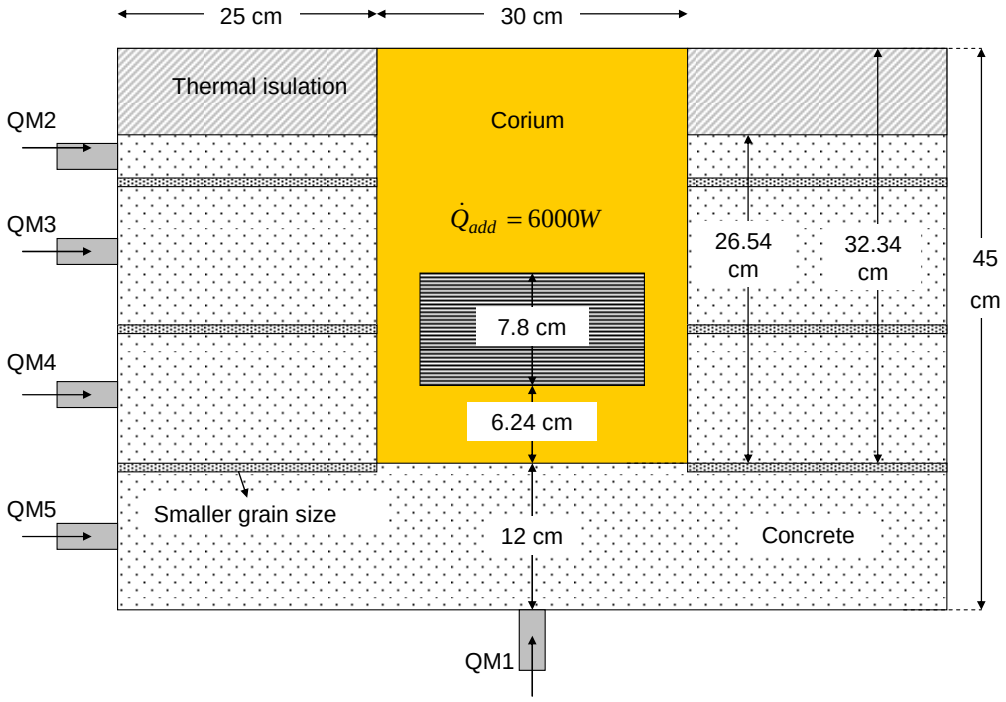

Figure 15. Schema d'ARTEMIS 11.

Principaux résultats obtenus sur l'ablation d'une paroi solide par un bain chauffé avec une composition uniforme et une percolation de gaz)

Les conclusions principales qui ont été faites à partir de l'analyse des données expérimentales d'ARTEMIS 11 sont :

- Tout d'abord, il existe des preuves d'une recirculation d'écoulement dans la cavité. Le fluide va vers le haut dans le centre de la cavité et vers le bas dans la couche limite existant le long de la paroi latérale.

- Deuxièmement, la température à l'interface de fond de la cavité reste à la température de fusion du béton et la température mesurée à l'interface latérale de la cavité est à quelques degrés au-dessus de la température de fusion du béton.

- Troisièmement, une analyse du transfert de chaleur dans la cavité a été réalisée et a abouti à la conclusion que:

- Pendant les premières 17 minutes dans ARTEMIS 11, il existe un mélange gaz-liquide dans la cavité et le transfert de chaleur est contrôlé par la convection de gaz-liquide. Les coefficients de transfert de chaleur déduits dans ARTEMIS 11 sont proches de ceux qui sont obtenus à partir des corrélations du nombre de Nusselt pour la convection de gaz-liquide.

- Cependant, pour t > 17 minutes, une comparaison avec des calculs CFD TRIO montre que la recirculation semble être proche de la convection naturelle. Les coefficients de transfert de chaleur deviennent nettement plus petits que le coefficient de transfert de chaleur par une convection de gaz-liquide.

- La transition entre la configuration de la convection de gaz-liquide et de la configuration de la convection naturelle semble être assez rapide.

- Les calculs de flux de gaz dans le milieu poreux du béton (avec des caractéristiques nominales) et de la vitesse superficielle à l'interface corium-béton par le code TRIO montrent une percolation de gaz dans la cavité du corium. Il convient de souligner qu'il existe probablement une augmentation significative de la perméabilité du béton poreux par la formation de fissures (qui peut permettre au gaz de contourner le béton) et / ou le colmatage possible de la porosité du béton fondu à l'interface liquide-solide (qui peut empêcher le gaz d'entrer dans la cavité du corium).

L'évolution de la température du corium est recalculée par un modèle 0D (Figure 16).

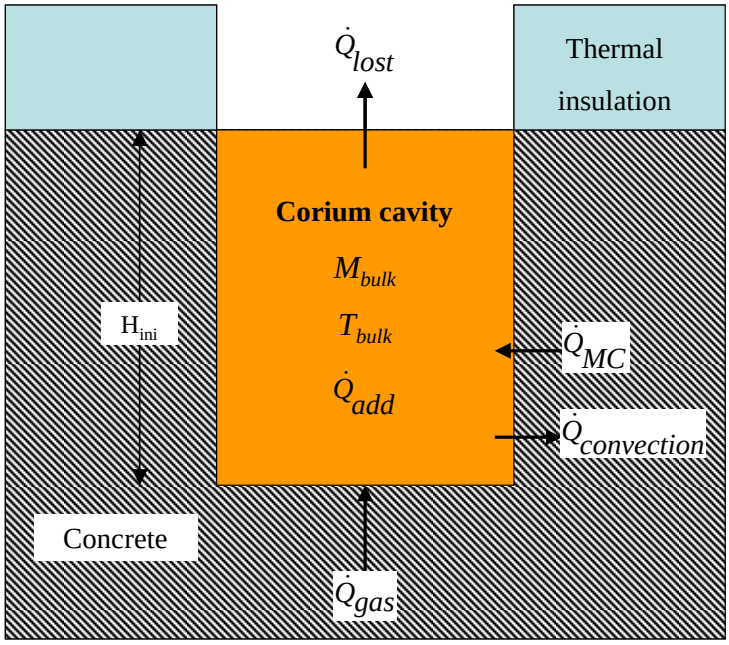

Figure 16. Configuration pour le modèle 0D d'ARTEMIS 11.

Les hypothèses suivantes sont utilisées pour l'approche:

- Le béton solide est attaqué toute la surface de la cavité du corium;
- La variation du rayon de la cavité du corium est calculée avec l'hypothèse d'une géométrie hémisphérique ou cylindrique et la hauteur du liquide dans la cavité est supposé constante ($H(t) = H_{ini}$ = 33 cm);
- La température à l'interface entre le corium liquide et le béton solide, T_i, est prise comme la température de fusion du béton;
- Puisque la température du corium n'est pas uniforme, une différence de température moyenne du corium (avec la température d'interface) est définie avec une hypothèse selon laquelle la variation de la différence de température moyenne et température d'interface de la cavité est proportionnelle à la variation de la différence de température maximale du corium, ou $\Delta\overline{T}_{bulk} = k_T \Delta T_{bulk,\max}$ où k_T est un coefficient qui est supposé indépendant du temps avec $\Delta\overline{T}_{bulk} = \overline{T}_{bulk} - T_i$ et $\Delta T_{bulk,\max} = T_{bulk,\max} - T_i$;
- La température moyenne du corium dans ARTEMIS 11 est prise comme la moyenne arithmétique des températures mesurées par les thermocouples situés à différents niveaux dans la cavité. Le calcul du rapport $\frac{\overline{T}_{bulk} - T_i}{T_{bulk,\max} - T_i}$ conduit à $k_T \approx 1$ au cours des premières 17 minutes et $k_T \approx 0{,}75$ pour le reste de l'essai (dans LIVE L3A, $k_T \approx 0.8$).

Le modèle a été développé sur la base de la conservation de la masse et de l'énergie dans la cavité comme suit:

$$\frac{dM_{bulk}}{dt} = \dot{m}_{MC} + \dot{m}_{gas,in} - \dot{m}_{gas,out} \quad (12)$$

et

$$\frac{d}{dt}(M_{bulk} H_{bulk}) = \dot{Q}_{add} + \dot{Q}_{gas} + \dot{Q}_{MC} - \dot{Q}_{lost} - \dot{Q}_{convection} \quad (13)$$

où:

- M_{bulk} est la masse du corium ;
- $\dot{m}_{MC}$ est le débit d'ablation du béton ;
- $\dot{m}_{gas,in}$ est le débit du gaz à l'entrée de la cavité ;
- $\dot{m}_{gas,in}$ est le débit du gaz à la sortie de la cavité ;
- H_{bulk} est l'enthalpie du corium ;
- $\dot{Q}_{add}$ est la puissance volumique dissipée dans la cavité ;
- $\dot{Q}_{gas}$ est la puissance thermique liée au flux de gaz ;
- $\dot{Q}_{MC}$ est la puissance thermique liée à l'entrée de la masse ablatée du béton dans la cavité ;
- $\dot{Q}_{convection}$ est la puissance transférée du bain vers l'interface de la cavité avec le béton solide par convection;
- $\dot{Q}_{lost}$ est la puissance perdue vers le haut de la cavité (qui est négligeable).

Le modèle développé a été appliqué pour les conditions d'essai ARTEMIS 11. Les principaux paramètres d'intérêt sont l'évolution de la température maximale du corium et l'évolution de la masse ablatée du béton. Les corrélations de transfert de chaleur par la convection naturelle ainsi que pour la convection de gaz-liquide ont été testées. Deux configurations seront considérées pour la cavité du corium, qui sont un hémisphère et un cylindre.

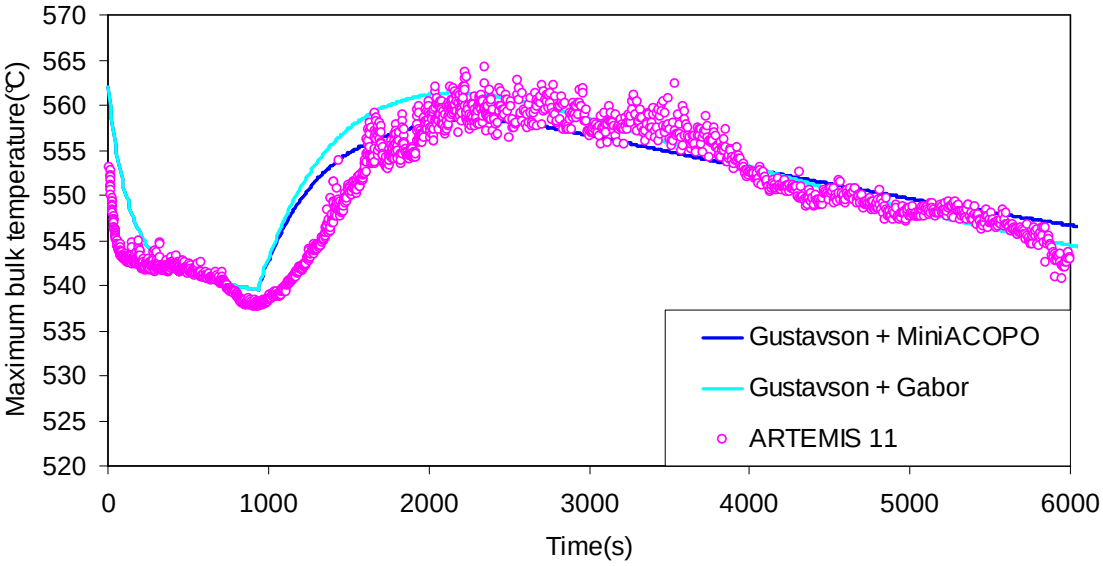

Figure 17. Evolution de la température maximale du corium dans ARTEMIS 11.

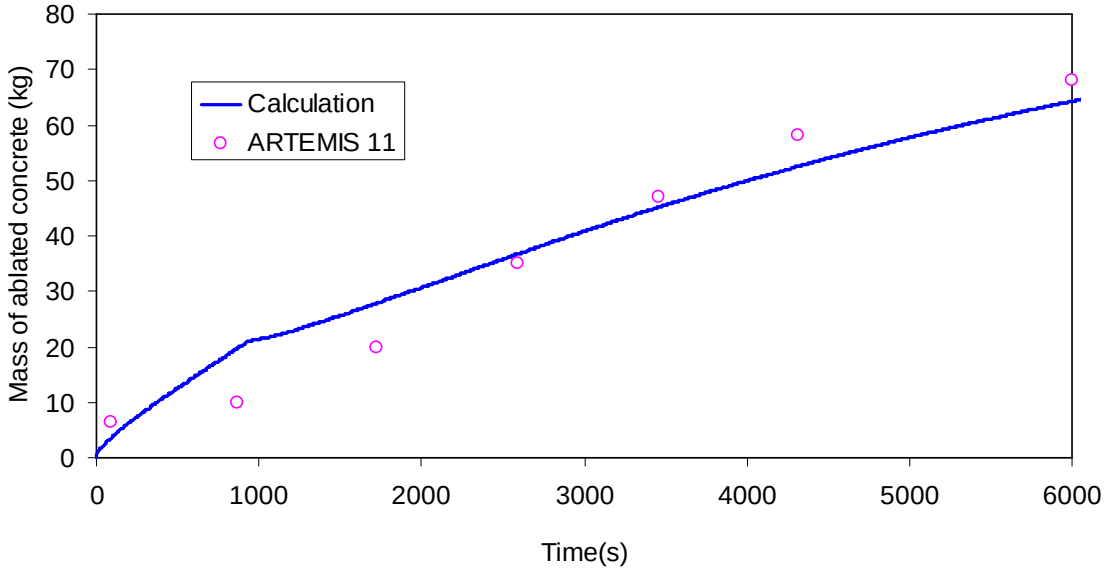

Figure 18. Evolution de la masse ablatée du béton dans ARTEMIS 11.

Il est confirmé, à partir de l'application du modèle, que le débit de recirculation dans la cavité du corium pendant t <17 minutes est contrôlée par une convection diphasique. A t > 17 minutes, le transfert de chaleur dans la cavité est gouverné par une convection naturelle. Les corrélations de transfert de chaleur introduites par [Gustavson et al., 1977] pour la convection de gaz-liquide et par [al. Gabor et, 1980] et Mini-ACOPO [Theofanous et al., 1997] pour la convection naturelle développées pour le régime permanent et pour la géométrie hémisphérique sont adoptées pour estimer

les évolutions de la température maximale du corium ainsi que la masse ablatée de béton dans ARTEMIS 11 (Figure 17, Figure 18).

L'augmentation de la température du corium vers t = 17 minutes est due à la diminution du coefficient de transfert de chaleur après la phase de la convection de gaz-liquide. La diminution de température pour t > 30 minutes est due à l'ablation du béton conduisant à l'élargissement de la cavité. Ces résultats sont valables quelle que soit la géométrie supposée (que ce soit un cylindre ou un hémisphère), ce qui signifie que les effets thermiques sont dominants.

Le modèle ne permet pas de décrire les paramètres locaux dans la cavité du corium telle que la température locale du corium, le flux de chaleur local et l'évolution du rayon local de la cavité, etc ... Par conséquent, un autre modèle tenant compte de l'évolution de ces paramètres locaux dans la cavité du corium a été développé.

L'application du modèle 1D déjà utilisé pour l'interprétation de test LIVE L3A a été effectuée. Les lois constitutives pour le coefficient de frottement et le coefficient de transfert de chaleur dérivées des profils de vitesse et de température introduites par Eckert pour la description de la couche limite le long d'une paroi verticale dans la convection naturelle laminaire sont appliquées.

- Le coefficient de frottement

$$F = \frac{96}{\mathrm{Re}} \tag{14}$$

- Le coefficient de transfert de chaleur

$$Nu_{bulk} = 4\frac{\delta}{\delta_T} = 4\,\mathrm{Pr}^{1/3} \approx 5.7 \tag{15}$$

En plus, la vitesse d'entraînement radial de liquide du bain à la couche limite pour Pr = 3 dans ARTEMIS 11 est donnée par :

$$j_{bulk} = 0.36\left[g\,\beta_T\,(T_{bulk} - T_{BL})\,\upsilon\right]^{1/3} \tag{16}$$

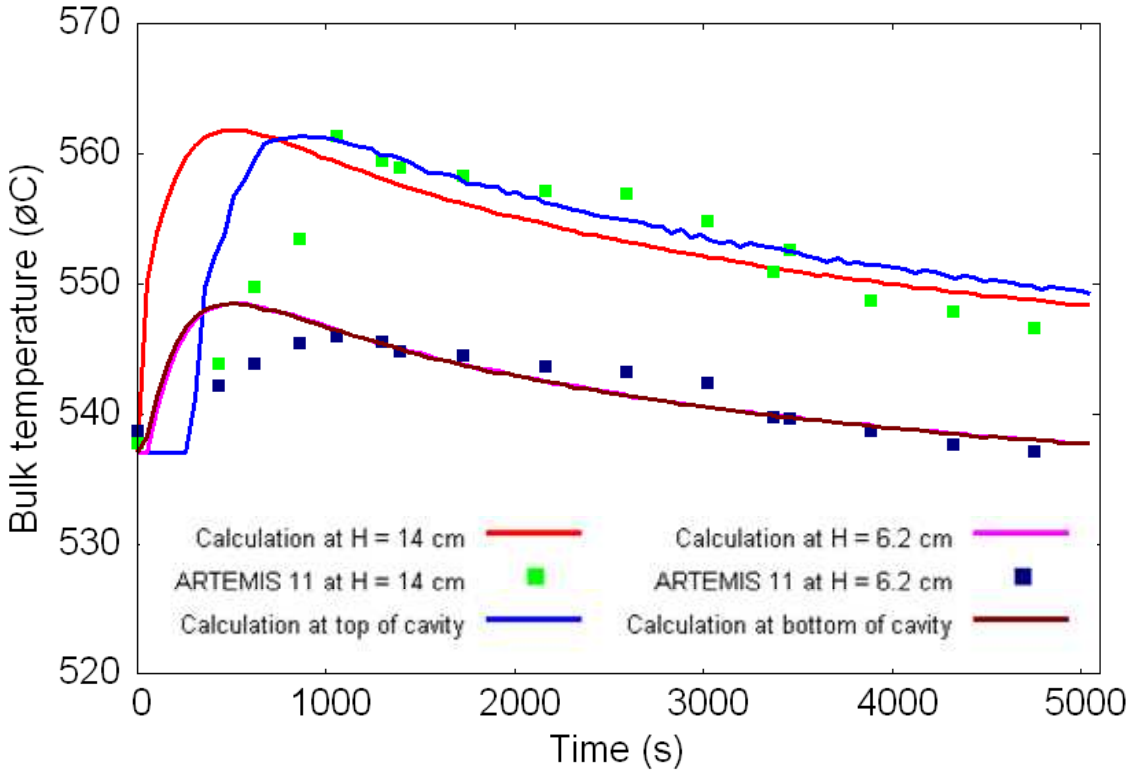

Figure 19. Evolutions des températures locales du bain.

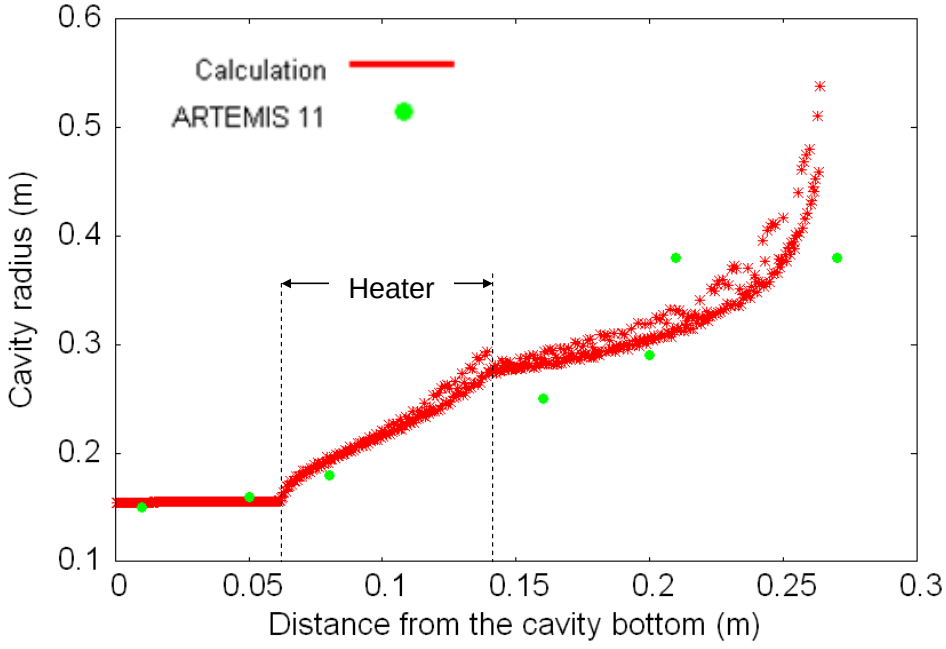

Figure 20. Evolution de la forme de la cavité à la fin d'ARTEMIS 11.

Les résultats des calculs du modèle 1D montrent une bonne reproduction de l'évolution de la température locale du corium (Figure 19) ainsi que de la forme de la cavité (Figure 20).

À partir de ces calculs, on conclut que l'ablation rapide en haut de la cavité du corium est liée à la distribution du flux de chaleur associée à l'écoulement de couche limite laminaire. La vitesse d'ablation au fond de la cavité du corium avec le béton solide est liée à la recirculation de liquide froid à partir de la couche limite au fond de la cavité.

6.1. ARTEMIS 10

La troisième situation concerne l'ablation 2D du béton par un corium réfractaire. Les deux aspects de la thermohydraulique et de la physico-chimique sont étudiés. Cette situation implique l'étude de l'ablation d'une paroi de béton eutectique à l'état solide en interaction avec un bain corium à l'état liquide en composition non-eutectique avec la présence d'une source de chaleur et l'injection de gaz. Cette situation est représentée par le test 10 ARTEMIS.

Description du test

Corium

- 100% en mole de $BaCl_2$ (100% en masse de $BaCl_2$)
- Température liquidus: 960 ° C
- Température initiale: 960 ° C
- Masse initiale: 97.1 kg
- Volume initial: 0,0316 m3

Béton

- Composition eutectique: 25% en mole de $BaCl_2$- 75% en mole de LiCl (62,04% en masse de $BaCl_2$, 37.96% en masse de LiCl)
- Température de fusion: 522 ° C
- Température initiale: 400 ° C
- Masse initiale: 259.25 kg

- Porosité: 46%
- Tailles des grains: 0,2 ~ 0,9 mm

Argon gazeux

- Température d'entrée: 400 ° C
- Vitesse superficielle à l'interface cavité du corium: 2 cm / s

	Densité	Coefficient de dilatation thermique	Coefficient de dilatation soluté	Viscosité cinématique	Capacité calorifique	Conductivité thermique	Chaleur latente de fusion	Température liquidus
	$kg.m^{-3}$	K^{-1}	$mol.mol^{-1}$	$kg.m^{-1}.s^{-1}$	$J.kg^{-1}.K^{-1}$	$W.m^{-1}.K^{-1}$	$J.kg^{-1}$	°C
$BaCl_2$ solide	3500				594	0.5 (at 400 °C)	$7.4\ 10^{4}$	960
$BaCl_2$ liquide	3150 (at 960 °C)	$3.2\ 10^{-4}$	0.9	$1.5\ 10^{-6}$	522	0.8		

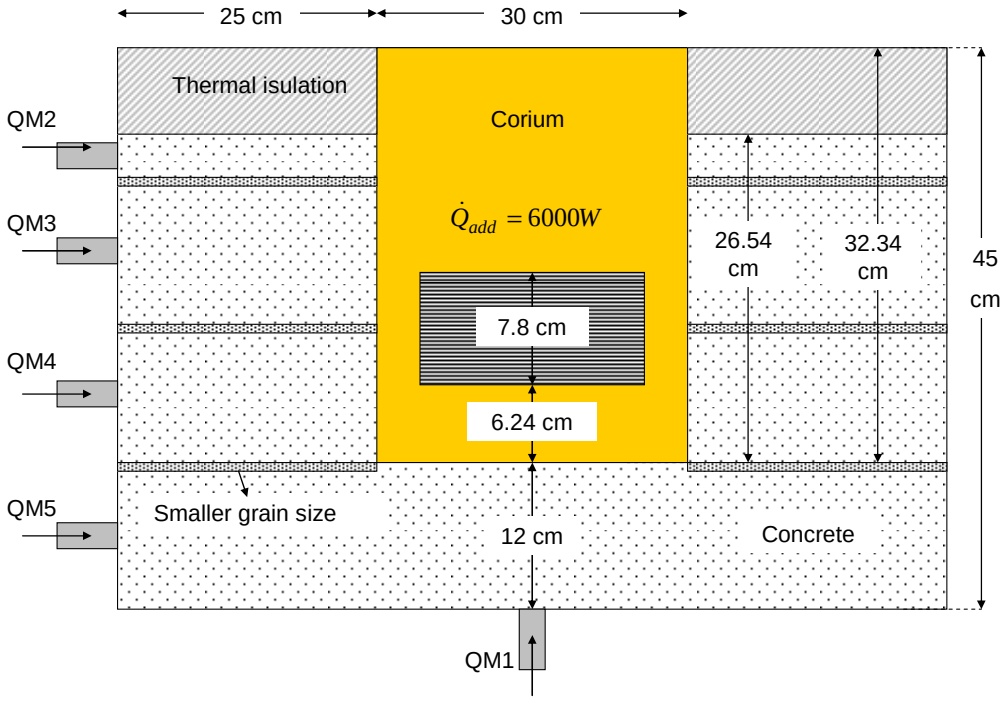

Figure 21. Schema d'ARTEMIS 10.

La cavité du corium a un diamètre de 30 cm et la hauteur initiale du corium dans la cavité est 44,3 cm (26,5 cm sont initialement à l'intérieur de la cavité de béton). Les éléments chauffants sont situés à une distance de 8,1 cm à 15,9 cm du fond initial de la cavité (Figure 21). La puissance dissipée dans ARTEMIS 10 est 6000 W et la vitesse superficielle du gaz à l'interface corium-béton est maintenue à 2 cm / s (comme dans ARTEMIS 11). La durée du test est de 1 h 31 mn 30 s.

Principaux résultats concernant la troisième situation (ablation d'une paroi solide par un bain liquide chauffé volumique avec une composition non-uniforme et une percolation de gaz)

L'expérience ARTEMIS 10 a pour but de représenter l'ablation d'une paroi solide en béton eutectique par un bain du corium non-eutectique et réfractaire. Une puissance volumique est dissipée dans la cavité du corium et une percolation de gaz est .

L'analyse de l'évolution de la distribution de température et du transfert de chaleur dans la cavité de corium montre que la convection naturelle monophasique est le mécanisme principal de transfert de chaleur. Deux boucles de recirculation ont été identifiées dans la cavité du corium. La composition et la température dans chaque zone sont quasi-uniformes mais différentes. Dans la zone supérieure, le fluide va vers le haut dans le centre de la cavité et vers le bas dans la couche limite. Dans la zone inférieure, le fluide va vers le bas dans le centre de la cavité et vers le haut dans la couche limite.

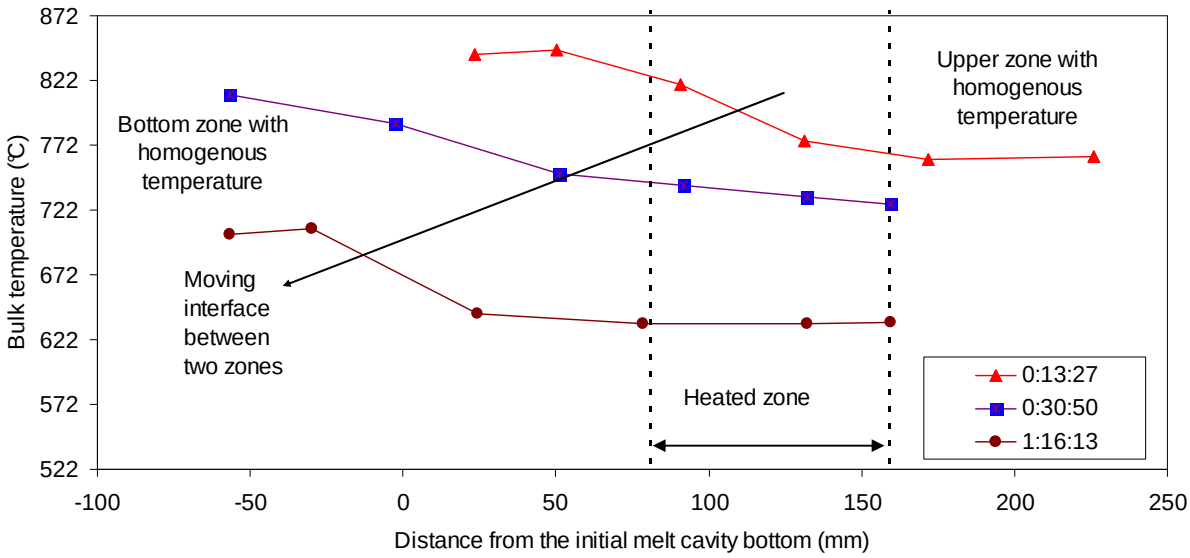

Figure 22. Deux zones avec des températures quasi-uniformes dans la cavité de corium.

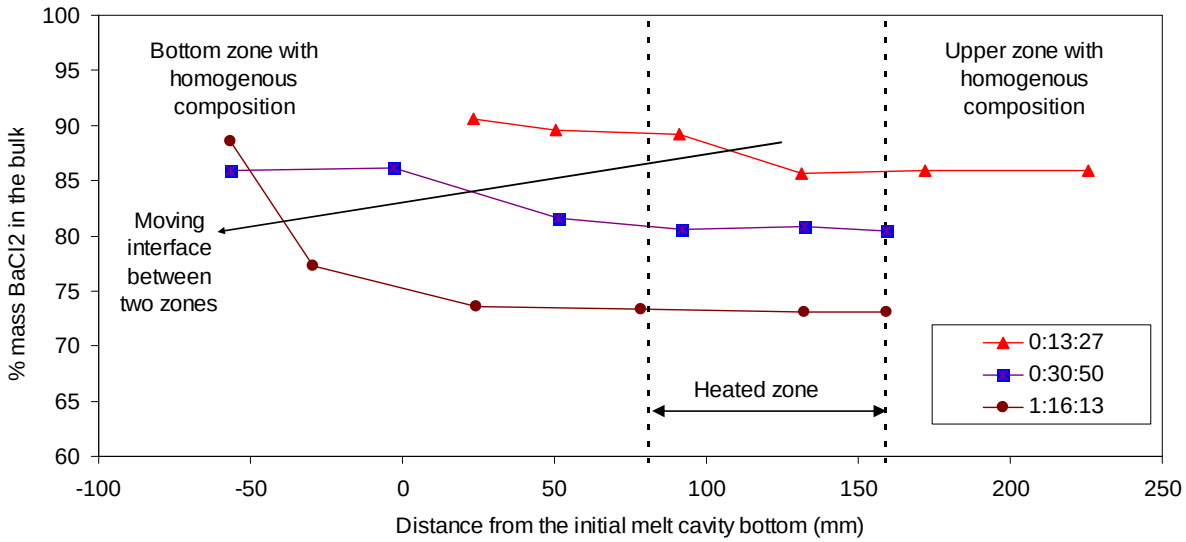

Figure 23. Deux zones avec des compositions quasi-uniformes dans la cavité de corium.

Un critère pour une densité limite du bain (ρ_{limit}) a été développé afin de déterminer la position de l'interface entre la zone supérieure et la zone inférieure.

$$\rho_{\text{limit}} = \rho_{MC}(T_{melt}) \left[1 + \frac{\beta_T \; L'_{melting}}{C^{bulk}_{p,liquid}} \right] \tag{17}$$

puis:

- $\rho_{bulk}(T_{bulk}) \geq \rho_{limit}$: écoulement vers le haut dans la couche limite
- $\rho_{bulk}(T_{bulk}) \leq \rho_{limit}$: écoulement vers le bas dans la couche limite

où:

- $\rho_{bulk}(T_{bulk})$ est la densité du corium à la température T_{bulk} et à la concentration du soluté w_{bulk}
- $\rho_{MC}(T_{corium})$ est la densité du béton fondu à la température de fusion du béton (T_{corium}) et à la concentration du soluté du béton fondu w_{MC}.

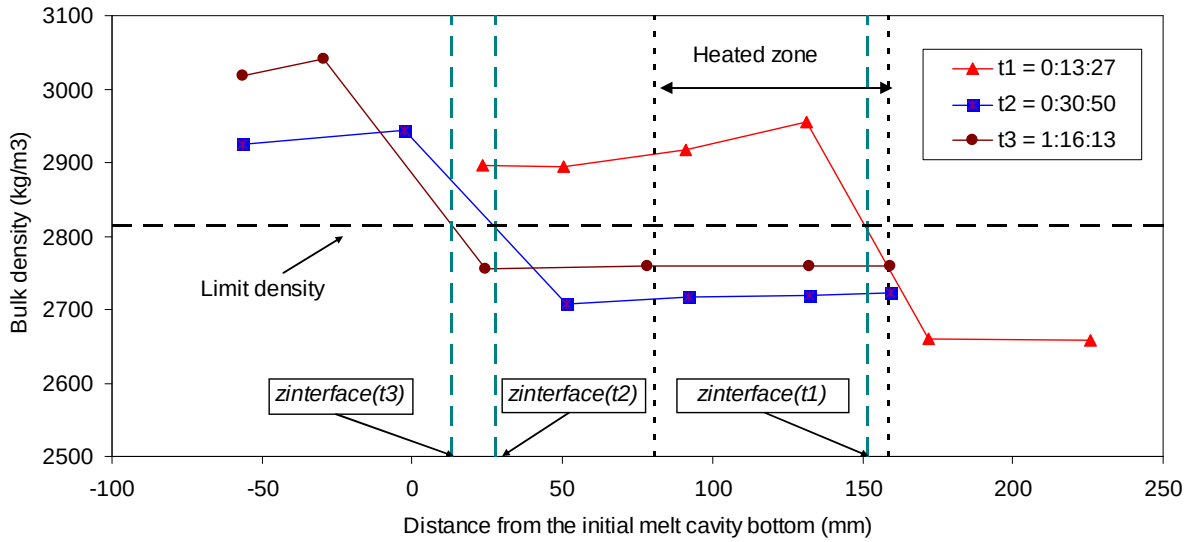

Figure 24. Densités dans les deux zones.

L'application du critère pour ARTEMIS 10 montre que l'interface entre les zones supérieure et inférieure se déplace vers le bas en fonction du temps (Figure 24), ce qui conduit à augmenter la puissance dissipée dans la zone supérieure et à une diminution dans la zone inférieure. Ceci contribue à expliquer la fin de l'ablation en partie basse et de l'accélération de l'ablation dans la partie supérieure de la cavité.

Un « cake » est formé au fond de la cavité du corium lié à un dépôt du réfractaire ($BaCl_2$). Bien que le « cake» est enrichi en $BaCl_2$, il n'est pas solide, mais un milieu poreux contenant à la fois solide et liquide à l'équilibre thermodynamique local. Le transfert de chaleur dans le « cake » est gouverné par la conduction et la convection de soluté (LiCl). La convection interne explique l'épaisseur du « cake », comme pour ARTEMIS 1D [Guillaumé, 2008].

L'évolution de la température du corium est recalculée par un modèle 0D comme avoir faite pour LIVE L3A et ARTEMIS 11. La configuration du modèle est donnée par Figure 25.

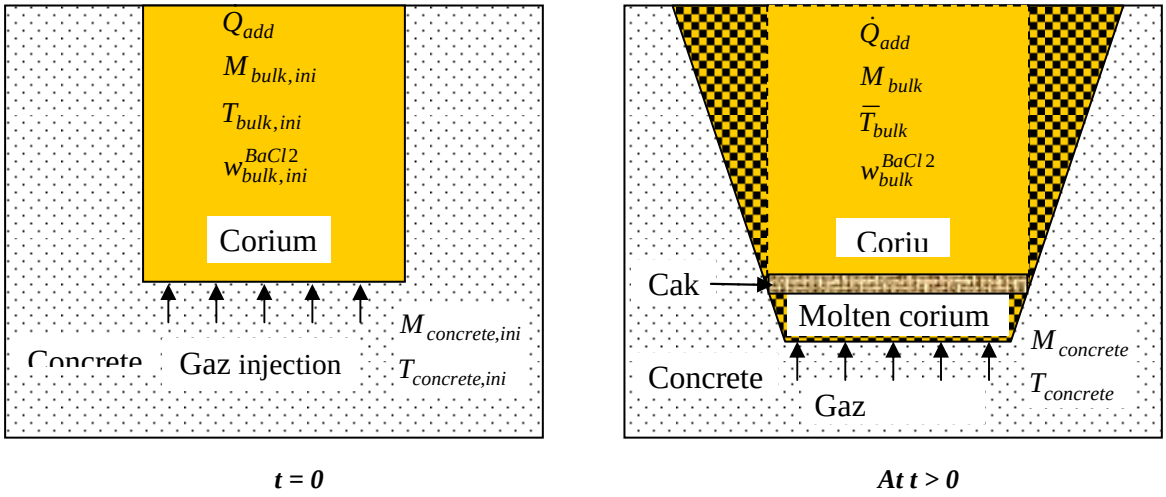

Figure 25. Configuration du modèle 0D d'ARTEMIS 10.

Les hypothèses suivantes sont utilisées pour l'approche du modèle simplifié:

- Le volume de contrôle est le volume du corium dans la cavité;
- Le béton solide est ablaté tout le long de la surface de la cavité;
- La variation du rayon de la cavité sera calculée avec l'hypothèse de géométrie hémisphérique ou de la géométrie cylindrique. La hauteur du liquide dans la cavité est constante et est considérée comme étant la hauteur initiale (i.e. $H(t) = H_{ini}$ = 45 cm);
- Une composition moyenne du corium dans la cavité liquide est supposée à un instant donné *t* (représentée par le pourcentage massique de $BaCl_2$, w_{bulk}^{BaCl2});
- Comme la température du corium n'est pas uniforme dans la cavité, une différence moyenne de température (entre le corium et l'interface liquide-solide) est définie ($\Delta\overline{T}_{bulk} = \overline{T}_{bulk} - T_i$) qui est proportionnelle à la différence de température maximale entre le corium et l'interface, i.e. $\Delta\overline{T}_{bulk} = k_T T_{bulk,\max}$ ou k_T = 0,7 est indépendante du temps. k_T peut être déterminée à partir de données expérimentales de mesure de la température du corium aux niveaux différents de la cavité (comme cela a été fait pour ARTEMIS 11).
- Le transfert de chaleur dans la cavité est contrôlé par la convection naturelle et le coefficient moyen de transfert de chaleur peut être estimé en utilisant des corrélations existantes du nombre de Nusselts développées pour le régime permanent.

Le calcul est effectué tout d'abord avec l'hypothèse de température liquidus correspondant à la composition moyenne du corium comme la température à l'interface liquide-solide. A long terme, cette hypothèse montre une bonne reproduction de l'évolution de la température moyenne du corium en comparaison avec les donnés expérimentales d'ARTEMIS 10. A court terme (t < 1000 s), la température liquidus surestimé la température d'interface et la température du corium. Le meilleur accord a été trouvé pour une évolution de la température d'interface en fonction de la température liquidus avec d'une correction liée au flux de chaleur:

$$T_i = T_{liquidus}(w_{bulk}^{LiCl}) - \frac{\overline{\varphi}\, D_{LiCl}}{k_M\, \lambda_{bulk}} \qquad (18)$$

Entre les quatre corrélations du nombre de Nusselt, on voit que la corrélation d'ACOPO donne le meilleur accord avec les données expérimentales d'ARTEMIS en termes d'évolution de la température moyenne du corium (Figure 26) ainsi que pour l'évolution de la masse ablatée du béton (Figure 27) et la variation de la concentration de $BaCl_2$ du corium (Figure 28).

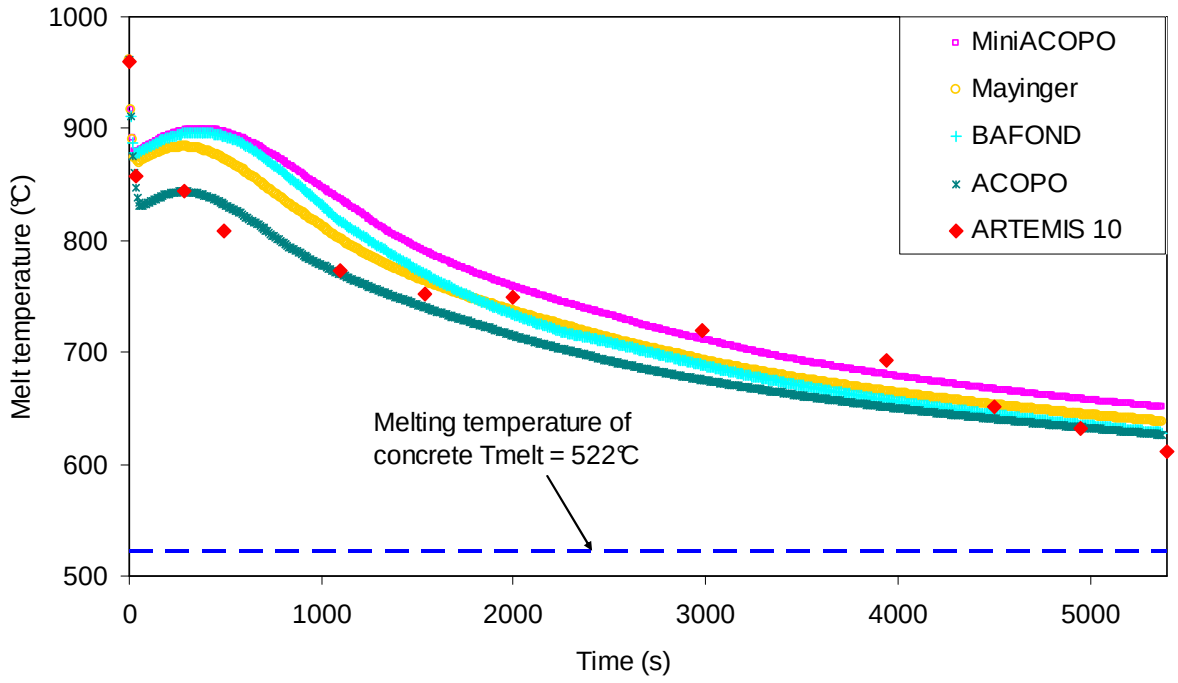

Figure 26. Evolution de la température moyenne du corium obtenue avec des corrélations différentes du nombre de Nusselt.

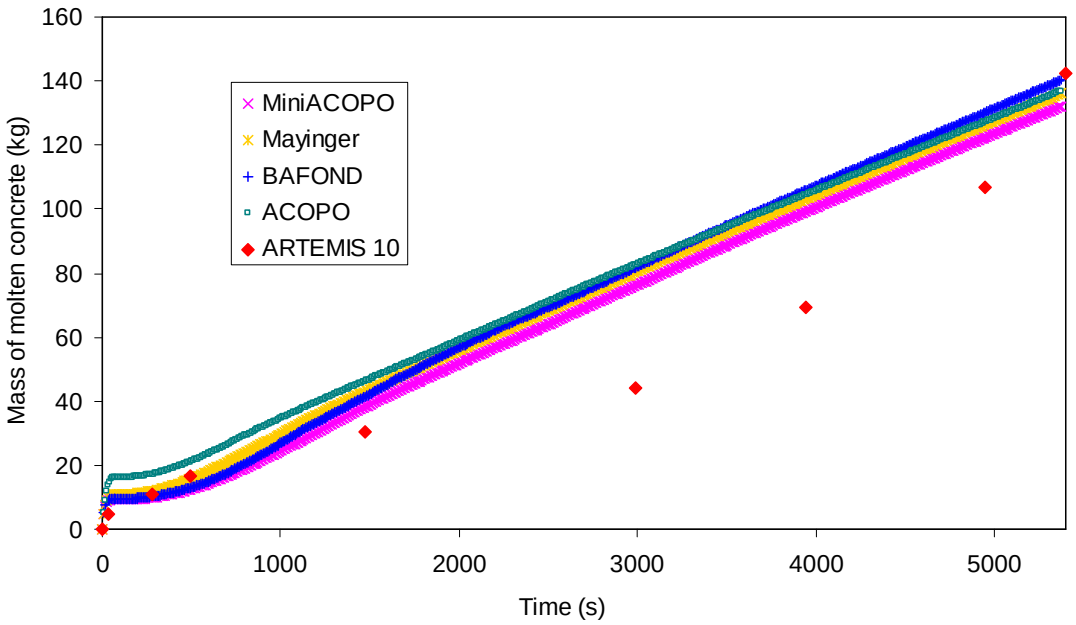

Figure 27. Evolution de la masse ablatée du béton calculée avec des différentes corrélations de Nusselt.

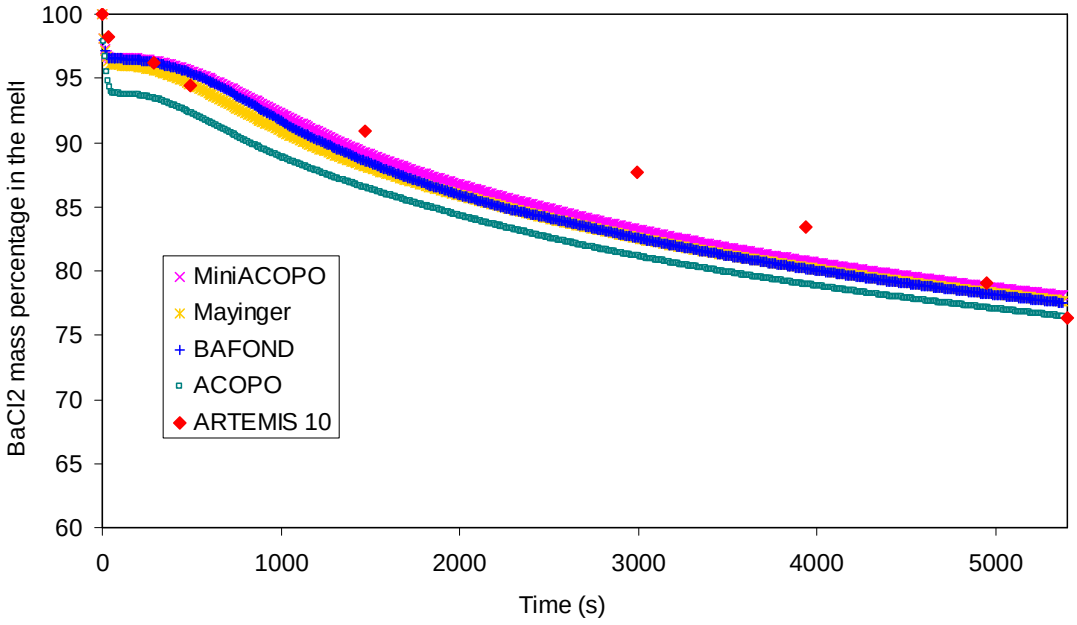

Figure 28. Evolution du pourcentage massique de $BaCl_2$ dans la cavité du corium.

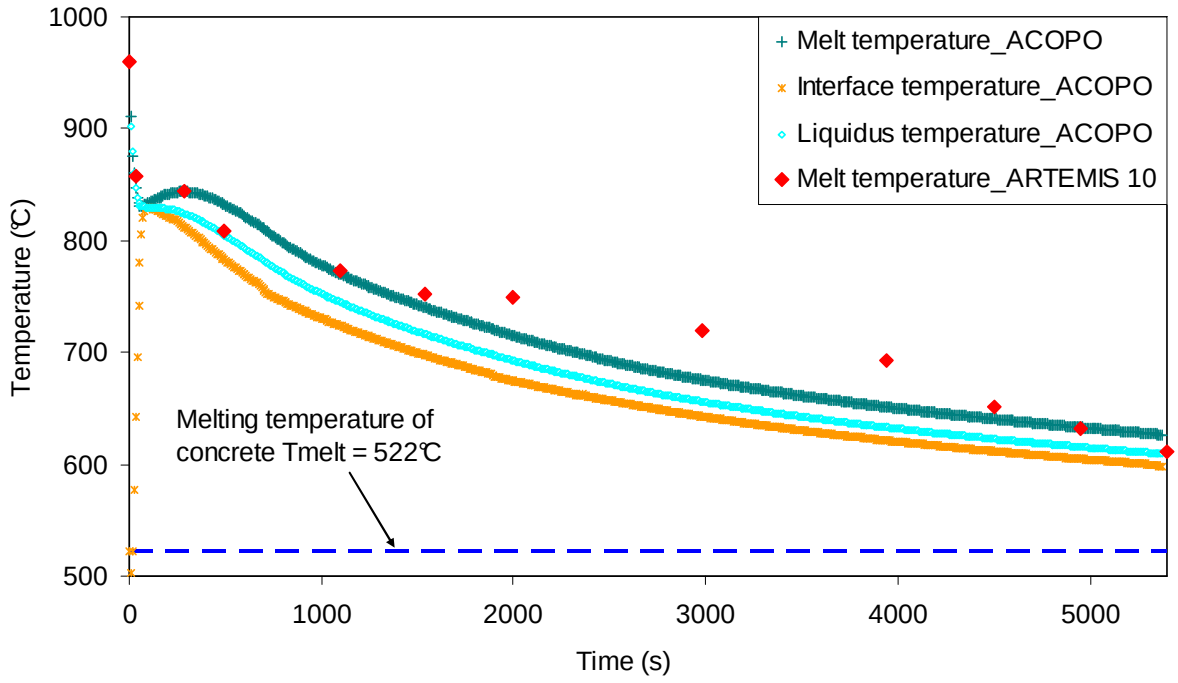

Figure 29. Evolutions des température d'ARTEMIS 10 avec correlation de Nusselt par ACOPO.

La température d'interface est sensiblement inférieure à la température liquidus par un flux de chaleur élevé, expliquant une diminution rapide de la température du corium au début d'essai (Figure 29). Après environ 1000 s, le flux de chaleur diminue et la température à l'interface liquide-solide peut être prise égale à la température liquidus correspondant à la composition moyenne du corium.

L'application du modèle 1D déjà utilisé pour l'interprétation des tests LIVE L3A et ARTEMIS 11 a aussi été faite pour ARTEMIS 10. Les lois constitutives appliquées pour l'interprétation de LIVE L3A et d'ARTEMIS 11 ont été considérés pour le coefficient de frottement, le coefficient de transfert de chaleur et la vitesse d'entraînement radial du liquide vers la couche limite dans ARTEMIS 10.

- Le coefficient de frottement

$$F = \frac{96}{\mathrm{Re}} \tag{19}$$

- Le coefficient de transfert de chaleur

$$Nu_{bulk} = 4\frac{\delta}{\delta_T} = 4\,\mathrm{Pr}^{1/3} \approx 6.4 \tag{20}$$

- La vitesse d'entraînement radiale du liquide du bulk vers la couche limite pour Pr = 4 dans ARTEMIS 10

$$j_{bulk} = 0.33\left[g\,\beta_T\,(T_{bulk} - T_{BL})\,\upsilon\right]^{1/3} \quad (21)$$

L'évolution de la température moyenne du corium est indiquée dans Figure 30. Par rapport à la température moyenne du corium obtenue dans ARTEMIS 10, pour t < 2000 s, une différence significative est observée entre le calcul et l'expérience. Cela est dû à l'hypothèse de la température liquidus à l'interface liquide-solide qui a prise dans le calcul.

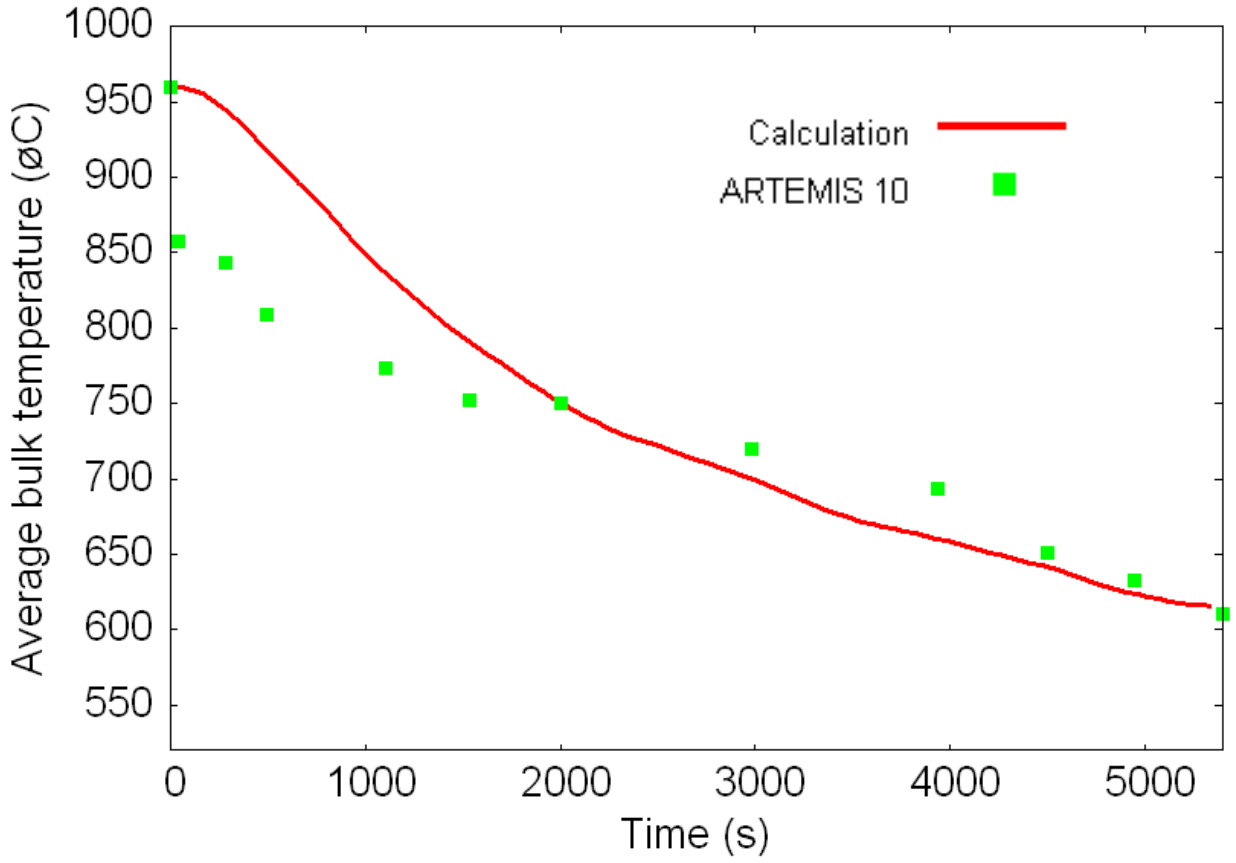

Figure 30. Evolution de la température moyenne du corium calculée par le modèle 1D.

Figure 31 représente la forme de la cavité du corium à t = 5400 s (à la fin d'ARTEMIS 10). En raison de 46% de la porosité du béton, la hauteur du corium dans la cavité est réduite à environ 30 cm (la hauteur initiale est 45 cm). Un assez bon accord est obtenu entre le profil d'ablation expérimentale et le calcul (dans le modèle 1D, la hauteur du corium liquide est calculée).

Les résultats de calculs du modèle montrent sa capacité à bien reproduire le profil d'ablation de la zone supérieure. À partir de ces calculs, il est conclu que l'ablation rapide en haut de la la cavité est liée à la

distribution du flux de chaleur associée à l'écoulement de couche limite laminaire, comme dans ARTEMIS 11.

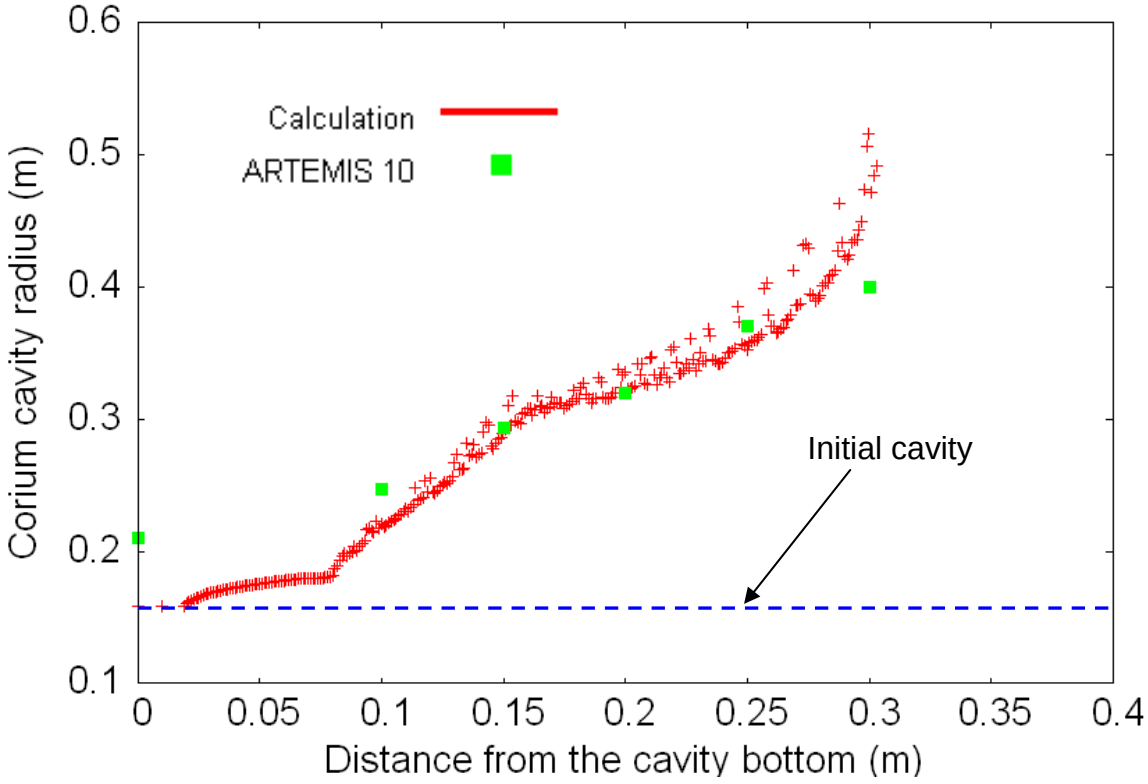

Figure 31. Forme de la cavité du corium à la fin d'ARTEMIS 10.

4. Conclusions

Conclusion concernant l'ablation

En termes de masse ablatée du béton, les paramètres de contrôle sont :

- La puissance dissipée dans la cavité du corium;
- L'inertie thermique du corium.

L'effet de l'inertie thermique du corium est liée à la diminution de la température du corium. La vitesse de diminution de la température du corium est associée à l'évolution de la température de l'interface et au transfert de chaleur dans la cavité.

Pour les matériaux avec la température de fusion unique, la température d'interface est fixée Pour les mélanges non-eutectiques, l'évolution de la température d'interface est plus difficile à prévoir, mais pour ARTEMIS 10, l'hypothèse que la température de l'interface suit la température liquidus donne de bons résultats en termes d'évolution de la masse ablatée de béton. À long terme, alors que la masse de béton ablatée devient grande, la température du corium tend vers la température de fusion du béton et la vitesse d'ablation du béton est ensuite entièrement contrôlée par la puissance dissipée.

Conclusions concernant le transfert de chaleur

En termes de transfert de chaleur du corium à l'interface liquide-solide, il a été conclu que le transfert de chaleur en régime permanent peut être une bonne approximation pour le transfert de chaleur transitoire. Les corrélations existantes du transfert de chaleur par convection naturelle ou par convection diphasique introduites pour le régime permanent peuvent être utilisées pour le calcul de la distribution du flux de chaleur et de l'évolution de la température du corium en régime transitoire. Ceci peut être expliqué par le fait que, dans les cas analysés dans ce travail, le temps de caractéristique requis pour établir la convection naturelle est plus courte que le temps caractéristique associé à l'échauffement du liquide (qui est lié à l'inertie thermique du liquide et à la puissance dissipée).

L'ablation de matière prédominante latérale observée dans ARTEMIS est liée à deux effets:

- Le fait que la convection naturelle domine dans la cavité (pas ou très peu de pénétration du gaz dans la cavité);
- Le fait que les effets de flottabilité sont plus importants que les effets de soluté (composition non uniforme) en raison de la faible vitesse d'ablation du béton par rapport à la vitesse d'entraînement radiale du liquide vers la couche limite et en raison d'une densité différence limitée entre le corium et le béton.

Cette analyse suggère que l'ablation préférentielle radiale observée dans les tests avec béton siliceux à petite échelle peut être due à un écoulement de convection naturelle dans la cavité qui signifie que le gaz ne peut probablement pas passer l'interface solide du corium. Cela peut expliquer les observations

de post-test que le corium fondu semble être très dense avec du béton siliceux (alors qu'il est très poreux avec du béton calcaire).

Conclusions concernant la température d'interface

Pour LIVE L3A, impliquant la formation de croûte solide sur une paroi du bain liquide chauffé en volume sans injection de gaz, il semble que la température à l'interface liquide-solide reste proche de la température liquidus pendant la formation de la croûte transitoire.

Pour ARTEMIS 11 (matériaux à composition eutectique uniforme, interface mobile), la température d'interface est égale à (ou proche de) la température de fusion du béton.

Pour ARTEMIS 10 (composition non-uniforme, avec une percolation de gaz, interface mobile), la situation est beaucoup plus complexe. La composition du corium n'est pas uniforme (une stratification de composition du corium dans la direction verticale et une variation de composition dans la couche limite). L'hypothèse que la température d'interface est égale à la température liquidus correspondant à la composition moyenne du corium conduit à une estimation de la température du corium raisonnable pour le long terme. Mais cette hypothèse conduit à une surestimation de la température du corium à court terme (< 1 heure). L'analyse 0D suggère que pour une courte durée, la température d'interface est inférieure à la température liquidus et que la différence de température avec le liquidus dépend du flux de chaleur. Une relation a été proposé pour une estimation approximative de la différence entre ces températures. Le calcul 1D montre que l'hypothèse de la température liquidus correspondant à la composition moyenne de la couche limite comme la température locale de l'interface ne suffit pas à expliquer l'écart à court terme.

Conclusion concernant la capacité de prévision du modèle 0D

On voit que le modèle 0D a une bonne capacité de prédire l'ablation du béton, la variation de composition du corium et l'évolution de la température moyenne du corium. Ceci peut être expliqué par les faits suivants:

- L'ablation de béton est entièrement contrôlée par la dissipation de puissance et l'inertie thermique du corium;

- La température d'interface est principalement liée aux propriétés de la matière, elles-mêmes liées à la composition du corium qui est régie par l’ablation du béton.

Ainsi, la prédiction de l'évolution de la masse ablatée du béton, la température moyenne du corium et la composition moyenne du corium peut être obtenue avec un modèle simple 0D. Toutefois, pour la prédiction de la vitesse locale d'ablation et d'évolution de la forme de la cavité du corium, au moins un modèle 1D est nécessaire.

5. Perspectives

Lorsque deux boucles de recirculation existent dans la cavité liquide comme observé dans ARTEMIS 10, en raison de la distribution non-uniforme de composition, la situation se complique et le modèle 1D introduit n'est pas suffisant. Tandis que l'ablation radiale du béton est très bien décrite par le modèle développé, l'ablation axiale au fond de la cavité du corium solide n'est pas encore décrite. En outre, la formation du « cake » en raison du dépôt d'espèces réfractaires observée expérimentalement dans ARTEMIS 10 n'est pas prise en compte dans ce modèle. Ce point devrait être inclus dans le futur modèle.

Il est à noter que, dans ARTEMIS 10 et ARTEMIS 11, le gaz ne traverse pratiquement pas n’existe que dans la cavité du corium (ou n'existent que dans une courte période au début de l'ARTEMIS 11). Par conséquent, l'effet du gaz sur le transfert de chaleur dans la cavité du corium et sur les conditions d'interface liquide-solide n'est pas étudié dans le cadre de la thèse. Les données expérimentales provenant d'un autre test dans lequel les effets du gaz sont plus clairs seraient à analyser via une étude complémentaire.